# Coherent Dynamical Control of Transport and Information in Composite Two-Level Quantum Systems

Dissertation
zur Erlangung des Doktorgrades
an der Fakultät für Mathematik, Informatik und Naturwissenschaften
Fachbereich Physik
der Universität Hamburg

vorgelegt von

## Lukas Broers

Hamburg

Dezember 2023

# Preface

The work in this cumulative dissertation has been conducted from March 2019 to December 2023 in the research group of Ludwig Mathey at the Center for Optical Quantum Technologies and the Institute of Quantum Physics of the University of Hamburg (Universität Hamburg). This work was funded by the Deutsche Forschungsgemeinschaft (DFG, German Research Foundation) – SFB-925 – project 170620586. This work was supervised by Prof. Dr. Ludwig Mathey and co-supervised by Prof. Dr. Henning Moritz. Throughout this work I use *I* when referring to results from works that I have first-authored, and *we* when referring to results from works that I have co-authored.

# Contents

6

# Abstract

A thorough understanding of non-equilibrium quantum mechanical phenomena provides the means to develop advanced and novel technologies. With growing expertise and improving controllability of quantum systems, a plethora of use-cases has emerged that employ and exploit physical processes for technological benefit. In this cumulative dissertation, I present my work on some of such research directions, such as controlling the non-equilibrium transport properties of graphene, engineering a non-equilibrium superradiant phase in driven two-band solids coupled to cavities, non-local quantum algorithm optimization on the native Hamiltonian level, and dynamics of superfluids in the presence of particle-hole symmetry.

We have devised a master equation approach for the driven dissipative electron dynamics in graphene, which recovers experimental non-equilibrium transport measurements. We have used this model to characterize the anomalous Hall response, in which the geometric contribution to the transversal current is determined by the non-equilibrium electron distribution across the light-induced topological Floquet-Bloch band structure. The light-induced gap at the Dirac point is often obscured in time-resolved angle-resolved photoelectron spectroscopy (trARPES) due to experimental limitations. I have predicted that strong driving leads to Floquet-Bloch band populations at the Dirac point which display an energy difference that extends far enough beyond Floquet replicas to overcome resolution limitations in trARPES setups. Similarly, I have studied the optical conductivity of driven graphene at terahertz frequencies, which displays the Floquet gap at the Dirac point in particular, due to resonant inter-band transitions across the Floquet-Bloch bands. In the presence of strong driving, the optical conductivity changes its sign and the system displays optical gain due to an effective population inversion of the Floquet-Bloch bands. This has motivated me to study a graphene-inspired quantum optical model, in which I have found that a non-equilibrium superradiant phase emerges due to the same mechanism of population inverted Floquet states which sustain a coherent state in a resonant cavity. I refer to this as the Floquet-assisted superradiant phase (FSP), and have studied its stability in the presence of environmental factors, such as inhomogeneous broadening, driving with finite decoherence, and dissipation. The FSP appears robust under realistic conditions, which suggests its utilization in a type of Floquet-assisted laser-like mechanism at terahertz frequencies in a graphene-cavity setup in future research.

Quantum computing faces the challenge of meticulously controlling quantum information across scalable systems. The more pragmatic near-term utilization of noisy intermediate-scale quantum (NISQ) devices draws attention to the potential of hybrid quantum-classical optimization algorithms. I have identified benefits of non-local quantum algorithm optimization approaches which act on the underlying Hamiltonian level

rather than in the circuit picture of variational quantum algorithms (VQAs). I have found that a parameterization that optimizes the Fourier coefficients of the control parameters of the Hamiltonian displays improved optimization behavior and indicates a mitigation of the barren plateau phenomenon which plagues conventional VQAs. Similarly, we have optimized high fidelity implementations of the controlled NOT gate in the quantum computing architecture of neutral atoms in tweezer arrays under realistic conditions. We have considered non-local restrictions on the control parameters, which do not affect the computational universality of the architecture. This motivates future proposals that involve less intricate and more easily constructed NISQ computers.

Superfluid states of matter such as Bose-Einstein condensates (BECs) and BCS-like condensates of neutral fermions display dynamics that are relevant for quantum simulation, superconducting devices such as Josephson junctions, and atomtronics. The order parameter of such superfluid phases is captured in effective field theories. We have developed a two-dimensional numerical simulation of an effective field theory which includes terms that interpolate between the presence and absence of particle-hole symmetry. The presence of this symmetry is accompanied by an amplitude mode that is present in BCS-like systems, but not in BECs. This theory thus captures both BEC-like and BCS-like superfluids in a manner that connects them continuously. We have demonstrated how the dynamics of defects such as vortices and solitons are affected considerably by the presence of particle-hole symmetry and the imbalance between particles and holes.

# Zusammenfassung

Ein tiefgreifendes Verständnis quantenmechanischer nicht-gleichgewichts Phänomene ist maßgebend für die Entwicklung fortgeschrittener und neuartiger Technologien. Mit wachsender Expertise und sich stets bessernder Kontrollierbarkeit von Quantensystemen, ergibt sich eine Vielzahl an Möglichkeiten physikalische Prozesse für technologischen Mehrwert zu nutzen. In dieser kumulativen Dissertation präsentiere ich meine Arbeit in hierzu verwandten Forschungsfeldern, wie die Kontrolle von nicht-gleichgewichts Transporteigenschaften in Graphen, das Konstruieren einer nicht-gleichgewichts superradianten Phase in getriebenen Zwei-Band Festkörpern in Resonatoren, nicht-lokale Quantenalgorithmusoptimierung auf der nativen Hamiltonian Ebene, und die Dynamik von Suprafluiden im Zusammenhang mit Teilchen-Loch Symmetrie.

Wir haben eine Master-Gleichung-Methode für die Beschreibung getriebener dissipativer Elektrondynamik in Graphen entwickelt, welche experimentelle nicht-gleichgewichts Transportmessungen reproduziert. Wir haben diese Methode genutzt um die anomale Hall-Leitfähigkeit zu charakterisieren, in welcher der geometrische Beitrag zum transversalen Strom durch die nicht-gleichgewichts Elektronverteilung in der lichtinduzierten topologischen Floquet-Bloch Bandstruktur gegeben ist. Die Floquet Bandlücke am Dirac-Punkt ist in zeit- und winkelaufgelöster Photoelektronspektroskopie (trARPES) erschwert aufgrund experimenteller Limitierungen. Ich habe gezeigt, dass starkes Treiben zu Besetzungen der Floquet-Bloch Bänder am Dirac-Punkt führt, die einen Energieabstand aufweisen welcher sich weit genug über die Floquet-Bloch Bandrepliken erstreckt um Auflösungslimitierungen in trARPES Experimenten zu überwinden. Ich habe ebenfalls die optische longitudinale Leitfähigkeit von Graphen untersucht, welches bei Frequenzen im Terahertz-Bereich getrieben wird und aufgrund resonanter Übergänge die Floquet-Bloch Bandlücken sichtbar macht. Unter starkem Treiben, ändert die optische Leitfähigkeit ihr Vorzeichen und das System weist optische Verstärkung aufgrund einer effektiven Populationsinversion in den Floquet-Bloch Bändern auf. Dieses Ergebnis hat mich motiviert ein von Graphen inspiriertes quantenoptisches Model zu untersuchen, in dem ich herausfand, dass sich eine nicht-gleichgewichts superradiante Phase aus dem selben Mechanismus populationsinvertierter Floquet Zustände ergibt, welche einen kohärenten Zustand in einem resonanten Hohlraumstrahler aufrecht erhalten. Ich bezeichne dies als die Floquet-assistierte superradiante Phase (FSP) und habe ihre Stabilität in der Gegenwart limitierender Außenwirkung in Form von inhomogener Verbreiterung, endlicher Dekohärenz im treibenden Feld, und erhöhter Dissipation untersucht. Die FSP stellt sich unter realistischen Konditionen als robust dar, was vermuten lässt, dass sie in weiterführender Forschung angewandt werden kann in einem Floquet-assistierten Laser-ähnlichen Mechanismus im Terahertz-Frequenzbereich in einer Graphen-Hohlraumstrahler-Konstruktion.

Quantencomputer stehen vor der Herausforderung Quanteninformation auf präzise Weise in skalierbaren Systemen zu kontrollieren. Die pragmatischere Nutzung existierender limitierter Quantensysteme (NISQ) zieht Aufmerksamkeit auf das Potential hybrider quanten-klassischer Optimierungsalgorithmen. Ich habe Vorteile identifiziert, nicht-lokale Quantenalgorithmusoptimierung welche auf der nativen Hamiltonian-Ebene agiert anzuwenden, anstatt der Schaltkreis-Variante variationeller Quantenalgorithmen (VQAs). Ich habe herausgefunden, dass eine Parameterisierung in der die Fourier-Koeffizienten von Parametern eines Hamiltonians optimiert werden ein verbessertes Optimierungsverhalten, so wie eine Reduktion des *barren plateau* Phänomen, welches ein Problem für konventionelle VQAs darstellt, aufweist. Auf ähnliche Weise haben wir Implementierungen des CNOT Quantengatter optimiert für die Quantencomputerarchitektur neutraler Atome in optischen Pinzetten unter realistischen Bedingungen. Wir haben nicht-lokale Restriktionen auf die Kontrolparameter angewandt, welche die Universalität der Rechnerarchitektur nicht beeinflussen, aber zukünftige Ansätze motivieren für weniger aufwändige und einfacher zu konstruierende NISQ Computer.

Suprafluide Aggregatszustände, wie Bose-Einstein Kondensate (BECs) und BCS-artige Kondensate neutraler Fermionen, weisen Dynamiken auf welche relevant sind für Quantensimulatoren, supraleitende Josephson junctions, und Atomtronik. Der Ordnungsparameter solcher Suprafluide kann mit Hilfe effektiver Feldtheorien beschrieben werden. Wir haben eine zweidimensionale Simulation einer effektiven Feldtheorie entwickelt, welche Terme beinhält die das Interpolieren zwischen der Anwesenheit und Abwesenheit von Teilchen-Loch Symmetrie erlauben. Die Anwesendheit dieser Symmetrie bedeutet das Vorhandensein einer Amplitudenmode, welche in BCS-artigen Systemen existiert, in BECs jedoch nicht. Diese Theorie beschreibt demnach sowohl BEC-artige als auch BCS-artige Suprafluide auf eine Weise die es erlaubt diese Limites kontinuierlich zu verknüpfen. Wir haben demonstriert, dass die Dynamik von Defekten wie Vortizes und Solitonen maßgeblich durch Teilchen-Loch Symmetrie und das Verhältnis aus Teilchen und Löchern beeinflusst wird.

# List of Publications

This cumulative dissertation is based on the publications listed below. Publications I — IV discuss the electronic transport properties of driven dissipative monolayer graphene. Publications V and VI discuss the emergence and robustness of the non-equilibrium Floquet-assisted superradiant phase in a driven dissipative Dicke-type model, inspired by solid-state physics. Publications VII and VIII discuss the non-local optimization of quantum algorithms on the native Hamiltonian level. Publication IX discusses the role of particle-hole symmetry in the dynamics of defects in superfluids.

- **Publication I**: M. Nuske, <u>L. Broers</u>, B. Schulte, G. Jotzu, S. A. Sato, A. Cavalleri, A. Rubio, J. W. McIver, and L. Mathey, *Floquet dynamics in light-driven solids*, Phys. Rev. Research 2, 043408 (2020)

- **Publication II**: <u>L. Broers</u> and L. Mathey, *Observing light-induced Floquet band gaps in the longitudinal conductivity of graphene*, Commun Phys 4, 248 (2021)

- **Publication III**: <u>L. Broers</u> and L. Mathey, *Detecting light-induced Floquet band gaps of graphene via trARPES*, Phys. Rev. Research 4, 013057 (2022)

- **Publication IV**: <u>L. Broers</u> and L. Mathey, *Non-linear photoconductivity of strongly driven graphene*, arXiv: 2312.13217 (Under review at SciPost Phys.) (2023)

- **Publication V**: <u>L. Broers</u> and L. Mathey, *Floquet engineering of non-equilibrium superradiance*, SciPost Phys. 14(2), 018 (2023)

- **Publication VI**: <u>L. Broers</u> and L. Mathey, *Robustness of the Floquet-assisted superradiant phase and possible laser operation*, arXiv:2211.01320 (Under review at Phys. Rev. A) (2022)

- **Publication VII**: <u>L. Broers</u> and L. Mathey, *Mitigated barren plateaus in the time-nonlocal optimization of analog quantum-algorithm protocols*, arXiv: 2111.08085 (Accepted in Phys. Rev. Research) (2021)

- **Publication VIII**: N. Heimann, <u>L. Broers</u>, N. Pintul, T. Petersen, K. Sponselee, A. Ilin, C. Becker, and L. Mathey, *Quantum Gate Optimization for Rydberg Architectures in the Weak-Coupling Limit*, arXiv: 2306.08691 (Under review at Phys. Rev. Research) (2023)

- **Publication IX**: J. Skulte, <u>L. Broers</u>, J. G. Cosme and L. Mathey, *Vortex and soliton dynamics in particle-hole symmetric superfluids*, Phys. Rev. Research 3, 043109 (2021)

# 1 Introduction

In the past decades, the fundamental understanding of, and the capability to control, quantum matter has been steadily advancing. This has enabled research on fundamental equilibrium phenomena in quantum mechanics. For example, it has become possible to control systems such as trapped clouds of ultra-cold atoms to a degree that has enabled the realization of the superfluid phase of matter of Bose-Einstein condensates [1, 2]. The fabrication of increasingly pristine two-dimensional quantum materials such as graphene, provides platforms for studying previously inaccessible electron dynamics [3–5]. Further, the utilization of high-finesse optical cavities has played a crucial role in understanding the interplay between light and matter, and has been essential to the field of quantum optics [6–8].

A central aspect of these advances was a deep understanding of the equilibrium and low-energy physics that characterize these systems. With the capability of controlling isolated quantum systems comes the hope of bringing these systems out of equilibrium in an equally well controlled fashion. The corresponding prospect of controlling emergent dynamics of quantum systems promises to provide deep fundamental insight into more intricate non-equilibrium quantum phenomena, and possibly also new functionalities with potential technological benefit. These intricacies may for instance take the form of a non-trivial interplay between coherent optical driving and dissipation which leads to tailoring quantum material properties [9, 10], or dynamical high-fidelity manipulation of quantum information in arrays of individually and optically trapped atoms [11, 12]. Understanding and engineering these types of non-equilibrium phenomena is at the heart of quantum technologies.

In this cumulative dissertation, I present my work which contributes to a range of these topics. I focus on the theoretical understanding of non-equilibrium quantum dynamics and the means to control emergent properties. This includes the driven dissipative electron dynamics in graphene irradiated at terahertz frequencies, which display intriguing transport properties such as an anomalous Hall effect, and optical gain. I have connected these results to solid-state-inspired quantum optics and the emergence of non-equilibrium superradiance. In the context of quantum information processing, I have studied quantum computational optimization methods that are constructed to operate non-locally and in bases beyond the quantum circuit paradigm. I have also studied the effects of particle-hole symmetry on the dynamics of superfluids. These topics largely find common ground in that they describe the coherent control of transport and information in systems that are described as ensembles of two-level quantum systems. I have separated these topics into different chapters that each introduce the necessary theoretical background, and motivate and contextualize my publications. My publications are included in these chapters and are each prefaced by a motivation, a summary of the work, and a

statement about my contribution.

Chapter 2 covers my work on the driven dissipative electron dynamics of graphene irradiated at terahertz frequencies. In that chapter, I provide an introduction into the topic of graphene and its transport properties, the description and effects of driving graphene with light, and how we capture dissipation in our master equation approach in order to capture solid-state phenomena. I have studied these setups numerically with a versatile code-base that has expanded throughout the years. In Publication I, this method was conceived, and we have studied an anomalous Hall effect under consideration of non-equilibrium electron distributions, in light of recent experimental results. I have implemented and maintained the calculations for the frequency- and momentum-resolved electron distribution in driven graphene, which reveals the non-equilibrium Floquet-Bloch band populations. In Publication II, I have expanded the numerical simulation of this setup in order to study the longitudinal optical response at terahertz frequencies. This was motivated by the prospects of observing the light-induced Floquet band gaps with respect to the driving intensity. I have found that the optical conductivity does display features that are resonant with the expected Floquet band gaps. This method reveals the gap at the Dirac point that displays a non-trivial band curvature and is associated with an anomalous Hall effect. Additionally, the results show that this system displays negative optical conductivity, i.e. optical gain at terahertz frequencies, which is the consequence of effective population inversions at Floquet band gaps in the presence of strong driving fields. In Publication III, I have studied the frequency- and momentum-resolved electron distribution of driven graphene under realistic conditions with the prospect of guiding time-resolved angle-resolved photoelectron spectroscopy (trARPES) experiments. According to my simulations, the population of the Floquet bands at the Dirac point remains primarily contained within the Floquet replicas that are continuously connected to the Dirac point as a function of driving intensity. As a consequence, this provides driving setups in which the energy difference of Floquet states that have non-zero occupation exceeds the size of the Floquet zones across which the spectrum repeats. This large separation of populated Floquet states at the Dirac point has promise of being observable under realistic experimental limitations. In Publication IV, I have studied the non-linear electron transport in graphene under strong driving and simultaneous strong direct bias. The presence of strong fields leads to a rich structure in the differential photoconductivity, as a result of the distinct dynamics that are captured by either the Floquet picture, or a driven Landau-Zener picture, depending on which external field is stronger. I have characterized the strong anisotropy of the momentum distribution to the current in a comoving frame, and provided approximations for the non-linear and temperature-dependent conductivity of graphene.

Chapter 3 covers my work on the emergence of a non-equilibrium superradiant phase in a driven dissipative Dicke model, motivated by the optical properties of driven graphene as discussed in Publication II. I introduce the theoretical framework of superradiance and the Dicke model, and I emphasize the prospect of coupling a system such as graphene to a cavity. In Publication V, I have extended the numerical method developed throughout Publications I — IV, to include a single-mode cavity in order to study this graphene-inspired Dicke model under consideration of solid-like dissipation. In this model, I have

identified the analogous mechanism as in Publication II that displays population inversion in the Floquet states, which explicitly depends on the particular choice of how to capture dissipative processes. Tuning the cavity to be resonant with the Floquet states results in the effective population inversion being depleted in order to sustain a coherent state in the cavity in a type of non-equilibrium superradiant phase. I refer to this as the Floquet-assisted superradiant phase (FSP), and have characterized this phenomenon in Publication V. In Publication VI, I have studied the robustness of the FSP under consideration of environmental factors such as inhomogeneous broadening, phase drift of the coherent driving field, and dissipation up to realistic values. The detuning of the transitional frequencies of the two-level system due to inhomogeneous broadening, and the finite linewidth of the driving field due to phase drift, do not destroy the FSP mechanism. While the phase transition is affected, in that it requires moderately increased coupling strengths, the FSP remains robust under realistic conditions and displays drastic line-narrowing across the phase transition. Notably, the FSP remains viable at dissipation rates that are comparable to those that we had used in Publication I to recover the experimental non-equilibrium transport in graphene.

Chapter 4 covers my work on quantum computational optimization algorithms on the native Hamiltonian level. I introduce the theoretical framework of quantum computing, variational quantum algorithms, the barren plateau phenomenon, quantum optimal control, and how these topics intertwine. I connect these topics through descriptions of non-local parameterizations of protocols on the native Hamiltonian level. In Publication VII, I have studied a time-nonlocal parameterization for variational quantum optimization on the native Hamiltonian level, that optimizes the Fourier coefficients of the controllable parameters. I have compared this to a piece-wise constant parameterization which is reminiscent of parameterized quantum circuits and optimal control methods. In this direct comparison I have found that the Fourier ansatz outperforms the piece-wise constant ansatz for the tasks of ground state preparation and quantum gate compilation in terms of convergence behavior and fidelity, while maintaining comparable efficiency of the resulting implementations. Further, I have compared the uniformly sampled variances of gradients of objective functions for both ansätze and found that the piece-wise constant ansatz expectedly displays exponential decay of the gradients, which is characteristic of the barren plateau phenomenon. However, in the Fourier ansatz these variances decrease at a slower rate, which suggests the mitigation of barren plateaus. In Publication VIII, we have studied the optimization of implementing quantum gates under realistic conditions in the quantum computing platform of neutral atoms trapped in optical tweezers. We have found high fidelity implementations of the controlled NOT gate in the limit of weak interaction between excited Rydberg states, and have demonstrated the robustness of these solutions in the presence of additional fluctuations in the interatomic distances. Our analysis shows that the error induced through such fluctuations grows drastically for intermediate distances between atoms. With a focus on addressability, we have demonstrated the viability of a restricted parameterization, in which the control parameters that drive the transitions into the Rydberg states are equal for all qubits instead of individually controllable. This restriction can be maintained for large systems, as this seemingly harsh constraint does not affect the

computational universality of the setup.

Chapter 5 covers my work on the dynamics of superfluids with respect to particle-hole (PH) symmetry, captured in an effective field theory. I introduce the Lagrangian that captures the PH symmetry via two dynamical terms. I reproduce how these terms affect the equation of motion of this effective field theory, and how they interpolate between the Gross-Pitaevskii equation that is used to describe Bose-Einstein condensates, and the Lorentz-invariant non-linear Klein-Gordon equation that describes BCS-type superfluids. This theory also provides a generalization of the conserved Noether charge, the low-energy excitations, and the spectra in confining potentials. In Publication IX, we have studied this model in two dimensions to understand the effect PH symmetry has on the dynamics of superfluids. In particular, we have studied the dynamics of vortices and solitons, which show that the absence of the Magnus force plays a large role in PH symmetric superfluids. Due to the lack of a Magnus force, vortex-anti-vortex pairs attract each other in the presence of PH symmetry, instead of propelling each other. In solitons, this leads to a modification of the characteristic snaking phenomenon.

Chapter 6 presents a conclusion and summary of the results put forth in Publications I — IX. I provide an outlook on future research directions based on these results.

# 2 Control of Electron Transport in Driven Dissipative Graphene

Graphene is a material that displays many interesting electronic properties and has been the subject of active research since its initial fabrication [3]. Studies often focus on the high electronic mobility [4, 5, 13–18], that is controlled via the back-gate-dependent charge carrier density, which has led to the demonstration of graphene transistor devices [19, 20]. Other remarkable results include the demonstration of the quantum Hall effect [21–24], quantum dot spin-qubits [25], spintronics [26–28], and the potential for valleytronics [29–31]. Further, the control of optical properties of graphene has been of great interest [32–38] and more recently, the Floquet engineering of topologically non-trivial states in graphene has been actively studied [39–44].

These phenomena rely on the peculiar electronic structure of graphene, which obeys an array of symmetries and displays mathematical equivalence to the Dirac physics of relativistic massless spin-1/2 particles [45–49]. Structural variants of graphene such as nanoribbons [50–53], nanotubes [54, 55], or more recently twisted bilayer graphene [56] are also actively being studied. The conceptual elegance and rich physics have turned graphene into a staple of modern material science.

Throughout this chapter, I provide an introduction into the electron dynamics of graphene as to motivate and contextualize Publications I — IV, in which I have studied different electronic transport properties of driven graphene and how they relate to the light-induced Floquet physics. This chapter focuses on the low-energy aspects and the driven dissipative physics of graphene, and the tools that are necessary to study such models. This chapter will also delve into the description of dissipative processes and Floquet physics. Introductory literature on the topic of graphene is widely available, and this chapter in large parts follows along the more in-depth discussions provided by the book of Katsnelson [57] and various review papers [58–60].

## 2.1 Electronic Description of Graphene

Graphene is made up of a two-dimensional hexagonal, or honeycomb, lattice of carbon atoms that occupy planar hybridized $sp^2$ orbitals that leave one electron per site in a perpendicular p-orbital, which forms $\pi$-bonds with the three equally spaced in-plane neighbors. In order to describe the hexagonal lattice structure of graphene in a way that obeys translational symmetry, a triangular construction of unit cell with two atoms is
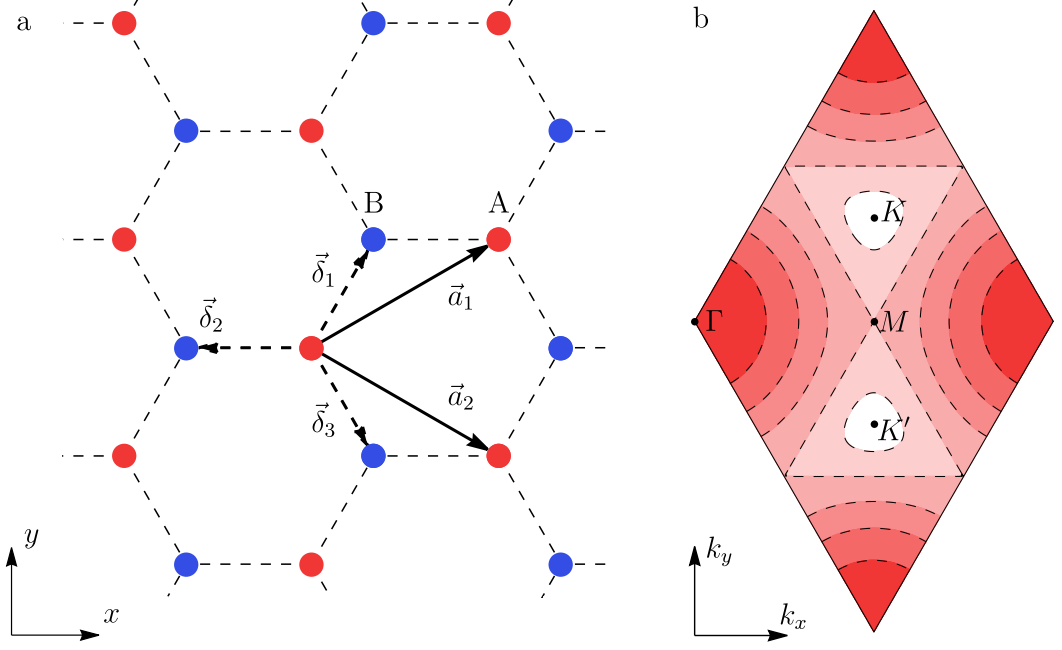
Figure 2.1: The structure of graphene. Panel (a) shows the real-space lattice structure spanned by the unit-vectors $\vec{a}_1$ and $\vec{a}_2$, and the nearest-neighbour vectors $\vec{\delta}_1$, $\vec{\delta}_2$, and $\vec{\delta}_3$. A and B denotes the sub-lattices. Panel (b) shows the Brillouin zone of graphene. $K$ and $K'$ are the exceptional points at which the valence and conduction bands touch.

necessary. In that case, the lattice is described by the unit-vectors

$$\vec{a}_1 = a\sqrt{3}\begin{pmatrix} \cos(\frac{\pi}{6}) \\ \sin(\frac{\pi}{6}) \end{pmatrix} \qquad\qquad \vec{a}_2 = a\sqrt{3}\begin{pmatrix} \cos(\frac{\pi}{6}) \\ -\sin(\frac{\pi}{6}) \end{pmatrix} \qquad (2.1)$$

with the lattice-spacing constant $a \approx 1.42\text{Å}$. The nearest-neighbor sites are separated by the vectors

$$\vec{\delta}_1 = a\begin{pmatrix} \cos(\frac{\pi}{3}) \\ \sin(\frac{\pi}{3}) \end{pmatrix} \qquad \vec{\delta}_2 = a\begin{pmatrix} -1 \\ 0 \end{pmatrix} \qquad \vec{\delta}_3 = a\begin{pmatrix} \cos(\frac{\pi}{3}) \\ -\sin(\frac{\pi}{3}) \end{pmatrix}. \qquad (2.2)$$

This structure is displayed in Fig. 2.1 (a). The low-lying electronic bands are captured well within the tight-binding approach. Due to the two-atomic unit cell, the appropriate wave function is described using two components $\psi_A$ and $\psi_B$ for the amplitudes within the respective sub-lattices, denoted as $A$ and $B$. To first order, the coupling between these components is due to nearest-neighbor, i.e. inter-sub-lattice, tunneling such that the dynamics are governed by the Hamiltonian

$$H(\vec{k}) = -t\begin{pmatrix} 0 & S^*(\vec{k}) \\ S(\vec{k}) & 0 \end{pmatrix}, \qquad (2.3)$$

where $\vec{k}$ is the two-dimensional momentum.[1] This Hamiltonian acts on the state vectors $|\psi\rangle = (\psi_A, \psi_B)^{\mathrm{T}}$. The tunneling amplitude is $t \approx 2.7\text{eV}$ and the momentum-dependent tight-binding coefficients are

$$S(\vec{k}) = \sum_{j=1}^{3} e^{i\vec{k}\vec{\delta}_j}. \tag{2.4}$$

The dispersion relation of the resulting two symmetric bands reads

$$\epsilon_\pm(\vec{k}) = \pm t |S(\vec{k})| = t|2e^{iak_x/2}\cos\left(ak_y\frac{\sqrt{3}}{2}\right) + e^{-iak_x}|. \tag{2.5}$$

Within the Brillouin zone are two exceptional points at which $|S(\vec{k})|$ vanishes and consequently the two bands touch. The Brillouin zone of graphene is illustrated in Fig. 2.1 (b). The two exceptional points are

$$\vec{K} = \frac{4\pi}{3\sqrt{3}a}\begin{pmatrix}\cos(\frac{\pi}{6})\\\sin(\frac{\pi}{6})\end{pmatrix} \qquad\qquad \vec{K}' = \frac{4\pi}{3\sqrt{3}a}\begin{pmatrix}\cos(\frac{\pi}{6})\\-\sin(\frac{\pi}{6})\end{pmatrix}. \tag{2.6}$$

Expanding the dispersion relation in the vicinity of these points provides the approximate linearized Hamiltonian that describes the low-energy physics of graphene. For momenta close to $\vec{K}$ or $\vec{K}'$ it is to first order

$$H(\vec{K}+\vec{k}) \approx \frac{3}{2}at\begin{pmatrix}0 & e^{i\frac{\pi}{6}}(k_x - ik_y)\\(k_x + ik_y)e^{-i\frac{\pi}{6}} & 0\end{pmatrix} \tag{2.7}$$

$$H(\vec{K}'+\vec{k}) \approx \frac{3}{2}at\begin{pmatrix}0 & e^{-i\frac{\pi}{6}}(k_x + ik_y)\\(k_x - ik_y)e^{i\frac{\pi}{6}} & 0\end{pmatrix}. \tag{2.8}$$

The phase factors $e^{\pm i\frac{\pi}{6}}$ are removed by a unitary transformation and the pre-factors are conventionally collected as $\hbar v_F = \frac{3}{2}at$, where $v_F \approx 10^6\text{ms}^{-1}$ is the Fermi velocity of the system. This results in the linearized Hamiltonian

$$H_{\vec{k}} = \hbar v_F\begin{pmatrix}0 & k_x - ik_y\\k_x + ik_y & 0\end{pmatrix} \tag{2.9}$$

at $\vec{K}$ and $H'_{\vec{k}} = H_{\vec{k}}^*$ at $\vec{K}'$. As the bands touch at $\vec{K}$ and $\vec{K}'$, the Fermi surface is reduced to a single point in the case of charge neutrality. Graphene is therefore classified as a gapless semimetal. The structure of this linearized Hamiltonian is paramount to the rich physics of graphene and the large interest it has gathered. This description of graphene[2] displays an inversion symmetry $H_K = \sigma_x H_{K'}\sigma_x$ and a time-reversal symmetry $H_K = H_{K'}^*$.

---

[1]Technically, $\vec{k}$ is the wave-number vector such that $\hbar\vec{k}$ is the momentum.

[2]These symmetries are also present prior to the linearization, however under exchange of $\vec{k} \leftrightarrow -\vec{k}$ instead of $K \leftrightarrow K'$.

Collecting the Pauli matrices into the vector representation $\vec{\sigma} = (\sigma_x, \sigma_y, \sigma_z)$ and replacing the momentum-operator by its real-space representation $\vec{k} = -i\vec{\nabla}$, provides the notation of

$$H = -i\hbar v_F(\partial_x \sigma_x + \tau_z \partial_y \sigma_y), \qquad (2.10)$$

where $\tau_z$ is the third Pauli matrix acting on the two-dimensional configuration space of $\vec{K}$ and $\vec{K}'$, i.e. $\tau_z = 1$ at $\vec{K}$ and $\tau_z = -1$ at $\vec{K}'$. This Hamiltonian then acts on a four-dimensional Hilbert space of states

$$|\psi\rangle = \begin{pmatrix} \psi_A \\ \psi_B \\ \psi'_A \\ \psi'_B \end{pmatrix}, \qquad (2.11)$$

where the prime indicates the associated exceptional point $K^{(\prime)}$. The Schrödinger equation takes the form

$$(v_F^{-1}\partial_t - \partial_x \sigma_x - \tau_z \partial_y \sigma_y)|\psi\rangle = 0, \qquad (2.12)$$

which is structurally reminiscent of the Dirac equation for a massless two-dimensional fermion at a fraction of the speed of light with $v_F \approx c/300$. This equivalence is the reason that the exceptional points $\vec{K}$ and $\vec{K}'$ are referred to as Dirac points. With respect to the Dirac equation, the occupation of the two Dirac points is analogous to particles and anti-particles, while the occupation of $A$ and $B$ sub-lattices is analogous to spin-up and spin-down states. This is the reason that in descriptions of graphene the state representation is referred to as a pseudo-spin. Note that the addition of a $\sigma_z$ component in the linearized graphene Hamiltonian produces a mass term that keeps the equivalence to the Dirac equation in-tact. The true electronic spin is naturally present as well, and could be considered, leading to a higher-dimensional description. However throughout this work, I consider no spin-interactions in graphene, which leaves a spin-degeneracy of $n_s = 2$.

In many applications, the dynamics at the $\vec{K}$ and $\vec{K}'$ sectors decouple and can be inferred from each other, due to the structural symmetry. Therefore, a reduced representation that covers the vicinity of $\vec{K}$ is sufficient in many cases. The Hamiltonian associated with this representation is

$$H_{\vec{k}} = \hbar v_F(k_x \sigma_x + k_y \sigma_y) = \hbar v_F k(e^{-i\phi_k}\sigma_+ + e^{i\phi_k}\sigma_-), \qquad (2.13)$$

where $k = |\vec{k}|$, $\phi_k = \arg(k_x + ik_y)$ and $\sigma_\pm = \frac{1}{2}(\sigma_x \pm i\sigma_y)$. In the polar representation of the momentum, the transformation

$$U_{\vec{k}} = \frac{1}{\sqrt{2}} \begin{pmatrix} e^{-\frac{i}{2}\phi_k} & e^{-\frac{i}{2}\phi_k} \\ e^{\frac{i}{2}\phi_k} & -e^{\frac{i}{2}\phi_k} \end{pmatrix} \qquad (2.14)$$

diagonalizes the Hamiltonian, i.e. $U_{\vec{k}}^{\dagger} H_{\vec{k}} U_{\vec{k}} = \hbar v_F |\vec{k}| \sigma_z$. The corresponding eigenstates are read off of $U_{\vec{k}}$ as

$$|+\rangle = \frac{1}{\sqrt{2}} \begin{pmatrix} e^{-\frac{i}{2}\phi_k} \\ e^{\frac{i}{2}\phi_k} \end{pmatrix} \qquad\qquad |-\rangle = \frac{1}{\sqrt{2}} \begin{pmatrix} e^{-\frac{i}{2}\phi_k} \\ -e^{\frac{i}{2}\phi_k} \end{pmatrix}. \qquad (2.15)$$

In the Bloch sphere representation, these states reside on the equator at an angle $\phi_k$ and $\phi_k + \pi$, respectively. Hence, the two eigenstates of linearized graphene have their pseudo-spin aligned parallel and antiparallel with their momentum. Note that in accordance with real spin degrees of freedom, a rotation about $2\pi$ provides a prefactor of $-1$.

## 2.2 Charge Transport and Electromagnetic Coupling

All momentum modes in graphene that are captured in this approach contribute to the overall charge transport through the material. From the continuity equation of the quantum mechanical wave-function in momentum space results the expression for the current operator, which in the case of linearized graphene evaluates to

$$\hat{j}_a = \frac{e}{\hbar} \frac{\partial H_{\vec{k}}^{(*)}}{\partial k_a} = e v_F \sigma_a^{(*)} \qquad (2.16)$$

with $a = x, y$. The complex conjugation is associated with the Dirac point $K'$. The expectation value is denoted as

$$j_a(\vec{k}) = \mathrm{Tr}(\rho_{\vec{k}} \hat{j}_a), \qquad (2.17)$$

whee $\rho_{\vec{k}}$ is the local density operator corresponding to the momentum $\vec{k}$, as explained in a later section. It is necessary to specifically distinguish between the current-density $j_a(\vec{k})$, resolved in momentum space, and the full current $J_a$ which is obtained by integrating over the Brillouin zone

$$J_a = \frac{n_s}{4\pi^2} \int_{\mathrm{BZ}} j_a(\vec{k}) dk_x dk_y. \qquad (2.18)$$

In the case of linearized graphene, the integral over the Brillouin zone is replaced by two integrals over sufficiently large areas $D_K$ and $D_{K'}$ around the Dirac points. The symmetries with respect to $K$ and $K'$ can be broken, which determines whether the contributions to the current are equal, opposite, or independent. The polarization of incoming light plays into this symmetry breaking. We have considered the effect of breaking time-reversal symmetry in Publication I in order to study an anomalous Hall effect in graphene. In the cases where the Dirac points contribute equally, the current reduces to

$$J_a = \frac{n_s n_v}{4\pi^2} \int_{D_K} j_a(\vec{k}) d^2 k, \qquad (2.19)$$

where $n_v = 2$ is the valley-degeneracy.

Graphene in its equilibrium state and in the absence of any electromagnetic potential will naturally yield zero net current. Current emerges as a response to the presence of electromagnetic fields that accelerate charge carriers. One method of studying linear responses consists of introducing a perturbation, e.g. a small electric field, and estimating the induced change from the equilibrium state. Analytically, perturbation-theoretical tools are well-suited for such calculations. It is also possible to numerically solve the steady states of dissipative systems and infer response functions from observables numerically. In the two-dimensional case of graphene, the linear conductivity tensor is written as

$$\bar{\sigma} = \begin{pmatrix} \sigma_{xx} & \sigma_{xy} \\ \sigma_{yx} & \sigma_{yy} \end{pmatrix}. \tag{2.20}$$

The generalized tensor-components $\sigma_{ab}(\vec{r}, t)$ are functions of time and space. The off-diagonal components $\sigma_{xy}$ and $\sigma_{yx}$ describe the transversal responses and become non-zero in Hall-type setups. Assuming spatial homogeneity gives the current as the linear response

$$\vec{J}(t) = \int \bar{\sigma}(t - t')\vec{E}(t')dt'. \tag{2.21}$$

This convolution simplifies in the Fourier representation, which reads

$$\vec{J}(\omega) = \bar{\sigma}(\omega)\vec{E}(\omega). \tag{2.22}$$

This equation denotes the frequency-local linear response given by the complex-valued conductivity tensor[3] $\bar{\sigma}(\omega)$. The DC conductivity is obtained as the small-frequency limit

$$\sigma_{ab} = \lim_{\omega \to 0} \frac{J_a(\omega)}{E_b(\omega)}. \tag{2.23}$$

For $\omega \neq 0$, the real part of the conductivity gives the in-phase response at that frequency, which corresponds to the conduction current of charge carriers. The imaginary part of the conductivity gives the out-of-phase response, which corresponds to the displacement current. In this regard, the diagonal components of Eq. 2.22 are equivalent to Ohm's law, where conductivity takes the role of the reciprocal value of the characteristic impedance.[4] In Publication II, I have identified circumstances under which the real part of the optical conductivity in graphene changes its overall sign. Such a negative conductivity means that the system becomes a gain medium that puts out energy as a consequence of non-equilibrium physics. This result has motivated my work in Publication V and Publication VI, as I discuss in section 3.

Tuning the chemical potential, and therefore the charge carrier density, of graphene is a reliable way to drastically increase the conductivity [61–68]. At the charge neutrality

---

[3]The units of conductivities of two-dimensional materials can be misleading. $\bar{\sigma}$ is in units of Siemens. However, this is not the *de facto* conductance of a graphene sample, where the geometry and the probing-axis enter such that units cancel to produce Siemens again.

[4]In electrical engineering jargon, conductance is only the real part, while the imaginary part is called susceptance and is closely related to the capacitance, as they only differ by a factor of $\omega$. The combined complex-valued quantity is called the admittance.

point, the Fermi surface reduces to a point and the conductivity of graphene takes its smallest value, which is referred to as the minimal conductivity $\sigma_0$. This has been the subject of some ambiguity as theories commonly predict values for the minimal conductivity of either $\sigma_0 = \frac{\pi e^2}{2h}$ [14, 69–71] or $\sigma_0 = \frac{4e^2}{\pi h}$ [4, 71, 72]. Experimental observations have found the minimal conductivity to be roughly $\sigma_0 \approx \frac{4e^2}{h}$ [13]. The optical conductivity of graphene is constant at $\sigma_0(\omega > 0) = \frac{e^2}{4\hbar}$, as a consequence of the constant density of states due to the linear dispersion relation [32]. The charge carrier density is also affected by incoherent pumping which transfers population into the excited bands and results in an increased conductivity, i.e. photoconductivity.

In order to study coherently driven charge transport phenomena it is necessary to introduce the presence of electromagnetic fields into this model of graphene. In lattice models, such as tight-binding, this is achieved via the Peierl's substitution, which in the limit of continuous momenta acts identically to minimal coupling in that the electromagnetic vector potential $\vec{A}(t)$ directly couples to the momentum. This is a consequence of the local gauge freedom of the complex phase of the quantum mechanical wave-function. The vector potential relates to the electric field as $\vec{E}(t) = -\partial_t \vec{A}(t) - \vec{\nabla}\Phi$. We gauge fix the potentials to be $\vec{\nabla}\vec{A} = 0$ and $\Phi = 0$ over the spatial extent of the theoretical material sample. An alternating field at frequency $\omega$ and field strength $\vec{E}$ relates to the vector potential as

$$\vec{A}_{\text{AC}}(t) = \frac{\vec{E}}{\omega}\sin(\omega t + \phi) \implies \vec{E}_{\text{AC}}(t) = -\vec{E}\cos(\omega t + \phi), \qquad (2.24)$$

with some arbitrary phase $\phi$. Similarly, a direct bias field yields $\vec{A}_{\text{DC}} = -\vec{E}_{\text{DC}}t$. This provides the means of describing the effects of applying periodic driving or constant electric fields to the system. One source of such an alternating bias field in graphene is the irradiation with polarized light. In my work, I considered in-plane fields only, i.e. $E_z = 0$. In this case, the incidence of the light onto the graphene is perpendicular to the sample.[5] This leads to the Hamiltonian

$$H_{\vec{k}} = \hbar v_F((k_x - \frac{e}{\hbar}A_x(t))\sigma_x + (k_y - \frac{e}{\hbar}A_y(t))\sigma_y) \qquad (2.25)$$

and in the particular case of irradiation with circularly polarized light at frequency $\omega_{\text{d}}$ and with the field strength $E_{\text{d}}$

$$H_{\vec{k}} = \hbar v_F((k_x - \frac{eE_{\text{d}}}{\hbar\omega_{\text{d}}}\cos(\omega_{\text{d}}t))\sigma_x + (k_y - \frac{eE_{\text{d}}}{\hbar\omega_{\text{d}}}\sin(\omega_{\text{d}}t))\sigma_y). \qquad (2.26)$$

The transport properties of graphene are drastically altered by driving with such an external field. This makes it possible to control the photoconductivity and charge carrier dynamics in a variety of ways [35, 37, 38, 73–87]. Capturing the effects of driving and probing graphene periodically, as well as constant in time, provides the

---

[5]In the case of linear polarization, the propagation axis of the light does not necessarily need to be perpendicular to the graphene sample. However, any inclination leads to spatial differences in phase fronts which need to be considered.

means of describing the different electronic transport phenomena [88–93]. It is possible to consider both steady state and transient transport for different types of polarization of the incoming light. Depending on the intensity of the applied fields, one can consider linear or non-linear responses in either longitudinal or transversal direction. Throughout my work, I have considered driving frequencies of up to $\omega_{\mathrm{d}} = 2\pi \times 50\mathrm{THz}$ and field strengths of up to $E_{\mathrm{d}} = 20\mathrm{MV\,m^{-1}}$, as inspired by the experiment by McIver *et al.* [44].

## 2.3 Floquet Physics

When studying the non-equilibrium physics of periodically driven systems, it is often very insightful to consider the perspective provided by Floquet theory. Floquet theory is a general framework for capturing crucial aspects of the dynamics of systems that are periodic in time. In general, these dynamics drastically differ from the undriven counterparts. A common example in classical mechanics is Kapitza's pendulum. In this system, a pendulum is driven by periodically moving its suspension point up and down. Depending on the details of the pendulum and the driving, this motion transforms the instable fix-point of the pendulum standing upright into a stable fix-point. Therefore, a small deviation will not make the pendulum roll down, but rather it will move back into the upright position. This popular example shows that periodic driving leads to profound phenomena in the resulting steady state physics. There is detailed literature available on the topic of Floquet physics [94, 95], which inspired this section.

Consider a Hamiltonian that is periodic in time, i.e. $H(t) = H(t + \tau)$, for some time $\tau$. The Floquet theorem states that fundamental solutions $\psi_n(t)$ to the time-dependent Schrödinger equation

$$i\hbar\partial_t\psi(t) = H(t)\psi(t) \tag{2.27}$$

display the same periodicity up to a phase factor, such that

$$\psi_n(t + \tau) = e^{-i\phi_n}\psi_n(t). \tag{2.28}$$

Introducing a periodic function $u_n(t) = u_n(t + \tau)$ allows one to write

$$\psi_n(t) = e^{-\frac{i}{\hbar}\epsilon_F^{(n)}t}u_n(t), \tag{2.29}$$

such that $\phi_n = \frac{2\pi\epsilon_F^{(n)}}{\hbar\omega}$ with the corresponding driving frequency $\omega = \frac{2\pi}{\tau}$. The expression $\epsilon_F^{(n)}$ is the Floquet energy of this $n$th state. An additional phase factor of $e^{-im\omega t}$, $m \in \mathbb{Z}$, leaves this solution in-tact as

$$e^{-im\omega\tau} = 1. \tag{2.30}$$

Therefore, for a Floquet state with energy $\epsilon_F^{(n)}$, a ladder of states exists with level-spacing equal to multiples of the driving photon energy $m\hbar\omega$, $m \in \mathbb{Z}$, and the emerging Floquet spectrum is periodic in frequency space. In particular, a solution can further be written as a linear combination

$$\psi_n(t) = \sum_{m\in\mathbb{Z}} u_m^{(n)}e^{-i(m\omega + \frac{1}{\hbar}\epsilon_F^{(n)})t}. \tag{2.31}$$

Transforming the Schrödinger equation into frequency space leads to the relation

$$(m\hbar\omega + \epsilon_F^{(n)})u_m^{(n)} = \sum_{l\in\mathbb{Z}} H_{m-l}u_l^{(n)}, \tag{2.32}$$

with the $m$th Fourier component of the time-dependent Hamiltonian

$$H_m = \frac{1}{\tau}\int_{t_0}^{t_0+\tau} e^{im\omega t}H(t)dt. \tag{2.33}$$

Note that the time $t_0$ is arbitrary, and a particular choice is referred to as the Floquet gauge. Eq. 2.32 can be represented using the Floquet Hamiltonian

$$H_F = \begin{pmatrix} \ddots & & & & & \\ & H_0+2\hbar\omega & H_1 & H_2 & H_3 & H_4 \\ & H_{-1} & H_0+\hbar\omega & H_1 & H_2 & H_3 \\ & H_{-2} & H_{-1} & H_0 & H_1 & H_2 \\ & H_{-3} & H_{-2} & H_{-1} & H_0-\hbar\omega & H_1 \\ & H_{-4} & H_{-3} & H_{-2} & H_{-1} & H_0-2\hbar\omega \\ & & & & & & \ddots \end{pmatrix} \tag{2.34}$$

with the solutions

$$\psi_n = (\ldots, u_1^{(n)}, u_0^{(n)}, u_{-1}^{(n)}, \ldots)^{\mathrm{T}}. \tag{2.35}$$

The eigenvalues of $H_F$ are the Floquet energies $\epsilon_F^{(n)}$ of the solutions of the driven system. However, the diagonalization of $H_F$ can in general only be performed approximately. The effective Floquet states describe the stroboscopic dynamics across the discrete points of periodicity $t = t_0 + m\tau$, $m \in \mathbb{Z}$. The dynamical structure in between these stroboscopic points in time is called micro-motion and is not covered by $H_F$. The micro-motion is relevant for the details of the dynamics, however the Floquet bands of $H_F$ by themselves provide deep structural insight into a driven system, particularly in the presence of dissipation. It is didactically valuable to consider the trivial edge-case of vanishing amplitude in the periodic terms, i.e. $H(t) = H_0$. Then $H_F$ is diagonalized using the same transformation as for diagonalizing $H_0$ and the resulting Floquet energies are just the bare eigenenergies up to multiples of the photon energy, albeit formally constrained within regions in frequency space of size $\hbar\omega$. By reintroducing finite amplitudes in the periodic terms in the Hamiltonian, the bare levels of different Floquet replicas that touch (or intersect) begin to repel each other. This leads to gaps at certain multi-photon resonances of the bare level structure. Floquet theory is often referred to as an analog to the Bloch theorem of solid-state physics, where a periodic potential in real-space leads to quasi-momentum that is periodic with the Brillouin zone. The consequences in Floquet theory are very similar with an emergent periodicity in the solutions in frequency rather than momentum.[6]

---

[6]The Floquet theorem in its original form predates the Bloch theorem by half a century and covers the effects of periodicity in partial differential equations agnostic to the physical nature of the parameters.

Floquet theory has gained particular attention in more recent literature of solid-state and condensed matter physics, as means of dynamically controlling various material properties, i.e. Floquet engineering [9, 10]. In particular, Floquet topological physics were actively studied [40–43, 96–99] in graphene. Similar approaches of designing Floquet topological insulators have been considered in a variety of setups [100–110]. Oka and Aoki showed how the topologically non-trivial Haldane model [111] is approximately reproduced in light-driven graphene [39]. The topological nature of this effective Floquet Hamiltonian predicts an anomalous Hall effect in graphene driven with circularly polarized light. This was experimentally studied by McIver *et al.* [44], who showed an anomalous Hall response slightly shy of quantization. An accurate description of the transport requires taking the non-equilibrium physics of the driven dissipative system into account, as well as the non-trivial Floquet-Bloch band occupations that it displays. This was the key motivation of our work in Publication I, where we devised a numerical model that captures the driven dissipative electron dynamics of graphene in order to explain the anomalous Hall transport measurements. The description of graphene used throughout these works is detailed in the following section.

## 2.4 Modelling Dissipative Processes

Dissipation plays a crucial role in the dynamics of practically any real system, and is in particular a substantial aspect of solid-state physics. Considering dissipation necessitates including processes of decoherence, decay, and loss into the model of a system. The Lindblad master equation [112] describes the non-unitary time evolution of density operators $\rho$ in a way that includes such processes phenomenologically. It reads

$$\dot{\rho} = i[\rho, H] + \sum_j \gamma_j (L_j \rho L_j^\dagger - \frac{1}{2}\{L_j^\dagger L_j, \rho\}), \qquad (2.36)$$

where $L_j$ are Lindblad operators that describe dissipative processes and $\gamma_j$ are the corresponding coefficients. It is commonly utilized in disciplines such as quantum optics, condensed matter, and quantum information processing. One condition for a proper model of dissipation is that it recovers the correct equilibrium state. In solid-state physics this would be reflected in the occupation of the Bloch bands. As discussed previously, the equilibrium state depends on the momentum which in turn is affected by semi-classical electromagnetic fields via minimal coupling. The decay into the ground state is therefore to be understood with respect to the vector potential, i.e. the dissipation has to act in a gauge invariant way. For this purpose, we consider dissipation that acts in the instantaneous eigenbasis of the time-dependent Hamiltonian under consideration of minimal coupling. We represent the system through a product of states that are local in momentum space

$$\rho = \otimes_{\vec{k} \in \mathcal{D}_K} \rho_{\vec{k}}, \qquad (2.37)$$

where $\mathcal{D}_K$ describes the vicinity of the Dirac point $K$, as mentioned in a previous section. We omit interaction terms between different momenta as might be mediated via phonons

for instance. Thus, the dynamics separate in momentum space with the Lindblad master equation acting locally.

To illustrate the choice of dissipation, consider a material such as graphene that is initially in its ground state and then quenched via an electric field corresponding to a vector potential that changes from $\vec{A}(t_{\text{initial}})$ to $\vec{A}(t_{\text{final}})$, but is constant in time before $t_{\text{inital}}$ and after $t_{\text{final}}$. Sufficiently long after the quench, the system will have relaxed into its equilibrium state, however at this point in time the vector potential will have the value $\vec{A}(t_{\text{final}})$ compared to it initial value of $\vec{A}(t_{\text{initial}})$. Consequently, the system acts as if the bands were shifted in momentum space by $\Delta\vec{k} = \frac{e}{\hbar}(\vec{A}(t_{\text{final}}) - \vec{A}(t_{\text{initial}}))$. The dissipative model of this type of system has to capture this and display relaxation with respect to the momentum that is translated by the vector potential. This consideration is necessary to recover fairly fundamental results of transport such as Ohm's law.

In the two-level description of graphene there is one electron per accessible momentum with two possible states. Treating these states as fermionic excitations invites a construction that considers two additional states. First, a state in which there are no electrons with a given momentum present, i.e. both bands are empty. And second, a state in which there are two electrons with a given momentum, i.e. both bands are occupied. Formally, this is written using fermionic operators for the two sub-lattices $c_{\vec{k},A}^{(\dagger)}$ and $c_{\vec{k},B}^{(\dagger)}$ with the anti-commutator relation

$$\{c_{\vec{k},i}, c_{\vec{k},j}^{\dagger}\} = \delta_{i,j}, \tag{2.38}$$

such that the Hilbert space is spanned by the states $|0\rangle$, $|A\rangle = c_{\vec{k},A}^{\dagger}|0\rangle$, $|B\rangle = c_{\vec{k},B}^{\dagger}|0\rangle$ and $|2\rangle = c_{\vec{k},B}^{\dagger}c_{\vec{k},A}^{\dagger}|0\rangle$ for a given momentum $\vec{k}$. In particular, the states $|A\rangle$ and $|B\rangle$ span the original two-dimensional Hilbert space. We introduce these additional states into the dynamics via coupling through dissipative channels. Physically, these channels describe electron exchange with a fermionic bath. Furthermore, in this four-level description it is straight-forward to include a chemical potential $\mu$. We write the corresponding four-level Hamiltonian

$$H_{\vec{\pi}(t)} = \begin{pmatrix} -2\mu & 0 & 0 & 0 \\ 0 & -\mu & \hbar v_F(\pi_x(x) - i\pi_y(t)) & 0 \\ 0 & \hbar v_F(\pi_x(t) + i\pi_y(t)) & -\mu & 0 \\ 0 & 0 & 0 & 0 \end{pmatrix} \tag{2.39}$$

with $\vec{\pi}(t) = \vec{k} - \frac{e}{\hbar}\vec{A}(t)$, acting on the space $\{|2\rangle, |A\rangle, |B\rangle, |0\rangle\}$. On this space we utilize the Lindblad operators

$$L_j' = \begin{pmatrix} 0 & \delta_{5,j} & \delta_{6,j} & 0 \\ \delta_{1,j} & \delta_{z,j} & \delta_{+,j} & \delta_{7,j} \\ \delta_{2,j} & \delta_{-,j} & -\delta_{z,j} & \delta_{8,j} \\ 0 & \delta_{3,j} & \delta_{4,j} & 0 \end{pmatrix}, \tag{2.40}$$

which cover the two-level processes of $\sigma_z$, $\sigma_+$, and $\sigma_-$ on the two-dimensional single-electron subspace $\{|A\rangle, |B\rangle\}$, but also the additional channels in and out of the sector

with zero or two electrons present. However, in this dissipative model the Lindblad operators act in the instantaneous eigenbasis that diagonalizes Eq. 2.39, i.e. we define $L_j = U^\dagger(t)L'_jU(t)$ where $U(t)$ diagonalizes $H_{\vec{\pi}(t)}$ at each point in time. The instantaneous eigenbasis reflects the presence of the vector potential, such that this method fulfills the desired gauge invariance. We introduce a temperature $T$ into this model by imposing restrictions onto opposing processes. It is

$$\gamma_+ = \gamma_- e^{-\frac{2\epsilon}{k_BT}} \tag{2.41}$$

and

$$\gamma_5 = \gamma_1 e^{\frac{\epsilon+\mu}{k_BT}} \qquad\qquad \gamma_6 = \gamma_2 e^{\frac{-\epsilon+\mu}{k_BT}} \tag{2.42}$$

$$\gamma_7 = \gamma_3 e^{\frac{-\epsilon+\mu}{k_BT}} \qquad\qquad \gamma_8 = \gamma_4 e^{\frac{\epsilon+\mu}{k_BT}}, \tag{2.43}$$

where $k_B$ is the Boltzmann constant and $\pm\epsilon$ are the instantaneous eigenenergies of the Hamiltonian $H_{\vec{\pi}}(t)$. This ensures that the undriven equilibrium state reproduces a Fermi-distribution at temperature $T$ around the chemical potential $\mu$. We have first introduced this dissipative model in Publication I, which was first-authored by Marlon Nuske, who played a major part in devising this method. I have continued expanding my own implementation of this method, and utilized it in Publication II—IV. Further, in Publication V and VI, I have used an extension of this method that includes a single-mode cavity in a type of Dicke model, as I discuss in Chapter 3.

Considering the dissipative processes on the two-level system alone and reducing the dynamics again to the two-dimensional sector provides a generalized expression. The instantaneous eigenbasis of any two-level Hamiltonian $H(t)$ with $\text{Tr}(H(t)) = 0$ is given by a transformation $U(t)$ such that

$$\epsilon\sigma_z = U^\dagger(t)H(t)U(t), \tag{2.44}$$

where $\pm\epsilon$ are the instantaneous eigenenergies of $H(t)$ given by $\vec{H}^2(t) = \epsilon^2$. This transformation makes it possible to rewrite the Lindblad master equation. I use the Bloch-sphere representation

$$\rho(t) = \frac{1}{2}(\mathbb{1} + \vec{\rho}(t)\vec{\sigma}) \qquad\qquad H(t) = \vec{H}(t)\vec{\sigma} \tag{2.45}$$

to write the general equation of motion in this dissipative model. It is

$$\dot{\vec{\rho}}(t) = 2\epsilon(\vec{h}(t) \times \vec{\rho}(t)) - \gamma_1\vec{\rho}(t) - \gamma_2\vec{h}(t) - \gamma_3(\vec{h}(t)\vec{\rho}(t))\vec{h}(t) \tag{2.46}$$

with the Hamiltonian axis $\vec{h}(t) = \vec{H}(t)\epsilon^{-1}$. The structure of this equation of motion is visualized in the Bloch sphere in Fig. 2.2.

$$\gamma_1 = (\gamma_+ + \gamma_-)/2 + 2\gamma_z \qquad \gamma_2 = \gamma_- - \gamma_+ \qquad \gamma_3 = (\gamma_+ + \gamma_-) - 2\gamma_z \tag{2.47}$$

emerge as the effective dissipation coefficients in this representation. I have derived this particular representation in Publication V and used it for analytical calculations in Publication IV and Publication V.
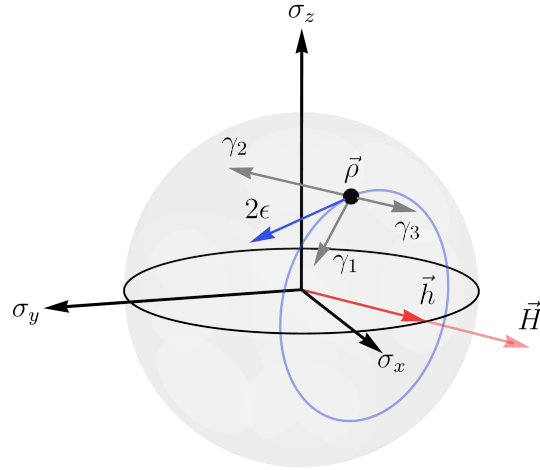
Figure 2.2: The Bloch-sphere representation of the generalized two-level Lindblad equation with dissipation in the instantaneous eigenbasis. The location of the density operator $\vec{\rho}$ is indicated with a black dot. The terms of Eq. 2.46 acting on $\vec{\rho}$ are depicted as gray and blue arrows. The gray arrows indicate the dissipative terms weighted with Lindblad coefficients. The term proportional to $\gamma_1$ is parallel to $\vec{\rho}$. The terms proportional to $\gamma_2$ and $\gamma_3$ are parallel to $\vec{h}$. The unitary action in the direction of $\vec{h} \times \vec{\rho}$ is proportional to $2\epsilon$ and by itself generates circular trajectories indicated in blue.

## 2.5 Momentum- and Frequency-resolved Electron Distribution

A crucial feature of the extended Hilbert-space in Eq. 2.39 and Eq. 2.40 is the capacity for calculating two-point correlation functions of the type $\langle c_{\vec{k},i}^{\dagger}(t_2)c_{\vec{k},j}(t_1)\rangle$, with $i,j \in \{A,B\}$. This provides access to frequency- and momentum-resolved electron distributions

$$n(\vec{k},\omega) = \frac{1}{(t_\text{f} - t_\text{i})^2} \int_{t_\text{i}}^{t_\text{f}} \int_{t_\text{i}}^{t_\text{f}} \mathcal{G}(\vec{k},t_1,t_2)e^{i\omega(t_2-t_1)}dt_2dt_1 \qquad (2.48)$$

where $t_\text{i}$ to $t_\text{f}$ provides a time-window across which the spectral information is evaluated. The correlation function in Eq. 2.48 is

$$\mathcal{G}(\vec{k},t_1,t_2) = \sum_{j\in\{A,B\}} \langle c_{\vec{k},j}^{\dagger}(t_2)c_{\vec{k},j}(t_1)\rangle. \qquad (2.49)$$

The expression in Eq. 2.48 is motivated by the theoretical study on the predictions of time- and angle-resolved photoelectron spectroscopy (trARPES) measurements by Freericks *et al.* [113]. trARPES is a well-established and state-of-the-art experimental method for observing band structures and their dynamics in solid-state systems [114–125]. It has been used to study the Floquet-Bloch states of strongly driven materials [126–134]. Experiments consistently show that the observed band structures match

the predictions of Floquet theory and trARPES has in particular been used to study graphene driven by circularly polarized light [135–138]. The particular light-induced gap at the Dirac point that is associated with an anomalous Hall effect in graphene [39] has however been difficult to observe in these experiments. This is attributed to an array of resolution- and signal-disambiguation limitations. These limitations cover various broadening effects, energy-resolution limitations, material defects [139–142], space charge effects due to many photoelectrons [143–146], and laser-assisted photoemission (LAPE) replica. This circumstance largely motivated Publication III, where I have studied means to circumvent some of these challenges and proposed a setup to observe said Floquet band gap using trARPES.

Note that as $n(\vec{k}, \omega)$ resolves the spectral function of a given system, I have used this quantity in Publications I — VI in order to obtain the population of light-induced Floquet states, which has provided valuable insight into the driven dynamics. In such two-level systems, this is achieved by integrating the spectral weight within bands of frequencies that are associated with a given Floquet-Bloch band

$$n_m^+(\vec{k}) = \int_{m\omega_d}^{(m+\frac{1}{2})\omega_d} n(\vec{k}, \omega)d\omega \qquad (2.50)$$

$$n_m^-(\vec{k}) = \int_{(m-\frac{1}{2})\omega_d}^{m\omega_d} n(\vec{k}, \omega)d\omega, \qquad (2.51)$$

where $\omega_d$ is the frequency of the driving term that induces the Floquet-Bloch bands. These expressions provide the population of the $m$th upper and lower Floquet-Bloch band, respectively.

## 2.6 Publication I: Floquet dynamics in light-driven solids

M. Nuske, <u>L. Broers</u>, B. Schulte, G. Jotzu, S. A. Sato, A. Cavalleri, A. Rubio, J. W. McIver, and L. Mathey — **Phys. Rev. Research 2, 043408 (2020)**

This collaboration was motivated by the experiment of McIver *et al.* [44] in which they studied an anomalous Hall effect in monolayer graphene driven with circularly polarized terahertz radiation. Oka and Aoki [39] had predicted, that the high-frequency limit of the Floquet band structure of this system is reminiscent of the Haldane model which presents a topologically insulating ground state. They had proposed that this would result in an anomalous Hall effect in graphene. The experimental results showed a non-quantized transversal conductivity attributed to the intricate non-equilibrium electron dynamics in driven systems.

In this work, first-authored by Marlon Nuske, we have numerically studied the Floquet physics of light-driven solids. We have conceived a numerical method for capturing driven dissipative dynamics and applied it to graphene irradiated by circularly polarized light. This numerical method is capable of simulating pump-probe transport measurements, as well as calculating the momentum- and frequency-resolved electron distribution, which resolves the population of the light-induced Floquet bands. In this setup we have reproduced the transport measurements of the experiment by McIver *et al.* [44].

We have found that the populations of the Floquet bands play a crucial role in the non-quantization of the anomalous Hall conductivity in this system. The electron distribution is highly non-trivial and far from an equilibrium distribution and corresponds to an effective electron temperature in the thousands of Kelvin, such that the system does not enter any topologically insulating state. We have identified two major contributions to the observed transversal current. First, a geometric contribution which consists of the Berry curvature of the Floquet bands weighted by their population. The Berry curvature is localized at the light-induced gaps and locally integrates to integer values. Secondly, there is a regular contribution which consist of the band velocity weighted by the population imbalance due to the non-equilibrium electron distribution. In this description we were able to reproduce the experimental results well and explain the deviations from the theoretical description. We have demonstrated that our numerical model captures the transport properties observed in the experiment, which motivated further research on the basis on this model.

My contribution to this work consisted of designing and implementing parts of the numerical methods together with MN. In particular, I devised the numerics for the momentum- and frequency-resolved electron distributions and for the two contributions to the Hall conductivity. All authors have contributed to this work and to writing the manuscript.

# Floquet dynamics in light-driven solids

M. Nuske [1,2,3] L. Broers,[1,2] B. Schulte [4] G. Jotzu,[4] S. A. Sato [5,4] A. Cavalleri,[4] A. Rubio [4,6]
J. W. McIver,[4] and L. Mathey[1,2,3]

[1]*Zentrum für Optische Quantentechnologien, Universität Hamburg, 22761 Hamburg, Germany*
[2]*Institut für Laserphysik, Universität Hamburg, 22761 Hamburg, Germany*
[3]*The Hamburg Center for Ultrafast Imaging, Luruper Chaussee 149, Hamburg 22761, Germany*
[4]*Max Planck Institute for the Structure and Dynamics of Matter, Luruper Chaussee 149, 22761 Hamburg, Germany*
[5]*Center for Computational Sciences, University of Tsukuba, Tsukuba 305-8577, Japan*
[6]*Center for Computational Quantum Physics (CCQ), Flatiron Institute, 162 Fifth Avenue, New York, New York 10010, USA*

We demonstrate how the properties of light-induced electronic Floquet states in solids impact natural physical observables, such as transport properties, by capturing the environmental influence on the electrons. We include the environment as dissipative processes, such as interband decay and dephasing, often ignored in Floquet predictions. These dissipative processes determine the Floquet band occupations of the emergent steady state, by balancing out the optical driving force. In order to benchmark and illustrate our framework for Floquet physics in a realistic solid, we consider the light-induced Hall conductivity in graphene recently reported by McIver *et al.* [Nat. Phys. **16**, 38 (2020)]. We show that the Hall conductivity is estimated by the Berry flux of the occupied states of the light-induced Floquet bands, in addition to the kinetic contribution given by the average band velocity. Hence, Floquet theory provides an interpretation of this Hall conductivity as a geometric-dissipative effect. We demonstrate this mechanism within a master equation formalism, and obtain good quantitative agreement with the experimentally measured Hall conductivity, underscoring the validity of this approach which establishes a broadly applicable framework for the understanding of ultrafast nonequilibrium dynamics in solids.

## I. INTRODUCTION

Light control of matter has emerged as a new chapter of condensed matter physics. While the established approach to solid state physics is to probe equilibrium or near-equilibrium properties of a given material, we now take a more active stance, to design nonequilibrium states with desired properties by periodic driving. This new vantage point is reflected in recent experimental work on light-controlled superconductivity (see, e.g., Refs. [1–5], where a superconducting state is either enhanced or induced by applying terahertz pulses). More generally, optical control provides a dynamical avenue towards creating functionalities on demand in materials [6], for which we provide an efficient theoretical framework and understanding.

A natural theoretical description of a periodically driven system utilizes Floquet theory to determine its quasienergy states. This approach formally represents a periodically driven, time-dependent Hamiltonian as a time-independent one, which allows the use of time-independent methodologies. If the quasienergy states are interpreted as the eigenstates of an effective Hamiltonian, this effective Hamiltonian can be qualitatively distinct from the unperturbed Hamiltonian. This approach constitutes "Floquet engineering" via periodic driving. Implementing this approach in nearly isolated cold atom systems has resulted in spectacular properties [7–15].

While this approach has a suggestive character, we demonstrate that a naive treatment of the Floquet states as energy states, which are then occupied by electrons with an equilibrium distribution, is in general not a correct prediction for the driven system. First, the measurable properties, such as transport properties, of the driven systems are generally different from the measurable properties of the effective Hamiltonian. The linear response to a probing term in the Hamiltonian, which models the physical probe, interferes with the driving term. The resulting linear response cannot be expressed as the linear response of the effective Hamiltonian, in general. Second, for a well-behaved effective Hamiltonian to describe the low-frequency dynamics, the high-frequency limit of the driving frequency is desirable. Typically that implies that the driving frequency is large compared to the electronic bandwidth, to avoid resonant driving of interband transitions. However, in this high-frequency limit a high driving intensity is required, so that the far off-resonant optical pumping has a noticeable effect on the system. This implies currently unrealistic experimental and material requirements. Third, the steady state of the electrons that emerges in the driven system is in general not an equilibrium distribution on the Floquet quasienergies. These properties of driven systems emphasize
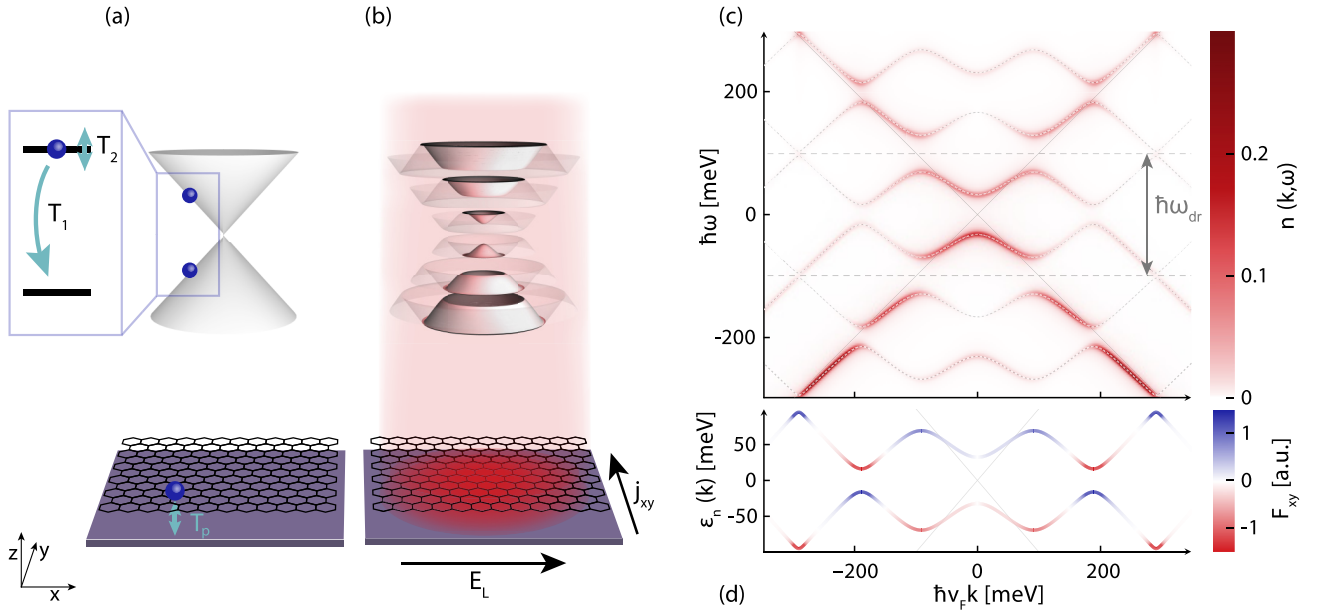
FIG. 1. Dirac cone of the (a) undriven and (b) driven graphene band structure (top) and the corresponding real-space lattice (bottom). The band structure of graphene driven with circularly polarized light develops gaps at each resonance and at the Dirac point. Applying a longitudinal field $E_L$ induces a transverse Hall current $j_{xy}$. (c) Electron distribution $n(\mathbf{k}, \omega)$ as a function of momentum times $\hbar v_F$. Note that $\hbar v_F k = 200$ meV corresponds to $k \approx 0.03/\text{Å}$. The distribution is shown after a steady state is achieved for a tanh-type ramp to the driven state. The parameters for (c) are inspired by the experimental ones used in Ref. [16]. Dotted gray lines show the numerically computed Floquet band structure (see Appendix E). The maxima of the electron distribution of the driven state agree perfectly with the Floquet band structure. We show a slice along the $k_x$ direction of the band structure shown in (b). Dashed gray lines separate the different Floquet replicas. (d) Floquet band structure colored by Berry curvature (for details, see Appendix E). The Berry curvature is integrated over ring segments of momentum space. This integrated quantity suppresses the curvature at the Dirac point. We only show the first Floquet replica since Berry curvature and Floquet energies are periodic with $\omega_{dr}$. We use $E_{dr} = 26$ MV/m, $\omega_{dr} = 2\pi \cdot 48$ THz $\approx 200$ meV$/\hbar$, $T_1 = 1$ ps, $T_2 = 0.2$ ps, $T_p = 0.4$ ps, temperature $T = 80$ K, and $\mu = 0$. Faint gray lines indicate the Dirac cone for undriven graphene.

clear distinctions between a system with a Floquet engineered Hamiltonian and a system with a static Hamiltonian.

In this paper, we present how the Floquet band properties manifest themselves in transport properties in an optically driven solid. As a central example we consider light control of graphene. References [17–21] have proposed to illuminate graphene with circularly polarized light with the purpose of inducing a topologically insulating state [22–26], with the same low-energy behavior as the Haldane model [27]. We note that these proposed experiments would only reproduce the behavior of the Haldane model in a band insulating state, under the above-mentioned assumption of a large driving frequency. As we demonstrate below, neither of these assumptions is fulfilled.

Our primary experimental motivation derives from the measurements of Ref. [16]. The authors report on a recently developed on-chip femtosecond technology to detect the Hall current of graphene illuminated with light with a frequency of tens of terahertz, which is orders of magnitude below the bandwidth of graphene. These measurements illustrate the realistic regime of current experiments, and are of guidance for our study. However, we emphasize that our conceptual approach directly applies to any light-driven Dirac material [28–32], and more broadly to any solid with well-defined electronlike quasiparticles. Theoretical studies on dissipative dynamics in graphene have been reported in Refs. [33–35].

## II. GEOMETRIC-DISSIPATIVE ORIGIN OF HALL CONDUCTIVITY

We develop a master equation description for the transport properties of illuminated graphene under realistic conditions. As a key addition to the unitary evolution we include several dissipative processes to provide an effective model for the relaxation and dephasing of the electronic states. These are shown schematically in Fig. 1(a). The form and the magnitude of the dissipative processes determine the steady state that is induced by the optical driving. For this steady state, we determine the Hall current $j_y$ by applying a dc probing field $E_L$ along the $x$ axis. From the linear response definition $\mathbf{j}_y = \sigma_{xy} E_L$, we determine the Hall conductivity $\sigma_{xy}$.

Furthermore, we determine the distribution of electrons in momentum and frequency space $n(\mathbf{k}, \omega)$, which is the Fourier transform of the single-particle correlation function. $n(\mathbf{k}, \omega)$ is depicted in Fig. 1(c). This distribution describes what frequencies and momenta are contained in the time evolution of the electrons, shown here for the steady state. This quantity is closely related to the quantity measured in time- and angle-resolved photoemission spectroscopy (trARPES) experiments [36]. We note that this distribution is consistent with the Floquet bands, depicted in Fig. 1(b) and shown as dashed lines in Fig. 1(c). Furthermore, the Floquet bands are populated primarily in regions that are close to the original Dirac dispersion. This implies that the predominantly

occupied Floquet band switches at each resonance. We refer to this property of the band occupation as a split-band picture. This is in contrast to the majority of previous works on Floquet theory where the properties of the continuously connected bands are studied. With these observations we determine the derived quantity $n_\sigma(\mathbf{k})$, with band index $\sigma = \pm 1$, which is determined by integrating the distribution $n(\mathbf{k}, \omega)$ for fixed $k$ in the vicinity of every second frequency maximum (see also Appendix D). This provides an estimate of the occupation of the Floquet states that includes the dissipative broadening of the bands.

As an additional property of the driven state, we determine the Floquet bands [see Figs. 1(b) and 1(c)]. From these, we determine the $y$ component of the band velocity $v_y^\sigma$ and the Berry curvature $\Omega^\sigma$. We combine these quantities and define

$$\Phi_{\mathrm{xy}} = \frac{1}{A} \sum_{\substack{\mathbf{k} \in 1.\mathrm{BZ} \\ \sigma = \pm 1}} \Omega^\sigma(\mathbf{k}) n_\sigma(\mathbf{k}),$$

$$\bar{v}_y = \frac{1}{nA} \sum_{\substack{\mathbf{k} \in 1.\mathrm{BZ} \\ \sigma = \pm 1}} v_y^\sigma(\mathbf{k}) n_\sigma(\mathbf{k}),$$

where $A$ is the lattice size and $n = 1/A \sum_{\mathbf{k},\sigma} n_\sigma(\mathbf{k})$ is the electron density. The Berry flux $\Phi_{\mathrm{xy}}$ is the sum over the Berry curvature of the Floquet bands, weighted with the band occupation $n_\sigma(\mathbf{k})$. Similarly, the average band velocity $\bar{v}_y$ is the sum over the $y$ component of the band velocity of the Floquet bands, weighted with the band occupation, and normalized with the electron density. The average band velocity term is nonzero for the light-driven state in the presence of the dc field $E_\mathrm{L}$, due to an occupation imbalance along the $y$ direction, contributing to the Hall current. The central result of our study is that the combination of these quantities provides a good estimate of the Hall conductivity,

$$\sigma_{\mathrm{xy}} \approx n\bar{v}_y/E_\mathrm{L} + \Phi_{\mathrm{xy}}. \tag{1}$$

Both the Berry flux and the average band velocity is a sum weighted with the steady state distribution of the driven state, which in turn is determined by the dissipative processes. Our result demonstrates that the Hall conductivity is a geometric-dissipative phenomenon. As we demonstrate below, for a small driving field $E_\mathrm{dr}$, the average band velocity dominates in this prediction, whereas for a large driving field, the Berry flux dominates. We note that the nonvanishing expectation value of $\bar{v}_y$ derives from an occupation imbalance in the transverse direction of the probe, which was also discussed in Ref. [34].

We note that the Floquet states not only display a topological band gap at the Dirac points, as they would for large driving frequencies (see Refs. [22–26]). In addition to this renormalization of the Dirac cone, additional resonances appear at integer multiples of the driving frequency. Frequency space naturally separates into Floquet zones of the size of the driving frequency, in analogy to Brillouin zones. Each Floquet zone contains two bands, corresponding to the underlying two-band structure of graphene. Each resulting Floquet band has an additional Berry curvature at the resonances, in addition to the curvature at the Dirac point. Integrating over the entire band gives the Chern number of each band. For

the example shown, there are about 80 resonances stemming from multiphoton absorption, and the Chern number of the Floquet bands is of the order of $10^2$–$10^3$. However, this is not the magnitude of the Hall conductivity, because the band is not occupied in a band insulating state, but rather has the electron distribution depicted in Fig. 1(c). For this example, we find that 99.8% of the Hall conductivity can be accounted for by summing the contributions from the Dirac point and the first four resonances. Higher-order resonances have no net contribution to the Hall conductivity. We note that the total Hall current has the opposite sign of that expected in the high-frequency limit. We observe that the Hall conductivity is not quantized in an obvious fashion, however, we find a soft plateau of the conductivity as a function of the driving field, more pronounced when depicted as a function of fluence (see Appendix L). While the magnitude of the conductivity at the plateau depends on the model assumptions, such as the choice of dissipative processes, the robustness of this feature might point to an underlying principle to be discussed elsewhere.

## III. RABI SOLUTION

The key qualitative difference to the proposals that utilize high-frequency driving, is the occurrence of resonances at integer multiples of the driving frequency. As depicted in Fig. 1(d), these resonances create a Berry curvature of the Floquet bands. To demonstrate this point we determine the Berry curvature at the single-photon resonance within a Rabi picture, which gives access to all properties near the single-photon resonance and provides analytical expressions. We expand on this analysis in a Floquet picture further down, which treats the full system within a numerical framework. We describe the graphene dispersion and the interaction of the electrons with the electromagnetic field via

$$H_R = \hbar v_\mathrm{F} k \sigma_z + \frac{\sigma_{\mathrm{pol}} e E_{\mathrm{dr}} v_\mathrm{F}}{2\omega_{\mathrm{dr}}} \begin{pmatrix} 0 & i e^{-i\omega_{\mathrm{dr}} t - i\tau_z \sigma_{\mathrm{pol}} \phi_k} \\ -i e^{i\omega_{\mathrm{dr}} t + i\tau_z \sigma_{\mathrm{pol}} \phi_k} & 0 \end{pmatrix},$$

and hence the solutions $|\psi_{R,\pm}(t)\rangle$ can be obtained in analogy to the Rabi problem (see Appendix B). Here, $k e^{i\phi_k} = k_x + i k_y$ and $\tau_z = \pm 1$ labels the two inequivalent Dirac points, $\sigma_{\mathrm{pol}} = \pm 1$ determines the polarization of the light, $v_\mathrm{F}$ denotes the Fermi velocity, and $e > 0$ is the elementary charge. We then compute the instantaneous Berry curvature within the Rabi approximation, which gives

$$\Omega^\pm(\mathbf{k}) = \mp \frac{e^2}{h} \frac{\sigma_{\mathrm{pol}} v_\mathrm{F} \lambda^2}{2k\Omega_R^3}, \tag{2}$$

where $\lambda = \frac{eE_{\mathrm{dr}} v_\mathrm{F}}{2\omega_{\mathrm{dr}}}$ is the bare Rabi frequency, $\Delta = \frac{\omega_{dr} - 2v_\mathrm{F} k}{2}$ is the detuning, and $\Omega_R = \sqrt{\lambda^2 + \Delta^2}$ is the Rabi frequency. We emphasize that this result applies directly to any light-driven Dirac material, and that similar considerations can be extended naturally to any material with electronic quasiparticles. As we discuss below, a Floquet analysis expands this analysis to all resonances numerically.

## IV. MASTER EQUATION

To evaluate the quantity $n\bar{v}/E_\mathrm{L} + \Phi_{\mathrm{xy}}$ of Eq. (1), we determine the steady state occupation $n_\sigma(\mathbf{k})$ numerically. Similarly,

we determine the Hall conductivity. We factorize the density matrix $\rho$ of the system as $\rho = \prod_{\mathbf{k}} \rho_{\mathbf{k}}$, where we choose a discrete lattice of momenta $\mathbf{k}$, centered around the Dirac point, of size $N \times N$. We represent each $\rho_{\mathbf{k}}$ in the four-dimensional basis of $|0\rangle$, $c_{\mathbf{k},+}^{\dagger}|0\rangle$, $c_{\mathbf{k},-}^{\dagger}|0\rangle$, $c_{\mathbf{k},+}^{\dagger}c_{\mathbf{k},-}^{\dagger}|0\rangle$. The operators $c_{\mathbf{k},\sigma}$ describe the upper and the lower band of momentum $\mathbf{k}$, depicted in Fig. 1(a). We note that using this four-dimensional basis enables us to determine the electron distribution $n(\mathbf{k}, \omega)$, and treat undoped and doped graphene in a systematic manner, by varying the chemical potential. For each $\rho_{\mathbf{k}}$, we solve the master equation. The master equation contains unitary contributions from the equilibrium Hamiltonian $H_0$ and the light-matter interaction $H_{em}$. The latter contains both the circularly polarized driving term, with electric-field strength $E_{dr}$, as well as a longitudinal dc probing field $E_L$. In addition to these unitary contributions, we introduce dissipative processes, depicted in Fig. 1(a), modeled via Lindblad operators (see Appendix A). The first describes decay from the upper to the lower band, with a rate $\gamma_1 = 1/T_1$. The second describes dephasing between the upper and the lower band, described by a rate $\gamma_z$, which we combine into $\gamma_2 = 1/T_2 = 1/(2T_1) + 2\gamma_z$. The third rate $\gamma_p = 1/T_p$ corresponds to a single-particle exchange with a fermionic bath of temperature $T$ and chemical potential $\mu$.

We first demonstrate that the experimental results of Ref. [16] are captured with this model. In Fig. 2 we compare the circular dichroism of the Hall conductivity, which is defined as one half the difference of the response for right- and left-handed circular polarization, of the measurement and our calculation. We find that both the peak-field dependence in Fig. 2(b) as well as the chemical potential dependence for high fluence in Fig. 2(a) are in quantitative agreement. The chosen $E_{dr}$ and $\omega_{dr}$ correspond to the peak driving field and central frequency of the laser pulses used in the experiment, respectively [16]. The dissipation rate $T_1$ is inspired by Ref. [37] and for $T_2$ we choose 20fs, which is chosen to be notably smaller than $T_1$. The decay rate $T_p$ is adjusted to match the experimental data. We find that $T_p = 30$–$50$fs are appropriate depending on the electric-field strength [see Fig. 2(b)]. We emphasize that the properties of the driven state crucially depend on the dissipative environment. Both the measurable properties, such as the transport behavior, and the steady state itself are shaped by the dissipation. This key result demonstrates the urgency of including the dissipative environment to model a material, and provides guidance for the design of light-induced material properties. On the conceptual side, it is this dissipative environment that is not captured in a Floquet analysis, but profoundly alters the physical behavior of the system.

## V. BERRY FLUX OF RABI STATES

In Fig. 3(b) we depict the contributions to the Hall conductivity in momentum space $\tilde{\sigma}_{xy}(\mathbf{k}) = \sigma_{xy}(\mathbf{k})/A$, as defined in Appendix A. In addition to the negative contributions near the Dirac point, which are not captured by the Rabi approach, there are negative contributions below the single-photon resonance, and positive contributions above the resonance. For comparison we depict the contributions to the Berry flux $\Phi_{xy}$ as determined within the Rabi approximation, in Fig. 3(a).
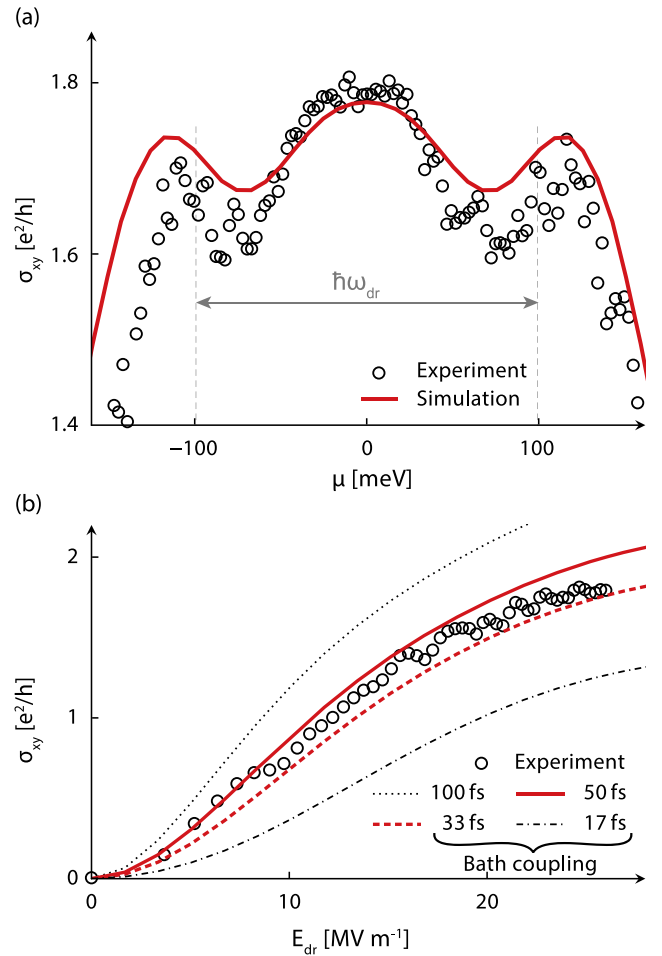


FIG. 2. (a) Circular dichroism of the transverse conductivity as a function of chemical potential. The data from the numerical simulation (red line) and experimental data [16] (open circles) agree quantitatively. (b) Electric-field dependence of the current dichroism for several values of the particle-exchange timescale $T_p$, as indicated in the legend. We see that a value in the range of $T_p = 30$–$50$ fs is consistent with the experiment. The parameters for the numerical simulation are $\omega_{dr} = 2\pi \cdot 48$ THz $\approx 200$ meV$/\hbar$, $T_1 = 100$ fs, $T_2 = 20$ fs, $T = 80$ K, $E_L = 1.7$ kV/m, and the driving pulse has a Gaussian envelope with electric-field strength full width at half maximum (FWHM) of $\sqrt{2}$ ps, corresponding to intensity FWHM of 1 ps. Finally, $E_{dr} = 26$ MV/m and $T_p = 36$ fs in (a) and chemical potential $\mu = 0$ in (b).

We find that the Rabi solution for the curvature gives a qualitatively correct description of the momentum-resolved conductivity. We note that the Rabi solution does not capture two-photon processes, which create the gap opening at the Dirac point, as well as higher-order gaps.

In Fig. 3(c) we depict a quantitative comparison. We show the momentum-resolved conductivity contributions integrated over a disk of radius $k_r$, i.e., we show $\sum_{|k|<k_r} \tilde{\sigma}_{xy}(\mathbf{k})$. Similarly, we show the contributions to the Berry flux $\Phi_{xy}$ integrated to $k_r$, as well as the sum of the curvature and band velocity contributions $\Phi_{xy} + n\bar{v}/E_L$, integrated up to $k_r$. We note that the integrated conductivity has been shifted up such that it has a zero crossing at $\hbar v k_r \approx 30$ meV, so that the behavior at the
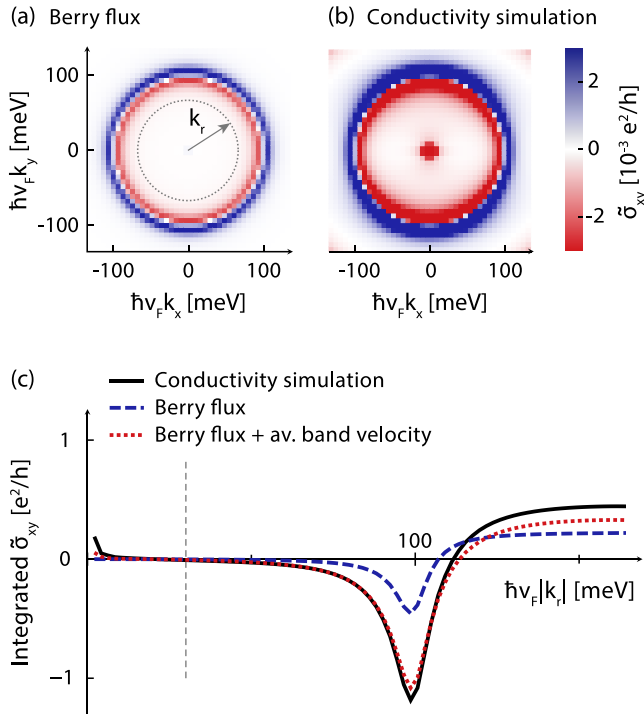
(a) Berry flux

(b) Conductivity simulation

(c)

FIG. 3. Comparison of the momentum-resolved Berry flux, depicted in (a), which is obtained within the Rabi approximation, and the momentum-resolved conductivity dichroism, depicted in (b). The Berry flux displays a qualitatively similar behavior as the conductivity dichroism, in particular a sign change at the single-photon resonance. The contribution near the Dirac point is not included in the Rabi approximation. (c) We depict the conductivity density, integrated over a disk in momentum space of radius $\mathbf{k}_r$, as shown in (a). For comparison, we show the momentum-resolved Berry flux, integrated over the same disk in momentum space, and the sum of the integrated Berry flux and the integrated average band velocity. The curves have been shifted such that their value vanishes at $\hbar v_F |k_r| = 30$ meV for a better comparison of the contribution of the first resonance. Consistent with the proposed estimate in Eq. (2), the sum of the Berry flux and the average band velocity predict the conductivity, even in a momentum-resolved manner. In all plots we use $E_{dr} = 3$ MV/m, $\omega_{dr} = 2\pi \cdot 48$ THz $\approx 200$ meV$/\hbar$, $T_1 = 50$ ps, $T_2 = 10$ ps, $T_p = 20$ ps, $T = 80$ K, $E_L = 0.84$ kV/m, $\mu = 0$, and the driving pulse is ramped with a tanh over 1 ps.

single-photon resonance can be compared directly to the Rabi solution.

We find that the momentum-resolved representation of $n\bar{v}_y/E_L + \Phi_{xy}$ gives a good prediction for the momentum-resolved conductivity. Generally, the agreement is good for small dissipation, in particular for small $\gamma_z$. The total value of the conductivity, which is the measurable conductivity of the system, is positive, and therefore of opposite sign than the contributions near the Dirac point. This implies that the positive contributions above the resonance, i.e., momentum states with $v_F k > \omega_{dr}/2$, exceed the negative contributions below the resonance, i.e., $v_F k < \omega_{dr}/2$. The sign change of the contributions is a direct consequence of the split-band picture depicted in Fig. 1(c). As mentioned above, in this picture the predominantly occupied band switches at each

resonance. The specific value of the conductivity depends continuously on the driving frequency and the dissipative properties of the system.

The momentum-resolved Berry flux, which is depicted in Fig. 3(a), derives from the Berry curvature and the occupation of the Floquet bands. The Rabi approximation describes the Floquet bands near the single-photon resonance. In Fig. 1(c) and 1(d), this resonance occurs at $\hbar v_F k \approx \pm 100$ meV. The Rabi approximation of the curvature, given in Eq. (2), predicts negative values of the curvature for the upper band, and positive curvature for the lower band, localized near the resonance. The occupation of the upper band $n_+(\mathbf{k})$ is larger than the occupation of the lower band $n_-(\mathbf{k})$ for momenta smaller than the resonance. For momenta larger than the resonance we have $n_+(k) < n_-(k)$. This change of predominant occupation results in a partial cancellation of the Berry flux. However, the lower-band contribution dominates, resulting in a positive contribution for the flux. Both the Berry curvature and the Berry flux are rotationally symmetric. In contrast, the average band velocity is manifestly anisotropic, since the band velocity $v_y^\sigma$ vanishes along the $k_x$ direction (see also Ref. [34]). This gives rise to the modest anisotropy of the Hall conductivity [see Fig. 3(b)].

## VI. BERRY FLUX OF FLOQUET STATES

We expand this analysis by determining the Floquet bands of the driven system, and their band velocity and curvature, as described in Appendix E. While the Rabi solution gives access to the properties of the single-photon resonance, the Floquet analysis gives the light-induced band properties to any order. We utilize the band velocities and the Berry curvature that is obtained from the Floquet bands, and combine them with the band occupations derived from $n(\mathbf{k}, \omega)$, as shown in Fig. 1(c), to determine the average band velocity and the Berry flux.

In Fig. 4(a), we display these quantities, and the sum of the average band velocity and the Berry flux. We find again that the sum of the Berry flux and the average band velocity gives a good prediction for the conductivity. The prediction is particularly good for small dissipation. We also display the Rabi approximation, which gives a good estimate at small $E_{dr}$. We note that for small $E_{dr}$ the band velocity contribution dominates, whereas for larger values of $E_{dr}$, the Berry flux dominates. The Berry-flux-dominated regime is achieved in the strongly driven regime, because the Floquet bands become flat, and the band velocities throughout the bands approach zero.

In Fig. 4(b) we display the momentum-resolved contributions to the conductivity for zero dephasing rate $\gamma_z = 0$. Our prediction for the conductivity based on Berry flux and average band velocity agrees almost perfectly with the simulated conductivity. We note that we find equally good agreement for nonzero $\gamma_z$, when considering only the momentum modes along the $k_y$ direction (see Appendix G). When considering all momenta and nonzero $\gamma_z$, the contributions to $n\bar{v}/E_L + \Phi_{xy}$ deviate from the contributions to the conductivity $\sigma_{xy}$, giving rise to the deviation between $n\bar{v}/E_L + \Phi_{xy}$ and $\sigma_{xy}$ in Fig. 4(a). This suggests an additional contribution due to the dephasing rate $\gamma_z$, possibly related to coherences between the Floquet bands, to be discussed elsewhere. We note that at
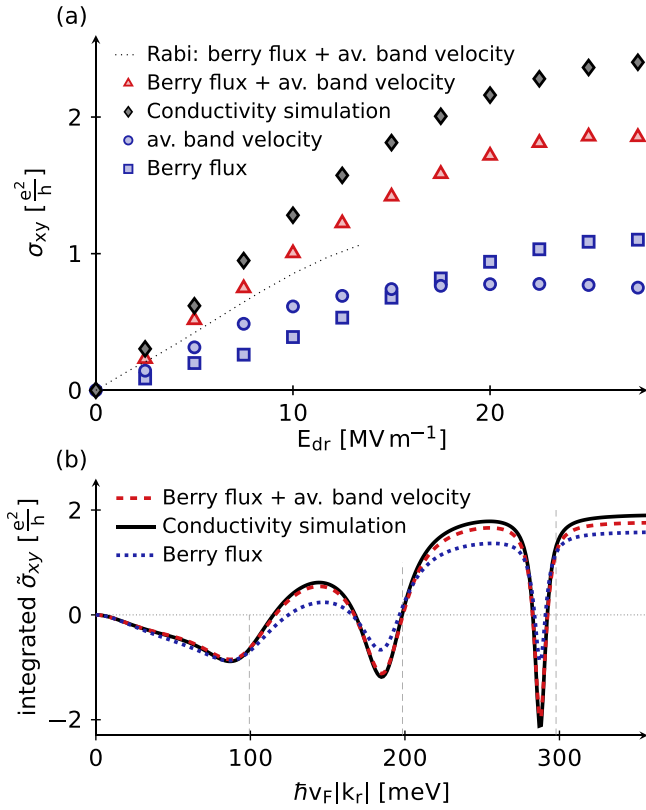
FIG. 4. (a) Comparison of the electric-field dependence of the conductivity dichroism, the Berry flux, and the average band velocity. Black diamonds show the simulated conductivity dichroism, and the faint dashed line the sum of the Berry flux and the average band velocity within the Rabi approximation. Red triangles show the sum of the Berry flux and the average band velocity, based on Floquet states. Blue squares show the Berry flux only and blue circles the average band velocity only. (b) We show the conductivity density $\tilde{\sigma}_{xy}$, integrated over a disk in momentum space with radius $\mathbf{k}_r$, for zero dephasing rate $\gamma_z = 0$. This integrated conductivity agrees with the sum over the Berry flux and the average band velocity, integrated over the same disk. For both panels the parameters are $\omega_{dr} = 2\pi \cdot 48\,\text{THz} \approx 200\,\text{meV}/\hbar$, $T_1 = 1\,\text{ps}$, $T_p = 0.4\,\text{ps}$, $T = 80\,\text{K}$ and $E_L = 1.7\,\text{kV/m}$. In (a) $T_2 = 0.2\,\text{ps}$ and in (b) $T_2 = 2\,\text{ps}$ and $E_{dr} = 26\,\text{MV/m}$. All observables are shown after a steady state is achieved for a tanh-type ramp of the driving field strength.

integer multiples of the resonance frequency at $2v_F k \approx n\omega_{dr}$, the momentum-resolved sum of the Berry flux and average band velocity changes sign. This behavior was described for the single-photon resonance above, and repeats itself for higher orders. We observe that while the momentum-resolved contribution to all three quantities is large, there is a near cancellation of these contributions for higher-order resonances.

## VII. CONCLUSION

The conceptual achievement that we put forth here is widely applicable for the description of light-induced dynamics in solids with well-defined electronic quasiparticles. We have presented a versatile and efficient master equation approach that includes the dissipative environment, enabling the description of light-driven solids under realistic conditions. The dissipative environment, which is ignored in the Floquet description of the driven system, shapes the emerging steady state by balancing out the light-induced force on the electrons. Furthermore, our approach is well suited to describe realistic driving frequencies that are small compared to the electronic bandwidth, and therefore induce resonant interband excitations, and treat the dynamics that are induced by probing processes explicitly.

Even though the construction of the light-induced Floquet states is an incomplete description of a light-driven solid, because the dissipative environment is ignored, we point out what features of Floquet states manifest themselves in its presence, resulting in Floquet physics in realistic materials. The key elements of our approach were exemplified for the recently observed light-induced Hall effect in graphene, for which we obtain a quantitative understanding. We have shown that the Hall conductivity is predicted by the sum of the average band velocity and the Berry flux of the light-induced Floquet bands. Therefore our prediction combines geometric properties of the Floquet bands, and dissipative properties of the material, which identify the Hall effect as a geometric-dissipative effect. This insight, derived from our master equation description, demonstrates the effectiveness of our approach, and motivates its application to a wide range of light-induced dynamics in solids.

## APPENDIX A: NUMERICAL ALGORITHM FOR THE COMPUTATION OF CURRENTS

We use the von Neumann equation for the unitary part of the time evolution and include interactions as well as other damping and dephasing effects by including Lindblad operators. When using the Weyl gauge the Hamiltonian does not couple different momentum points. As mentioned in the main text we therefore consider the ansatz $\rho = \prod_{\mathbf{k}} \rho_{\mathbf{k}}$ for the density matrix $\rho$ of the system. The full time evolution of the density matrix is then governed by the master equation [38]

$$\frac{d}{dt}\rho_{\mathbf{k}} = \frac{i}{\hbar}[\rho_{\mathbf{k}}, H_{\mathbf{k}}] - \frac{1}{2}\sum_{\alpha}(L^{\alpha\dagger}L^{\alpha}\rho_{\mathbf{k}} + \rho_{\mathbf{k}}L^{\alpha\dagger}L^{\alpha} - 2L^{\alpha}\rho_{\mathbf{k}}L^{\alpha\dagger}).$$

The first line of this equation describes the unitary part of the time evolution, fully determined by the Hamiltonian of
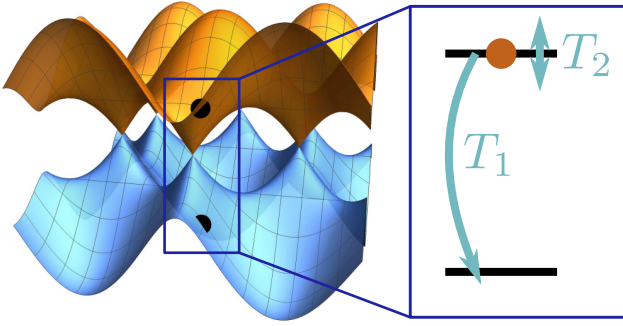
FIG. 5. Sketch of the graphene dispersion relation (left). In the Weyl gauge the Hamiltonian decouples in momentum space such that we can treat each momentum point as a two-level system (sketch on the right-hand side). We also sketch the effect of damping ($T_1$) and dephasing ($T_2$) effects.

the system. The second line with the Lindblad operators $L^\alpha$ accounts for damping and dephasing effects.

In the Weyl gauge (for details, see Appendix F) the graphene Hamiltonian with light field coupled via minimal coupling can be written such that it remains diagonal in momentum space,

$$H = \sum_{\mathbf{k}} H_{\mathbf{k}}.$$

Each momentum mode is modeled by a two-level system (see Fig. 5) and hence there are four possible fermionic states, that correspond to an empty mode, a particle on the $A$ sublattice, a particle on the $B$ sublattice, and a fully occupied mode,

$$\Psi_{\mathbf{k}} = (|11\rangle \quad |01\rangle \quad |10\rangle \quad |00\rangle),$$

where $|11\rangle = c^\dagger_{\mathbf{k},A} c^\dagger_{\mathbf{k},B}|0\rangle$ and $c^\dagger_{\mathbf{k},\sigma}$ creates an electron with momentum $\mathbf{k}$ in band $\sigma$.

In order to write the Hamiltonian with respect to this basis we introduce a set of Pauli-type matrices,

$$\sigma_x = \begin{pmatrix} 0 & 0 & 0 & 0 \\ 0 & 0 & 1 & 0 \\ 0 & 1 & 0 & 0 \\ 0 & 0 & 0 & 0 \end{pmatrix}, \quad \sigma_y = \begin{pmatrix} 0 & 0 & 0 & 0 \\ 0 & 0 & -i & 0 \\ 0 & i & 0 & 0 \\ 0 & 0 & 0 & 0 \end{pmatrix},$$

$$\sigma_z = \begin{pmatrix} 0 & 0 & 0 & 0 \\ 0 & 1 & 0 & 0 \\ 0 & 0 & -1 & 0 \\ 0 & 0 & 0 & 0 \end{pmatrix}, \quad \sigma_z^{(0)} = \begin{pmatrix} 0 & 0 & 0 & 0 \\ 0 & 0 & 0 & 0 \\ 0 & 0 & 1 & 0 \\ 0 & 0 & 0 & -1 \end{pmatrix},$$

$$\sigma_z^{(2)} = \begin{pmatrix} 1 & 0 & 0 & 0 \\ 0 & -1 & 0 & 0 \\ 0 & 0 & 0 & 0 \\ 0 & 0 & 0 & 0 \end{pmatrix}, \quad \sigma_g = \begin{pmatrix} 0 & 0 & 0 & 0 \\ 0 & 1/2 & 0 & 0 \\ 0 & 0 & 1/2 & 0 \\ 0 & 0 & 0 & 0 \end{pmatrix}.$$

For the linearized dispersion relation the Hamiltonian for each momentum point further splits into a sum of two terms,

$$H_{\mathbf{k}} = H_{0,\mathbf{k}} + H_{em}(t), \tag{A1}$$

where

$$H_{em}(t) = H_{dr,\mathbf{k}}(t) + H_{L,\mathbf{k}}(t). \tag{A2}$$

The first contribution is the equilibrium Hamiltonian without any light field applied. Except for the chemical potential it contains only terms of type $\sigma_{x,y,z}$ because the empty and the fully occupied sector do not have a unitary time evolution. In our calculations we include the chemical potential in $H_{0,\mathbf{k}}$, such that it becomes

$$H_{0,\mathbf{k}} = \Psi_k^\dagger \big[ \hbar v_F (\tau_z k_x \sigma_x + k_y \sigma_y) \\ - \mu \big( 1 + \sigma_z + \sigma_z^{(0)} + \sigma_z^{(2)} \big) \big] \Psi_k.$$

Here, $\tau_z = \pm 1$ is the valley index, describing the two Dirac points, $\mathbf{k}$ is the momentum relative to the Dirac momenta $\mathbf{K}$ and $\mathbf{K}'$, and $v_F \approx 10^6$ m/s is the Fermi velocity. We suppress spin indices.

The second and third terms represent the two light fields, that are coupled through the Peierls substitution $\mathbf{k} \to \mathbf{k} - \frac{q}{\hbar}\mathbf{A}(\mathbf{r}, t)$, with charge $q = -e$ and $e > 0$ being the elementary charge. The second term resembles the experimental driving or pump pulse and is a circularly polarized electromagnetic field propagating along the $z$ direction,

$$H_{dr,\mathbf{k}}(t) = e v_F \Psi_k^\dagger (\tau_z A_{dr,x} \sigma_x + A_{dr,y} \sigma_y) \Psi_k,$$

where

$$\mathbf{A}_{dr} = \begin{pmatrix} A_{dr,x} \\ A_{dr,y} \end{pmatrix} = -\int_0^t dt' \, \mathbf{E}_{dr}(t),$$

$$\mathbf{E}_{dr}(t) = -E_{dr}\, g_{env}(t)[\cos(\omega_{dr}t)\mathbf{e}_x + \sigma_{pol} \sin(\omega_{dr}t)\mathbf{e}_y],$$

$\sigma_{pol}$ defines the polarization of the light, $\mathbf{e}_{x,y}$ are unit vectors in the $x$ and $y$ directions, and $g_{env}(t)$ is the envelope of the pulse. The envelope $g_{env}(t)$ is either chosen to be a Gaussian envelope or a tanh-type switch on. Furthermore, we only give the fields in the $x$-$y$ plane (at $z = 0$) as, without loss of generality, we choose the graphene sheet to lie in this plane.

For $g_{env}(t) = 1$ we obtain

$$H_{dr,\mathbf{k}} = \frac{e E_{dr} v_F}{\omega_{dr}} \Psi_{\mathbf{k}}^\dagger [\tau_z \sin(\omega_{dr}t)\sigma_x - \sigma_{pol} \cos(\omega_{dr}t)\sigma_y] \Psi_{\mathbf{k}}.$$

$$\tag{A3}$$

The third term is a dc longitudinal field, that resembles the experimental probe field

$$H_{L,\mathbf{k}} = e v_F s_{switch}(t)\Psi_k^\dagger (\tau_z A_{L,x}\sigma_x + A_{L,y}\sigma_y)\Psi_k,$$

where

$$\mathbf{E}_L(t) = E_L \mathbf{e}_x,$$

$$\mathbf{A}_L(t) = -\int_0^t dt' \, E_L(t) = -E_L t \, \mathbf{e}_x,$$

and $s_{switch}(t)$ denotes a switch-on during the first 0.1 ps.

In the high-frequency limit for the pump pulse the second term of the Hamiltonian can be approximated by an effective Hamiltonian describing the low-frequency dynamics of the system [22,23],

$$H_{eff,\mathbf{k}} = -g_{env}(t)\,\sigma_{pol}\Delta_{hf}\, \Psi_k^\dagger \sigma_z \Psi_k,$$

where $\Delta_{hf} = (\hbar v_F e E_{dr})^2/(\hbar\omega_{dr})^3$.

In addition to the unitary time evolution governed by the Hamiltonian $H_{\mathbf{k}}$ we include Lindblad operators defined

in the basis that diagonalizes the instantaneous Hamiltonian $H_{\mathrm{dr},\mathbf{k}}(t)$,

$$\Phi_{\mathbf{k}} = U_{\mathbf{k}}\Psi_{\mathbf{k}},$$

where

$$U_{\mathbf{k}} = \begin{pmatrix} 1 & 0 & 0 & 0 \\ 0 & 1/\sqrt{2} & \tau_z e^{-i\tau_z\phi_k}/\sqrt{2} & 0 \\ 0 & \tau_z e^{i\tau_z\phi_k}/\sqrt{2} & -1/\sqrt{2} & 0 \\ 0 & 0 & 0 & 1 \end{pmatrix}, \quad \text{(A4)}$$

and $\phi_{\mathbf{k}}$ is defined via

$$|\mathbf{k} + e/\hbar\mathbf{A}|e^{i\phi_{\mathbf{k}}} = \left[ k_x + \frac{e}{\hbar}A_x + i\left( k_y + \frac{e}{\hbar}A_y \right) \right].$$

In this basis we introduce

$$L^\alpha = \sqrt{c_\alpha} \begin{pmatrix} 0 & \delta_{\alpha,1} & \delta_{\alpha,3} & 0 \\ \delta_{\alpha,2} & 0 & \delta_{\alpha,5} & \delta_{\alpha,7} \\ \delta_{\alpha,4} & \delta_{\alpha,6} & 0 & \delta_{\alpha,9} \\ 0 & \delta_{\alpha,8} & \delta_{\alpha,10} & 0 \end{pmatrix} \text{ for } \alpha = 1, 2, \ldots, 10,$$

$$L^{11} = \sqrt{\gamma_z}\sigma_z.$$

with for now arbitrary constants $c_\alpha$. Here, $c_5$ and $c_6$ correspond to decay effects and $\gamma_z$ corresponds to dephasing effects in the singly occupied sector. Additionally, we explicitly allow for the exchange of particles with the back gate. The timescale and dynamics for the exchange of particles are set by the damping constants $c_1$–$c_4$ and $c_7$–$c_{10}$.

We note that the transformation in Eq. (A4) is ill defined when $|\mathbf{k} + e/\hbar\mathbf{A}| = 0$. In this case $H_{\mathbf{k}} = 0$ and the instantaneous Hamiltonian is diagonal with respect to any basis. We choose to implement the same Lindblad operators as above in the original $AB$ basis for this case.

We find that the resulting equations of motion for the density matrix decouple into different sectors and write the density matrix in the sector that is relevant for computing the current as

$$\rho_{\mathbf{k}} = \sigma_g + \rho_{\mathbf{k},x}\sigma_x + \rho_{\mathbf{k},y}\sigma_y + \rho_{\mathbf{k},z}\sigma_z + \rho_{\mathbf{k},0}\sigma_z^{(0)} + \rho_{\mathbf{k},2}\sigma_z^{(2)}.$$

The resulting equations of motion are

$$\hbar\partial_t\rho_{\mathbf{k},x} = \delta_{\mathbf{k}+e\mathbf{A}}\rho_{\mathbf{k},z} - \epsilon_{\mathbf{k}+e\mathbf{A}}\rho_{\mathbf{k},y} - [\Gamma + (c_1 + c_3 + c_8 + c_{10})/2]\rho_{\mathbf{k},x},$$

$$\hbar\partial_t\rho_{\mathbf{k},y} = \epsilon_{\mathbf{k}+e\mathbf{A}}\rho_{\mathbf{k},x} - [\Gamma + (c_1 + c_3 + c_8 + c_{10})/2]\rho_{\mathbf{k},y},$$

$$\hbar\partial_t\rho_{\mathbf{k},z} = \delta_{\mathbf{k}+e\mathbf{A}}\rho_{\mathbf{k},x} + c_3(1/2 + \rho_{\mathbf{k},0} - \rho_{\mathbf{k},z}) - c_4\rho_{\mathbf{k},2} + c_5(1/2 + \rho_{\mathbf{k},0} - \rho_{\mathbf{k},z}) - c_6(1/2 + \rho_{\mathbf{k},z} - \rho_{\mathbf{k},2})$$
$$- c_7\rho_{\mathbf{k},0} - c_8(1/2 + \rho_{\mathbf{k},z} - \rho_{\mathbf{k},2}),$$

$$\hbar\partial_t\rho_{\mathbf{k},0} = -(c_7 + c_9)\rho_{\mathbf{k},0} - c_{10}(1/2 + \rho_{\mathbf{k},0} - \rho_{\mathbf{k},z}) - c_8(1/2 + \rho_{\mathbf{k},z} - \rho_{\mathbf{k},2}),$$

$$\hbar\partial_t\rho_{\mathbf{k},2} = -(c_2 + c_4)\rho_{\mathbf{k},2} + c_3(1/2 + \rho_{\mathbf{k},0} - \rho_{\mathbf{k},z}) + c_1(1/2 + \rho_{\mathbf{k},z} - \rho_{\mathbf{k},2}),$$

where

$$\gamma_2 = (c_5 + c_6)/2 + 2\gamma_z,$$
$$\epsilon_{\mathbf{k}+e\mathbf{A}} = 2\tau_z v_{\mathrm{F}}[\hbar|\mathbf{k}| + e\mathbf{k}\cdot\mathbf{A}/|\mathbf{k}|],$$
$$\delta_{\mathbf{k}+e\mathbf{A}} = 2\tau_z v_{\mathrm{F}}[e\mathbf{A}\times\mathbf{k}/|\mathbf{k}|].$$

We note that while we give the equations of motion in the basis diagonalizing $H_{0,\mathbf{k}}$ here, we implement them in the original $AB$ basis in the numerical simulations.

We choose the damping constants Boltzmann distributed

$$\gamma_2 = 1/T_2,$$
$$c_5 = c_6\exp(-2\beta\epsilon), \quad c_5 + c_6 = 1/T_1,$$
$$c_1 = c_2\exp[-\beta(-\epsilon - \mu)], \quad c_1 + c_2 = 1/T_p,$$
$$c_3 = c_4\exp[-\beta(\epsilon - \mu)], \quad c_3 + c_4 = 1/T_p,$$
$$c_7 = c_8\exp[-\beta(\epsilon - \mu)], \quad c_7 + c_8 = 1/T_p,$$

and

$$c_9 = c_{10}\exp[-\beta(-\epsilon - \mu)], \quad c_9 + c_{10} = 1/T_p,$$

where $\epsilon = v_{\mathrm{F}}\sqrt{(\hbar k_x + eA_x)^2 + (\hbar k_y + eA_y)^2}$ are the instantaneous eigenenergies.

This ensures that the ground state of the system without the light field is Fermi distributed with chemical potential $\mu$ and inverse temperature $\beta = 1/(k_BT)$.

Note that $T_1$ and $T_2$ are the commonly introduced decoherence measures. In analogy we define a third timescale $T_p$ for the exchange of particles with the back gate.

We solve the master equation numerically and then compute the current for each momentum point,

$$\mathbf{j}_{\mathbf{k}} = \left\langle \frac{\partial H_{\mathbf{k}}}{\partial\mathbf{A}} \right\rangle = ev_{\mathrm{F}}(\tau_z\langle\sigma_x\rangle\mathbf{e}_x + \langle\sigma_y\rangle\mathbf{e}_y),$$

where the Pauli matrices here refer to the singly occupied sector and empty and doubly occupied modes do not contribute to the current. The conductivity is then obtained as $\sigma_{\mathrm{xy}}(\mathbf{k}) = \lim_{E_L\to 0}\mathbf{j}_{y,\mathbf{k}}/E_L$. We perform the calculation of $\mathbf{j}_{y,\mathbf{k}}$ at experimentally realistic values of $E_L$, and have checked that these values realize the linear response limit. Finally, we define the conductivity density

$$\tilde{\sigma}_{\mathrm{xy}} = \frac{1}{A}\sigma_{\mathrm{xy}}(\mathbf{k}),$$

where $A$ is the lattice size and the full conductivity

$$\sigma_{\mathrm{xy}} = \sum_{\mathbf{k}}\tilde{\sigma}_{\mathrm{xy}}.$$

We note that a similar method for the calculation of current has been used in Ref. [34]. The crucial difference is that we explicitly allow for the exchange of particles by including the empty and the fully occupied mode. In particular this also implies that we introduce a separate timescale for particle-exchange processes $T_p$. Also in our case the trace of the density matrix is ensured to be 1 at all times as in Ref. [34]. Quantitatively the approach presented here yields better agreement to experimental data from Ref. [16]. Furthermore, including the empty and doubly occupied mode is crucial for the calculation of the single-particle correlation function.

## APPENDIX B: ROTATING-WAVE APPROXIMATION FOR GRAPHENE: RABI-BLOCH BANDS

We start from the graphene Hamiltonian from Eq. (A1) with no longitudinal field,

$$H_{\mathbf{k}} = H_{0,\mathbf{k}} + H_{\mathrm{dr},\mathbf{k}}(t).$$

The undriven Hamiltonian is diagonalized by

$$H_0^d = U^\dagger H_0 U = \hbar v_{\mathrm{F}} k \sigma_z,$$

$$U = 1/\sqrt{2}\begin{pmatrix} 1 & 1 \\ e^{i\phi_k} & -e^{i\phi_k} \end{pmatrix},$$

$$e^{i\phi_k} = \frac{\tau_z k_x + i k_y}{k}.$$

In this basis the driving Hamiltonian is

$$H_{\mathrm{dr},\mathbf{k}}(t) = \frac{eE_{\mathrm{dr}}v_{\mathrm{F}}}{\omega_{\mathrm{dr}}}\begin{pmatrix} \tau_z s_{\mathrm{dr}} & -i\sigma_{\mathrm{pol}}c_{\mathrm{dr}} \\ i\sigma_{\mathrm{pol}}c_{\mathrm{dr}} & -\tau_z s_{\mathrm{dr}} \end{pmatrix},$$

where

$$s_{\mathrm{dr}} = \sin(\omega_{\mathrm{dr}}t - \tau_z\sigma_{\mathrm{pol}}\phi_k),$$

$$c_{\mathrm{dr}} = \cos(\omega_{\mathrm{dr}}t - \tau_z\sigma_{\mathrm{pol}}\phi_k).$$

Next, we do the rotating-wave approximation, keeping only those terms nonoscillatory in the rotating frame. Then

$$H_{\mathrm{dr},\mathbf{k}}(t) \approx \frac{\sigma_{\mathrm{pol}}eE_{\mathrm{dr}}v_{\mathrm{F}}}{2\omega_{\mathrm{dr}}}\begin{pmatrix} 0 & -ie^{-i\omega_{\mathrm{dr}}t+i\tau_z\sigma_{\mathrm{pol}}\phi_k} \\ ie^{i\omega_{\mathrm{dr}}t-i\tau_z\sigma_{\mathrm{pol}}\phi_k} & 0 \end{pmatrix}.$$

In analogy to the Rabi problem the system can now be solved analytically. The eigenenergies are $E_{\mathrm{R},\pm} = -\hbar\omega_{\mathrm{dr}}/2 \pm \hbar\Omega_{\mathrm{R}}$ and the eigenstates are

$$|\psi(t)\rangle = |\psi_{\mathrm{R},+}(t)\rangle e^{-i\Omega_{\mathrm{R}}t} + |\psi_{\mathrm{R},-}(t)\rangle e^{i\Omega_{\mathrm{R}}t},$$

where

$$|\psi_{\mathrm{R},\pm}(t)\rangle = \begin{pmatrix} -i\sigma_{\mathrm{pol}}e^{i\tau_z\sigma_{\mathrm{pol}}\phi_k}\left(a \mp \frac{a\Delta - b\lambda}{\Omega_{\mathrm{R}}}\right)e^{-i\omega_{\mathrm{dr}}t/2} \\ \left(b \pm \frac{b\Delta + a\lambda}{\Omega_{\mathrm{R}}}\right)e^{i\omega_{\mathrm{dr}}t/2} \end{pmatrix}.$$

Furthermore,

$$\Delta = \frac{\omega_{\mathrm{dr}} - 2v_{\mathrm{F}}k}{2},$$

$$\Omega_{\mathrm{R}} = \sqrt{\lambda^2 + \Delta^2},$$

$$\lambda = \frac{eE_{\mathrm{dr}}v_{\mathrm{F}}}{2\hbar\omega_{\mathrm{dr}}},$$

and the constants $a$ and $b$ are integration constants constrained by normalizing $|\psi_{\mathrm{R},\pm}(t)\rangle$. The remaining freedom in $a$ and $b$ determines the initial state. The band velocity in the $y$ direction is immediately obtained as

$$v_y^\pm(\mathbf{k}) = \partial_y E_{\mathrm{R},\pm}.$$

Further, note that

$$\sigma_{\mathrm{pol}}e^{i\tau_z\sigma_{\mathrm{pol}}\phi_k} = \frac{\tau_z(\sigma_{\mathrm{pol}}k_x + ik_y)}{k}.$$

Next, we determine the instantaneous Berry curvature. For this we need the eigenstates with respect to the original $AB$ basis,

$$\left|\psi_{\mathrm{R},\pm}^{AB}(t)\right\rangle = U\left|\psi_{\mathrm{R},\pm}(t)\right\rangle.$$

The Berry connection is now given by

$$A_j^\pm = i\left\langle\psi_{\mathrm{R},\pm}^{AB}|\partial_j|\psi_{\mathrm{R},\pm}^{AB}\right\rangle,$$

and as a result we obtain the Berry curvature as

$$\Omega^\pm(\mathbf{k}) = \partial_y A_x - \partial_x A_y$$
$$= \pm\frac{\sigma_{\mathrm{pol}}v_{\mathrm{F}}\lambda^2}{2k\Omega_{\mathrm{R}}^3} \pm \frac{\mathrm{Re}[(k_y + i\sigma_{\mathrm{pol}}k_x)e^{i\omega_{\mathrm{dr}}t}]v_{\mathrm{F}}\lambda\Delta}{2k^2\Omega_{\mathrm{R}}^3}.$$

Finally, we can compute the resulting Hall conductivity from Eq. (1) from the main text, where the Rabi occupations are computed from the density matrix $\rho_{\mathbf{k}}$ as

$$n_{\mathrm{R},\pm}(\mathbf{k}) = \left\langle\psi_{\mathrm{R},\pm}^{AB}|\rho_{\mathbf{k}}|\psi_{\mathrm{R},\pm}^{AB}\right\rangle.$$

Note that both the Berry curvature and the occupations are time dependent. Therefore there is a time-independent contribution from time-dependent curvature and occupations. We have checked that this contribution is at least an order of magnitude smaller than the time-independent contribution and hence the quantities can be averaged independently $\overline{\Omega^\pm(\mathbf{k},t)n_{\mathrm{R},\pm}(\mathbf{k},t)} \approx \overline{\Omega^\pm(\mathbf{k},t)}\ \overline{n_{\mathrm{R},\pm}(\mathbf{k},t)}$. Hence we can drop the second, time-dependent contribution to the Berry curvature.

## APPENDIX C: NUMERICAL RESULTS WITHIN THE RABI APPROXIMATION

As described in the main text, mapping graphene onto the Rabi problem is a good approximation close to the first resonance. By the nature of the approximations made the Rabi results are not valid close to the Dirac point and hence the contribution of the Dirac point cannot be captured. We have therefore shifted the curves in Fig. 3(b), such that only the conductivity density of the first resonance is integrated. For completeness we show the unshifted version in Fig. 6(a). For the low dissipation considered the Dirac point obtains a significant contribution that is larger than the contribution of the first resonance. We also show results for higher dissipation in Figs. 6(b) and 6(c), where the contribution of the Dirac point is small.

## APPENDIX D: CALCULATION OF SINGLE-PARTICLE CORRELATION FUNCTION

Given a density matrix at a certain time $\rho(t_1)$ by the numerical methods of Appendix A, the single-particle correlation
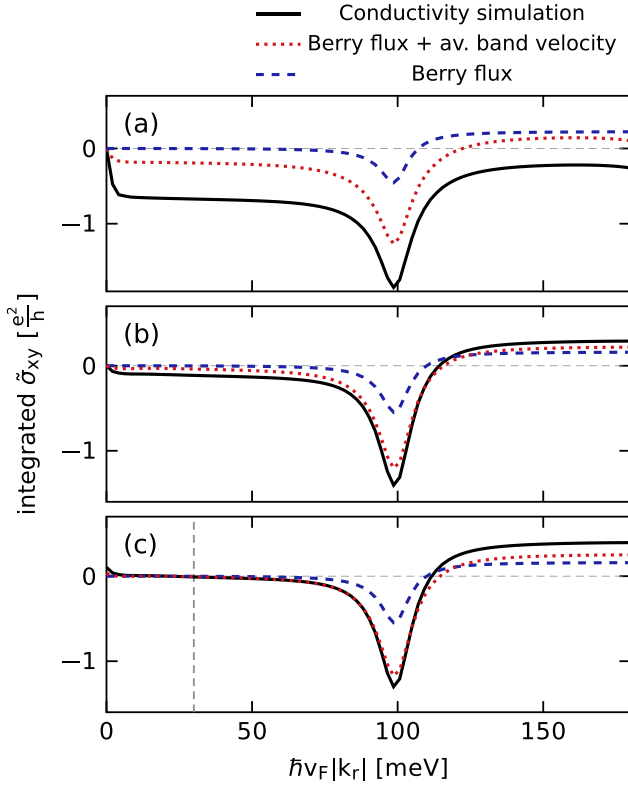
FIG. 6. We depict the conductivity density, integrated over a disk in momentum space of radius $\mathbf{k}_r$. For comparison, we show the momentum-resolved Berry flux, integrated over the same disk in momentum space, and the sum of the integrated Berry flux and the integrated average band velocity. Both are obtained within the Rabi approximation. In (c) the curves have been shifted such that their value vanishes at $\hbar v_F |k_r| = 30$ meV for a better comparison of the contribution of the first resonance. In all plots we use $E_{\mathrm{dr}} = 3$ MV/m, $\omega_{\mathrm{dr}} = 2\pi \cdot 48$ THz $\approx 200$ meV/$\hbar$, $T = 80$ K, $E_L = 0.84$ kV/m, $\mu = 0$, and the driving pulse is ramped with a tanh over 1 ps. (a) shows $T_1 = 50$ ps, $T_2 = 10$ ps, $T_p = 20$ ps, while (b) and (c) show $T_1 = 4$ ps, $T_2 = 0.8$ ps, $T_p = 1.6$ ps.

function $\langle c(t_2)^\dagger c(t_1) \rangle$ can be calculated. The state is acted upon with an annihilation operator $c$ which gives a matrix of the shape

$$c\rho(t_1) = \begin{pmatrix} 0 & 0 & 0 & 0 \\ r_1 & 0 & 0 & 0 \\ r_2 & 0 & 0 & 0 \\ 0 & r_3 & r_4 & 0 \end{pmatrix}.$$

This object is evolved to a later time $t_2$ using the equations of motion

$$\dot{r}_1 = -r_1(i\mu + \Gamma_1 + \Gamma_3 + \Gamma_4) - e^{-i\phi} r_2(+iv_F|q| + \Gamma_3 - \Gamma_4),$$
$$\dot{r}_2 = -r_2(i\mu + \Gamma_1 + \Gamma_3 + \Gamma_4) - e^{+i\phi} r_1(+iv_F|q| + \Gamma_3 - \Gamma_4),$$
$$\dot{r}_3 = -r_3(i\mu + \Gamma_2 + \Gamma_3 + \Gamma_4) - e^{+i\phi} r_4(-iv_F|q| + \Gamma_3 - \Gamma_4),$$
$$\dot{r}_4 = -r_4(i\mu + \Gamma_2 + \Gamma_3 + \Gamma_4) - e^{-i\phi} r_3(-iv_F|q| + \Gamma_3 - \Gamma_4),$$

where

$$\Gamma_1 = \tfrac{1}{2}(\gamma_-^{(ud)} + \gamma_-^{(ld)} + \gamma_z), \quad \Gamma_2 = \tfrac{1}{2}(\gamma_+^{(uu)} + \gamma_+^{(lu)} + \gamma_z),$$
$$\Gamma_3 = \tfrac{1}{4}(\gamma_-^{(b)} + \gamma_-^{(uu)} + \gamma_+^{(ud)}), \quad \Gamma_4 = \tfrac{1}{4}(\gamma_+^{(b)} + \gamma_-^{(lu)} + \gamma_+^{(ld)}).$$

Here, it is $q = q_x + iq_y$ the momentum and $\phi = \arg(q)$ its phase. $\mu$ is the chemical potential.

At any time $t_2$ this state can be acted upon with $c^\dagger$ and traced over to give the correlation function.

The occupations of the system are then calculated using an approach inspired by trARPES [36],

$$n(\mathbf{k}, \omega) = \frac{1}{t - t_0} \int_{t_0}^t \int_{t_0}^t \langle c^\dagger(t_2)c(t_1) \rangle e^{i\omega(t_2 - t_1)} dt_1 dt_2$$

$$= \frac{2}{t - t_0} \mathrm{Re}\left[ \int_{t_0}^t \int_{t_1}^t \langle c^\dagger(t_2)c(t_1) \rangle e^{i\omega(t_2 - t_1)} dt_2 dt_1 \right].$$

The occupations of the individual Floquet bands are assigned by integrating $n(\mathbf{k}, \omega)$ over frequency intervals of multiples of $\omega_d/2$, starting and ending centered at the band gaps,

$$n_{\alpha, \pm}(\mathbf{k}) = \int_{(\alpha - \frac{1}{4} \pm \frac{1}{4})\omega_d}^{(\alpha + \frac{1}{4} \pm \frac{1}{4})\omega_d} n(\mathbf{k}, \omega) d\omega.$$

The effective Floquet band occupations are found by summation over the Floquet index,

$$n_\pm(\mathbf{k}) = \sum_\alpha n_{\alpha, \pm}(\mathbf{k}).$$

## APPENDIX E: FLOQUET-BERRY CURVATURE CALCULATION

Here, we present the details on the calculation of the Berry curvature of Floquet bands. For each momentum $\mathbf{k}$ we use the quasienergy operator in the extended Floquet-Hilbert space (for details, see, for example, Ref. [39])

$$Q = \begin{pmatrix} \ddots & \vdots & \vdots & \ddots \\ \cdots & H_0 & H_1 & \cdots \\ \cdots & H_{-1} & H_0 + \hbar\omega_{\mathrm{dr}} & \cdots \\ \ddots & \vdots & \vdots & \ddots \end{pmatrix},$$

where

$$H_m = \int dt \, e^{-im\omega_{\mathrm{dr}}t}[H_{0,\mathbf{k}} + H_{\mathrm{dr},\mathbf{k}}(t)]$$

and

$$g_{\mathrm{env}}(t) = 1.$$

In order to get the Floquet eigenstates and eigenenergies we diagonalize $Q$ after truncating such that $-4 \leqslant m \leqslant 4$. The Floquet band structure is obtained from combining the eigenenergies of different momentum points. Subsequently we use the method presented in Ref. [40] in order to determine the Berry curvature numerically. Finally, the Floquet band velocity is obtained by numerically computing the momentum derivative of the Floquet eigenenergies.
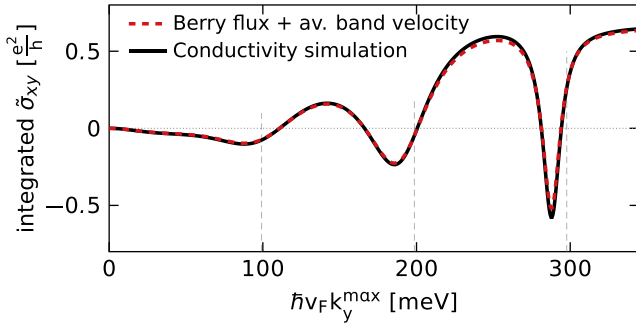
FIG. 7. We show the conductivity density $\tilde{\sigma}_{xy}$ integrated over momenta in an interval on the $y$ axis, specifically fulfilling $k_x = 0$, $|k_y| < k_y^{max}$. This integrated conductivity agrees with the sum over the Berry flux and the average band velocity, integrated over the same interval. The parameters are $E_{dr} = 26$ MV/m, $\omega_{dr} = 2\pi \cdot 48$ THz $\approx 200$ meV$/\hbar$, $T_1 = 1$ ps, $T_2 = 0.2$ ps and $T_p = 0.4$ ps, $T = 80$ K, and $E_L = 1.7$ kV/m. All observables are shown after a steady state is achieved for a tanh-type ramp of the driving field strength.

## APPENDIX F: WEYL GAUGE

Here, we discuss the meaning of different gauge choices and their importance for our method. For all our calculations we choose the Weyl gauge, i.e., we choose the scalar potential $\phi = 0$ and the time-dependent vector potential $\mathbf{A}(\mathbf{r}, t) = -\int dt\, \mathbf{E}(\mathbf{r}, t)$. Using the Peierls substitution $\mathbf{k} \to \mathbf{k} - \frac{q}{\hbar}\mathbf{A}(\mathbf{r}, t)$ this leads to a time-dependent shift of the momentum in the Hamiltonian. This can be viewed as a time-dependent shift of the band structure. The Weyl gauge is particularly useful for an electric field that is spatially constant within the graphene sheet in the $x$-$y$ plane. In this case the vector potential within the $x$-$y$ plane can also be chosen independent of position and hence the contribution to the Hamiltonian decouples in momentum space. As an example for the choice of gauge we consider a uniform electric field $\mathbf{E} = E\hat{\mathbf{e}}_x$ and vanishing magnetic field $\mathbf{B} = 0$. For this case the Weyl gauge implies $\mathbf{A} = -\mathbf{E}t$. The vector potential is indeed independent of position. An alternative gauge choice would be a special case of the Coulomb gauge, $\mathbf{A} = 0$. This choice implies $\phi = Ex$ which can be viewed as a tilt of the lattice potential. The resulting Hamiltonian obtains a nontrivial spatial dependence and hence is no longer diagonal in momentum space.

## APPENDIX G: HALL CONDUCTIVITY FOR A CUT ALONG THE $Y$ DIRECTION

In Fig. 7 we display the momentum-resolved contributions to the conductivity, integrated over the momentum state interval from $-k_y^{max}$ to $k_y^{max}$ on the $k_y$ axis. The corresponding integral over the contributions to $n\bar{v}/E_L + \Phi_{xy}$ are depicted as well. We find essentially perfect agreement for these quantities. Hence, the deviations between these quantities in Fig. 4(a) in the main text arise predominantly from the $k_x$ direction, where the average band velocity vanishes and only the Berry flux contributes.
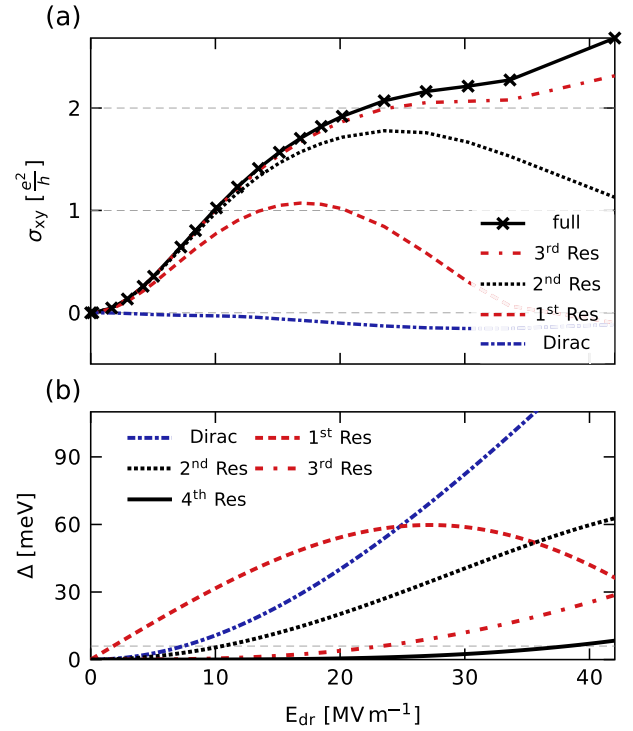


FIG. 8. (a) Resonance-resolved conductivity dichroism as a function of electric-field strength. The solid black line shows the full current, while the dashed-dotted blue line shows only the contribution from the gap at the Dirac point and other lines show the contributions up to and including the $n$th resonance as indicated in the legend. (b) Gap sizes as a function of electric-field strength. The dashed-dotted blue line shows the gap at the Dirac point, while other lines show the gaps at the $n$th resonance as indicated in the legend. The dashed gray line shows the approximate scale of temperature, damping, and dephasing effects $k_B T \approx \hbar/T_1 \approx 6$ meV. The parameters used are $\omega_{dr} = 2\pi \cdot 48$ THz $\approx 200$ meV$/\hbar$, $T_1 = 100$ fs, $T_2 = 20$ fs, $T_p = 40$ fs $T = 80$ K, $E_L = 1.7$ kV/m, $\mu = 0$, and the envelope of the driving pulse is a tanh-type interpolation from 0 to 1, that reaches 1 after 1 ps.

## APPENDIX H: SUBSEQUENT OPENING OF GAPS

For larger electric field strength it is no longer sufficient to consider the first resonance only. The contribution in the high-frequency limit without damping has been analyzed in Refs. [22–26]. In this limit there are no resonant contributions and the total Hall current is $\sigma_{xy} = -2\frac{e^2}{h}$. For this result it is assumed that only the lower graphene band is occupied. Under experimental conditions finite frequency driving leads to excitations into the upper graphene band. For intermediate driving strength the Berry curvature is still well localized around the Dirac point and individual resonances. We can therefore investigate each of the contributions separately. Depending on the strength of damping and dephasing effects one obtains a steady state with significant occupation in the upper graphene band close to the Dirac point [see Fig. 1(a)]. The upper band has opposite Berry curvature and hence contributes to the Hall current with opposite sign. Hence the Hall current arising from the Dirac point is significantly reduced for experimental conditions. Since the occupation of the lower band is always
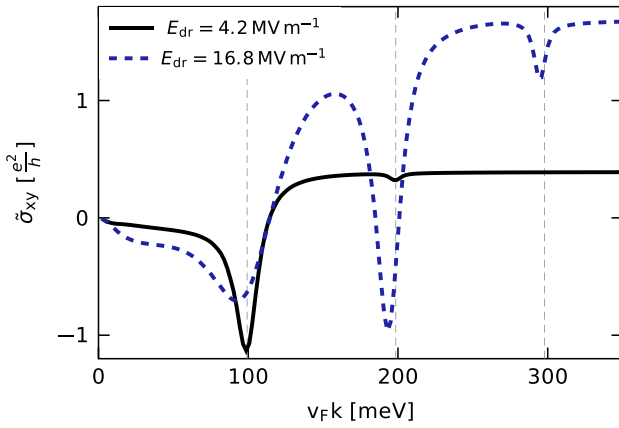
FIG. 9. Integrated Hall conductivities. We show the sum of the conductivity for all momenta smaller than a threshold value as a function of threshold momentum. The first, second, and third resonance are indicated by dashed lines. We use $\omega_{dr} = 2\pi \cdot 48$ THz $\approx 200$ meV$/\hbar$, $T_1 = 1$ ps, $T_2 = 200$ fs, $T_p = 200$ fs, $T = 80$ K, $E_L = 1.7$ kV/m, $\mu = 0$, and the envelope of the driving pulse is a tanh-type interpolation from 0 to 1, that reaches 1 after 1 ps.

larger than the one of the upper band the net contribution from the Dirac point is always negative.

The main resonant contribution comes from those gaps that are lying on the original lower Dirac cone. For these gaps the Floquet band below the gap has positive curvature while the band above has equal and opposite curvature. Hence for equal occupation of both bands close to the gap, there is no net contribution to the current. This is the case for higher-order

gaps with a magnitude smaller than temperature and damping. We say that these gaps are closed [see Fig. 8(b)]. In Fig. 8 only the first gap is open for electric-field strengths smaller than 8 MV/m. In this regime the current is well described by the Rabi-Berry curvature. For field strengths larger than 10 MV/m we expect the current arising from the first resonance to saturate. The reduction that can be seen in this regime in Fig. 8 is a numerical artifact that we explain in Appendix I. While the current arising from the first resonance saturates, the second resonance gap opens and for higher $E_{dr}$ leads to a further increase of the Hall conductivity. At even higher field strengths the higher-order gaps open subsequently. For each gap the net contribution to the current is positive since there is more occupation in the band below the gap than in the one above. Hence the total resonant contribution is opposite to the high-frequency contribution. Furthermore, we find numerically that the magnitude of the high-frequency contribution is always smaller than the magnitude of the resonant contributions and usually is a minor effect. This is in agreement with the sign of the current in Ref. [16].

## APPENDIX I: RESONANCE-RESOLVED CONDUCTIVITY AND RESONANCE BROADENING

For low driving field strength $E_{dr}$ the current is well localized around individual resonances. In contrast, for large $E_{dr}$ resonances start overlapping and it is therefore difficult to identify the current arising from individual resonances. We show an example of this phenomenon in Fig. 9. For low values of $E_{dr}$ there is no contribution to the current in between resonances. Hence the integrated conductivity shown in Fig. 9 is constant. For larger values of $E_{dr}$ resonances get broadened
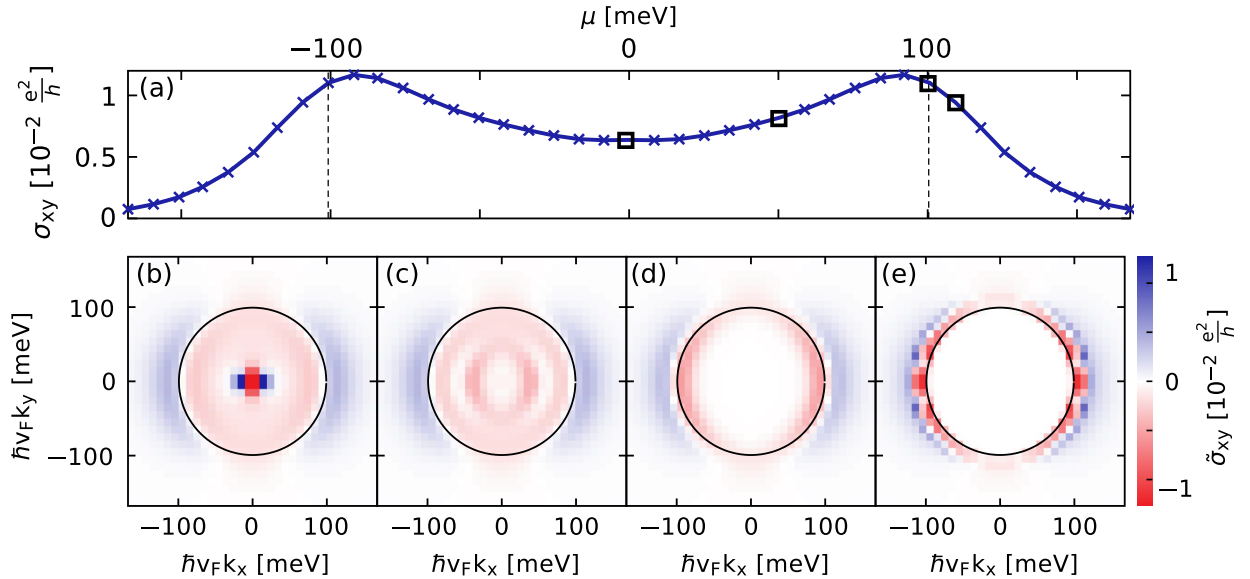


FIG. 10. Circular dichroism of the transverse conductivity. (a) shows the total conductivity as a function of applied chemical potential. (b)–(e) show the momentum-resolved conductivity for several different chemical potentials as indicated by black squares in (a). The panels are aligned in the same order as the squares in (a). Black circles denote the position of the first bare resonance $2v_F k = \omega_{dr}$. For these panels we average the conductivity of opposite momentum modes $\overline{\sigma}_y(\mathbf{k}) = [\sigma_y(\mathbf{k}) + \sigma_y(-\mathbf{k})]/2$ and for both Dirac points. The center of each panel (0,0) is positioned at the Dirac point. The parameters for all panels are $E_{dr} = 1$ MV/m, $\omega_{dr} = 2\pi \cdot 48$ THz, $T_1 = 100$ fs, $T_2 = 20$ fs, $T_p = 25$ fs, $T = 80$ K, $E_L = 840$ V/m, and $g_{env}(t)$ is a Gaussian envelope with a full width at half maximum $t_{FWHM} = 1$ ps.
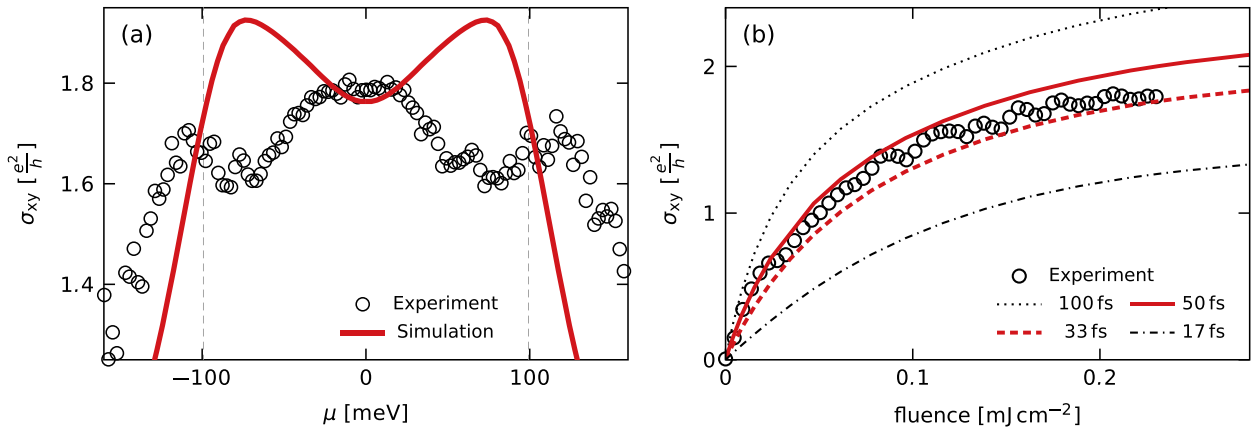
FIG. 11. (a) Chemical-potential-resolved circular dichroism of the transverse conductivity. Black circles show experimental data from Ref. [16] and the solid red line shows results from our numerical simulation. Here, $\mu$ is the chemical potential of the initial state and we do not allow for the exchange of particles during the simulation. (b) Fluence dependence of the current dichroism for several values of the particle-exchange timescale $T_p$, as indicated in the legend. We see that a value in the range of $T_p = 30$–50 fs is consistent with the experiment. For both panels the parameters for the numerical simulation are $\omega_{dr} = 2\pi \cdot 48$ THz $\approx 200$ meV$/\hbar$, $T_1 = 100$ fs, $T_2 = 20$ fs, $T = 80$ K, $E_L = 1.7$ kV/m, and the driving pulse has a Gaussian envelope with electric-field strength FWHM of $\sqrt{2}$ ps, corresponding to intensity FWHM of 1 ps. Furthermore, we use $E_{dr} = 26$ MV/m and $T_p = 36$ fs in (a) and $\mu = 0$ in (b). For details on the experimental data, see Ref. [16].

and there is no such constant regime. This is an indication that the contribution of neighboring resonances is now overlapping. Since the contribution from resonances is always negative below and positive above the resonance, overlapping resonances lead to canceling contributions.

When we compute the resonance-resolved conductivity as in Fig. 8, we do this by integrating the current up to the momentum value halfway in between the corresponding resonances. In other words we use the corresponding value of the curve in Fig. 9. Once resonances start overlapping the contributions cancel and hence lead to decreasing contributions of the inner resonances. This is the reason why the curves in Fig. 8 decrease.

## APPENDIX J: CHEMICAL POTENTIAL DEPENDENCE AT LOW FLUENCE

The momentum-resolved conductivity allowed us to identify the different contributions to the transverse current. In experiment, however, such data are not easily accessible. Instead it is possible to tune the applied back gate, i.e., the chemical potential [16]. When increasing the chemical potential, momenta close to the Dirac point are fully occupied and, due to Pauli blocking, do not contribute to the conductivity. For momentum modes smaller than the first bare resonance negative contributions to the conductivity dominate. For increasing chemical potential conductivity from these modes

becomes suppressed and the total conductivity increases (see Fig. 10). Near the first resonance the situation reverses. Now momentum modes above the resonance become fully occupied and increasing the chemical potential further leads to decreasing total conductivity. Hence the chemical-potential-resolved transverse conductivity shows a clear signature of the resonant behavior.

## APPENDIX K: COMPARISON OF FIXED CHEMICAL POTENTIAL AND FIXED DENSITY

For the simulation of the experiment from Ref. [16] it is crucial to work at a fixed chemical potential instead of a fixed density. To illustrate the difference we show a simulation enforcing fixed density for each momentum mode during the time evolution in Fig. 11(a). The parameters are the same as in Fig. 2(a) in the main text. The shape of the curve is fundamentally different from the experimental data. We conclude that the exchange of electrons with nonilluminated regions of the graphene sample as well as with the substrate is important even on the short timescales of the circularly polarized pulse.

## APPENDIX L: FLUENCE DEPENDENCE

For completeness and for better comparison to the experiments in Ref. [16] we show the data from Fig. 2(b) in the main text as a function of fluence instead of peak driving field in Fig. 11(b).

[1] D. Fausti, R. I. Tobey, N. Dean, S. Kaiser, A. Dienst, M. C. Hoffmann, S. Pyon, T. Takayama, H. Takagi, and A. Cavalleri, Light-induced superconductivity in a stripe-ordered cuprate, Science **331**, 189 (2011).

[2] W. Hu, S. Kaiser, D. Nicoletti, C. R. Hunt, I. Gierz, M. C. Hoffmann, M. Le Tacon, T. Loew, B. Keimer, and A. Cavalleri,

Optically enhanced coherent transport in YBa$_2$Cu$_3$O$_{6.5}$ by ultrafast redistribution of interlayer coupling, Nat. Mater. **13**, 705 (2014).

[3] M. Mitrano, A. Cantaluppi, D. Nicoletti, S. Kaiser, A. Perucchi, S. Lupi, P. Di Pietro, D. Pontiroli, M. Riccò, S. R. Clark, D. Jaksch, and A. Cavalleri, Giant THz photoconductivity and

possible non-equilibrium superconductivity in metallic $K_3C_{60}$, Nature (London) **530**, 461 (2016).

[4] J.-i. Okamoto, A. Cavalleri, and L. Mathey, Theory of Enhanced Interlayer Tunneling in Optically Driven High-$T_c$ Superconductors, Phys. Rev. Lett. **117**, 227001 (2016).

[5] J.-i. Okamoto, W. Hu, A. Cavalleri, and L. Mathey, Transiently enhanced interlayer tunneling in optically driven high-$T_c$ superconductors, Phys. Rev. B **96**, 144505 (2017).

[6] D. N. Basov, R. D. Averitt, and D. Hsieh, Towards properties on demand in quantum materials, Nat. Mater. **16**, 1077 (2017).

[7] M. Aidelsburger, M. Atala, S. Nascimbène, S. Trotzky, Y.-A. Chen, and I. Bloch, Experimental Realization of Strong Effective Magnetic Fields in an Optical Lattice, Phys. Rev. Lett. **107**, 255301 (2011).

[8] L. Tarruell, D. Greif, T. Uehlinger, G. Jotzu, and T. Esslinger, Creating, moving and merging Dirac points with a Fermi gas in a tunable honeycomb lattice, Nature (London) **483**, 302 (2012).

[9] T. Uehlinger, D. Greif, G. Jotzu, L. Tarruell, T. Esslinger, L. Wang, and M. Troyer, Double transfer through Dirac points in a tunable honeycomb optical lattice, Eur. Phys. J.: Spec. Top. **217**, 121 (2013).

[10] J. Struck, M. Weinberg, C. Ölschläger, P. Windpassinger, J. Simonet, K. Sengstock, R. Höppner, P. Hauke, A. Eckardt, M. Lewenstein, and L. Mathey, Engineering Ising-XY spin-models in a triangular lattice using tunable artificial gauge fields, Nat. Phys. **9**, 738 (2013).

[11] G. Jotzu, M. Messer, R. Desbuquois, M. Lebrat, T. Uehlinger, D. Greif, and T. Esslinger, Experimental realization of the topological Haldane model with ultracold fermions, Nature (London) **515**, 237 (2014).

[12] M. Aidelsburger, M. Lohse, C. Schweizer, M. Atala, J. T. Barreiro, S. Nascimbène, N. R. Cooper, I. Bloch, and N. Goldman, Measuring the Chern number of Hofstadter bands with ultracold bosonic atoms, Nat. Phys. **11**, 162 (2015).

[13] M. Lohse, C. Schweizer, O. Zilberberg, M. Aidelsburger, and I. Bloch, A Thouless quantum pump with ultracold bosonic atoms in an optical superlattice, Nat. Phys. **12**, 350 (2016).

[14] C. Grossert, M. Leder, S. Denisov, P. Hänggi, and M. Weitz, Experimental control of transport resonances in a coherent quantum rocking ratchet, Nat. Commun. **7**, 10440 (2016).

[15] S. Nakajima, T. Tomita, S. Taie, T. Ichinose, H. Ozawa, L. Wang, M. Troyer, and Y. Takahashi, Topological Thouless pumping of ultracold fermions, Nat. Phys. **12**, 296 (2016).

[16] J. W. McIver, B. Schulte, F.-U. Stein, T. Matsuyama, G. Jotzu, G. Meier, and A. Cavalleri, Light-induced anomalous Hall effect in graphene, Nat. Phys. **16**, 38 (2020).

[17] H. L. Calvo, H. M. Pastawski, S. Roche, and L. E. F. Foa Torres, Tuning laser-induced band gaps in graphene, Appl. Phys. Lett. **98**, 232103 (2011).

[18] G. Usaj, P. M. Perez-Piskunow, L. E. F. Foa Torres, and C. A. Balseiro, Irradiated graphene as a tunable Floquet topological insulator, Phys. Rev. B **90**, 115423 (2014).

[19] P. M. Perez-Piskunow, G. Usaj, C. A. Balseiro, and L. E. F. Foa Torres, Floquet chiral edge states in graphene, Phys. Rev. B **89**, 121401(R) (2014).

[20] H. Dehghani, T. Oka, and A. Mitra, Dissipative Floquet topological systems, Phys. Rev. B **90**, 195429 (2014).

[21] K. Kristinsson, O. V. Kibis, S. Morina, and I. A. Shelykh, Control of electronic transport in graphene by electromagnetic dressing, Sci. Rep. **6**, 20082 (2016).

[22] T. Oka and H. Aoki, Photovoltaic Hall effect in graphene, Phys. Rev. B **79**, 081406(R) (2009).

[23] T. Kitagawa, E. Berg, M. Rudner, and E. Demler, Topological characterization of periodically driven quantum systems, Phys. Rev. B **82**, 235114 (2010).

[24] T. Kitagawa, T. Oka, A. Brataas, L. Fu, and E. Demler, Transport properties of nonequilibrium systems under the application of light: Photoinduced quantum Hall insulators without Landau levels, Phys. Rev. B **84**, 235108 (2011).

[25] H. Dehghani, T. Oka, and A. Mitra, Out-of-equilibrium electrons and the Hall conductance of a Floquet topological insulator, Phys. Rev. B **91**, 155422 (2015).

[26] T. Mikami, S. Kitamura, K. Yasuda, N. Tsuji, T. Oka, and H. Aoki, Brillouin-Wigner theory for high-frequency expansion in periodically driven systems: Application to Floquet topological insulators, Phys. Rev. B **93**, 144307 (2016).

[27] F. D. M. Haldane, Model for a Quantum Hall Effect without Landau Levels: Condensed-Matter Realization of the "Parity Anomaly", Phys. Rev. Lett. **61**, 2015 (1988).

[28] T. O. Wehling, A. M. Black-Schaffer, and A. V. Balatsky, Dirac materials, Adv. Phys. **63**, 1 (2014).

[29] O. Vafek and A. Vishwanath, Dirac fermions in solids: From high-$T_c$ cuprates and graphene to topological insulators and Weyl semimetals, Annu. Rev. Condens. Matter Phys. **5**, 83 (2014).

[30] W. Zawadzki, Semirelativity in semiconductors: A review, J. Phys.: Condens. Matter **29**, 373004 (2017).

[31] N. P. Armitage, E. J. Mele, and A. Vishwanath, Weyl and Dirac semimetals in three-dimensional solids, Rev. Mod. Phys. **90**, 015001 (2018).

[32] A. V. Balatsky, B. Brena, H. C. Herper, and B. Sanyal, Functional Dirac materials: Status and perspectives, Phys. Status Solidi RRL **12**, 1870334 (2018).

[33] I. Esin, M. S. Rudner, G. Refael, and N. H. Lindner, Quantized transport and steady states of Floquet topological insulators, Phys. Rev. B **97**, 245401 (2018).

[34] S. A. Sato, J. W. McIver, M. Nuske, P. Tang, G. Jotzu, B. Schulte, H. Hübener, U. De Giovannini, L. Mathey, M. A. Sentef, A. Cavalleri, and A. Rubio, Microscopic theory for the light-induced anomalous Hall effect in graphene, Phys. Rev. B **99**, 214302 (2019).

[35] S. A. Sato, P. Tang, M. A. Sentef, U. D. Giovannini, H. Hübener, and A. Rubio, Light-induced anomalous Hall effect in massless Dirac fermion systems and topological insulators with dissipation, New J. Phys. **21**, 093005 (2019).

[36] J. K. Freericks, H. R. Krishnamurthy, and T. Pruschke, Theoretical Description of Time-Resolved Photoemission Spectroscopy: Application to Pump-Probe Experiments, Phys. Rev. Lett. **102**, 136401 (2009).

[37] I. Gierz, J. C. Petersen, M. Mitrano, C. Cacho, E. Turcu, E. Springate, A. Stöhr, A. Köhler, U. Starke, and A. Cavalleri, Snapshots of non-equilibrium Dirac carrier distributions in graphene, Nat. Mater. **12**, 1119 (2013).

[38] P. Pearle, Simple derivation of the Lindblad equation, Eur. J. Phys. **33**, 805 (2012).

[39] A. Eckardt and E. Anisimovas, High-frequency approximation for periodically driven quantum systems from a Floquet-space perspective, New J. Phys. **17**, 093039 (2015).

[40] T. Fukui, Y. Hatsugai, and H. Suzuki, Chern numbers in discretized Brillouin zone: Efficient method of computing (spin) Hall conductances, J. Phys. Soc. Jpn. **74**, 1674 (2005).

## 2.7 Publication II: Observing light-induced Floquet band gaps in the longitudinal conductivity of graphene

<u>L. Broers</u> and L. Mathey — **Commun Phys 4, 248 (2021)**

This work was motivated by the prospect of the direct experimental observation of the light-induced Floquet band gap at the Dirac point of graphene driven by circularly polarized light. This Floquet gap displays non-trivial topological properties and is of particular interest in the context of the anomalous Hall effect, studied in Publication I.

In this work, I have studied the longitudinal optical conductivity at terahertz frequencies of driven dissipative graphene as means of observing the light-induced Floquet band gaps. I have implemented and utilized numerical methods expanding on those of Publication I, and found that inter-band transitions across the Floquet-Bloch bands lead to resonant features in the optical conductivity. The locations of these features agree with the predicted locations of the gaps of the Floquet-Bloch band structure as a function of driving intensity. However, the signals of the many light-induced Floquet band gaps occur on comparable energy scales, such that their signals in the optical conductivity tend to obscure each other. I have identified a particular regime of probing at which the gap at the Dirac point is clearly visible and observable in isolation of the higher-order Floquet gaps. This is achieved by driving the system with an intensity such that the size of the gap at the Dirac point is half the size of the driving photon energy, which is a regime the other light-induced gaps do not reach. This leaves the signal provided by the gap at the Dirac point observable under realistic conditions.

Further, my results show that the optical conductivity reverses its sign under certain driving and probing conditions. In general, increasing the driving field strength leads to Floquet band gaps opening and increasing in size up to a certain point. Increasing the driving field strength beyond this leads to the Floquet band gaps decreasing in size as a function of the field strength. It is in this regime of decreasing gap size, where the Floquet band population located at a given gap becomes inverted in this model and the resulting inter-band transitions contribute to the longitudinal current negatively. Probing at such a negatively contributing Floquet band transition under the condition that there is no other gap comparable in size obscuring the signal, leads to a sign change of the optical longitudinal conductivity. Such a negative optical conductivity is equivalent to optical gain at the corresponding frequency, which suggests the possibility of utilizing this effect in a type of graphene-based gain medium. This has motivated further work in exploring the possibility of obtaining coherent optical gain at terahertz frequencies from driven graphene or similar materials by this Floquet-Bloch band inversion mechanism.

My contribution to this work consisted of conceiving the project, creating the numerical code, performing the numerical studies, performing the analytical calculations, analyzing and presenting the results, and writing the manuscript. All of this was done under the supervision and with the guidance of LM.

### ARTICLE

**OPEN**

Check for updates

# Observing light-induced Floquet band gaps in the longitudinal conductivity of graphene

Lukas Broers [iD] [1,2✉] & Ludwig Mathey[1,2,3]

Floquet engineering presents a versatile method of dynamically controlling material properties. The light-induced Floquet-Bloch bands of graphene feature band gaps, which have not yet been observed directly. We propose optical longitudinal conductivity as a realistic observable to detect light-induced Floquet band gaps in graphene. These gaps manifest as resonant features in the conductivity, when resolved with respect to the probing frequency and the driving field strength. The electron distribution follows the light-induced Floquet-Bloch bands, resulting in a natural interpretation as occupations of these bands. Furthermore, we show that there are population inversions of the Floquet-Bloch bands at the band gaps for sufficiently strong driving field strengths. This strongly reduces the conductivity at the corresponding frequencies. Therefore our proposal puts forth not only an unambiguous demonstration of light-induced Floquet-Bloch bands, which advances the field of Floquet engineering in solids, but also points out the control of transport properties via light, that derives from the electron distribution on these bands.

[1] Center for Optical Quantum Technologies, University of Hamburg, Hamburg, Germany. [2] Institute for Laser Physics, University of Hamburg, Hamburg, Germany. [3] The Hamburg Center for Ultrafast Imaging, Hamburg, Germany. ✉email: lbroers@physnet.uni-hamburg.de

Controlling solids with light constitutes a modern approach to induce novel functionalities. A specific framework within this broader effort is Floquet engineering. Floquet engineering refers to inducing dynamics that are captured by an effective Floquet Hamiltonian in a system by periodic driving. For a non- or weakly interacting system this approach describes effective single-particle states that form a natural basis for the driven system. These states are the Floquet-Bloch bands of the electrons, in analogy to the Bloch bands of the equilibrium system. These Floquet-Bloch bands can have qualitatively distinct features from the Bloch bands of the non-driven system[1–4]. A striking example are Floquet topological insulators[5–7], for which applications in spintronics[8] have been discussed. A general overview on spintronics can be found in[9]. A specific realization of Floquet topological insulators is monolayer graphene illuminated with circularly polarized light, for which the band structure approaches the Haldane model in the high-frequency limit[10,11]. However, while the ground state of the equilibrium Haldane model forms indeed a topological insulator, which manifests in a quantized Hall conductance, the Hall conductance of optically driven graphene is not topologically quantized, but of geometric-dissipative origin[12,13]. This observation is part of the larger challenge of an unambiguous detection of the Floquet-Bloch bands in a solid. We note that the geometric properties of bands in periodically driven lattices have been demonstrated in ultracold atom experiments[14–16] as well as helical wave guides[17,18] and classical settings[19]. Signatures of Floquet-Bloch bands have been seen in angle-resolved photoelectron spectroscopy[20] and approaches for observing related pseudospin textures have been proposed[21,22]. In this context, the effects of Auger recombination[23] and scattering decoherence[24] on the electron dynamics in graphene have been discussed. The transport properties of similar Floquet systems have been discussed[25] and the high-frequency probing limit has been explored[26]. However, a smoking-gun in the transport measurements of solids is lacking.

In this paper, we propose to detect light-induced Floquet band gaps in graphene via the optical longitudinal transport. We determine the optical conductivity as a function of the probing frequency and the driving field strength, which displays resonant features. We present an interpretation of these features in terms of the Floquet-Bloch band dispersion and the effective occupation of these states. These occupations are determined by the dissipation and the driving field, which balance out to form the steady state. We include the dissipation processes in our master equation approach that we use to describe the system. With this, we attribute the observable resonant features in the optical conductivity to two transition processes. One occurs between bands inside the same Floquet zone and the other between adjacent bands of neighboring Floquet zones. These processes compete in their impact on the optical conductivity, which can result in vanishing and even negative optical conductivity for specific frequencies and driving field strengths. In general, we show that the conductivity depends on the relative occupation of the Floquet bands. We also point out that the relative occupation is in qualitative agreement with a comoving band velocity, to be defined below. In particular, we show that there are regimes of driving field strengths that show an effective inversion of Floquet band populations. These are in the regimes in which negative optical conductivity is achieved. Therefore, as a second point besides the demonstration of Floquet-Bloch bands in solids, our proposal shows non-trivial control of the transport properties of solids, induced by light.

## Results and discussion

**Model Hamiltonian**. We consider a circularly polarized laser with frequency $\omega_d = 2\pi \times 48\,\text{THz} \approx 200\,\text{meV}$ and variable field strength $E_d$, which illuminates a graphene layer from perpendicular direction. The electromagnetic forces drive the electrons into a steady state. We propose to measure the longitudinal AC conductivity of this steady state in the optical frequency domain. The conductivity displays frequency regimes in which its magnitude is increased compared to the non-driven graphene layer, and regimes in which it is decreased. These frequency regimes derive from resonances between the Floquet states, which in turn depend on the driving field strength. As a result, these frequency regimes can be tuned to overlap, resulting in a partial cancellation. In particular, the band gap $\Delta_0$ at the Dirac point can be overshadowed, in general, by other features. However, we point out a regime in which it can be identified unambiguously.

The Hamiltonian of light-driven graphene, close to the Dirac point is given by

$$H = \sum_k c_k^\dagger \mathbf{h}(\mathbf{k}) c_k, \tag{1}$$

where $c_k = (c_{k,A}, c_{k,B})^T$ and $c_{k,i}$ are the fermionic annihilation operators of an electron with momentum $\mathbf{k}$ and sublattice index $i = A, B$. Invoking the edge-bulk correspondance, the transport properties of the periodic bulk captured by Eq. (1) directly translate to localized edge modes of finite systems. The Hamiltonian of a single momentum $\mathbf{k}$ is

$$\mathbf{h}(\mathbf{k}) = \hbar v_F (q_x \sigma_x + q_y \sigma_y), \tag{2}$$

with

$$q_x = k_x + \frac{E_d}{\omega_d} \sin(\omega_d t) - \frac{E_L}{\omega_L} \cos(\omega_L t), \tag{3}$$

$$q_y = k_y + \frac{E_d}{\omega_d} \cos(\omega_d t), \tag{4}$$

where $v_F \approx 10^6\,\text{m s}^{-1}$ is the Fermi velocity. $k_i$ are the momentum components and $\sigma_i$ are the Pauli matrices. $E_d$ and $\omega_d$ are field strength and frequency of the driving laser. $E_L$ and $\omega_L$ are the same quantities for the longitudinal probing field.

We simulate the dynamics via a master equation approach, expanding on previous work by some of the authors[12]. The density matrix of the system factorizes in momentum space, as $\rho = \prod_k \rho_k$. Each $\rho_k$ matrix operates on a four dimensional Hilbert space, given by the states $|0\rangle$, $c_{k,A}^\dagger |0\rangle$, $c_{k,B}^\dagger |0\rangle$, $c_{k,B}^\dagger c_{k,A}^\dagger |0\rangle$. We include doubly and unoccupied states to determine two-time correlation functions, and thereby frequency-resolved quantities.

In addition to the unitary time evolution induced by the Hamiltonian in Eq. (2), we include dissipation via Lindblad operators defined in the instantaneous eigenbasis of the driven system, to describe the dissipative environment due to degrees of freedom not included in the Hamiltonian. We include a dephasing term $\gamma_z$, a decay term $\gamma_-$ and a term with decay rate $\gamma_{bg}$ that models particle exchange of the graphene layer to a supporting substrate backgate. This model provides a realistic discription of the non-equilibrium electron dynamics[12].

We choose the coefficients $\gamma_z = 1\,\text{THz}$, $\gamma_- = 2.25\,\text{THz}$ and $\gamma_{bg} = 2.5\,\text{THz}$. This sets the scale for the broadening of the effective bands in the single-particle correlation function as well as the optical conductivity. These values are a factor of 10 smaller than those estimated[12] for the experimental setup of McIver et al.[13]. Our predictions apply to high-mobility samples, e.g., BN-encapsulated graphene. For larger values, such as those that are realized in the work of McIver et al.[13], resolving the gap features that we describe in the following, would require larger driving frequencies and stronger driving. Throughout this work we use the temperature $T = 80\,\text{K}$, which is the same as the setup of
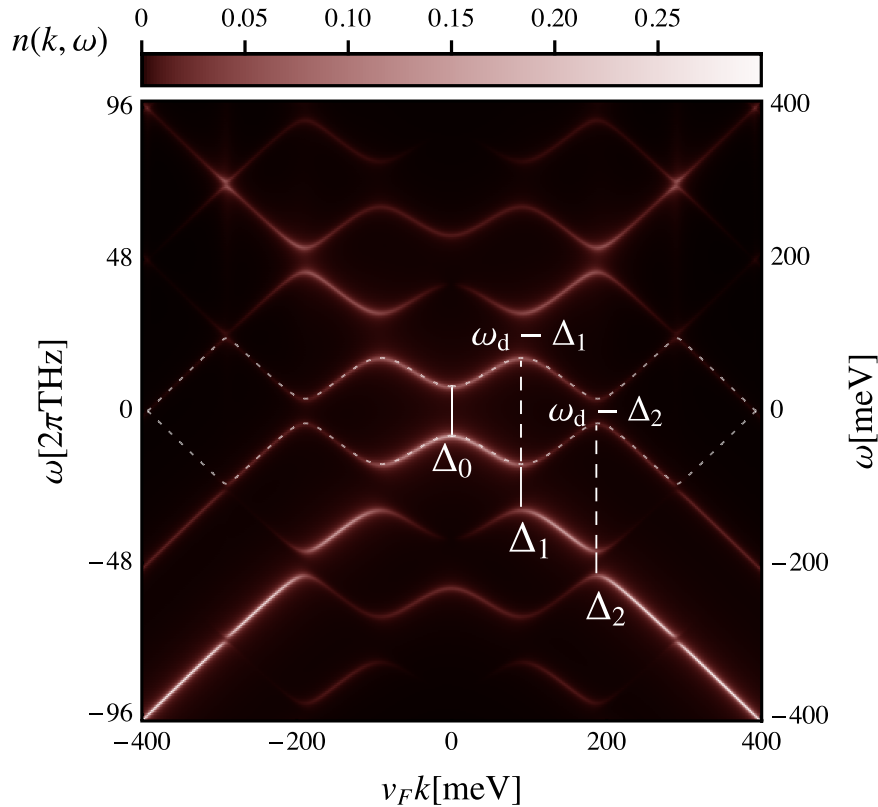
**Fig. 1 Electron distribution of light-driven graphene, revealing its Floquet states.** The electron distribution $n(\mathbf{k}, \omega)$ of graphene driven with circularly polarized light at the driving frequency $\omega_d = 2\pi \times 48$ THz $\approx 200$ meV and field strength $E_d = 26$ MV m$^{-1}$. The distribution $n(\mathbf{k}, \omega)$ depends only on the momentum $k = |\mathbf{k}|$. This quantity displays the steady state occupation of the Floquet-Bloch band structure. The one-photon resonance gap $\Delta_1$ at $k = \omega_d/(2v_F)$, the two-photon gap $\Delta_0$ at the Dirac point, and the two-photon gap at $k = \omega_d/v_F$ are highlighted for clarity. $v_F$ is the Fermi velocity. Additionally, the complementary gaps $\omega_d - \Delta_1$ and $\omega_d - \Delta_2$ are indicated. The dotted lines indicate the Floquet energies of the first Floquet zone.

McIver et al.[13]. We fix the value of the chemical potential at $\mu = 0$.

**Electron distribution**. As a first observable we display the momentum-resolved and energy-resolved electron distribution inspired by Freericks et al.[27]

$$n(\mathbf{k}, \omega) = \int_{\tau_1}^{\tau_2} \int_{\tau_1}^{\tau_2} \mathcal{G}(\mathbf{k}, t_2, t_1) \frac{e^{i\omega(t_2 - t_1)}}{(\tau_2 - \tau_1)^2} dt_2 dt_1, \quad (5)$$

which is manifestly real-valued with

$$\mathcal{G}(\mathbf{k}, t_2, t_1) = \langle c_{\mathbf{k},A}^\dagger(t_2) c_{\mathbf{k},A}(t_1) \rangle + \langle c_{\mathbf{k},B}^\dagger(t_2) c_{\mathbf{k},B}(t_1) \rangle \quad (6)$$

for which its complex conjugate corresponds to the exchange of $t_1$ and $t_2$. We use the time interval $[\tau_1, \tau_2]$ as the probing interval. We choose $\tau_1$ such that the system has reached its steady state. $\tau_2 - \tau_1$ is a sufficiently long probing time of the order of hundreds of driving periods $2\pi/\omega_d$ that is also commensurate with the probing period $2\pi/\omega_L$. We note that this quantity provides a prediction for trARPES measurements[27]. In Fig. 1 we show $n(k = |\mathbf{k}|, \omega)$ for the driving field strength $E_d = 26$ Me V m$^{-1}$. We note that a similar result was presented in previous work by some of the authors[12]. The electron distribution of the steady state is consistent with the effective band structure predicted by Floquet theory and identifies the non-equilibrium electron occupation of these Floquet-Bloch bands.

We label the band gaps as $\Delta_m$, based on their location $m\omega_d/(2v_F)$ in momentum space for small driving field strength $E_d \to 0$, as shown in Fig. 1. Due to the periodicity in frequency space of the Floquet spectrum, there is a complementary gap $\omega_d - \Delta_m$ for any given band gap $\Delta_m$, with $m > 0$. These complementary gaps

are also visible in the optical conductivity of the system. They reduce the conductivity at the corresponding frequency, rather than enhance it. The gap $\Delta_0$ at the Dirac point does not exhibit this behavior, as discussed later.

**Optical conductivity**. The second observable that we present is the longitudinal optical conductivity. We propose to measure this quantity experimentally, to compare to the predictions made here. In Fig. 2 we show the real part of the total optical conductivity of the system as a function of the driving field strength $E_d$. This is obtained from our master equation approach as

$$\sigma_r(\omega_L) = \text{Re}\left[\frac{j_x(\omega_L)}{E_x(\omega_L)}\right], \quad (7)$$

with the longitudinal current and electric field

$$j_x(\omega_L) = n_s n_v e v_F \sum_{\mathbf{k}} \int_\tau^{\tau + \frac{2\pi}{\omega_L}} \text{Tr}(\rho_{\mathbf{k}}(t)\sigma_x) e^{i\omega_L t} dt, \quad (8)$$

$$E_x(\omega_L) = \int_\tau^{\tau + \frac{2\pi}{\omega_L}} (E_d \cos(\omega_d t) + E_L \sin(\omega_L t)) e^{i\omega_L t} dt, \quad (9)$$

where $\tau$ is a point in time where the system has reached its steady state. $n_s = n_v = 2$ are the spin- and valley-degeneracies. $e$ is the electron charge. $\sigma_r(\omega_L)$ is obtained for the probing field $E_L = 10$ V m$^{-1}$. We have verified that the conductivity obtained in this manner is the linear response and that the sum over $k$ includes sufficiently many points surrounding the Dirac point.

As we demonstrate in Fig. 2a, $\sigma_r(\omega_L)$ displays resonant features that match the band gaps of the Floquet spectrum. The energy gap $\Delta_0$ increases with increasing field strength $E_d$, in a
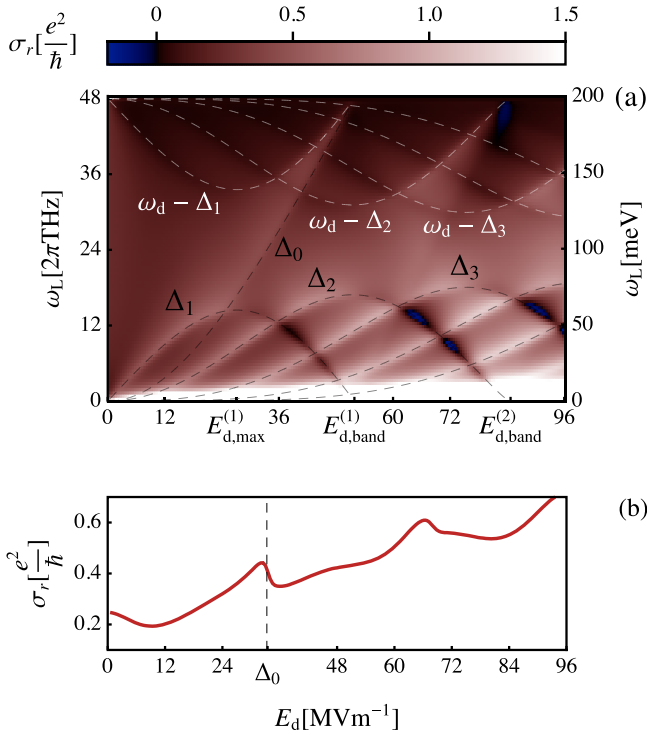
**Fig. 2 Longitudinal optical conductivity of light-driven graphene.** The real part of the optical conductivity of graphene driven at the frequency $\omega_d = 2\pi \times 48$ THz $\approx 200$ meV as a function of the driving field strength $E_d$ (a) and a cut at half the driving frequency $\omega_L = \omega_d/2 = 2\pi \times 24$ THz (b). The dashed lines show the various band gaps $\Delta_m$ as given by Floquet theory. The gap $\Delta_0$ becomes clearly visible above values of $\omega_L \approx 2\pi \times 14$ THz $\approx 60$ meV and $E_d \approx 28$ MV m$^{-1}$. We also see the complementary resonant features at $\omega_d - \Delta_m$, with $m > 0$.



**Fig. 3 Electron distribution at the Dirac point.** The electron distribution $n(k = 0, \omega)$ at the Dirac point as a function of the driving field strength $E_d$. The driving frequency is $\omega_d = 2\pi \times 48$ THz $\approx 200$ meV. The scaling behavior of the gap at the Dirac point is $\Delta_0 = 2\sqrt{v_F^2 E_d^2/\omega_d^2 + \omega_d^2/4} - \omega_d$, where $v_F$ is the Fermi velocity. The vertical dotted line indicates $E_d = E_{d,band}^{(1)}$. The horizontal dotted lines indicate Floquet zone boundaries. The dashed lines show the Floquet energies at the Dirac point (See Supplementary Note 1) that are formally constrained to be inside the first Floquet zone. The occupations stay confined within the Floquet bands adiabatically connected to the bare graphene and one replica outwards. There are no complementary gaps at $k = 0$.

monotonuous fashion. The energy gaps $\Delta_m$, with $m > 0$, first increase with $E_d$, then reach a maximum at $E_d = E_{d,max}^{(m)}$, then decrease, and ultimately reach 0 at $E_d = E_{d,band}^{(m)}$. At this driving strength the gap is located at $k = 0$ and merges with $\Delta_0$.
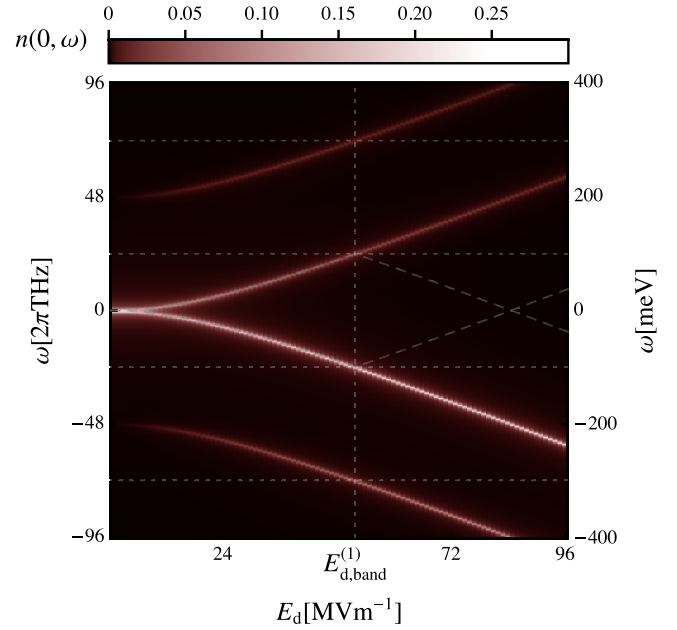
The magnitude of $\sigma_r(\omega_L)$ at the resonance $\Delta_1$, i.e., the magnitude of $\sigma_r(\Delta_1)$, displays a maximum for $E_d < E_{d,max}^{(1)}$, relative to its background, and a minimum for $E_d > E_{d,max}^{(1)}$. The magnitude of $\sigma_r(\omega_L)$ at $\omega_d - \Delta_1$, displays the complementary behavior. $\sigma_r(\omega_d - \Delta_1)$ has a minimum for $E_d < E_{d,max}^{(1)}$, and a maximum for $E_d > E_{d,max}^{(1)}$. Note that this does not happen for $\Delta_0$ due to the lack of a complementary gap $\omega_d - \Delta_0$ as can be seen in Figs. 1 and 3.

We note that in the limit of $E_d \to 0$, the optical conductivity $\sigma_r(\omega_L)$ approaches the value $\frac{1}{4}\frac{e^2}{\hbar}$ for non-zero frequencies. An example for this is visible in Fig. 2b, for $\omega_L = 2\pi \times 24$ THz. Additionally, we obtain a peak at $\omega_L = 0$, which is the Drude peak broadened by the dissipative terms. We show the real part of the longitudinal conductivity $\sigma_r(\omega_L)$ for $E_d = 0$ in Supplementary Note 2.

We obtain analytical expressions for $\Delta_0$ and $E_{d,band}^{(m)}$ by considering the Hamiltonian in Eq. (2) at the Dirac point and without probing, i.e., $k = 0$ and $E_L = 0$. This has the time-dependent Rabi solutions

$$|+\rangle \sim e^{i(\omega_d t/2 + \pi/4)} \begin{pmatrix} \cos(\Omega t) - \frac{i\omega_d \sin(\Omega t)}{2\Omega} \\ e^{-i\omega_d t}\frac{E_d \sin(\Omega t)}{\Omega\omega} \end{pmatrix}, \quad (10)$$

$$|-\rangle \sim e^{-i(\omega_d t/2 + \pi/4)} \begin{pmatrix} -e^{i\omega_d t}\frac{E_d \sin(\Omega t)}{\Omega\omega_d} \\ \cos(\Omega t) + \frac{i\omega_d \sin(\Omega t)}{2\Omega} \end{pmatrix}, \quad (11)$$

where

$$\Omega = \sqrt{\frac{v_F^2 E_d^2}{\omega_d^2} + \frac{\omega_d^2}{4}}. \quad (12)$$

The gap at the Dirac point is given by $\Delta_0 = 2\Omega - \omega_d$. This expression is also the Aharanov-Anandan phase of this system[2]. In the weak driving limit this gap follows the expected perturbative behavior[11] $\Delta_0 \approx v_F^2 E_d^2/\omega_d^3$ whereas in the strong driving limit it develops a linear dependence on $E_d$ as $\Delta_0 \approx v_F E_d/\omega_d$. We use the full expression for $\Delta_0$ to find the driving strengths $E_{d,band}^{(m)}$, since they occur whenever the gap $\Delta_0$ spans a multiple of $\omega_d$. By setting $2\Omega - \omega_d = m\omega_d$, $m \in \mathbb{N}$, we find

$$E_{d,band}^{(m)} = v_F^{-1}\sqrt{\frac{m}{2} + \frac{m^2}{4}}\omega_d^2. \quad (13)$$

We display the Dirac gap in Fig. 3, and compare it to the electron distribution at $\mathbf{k} = 0$, of the steady state. We observe that the two maxima of the electron distribution that emerge from $\omega = 0$ follow the prediction of $\pm\Delta_0$, even as $\Delta_0$ grows larger than the Floquet zone boundary at $\omega_d$. Therefore, $\Delta_0$ is a more natural energy scale to predict the resonances at $\mathbf{k} = 0$ for large driving intensities, than the direct band gap that is strictly smaller than $\omega_d$. For increasing field strength $E_d$, the occupation of the upper
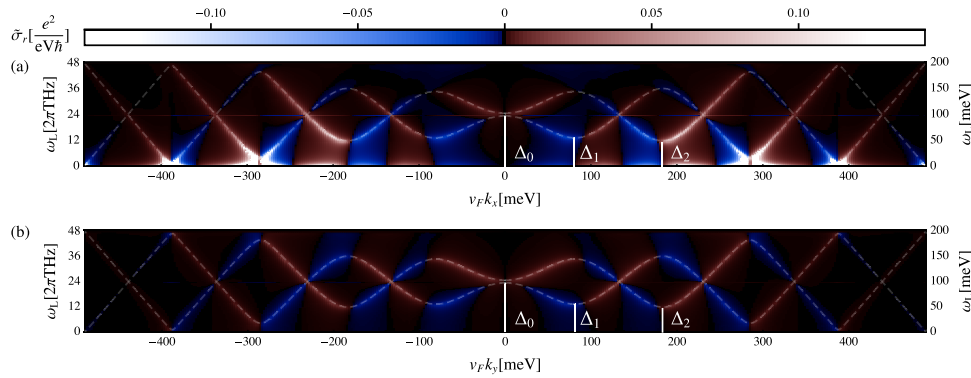
**Fig. 4 Momentum-resolved optical conductivity of light-driven graphene.** The momentum-resolved contributions to the optical conductivity of driven graphene along the $k_x$ (**a**) and $k_y$ (**b**) momentum directions. The driving frequency is $\omega_d = 2\pi \times 48$ THz $\approx 200$ meV and the field strength is $E_d = 34$ MV m$^{-1}$. For these parameters the gap at the Dirac point roughly matches half the driving frequency such that $\Delta_0 \approx \omega_d/2$. The dashed lines indicate the Floquet band energy differences $\Delta\epsilon(k)$ and $\omega_d - \Delta\epsilon(k)$ (See Supplementary Note 1).

two bands decreases. The occupation of complementary gaps is zero throughout Fig. 3.

As visible in Fig. 2a, the conductivity vanishes around the probing frequency $\omega_L \approx 2\pi \times 12$ THz $\approx 50$ meV and the driving field strength of $E_d \approx 39$ MV m$^{-1}$. Here the first gap $\Delta_1$ decreases with increasing $E_d$ and creates a negative contribution that suppresses $\sigma_r(\omega_L)$ to zero. For higher order gaps, e.g., $\Delta_2$ and $\Delta_3$ in Fig. 2a, the same phenomenon even leads to a sign change in the conductivity. Whenever a gap is in the regime of decreasing with increasing $E_d$, and no other resonance contributes positively and too strongly to the conductivity, the negative contributions can cancel the background and result in net negative optical conductivity. Such a total negative conductivity in the system amounts to an out-of-phase response to a probing field with a probing frequency in the regime in which $\sigma_r(\omega_L)$ is negative. In principle this can be utilized to obtain electrical gain out of the system, where the required energy is effectively taken from the driving.

**Momentum-resolved conductivity.** In order to gain further insight into the origin of the features in the total optical conductivity shown in Fig. 2, we explore the momentum resolved contributions to the conductivity. In Fig. 4 we resolve the contributions to the conductivity along the $k_x$ and $k_y$ directions relative to the Dirac point in momentum space, defined as

$$\tilde{\sigma}_r(\mathbf{k}, \omega_L) = \frac{n_s n_v e v_F |\mathbf{k}|}{E_x(\omega_L)} \int_\tau^{\tau + \frac{2\pi}{\omega_L}} \text{Tr}(\rho_\mathbf{k}(t)\sigma_x) e^{i\omega_L t} dt. \quad (14)$$

Here, we include the linear scaling with the absolute momenta $|\mathbf{k}|$ in polar coordinates. Direct interband transitions between neighboring Floquet bands give rise to resonant features in $\tilde{\sigma}_r(\mathbf{k}, \omega_L)$ that match the Floquet band energy differences $\Delta\epsilon(k)$ and $\omega_d - \Delta\epsilon(k)$ (See Supplementary Note 1). These resonant features contribute to the conductivity with alternating signs. The sign changes occur close to the band gap locations, but slightly shifted towards (away from) the Dirac point in case the gap size increases (decreases) with respect to the field strength $E_d$. For gaps that do not change with respect to $E_d$, i.e., gaps at their maximum, this shift vanishes. Therefore, the accumulated contributions across gaps net either positive or negative conductivity depending on the change in gap size with respect to field strength $E_d$. This is consistent with the enhancements and reductions in $\sigma_r(\omega_L)$ at the gaps $\Delta_m$, with $m > 0$, and their complementary gaps $\omega_d - \Delta_m$, seen in Fig. 2a.

For probing frequencies $\omega_L$ that are not resonant with a given band gap, $\tilde{\sigma}_r(\mathbf{k}, \omega_L)$ does not vanish in general. This results in a background conductivity that can obscure the gap $\Delta_0$ at the Dirac point in particular, as is the case for $E_d < E_{d,max}^{(1)}$ in Fig. 2a. Since the band gaps $\Delta_m$, with $m > 0$, and their complementary gaps $\omega_d - \Delta_m$ have a maximum at the field strength $E_d = E_{d,max}^{(m)}$, there is always a range that no gap $\Delta_m$, with $m > 0$, reaches that is centered around $\omega_L = \omega_d/2$. In this range, it is the gap $\Delta_0$ that is visible predominantly. The overall behavior of the gaps is self-similar with respect to the driving frequency $\omega_d$. Therefore in this system, there always exists a reliable range of probing frequencies where the gap $\Delta_0$ can be observed.

The Floquet interband transitions resonant with $\Delta\epsilon(k)$ occur inside a given Floquet zone. The ones resonant with $\omega_d - \Delta\epsilon(k)$ occur across Floquet zone boundaries. Hence, we refer to them as intra-Floquet $\tilde{\sigma}_r^{intra}(\mathbf{k}, \omega_L)$ and inter-Floquet $\tilde{\sigma}_r^{inter}(\mathbf{k}, \omega_L)$ contributions to the conductivity, respectively. To distinguish the two we write

$$\tilde{\sigma}_r(\mathbf{k}, \omega_L) = \tilde{\sigma}_r^{intra}(\mathbf{k}, \omega_L) + \tilde{\sigma}_r^{inter}(\mathbf{k}, \omega_L) + \tilde{\sigma}_r^{bg}(\mathbf{k}, \omega_L), \quad (15)$$

where $\tilde{\sigma}_r^{bg}(\mathbf{k}, \omega_L)$ is a remaining background contribution accounting for the $\omega_L \to 0$ behavior in $\tilde{\sigma}_r(\mathbf{k}, \omega_L)$. Figure 4b shows that $\sigma_r^{bg}(k_y, \omega_L) \approx 0$. We fit a function of two Lorentzians located at $\Delta\epsilon(k)$ and $\omega_d - \Delta\epsilon(k)$ with the same fixed width $\Gamma = 1$ THz to the numerical results of $\tilde{\sigma}_r(k_y, \omega_L)$. Specifically, we use

$$\tilde{\sigma}_r^{fit}(k_y, \omega_L) = \frac{\Gamma}{\pi} \frac{\tilde{\sigma}_r^{intra}(k_y)}{\Gamma^2 + (\omega_L - \Delta\epsilon)^2} + \frac{\Gamma}{\pi} \frac{\tilde{\sigma}_r^{inter}(k_y)}{\Gamma^2 + (\omega_L - \omega_d + \Delta\epsilon)^2} \quad (16)$$

as a fitting function.

The conductivity features derive from the transitions between the Floquet bands, and are therefore related to the occupation of these bands. We define the relative occupation

$$\Delta n(k) = \sum_{m \in \mathbb{Z}} n_m^-(k) - n_m^+(k), \quad (17)$$

where $n_m^\pm(k)$ is the occupation at momentum $k$ of the $m$th upper (lower) Floquet band given by integrating $n(k, \omega)$ from $(m - \frac{1}{4} \pm \frac{1}{4})\omega_d$ to $(m + \frac{1}{4} \pm \frac{1}{4})\omega_d$.

Figure 5 shows the momentum-resolved intra-Floquet conductivity $\tilde{\sigma}_r^{intra}(k_y)$ which is determined via fitting as described above, as well as the effective relative occupation $\Delta n(k)$ of the

5
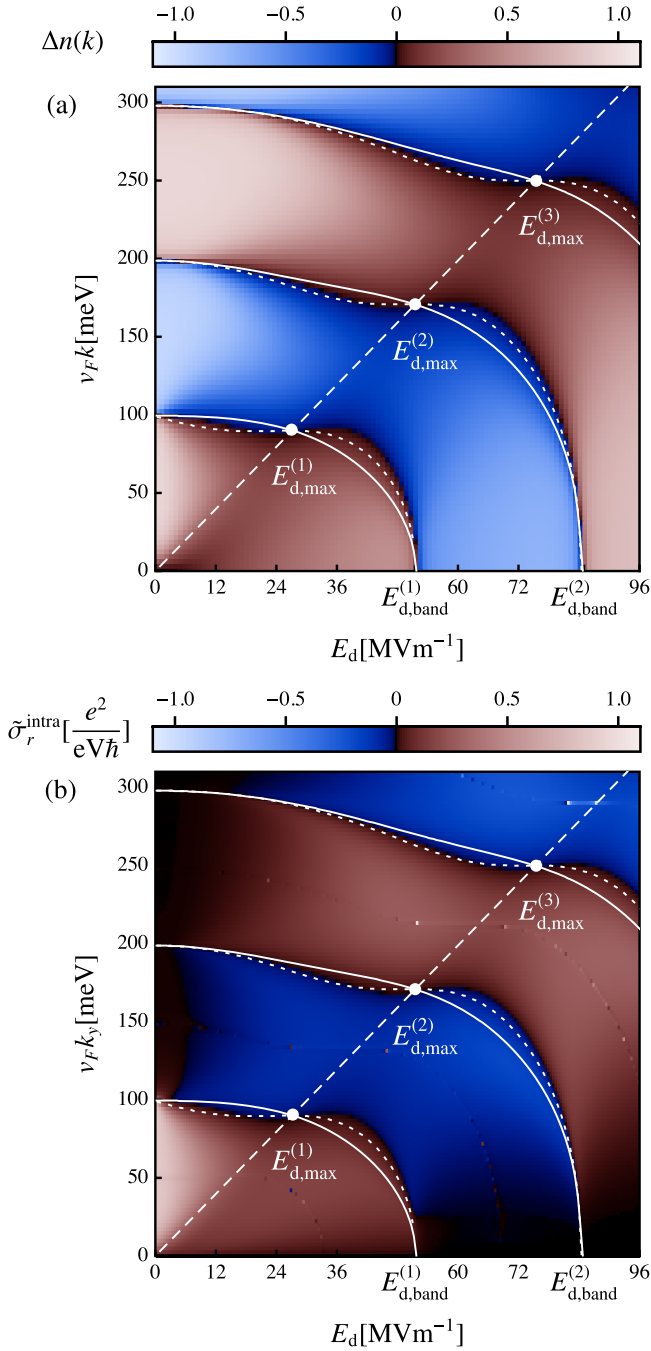
**Fig. 5 Effective Floquet state occupation and intra-Floquet conductivity.**
The effective occupation $\Delta n(k)$ (**a**) and the fitted intra-Floquet conductivity $\tilde{\sigma}_r^{\text{intra}}(k_y)$ (**b**) as functions of the field strength $E_d$. The solid white lines are given by the locations in momentum space of the band gaps $\Delta_m$, with $m > 0$. The dotted white lines are given by the zero-crossings of a type of comoving band velocity $\partial_\Pi \Delta \epsilon = 0$, where $\Pi = v_F(k + E_d/\omega_d)$ (See Supplementary Note 1). The dashed line is given by $k = \frac{E_d}{\omega_d}$.

Floquet bands as functions of the field strength $E_d$. They are in good qualitative agreement with each other. Both quantities display tongues with alternating signs and zero-crossings seperating them that agree very well between $\Delta n(k)$ and $\tilde{\sigma}_r^{\text{intra}}(k_y)$. The zero-crossings touch the $v_F k$-axis at $m\omega_d/2$ and the $E_d$-axis at $E_{d,\text{band}}^{(m)}$, $m \in \mathbb{N}$. The solid white lines show the location of the Floquet band gaps, i.e., where the radial band velocity vanishes, i.e., $\partial_k \epsilon = 0$. They roughly follow the zero-crossings of $\Delta n(k)$ and $\tilde{\sigma}_r^{\text{intra}}(k_y)$ while showing small, but clear deviations. We observe that for $E_{d,\text{max}}^{(m)} < E_d < E_{d,\text{band}}^{(m)}$ the steady state displays an inversion of the Floquet bands, which creates a negative contribution to the optical conductivity. The dotted white lines indicate where the comoving radial band velocity $\partial_\Pi \epsilon$ with $\Pi = v_F(k + E_d/\omega_d)$ vanishes, i.e., $\partial_\Pi \epsilon = 0$. These lines show improved agreement with the zero-crossings of $\Delta n(k)$ and $\tilde{\sigma}_r^{\text{intra}}(k_y)$. Further, there is an overall resemblance between $\partial_\Pi \epsilon(k)$, $\Delta n(k)$, and $\tilde{\sigma}_r^{\text{intra}}(k_y)$ (See Supplementary Note 1).

We summarize that the momentum-resolved optical conductivity shows two types of interband processes across the effective Floquet band structure. These resonant processes correspond to the energy differences $\Delta \epsilon(k)$ and $\omega_d - \Delta \epsilon(k)$ between Floquet bands and contribute both positively and negatively. We relate these conductivities to the effective relative occupation of the Floquet bands $\Delta n(k)$. We find that effective inversions of the Floquet bands correspond to reductions in the conductivity which can lead to a sign change in the total optical conductivity. These band inversions at the Floquet gaps and their reductions of the optical conductivity systematically occur in regimes of decreasing gap sizes with respect to the driving field strength.

## Conclusion

In conclusion, we have proposed the longitudinal optical conductivity of illuminated graphene as a realistic observable to detect Floquet band gaps. We have shown that this quantity displays the Floquet gaps as functions of the driving intensity and the probing frequency. In particular, we have pointed out a regime in which the band gap at the Dirac point can be detected. All band gaps except for the band gap at the Dirac point, first increase with the driving intensity, approach a maximal value, and then decrease. For the increasing regime, the optical conductivity displays a positive contribution. For the decreasing regime, it displays a negative contribution that can amount to a total negative conductivity at the given frequency. We point out that this negative contribution derives from an inversion of the occupation of the Floquet bands. Therefore, the proposed experiment not only provides an unambiguous detection of Floquet bands, but also demonstrates dynamical control of transport in solids with light.

## Methods

**Driven graphene dynamics.** We express the driven graphene Hamiltonian in a four-level description, spanned by the states $|0\rangle$, $c_{\mathbf{k},A}^\dagger |0\rangle$, $c_{\mathbf{k},B}^\dagger |0\rangle$ and $c_{\mathbf{k},B}^\dagger c_{\mathbf{k},A}^\dagger |0\rangle$. The $c_{\mathbf{k},A/B}^{(\dagger)}$ are the annihilation (creation) operators at the momentum $\mathbf{k}$ in the sublattice A/B. The Hamiltonian $H$ is defined in Eq. (1). We factorize the density matrix in momentum space as $\rho = \Pi_k \rho_k$ and simulate the dissipative dynamics using the Lindblad-von Neumann master equation

$$\dot{\rho} = i[\rho, H] + \sum_j c_j(L_j \rho L_j^\dagger - \frac{1}{2}\{L_j^\dagger L_j, \rho\}),$$

where the sum over $j$ goes over the momentum-dependent Lindblad operators

$$L_z = V(c_{\mathbf{k},A}^\dagger c_{\mathbf{k},A} - c_{\mathbf{k},B}^\dagger c_{\mathbf{k},B})V^\dagger$$
$$L_+ = V(c_{\mathbf{k},B}^\dagger c_{\mathbf{k},A})V^\dagger$$
$$L_- = V(c_{\mathbf{k},A}^\dagger c_{\mathbf{k},B})V^\dagger$$
$$L_l = V \begin{pmatrix} 0 & \delta_{l,-1} & \delta_{l,-2} & 0 \\ \delta_{l,1} & 0 & 0 & \delta_{l,-3} \\ \delta_{l,2} & 0 & 0 & \delta_{l,-4} \\ 0 & \delta_{l,3} & \delta_{l,4} & 0 \end{pmatrix} V^\dagger$$

with $l = \pm 1, \pm 2, \pm 3, \pm 4$. $\delta_{l,i}$ is the Kronecker-Delta and $V$ is the transformation into the instantaneous eigenbasis of $\mathbf{h}(\mathbf{k})$ defined in Eq. (2). The dissipation coefficients

$c_j$ fulfill the conditions

$$c_z = \gamma_z$$
$$c_+ + c_- = \gamma_- \qquad c_+ = c_- \exp\{-2\epsilon\beta\}$$
$$c_1 + c_{-1} = \gamma_{bg} \qquad c_{-1} = c_1 \exp\{+\epsilon\beta\}$$
$$c_2 + c_{-2} = \gamma_{bg} \qquad c_{-2} = c_2 \exp\{-\epsilon\beta\}$$
$$c_3 + c_{-3} = \gamma_{bg} \qquad c_{-3} = c_3 \exp\{-\epsilon\beta\}$$
$$c_4 + c_{-4} = \gamma_{bg} \qquad c_{-4} = c_4 \exp\{+\epsilon\beta\}$$

with $\beta = (k_B T)^{-1}$. $\pm\epsilon$ are the instantaneous eigenenergies of $\mathbf{h}(\mathbf{k})$. This approach is also detailed in previous work[12].

In order to calculate the electron distribution, we first calculate the two-point correlation functions $\langle c_{\mathbf{k},i}^\dagger(t_2) c_{\mathbf{k},i}(t_1)\rangle$. We do this by acting with $c_{\mathbf{k},i}$ on the density matrix $\rho_\mathbf{k}(t_1)$ and continuing the time-evolution with the same master equation until the time $t_2$ at which we act on the resulting density with the operator $c_{\mathbf{k},i}^\dagger$. We do this for all pairs of times $t_1$ and $t_2$ in the interval $[\tau_1, \tau_2]$ and calculate the electron distribution as detailed in Eq. (5).

## Data availability
The data that support the findings of this study are available from the corresponding author upon reasonable request.

## Code availability
The code used to generate the data presented in this study is available from the corresponding author upon reasonable request.

## References

1. Basov, D. N., Averitt, R. D. & Hsieh, D. Towards properties on demand in quantum materials. *Nat. Mater.* **16**, 1077–1088 (2017).
2. Oka, T. & Kitamura, S. Floquet engineering of quantum materials. *Tech. Rep.* https://doi.org/10.1146/annurev-conmatphys-031218-013423 (2019).
3. Wackerl, M., Wenk, P. & Schliemann, J. Floquet-drude conductivity. *Phys. Rev. B* **101**, 184204 (2020).
4. Chen, Q., Du, L. & Fiete, G. A. Floquet band structure of a semi-dirac system. *Phys. Rev. B* **97**, 035422 (2018).
5. Kitagawa, T., Oka, T., Brataas, A., Fu, L. & Demler, E. Transport properties of nonequilibrium systems under the application of light: photoinduced quantum hall insulators without landau levels. *Phys. Rev. B* **84**, 235108 (2011).
6. Lindner, N. H., Refael, G. & Galitski, V. Floquet topological insulator in semiconductor quantum wells. *Nat. Phys.* **7**, 490–495 (2011).
7. Rudner, M. & Lindner, N. Band structure engineering and non-equilibrium dynamics in floquet topological insulators. *Nat. Rev. Phys.* **2**, 229–244 (2020).
8. Sameti, M. & Hartmann, M. J. Floquet engineering in superconducting circuits: from arbitrary spin-spin interactions to the kitaev honeycomb model. *Phys. Rev. A* **99**, 012333 (2019).
9. Žutić, I., Fabian, J. & Das Sarma, S. Spintronics: fundamentals and applications. *Rev. Mod. Phys.* **76**, 323–410 (2004).
10. Haldane, F. D. M. Model for a quantum hall effect without landau levels: condensed-matter realization of the "parity anomaly". *Phys. Rev. Lett.* **61**, 2015–2018 (1988).
11. Oka, T. & Aoki, H. Photovoltaic hall effect in graphene. *Phys. Rev. B* **79**, 081406 (2009).
12. Nuske, M. et al. Floquet dynamics in light-driven solids. *Phys. Rev. Res.* **2**, 043408 (2020).
13. McIver, J. W. et al. Light-induced anomalous hall effect in graphene. *Nat. Phys.* **16**, 38–41 (2019).
14. Fläschner, N. et al. Experimental reconstruction of the berry curvature in a floquet bloch band. *Science* **352**, 1091–1094 (2016).
15. Jotzu, G. et al. Experimental realization of the topological haldane model with ultracold fermions. *Nature* **515**, 237–240 (2014).
16. Aidelsburger, M. et al. Realization of the hofstadter hamiltonian with ultracold atoms in optical lattices. *Phys. Rev. Lett.* **111**, 185301 (2013).
17. Rechtsman, M. C. et al. Photonic floquet topological insulators. *Nature* **496**, 196–200 (2013).
18. Mukherjee, S. et al. Experimental observation of anomalous topological edge modes in a slowly driven photonic lattice. *Nat. Commun.* **8**, 13918 (2017).
19. Ma, G., Xiao, M. & Chan, C. T. Topological phases in acoustic and mechanical systems. *Nat. Rev. Phys.* **1**, 281–294 (2019).
20. Wang, Y. H., Steinberg, H., Jarillo-Herrero, P. & Gedik, N. Observation of floquet-bloch states on the surface of a topological insulator. *Science* **342**, 453–457 (2013).
21. Schüler, M. et al. How circular dichroism in time- and angle-resolved photoemission can be used to spectroscopically detect transient topological states in graphene. *Phys. Rev. X* **10**, 041013 (2020).
22. Sentef, M. A. et al. Theory of floquet band formation and local pseudospin textures in pump-probe photoemission of graphene. *Nat. Commun.* **6**, 7047 (2015).
23. Keunecke, M. et al. Direct access to auger recombination in graphene (2020). https://arxiv.org/abs/2012.01256 (2020).
24. Aeschlimann, S. et al. Survival of floquet-bloch states in the presence of scattering. *Nano Lett.* **21**, 5028–5035 (2021).
25. Kumar, A., Rodriguez-Vega, M., Pereg-Barnea, T. & Seradjeh, B. Linear response theory and optical conductivity of floquet topological insulators. *Phys. Rev. B* **101**, 174314 (2020).
26. Zhou, Y. & Wu, M. W. Optical response of graphene under intense terahertz fields. *Phys. Rev. B* **83**, 245436 (2011).
27. Freericks, J. K., Krishnamurthy, H. R. & Pruschke, T. Theoretical description of time-resolved photoemission spectroscopy: application to pump-probe experiments. *Phys. Rev. Lett.* **102**, 136401 (2009).

## Author contributions
L.B. and L.M. conceived the project. L.B. performed the calculations, simulations, and analysis, supervised by L.M.

## Competing interests
The authors declare no competing interests.

## Additional information
**Supplementary information** The online version contains supplementary material available at https://doi.org/10.1038/s42005-021-00746-6.

**Correspondence** and requests for materials should be addressed to Lukas Broers.

**Peer review information** Communications Physics thanks the anonymous reviewers for their contribution to the peer review of this work. Peer reviewer reports are available.

**Reprints and permission information** is available at http://www.nature.com/reprints

**Publisher's note** Springer Nature remains neutral with regard to jurisdictional claims in published maps and institutional affiliations.

## 2.8 Publication III: Detecting light-induced Floquet band gaps of graphene via trARPES

L. Broers and L. Mathey — **Phys. Rev. Research 4, 013057 (2022)**

This work was motivated by the prospect of direct experimental observation of the light-induced Floquet band gap at the Dirac point of graphene driven by circularly polarized light, similar to Publication II. While many similar observations have been made in different materials, the observation of the Floquet gap at the Dirac point of light-driven graphene has not been achieved due to a set of challenges and limitations in photoelectron spectroscopy techniques.

In this work, I have studied the numerical predictions of time-resolved angle-resolved photoelectron spectroscopy (trARPES), which is a state-of-the-art tool for studying material band structures. It is also a naturally accessible observable in the numerical methods devised in Publication I and Publication II. I have demonstrated a particular regime of parameters that promises to reveal the Floquet band gap, while also being experimentally feasible. This proposed regime takes the experimental limitations of mobility, Fourier broadening, laser-assisted photoemission, probe-pulse energy resolution, and space-charge effects into account. In general, the driving frequency needs to be large enough such that the light-induced Floquet band gaps overcome broadening effects. In an undesirable compromise, a large driving frequency however necessitates a disproportionately larger driving field strength, which induces undesired space-charge effects and laser-assisted photoelectrons that obscure the ARPES signal.

A key result of this work is that my numerics have shown a lack of population in the vicinity of the Dirac point in lower-order Floquet bands, provided the driving is strong enough. The population at the Dirac points remains predominantly in the Floquet-Bloch bands that are continuously connected to the Dirac point as a function of the driving field strength. As a consequence, the energy difference of populated Floquet-Bloch bands at vanishing momenta effectively surpassed the size of the Floquet zones and thus the experimental limitations in resolution. This circumstance makes the gap in principle visible even in the presence of broadening and resolution limitations in moderately clean graphene samples.

My contribution to this work consisted of conceiving the project, creating the numerical code, performing the numerical studies, performing the analytical calculations, analyzing and presenting the results, and writing the manuscript. All of this was done under the supervision and with the guidance of LM.

# Detecting light-induced Floquet band gaps of graphene via trARPES

Lukas Broers [1,2] and Ludwig Mathey[1,2,3]

[1]*Center for Optical Quantum Technologies, University of Hamburg, 22761 Hamburg, Germany*
[2]*Institute for Laser Physics, University of Hamburg, 22761 Hamburg, Germany*
[3]*The Hamburg Center for Ultrafast Imaging, Luruper Chaussee 149, 22761 Hamburg, Germany*

We propose a realistic regime to detect the light-induced topological band gap in graphene via time-resolved angle-resolved photoelectron spectroscopy (trARPES), which can be achieved with current technology. The direct observation of Floquet-Bloch bands in graphene is limited by low-mobility, Fourier-broadening, laser-assisted photoemission (LAPE), probe-pulse energy-resolution bounds, space-charge effects, and more. We characterize a regime of low driving frequency and high amplitude of the circularly polarized light that induces an effective band gap at the Dirac point that exceeds the Floquet zone. This circumvents limitations due to energy resolutions and band broadening. The electron distribution across the Floquet replicas in this limit allows for distinguishing LAPE replicas from Floquet replicas. We derive our results from a dissipative master equation approach that gives access to two-point correlation functions and the electron distribution relevant for trARPES measurements.

## I. INTRODUCTION

Floquet engineering constitutes a novel approach to control material properties via light [1–4]. A prominent example is the proposed light-induced topologically insulating state of monolayer graphene [5–7]. The resulting anomalous Hall effect in this system has been observed experimentally [8] and has been explained as a geometric-dissipative effect [9] in accordance with Floquet theory. Meanwhile, time-resolved angle-resolved photoemission spectroscopy (trARPES) has been established as the prime method for resolving dynamical changes in effective band structures of solid-state systems [10–16]. Experimental trARPES setups are constantly improving and being used for investigating the dynamical electronic processes in two-dimensional Dirac materials such as graphene [17–21], $WSe_2$ [20–24], and $Bi_2Se_3$ [25–28]. Approaches related to observing pseudospin textures in ARPES were discussed in Refs. [29–32]. In $Bi_2Se_3$, Floquet replicas of electronic bands were observed using trARPES setups [33]. However, the direct observation of both the replicas and the topological gap at the Dirac point has been met with intricate challenges in graphene and remains unachieved to date.

In this work we determine the regime of trARPES measurements for observing the topological band gap at the Dirac point of irradiated graphene. We propose to perform these measurements in the regime of low driving frequencies and high driving field strengths. In this previously unexplored

regime the dominant Floquet-Bloch band occupations are spaced farther apart than the driving frequency. They are therefore outside of the first Floquet zone. We propose to detect this light-induced energy gap beyond the Floquet zone in experiment because the different spectral features are well resolved in this regime. We discuss the dependence of our predictions on the system parameters, specifically how they affect the systematic limitations of the energy resolution of photoemission spectroscopy. These parameters include the driving frequency and field strength, which determine the Floquet-Bloch band structure, the dissipation coefficients that broaden the band signals, and the pulse lengths of drive and probe lasers. For the pulse lengths we point out a desirable regime with sufficient energy resolution and high enough repetition rates. These repetition rates are necessary to avoid undesired space-charge effects, where the photoemitted electrons interact and affect each other's trajectories [23,34–36]. In particular, it is possible to distinguish the laser-assisted photoemission (LAPE) replicas from the Floquet replicas within the gap at the Dirac point in our suggested regime.

We consider a single layer of graphene irradiated by a circularly polarized infrared laser from a perpendicular direction. We consider a laser pulse with a temporal Gaussian envelope of pulse length $\tau_d$. The pulse length is assumed to be much longer than the driving period, so that it induces Floquet-Bloch states that vary with the envelope function of the pulse. The graphene sample is probed by a tunable extreme ultraviolet laser pulse from the same direction. It has a shorter pulse length and excites photoelectrons out of the driven graphene over a time span during which the driving intensity is approximately constant. This is necessary for resolving the time-dependent Floquet-Bloch bands, which are sensitive to the driving amplitude. This is considered the standard approach to trARPES experiments [37] and is illustrated
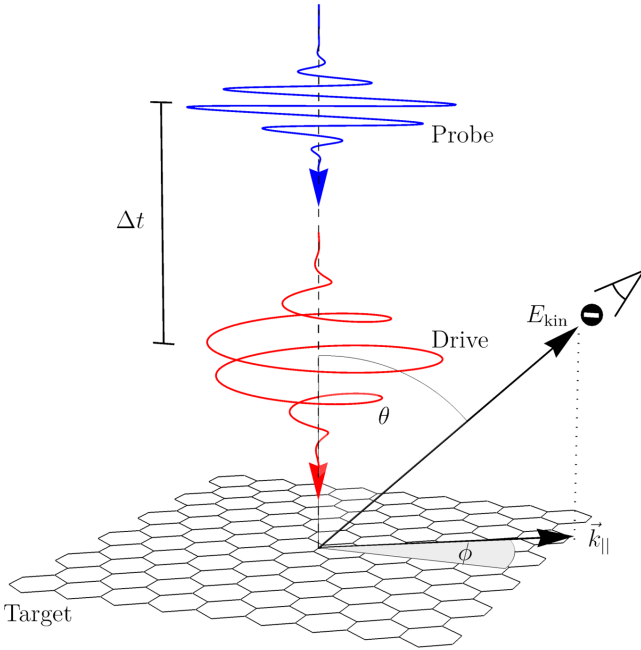
---

FIG. 1. An illustration of the trARPES principle. A circularly polarized infrared drive pulse (red) hits the graphene target from a perpendicular direction, exciting a transient state in the illuminated region. After a time delay of $\Delta t$, an ultraviolet probe pulse (blue) hits the target and excites photoelectrons. A given electron leaves the target with a kinetic energy $E_{\text{kin}}$ at an inclination $\theta$ to the graphene target and at an azimuthal angle $\phi$. The momentum component $\vec{k}_{||}$ parallel to the target is that of the preprobe transient state of the electron bound in the graphene layer.

in Fig. 1. The emitted photoelectrons corresponding to a probe frequency $\omega_{\text{p}}$ have the kinetic energy

$$E_{\text{kin}} = \hbar\omega_{\text{p}} - E_{\text{b}} - \Phi, \tag{1}$$

where $E_{\text{b}}$ is the binding energy and $\Phi$ is the work function of the material, which is the energy required to remove the electron from the graphene. In addition, a photoelectron has momentum $\vec{k}$ with components

$$\vec{k}_{||} = \sqrt{2mE_{\text{kin}}}\hbar^{-1}\sin(\theta)(\cos(\phi), \sin(\phi))^{\text{T}} \tag{2}$$

parallel to the graphene layer. $m$ is the electron mass, and $\theta$ and $\phi$ are the inclination and azimuthal angles of the momentum with respect to the graphene layer. Measuring the photoelectron counts at these angles and energies gives access to the time-resolved Floquet-Bloch bands. The momentum $\vec{k}_{||}$ is the electron momentum prior to the excitation process. For simplicity this is denoted as **k** in the following.

## II. PREDICTIONS FOR trARPES MEASUREMENTS

We describe the electron dynamics in graphene with the Hamiltonian

$$H(t) = \sum_{\mathbf{k}} c_{\mathbf{k}}^{\dagger} h(\mathbf{k}, t) c_{\mathbf{k}}, \tag{3}$$

where $c_{\mathbf{k}} = (c_{\mathbf{k},A}, c_{\mathbf{k},B})^{\text{T}}$. Here $c_{\mathbf{k},i}^{(\dagger)}$, with $i \in \{A, B\}$, are the annihilation (creation) operators of the graphene sublattices.

The single-particle Hamiltonian is given by

$$h(\mathbf{k}, t) = \hbar v_F [q_x(t)\sigma_x + q_y(t)\sigma_y], \tag{4}$$

with

$$q_x(t) = k_x + \frac{e}{\hbar}A_{\text{d}}(t)\sin(\omega_{\text{d}}t), \tag{5}$$

$$q_y(t) = k_y + \frac{e}{\hbar}A_{\text{d}}(t)\cos(\omega_{\text{d}}t), \tag{6}$$

where $v_F \approx 10^6\,\text{ms}^{-1}$ is the Fermi velocity and $k_x = |\mathbf{k}|\cos(\phi)$ and $k_y = |\mathbf{k}|\sin(\phi)$ are the momentum components. $\sigma_i$ are the Pauli matrices. The pulsed vector potential amplitude is given by

$$A_{\text{d}}(t) = \frac{E_{\text{d}}}{\omega_{\text{d}}} \exp\left\{-t^2\tau_{\text{d}}^{-2}4\ln(2)\right\}, \tag{7}$$

where $\tau_{\text{d}}$ is the driving pulse full width at half maximum (FWHM). For the pulse length we use the value $\tau_{\text{d}} = 500\,\text{fs}$ as a realistic value for driving frequencies in the range of tens to hundreds of terahertz. Note that the specific choice of a temporal Gaussian envelope is not crucial for the results. However, more quickly varying temporal envelopes may induce transient behavior that potentially obscure band signals.

We consider a product state $\rho = \Pi_{\mathbf{k}}\rho_{\mathbf{k}}$ and evolve the system using a Lindblad–von Neumann master equation that includes dissipation. The dissipation channels amount to dephasing, decay, and electron exchange with a back gate. The corresponding coefficients are chosen to be $\gamma_z = 22.5\,\text{THz} \approx (44.4\,\text{fs})^{-1}$, $\gamma_{\pm} = 10\,\text{THz} = (100\,\text{fs})^{-1}$ and $\gamma_{\text{bg}} = 25\,\text{THz} = (40\,\text{fs})^{-1}$. These are the values that were demonstrated to describe the experimental realization of Ref. [8] in Ref. [9]. Hence, this approach is well suited to describing the dynamics in realistic solid-state samples, despite the potential intricacies of material defects [38–41]. These values for the dissipation coefficients also agree with the relaxation times of 20 to 40 fs found in Refs. [42–45] and the electron-phonon channel relaxation estimated to be on the order of 100 fs [44–46]. This also gives the timescale of the system to form a steady state with an effective Floquet spectrum. We include a nonzero temperature in the system by giving corresponding Boltzmann factors to complementary dissipation coefficients so that the equilibrium states realize the desired temperature $T$. Throughout this work we use room temperature $T = 300\,\text{K}$. For details of this approach, see Ref. [9] or Appendix A.

Our predictions for the trARPES measurements are based on the momentum- and energy-resolved electron distribution calculated as [47]

$$n(k, \omega) = \int_{-t_0}^{t_0}\int_{-t_0}^{t_0} s(t_1)s(t_2)\mathcal{G}(k, t_2, t_1)\frac{e^{i\omega(t_2-t_1)}}{4t_0^2}dt_2 dt_1 \tag{8}$$

with the correlator [48]

$$\mathcal{G}(\mathbf{k}, t_2, t_1) = \sum_{i \in \{A,B\}} \langle c_{\mathbf{k},i}^{\dagger}(t_2)c_{\mathbf{k},i}(t_1)\rangle \tag{9}$$

and the probe pulse envelope

$$s(t) = \exp\left\{-(t - \Delta t)^2\tau_{\text{p}}^{-2}4\ln(2)\right\}, \tag{10}$$

where $\tau_{\text{p}}$ is the probe pulse length (FWHM) and $\Delta t$ is the delay time between the incidence of the drive and probe pulses. For the probe length we use the value $\tau_{\text{p}} = 100\,\text{fs}$. $t_0$ is the
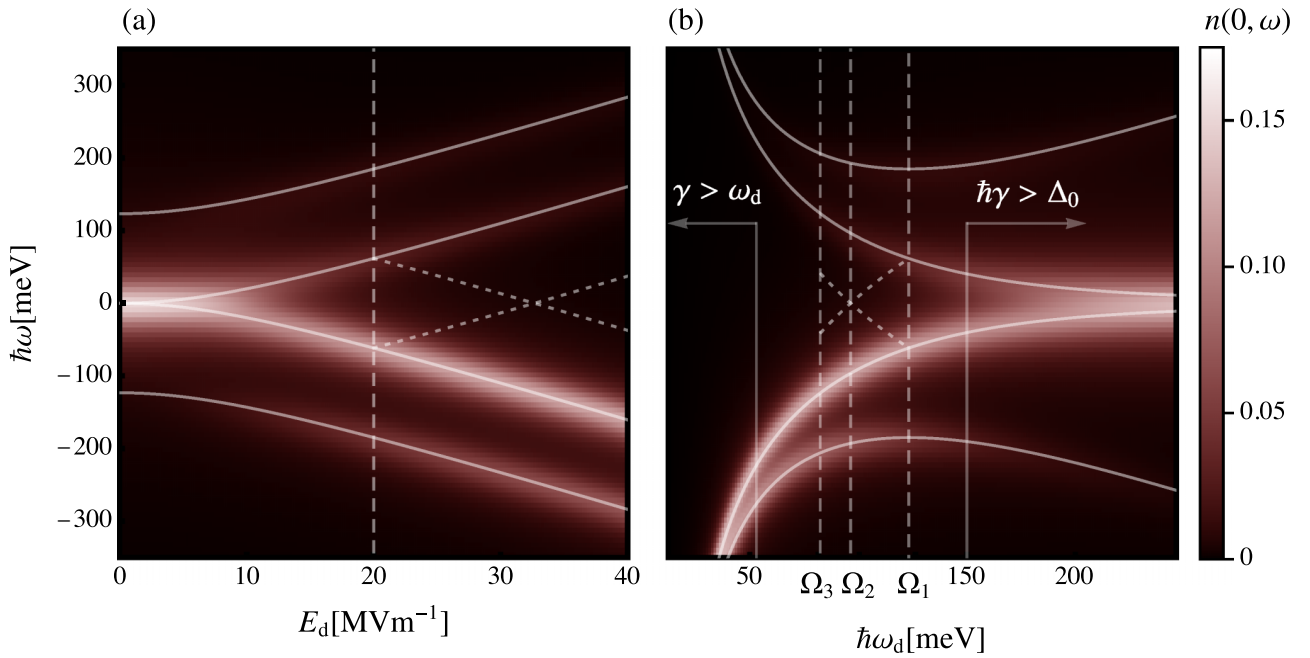
FIG. 2. The electron distribution at the Dirac point $n(\mathbf{k} = 0, \omega)$ for zero delay ($\Delta t = 0$) (a) as a function of the driving field strength at the driving frequency $\omega_d = 2\pi \times 29.8\,\mathrm{THz} \approx 123\,\mathrm{meV}\hbar^{-1}$ and (b) as a function of the driving frequency at driving field strength $E_d = 20\,\mathrm{MV\,m^{-1}}$. The solid lines show the expected Floquet energies $\pm\sqrt{(ev_F E_d/\omega_d)^2 + (\hbar\omega_d/2)^2} \pm \hbar\omega_d/2$. The dotted lines show the Floquet energies confined within the first Floquet zone of width $\hbar\omega_d$. The dashed lines indicate the field strength at which $\Delta_0 = \hbar\omega_d$ in (a) and the driving frequencies $\Omega_{m=1,2,3}$ in (b). The frequencies $\Omega_{m=1,2,3}$ are defined in Eq. (14). The examples shown in Figs. 3 and 4 also use these frequencies.

temporal integration range, for which we choose $t_0 = 3\tau_d$ to support the probe pulse sufficiently well.

We choose the pulse lengths of the drive and the pump pulse to fulfill two requirements. First, the probe pulse length is chosen to be short compared to the drive pulse length, so that the drive-induced dynamics is resolved. Second, the probe pulse length is chosen to be large compared to the driving period. These conditions are expressed as

$$\tau_d \gg \tau_p \gg \frac{2\pi}{\omega_d}. \tag{11}$$

When the probe pulse length $\tau_p$ and the driving period $2\pi/\omega_d$ are comparable, Eq. (8) no longer resolves Floquet-Bloch bands but rather resolves subdriving period electron occupations. We note that increasing the pulse lengths requires increasing the drive pulse energies, which are experimentally limited. This also leads to a reduced repetition rate, which results in undesirable space-charge effects that greatly decrease the resolution due to electron scattering [34,35,49]. We do not include this effect in our numerics but acknowledge that it necessitates a compromise in the pulse lengths, which is reached with the given values of $\tau_p$ and $\tau_d$.

## III. NONEQUILIBRIUM ELECTRON DISTRIBUTION NEAR THE DIRAC POINT

In Fig. 2(a), we show the electron distribution $n(\mathbf{k} = 0, \omega)$ at the Dirac point at zero delay, i.e., $\Delta t = 0$. We choose the driving frequency $\omega_d = 2\pi \times 29.8\,\mathrm{THz}$ and display the electron distribution as a function of the driving field strength

$E_d$. We refer to the energy difference of the two distribution maxima that emerge at $\mathbf{k} = 0$ as the energy gap $\Delta_0$. We see that this gap $\Delta_0$ grows monotonously as a function of $E_d$ rather than being confined within the first Floquet zone of width $\omega_d$, as also discussed in Ref. [50]. We derive the Floquet energy gap at the Dirac point from $h(\mathbf{k} = 0, t)$ with a fixed vector potential amplitude $A_d = E_d/\omega_d$. Using the Rabi solution, we obtain the energy (see Appendix B)

$$\Delta_0/2 = \sqrt{(ev_F E_d/\omega_d)^2 + (\hbar\omega_d/2)^2} - \hbar\omega_d/2. \tag{12}$$

In the following, we point out the most promising regime in which this gap can be detected. As we display in Fig. 2(a), the gap $\Delta_0$ grows with increasing driving strength $E_d$; in particular it grows beyond the Floquet zone boundary at $\omega_d/2$. We propose to detect the energy gap $\Delta_0$ in this strongly driven regime in which $\hbar\omega_d \approx \Delta_0$. While the Floquet quasienergies are confined to the Floquet zone, the maxima of the electron distribution continue to be shifted to higher frequencies with increasing $E_d$ so that they can be resolved despite broadening effects and energy resolution limitations. For very large field strengths with $\Delta_0 \gg \hbar\omega_d$, the electrons will predominantly populate the lower bands at the Dirac point. Therefore, intermediate values of $E_d$ are desirable, such that $\Delta_0 \approx \hbar\omega_d$, as we discuss throughout this paper.

In Fig. 2(b), we show the electron distribution $n(\mathbf{k} = 0, \omega)$ at zero delay, i.e., $\Delta t = 0$, at the Dirac point for driving field strength $E_d = 20\,\mathrm{MV\,m^{-1}}$ as a function of the driving frequency $\omega_d$. We display the energies $\pm\sqrt{(ev_F E_d/\omega_d)^2 + (\hbar\omega_d/2)^2} \pm \hbar\omega_d/2$, which reproduce the

maxima of the electron distribution. We see the expected scaling behavior of the gap at the Dirac point $\Delta_0$ of Eq. (12) as well as the spacing between the nearest Floquet replica $\Delta_0 + \hbar\omega_d$. We propose to measure the electron distribution in the regime that is given by $\omega_d > \gamma$ and $\Delta_0 > \hbar\gamma$. $\gamma$ is given by $\gamma = \gamma_\pm/2 + 2\gamma_z + \gamma_{bg} = 75\,\text{THz} \approx 50\,\text{meV}/\hbar \approx (13.3\,\text{fs})^{-1}$ as an overall metric for the decay rate. This value for $\gamma$ is comparable to the coherence times of 22 fs found in Ref. [51]. With increasing $\omega_d$ and for fixed $E_d$, $\Delta_0$ decreases. This dependence is predicted by Eq. (12). If $\Delta_0$ is smaller than $\hbar\gamma$, the two maxima of the electron distribution are not resolved and are not detectable via trARPES. With decreasing $\omega_d$, $\Delta_0$ increases and becomes easier to resolve. However, the driving period $2\pi/\omega_d$ needs to be shorter than the characteristic timescale of the dissipative processes, i.e., $\omega_d > \gamma$. Otherwise, the picture of a close to adiabatically stirred Dirac cone in equilibrium is more appropriate than that of emerging Floquet-Bloch bands. Long scattering times have also been connected to the visibility of $\Delta_0$ in Ref. [52]. The range of feasible driving frequencies given by these two conditions decreases for increasing $\gamma$ but increases for increasing $E_d$.

In general, the $m$-photon gaps $\Delta_m$ open up at momenta of $v_F|\mathbf{k}| = m\omega_d/2$, with $m > 0$, for small field strengths $E_d$. These gaps move inwards towards the Dirac point for increasing field strengths. Thus, increasing $E_d$ increases the gap at the Dirac point but at the same time decreases the distance in momentum space to higher-order gaps. For the driving field strength [50]

$$E_d = \frac{\hbar\omega_d^2}{ev_F}\sqrt{\frac{m^2}{4} + \frac{m}{2}} \qquad (13)$$

the $m$th gap is located at $\mathbf{k} = 0$ and merges with the gap $\Delta_0$. The next gap $\Delta_{m+1}$ is then the gap closest to the Dirac point with its distance maximized with respect to $E_d$. This further enhances the visibility of the gap at the Dirac point and makes this relation between driving field strength and frequency desirable. We rewrite Eq. (13) to find the driving frequency that is necessary for a given field strength $E_d$ to have the gap $\Delta_0$ be equal to $m$ times the driving frequency $\omega_d$. It is

$$\Omega_m = \left(\frac{m^2}{4} + \frac{m}{2}\right)^{-\frac{1}{4}}\sqrt{ev_F\hbar^{-1}E_d}. \qquad (14)$$

The driving frequencies $\omega_d = \Omega_m$ have the highest distinguishability and are indicated in Fig. 2(b) as vertical dashed lines. Additionally, at the frequency $\omega_d = \Omega_1 = (\frac{4}{3})^{\frac{1}{4}}\sqrt{ev_F\hbar^{-1}E_d}$, the energy of the first Floquet replica at $\Delta_0/2 + \hbar\omega_d$ is minimized. This point denotes a regime that is well suited for trARPES probing, and the conditions for resolvability simplify to $\gamma < (\frac{4}{3})^{\frac{1}{4}}\sqrt{ev_F\hbar^{-1}E_d}$. For $\gamma = 75\,\text{THz}$ and $E_d \approx 20\,\text{MV m}^{-1}$, this suggests a driving frequency close to $\omega_d = \Omega_1 \approx 2\pi \times 29.8\,\text{THz} \approx 123\,\text{meV}\hbar^{-1}$ or $\omega_d = \Omega_2 \approx 2\pi \times 23\,\text{THz} \approx 96\,\text{meV}\hbar^{-1}$.

To demonstrate the steady state that emerges for driving at frequencies $\omega_d = \Omega_1$, $\Omega_2$, and $\Omega_3$, we show the electron distribution $n(\mathbf{k}, \omega)$ in Fig. 3. This expands on the steady-state behavior of the electron distribution $n(\mathbf{k} = 0, \omega)$ that we displayed in Fig. 2. We choose driving field strength $E_d = 20\,\text{MV m}^{-1}$. In the vicinity of the Dirac point, band
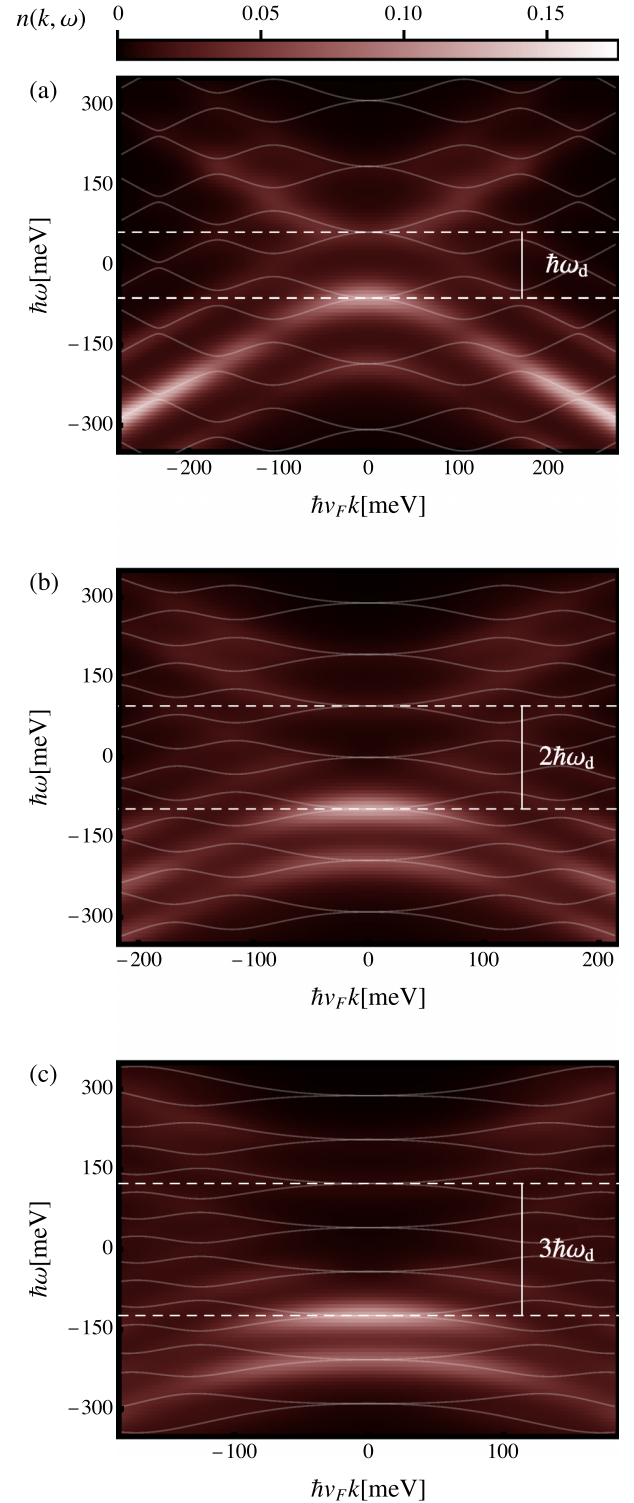


FIG. 3. The electron distribution $n(\mathbf{k}, \omega)$ for zero delay ($\Delta t = 0$) and driving field strength $E_d = 20\,\text{MV m}^{-1}$. The driving frequencies are (a) $\omega_d = \Omega_1$, (b) $\omega_d = \Omega_2$, and (c) $\omega_d = \Omega_3$. The dashed lines indicate an effective gap $\Delta_0$ of size $\hbar\omega_d$ in (a), $2\hbar\omega_d$ in (b), and $3\hbar\omega_d$ in (c). The solid lines indicate the instantaneous spectra obtained from the Floquet Hamiltonian.

occupations of the lower Floquet replicas are suppressed. The Floquet replicas with sizable electron occupation are two upper and two lower effective bands at the Dirac point, which are the four bands shown in Fig. 2. As the gap $\Delta_0$ increases, the population is predominantly distributed among the two lower bands. Away from the Dirac point, for nonzero $\mathbf{k}$, the additional Floquet bands have sizable electron occupation and are visible in Fig. 3. The finite values of the electron distribution inside the Floquet gaps is a consequence of the broadening that occurs due to dissipative processes.

Having pointed out the regime that we propose to use to detect the energy gap at the Dirac point in terms of the driving field strength and the driving frequency, we now present the time-resolved response of the system. Figure 4 shows the electron distribution at the Dirac point $n(\mathbf{k} = 0, \omega)$ as a function of the pulse delay time $\Delta t$ for the same driving field strength and driving frequencies as in Fig. 3, i.e., $\Omega_1$, $\Omega_2$, and $\Omega_3$ for $E_d = 20\,\text{MV m}^{-1}$. This gives an estimate of the time-resolved Floquet-Bloch band occupations at the Dirac point. The dashed lines indicate the corresponding Floquet energies expected from static driving field strengths given by the drive pulse at the delay time $\Delta t$, i.e.,

$$
\epsilon(\Delta t) = \pm \sqrt{\exp\left\{-\frac{\Delta t^2}{\tau_d^2} 8\ln(2)\right\}\left(\frac{ev_F E_d}{\omega_d}\right)^2 + \left(\frac{\hbar\omega_d}{2}\right)^2}
$$
$$
\pm \frac{\hbar\omega_d}{2}. \tag{15}
$$

The electron distributions that we show in Fig. 4 are close to the instantaneous steady-state distribution for this value of $\gamma$. Deviations from the instantaneous steady-state distribution manifest themselves as features that are asymmetric during the pulse rise and pulse decay. For this choice of $\gamma$ and of the pulse lengths, these features are small.

## IV. LIMITATIONS OF RESOLUTION

One common phenomenon that obscures the results of trARPES is LAPE [53]. The essentially free photoelectrons emitted in a trARPES experiment respond to the drive pulse with driving frequency $\omega_d$. This may result in the photoelectron energy being shifted by one unit of the photon energy $\pm\hbar\omega_d$. These energy shifts are detected in trARPES measurements as band replicas, whose similarities to Floquet replicas might hinder identifying the signatures of Floquet physics unambiguously. However, in contrast to Floquet replicas, these LAPE replicas are not related to band gaps [37]. The magnitude of the light-induced Floquet band gaps is tunable via the field strength $E_d$ [see Eq. (12)]. We propose to use this tunability to distinguish the LAPE and Floquet replicas. More specifically, the Floquet replicas at the Dirac point are at $\pm\Delta_0/2$ and $\pm(\Delta_0/2 + \hbar\omega_d)$, as we show in Fig. 3. The monotonous behavior of the Dirac gap $\Delta_0$ makes it possible to distinguish between LAPE and Floquet replicas.

The Floquet-Bloch bands resolved in $n(\mathbf{k}, \omega)$ are broadened due to dissipation. In addition they are Fourier broadened with the probe pulse length. The combined result is a Voigt



FIG. 4. The electron distribution $n(\mathbf{k} = 0, \omega)$ at the Dirac point as a function of the delay time $\Delta t$ for a peak driving field strength of $E_d = 20\,\text{MV m}^{-1}$. The driving frequencies are (a) $\omega_d = \Omega_1$, (b) $\omega_d = \Omega_2$, and (c) $\omega_d = \Omega_3$. The dashed lines indicate the static Floquet energies corresponding to the driving field strengths at the center of the probe pulse.

profile of approximate width

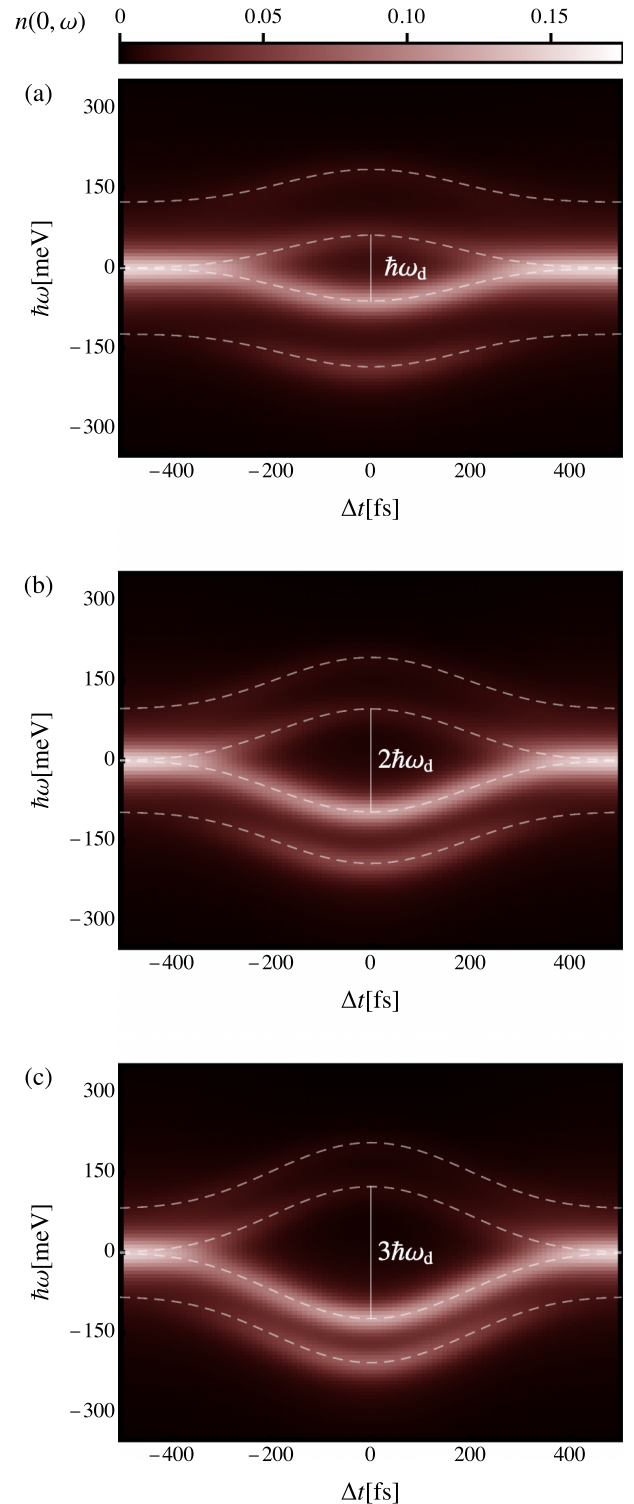$$\Gamma \approx \frac{\gamma}{2} + \sqrt{\frac{\gamma^2}{4} + \frac{4}{\tau_p^2}}, \qquad (16)$$

with $\gamma = \gamma_{\pm}/2 + 2\gamma_z + \gamma_{bg}$. For our specified values this is $\Gamma = 80\,\text{THz} = (12.5\,\text{fs})^{-1} \approx 53\,\text{meV}\,\hbar^{-1}$. In order to successfully resolve the effective bands in $n(\mathbf{k}, \omega)$ it is crucial that the bands gaps are large compared to $\Gamma$. For probe pulses long enough that their contribution to $\Gamma$ can be neglected, the broadening is $\gamma$ due to intrinsic dissipation. Reducing $\gamma$ can be achieved by using cleaner graphene samples with higher mobility, which is technologically challenging.

Furthermore, trARPES experiments are, in general, limited by a Gaussian pulse energy resolution of the order [37]

$$\Delta E \approx \tau_p^{-1} 1825\,\text{meV fs}. \qquad (17)$$

The energy resolution of the measurement has to exceed the band gap $\Delta_0$, the Floquet replica spacing $\omega_d$, and the Floquet-Bloch band Voigt width $\Gamma$. These requirements are realistically achieved in the proposed regime of $\Delta_0 > \hbar\omega_d$. For instance, fulfilling the resolvability conditions $\Gamma \ll \omega_d$ and $\Delta E \ll \hbar\omega_d$ is not a necessity for identifying signatures of Floquet physics for this regime.

To determine the minimal probe length that is necessary to achieve an energy resolution equal to the gap, we insert the expression for the gap $\Delta_0$ at the Dirac point into Eq. (17). It is

$$\tau_p^{min} = \frac{1825\,\text{meV fs}}{\sqrt{4e^2 v_F^2 E_d^2/\omega_d^2 + \hbar^2 \omega_d^2} - \hbar\omega_d}. \qquad (18)$$

An energy resolution several times better is necessary to clearly identify the Floquet-Bloch bands, which corresponds to probe pulse lengths several times larger than the minimal length, e.g., $\tau_p \approx 10\tau_p^{min}$.

## V. CONCLUSION

In conclusion, we have pointed out a realistic regime for the detection of the light-induced topological gap in graphene via time- and angle-resolved photoelectron spectroscopy. Our proposed regime addresses the limitations of band broadening, energy and momentum resolution, and intrinsic limitations of the detection method for realistic estimates of dissipative processes. We find that these limitations are overcome by increasing the driving field strength and decreasing the driving frequency so that the energy difference between finitely occupied Floquet-Bloch bands is larger than the Floquet zone. The timescales associated with the dissipative processes set the limits of this regime. On the one hand, the driving frequency has to be large enough that many driving cycles occur during one characteristic timescale of the dissipation. On the other, decreasing the driving frequency increases the gap size at the Dirac point, which has to exceed the band broadening. As the gap becomes larger than multiples of the driving frequency, limitations such as band broadening and inherent energy resolutions no longer obstruct the identifica-

tion of signatures of Floquet physics. This regime also allows undesired laser-assisted photoemission replicas in trARPES measurements to be unambiguously identified as such at the Dirac point and to be clearly distinguished from the Floquet replicas. The detection of Floquet bands via trARPES would constitute a profound insight in light-driven solids, which would complement the measurements of transport reported in Ref. [8] and thereby advance the field of optical control of solids.

## APPENDIX A: MASTER EQUATION

We base our numerics on the Lindblad–von Neumann master equation

$$\dot{\rho} = i[\rho, H] + \sum_j c_j (L_j \rho L_j^\dagger - \frac{1}{2}\{L_j^\dagger L_j, \rho\}), \qquad (A1)$$

where $j \in \{z, +, -, \pm 1, \pm 2, \pm 3, \pm 4\}$. We consider a product state in momentum space $\rho = \prod_k \rho_k$ and the Hamiltonian in Eq. (3) in the extended basis spanned by the states $|0\rangle$, $c_{\mathbf{k},A}^\dagger |0\rangle$, $c_{\mathbf{k},B}^\dagger |0\rangle$, and $c_{\mathbf{k},B}^\dagger c_{\mathbf{k},A}^\dagger |0\rangle$. The transformation $V$ into the instantaneous eigenbasis diagonalizes the Hamiltonian at any given time and determines the momentum-dependent Lindblad operators as

$$L_z = V(c_{\mathbf{k},A}^\dagger c_{\mathbf{k},A} - c_{\mathbf{k},B}^\dagger c_{\mathbf{k},B})V^\dagger, \qquad (A2)$$

$$L_+ = V c_{\mathbf{k},B}^\dagger c_{\mathbf{k},A} V^\dagger, \qquad (A3)$$

$$L_- = V c_{\mathbf{k},A}^\dagger c_{\mathbf{k},B} V^\dagger, \qquad (A4)$$

$$L_l = V \begin{pmatrix} 0 & \delta_{-1,l} & \delta_{-2,l} & 0 \\ \delta_{1,l} & 0 & 0 & \delta_{-3,l} \\ \delta_{2,l} & 0 & 0 & \delta_{-4,l} \\ 0 & \delta_{3,l} & \delta_{4,l} & 0 \end{pmatrix} V^\dagger. \qquad (A5)$$

The coefficients $c_j$ are

$$c_z = \gamma_z, \qquad (A6)$$

$$c_+ + c_- = \gamma_{\pm}, \quad c_+ = c_- e^{-2\epsilon\beta}, \qquad (A7)$$

$$c_j + c_{-j} = \gamma_{bg}, \quad c_{-1,2,3,-4} = c_{1,-2,-3,4} e^{\epsilon\beta}, \qquad (A8)$$

with $\beta = (k_B T)^{-1}$ and the instantaneous level spacing $\epsilon$. This four-dimensional description makes two-point correlation functions and therefore the electron distributions via Eqs. (8) and (9) accessible.

## APPENDIX B: FLOQUET ENERGIES

At the Dirac point, the graphene Hamiltonian in Eq. (3) with constant amplitude simplifies to

$$h(\mathbf{k} = 0, t) = \frac{ev_F}{\hbar} A_{\mathrm{d}}[\sin(\omega_{\mathrm{d}}t)\sigma_x + \cos(\omega_{\mathrm{d}}t)\sigma_y], \quad (\mathrm{B1})$$

which is the Rabi-Hamiltonian

$$H_{\mathrm{R}} = \hbar \begin{pmatrix} \omega_0/2 & \Omega e^{-i\omega_{\mathrm{d}}t} \\ \Omega e^{+i\omega_{\mathrm{d}}t} & -\omega_0/2 \end{pmatrix}, \quad (\mathrm{B2})$$

with $\omega_0 = 0$. In the rotating frame given by $\exp\{-i\sigma_z\omega_{\mathrm{d}}t/2\}$, the corresponding dynamics are governed by the static Hamiltonian

$$H'_{\mathrm{R}} = \hbar \begin{pmatrix} -\omega_{\mathrm{d}}/2 & \Omega \\ \Omega & +\omega_{\mathrm{d}}/2 \end{pmatrix} \quad (\mathrm{B3})$$

with eigenenergies

$$\epsilon = \hbar\sqrt{\Omega^2 + \omega_{\mathrm{d}}^2/4}. \quad (\mathrm{B4})$$

In the original frame of Eq. (B2) the solutions to the Schrödinger equation then rotate with the energies

$$\epsilon = \pm\hbar\left(\sqrt{\Omega^2 + \omega_{\mathrm{d}}^2/4} - \omega_{\mathrm{d}}/2\right), \quad (\mathrm{B5})$$

which gives Eq. (12) for $\Omega = ev_F\hbar^{-1}E_{\mathrm{d}}/\omega_{\mathrm{d}}$.

This expression increases monotonously as a function of $E_{\mathrm{d}}$, and the Floquet energies are given by this expression modulo the driving frequency $\omega_{\mathrm{d}}$. Put differently, $\epsilon \pm m\hbar\omega_{\mathrm{d}}$ gives the various Floquet replicas at the Dirac point. Whenever $\epsilon = m\hbar\omega_{\mathrm{d}}/2$, the expression of $\epsilon$ in Eq. (B5) crosses a Floquet zone boundary. We solve this condition for $E_{\mathrm{d}}$ to find the driving field strengths at which this occurs for the $m$th Floquet zone boundary. This gives us Eq. (13).

In the case of a time-dependent driving amplitude such as in Eq. (7) and under the assumption that the Floquet states form instantly, we insert the driving amplitude envelope at a given point in time $\Delta t$ expressed relative to the amplitude peak, such that

$$\Omega(\Delta t) = \frac{ev_F}{\hbar}\frac{E_{\mathrm{d}}}{\omega_{\mathrm{d}}} \exp\left\{-(\Delta t)^2\tau_{\mathrm{d}}^{-2}4\ln(2)\right\}. \quad (\mathrm{B6})$$

This leads to the expression $\epsilon(\Delta t)$ in Eq. (15).

[1] D. N. Basov, R. D. Averitt, and D. Hsieh, Towards properties on demand in quantum materials, Nat. Mater. **16**, 1077 (2017).

[2] N. H. Lindner, G. Refael, and V. Galitski, Floquet topological insulator in semiconductor quantum wells, Nat. Phys. **7**, 490 (2011).

[3] T. Kitagawa, T. Oka, A. Brataas, L. Fu, and E. Demler, Transport properties of nonequilibrium systems under the application of light: Photoinduced quantum hall insulators without landau levels, Phys. Rev. B **84**, 235108 (2011).

[4] M. Bukov, L. D'Alessio, and A. Polkovnikov, Universal high-frequency behavior of periodically driven systems: From dynamical stabilization to Floquet engineering, Adv. Phys. **64**, 139 (2015).

[5] T. Oka and H. Aoki, Photovoltaic Hall effect in graphene, Phys. Rev. B **79**, 081406(R) (2009).

[6] G. Usaj, P. M. Perez-Piskunow, L. E. F. Foa Torres, and C. A. Balseiro, Irradiated graphene as a tunable Floquet topological insulator, Phys. Rev. B **90**, 115423 (2014).

[7] M. Vogl, M. Rodriguez-Vega, and G. A. Fiete, Effective Floquet Hamiltonian in the low-frequency regime, Phys. Rev. B **101**, 024303 (2020).

[8] J. W. McIver, B. Schulte, F.-U. Stein, T. Matsuyama, G. Jotzu, G. Meier, and A. Cavalleri, Light-induced anomalous Hall effect in graphene, Nat. Phys. **16**, 38 (2019).

[9] M. Nuske, L. Broers, B. Schulte, G. Jotzu, S. A. Sato, A. Cavalleri, A. Rubio, J. W. McIver, and L. Mathey, Floquet dynamics in light-driven solids, Phys. Rev. Res. **2**, 043408 (2020).

[10] D. Kutnyakhov *et al.*, Time- and momentum-resolved photoemission studies using time-of-flight momentum microscopy at a free-electron laser, Rev. Sci. Instrum. **91**, 013109 (2020).

[11] C. M. Cacho, I. C. E. Turcu, C. A. Froud, W. A. Bryan, G. R. A. J. Nemeth, J. C. Petersen, N. Dean, A. Cavalleri, S. Kaiser, A. Simoncig, H. Y. Liu, A. L. Cavalieri, S. Dhesi, L. Poletto, P. Villoresi, F. Frassetto, and E. Springate, Ultrafast tr-ARPES with Artemis xuv beamline, in *Research in Optical Sciences* (Optical Society of America, Washington, DC, 2012), p. JT2A.43.

[12] S. Peli, D. Puntel, D. Kopic, B. Sockol, F. Parmigiani, and F. Cilento, Time-resolved vuv ARPES at 10.8 eV photon energy and mHz repetition rate, J. Electron Spectrosc. Relat. Phenom. **243**, 146978 (2020).

[13] G. Rohde, A. Hendel, A. Stange, K. Hanff, L.-P. Oloff, L. X. Yang, K. Rossnagel, and M. Bauer, Time-resolved ARPES with sub-15 fs temporal and near Fourier-limited spectral resolution, Rev. Sci. Instrum. **87**, 103102 (2016).

[14] S. Eich, A. Stange, A. V. Carr, J. Urbancic, T. Popmintchev, M. Wiesenmayer, K. Jansen, A. Ruffing, S. Jakobs, T. Rohwer, S. Hellmann, C. Chen, P. Matyba, L. Kipp, K. Rossnagel, M. Bauer, M. M. Murnane, H. C. Kapteyn, S. Mathias, and M. Aeschlimann, Time- and angle-resolved photoemission spectroscopy with optimized high-harmonic pulses using frequency-doubled Ti:sapphire lasers, J. Electron Spectrosc. Relat. Phenom. **195**, 231 (2014).

[15] M. Puppin, Y. Deng, C. W. Nicholson, J. Feldl, N. B. M. Schröter, H. Vita, P. S. Kirchmann, C. Monney, L. Rettig, M. Wolf, and R. Ernstorfer, Time- and angle-resolved photoemission spectroscopy of solids in the extreme ultraviolet at 500 kHz repetition rate, Rev. Sci. Instrum. **90**, 023104 (2019).

[16] C. W. Nicholson, A. Lücke, W. G. Schmidt, M. Puppin, L. Rettig, R. Ernstorfer, and M. Wolf, Beyond the molecular movie: Dynamics of bands and bonds during a photoinduced phase transition, Science **362**, 821 (2018).

[17] I. Gierz, S. Link, U. Starke, and A. Cavalleri, Non-equilibrium Dirac carrier dynamics in graphene investigated with time- and

angle-resolved photoemission spectroscopy, Faraday Discuss. **171**, 311 (2014).

[18] S. Ulstrup, J. C. Johannsen, A. Crepaldi, F. Cilento, M. Zacchigna, C. Cacho, R. T. Chapman, E. Springate, F. Fromm, C. Raidel, T. Seyller, F. Parmigiani, M. Grioni, and P. Hofmann, Ultrafast electron dynamics in epitaxial graphene investigated with time- and angle-resolved photoemission spectroscopy, J. Phys.: Condens. Matter **27**, 164206 (2015).

[19] I. Gierz, Probing carrier dynamics in photo-excited graphene with time-resolved ARPES, J. Electron Spectrosc. Relat. Phenom. **219**, 53 (2017).

[20] S. Aeschlimann, A. Rossi, M. Chávez-Cervantes, R. Krause, B. Arnoldi, B. Stadtmüller, M. Aeschlimann, S. Forti, F. Fabbri, C. Coletti, and I. Gierz, Direct evidence for efficient ultrafast charge separation in epitaxial WS$_2$/graphene heterostructures, Sci. Adv. **6**, 20 (2020).

[21] R. Krause, M. Chávez-Cervantes, S. Aeschlimann, S. Forti, F. Fabbri, A. Rossi, C. Coletti, C. Cacho, Y. Zhang, P. E. Majchrzak, R. T. Chapman, E. Springate, and I. Gierz, Ultrafast charge separation in bilayer WS$_2$/graphene heterostructure revealed by time- and angle-resolved photoemission spectroscopy, Front. Phys. **9**, 184 (2021).

[22] S. Dong, M. Puppin, T. Pincelli, S. Beaulieu, D. Christiansen, H. Hübener, C. W. Nicholson, R. P. Xian, M. Dendzik, Y. Deng, Y. W. Windsor, M. Selig, E. Malic, A. Rubio, A. Knorr, M. Wolf, L. Rettig, and R. Ernstorfer, Direct measurement of key exciton properties: Energy, dynamics, and spatial distribution of the wave function, Nat. Sci. **1**, e10010 (2021).

[23] J. Maklar, S. Dong, S. Beaulieu, T. Pincelli, M. Dendzik, Y. W. Windsor, R. P. Xian, M. Wolf, R. Ernstorfer, and L. Rettig, A quantitative comparison of time-of-flight momentum microscopes and hemispherical analyzers for time- and angle-resolved photoemission spectroscopy experiments, Rev. Sci. Instrum. **91**, 123112 (2020).

[24] R. Liu, Y. Ogawa, P. Chen, K. Ozawa, T. Suzuki, M. Okada, T. Someya, Y. Ishida, K. Okazaki, S. Shin, T. Chiang, and I. Matsuda, Femtosecond to picosecond transient effects in WSe$_2$ observed by pump-probe angle-resolved photoemission spectroscopy, Sci. Rep. **7**, 15981 (2017).

[25] I. Gierz, M. Mitrano, J. C. Petersen, C. Cacho, I. C. E. Turcu, E. Springate, A. Stöhr, A. Köhler, U. Starke, and A. Cavalleri, Population inversion in monolayer and bilayer graphene, J. Phys.: Condens. Matter **27**, 164204 (2015).

[26] F. Mahmood, C. Chan, Z. Alpichshev, D. Gardner, Y. Lee, P. A. Lee, and N. Gedik, Selective scattering between Floquet–Bloch and Volkov states in a topological insulator, Nat. Phys. **12**, 306 (2016).

[27] H. Soifer, A. Gauthier, A. F. Kemper, C. R. Rotundu, S.-L. Yang, H. Xiong, D. Lu, M. Hashimoto, P. S. Kirchmann, J. A. Sobota, and Z.-X. Shen, Band-Resolved Imaging of Photocurrent in a Topological Insulator, Phys. Rev. Lett. **122**, 167401 (2019).

[28] Y. H. Wang, D. Hsieh, D. Pilon, L. Fu, D. R. Gardner, Y. S. Lee, and N. Gedik, Observation of a Warped Helical Spin Texture in Bi$_2$Se$_3$ from Circular Dichroism Angle-Resolved Photoemission Spectroscopy, Phys. Rev. Lett. **107**, 207602 (2011).

[29] M. A. Sentef, M. Claassen, A. F. Kemper, B. Moritz, T. Oka, J. K. Freericks, and T. P. Devereaux, Theory of Floquet band

formation and local pseudospin textures in pump-probe photoemission of graphene, Nat. Commun. **6**, 7047 (2015).

[30] L. P. Gavensky, G. Usaj, and C. A. Balseiro, Photo-electrons unveil topological transitions in graphene-like systems, Sci. Rep. **6**, 36577 (2016).

[31] M. Schüler, U. De Giovannini, H. Hübener, A. Rubio, M. A. Sentef, T. P. Devereaux, and P. Werner, How Circular Dichroism in Time- and Angle-Resolved Photoemission Can Be Used to Spectroscopically Detect Transient Topological States in Graphene, Phys. Rev. X **10**, 041013 (2020).

[32] S. Beaulieu, J. Schusser, S. Dong, M. Schüler, T. Pincelli, M. Dendzik, J. Maklar, A. Neef, H. Ebert, K. Hricovini, M. Wolf, J. Braun, L. Rettig, J. Minár, and R. Ernstorfer, Revealing Hidden Orbital Pseudospin Texture with Time-Reversal Dichroism in Photoelectron Angular Distributions, Phys. Rev. Lett. **125**, 216404 (2020).

[33] Y. H. Wang, H. Steinberg, P. Jarillo-Herrero, and N. Gedik, Observation of Floquet-Bloch states on the surface of a topological insulator, Science **342**, 453 (2013).

[34] S. Hellmann, T. Ott, L. Kipp, and K. Rossnagel, Vacuum space-charge effects in nano-ARPES, Phys. Rev. B **85**, 075109 (2012).

[35] S. Hellmann, K. Rossnagel, M. Marczynski-Bühlow, and L. Kipp, Vacuum space-charge effects in solid-state photoemission, Phys. Rev. B **79**, 035402 (2009).

[36] L.-P. Oloff, K. Hanff, A. Stange, G. Rohde, F. Diekmann, M. Bauer, and K. Rossnagel, Pump laser-induced space-charge effects in HHG-driven time- and angle-resolved photoelectron spectroscopy, J. Appl. Phys. **119**, 225106 (2016).

[37] B. Lv, T. Qian, and H. Ding, Angle-resolved photoemission spectroscopy and its application to topological materials, Nat. Rev. Phys. **1**, 609 (2019).

[38] T. O. Wehling, A. V. Balatsky, M. I. Katsnelson, A. I. Lichtenstein, K. Scharnberg, and R. Wiesendanger, Local electronic signatures of impurity states in graphene, Phys. Rev. B **75**, 125425 (2007).

[39] S. Ihnatsenka and G. Kirczenow, Dirac point resonances due to atoms and molecules adsorbed on graphene and transport gaps and conductance quantization in graphene nanoribbons with covalently bonded adsorbates, Phys. Rev. B **83**, 245442 (2011).

[40] M. Inglot and V. K. Dugaev, Impurity states in graphene with intrinsic spin-orbit interaction, J. Appl. Phys. **109**, 123709 (2011).

[41] Y. G. Pogorelov, V. M. Loktev, and D. Kochan, Impurity resonance effects in graphene versus impurity location, concentration, and sublattice occupation, Phys. Rev. B **102**, 155414 (2020).

[42] T. Higuchi, C. Heide, K. Ullmann, H. B. Weber, and P. Hommelhoff, Light-field-driven currents in graphene, Nature (London) **550**, 224 (2017).

[43] I. Gierz, F. Calegari, S. Aeschlimann, M. Chávez Cervantes, C. Cacho, R. T. Chapman, E. Springate, S. Link, U. Starke, C. R. Ast, and A. Cavalleri, Tracking Primary Thermalization Events in Graphene with Photoemission at Extreme Time Scales, Phys. Rev. Lett. **115**, 086803 (2015).

[44] M. Breusing, C. Ropers, and T. Elsaesser, Ultrafast Carrier Dynamics in Graphite, Phys. Rev. Lett. **102**, 086809 (2009).

[45] I. Gierz, J. C. Petersen, M. Mitrano, C. Cacho, I. C. E. Turcu, E. Springate, A. Stöhr, A. Köhler, U. Starke, and A. Cavalleri, Snapshots of non-equilibrium Dirac carrier distributions in graphene, Nat. Mater. **12**, 1119 (2013).

[46] M. Breusing, S. Kuehn, T. Winzer, E. Malić, F. Milde, N. Severin, J. P. Rabe, C. Ropers, A. Knorr, and T. Elsaesser, Ultrafast nonequilibrium carrier dynamics in a single graphene layer, Phys. Rev. B **83**, 153410 (2011).

[47] J. K. Freericks, H. R. Krishnamurthy, and Th. Pruschke, Theoretical Description of Time-Resolved Photoemission Spectroscopy: Application to Pump-Probe Experiments, Phys. Rev. Lett. **102**, 136401 (2009).

[48] This expression for $\mathcal{G}(k, t_2, t_1)$ omits coherence terms such as $c_{k,A}^\dagger(t_2)c_{k,B}(t_1)$, which are responsible for the dark corridor in graphene.

[49] J. Graf, S. Hellmann, C. Jozwiak, C. L. Smallwood, Z. Hussain, R. A. Kaindl, L. Kipp, K. Rossnagel, and A. Lanzara, Vacuum space charge effect in laser-based solid-state photoemission spectroscopy, J. Appl. Phys. **107**, 014912 (2010).

[50] L. Broers and L. Mathey, Observing light-induced Floquet band gaps in the longitudinal conductivity of graphene, Comm. Phys. **4**, 248 (2021).

[51] C. Heide, T. Eckstein, T. Boolakee, C. Gerner, H. B. Weber, I. Franco, and P. Hommelhoff, Electronic coherence and coherent dephasing in the optical control of electrons in graphene, Nano Lett. **21**, 9403 (2021).

[52] S. Aeschlimann, S. A. Sato, R. Krause, M. Chávez-Cervantes, U. De Giovannini, H. Hübener, S. Forti, C. Coletti, K. Hanff, K. Rossnagel, A. Rubio, and I. Gierz, Survival of Floquet-Bloch states in the presence of scattering, Nano Lett. **21**, 5028 (2021).

[53] G. Saathoff, L. Miaja-Avila, M. Aeschlimann, M. M. Murnane, and H. C. Kapteyn, Laser-assisted photoemission from surfaces, Phys. Rev. A **77**, 022903 (2008).

## 2.9 Publication IV: Non-linear photoconductivity of strongly driven graphene

L. Broers and L. Mathey — **arXiv:2312.13217 (Under review at SciPost Phys.)**

This work was motivated by the prospect of obtaining a more detailed understanding of the non-linear electronic transport properties of strongly driven dissipative graphene. Non-linear charge transport plays a crucial role in the light-controlled transport with few-cycle pulses, and coherent electronics. A detailed understanding of driven graphene is paramount for the development of new devices based on these effects. This work is a preprint, and potentially subject to changes.

I have studied the non-linear photoconductivity of graphene in the presence of both linearly polarized strong driving, and a strong direct bias in parallel direction. This non-linear AC-DC transport setup provides a rich structure in the differential photoconductivity with distinct limits where either the AC field or the DC field outweighs the other. I have captured the dynamics in these two limits by using distinct descriptions, that present good agreement with simulated results. In the limit of a dominant DC field, I have explained the non-linear conductivity using a picture of modulated Landau-Zener transitions. I have presented an analytical calculation that agrees with the structure of the non-linear differential photoconductivity as a function of the electrical field strengths. The DC field leads to a strong anisotropy of the momentum-distribution of currents, reminiscent of wake-fields of current density in momentum-space emerging at the Dirac point. Based on this observation, I have provided an analytical calculation of the conductivity of undriven graphene as a function of temperature and DC field strength in the non-linear regime, which recovers the distinct features of the numerical results. In the opposite limit of a dominant AC field, I have provided a description rooted in Floquet physics that is reminiscent of the Tien-Gordon effect of photon-assisted tunneling and qualitatively agrees well with analytical estimates. The differential photoconductivity displays a checkerboard pattern that emerges from the displacement in momentum space due to the DC field within the Floquet-Bloch band structure in the presence of high intensity driving.

My contribution to this work consisted of conceiving the project, creating the numerical code, performing the numerical studies, performing the analytical calculations, analyzing and presenting the results, and writing the manuscript. All of this was done under the supervision and with the guidance of LM.

# Non-linear photoconductivity of strongly driven graphene

Lukas Broers[1,2,*], Ludwig Mathey[1,2,3]

**1** Center for Optical Quantum Technologies, University of Hamburg, Hamburg, Germany
**2** Institute for Quantum Physics, University of Hamburg, Hamburg, Germany
**3** The Hamburg Center for Ultrafast Imaging, Hamburg, Germany
* lbroers@physnet.uni-hamburg.de

December 21, 2023

## Abstract

We present the non-linear DC photoconductivity of graphene under strong infra-red (IR) radiation. The photoconductivity is obtained as the response to a strong DC electric field, with field strengths outside of the linear-response regime, while the IR radiation is described by a strong AC electric field. The conductivity displays two distinct regimes in which either the DC or the AC field dominates. We explore these regimes and associate them with the dynamics of driven Landau-Zener quenches in the case of a large DC field. In the limit of large AC field, we describe the conductivity in a Floquet picture and compare the results to the closely related Tien-Gordon effect. We present analytical calculations for the non-linear differential photoconductivity, for both regimes based on the corresponding mechanisms. As part of this discussion of the non-equilibrium state of graphene, we present analytical estimates of the conductivity of undriven graphene as a function of temperature and DC bias field strength that show very good agreement with our simulations.

## Contents

# 1 Introduction

Graphene displays a wide range of remarkable properties, which have been the subject of basic research and of technological interest, since its discovery [1–6]. A key interest have been the electronic transport properties [7–26], as well as the optical properties [27–34], including the more recent shift of interest towards optical driving [35–41]. As a key example we mention circularly polarized light which generates topological Floquet band gaps leading to an anomalous Hall effect [42–45]. Control of transport has been demonstrated by driving graphene with short pulses, which leads to charge-envelope-phase-dependent Stückelberg interferometrically induced currents [46–49]. The coherent destruction of tunneling [50–52] has been proposed in strongly driven graphene [53], as well as photon-assisted tunneling [54]. Given the recent studies of light-controlled phenomena in graphene, a comprehensive characterization of the non-linear photoconductivity and coherent dynamics and transport in periodically driven graphene is imperative, and is also motivated by future technologies based on high-intensity driving.

In this work, we present the non-linear longitudinal DC photoconductivity of monolayer graphene driven with linearly polarized terahertz radiation at the charge neutrality point. The polarization of the driving radiation is parallel to the probing polarization. We utilize a Master equation approach that explicitly models the dissipative properties of the material, see [45]. We identify a rich structure in the differential conductivity which features two limits, in which either the DC probing field strength or the AC driving field strength dominates. These two limits are separated by a regime in which the two fields are comparatively strong, and the dynamics display a subtle competition. In the regime in which the DC field dominates, we describe the dynamics via Landau-Zener (LZ) transitions that are modulated by the radiation field, and affected by the dissipative properties of the system. Due to the modulation by the radiation field, dynamical patterns in momentum space, in the vicinity of the Dirac points, emerge with a periodicity that is equal to the accumulated momentum shift during one driving cycle. We present an analytical solution to leading order in the transverse momentum component, i.e. the momentum component orthogonal to the probing direction relative to one of the Dirac points. This analytical solution reproduces the characteristic patterns in the differential photoconductivity. In the absence of the radiation field, we estimate this current density pattern analytically and derive an expression for the non-linear conductivity of strongly biased undriven graphene. Further, we provide analytical calculations for the dependence on temperature of the undriven conductivity. For a weak DC probing field, we find that the conductivity scales linearly with temperature down to small temperatures at which the conductivity converges to the analytical minimal conductivity of $\frac{\pi e^2}{2h}$. In the regime in which the AC driving field dominates, we find that the differential photoconductivity displays a type of checkerboard pattern. The DC field provides a shift in momentum space across the strongly driven Floquet band structure, such that the conductivity pattern emerges from an interplay of Floquet and transport dynamics. We note that the checkerboard pattern in the differential conductivity shows strong qualitative similarities to predictions for this system of the distinct Tien-Gordon effect [55].

# 2 Methods

We consider monolayer graphene in the presence of a constant electric field, i.e. a direct (DC) bias, in addition to continuous terahertz radiation, i.e. an alternating (AC) bias, which is linearly polarized in parallel to the DC field. We write the linearized Hamiltonian
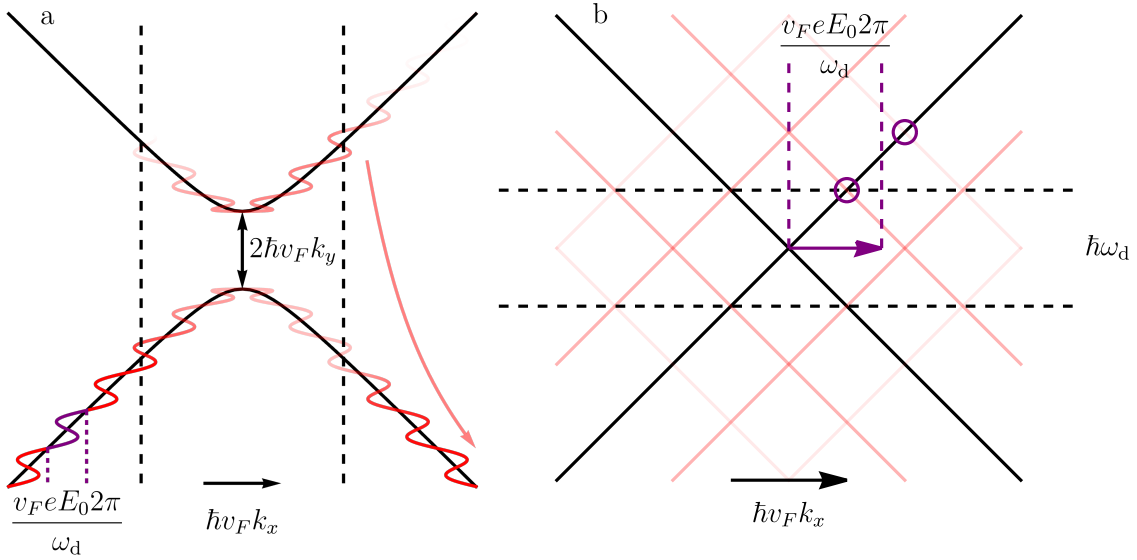
Figure 1: Illustrations of the dynamics in the two regimes of either dominating DC field strength $E_0$ or AC field strength $E_d$. Panel (a) shows the structure of the modified Landau-Zener quench in the limit of dominating DC field strength $E_0$. An electron in the ground state with initial momentum far away from the gap is accelerated due to $E_0$ and displays quenched dynamics across the gap. Due to the additional AC field, the quench is modulated. Panel (b) shows the structure of the Floquet band structure in the limit of large and dominating AC field strength $E_d$. The DC field $E_0$ accelerates electrons across this effective band structure.

for a single momentum mode $\mathbf{k} = (k_x, k_y)$ near one of the Dirac points, as

$$\frac{1}{\hbar} H_{\mathbf{k}}(t) = v_F \left( k_x + \frac{eE_0}{\hbar} t + \frac{eE_d}{\hbar \omega_d} \cos(\omega_d t) \right) \sigma_x + v_F k_y \sigma_y. \tag{1}$$

A similar model applies to the other Dirac point, with $\sigma_y \to -\sigma_y$. Here $e$ is the elementary charge, $\hbar$ is the reduced Planck constant and $v_F \approx 10^6 \mathrm{m\,s^{-1}}$ is the Fermi velocity of graphene. $E_0$ is the DC field strength, $E_d$ is the AC field strength and $\omega_d$ is the driving frequency. $\sigma_x$ and $\sigma_y$ are Pauli matrices. We propagate the density operator of the system using the Lindblad-von Neumann master equation

$$\dot{\rho}_{\mathbf{k}} = \frac{i}{\hbar} [\rho_{\mathbf{k}}, H_{\mathbf{k}}(t)] + \sum_l \gamma_l (L_l \rho_{\mathbf{k}} L_l^\dagger - \frac{1}{2} \{ L_l^\dagger L_l, \rho_{\mathbf{k}} \}). \tag{2}$$

The indices $l$ of the Lindblad operators describe the dissipative processes of spontaneous decay and excitation, dephasing and incoherent exchange to an electronic backgate. The associated dissipation rates are $\gamma_-$, $\gamma_+$, $\gamma_z$ and $\gamma_{bg}$, respectively. The temperature $T$ of the system enters the model through Boltzmann factors of conjugate processes, e.g. $\gamma_+ = \gamma_- \exp\{-\frac{2\epsilon}{k_B T}\}$, where $\epsilon$ is the instantaneous eigenenergy scale of the driven Hamiltonian. The Lindblad operators $L_l$ act in the instantaneous eigenbasis of the Hamiltonian. For further details of this method we refer to App. C and previous works [45, 56, 57]. Throughout this work we use the parameters $\omega_d = 2\pi \times 12$THz, $\gamma_z = 11.25$THz, $\gamma_+ + \gamma_- = 5$THz, $\gamma_{bg} = 12.5$THz and $T = 80$K unless stated otherwise. We explore values for the electric field strengths $E_0$ and $E_d$ up to a few megavolts per meter.

We calculate the total longitudinal current of the system by integrating the momentum-resolved contributions of the current operator

$$j_x = e v_F \sigma_x \tag{3}$$

over momentum space. Note that the periodicity of the AC field requires integration over one driving period to obtain the DC component of the total current. It is

$$J_x = n_v n_s \frac{e v_F \omega_{\mathrm{d}}}{8\pi^3} \sum_{\mathbf{k} \in \mathcal{D}} \int_\tau^{\tau + \frac{2\pi}{\omega_{\mathrm{d}}}} \mathrm{Tr}(\sigma_x \rho_{\mathbf{k}}(t)) dt \Delta k_x \Delta k_y, \tag{4}$$

with the valley- and spin-degeneracy $n_v = n_s = 2$. $\Delta k_x$ and $\Delta k_y$ are the numerical discretization of momentum space. We note that both the two spin states, as well as both Dirac points give the same contribution for all observables in this paper. $\mathcal{D}$ is a sufficiently large neighborhood in momentum space around the Dirac point $K$ to ensure convergence. $\tau$ is a time that is large enough that the system has formed a steady state in the comoving frame $k_x \to k_x - \frac{e}{\hbar} E_0 t$. We calculate the differential conductivity of the system as

$$G_{xx} = \frac{dJ_x}{dE_0} \tag{5}$$

and in the absence of driving as

$$G_{xx}^0 = G_{xx}|_{E_{\mathrm{d}}=0}. \tag{6}$$

We further introduce the differential photoconductivity with respect to the AC field strength as

$$g_{xx} = \frac{dG_{xx}}{dE_{\mathrm{d}}}. \tag{7}$$

We obtain the derivatives of Eqs. 5 and 7 numerically as central finite differences. Since in this model we are considering graphene at its charge neutrality point, i.e. at vanishing chemical potential, the conductivity we calculate is commonly referred to as the minimal conductivity of graphene, in relation to the possible enhancement of the conductivity by increasing the charge carrier density by means of a non-zero chemical potential.

## 3 Results

We calculate the overall current $J_x$ as a function of the DC field strength $E_0$ and the AC field strength $E_{\mathrm{d}}$ up to values of $4\mathrm{MV\,m^{-1}}$ and $20\mathrm{MV\,m^{-1}}$, respectively. This range of the DC probing field includes the nonlinear DC conductivity of driven graphene well beyond the linear response regime. In Fig. 2 (a) and (b) we show the differential photoconductivity $g_{xx}$ and the change in differential conductivity

$$\Delta G_{xx} = G_{xx} - G_{xx}^0, \tag{8}$$

respectively. The structure of these observables is rich and there are two distinct regimes which correspond to the cases of $E_{\mathrm{d}} \gg E_0$ and $E_0 \gg E_{\mathrm{d}}$, in which qualitative structural dependencies can clearly be identified. Depending on whether the DC field or the AC field dominates, the steady state dynamics change significantly. As we discuss below, the AC and DC fields are on equal scales when $E_{\mathrm{d}} = 2\pi E_0$. This condition is met when the momentum shift due to the DC field that is accumulated during one driving period is equal to the momentum displacement amplitude due to the AC field. We indicate this condition
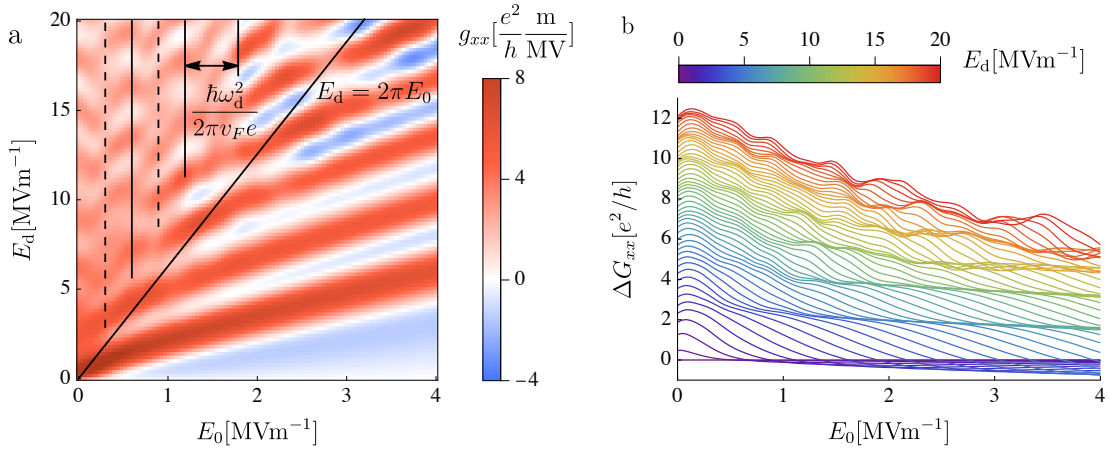
Figure 2: The differential conductivities of strongly driven graphene. Panel (a) shows the differential photoconductivity $g_{xx}$ as a function of the DC field strength $E_0$ and the AC field strength $E_\mathrm{d}$. The diagonal line is given by $E_\mathrm{d} = 2\pi E_0$ and separates the results into the two regimes where either the DC field strength $E_0$ or the AC field strength $E_\mathrm{d}$ dominates. Panel (b) shows the change in differential conductivity $\Delta G_{xx}$ as a function of $E_0$ for various values of $E_\mathrm{d}$.

with the diagonal line in Fig. 2 (a). The structure of the differential photoconductivity $g_{xx}$ in these two regimes is intricate and can be understood from different perspectives in analyzing the corresponding dynamics. The following subsections discuss these two regimes.

## 3.1 Dominant DC Field

We first analyze the regime in which the AC field strength $E_0$ is significantly larger than the AC field strength $E_\mathrm{d}$. In this regime, the differential photoconductivity $g_{xx}$ in Fig. 2 (a) shows a striped pattern as a function of $E_\mathrm{d}$ and $E_0$ which leads to step-like features in the change in differential conductivity $\Delta G_{xx}$ that we show in Fig. 2 (b). The dynamics of this case are captured naturally in the comoving frame $k_x \to k_x - \frac{eE_0}{\hbar}t$, produced by the large momentum shift due to the DC field $E_0$. In this frame, an electron with a momentum far to one side of the Dirac point and initially in thermal equilibrium accelerates due to the DC field and eventually passes the Dirac point. These dynamics are a type of Landau-Zener (LZ) quench across the gap given by the transverse momentum component, i.e. $\Delta = 2\hbar v_F k_y$. The driving term is linearly polarized in parallel with the DC field, such that the LZ quench is further modified by an undulating motion in $k_x$ as depicted in Fig. 1 (a). As the relative phase of the AC field during the quench depends on the initial value of $k_x$, the transition probability is periodic in momentum with $eE_0\hbar^{-1}2\pi\omega_\mathrm{d}^{-1}$, which is the momentum shift induced by the DC field during one driving period. Therefore, the temporal periodicity of the AC field leads to a periodic current density pattern in momentum space.

In Fig. 3, we show examples of such patterns in the quantity

$$\overline{\Delta j_x}(\mathbf{k}) = \frac{\omega_\mathrm{d}}{2\pi} \int_\tau^{\tau+\frac{2\pi}{\omega_\mathrm{d}}} \Delta j_x(\mathbf{k})dt, \tag{9}$$

which is the time-average of the momentum-resolved photocurrent density

$$\Delta j_x(\mathbf{k}) = j_x(\mathbf{k}) - j_x(\mathbf{k})|_{E_0,E_\mathrm{d}=0}, \tag{10}$$
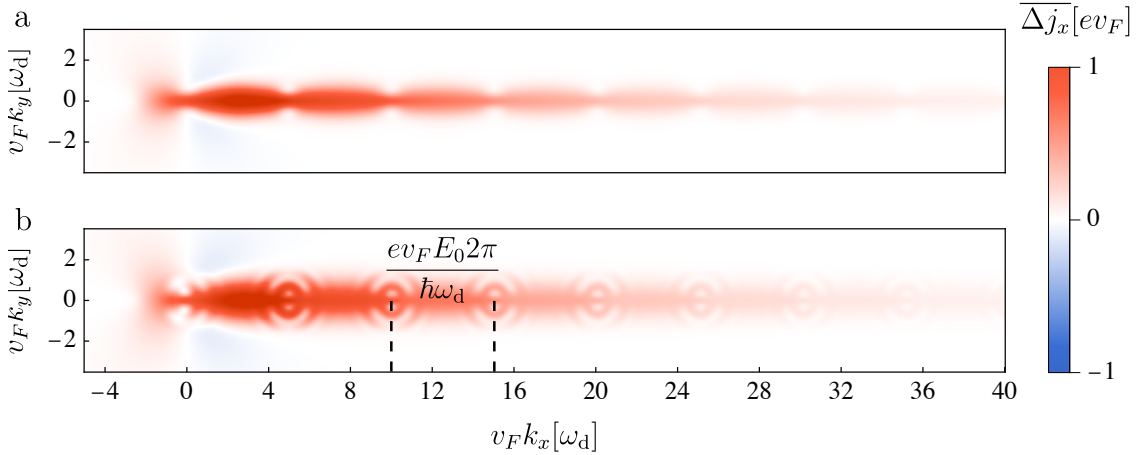
Figure 3: The momentum-resolved photocurrent density in the presence of a strong DC field of $E_0 = 3\,\mathrm{MV\,m^{-1}}$ and an AC field strength of $E_\mathrm{d} = 2\,\mathrm{MV\,m^{-1}}$ (a) and $E_\mathrm{d} = 6\,\mathrm{MV\,m^{-1}}$ (b) averaged over one driving period. Here the dissipation coefficients are reduced by a factor of five compared to the values in the main text, for visual clarity. The dashed lines indicate the momentum shift that is accumulated during one driving period, which corresponds to the periodic patterns that occurs due to the AC field.

in which we subtract the equilibrium current density which integrates to zero. $\tau$ is a time large enough that a steady state has formed in the comoving frame $k_x \to k_x - \frac{eE_0}{\hbar}t$. In the case of large values of $E_0$ and comparatively small dissipation, the steady state current density pattern stretches very far across momentum space before significantly decaying. Note that for increasing AC field strength $E_\mathrm{d}$ the pattern becomes more intricate.

In the picture of modified LZ quenches, the integrated current in Eq. 4 consists of a contribution close to the gap, and a much larger contribution from the decaying tail of the current density pattern as is clearly visible in Fig. 3. We neglect the first part and estimate the current as a product of the periodic current density pattern and exponential decay with a dissipation rate $\Gamma = \frac{1}{2}\gamma_- + \gamma_\mathrm{bg}$. We present the details of this calculation in App. A. We write the total current as

$$J_x^\mathrm{LZ} \approx n_v n_s \frac{e v_F \omega_\mathrm{d}}{8\pi^3} \int_0^{\frac{eE_0 2\pi}{\hbar\omega_\mathrm{d}}} \int_{\mathbb{R}^2} 2P(k_{x,0} + \kappa, k_y)e^{-\Gamma\frac{\hbar k_x}{eE_0}}dk_x dk_y d\kappa, \qquad (11)$$

where $P(k_x, k_y)$ is the transition probability into the excited state of a system initially in the ground state at momentum $k_x$. It is

$$P(k_x, k_y) = \lim_{t\to\infty} |\langle+| U(t,0) |-\rangle|^2, \qquad (12)$$

where $U(t_2, t_1)$ is the time-evolution operator of the Hamiltonian in Eq. 1 from time $t_1$ to $t_2$ and $|\pm\rangle$ are the eigenstates of the $\sigma_x$ Pauli matrix. $k_{x,0}$ is an initial momentum component that is negative and large enough such that the dynamics are initially adiabatic, in order to capture the quenched dynamics in their entirety. $\kappa$ is an additional momentum offset in order to average over the periodicity of the density pattern.

We calculate $P(k_x, k_y)$ from the modified LZ problem (See App. A). To leading order in $k_y$ it is

$$|\langle+|U(t,0)|-\rangle|^2 = \exp\{-\frac{\pi\hbar v_F k_y^2}{eE_0}|\int_0^t e^{i\frac{2}{\hbar}\Pi(t')}dt'|^2\} \qquad (13)$$
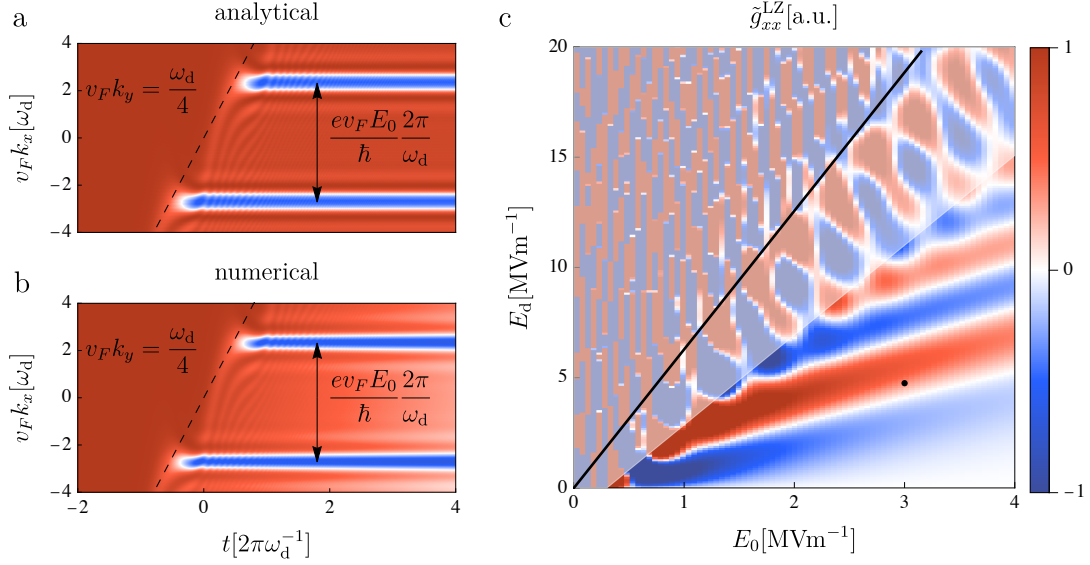
Figure 4: Comparison of the quenched dynamics for $E_0 = 3\text{MV m}^{-1}$ and $E_\text{d} = 4.75\text{MV m}^{-1}$ as a function of the initial momentum component $k_x$ at $v_F k_y = \omega_\text{d}/4$. Panel (a) shows the analytical solution to the modified Landau-Zener quenched dynamics (See App. A) that lead to the expression in Eq. 13. Panel (b) shows the numerical results in the presence of weak dissipation. A weak exponential decay due to the dissipation is visible, and the overall structure agrees well with the analytical estimate in panel (a). Panel (c) shows the analytical estimate for the differential photoconductivity from the modified Landau-Zener quench to leading order in $k_y$ as given by Eq. 17. The striped structure agrees qualitatively with the numerical results in Fig. 2 (a) for large values of $E_0$. The black line is given by $E_\text{d} = 2\pi E_0$. The black dot indicates the parameters used in panels (a) and (b). The shaded area indicates the regime in which Eq. 17 is not a valid approximation.

with the integrated dynamical momentum of Eq. 1,

$$\Pi(t) = \hbar v_F \int_0^t (k_x + \frac{eE_0 t'}{\hbar} + \frac{eE_\text{d}}{\hbar\omega_\text{d}}\cos(\omega_\text{d}t'))dt \qquad (14)$$

such that we find the full transition probability

$$P(k_x, k_y) \approx \exp\left\{ -\frac{\pi\hbar v_F k_y^2}{eE_0} \sum_{n\in\mathbb{Z}} J_n\left(\frac{-4v_F eE_\text{d}}{\hbar\omega_\text{d}^2}\sin(n\frac{\hbar\omega_\text{d}^2}{4v_F eE_0})\right) e^{in\hbar\omega_\text{d}\frac{k_x}{eE_0}}\right\}, \qquad (15)$$

for values of $k_x$ that are negative and large enough for the initial state to be in equilibrium prior to the quench transition. $J_n$ is the $n$th Bessel function of the first kind. This expression explicitly displays the periodicity of $eE_0\hbar^{-1}2\pi\omega_\text{d}^{-1}$ in $k_x$ that is induced by the AC field. For the total current we average the transition probability over this periodicity and to leading order find the expression

$$\bar{P}(k_y) = \int_0^{\frac{eE_0 2\pi}{\hbar\omega_\text{d}}} P(k_x, k_y)dk_x \approx c_0 + \frac{\pi^2\hbar^2 v_F^2 k_y^4}{e^2 E_0^2}\sum_{n\in\mathbb{Z}} J_n^2\left(\frac{-4v_F eE_\text{d}}{\hbar\omega_\text{d}^2}\sin(n\frac{\hbar\omega_\text{d}^2}{4v_F eE_0})\right), \qquad (16)$$

7

where we ignore $c_0$ as it is constant with respect to $E_d$ and does not contribute to the photoconductivity (See App. A). In Fig. 4 (c), we show the resulting contribution to the differential photoconductivity for small $k_y$

$$\tilde{g}_{xx}^{\text{LZ}} \propto \frac{d^2}{dE_d dE_0} \frac{\pi^2 \hbar v_F^2}{4e\Gamma E_0} \sum_{n\in\mathbb{Z}} J_n^2 \left( \frac{-4v_F e E_d}{\hbar \omega_d^2} \sin(n\frac{\hbar \omega_d^2}{4v_F e E_0}) \right). \tag{17}$$

In the case of $E_0 \gg E_d$, $\tilde{g}_{xx}^{\text{LZ}}$ displays a striped structure that is consistent with the differential conductivity in Fig. 2 (a). For values of $2\pi E_0 \gtrsim E_d$, the prediction starts to deviate as the contributions from momenta with larger $k_y$ component are not captured by the leading order calculation for the transition probability in the modified LZ quench. The oscillating terms proportional to $E_0^{-1}$ in Eq. 17 result in erratic behavior for small DC fields, which leads to the chaotic results in the regime of $2\pi E_0 < E_d$. This demonstrates that the modified LZ quench is not a good description in the limit of $E_0 \ll E_d$, where many driving oscillations happen during the transition and dissipation cannot be neglected as a driven steady state forms.

In Figs. 4 (a) and (b) we show the time-evolution of the current density $j_x(t)$ as a function of the initial value of $k_x$ and for $v_F k_y = \omega_d/4$. We show this for $E_0 = 3\text{MV m}^{-1}$ and $E_d = 4.75\text{MV m}^{-1}$. Fig. 4 (a) shows the analytical solution of Eq. 13 to leading order in $k_y$, whereas Fig. 4 (b) shows the numerical simulation in the presence of weak dissipation. The dashed line indicates the points in time at which the drift of the momentum mode passes the band gap. Note the periodicity in the transition probability pattern as a function of $k_x$. The results agree very well with each other and display how dissipation acts as simple decay when the drift occurs quickly relative to the dissipation time scales. For larger values of $E_d$, momentum modes with large transversal components contribute to the current. The patterns at these large values of $k_y$ are not captured by the approximation to leading order in $k_y$. This explains the discrepancies of the striped patterns in Fig. 4 (c) and Fig. 2 (a) for increasing values of $E_d$.

In the limit of vanishing driving, i.e. $E_d \to 0$, the expression in Eq. 15 reproduces the well-known approximation of the transition probability of the LZ problem $P(k_y) \propto \exp\{-\pi \hbar v_F k_y^2 e^{-1} E_0^{-1}\}$. In this limit, we calculate the bare, i.e. undriven, non-linear conductivity of graphene for large $E_0$ (See App. A) and find

$$G_{xx}^{E_0 \gg 0} = \frac{dJ_x|_{E_d=0}}{dE_0} \approx 6\sqrt{\frac{eE_0 v_F}{(\gamma_{\text{bg}} + \frac{1}{2}\gamma_-)^2 \hbar \pi^2}} \frac{e^2}{h}. \tag{18}$$

In the undriven, i.e. $E_d \to 0$, and linear limit, i.e. $E_0 \to 0$, we calculate the conductivity as a function of temperature (See App. A) and find

$$G_{xx}^{E_0 \to 0} \approx \frac{e^2}{h} \left( \frac{\pi}{2} - \arctan((\frac{k_B T}{\hbar \gamma_1})^{\frac{3}{4}}) + \frac{k_B T}{\hbar} \frac{\log(4)}{\gamma_-} \right). \tag{19}$$

A linear dependence of the minimal conductivity on the temperature in graphene as we find here is consistent with the literature [16–24]. In gated graphene this behavior reverses and the conductivity is found to decrease as a function of temperature [25,26]. In the case of $T = 0$, Eq. 19 recovers the analytical result of the minimal conductivity of graphene

$$G_{xx}^{E_0 \to 0}\big|_{T\to 0} = \frac{\pi}{2} \frac{e^2}{h}. \tag{20}$$

The minimal conductivity of graphene has been the subject of many studies and theory commonly produces the values $\frac{\pi}{2} \frac{e^2}{h}$ [7–10] or $\frac{4}{\pi} \frac{e^2}{h}$ [10–12], while experiments consistently find $\frac{4e^2}{h}$.
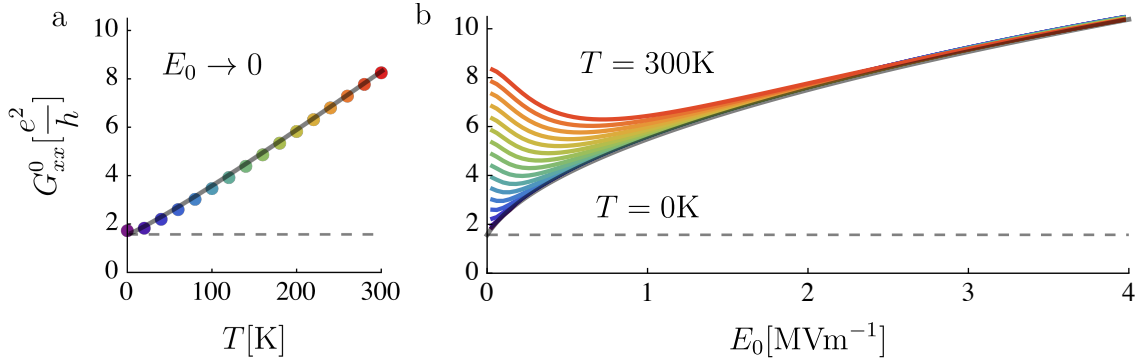
Figure 5: The undriven differential conductivity $G_{xx}^0$ of graphene for various temperatures. Panel (a) shows the linear conductivity as a function of temperature. The black line indicates the analytical solution in Eq. 19 (See App. A). Panel (b) shows the non-linear differential conductivity as a function of $E_0$ for various temperatures. In the limit of large $E_0$ the conductivity becomes temperature-independent. The black line shows the analytical expression for the conductivity presented in Eq. 21. The dashed lines indicate the bare conductivity of $\frac{\pi}{2}\frac{e^2}{h}$.

In Fig. 5 we show the conductivity in the absence of any AC field, i.e. $G_{xx}^0$ as in Eq. 6, for different temperatures. In Fig. 5 (a) we show the linear conductivity, i.e. $E_0 \to 0$, as a function of temperature. Note that the expression in Eq. 19 is derived in the case of $\gamma_{\mathrm{bg}} = 0$. Therefore, we introduce a parameter $\gamma'$ as $\gamma_- \to \gamma_- + \gamma'$ and fit this to the numerical results of the Lindblad master equation. We find very good agreement for $\gamma' = \gamma_{\mathrm{bg}}/6$. The gray line in Fig. 5 (a) shows this fitted analytical prediction. In Fig. 5 (b) we show $G_{xx}^0$ as a function of $E_0$ for different temperatures. For small and intermediately large values of $E_0$ there is a clear dependency on the temperature. This is expected, since for large $E_0$ the current is dominated by contributions at momenta where the level spacing is large enough to suppress any thermal excitation. In general, the conductivity initially decreases with $E_0$, reaches a minimal value at some value of $E_0$ which increases with temperature. The conductivity then increases again while approaching the asymptotic behavior of Eq. 18. For $T = 300$K, the minimum of the differential conductivity is approximately located at $E_0 \approx 0.6 \mathrm{MV\,m}^{-1}$. This qualitative structure is consistent with recent results [58]. We combine the analytical results of Eqs. 18 and 19 into an expression for the differential conductivity at $T = 0$K

$$G_{xx}^0 \approx \frac{e^2}{h}\left( \alpha\frac{\pi}{2} + \sqrt{\frac{(1-\alpha)^2\pi^2}{4} + \frac{36eE_0 v_F}{(\gamma_{\mathrm{bg}} + \frac{1}{2}\gamma_-)^2\hbar\pi^2}} \right), \tag{21}$$

where the construction of the parameter $\alpha$ ensures that for vanishing $E_0$ the numerical and analytical result is recovered, i.e. $G_{xx}^0|_{E_0 \to 0} = \frac{\pi}{2}\frac{e^2}{h}$ as in Eq. 20. We find very good agreement with the numerical results for $\alpha = \frac{1}{4}$ and show this estimate in Fig. 5 (b) as a black line. Note that this scaling behavior can in principle be used to determine the scale of dissipation $\Gamma$ in a given graphene sample. The expression in Eq. 21 for the differential conductivity is necessary in the context of the Tien-Gordon effect [55] as we discuss later.

## 3.2   Dominant AC Field

Here we analyze the regime in which the AC field is dominant, and the differential photoconductivity displays a checkerboard pattern as we show in Fig. 2 (a). As the AC field strength $E_{\mathrm{d}}$ greatly exceeds the DC field strength $E_0$, we describe the system as primarily
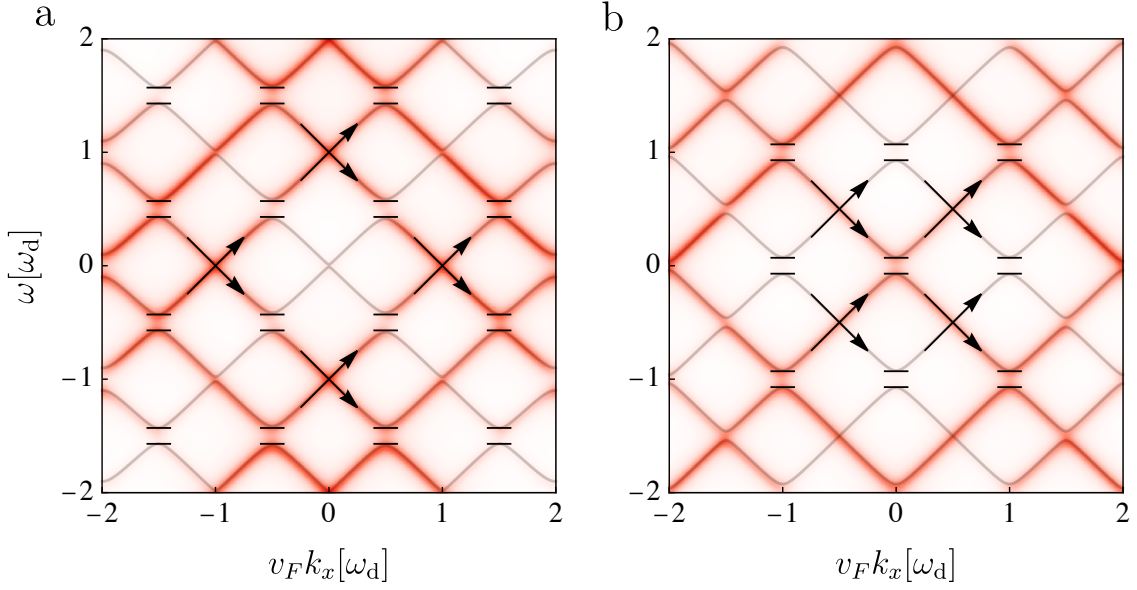
Figure 6: The electron distribution $n(\mathbf{k}, \omega)$ (See App. C) as a function of $k_x$ for $k_y = \omega_\mathrm{d}/4v_F$ and for the AC field strengths $E_\mathrm{d} = 10\mathrm{MV\,m^{-1}}$ (a) and $E_\mathrm{d} = 13\mathrm{MV\,m^{-1}}$ (b). The solid lines show the Floquet spectra of the Hamiltonian in Eq. 24. Here the dissipation coefficients are reduced by a factor of five compared to the values in the main text, for visual clarity. For increasing dissipation the gaps become increasingly indiscernible.

driven periodically and perturbed by the comparatively weak DC field $E_0$. This naturally suggests describing the system in the Floquet picture, in which dynamics are captured via the effective Floquet Hamiltonian

$$H_F = \begin{pmatrix} \ddots & & & & \\ & H_0 + \hbar\omega_\mathrm{d} & H_1 & H_2 & \\ & H_{-1} & H_0 & H_1 & \\ & H_{-2} & H_{-1} & H_0 - \hbar\omega_\mathrm{d} & \\ & & & & \ddots \end{pmatrix}, \tag{22}$$

which has an effective band structure that deviates from the undriven Hamiltonian. Here $H_m$ is the $m$th Fourier component of the original Hamiltonian $H(t)$ such that

$$H_m = \frac{\omega_\mathrm{d}}{2\pi} \int_0^{\frac{2\pi}{\omega_\mathrm{d}}} e^{im\omega_\mathrm{d}t} H(t) dt. \tag{23}$$

The structure of the Floquet Hamiltonian explicitly includes infinitely many replicas of the bare bands coupled to each other by the components $H_{m \neq 0}$ and separated by multiples

of the photon energy $\hbar\omega_\mathrm{d}$. In the case of Eq. 1 it is $H_{m,|m|>1} = 0$, and we explicitly write

$$\frac{H_F}{\hbar} = \begin{pmatrix} \ddots & & & & & & \\ & \omega_\mathrm{d} & v_F\bar{\mathbf{k}} & 0 & \Omega & 0 & 0 \\ & v_F\mathbf{k} & \omega_\mathrm{d} & \Omega & 0 & 0 & 0 \\ & 0 & \Omega & 0 & v_F\bar{\mathbf{k}} & 0 & \Omega \\ & \Omega & 0 & v_F\mathbf{k} & 0 & \Omega & 0 \\ & 0 & 0 & 0 & \Omega & -\omega_\mathrm{d} & v_F\bar{\mathbf{k}} \\ & 0 & 0 & \Omega & 0 & v_F\mathbf{k} & -\omega_\mathrm{d} \\ & & & & & & \ddots \end{pmatrix} \tag{24}$$

with $\mathbf{k} = k_x + ik_y$ and $\Omega = \frac{ev_F E_\mathrm{d}}{2\hbar\omega_\mathrm{d}}$.

In the case of very large AC field strengths, the Floquet band structure approaches an increasingly regular pattern in which the Floquet band gaps align with the quasi-resonant condition of $v_F k_x = m\omega_\mathrm{d}/2$, $m \in \mathbb{Z}$. In Fig. 6 (a) and (b), we show the momentum- and frequency-resolved electron distributions $n(\mathbf{k},\omega)$ (See App. C) at $v_F k_y = \omega_\mathrm{d}/4$ for $E_\mathrm{d} = 10\mathrm{MV\,m^{-1}}$ and $E_\mathrm{d} = 13\mathrm{MV\,m^{-1}}$, respectively. We also show the eigenvalues of the Floquet Hamiltonian in Eq. 24 for the same parameters as solid lines. Note that for $E_\mathrm{d} = 0$ the gap at $k_x = 0$ in this example is $\Delta = \hbar\omega_\mathrm{d}/2$, which is fully suppressed in the effective Floquet band structure in Fig. 6. We calculate the Floquet energies at the quasi-resonant conditions in first order of $k_y$ (See App. B) and find that the $m$th Floquet band gap is given by

$$\Delta\epsilon^{(m)} = 2\hbar v_F k_y J_m(2\frac{ev_F E_\mathrm{d}}{\hbar\omega_\mathrm{d}^2}) + \mathcal{O}(k_y^2), \tag{25}$$

where $J_m$ is the $m$th Bessel function of the first kind. For increasing $E_\mathrm{d}$, the range of values of $k_y$ for which this expression remains valid increases. For those values of $E_\mathrm{d}$ for which the $m$th Bessel function evaluates to zero, the transition probability becomes unity as a form of coherent destruction of tunneling [50,53].

Fig. 2 (a) shows that the differential photoconductivity displays a type of checkerboard pattern in the regime that we consider in this section. The regularity of this pattern with respect to $E_0$ aligns along values of

$$E_0^{(m)} = \frac{m\hbar\omega_\mathrm{d}^2}{4\pi ev_F} \tag{26}$$

with $m \in \mathbb{N}$, as we indicate with vertical lines. These values of $E_0^{(m)}$ are the DC field strengths for which during one driving period $\frac{2\pi}{\omega_\mathrm{d}}$, a shift in momentum equivalent to the difference in location between $m$ resonances is accumulated. In consideration of the Floquet band gaps in Eq. 25, this translates into a momentum shift that is commensurate with $m$ Floquet band gaps for small $k_y$.

We demonstrate that the contributions to the photoconductivity are located at these Floquet band gaps in Fig. 7 (a), where we show the photocurrent density $\Delta j_x(\mathbf{k})$, as defined in Eq. 10, integrated over $k_y$ as a function of $k_x$, and the AC field strength $E_\mathrm{d}$ in the limit of small $E_0$. We see a clear structure of dominant contributions to the differential photoconductivity at momentum components $k_x = m\omega_\mathrm{d}/v_F$, i.e. at locations of the Floquet band gaps for small $k_y$ as given in Eq. 25. With increasing $E_\mathrm{d}$, contributions at higher-order resonances start to emerge that are aligned with the locations of Floquet band gaps. The regularity in the differential photoconductivity $g_{xx}$ with respect to $E_\mathrm{d}$ emerges as a consequence of these quasi-resonant contributions, which relate to the size of the Floquet band gaps in Eq. 25. For large values of $E_\mathrm{d}$ the roots of the even-order Bessel
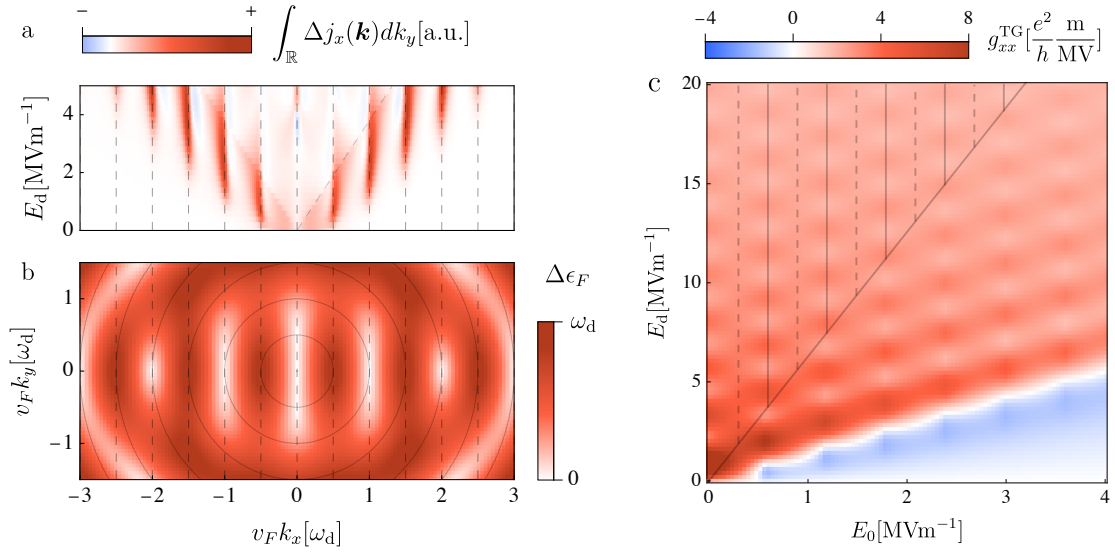
Figure 7: The distribution of current contributions in momentum space. In panel (a), we show the photocurrent density in momentum space integrated over only the $k_y$ component as a function of the $k_x$ component, and the AC field strength $E_d$. The dominant contributions are located at the multi-photon resonances indicated by the vertical dashed lines. In panel (b), we show the Floquet band energy differences resolved in $k$-space for large AC field strength $E_d = 10 \text{MV m}^{-1}$. The Floquet gap locations align with the resonance conditions for $k_y = 0$, giving rise to a striped pattern of Floquet band gaps. The circles indicate the original resonance conditions in bare graphene. In panel (c), we show the differential photoconductivity as given by the Tien-Gordon expression in Eq. 28 using the expression for the bare differential conductivity in Eq. 21. Note the similarities in the regular checkerboard pattern to the differential photoconductivity in Fig. 2.

functions in Eq. 25 become increasingly aligned, as do the roots of the odd-order Bessel functions. This results in an odd-even pattern of dominant contributions with respect to $E_0^{(m)}$, i.e. the checkerboard pattern in Fig. 2 (a). In Fig. 7 (b), we show the Floquet band energy differences for $E_d = 10 \text{MV m}^{-1}$, where it is clearly visible how the Floquet band gaps for small $k_y$ align in the regular pattern along $k_x$ at which the dominant contributions to the photocurrent occur. This is consistent with pulsed two-level systems, in which LZ transitions across instantaneous Floquet band structures provide an accurate description of the dynamics [59].

For comparison, we consider the predictions of the Tien-Gordon effect. In semiconducting nanostructures that are AC and DC biased simultaneously, the DC $I$-$V$ curves without an AC driving field taking into account photon-assisted tunneling. The original discussion put forth by Tien and Gordon discussed the dynamics of superconducting junctions in a perpendicular electric field [55]. For a bias voltage $V(t) = V_0 + \frac{V_d}{\omega_d} \sin(\omega_d t)$ they approximate the driven $I$-$V$ curve as

$$I(V_0) = \sum_m J_m^2 \left(\frac{V_d}{\omega_d}\right) I_0(V_0 + m\omega_d). \tag{27}$$

A similar analysis has been put forth for graphene in the presence of an oscillating chemical potential [60], i.e. an alternating gate bias. The expression in Eq. 27 translates into the

conductivity

$$G_{xx}^{\text{TG}} = \sum_m J_m^2 \left( \frac{ev_F E_{\text{d}}}{\hbar \omega_{\text{d}}^2} \right) G_{xx}^0 \left( E_0 + \frac{m\hbar\omega_{\text{d}}^2}{2\pi v_F e} \right). \tag{28}$$

In Fig. 7 (c) we show the differential photoconductivity as it is predicted by Eq. 28 using the approximate expression for the bare conductivity in Eq. 21. We find that the characteristic structure shows a similar checkerboard pattern to that in Fig. 2 (a). In particular, the regularity with respect to $E_0$ is identical, as in Eq. 28 the same multi-photon offset to the DC field strength $E_0$ occurs as in Eq. 26. The regularity with respect to $E_{\text{d}}$ agrees with the results in Fig. 2 (a) and the Floquet band gap scaling in Eq. 25, despite the distinct nature of the two phenomena. Note that the Tien-Gordon prediction in Eq. 28 becomes increasingly inaccurate towards the regime where it is $2\pi E_0 > E_{\text{d}}$, which is where the checkerboard pattern is lost in the differential photoconductivity in Fig. 2 (a).

# 4   Conclusion

We have presented the non-linear longitudinal differential DC photoconductivity of light-driven monolayer graphene. We model the electron dynamics near the Dirac points of the graphene dispersion, in the presence of a DC probing field and an AC driving field. The driving field has the same linear polarization as the probing field. The differential photoconductivity displays two regimes as a function of the AC driving field strength, and the DC probing field strength, depending on which of these field strengths is dominant. The dynamics of these two regimes are captured well in two very distinct pictures, which we have explored analytically, and compared to the numerical result.

In the regime in which the direct bias dominates, the photoconductivity displays a striped pattern. It derives from the Landau-Zener dynamics of the electrons across the Dirac cone, driven by the two electric fields. We presented an analytical calculation that reproduces the formation of the striped patterns in the photoconductivity. We put forth an analytical prediction for the formation of current density patterns in momentum space in the limit of large direct biases. From this we have approximated the non-linear conductivity in the absence of an alternating bias, which shows behavior that is independent of temperature. Further, in the limit of a small direct bias and no alternating bias, i.e. the undriven linear case, we have calculated that the minimal conductivity increases linearly with the temperature and recovers the value of $\frac{\pi}{2}\frac{e^2}{h}$ for vanishing temperature.

In the regime of the dominant AC driving field, the photoconductivity displays a checkerboard pattern. In this regime, we use a Floquet picture to describe the dynamics. The regularity as a function of the direct bias is given by values which during one driving period accumulate a shift in momentum that is equal to the differences of Floquet band gap locations. We have shown that for large alternating bias and small transverse momenta, the Floquet band gaps align along the corresponding values of equal longitudinal momenta at which the dominant contributions to the photoconductivity are located. Further we have compared these results to the Tien-Gordon effect. We have used the analytic expression of the non-linear conductivity to calculate the differential photoconductivity using the expression put forth by Tien and Gordon, which displays a similar checkerboard pattern. In particular, the regularity as a function of the direct bias is manifestly identical. The regularity as a function of the alternating bias is very similar, and agrees with the analytic expression of the Floquet band gaps to leading order in transverse momentum.

The results we have put forth provide insight into the non-linear electronic transport properties of strongly driven graphene. The insights presented here support the engineering of non-equilibrium quantum electronic devices in the future.

# A  Analytical Approaches to the Differential Photoconductivity

**Transition Probability for Generalized Quenches**

We consider a two-level Hamiltonian with energy spacing $\Delta$ and a time-dependent quench $\pi(t)$ that we write as

$$H = \Delta\sigma_x + \pi(t)\sigma_z \tag{29}$$

such that the second time-derivative of any state is given by

$$\partial_t^2 |\psi\rangle = -\frac{i}{\hbar}\partial_t(H|\psi\rangle) = -\frac{1}{\hbar}\Big(\frac{1}{\hbar}\epsilon(t)^2 + i\sigma_z\dot{\pi}(t)\Big)|\psi\rangle, \tag{30}$$

where we have used that $H^2 = \epsilon^2 = \Delta^2 + \pi(t)^2$ in centered two-level systems, i.e. when $\mathrm{Tr}(H) = 0$. For the components of $|\psi\rangle = (\psi_+, \psi_-)$ it is

$$\ddot{\psi}_\pm = -\frac{1}{\hbar^2}(\Delta^2 + \pi(t)^2 \pm i\hbar\dot{\pi}(t))\psi_\pm \tag{31}$$

$$\dot{\psi}_\pm = -\frac{i}{\hbar}(\pm\pi(t)\psi_\pm + \Delta\psi_\mp) \tag{32}$$

such that for initial conditions $\psi_\pm(0)$ we have

$$\dot{\psi}_\pm(0) = -\frac{i}{\hbar}(\pm\pi(0)\psi_\pm(0) + \Delta\psi_\mp(0)). \tag{33}$$

We write $\psi_\pm(t) = \exp\{\xi_\pm(t)\}$ such that Eq. 31 yields

$$\ddot{\xi}_\pm + \dot{\xi}_\pm^2 = -\frac{\Delta^2}{\hbar^2} - \frac{\pi^2}{\hbar^2} \mp \frac{i\dot{\pi}}{\hbar} \tag{34}$$

$$\xi_\pm(0) = \ln(\psi_\pm(0)) \tag{35}$$

$$\dot{\xi}_\pm(0) = -\frac{i}{\hbar}\Big(\pm\pi(0) + \Delta\frac{\psi_\mp(0)}{\psi_\pm(0)}\Big). \tag{36}$$

We expand $\xi = \sum_{m=0}^{\infty} \xi_m \Delta^m$ in orders of $\Delta$ and write

$$\ddot{\xi}_{\pm,m} + \sum_{n=0}^{m} \dot{\xi}_{\pm,m-n}\dot{\xi}_{\pm,n} = -\delta_{m,2} - \delta_{m,0}(\pi^2 \pm i\dot{\pi}). \tag{37}$$

The case $m = 0$ gives

$$\ddot{\xi}_{\pm,0} + \dot{\xi}_{\pm,0}^2 = \mp i\dot{\pi} - \pi^2 \implies \dot{\xi}_{\pm,0} = \mp i\pi \tag{38}$$

$$\implies \xi_{\pm,0} = \ln(\psi_\pm(0)) \mp i\Pi(t) \tag{39}$$

with

$$\Pi(t) = \int_0^t \pi(t')dt'. \tag{40}$$

The case $m = 1$ is solved to satisfy the initial condition Eq. 36 such that

$$\ddot{\xi}_{\pm,1} \mp i2\pi\dot{\xi}_{\pm,1} = 0 \implies \dot{\xi}_{\pm,1} = -i\frac{\psi_{\mp}}{\psi_{\pm}}e^{\pm 2\frac{i}{\hbar}\Pi(t)} \tag{41}$$

$$\implies \xi_{\pm,1} = -i\frac{\psi_{\mp}}{\psi_{\pm}}\int_0^t e^{\pm 2\frac{i}{\hbar}\Pi(t')}dt' \tag{42}$$

The case $m = 2$ is solved as

$$\ddot{\xi}_{\pm,2} \mp i2\pi\dot{\xi}_{\pm,2} = -1 - (-i\frac{\psi_{\mp}}{\psi_{\pm}}e^{\pm 2\frac{i}{\hbar}\Pi(t)})^2 \tag{43}$$

$$\implies \dot{\xi}_{\pm,2} = -e^{\pm i2\Pi(t)}\int_0^t e^{\mp i2\Pi(t')} - \frac{\psi_{\mp}^2}{\psi_{\pm}^2}e^{\pm 2i\Pi(t')}dt' \tag{44}$$

$$\implies \xi_{\pm,2} = \underbrace{-\int_0^t e^{\pm i2\Pi(t')}\int_0^{t'} e^{\mp i2\Pi(t'')}dt''dt'}_{\xi'_{\pm,2}} + \underbrace{\frac{\psi_{\mp}^2}{\psi_{\pm}^2}\int_0^t e^{\pm i2\Pi(t')}\int_0^{t'} e^{\pm i2\Pi(t'')}dt''dt'}_{\xi''_{\pm,2}} \tag{45}$$

We note that $\xi'_{\pm,2} = \xi'^*_{\mp,2}$ such that we define $\xi'_2 = \text{Re}[\xi'_{+,2}] = \text{Re}[\xi'_{-,2}]$.
Higher orders of $m > 2$ are solved iteratively by

$$\ddot{\xi}_{\pm,m} \mp i2\pi\dot{\xi}_{\pm,m} = -\sum_{n=1}^{m-1}\dot{\xi}_{\pm,m-n}\dot{\xi}_{\pm,n} \tag{46}$$

$$\implies \dot{\xi}_{\pm,m} = -e^{\pm i2\Pi(t)}\int_0^t e^{\mp i2\Pi(t')}\sum_n \dot{\xi}_{\pm,m-n}\dot{\xi}_{\pm,n}dt' \tag{47}$$

$$\implies \xi_{\pm,m} = -\int_0^t e^{\pm i2\Pi(t')}\int_0^{t'} e^{\mp i2\Pi(t'')}\sum_n \dot{\xi}_{\pm,m-n}\dot{\xi}_{\pm,n}dt''dt'. \tag{48}$$

Here, we consider $\xi_-$ up to second order with the boundary conditions $\psi_-(0) = 1$ and $\psi_+(0) = 0$. We calculate the amplitude square

$$|a(t)|^2 = \exp\{(\xi_{-,0} + \xi_{-,2}\frac{\Delta^2}{\hbar^2})\}\exp\{(\bar{\xi}_{-,0} + \bar{\xi}_{-,2}\frac{\Delta^2}{\hbar^2})\} = \exp\{2\frac{\Delta^2}{\hbar^2}\text{Re}[\xi'_2]\} \tag{49}$$

$$= \exp\{-\frac{\Delta^2}{\hbar^2}\int_0^t(\cos(\frac{2}{\hbar}\Pi(t'))\int_0^{t'}\cos(\frac{2}{\hbar}\Pi(t''))dt'' + \sin(\frac{2}{\hbar}\Pi(t'))\int_0^{t'}\sin(\frac{2}{\hbar}\Pi(t''))dt''\}dt'\} \tag{50}$$

$$= \exp\{-\frac{\Delta^2}{\hbar}([\int_0^t\cos(\frac{2}{\hbar}\Pi(t'))dt']^2 + [\int_0^t\sin(\frac{2}{\hbar}\Pi(t'))dt']^2)\} \tag{51}$$

$$= \exp\{-\frac{\Delta^2}{\hbar}|\int_0^t e^{i\frac{2}{\hbar}\Pi(t')}dt'|^2\}. \tag{52}$$

We apply this to the explicit case of

$$\pi(t) = \hbar v_F k_x + ev_F E_0 t + \frac{ev_F E_\text{d}}{\omega_\text{d}}\sin(\omega_\text{d}t) \tag{53}$$

$$\Pi(t) = \hbar v_F k_x t + \frac{ev_F E_0 t^2}{2} - \frac{ev_F E_\text{d}}{\omega_\text{d}^2}\cos(\omega_\text{d}t) + \frac{ev_F E_\text{d}}{\omega_\text{d}^2}. \tag{54}$$

This constitutes a Landau-Zener quench with an additional alternating motion. The construction of the parameters is chosen to invoke the similarities to graphene. In particular,

we write $\Delta = \hbar v_F k_y$ to emphasize this connection. Note that the Hamiltonian in Eq. 29 then becomes equivalent to that in Eq. 1 under a simple basis rotation around $\sigma_y$. We continue by writing the central exponential function as

$$\exp\{i\frac{2}{\hbar}\Pi(t)\} = e^{i2\frac{ev_F E_{\rm d}}{\hbar\omega_{\rm d}^2}} e^{i2v_F k_x t} e^{\frac{i}{\hbar}ev_F E_0 t^2} e^{-i\frac{2ev_F E_{\rm d}}{\hbar\omega_{\rm d}^2}\cos(\omega_{\rm d}t))} \tag{55}$$

$$= e^{i2\frac{ev_F E_{\rm d}}{\hbar\omega_{\rm d}^2}} \sum_{n\in\mathbb{Z}} i^n J_n\left(\frac{-2ev_F E_{\rm d}}{\hbar\omega_{\rm d}^2}\right) e^{i(n\omega_{\rm d}+2v_F k_x)t} e^{\frac{i}{\hbar}ev_F E_0 t^2}. \tag{56}$$

We integrate this product of exponential functions for a fixed value of $n$, which gives

$$\int_0^t e^{i(n\omega_{\rm d}+2v_F k_x)t'} e^{\frac{i}{\hbar}ev_F E_0 t'^2} dt' = \sqrt{\frac{i\pi\hbar}{4ev_F E_0}} e^{-\frac{i\hbar(n\omega_{\rm d}+2v_F k_x)^2}{4ev_F E_0}} \tag{57}$$

$$\times \left(\operatorname{erf}\left(\sqrt{\frac{-i}{4E_0}}(n\omega_{\rm d}+2k_x)\right) - \operatorname{erf}\left(\sqrt{\frac{-i}{4E_0}}(n\omega_{\rm d}+2k_x+2E_0 t)\right)\right). \tag{58}$$

In order to consider the transition amplitude across the quench, we assume that $|k_x|$, with $k_x < 0$, and $t$ are both large enough such that the error functions approach $-1$ and $1$ for large times. Then the absolute square of the integral becomes

$$\left|\int_0^\infty \exp\{i2\Pi(t)\}dt\right|^2 \approx \frac{\hbar\pi}{ev_F E_0}\left|\sum_{n\in\mathbb{Z}} i^n J_n\left(\frac{-2ev_F E_{\rm d}}{\hbar\omega_{\rm d}^2}\right) e^{-\frac{i\hbar n^2\omega_{\rm d}^2}{4ev_F E_0}} e^{-\frac{in\hbar\omega_{\rm d}k_x}{eE_0}}\right|^2. \tag{59}$$

In the undriven case of $E_{\rm d} = 0$ we correctly recover the first order correction to the transition amplitude as predicted in the Landau-Zener problem. In that case it is $J_0(-2E_{\rm d}\omega_{\rm d}^{-2}) = 1$ and $J_{n>0}(-2E_{\rm d}\omega_{\rm d}^{-2}) = 0$, such that

$$|a(t\to\infty)|^2 = e^{-\frac{\pi\hbar v_F k_y^2}{eE_0}}. \tag{60}$$

In the driven case the calculation is more intricate. Remember that the expression Eq. 59 is periodic in $k_x$. We take the expression for the transition probability and simplify the absolute squared expression. It is

$$|a|^2 = \exp\left\{-\frac{\pi\hbar v_F k_y^2}{2eE_0}\left|\sum_{n\in\mathbb{Z}} i^n J_n(-\frac{2v_F eE_{\rm d}}{\hbar\omega_{\rm d}^2})e^{-i\frac{\hbar n^2\omega_{\rm d}^2}{4v_F eE_0}}e^{-i\frac{n\hbar\omega_{\rm d}k_x}{eE_0}}\right|^2\right\} \tag{61}$$

$$= \exp\left\{-\frac{\pi\hbar v_F k_y^2}{2eE_0}\sum_{n,m\in\mathbb{Z}} i^{n-m} J_n(-\frac{2v_F eE_{\rm d}}{\hbar\omega_{\rm d}^2})J_m(-\frac{2v_F eE_{\rm d}}{\hbar\omega_{\rm d}^2})e^{-i\frac{\hbar(n^2-m^2)\omega_{\rm d}^2}{4v_F eE_0}}e^{-i\frac{\hbar(n-m)\omega_{\rm d}k_x}{eE_0}}\right\} \tag{62}$$

$$= \exp\left\{-\frac{\pi\hbar v_F k_y^2}{2eE_0}\sum_{n,m\in\mathbb{Z}} i^n J_{n+m}(-\frac{2v_F eE_{\rm d}}{\hbar\omega_{\rm d}^2})J_m(-\frac{2v_F eE_{\rm d}}{\hbar\omega_{\rm d}^2})e^{-i\frac{n\hbar(n+2m)\omega_{\rm d}^2}{4v_F eE_0}}e^{-i\frac{n\hbar\omega_{\rm d}k_x}{eE_0}}\right\} \tag{63}$$

$$= \prod_{n\in\mathbb{Z}}\exp\left\{-\frac{\pi\hbar v_F k_y^2}{2eE_0}J_n(-\frac{4v_F eE_{\rm d}}{\hbar\omega_{\rm d}^2}\sin(\frac{n\hbar\omega_{\rm d}^2}{4v_F eE_0}))e^{-i\frac{n\hbar\omega_{\rm d}k_x}{eE_0}}\right\} \tag{64}$$

$$= e^{-\frac{\pi\hbar v_F k_y^2}{2eE_0}}\prod_{n=1}^{\infty}\exp\left\{-\frac{\pi\hbar v_F k_y^2}{eE_0}J_n(-\frac{4v_F eE_{\rm d}}{\hbar\omega_{\rm d}^2}\sin(\frac{n\hbar\omega_{\rm d}^2}{4v_F eE_0}))\cos(\frac{n\hbar\omega_{\rm d}k_x}{eE_0})\right\} \tag{65}$$

where we have used that

$$i^n \sum_{m \in \mathbb{Z}} J_{n+m}(-\frac{2E_{\mathrm{d}}}{\omega_{\mathrm{d}}^2}) J_m(-\frac{2E_{\mathrm{d}}}{\omega_{\mathrm{d}}^2}) e^{-i\frac{n(n+2m)\omega_{\mathrm{d}}^2}{4E_0}} = J_n(\frac{4E_{\mathrm{d}}}{\omega_{\mathrm{d}}^2} \sin(n\frac{\omega_{\mathrm{d}}^2}{4E_0})), \tag{66}$$

which we obtain by invoking the relations

$$J_\mu(z) = \frac{1}{2\pi} \int_0^{2\pi} e^{i\mu\tau - iz\cos(\tau)} d\tau \tag{67}$$

$$J_\mu(z) J_\nu(z) = \frac{2}{\pi} \int_0^{\frac{\pi}{2}} J_{\mu+\nu}(2z\cos(t)) \cos((\mu-\nu)t) dt. \tag{68}$$

In the following, we use the expression in Eq. 65 to approximate contributions to the conductivity.

## Integrated Contributions from Modulated Quench Transitions

We estimate the conductivity by first integrating the transition probability over momentum-space, which gives the total current. Afterwards we take the derivative with respect to the two bias strengths $E_0$ and $E_{\mathrm{d}}$. However, that expression is only finite in the presence of dissipation which relaxes the excited states after the quench. Therefore, we consider this calculation in a two-step model, where the transition occurs in full and only afterwards dissipation starts to act, decaying any population that was excited. This is modeled by exponential decay by a phenomenological dampening coefficient $\Gamma$. Note that $k_x$ in $|a|^2$ is the initial value of the momentum component. We calculate the transition probability averaged over this initial value by writing

$$|a|^2 = \exp\left\{-\frac{\pi\hbar v_F k_y^2}{2eE_0} \sum_{n \in \mathbb{Z}} J_n(-\frac{4v_F eE_{\mathrm{d}}}{\hbar\omega_{\mathrm{d}}^2} \sin(\frac{n\hbar\omega_{\mathrm{d}}^2}{4v_F eE_0})) e^{-i\frac{n\hbar\omega_{\mathrm{d}} k_x}{eE_0}}\right\} \tag{69}$$

$$= \sum_{l=0}^{\infty} \frac{(-\frac{\pi\hbar v_F k_y^2}{2eE_0})^l}{l!} \sum_{\substack{\{n_j \in \mathbb{Z}\} \\ j \in \{1,\dots,l\}}} e^{-i\frac{(\sum_{j=1}^l n_j)\hbar\omega_{\mathrm{d}} k_x}{eE_0}} \prod_{j=1}^l J_{n_j}(-\frac{4v_F eE_{\mathrm{d}}}{\hbar\omega_{\mathrm{d}}^2} \sin(\frac{n_j \hbar\omega_{\mathrm{d}}^2}{4v_F eE_0})) \tag{70}$$

and integrating this expression to leading order such that

$$\overline{|a|^2} = \frac{\hbar\omega_{\mathrm{d}}}{2\pi eE_0} \int_0^{\frac{2\pi eE_0}{\hbar\omega_{\mathrm{d}}}} |a|^2 dk_{x,0} \tag{71}$$

$$= \sum_{l=0}^{\infty} \frac{(-\frac{\pi\hbar v_F k_y^2}{2eE_0})^l}{l!} \sum_{\substack{\{n_j \in \mathbb{Z}\} \\ j \in \{1,\dots,l\}}} \delta(\sum_{j=1}^l n_j) \prod_{j=1}^l J_{n_j}(-\frac{4v_F eE_{\mathrm{d}}}{\hbar\omega_{\mathrm{d}}^2} \sin(\frac{n_j \hbar\omega_{\mathrm{d}}^2}{4v_F eE_0})) \tag{72}$$

$$= 1 - \frac{\pi\hbar v_F k_y^2}{2eE_0} + (\frac{\pi\hbar v_F k_y^2}{2eE_0})^2 \sum_{n \in \mathbb{Z}} J_n^2(-\frac{4v_F eE_{\mathrm{d}}}{\hbar\omega_{\mathrm{d}}^2} \sin(\frac{n\hbar\omega_{\mathrm{d}}^2}{4v_F eE_0})) + \mathcal{O}(k_y^6). \tag{73}$$

In the first step we evaluated the integral and found that the exponential functions lead to vanishing integration unless the exponent is zero. This condition is expressed through the delta-function $\delta(\sum_{j=1}^l n_j)$. In the following step we have evaluated the first three terms of the series. Note that the $l=1$ term is proportional to $J_0(0) = 1$ and for the $l=2$ term the sum reduces since $n_2 = -n_1$ and a sign change in both the index of the Bessel function and the sine in the argument of the same Bessel function cancel each other. As we are interested in the differential photoconductivity, we first notice that the first two

terms vanish when differentiating with respect to $E_d$, such that we can ignore them. We consider the conductivity in the limit, where the quench occurs fast and dissipation acts afterwards with a simple exponential decay such that we integrate current contributions over all $k_x$ as

$$\tilde{g}_{xx} \propto \partial_{E_d} \partial_{E_0} \overline{|a|^2} \int_0^\infty e^{-\Gamma \frac{\hbar k_x}{eE_0}} dk_x \tag{74}$$

$$= \partial_{E_d} \partial_{E_0} (\overline{|a|^2} \frac{eE_0}{\hbar\Gamma}) \tag{75}$$

$$\approx k_y^4 \frac{\pi^2 \hbar v_F^2}{4e\Gamma} \partial_{E_d} \partial_{E_0} \sum_{n \in \mathbb{Z}} \frac{1}{E_0} J_n^2 (-\frac{4v_F eE_d}{\hbar\omega_d^2} \sin(\frac{n\hbar\omega_d^2}{4v_F eE_0})). \tag{76}$$

This expression provides the contributions to the differential photoconductivity as a function of $k_y$ for small values of $k_y$. In order to access higher order contributions it is necessary to evaluate Eq. 48 and then perform the analogous calculation of the conductivity.

## Non-Linear Conductivity in the Large-DC-Bias Limit

For large values of $ev_F E_0 \hbar^{-1} \gg \Gamma\omega_d$, we can approximate the transition probability of a ground state at $t \to -\infty$ towards $t \to \infty$ as a function of $k_y$. We assume that the transition happens fast enough such that the entire transition process happens and then decay starts acting. In a comoving frame, time translates into $k_x$-momentum and the transition probability is proportional to the conductivity density. We take the result for the transition probability for $E_d = 0$ and multiply this by an exponential decay in $k_x$ starting at $k_x = 0$. It is

$$|a(k_x, k_y)|^2 = e^{-\frac{\pi v_F \hbar k_y^2}{eE_0}} e^{-\Gamma \frac{\hbar k_x}{eE_0}} \Theta(k_x) \tag{77}$$

where $\Theta(k_x)$ is the Heaviside function. This integrates over momentum space to

$$J_x = n_s n_v \frac{ev_F}{4\pi^2} \int_{-\infty}^\infty \int_0^\infty 2|a(k_x, k_y)|^2 dk_x dk_y = 2\sqrt{\frac{e^5 E_0^3 v_F}{\Gamma^2 \hbar^3 \pi^4}} \tag{78}$$

Hence the conductivity from this main contributions is

$$G_{xx}^0 = \frac{dJ_x}{dE_0} = 6\sqrt{\frac{eE_0 v_F}{\Gamma^2 \hbar \pi^2}} \frac{e^2}{h}. \tag{79}$$

This is in agreement with the large $E_0$ limit of Fig. 5 (b) up to some constant offset provided by the current density close to the Dirac point which we neglected here. This calculation holds only in the limit where the exponential decay in $k_x$-direction happens close enough to the Dirac point that a linear dispersion is still a valid approximation. From the Lindbladian in the $4 \times 4$ basis it is easy to see, that $\Gamma = \gamma_\pm + \gamma_{bg}$.

## Temperature-dependent Conductivity Without Driving

In the limit of small $E_0$, dissipation acts significantly during the transition and the previous approximation is no longer valid. Also, temperature starts to become relevant in this limit. In the comoving frame $k_x \to k_x - eE_0\hbar^{-1}t$, the solution is a stationary state such that $\hbar\partial_t\rho = eE_0\partial_{k_x}\rho$. To approach this problem analytically we neglect the expanded sector of the Hilbert space and only consider the original $2 \times 2$ system, i.e. $\gamma_{bg} = 0$. In this case the Lindblad-von Neumann master equation can be cast into the form

$$\hbar\partial_t\vec{\rho} = 2\vec{H} \times \vec{\rho} - \hbar\gamma_1\vec{\rho} - \hbar\gamma_2\vec{h} - \hbar\gamma_3(\vec{\rho}\vec{h})\vec{h} \tag{80}$$

for the density operator representation

$$\rho = \frac{1}{2}(\mathbb{1} + \vec{\rho}\vec{\sigma}) \tag{81}$$

where $\vec{\sigma} = (\sigma_x, \sigma_y, \sigma_z)$ is a vector containing the Pauli matrices. Similarly, it is

$$H = \vec{H}\vec{\sigma} \tag{82}$$

and $\vec{h} = \epsilon^{-1}\vec{H}$ with $\epsilon = \sqrt{\vec{H}.\vec{H}}$. For details on and a derivation of this representation of the master equation we refer to previous work [61]. We invoke this representation in the comoving frame and write

$$eE_0\partial_{k_x}\vec{\rho} = 2\vec{H} \times \vec{\rho} - \hbar\gamma_1\vec{\rho} - \hbar\gamma_2\vec{h} - \hbar\gamma_3(\vec{\rho}\vec{h})\vec{h}. \tag{83}$$

In the case of finite temperature the dissipation coefficient $\gamma_2$ depends on the temperature $T$ as

$$\gamma_2 = \gamma_{\pm}\tanh\left(\frac{\epsilon}{k_BT}\right), \tag{84}$$

where $\epsilon = \sqrt{(\hbar v_F k_x + e v_F E_0 t)^2 + (\hbar v_F k_y)^2}$. We consider this in the expansion in orders of $E_0$ and find

$$e\partial_{k_x}\vec{\rho}_{m-1} = 2(\vec{H}_0 \times \vec{\rho}_m + \vec{H}_1 \times \vec{\rho}_{m-1}) - \hbar\gamma_1\vec{\rho}_m - \hbar\gamma_{2,m}\vec{h}_{m-n} - \hbar\sum_{n,l}\gamma_3(\vec{\rho}_{m-n-l}\vec{h}_n)\vec{h}_l. \tag{85}$$

We solve this for $m = 0$ and find the thermal state

$$\vec{\rho}_0 = -\tanh\left(\frac{\hbar v_F k}{k_BT}\right)\vec{h}. \tag{86}$$

We continue to find the solution for $m = 1$, which expressed in polar coordinates $k_x + ik_y = ke^{i\phi}$, has the $x$-component

$$\rho_{1,x} = \frac{e}{2}\text{sech}^2\left(\frac{\hbar v_F k}{k_BT}\right)\left(\frac{2\hbar^2 v_F^2\cos^2(\phi)}{\hbar^2 k_BT(\gamma_1 + \gamma_3)} + \frac{\gamma_1\hbar^2 v_F^2\sin^2(\phi)\sinh\left(\frac{2\hbar v_F k}{k_BT}\right)}{\hbar^2\gamma_1^2\hbar v_F k + 4\hbar^3 v_F^3 k^3}\right). \tag{87}$$

In order to obtain the conductivity we have to integrate this expression over momentum space. This expression integrates angularly to

$$\frac{1}{e}\int_0^{2\pi}\rho_{1,x}d\phi = \frac{\pi\hbar^2 v_F^2\text{sech}^2\left(\frac{\hbar v_F k}{k_BT}\right)}{\hbar^2 k_BT(\gamma_1 + \gamma_3)} + \frac{\pi\hbar^2 v_F^2\gamma_1\tanh\left(\frac{\hbar v_F k}{k_BT}\right)}{\hbar^3 v_F k\gamma_1^2 + 4\hbar^3 v_F^3 k^3}. \tag{88}$$

The first term integrates radially to

$$\int_0^{\infty}k\frac{\pi\hbar^2 v_F^2\text{sech}^2\left(\frac{\hbar v_f k}{k_BT}\right)}{\hbar^2 k_BT(\gamma_1 + \gamma_3)}dk = \frac{k_BT}{\hbar^2}\frac{\pi\log(2)}{\gamma_1 + \gamma_3}. \tag{89}$$

The second term relies on some approximation of the hyperbolic tangent, we use to good approximation that

$$\int_0^{\infty}\frac{\pi\hbar^2 v_F^2\gamma_1\tanh\left(\frac{\hbar v_F k}{k_BT}\right)}{\hbar^3 v_F\gamma_1^2 + 4\hbar^3 v_F^3 k^2}dk \approx \left(\frac{\pi^2}{4} - \frac{\pi}{2}\arctan\left(\left(\frac{k_BT}{\hbar\gamma_1}\right)^{\frac{3}{4}}\right)\right)\frac{1}{\hbar v_F}. \tag{90}$$

We collect the terms and write the conductivity as

$$G_{xx}^0 = n_v n_s \frac{e v_F}{4\pi^2} \int_0^\infty \int_0^{2\pi} k \rho_{1,x}(k) d\phi dk \tag{91}$$

with the valley- and spin-degeneracy $n_v = n_s = 2$. With this we insert the derived expressions and get the final result

$$G_{xx}^0 \approx \left( \frac{\pi}{2} \left( 1 - \frac{2}{\pi} \arctan((\frac{k_B T}{\hbar \gamma_1})^{\frac{3}{4}}) \right) + \frac{k_B T}{\hbar} \frac{2 \log(2)}{\gamma_1 + \gamma_3} \right) \frac{e^2}{h}. \tag{92}$$

## B  Floquet Band Gaps at Small Transverse Momenta

We want to calculate the Floquet band structure in the limit of small $k_y$ for the driven Hamiltonian

$$\frac{1}{\hbar} H = v_F (k_x + \frac{e E_d}{\hbar \omega_d} \cos(\omega_d t)) \sigma_x + v_F k_y \sigma_y. \tag{93}$$

We start by going into the time-dependent basis under the transformation

$$V = \exp\{-i v_F (k_x t + \frac{e E_d}{\hbar \omega_d^2} \sin(\omega_d t) \sigma_x)\} \tag{94}$$

such that the Schrödinger equation becomes

$$\partial_t \psi = -i v_F k_y V^\dagger \sigma_y V \psi \tag{95}$$

with the effective Hamiltonian proportional to

$$V^\dagger \sigma_y V = \sin(2(v_F k_x t + \frac{e v_F E_d}{\hbar \omega_d^2} \sin(\omega_d t))) \sigma_z + \cos(2(v_F k_x t + \frac{e v_F E_d}{\hbar \omega_d^2} \sin(\omega_d t))) \sigma_y. \tag{96}$$

In this basis the time-evolution operator after one driving period describes the same transformation as the effective static Floquet Hamiltonian. The formal solution yields

$$U \left( \frac{2\pi}{\omega_d} \right) = \hat{T}[\exp\{-i v_F k_y \int_0^{\frac{2\pi}{\omega_d}} V^\dagger \sigma_y V dt\}], \tag{97}$$

where $\hat{T}$ indicates time-ordering. This expression is a formal notation for an infinite series of nested integrals. We approximate this transformation by the Magnus expansion to first order in $k_y$. It then suffices to calculate

$$U \left( \frac{2\pi}{\omega_d} \right) = \exp\{-i v_F k_y \int_0^{\frac{2\pi}{\omega_d}} V^\dagger \sigma_y V dt\}, \tag{98}$$

where the integral in the exponential is now a closed expression that can be integrated by itself before exponentiation. We calculate the integral by first writing

$$\sin(2(v_F k_x t + \frac{e v_F E_{\rm d}}{\hbar \omega_{\rm d}^2} \sin(\omega_{\rm d} t))) = \frac{1}{2i} \sum_{n \in \mathbb{Z}} i^n e^{i 2 v_F k_x t} J_n(2 \frac{e v_F E_{\rm d}}{\hbar \omega_{\rm d}^2}) e^{in(\omega_{\rm d} t - \frac{\pi}{2})} \tag{99}$$

$$- i^n e^{-i 2 v_F k_x t} J_n(2 \frac{e v_F E_{\rm d}}{\hbar \omega_{\rm d}^2}) e^{in(-\omega_{\rm d} t - \frac{\pi}{2})} \tag{100}$$

$$= \sum_{n \in \mathbb{Z}} J_n(2 \frac{e v_F E_{\rm d}}{\hbar \omega_{\rm d}^2}) \sin(2 v_F k_x t - n \omega_{\rm d} t) \tag{101}$$

$$\int_0^{\frac{2\pi}{\omega_{\rm d}}} \to \frac{2\pi}{\omega_{\rm d}} \sum_{n \in \mathbb{Z}} J_n(2 \frac{e v_F E_{\rm d}}{\hbar \omega_{\rm d}^2}) \frac{1 - \cos(2\pi(\frac{2 v_F k_x}{\omega_{\rm d}} - n))}{\frac{2 v_F k_x}{\omega_{\rm d}} - n} \tag{102}$$

and analogously

$$\cos(2(v_F k_x t + \frac{e v_F E_{\rm d}}{\hbar \omega_{\rm d}^2} \sin(\omega_{\rm d} t))) \to \frac{2\pi}{\omega_{\rm d}} \sum_{n \in \mathbb{Z}} J_n(2 \frac{e v_F E_{\rm d}}{\hbar \omega_{\rm d}^2}) \frac{\sin(2\pi(\frac{2 v_F k_x}{\omega_{\rm d}} - n))}{\frac{2 v_F k_x}{\omega_{\rm d}} - n}. \tag{103}$$

The final transformation in the original basis is

$$V^\dagger(\frac{2\pi}{\omega_{\rm d}}) U(\frac{2\pi}{\omega_{\rm d}}) \tag{104}$$

which has the eigenvalues $\lambda_\pm = e^{\pm i \epsilon \frac{2\pi}{\hbar \omega_{\rm d}}}$, where $\epsilon$ are the Floquet energies. Hence, the Floquet energies can be calculated as

$$\epsilon_\pm = \frac{\hbar \omega_{\rm d}}{i 2\pi} \log(\lambda_\pm). \tag{105}$$

In the case in which $2 v_F k_x \omega_{\rm d}^{-1}$ is integer valued, we simplify

$$\frac{2\pi}{\omega_{\rm d}} \sum_{n \in \mathbb{Z}} J_n(2 \frac{e v_F E_{\rm d}}{\hbar \omega_{\rm d}^2}) \frac{1 - \cos(2\pi(l - n))}{l - n} = 0 \tag{106}$$

$$\frac{2\pi}{\omega_{\rm d}} \sum_{n \in \mathbb{Z}} J_n(2 \frac{e v_F E_{\rm d}}{\hbar \omega_{\rm d}^2}) \frac{\sin(2\pi(l - n))}{l - n} = \frac{2\pi}{\omega_{\rm d}} J_{2l}(2 \frac{e v_F E_{\rm d}}{\hbar \omega_{\rm d}^2}) \tag{107}$$

and similarly in the case where $2 v_F k_x \omega_{\rm d}^{-1}$ is half-integer we write

$$\frac{2\pi}{\omega_{\rm d}} \sum_{n \in \mathbb{Z}} J_n(2 \frac{e v_F E_{\rm d}}{\hbar \omega_{\rm d}^2}) \frac{1 - \cos(2\pi(l - n))}{l - n} = \frac{2\pi}{\omega_{\rm d}} J_{2l+1}(2 \frac{e v_F E_{\rm d}}{\hbar \omega_{\rm d}^2}) \tag{108}$$

$$\frac{2\pi}{\omega_{\rm d}} \sum_{n \in \mathbb{Z}} J_n(2 \frac{e v_F E_{\rm d}}{\hbar \omega_{\rm d}^2}) \frac{\sin(2\pi(l - n))}{l - n} = 0 \tag{109}$$

In either of these case it is $V(\frac{2\pi}{\omega_{\rm d}}) \propto \mathbb{1}$ and we therefore find

$$U(\frac{2\pi}{\omega_{\rm d}}) = e^{-i \frac{2\pi \hbar v_F k_y}{\hbar \omega_{\rm d}} J_l\left(2 \frac{e v_F E_{\rm d}}{\hbar \omega_{\rm d}^2}\right) \sigma_y} \tag{110}$$

which has the eigenvalues

$$\lambda_\pm = e^{\mp i \frac{2\pi \hbar v_F k_y}{\hbar \omega_{\rm d}} J_l\left(2 \frac{e v_F E_{\rm d}}{\hbar \omega_{\rm d}^2}\right)} \tag{111}$$

and we therefore find the Floquet energies

$$\epsilon_\pm = \hbar v_F k_y J_l\left(2 \frac{e v_F E_{\rm d}}{\hbar \omega_{\rm d}^2}\right). \tag{112}$$

Note that $\frac{2 v_F k_y}{\omega_{\rm d}} < 1$ and $J_l(z) \le 1$, such that analytic continuation in the complex plane does not have to be considered and the eigenvalues take this simple shape.

# C  Dissipative Calculations

The model of graphene that we use in this work employs of a Hilbert space that includes two additional states. We consider fermionic operators $c^{(\dagger)}_{\mathbf{k},A}$ and $c^{(\dagger)}_{\mathbf{k},B}$ that annihilate (create) electrons at momentum $\mathbf{k}$ in sublattice $A$ and $B$, respectively. The Hilbert space is then spanned by the states $|0\rangle$, $c^\dagger_A|0\rangle$, $c^\dagger_B|0\rangle$ and $c^\dagger_B c^\dagger_A|0\rangle$. In particular, the first and fourth states describe the situation in which either no electrons or two electrons are occupying a given momentum mode $\mathbf{k}$. In this space we define the dissipation operators in the instantaneous eigenbasis of the driven Hamiltonian, e.g. $L_-$ describes decay from the excited single-electron eigenstate to the single-electron ground state. It is

$$L_- = \begin{pmatrix} 0 & 0 & 0 & 0 \\ 0 & 0 & 0 & 0 \\ 0 & 1 & 0 & 0 \\ 0 & 0 & 0 & 0 \end{pmatrix} \qquad L_+ = \begin{pmatrix} 0 & 0 & 0 & 0 \\ 0 & 0 & 1 & 0 \\ 0 & 0 & 0 & 0 \\ 0 & 0 & 0 & 0 \end{pmatrix} \qquad L_z = \begin{pmatrix} 0 & 0 & 0 & 0 \\ 0 & 1 & 0 & 0 \\ 0 & 0 & -1 & 0 \\ 0 & 0 & 0 & 0 \end{pmatrix}$$
(113)

$$L_{\downarrow,j} = \begin{pmatrix} 0 & \delta_{j,1} & 0 & 0 \\ 0 & 0 & 0 & 0 \\ \delta_{j,2} & 0 & 0 & \delta_{j,3} \\ 0 & \delta_{j,4} & 0 & 0 \end{pmatrix} \quad L_{\uparrow,j} = \begin{pmatrix} 0 & 0 & \delta_{j,2} & 0 \\ \delta_{j,1} & 0 & 0 & \delta_{j,4} \\ 0 & 0 & 0 & 0 \\ 0 & 0 & \delta_{j,3} & 0 \end{pmatrix}.$$
(114)

$L_{\uparrow/\downarrow,j}$ describe the individual transitions in and out of the single-electron sector. In the master equation these particular processes are weighted by the dissipation rate $\gamma_{\mathrm{bg}} = \gamma_\downarrow + \gamma_\uparrow$ and $\gamma_\pm = \gamma_+ + \gamma_-$ We weight opposing processes by Boltzmann factors that ensure a Fermi distribution with temperature $T$ in the equilibrium state

$$\gamma_\uparrow = \gamma_\downarrow \exp\{-\frac{\epsilon}{k_B T}\}$$
(115)

$$\gamma_+ = \gamma_- \exp\{-\frac{2\epsilon}{k_B T}\}.$$
(116)

$k_B$ is the Boltzmann constant and $\pm\epsilon$ are the instantaneous eigenenergies of the Hamiltonian, e.g. Eq. 1. For further details on this dissipative model we refer to previous work that employ the same model [45, 56, 57].

Further, this description allows us to calculate two-point correlation functions using these fermionic operators, such as $\langle c^\dagger_A(t_2) c_A(t_1)\rangle$ and $\langle c^\dagger_B(t_2) c_B(t_1)\rangle$. We use these correlation functions to calculate the momentum- and frequency-resolved electron distribution in the steady state of the driven dissipative system.

$$n(\mathbf{k},\omega) = \frac{1}{(t_f - t_i)^2} \int_{t_i}^{t_f} \int_{t_i}^{t_f} \sum_{j=A,B} \langle c^\dagger_{\mathbf{k},j}(t_2) c_{\mathbf{k},j}(t_1)\rangle \, e^{i\omega(t_2-t_1)} dt_1 dt_2$$
(117)

This electron distribution reveals the Floquet band structure of the system and the electron population in these bands. This quantity is reminiscent of time- and angle-resolved photoelectron spectroscopy [62]. For further details on this method see previous works [45,56,57]. We use this calculation for Fig. 7 in the main text.

# References

[1] K. S. Novoselov, A. K. Geim, S. V. Morozov, D. Jiang, Y. Zhang, S. V. Dubonos, I. V. Grigorieva and A. A. Firsov, *Electric field effect in atomically thin carbon films*,

Science **306**(5696), 666 (2004), doi:10.1126/science.1102896, `https://www.science.org/doi/pdf/10.1126/science.1102896`.

[2] A. K. Geim and K. S. Novoselov, *The rise of graphene*, Nature Materials **6**(3), 183 (2007), doi:10.1038/nmat1849.

[3] A. H. Castro Neto, F. Guinea, N. M. R. Peres, K. S. Novoselov and A. K. Geim, *The electronic properties of graphene*, Rev. Mod. Phys. **81**, 109 (2009), doi:10.1103/RevModPhys.81.109.

[4] M. J. Allen, V. C. Tung and R. B. Kaner, *Honeycomb carbon: A review of graphene*, Chemical Reviews **110**(1), 132 (2010), doi:10.1021/cr900070d.

[5] D. Abergel, V. Apalkov, J. Berashevich, K. Ziegler and T. Chakraborty, *Properties of graphene: a theoretical perspective*, Advances in Physics **59**(4), 261 (2010), doi:10.1080/00018732.2010.487978, `https://doi.org/10.1080/00018732.2010.487978`.

[6] V. Kumar, *Linear and nonlinear optical properties of graphene: A review*, Journal of Electronic Materials **50**(7), 3773 (2021), doi:10.1007/s11664-021-08904-w.

[7] P. M. Ostrovsky, I. V. Gornyi and A. D. Mirlin, *Electron transport in disordered graphene*, Phys. Rev. B **74**, 235443 (2006), doi:10.1103/PhysRevB.74.235443.

[8] K. Ziegler, *Minimal conductivity of graphene: Nonuniversal values from the kubo formula*, Phys. Rev. B **75**, 233407 (2007), doi:10.1103/PhysRevB.75.233407.

[9] G. L. Klimchitskaya and V. M. Mostepanenko, *Conductivity of pure graphene: Theoretical approach using the polarization tensor*, Phys. Rev. B **93**, 245419 (2016), doi:10.1103/PhysRevB.93.245419.

[10] J. Cserti, *Minimal longitudinal dc conductivity of perfect bilayer graphene*, Phys. Rev. B **75**, 033405 (2007), doi:10.1103/PhysRevB.75.033405.

[11] N. M. R. Peres, F. Guinea and A. H. Castro Neto, *Electronic properties of disordered two-dimensional carbon*, Phys. Rev. B **73**, 125411 (2006), doi:10.1103/PhysRevB.73.125411.

[12] M. I. Katsnelson, *Zitterbewegung, chirality, and minimal conductivity in graphene*, The European Physical Journal B - Condensed Matter and Complex Systems **51**(2), 157 (2006), doi:10.1140/epjb/e2006-00203-1.

[13] T. Stauber, N. M. R. Peres and F. Guinea, *Electronic transport in graphene: A semiclassical approach including midgap states*, Phys. Rev. B **76**, 205423 (2007), doi:10.1103/PhysRevB.76.205423.

[14] R. Danneau, F. Wu, M. F. Craciun, S. Russo, M. Y. Tomi, J. Salmilehto, A. F. Morpurgo and P. J. Hakonen, *Evanescent wave transport and shot noise in graphene: Ballistic regime and effect of disorder*, Journal of Low Temperature Physics **153**(5), 374 (2008), doi:10.1007/s10909-008-9837-z.

[15] S. V. Morozov, K. S. Novoselov, M. I. Katsnelson, F. Schedin, D. C. Elias, J. A. Jaszczak and A. K. Geim, *Giant intrinsic carrier mobilities in graphene and its bilayer*, Phys. Rev. Lett. **100**, 016602 (2008), doi:10.1103/PhysRevLett.100.016602.

[16] K. Nomura and A. H. MacDonald, *Quantum transport of massless dirac fermions*, Phys. Rev. Lett. **98**, 076602 (2007), doi:10.1103/PhysRevLett.98.076602.

[17] F. T. Vasko and V. Ryzhii, *Voltage and temperature dependencies of conductivity in gated graphene*, Phys. Rev. B **76**, 233404 (2007), doi:10.1103/PhysRevB.76.233404.

[18] X. Du, I. Skachko, A. Barker and E. Y. Andrei, *Approaching ballistic transport in suspended graphene*, Nature Nanotechnology **3**(8), 491 (2008), doi:10.1038/nnano.2008.199.

[19] K. I. Bolotin, K. J. Sikes, J. Hone, H. L. Stormer and P. Kim, *Temperature-dependent transport in suspended graphene*, Phys. Rev. Lett. **101**, 096802 (2008), doi:10.1103/PhysRevLett.101.096802.

[20] I. Jung, D. A. Dikin, R. D. Piner and R. S. Ruoff, *Tunable electrical conductivity of individual graphene oxide sheets reduced at "low" temperatures*, Nano Letters **8**(12), 4283 (2008), doi:10.1021/nl8019938.

[21] M. Müller, M. Bräuninger and B. Trauzettel, *Temperature dependence of the conductivity of ballistic graphene*, Phys. Rev. Lett. **103**, 196801 (2009), doi:10.1103/PhysRevLett.103.196801.

[22] J. Horng, C.-F. Chen, B. Geng, C. Girit, Y. Zhang, Z. Hao, H. A. Bechtel, M. Martin, A. Zettl, M. F. Crommie, Y. R. Shen and F. Wang, *Drude conductivity of dirac fermions in graphene*, Phys. Rev. B **83**, 165113 (2011), doi:10.1103/PhysRevB.83.165113.

[23] S. Sibilia, F. Bertocchi, S. Chiodini, F. Cristiano, L. Ferrigno, G. Giovinco and A. Maffucci, *Temperature-dependent electrical resistivity of macroscopic graphene nanoplatelet strips*, Nanotechnology **32**(27), 275701 (2021), doi:10.1088/1361-6528/abef95.

[24] D. J. Sánchez-Trujillo, L. V. Osorio-Maldonado and J. J. Prías-Barragán, *Temperature dependence of electrical conductivity and variable hopping range mechanism on graphene oxide films*, Scientific Reports **13**(1), 4810 (2023), doi:10.1038/s41598-023-31778-3.

[25] J.-H. Chen, C. Jang, S. Xiao, M. Ishigami and M. S. Fuhrer, *Intrinsic and extrinsic performance limits of graphene devices on sio2*, Nature Nanotechnology **3**(4), 206 (2008), doi:10.1038/nnano.2008.58.

[26] J. Schiefele, F. Sols and F. Guinea, *Temperature dependence of the conductivity of graphene on boron nitride*, Phys. Rev. B **85**, 195420 (2012), doi:10.1103/PhysRevB.85.195420.

[27] T. Stauber, N. M. R. Peres and A. K. Geim, *Optical conductivity of graphene in the visible region of the spectrum*, Phys. Rev. B **78**, 085432 (2008), doi:10.1103/PhysRevB.78.085432.

[28] S. A. Mikhailov and K. Ziegler, *Nonlinear electromagnetic response of graphene: frequency multiplication and the self-consistent-field effects*, Journal of Physics: Condensed Matter **20**(38), 384204 (2008), doi:10.1088/0953-8984/20/38/384204.

[29] L. E. F. Foa Torres and G. Cuniberti, *Controlling the conductance and noise of driven carbon-based fabry–pérot devices*, Applied Physics Letters **94**(22), 222103 (2009), doi:10.1063/1.3147865, https://doi.org/10.1063/1.3147865.

[30] E. G. Mishchenko, *Dynamic conductivity in graphene beyond linear response*, Phys. Rev. Lett. **103**, 246802 (2009), doi:10.1103/PhysRevLett.103.246802.

[31] E. Hendry, P. J. Hale, J. Moger, A. K. Savchenko and S. A. Mikhailov, *Coherent nonlinear optical response of graphene*, Phys. Rev. Lett. **105**, 097401 (2010), doi:10.1103/PhysRevLett.105.097401.

[32] C. G. Rocha, L. E. F. F. Torres and G. Cuniberti, *ac transport in graphene-based fabry-pérot devices*, Phys. Rev. B **81**, 115435 (2010), doi:10.1103/PhysRevB.81.115435.

[33] M. Freitag, T. Low, F. Xia and P. Avouris, *Photoconductivity of biased graphene*, Nature Photonics **7**(1), 53 (2013), doi:10.1038/nphoton.2012.314.

[34] J. N. Heyman, J. D. Stein, Z. S. Kaminski, A. R. Banman, A. M. Massari and J. T. Robinson, *Carrier heating and negative photoconductivity in graphene*, Journal of Applied Physics **117**(1), 015101 (2015), doi:10.1063/1.4905192, https://pubs.aip.org/aip/jap/article-pdf/doi/10.1063/1.4905192/13706672/015101_1_online.pdf.

[35] H. K. Avetissian, A. K. Avetissian, G. F. Mkrtchian and K. V. Sedrakian, *Creation of particle-hole superposition states in graphene at multiphoton resonant excitation by laser radiation*, Phys. Rev. B **85**, 115443 (2012), doi:10.1103/PhysRevB.85.115443.

[36] G. Jnawali, Y. Rao, H. Yan and T. F. Heinz, *Observation of a transient decrease in terahertz conductivity of single-layer graphene induced by ultrafast optical excitation*, Nano Letters **13**(2), 524 (2013), doi:10.1021/nl303988q.

[37] K. Kristinsson, O. V. Kibis, S. Morina and I. A. Shelykh, *Control of electronic transport in graphene by electromagnetic dressing*, Scientific Reports **6**(1), 20082 (2016), doi:10.1038/srep20082.

[38] S. F. Islam and A. Saha, *Driven conductance of an irradiated semi-dirac material*, Phys. Rev. B **98**, 235424 (2018), doi:10.1103/PhysRevB.98.235424.

[39] M. S. Mrudul, Álvaro Jiménez-Galán, M. Ivanov and G. Dixit, *Light-induced valleytronics in pristine graphene*, Optica **8**(3), 422 (2021), doi:10.1364/OPTICA.418152.

[40] H. Tang, S. G. Menabde, T. Anwar, J. Kim, M. S. Jang and G. Tagliabue, *Photo-modulated optical and electrical properties of graphene*, Nanophotonics **11**(5), 917 (2022), doi:doi:10.1515/nanoph-2021-0582.

[41] B. Zhou, M. Rasmussen, P. R. Whelan, J. Ji, A. Shivayogimath, P. Bøggild and P. U. Jepsen, *Non-linear conductivity response of graphene on thin-film pet characterized by transmission and reflection air-plasma thz-tds*, Sensors **23**(7) (2023), doi:10.3390/s23073669.

[42] T. Oka and H. Aoki, *Photovoltaic hall effect in graphene*, Phys. Rev. B **79**, 081406 (2009), doi:10.1103/PhysRevB.79.081406.

[43] J. W. McIver, B. Schulte, F. U. Stein, T. Matsuyama, G. Jotzu, G. Meier and A. Cavalleri, *Light-induced anomalous hall effect in graphene*, Nature Physics **16**(1), 38 (2020), doi:10.1038/s41567-019-0698-y.

[44] S. A. Sato, J. W. McIver, M. Nuske, P. Tang, G. Jotzu, B. Schulte, H. Hübener, U. De Giovannini, L. Mathey, M. A. Sentef, A. Cavalleri and A. Rubio, *Microscopic theory for the light-induced anomalous hall effect in graphene*, Phys. Rev. B **99**, 214302 (2019), doi:10.1103/PhysRevB.99.214302.

[45] M. Nuske, L. Broers, B. Schulte, G. Jotzu, S. A. Sato, A. Cavalleri, A. Rubio, J. W. McIver and L. Mathey, *Floquet dynamics in light-driven solids*, Phys. Rev. Res. **2**, 043408 (2020), doi:10.1103/PhysRevResearch.2.043408.

[46] T. Higuchi, C. Heide, K. Ullmann, H. B. Weber and P. Hommelhoff, *Light-field-driven currents in graphene*, Nature **550**(7675), 224 (2017), doi:10.1038/nature23900.

[47] C. Heide, T. Higuchi, H. B. Weber and P. Hommelhoff, *Coherent electron trajectory control in graphene*, Phys. Rev. Lett. **121**, 207401 (2018), doi:10.1103/PhysRevLett.121.207401.

[48] C. Heide, T. Boolakee, T. Higuchi, H. B. Weber and P. Hommelhoff, *Interaction of carrier envelope phase-stable laser pulses with graphene: the transition from the weak-field to the strong-field regime*, New Journal of Physics **21**(4), 045003 (2019), doi:10.1088/1367-2630/ab13ce.

[49] C. Heide, T. Boolakee, T. Eckstein and P. Hommelhoff, *Optical current generation in graphene: Cep control vs. w + 2w control*, Nanophotonics **10**(14), 3701 (2021), doi:doi:10.1515/nanoph-2021-0236.

[50] F. Grossmann, T. Dittrich, P. Jung and P. Hänggi, *Coherent destruction of tunneling*, Phys. Rev. Lett. **67**, 516 (1991), doi:10.1103/PhysRevLett.67.516.

[51] J. C. A. Barata and W. F. Wreszinski, *Strong-coupling theory of two-level atoms in periodic fields*, Phys. Rev. Lett. **84**, 2112 (2000), doi:10.1103/PhysRevLett.84.2112.

[52] M. Frasca, *Perturbative results on localization for a driven two-level system*, Phys. Rev. B **68**, 165315 (2003), doi:10.1103/PhysRevB.68.165315.

[53] D. Gagnon, F. Fillion-Gourdeau, J. Dumont, C. Lefebvre and S. MacLean, *Coherent destruction of tunneling in graphene irradiated by elliptically polarized lasers*, Journal of Physics: Condensed Matter **29**(3), 035501 (2016), doi:10.1088/0953-8984/29/3/035501.

[54] A. Iurov, G. Gumbs, O. Roslyak and D. Huang, *Anomalous photon-assisted tunneling in graphene*, Journal of Physics: Condensed Matter **24**(1), 015303 (2011), doi:10.1088/0953-8984/24/1/015303.

[55] P. K. Tien and J. P. Gordon, *Multiphoton process observed in the interaction of microwave fields with the tunneling between superconductor films*, Phys. Rev. **129**, 647 (1963), doi:10.1103/PhysRev.129.647.

[56] L. Broers and L. Mathey, *Observing light-induced floquet band gaps in the longitudinal conductivity of graphene*, Communications Physics **4**(1), 248 (2021), doi:10.1038/s42005-021-00746-6.

[57] L. Broers and L. Mathey, *Detecting light-induced floquet band gaps of graphene via trarpes*, Phys. Rev. Res. **4**, 013057 (2022), doi:10.1103/PhysRevResearch.4.013057.

[58] S. A. Sato and A. Rubio, *Nonlinear electric conductivity and thz-induced charge transport in graphene*, New Journal of Physics **23**(6), 063047 (2021), doi:10.1088/1367-2630/ac03d0.

[59] T. N. Ikeda, S. Tanaka and Y. Kayanuma, *Floquet-landau-zener interferometry: Usefulness of the floquet theory in pulse-laser-driven systems*, Phys. Rev. Res. **4**, 033075 (2022), doi:10.1103/PhysRevResearch.4.033075.

[60] B. Trauzettel, Y. M. Blanter and A. F. Morpurgo, *Photon-assisted electron transport in graphene: Scattering theory analysis*, Phys. Rev. B **75**, 035305 (2007), doi:10.1103/PhysRevB.75.035305.

[61] L. Broers and L. Mathey, *Floquet engineering of non-equilibrium superradiance*, SciPost Phys. **14**, 018 (2023), doi:10.21468/SciPostPhys.14.2.018.

[62] J. K. Freericks, H. R. Krishnamurthy and T. Pruschke, *Theoretical description of time-resolved photoemission spectroscopy: Application to pump-probe experiments*, Phys. Rev. Lett. **102**, 136401 (2009), doi:10.1103/PhysRevLett.102.136401.

# 3 The Floquet-assisted Superradiant Phase

A central result of Publication II was that the longitudinal optical conductivity of strongly driven dissipative graphene can display a sign reversal at probing frequencies that are resonant with light-induced band gaps. From this, the question emerged whether the corresponding optical gain can be utilized to build a gain medium or a coherent light-source by exploiting the underlying mechanism of population inverted Floquet bands in solids. A possible construction would consider coupling the material to a single-mode cavity that is resonant to these population-inverted Floquet states, in order for a coherent light-field in the cavity to be sustained by depleting the population inversion in a type of laser-like mechanism. This consideration motivated Publication V, and subsequently Publication VI, in which I have studied a modified driven dissipative Dicke model that is inspired by the physics of circularly driven dissipative graphene. In this quantum optical model the same mechanism does occur, leading to a population inversion in the Floquet states, which in fact culminates in a non-equilibrium superradiant phase, to which I refer as the Floquet-assisted superradiant phase (FSP). The emergence, characterization, and robustness of the FSP are the focus of Publication V and Publication VI.

Throughout this chapter I provide an overview of the necessary background in quantum optics, with a focus on the Dicke model and the superradiant phase. This invites a discussion on non-equilibrium phenomena, superradiance, and different types of laser mechanisms. I also address the challenges of realizing the Dicke model and how this connects to a graphene-based setup such as the one that motivates Publication V and Publication VI. Quantum optics is a large and well-established field of research, and detailed books as well as extensive reviews of the Dicke model, superradiance, and laser phenomena are widely available [147–151] and have inspired the content of this chapter.

## 3.1 The Dicke Model and Superradiance

The Dicke model [152, 153] is one of the quintessential quantum optical models. It describes $N$ identical two-level systems with level-spacing $\omega_z$ that are placed inside, and coupled to, a single-mode cavity with frequency $\omega_c$. The Hamiltonian reads[1]

$$H = \hbar\frac{\omega_z}{2}\sum_{j=1}^{N}\sigma_z^j + \hbar\omega_c a^\dagger a + \frac{\lambda}{\sqrt{N}}\sum_{j=1}^{N}(\sigma_+^j + \sigma_-^j)(a + a^\dagger), \tag{3.1}$$

where $\sigma_\pm^j = \frac{1}{2}(\sigma_x^j \pm i\sigma_y^j)$ and $\sigma_{x,y,z}^j$ are the local Pauli matrices of the $j$th two-level system. $\lambda$ is the coupling strength and $a^{(\dagger)}$ are the annihilation (creation) operators

---

[1]Note that I use the definition of the Pauli matrices that fulfills $\sigma_j^2 = \mathbb{1}$, and not $\sigma_j^2 = \frac{\mathbb{1}}{4}$.

of the cavity mode. Note that the interaction contains four terms of the form $\sigma_\pm^j a^{(\dagger)}$. The two so-called counter-rotating terms $\sigma_-^j a$ and $\sigma_+^j a^\dagger$ are sometimes neglected in the rotating-wave approximation (RWA), as they describe relaxation and excitation processes by two quanta at once and are therefore fast-oscillating compared to the remaining two interaction terms. Applying this approximation recovers the Tavis-Cummings model [154]. Considering the edge-case of $N = 1$ of the Tavis-Cummings model recovers the Jaynes-Cummings model [155]. Considering the case of $N = 1$, while keeping the counter-rotating terms produces the quantum Rabi model.

The Hamiltonian in Eq. 3.1 is sometimes referred to as the Dicke-Lieb-Hepp model, as it was first proposed in this form by Lieb and Hepp [153][2] two decades after the original model of superradiance proposed by Dicke [152], which did not consider the presence of a cavity. This semantic ambiguity extends into the nomenclature of superradiance, which refers to the two distinct phenomena of transient superradiant flashing and the steady-state superradiant phase, which occur in these models. The former, also referred to as superradiant bursting or just superradiance, occurs in the original Dicke model as a collective spontaneous emission of $N$ excited emitters in proximity which leads to a coherent burst of radiation that scales with $N^2$ in intensity. I am not concerned with this phenomenon throughout my work. The superradiant phase on the other hand, also referred to as superradiance, is an equilibrium phenomenon of the Dicke-Lieb-Hepp model. It describes a second-order phase transition characterized by the occupation of the cavity. For coupling strengths that exceed the critical value $\lambda > \lambda_c = \frac{1}{2}\sqrt{\omega_c \omega_z}$ [153, 156, 157] the system displays a new ground state. This ground state consists of a coherent state in the cavity and substantial component along the $\sigma_x$ direction in the two-level systems, which represents finite polarization in case the model is used to describe atoms inside an optical cavity. Note that the coherent state in the cavity emerges, while the two-level systems show no population inversion, i.e. $\langle \sigma_z \rangle < 0$. For $\lambda < \lambda_c$, the system is in its normal phase where the ground state is trivial and consists of an empty cavity and all two-level systems in their local ground state. Throughout this section I am concerned with the Dicke-Lieb-Hepp model as written in Eq. 3.1, to which I refer to as the Dicke model.

When quantum optical models of this type were first studied, it was noticed that experimental realizations of the Dicke model are faced with a no-go argument [158–160], which sparked an intricate discussion about the relevance of gauge-fixing [161] that is still attracting attention [162, 163]. The outline of the argument goes as follows. Historically, the Dicke model was derived for a set of atoms inside an optical cavity coupled through the electric transition dipole moment. In minimal coupling, the electromagnetic vector potential $\vec{A}$ couples to momentum as

$$\vec{p} \to \vec{\pi} = \vec{p} - e\vec{A}, \tag{3.2}$$

where $\vec{\pi}$ is the dynamical momentum. In the parabolic kinetic term of non-relativistic

---

[2]In fact in the work by Lieb and Hepp, the RWA was used which makes it also a study on the Tavis-Cummings model.

Hamiltonians this leads to the transformation

$$\frac{\vec{p}^2}{2m} \to \frac{\vec{\pi}^2}{2m} = \frac{1}{2m}(\vec{p}^2 - 2e\vec{p}\vec{A} + e^2\vec{A}^2). \tag{3.3}$$

The quadratic term $\propto \vec{A}^2$ may be neglected when it is considered to be small. The vector potential is then quantized as

$$\vec{A}(\vec{r},t) = \sum_{j,\lambda} \sqrt{\frac{\hbar}{2\epsilon_0\omega_j V}} \vec{\epsilon}_{j,\lambda}(a_{j,\lambda}e^{i(\vec{k}_j\vec{r}-\omega_j t)} + a^\dagger_{j,\lambda}e^{-i(\vec{k}_j\vec{r}-\omega_j t)}), \tag{3.4}$$

where $\lambda \in \{1,2\}$ denotes the index of the polarization vectors $\vec{\epsilon}_{j,\lambda}$ which describe transversal modes, i.e. $\vec{k}_j\vec{\epsilon}_{j,\lambda} = 0$. $V$ is the mode volume of the cavity and $\epsilon_0$ is the vacuum permittivity. It is $\omega_j = c|\vec{k}_j|$ with the speed of light $c$. In considering a single-mode cavity this expression of the vector potential reduces to one operator $a$ with frequency $\omega$, momentum $\vec{k}$, and polarization vector $\vec{\epsilon}$.

At the same time an atomic potential is assumed, which is solved to identify two low-lying states, $|e\rangle$ and $|g\rangle$ with the level-spacing $E_e - E_g = \hbar\omega_z$. Assuming that the spatial extent of the set of atoms is much smaller than the wavelength of the cavity mode, i.e. the Dipole approximation, leads to the cross-term of Eq. 3.3

$$\langle e|\vec{p}\vec{A}(\vec{r},t)|g\rangle = \sqrt{\frac{\hbar}{2\epsilon_0\omega V}} \langle e|\vec{p}e^{i\vec{k}\vec{r}_0}a + \vec{p}e^{-i\vec{k}\vec{r}_0}a^\dagger|g\rangle. \tag{3.5}$$

Here, $\vec{r}_0$ is the approximate location of the two-level systems which is chosen to set the phase of the dipole element $\vec{d}_{eg} = e\langle e|\vec{r}|g\rangle = \frac{ie}{\hbar\omega_z m}\langle e|\vec{p}|g\rangle$ such that the coupling term in Eq. 3.3 becomes

$$-\frac{e}{m}(|e\rangle\langle e|\vec{p}\vec{A}(\vec{r},t)|g\rangle\langle g| + \text{h.c.}) = \omega_z\sqrt{\frac{\hbar}{2\epsilon_0\omega V}}|\vec{d}_{eg}|\sigma_x(a + a^\dagger), \tag{3.6}$$

with the polarization vector parallel to the dipole element, i.e. $\vec{\epsilon}\vec{d}_{eg} = |\vec{d}_{eg}|$. The prefactors in Eq. 3.6 are collected as the coupling strength $\lambda$. When this calculation is performed for $N$ identical systems, this recovers the Dicke Hamiltonian in Eq. 3.1. The no-go argument then states, that the quadratic term in Eq. 3.3 can in fact not be neglected in this derivation, as it becomes dominant in the would-be superradiant phase of the Dicke model. Deriving the model while not neglecting the quadratic term and quantizing the vector potential results in an additional term $\propto (a + a^\dagger)^2$ that prevents the superradiant phase transition from occurring in the first place. Note that this argument addresses the realization of the Dicke model through this equilibrium description of atoms inside optical cavities and does not immediately extend to other systems or non-equilibrium setups.

Consequently, experimental realizations of the Dicke model are fairly sparse and solutions to this conundrum usually consist of the light-matter coupling being generated by intricate pumping mechanisms, such that the Dicke model emerges effectively. Successful realizations include setups utilizing hyperfine states of atoms confined in an optical

cavity [164–166], circuit QED setups [167], or trapped ion systems [168, 169]. A prevalent realization consists of trapping a Bose-Einstein condensate inside a perpendicularly oriented optical cavity [170–178], where the two-level sector consists of momentum-state superpositions that form checkerboard patterns and lead to scattering into the cavity.

## 3.2 Non-equilibrium Models and Laser Mechanisms

Beyond the equilibrium phenomena of quantum optics, such as the Dicke superradiant phase, lies the introduction of driving terms to study more intricate physics. The non-equilibrium dynamics of quantum optical models in the presence of additional driving have been [179–184] and continue to be [185–196] an active field of study. In realizations of the Dicke model, different driving schemes have been demonstrated to lead to various non-equilibrium phases [197–203] and time-crystalline phenomena [203–208]. With the recently growing interest in Floquet engineering and non-equilibrium superradiance, the distinction between various classes of coherent-light sources becomes increasingly subtle.

It is common practice to consider quantum optical models in the presence of incoherent driving which pumps the population of the excited states. This leads for instance to the construction of lasing mechanisms, which are approximated analytically in the form of rate equations, where optical gain is the result of the pump-induced population inversion and stimulated emission. The quantum theory of regular lasing emerges in its original manner from the Jaynes-Cummings model in the presence of repeated injection of population inverted atoms as put forth by Lamb and Scully [209]. There have been countless realizations of conventional laser mechanism throughout the decades. However, there are also various unconventional laser mechanisms, such as lasing without inversion [210–214], counter-lasing [215, 216], dressed-state lasing [185, 217–222], and more [223–230]. A noteworthy mechanism is superradiant lasing [231–245], which is achieved by pumping the two-level systems of the Dicke model to engineer continuous steady-state superradiance[3] that characteristically displays an ultra-narrow linewidth.

An important distinction between incoherent and coherent driving is that in a system with coherent periodic driving, the Floquet theorem applies. As previously laid out in Section 2.3, this leads to the formation of hybridized states of the bare system in the presence of the interaction with the driving. In quantum optics, these are also referred to as dressed states, whereas in solid-state systems the term Floquet bands or Floquet states is often used. Note that the term dressed states is also used to refer to the corresponding eigenstates of quantum optical models in which quantized light-modes and orbitals hybridize. Including semi-classical coherent driving in quantum optical systems has been considered since the early days of the field of quantum optics. The Rabi model [246] is arguably the most minimalistic quantum optical model in that it describes a single simplified atom that is coherently irradiated by semi-classical light.

---

[3]Superradiant lasing is engineered in the Dicke-Lieb-Hepp or Tavis-Cummings model, and is a steady-state superradiance phenomenon distinct from the Dicke superradiant phase. It builds on the transient superradiant flashing phenomenon of the original Dicke model, which did not consider a cavity. This is one manifestation of the aforementioned semantic ambiguities that surround this topic.

The Hamiltonian consists of a two-level system in the presence of a periodic driving term and reads

$$H_R = \frac{\hbar\omega_z}{2}\sigma_z + \frac{\omega_z}{2\omega}\vec{d}\vec{E}(e^{i\omega t} + e^{-i\omega t})\sigma_x. \tag{3.7}$$

$\vec{E}$ is the electric field of the semi-classical driving term and $\vec{d}$ is the electric transition dipole moment of the atom. The conventional approach to solving this system consists of going into the rotating frame given by $V = e^{-i\sigma_z\frac{\omega}{2}t}$ and in the classical rotating-wave approximation (cRWA) dropping the counter-rotating terms that oscillate at the frequencies $\pm 2\omega$. This approximation is valid in the limit of weak driving, i.e. low field strengths, and has been widely used to study the behavior of absorption spectra of driven systems since the early days of quantum optics. However, this approximation breaks down for strong driving, at which point the counter-rotating term has to be considered. The details of Floquet states depend on the structure of the driving term, such that for instance the Rabi model after the cRWA leads to qualitatively distinct Floquet states compared to the Rabi model prior to this approximation. This is relevant in the following section, where I motivate a connection from quantum optics to two-band materials, in particular graphene, which displays a similar expression to that in Eq. 3.7.

## 3.3 Towards a Graphene-based Dicke model

As discussed in Chapter 2, I have studied a setup of driven graphene in Publication II that displays optical gain through a mechanism of population inverted Floquet states. This motivated studying this mechanism in a coherently driven quantum optical setup, where a single layer of graphene couples to a single-mode cavity. This is also in light of the more recent interest into engineering non-equilibrium dynamics [247–249], where the control of population of Floquet states has also been studied in different setups [250–254]. In Publication V and Publication VI, I have considered a driven dissipative Dicke-like model that contains a coherent driving term in the two-level systems in a manner that is inspired by the circularly polarized irradiation of graphene as in Eq. 2.26. The Hamiltonian reads

$$H = \sum_{j=1}^{N}\frac{\hbar\omega_z}{2}\sigma_z^j + \frac{\hbar\Omega}{2}(e^{-i\omega_\mathrm{d}t}\sigma_+ + e^{i\omega_\mathrm{d}t}\sigma_-) + \hbar\omega_c a^\dagger a + \frac{\lambda}{\sqrt{N}}\sum_{j=1}^{N}\sigma_x^j(a + a^\dagger) \tag{3.8}$$

and is locally structurally reminiscent of the Rabi model in Eq. 3.7 in the cRWA. Here $\Omega$ is a frequency that represents the intensity of the driving term, agnostic to its realization. The connection of this coherently driven Dicke model to graphene manifests itself in different ways and is well-motivated. First, note that in graphene no counter-rotating driving term exists, due to the nature of the linear dispersion relation and the minimal coupling, such that the resulting term in Eq. 3.8 should not be confused with the results of an approximation. This is crucial, since in contrast to the Rabi model in the cRWA, this term remains valid in the presence of strong driving, such that the two systems display distinct Floquet physics. However, the structure makes it straight-forward to

analyze the Floquet states in this system and their population inversion in order to gain insight into the underlying non-equilibrium physics.

Second, note that due to the linear dispersion relation of graphene, the minimal coupling does not produce any quadratic term $\propto \vec{A}^2$ to begin with. Hence, the interaction term in Eq. 3.8 is not the result of an approximation that neglects a quadratic term as the one presumed in the no-go argument of the Dicke superradiant phase. As a side remark, the linear dispersion in graphene has lead to discussions about a cyclotronic realization of the Dicke model using the non-equidistant Landau levels of graphene in a strong magnetic field [255, 256]. The arguments that are put forth as a no-go theorem of this cyclotronic realization [256] do not make statements about other realizations utilizing graphene, in particular non-equilibrium cases. Graphene has also been proposed as an alternative to realizing the bosonic mode[4] in the Dicke model, by utilizing surface-plasmonic excitations [257].

Finally, the connection to graphene is particularly emphasized through the dissipation that I employ in this model, which is the same as the one used to describe the dynamics of driven dissipative graphene in Publications I through IV. This dissipative model is implemented via the Lindblad master equation and is distinct in that the Lindblad operators act in the instantaneous eigenbasis of the Hamiltonian, as discussed in Section 2.4. In the description of two-band materials such as graphene, this model reproduces steady states in the presence of bias fields in a gauge-invariant manner. This choice of dissipation directly affects the emergence of population inverted Floquet states. The remaining distinction of this Dicke-like model and graphene consequently lies primarily in the bare Hamiltonian of the two-level systems in Eq. 3.8, which makes the system more accessible analytically while still providing meaningful insight. All of these considerations motivate this model as means of studying the behavior of driven two-band materials inside a cavity.

In a mean-field description, the Hamiltonian in Eq. 3.8 separates into two sectors describing the dynamics of the two-level systems and the cavity, respectively. I write for the individual two-level systems the locally identical Hamiltonian

$$H_a = \frac{\hbar\omega_z}{2}\sigma_z + \frac{\hbar\Omega}{2}(e^{-i\omega_d t}\sigma_+ + e^{i\omega_d t}\sigma_-) + \frac{\lambda}{\sqrt{N}}\sigma_x \langle a + a^\dagger \rangle \tag{3.9}$$

and for the cavity

$$H_c = \hbar\omega_c a^\dagger a + \lambda\sqrt{N} \langle \sigma_x \rangle (a + a^\dagger). \tag{3.10}$$

I assume that the cavity hosts a coherent state that is fully characterized by the parameter $\alpha = \langle a \rangle$, such that the equation of motion of the coherent state reads

$$\dot{\alpha} = -(i\omega_c + \kappa)\alpha - i\lambda\sqrt{N}\rho_x, \tag{3.11}$$

where $\kappa$ is a cavity loss rate that I include to describe a potentially dissipative cavity. $\rho_x = \langle \sigma_x \rangle$ is the $\sigma_x$ expectation value of the identical two-level systems. This equation

---

[4]At face value, the Hamiltonian in Eq. 3.8 considers a single bosonic mode coupled to $N$ two-level systems. What type of physical system is used to realize the bosonic mode is in principle unspecified, although it will relate to the origin of the coupling term.
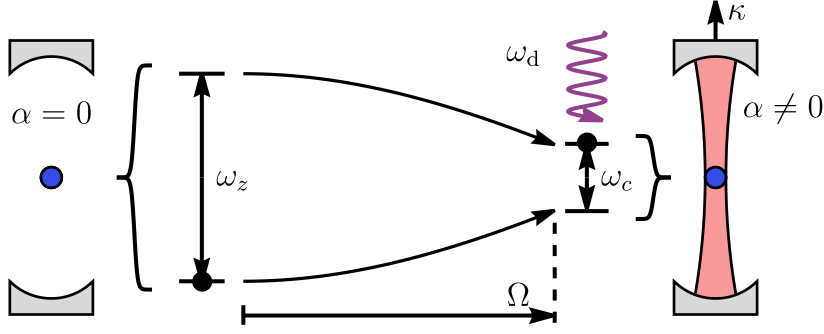
Figure 3.1: Schematic overview of the FSP mechanism. The two-level systems inside the cavity have a transitional frequency $\omega_z$ and are driven with an intensity of $\Omega$ at a frequency $\omega_\mathrm{d} > \omega_z$. The Floquet states change as a function of $\Omega$ as indicated by the curved arrows, and in the presence of dissipation in the instantaneous eigenbasis, display population inversion. The single-mode cavity at $\omega_c$ is resonant to the population inverted Floquet states, which leads to a depletion of the inversion in order to sustain a coherent state $\alpha$ inside the cavity. The cavity loss rate $\kappa$ results in a photonic output.

of motion is coupled to that of the density operators

$$\rho = \frac{1}{2}(\mathbb{1} + \vec{\rho}\vec{\sigma}) \tag{3.12}$$

of the two-level systems, where $\vec{\sigma}$ is the vector containing the Pauli matrices. I write this in the general representation that I provided for the solid-like dissipation in Section 2.4 in Eq. 2.46. It reads

$$\dot{\vec{\rho}} = 2\epsilon_a \vec{h}_a \times \vec{\rho} - \gamma_1 \vec{\rho} - \gamma_2 \vec{h}_a - \gamma_3(\vec{h}_a\vec{\rho})\vec{h}_a, \tag{3.13}$$

where $\epsilon_a$ is the instantaneous level spacing of the Hamiltonian $H_a = \epsilon_a \vec{h}_a \vec{\sigma}$ given for instance by the relation $H_a^2 = \epsilon_a^2$, since $\mathrm{Tr}(H_a) = 0$. The dissipation coefficients in this representation are

$$\gamma_1 = \frac{\gamma_+ + \gamma_-}{2} + 2\gamma_z \qquad \gamma_2 = \gamma_- - \gamma_+ \qquad \gamma_3 = \frac{\gamma_+ + \gamma_-}{2} - 2\gamma_z, \tag{3.14}$$

where $\gamma_{\pm,z}$ are the coefficients of the processes modeled by the Lindblad operators $\sigma_{\pm,z}$ in the instantaneous eigenbasis, see Section 2.4.

Equations 3.11 and 3.13 recover the Dicke superradiant phase correctly, but also display the emergence of a non-equilibrium superradiant phase for strong driving, i.e. large $\Omega$, through the mechanism depicted in Fig. 3.1. For strong driving, the Floquet states of the two-level system become population inverted, in a mechanism analogous to the one I had identified in graphene in Publication II. This mechanism depends on the relation between the characteristic frequencies of the system. I have studied the case in which

$\omega_{\mathrm{d}} > \omega_z > \omega_c$. The cavity is tuned to be resonant to the light-induced Floquet states and hosts a coherent state with a photonic population that matches the depletion of the population inversion, in a type of laser-like mechanism. Notably, the complex order parameter $\alpha$, given by the coherent state, oscillates at a frequency close to the Floquet state transition frequency. The two-level systems experience this oscillating order parameter as an additional driving term which leads to further modification of the Floquet states and to a type of hole-burning effect in the two-level systems. I refer to this non-equilibrium phase as the Floquet-assisted superradiant phase (FSP) and it is the focus of Publication V, where I characterize this phenomenon analytically and numerically. In Publication VI, I have further studied this model, in particular with respect to the robustness against environmental factors such as homogeneous broadening, noisy driving, and increased dissipation, all of which might affect the viability and stability of the FSP. Inhomogeneous broadening enters this model through normal-distributed detuning of the transitional frequencies of the individual two-level systems. Noisy driving is included via random phase drift and leads to a finite linewidth in the semi-classical driving field as well as the light-field inside the cavity. I find that the power spectrum of the light-field in the cavity experiences drastic line-narrowing across the FSP transition which overcomes the intrinsic linewidths of the system. Such line-narrowing corresponds to increased spectral coherence and is characteristic of laser mechanisms. The critical coupling strength at which the FSP occurs decreases with decreasing dissipation, which presents the prospect of realizing the FSP in the presence of very weak coupling in sufficiently clean materials and high-finesse cavities. Notably, in the case of large dissipation coefficients that are on the order of the values that we used to described graphene in Publication I, the FSP remains reasonably accessible under realistic conditions with a critical coupling comparable to that of the equilibrium Dicke superradiant phase. The results of Publication V and Publication VI are promising, and pave the road for demonstrating the FSP mechanism in a full construction of driven dissipative graphene coupled to a cavity under realistic conditions.

## 3.4 Publication V: Floquet engineering of non-equilibrium superradiance

L. Broers and L. Mathey — **SciPost Phys. 14(2), 018 (2023)**

This work was motivated by the observation of a negative longitudinal optical conductivity due to inverted Floquet band populations in graphene driven at terahertz frequencies in Publication II. The prospect of obtaining optical gain out of driven dissipative two-band materials such as graphene prompted me to try and better understand the underlying mechanism from a quantum optical perspective. This also raised the question if this effect could be utilized to construct a type of coherent light-source.

I have introduced a coherently and strongly driven Dicke model as a simplified model of a two-band material coupled to a single-mode cavity. In particular, I have considered solid-like dissipation as I had used for graphene in Publication I — IV. I studied this model numerically and analytically with a focus on the emergence of a non-equilibrium superradiant phase in the presence of strong driving. I have found that the mechanism of population inverted Floquet states as in Publication II does appear in this system as well. Further, I have shown that tuning the cavity into resonance with the Floquet state energy differences leads to the effective population inversion being depleted in order to sustain a coherent steady state in the cavity. This leads to a non-equilibrium superradiant phase to which I refer to as the Floquet-assisted superradiant phase (FSP). I have characterized the FSP with respect to the coupling strength and the driving field strength, as well as the dependency on the cavity frequency and the transition frequency of the two-level systems. The phase diagram of the photonic field in the cavity shows that the FSP emerges for small values of the coupling strength, compared to the equilibrium Dicke superradiant phase. I have identified the conditions under which the FSP emerges in the weak coupling regime, and how this relates to the mechanism of population inverted Floquet states. Further, the phase diagram displays the FSP within the analytical boundaries that I have predicted for the regime in which the population inversion in the Floquet states occurs. The FSP presents an intriguing mechanism for coherent light-sources that could in future work be studied in driven graphene coupled to a cavity as a realistic platform.

My contribution to this work consisted of conceiving the project, creating the numerical code, performing the numerical studies, performing the analytical calculations, analyzing and presenting the results, and writing the manuscript. All of this was done under the supervision and with the guidance of LM.

# Floquet engineering of non-equilibrium superradiance

Lukas Broers[1,2]⋆ and Ludwig Mathey[1,2,3]

**1** Center for Optical Quantum Technologies, University of Hamburg, Hamburg, Germany
**2** Institute for Laser Physics, University of Hamburg, Hamburg, Germany
**3** The Hamburg Center for Ultrafast Imaging, Hamburg, Germany

⋆ lbroers@physnet.uni-hamburg.de

## Abstract

We demonstrate the emergence of a non-equilibrium superradiant phase in the dissipative Rabi-Dicke model. This phase is characterized by a photonic steady state that oscillates with a frequency close to the cavity frequency, in contrast to the constant photonic steady state of the equilibrium superradiant phase in the Dicke model. We relate this superradiant phase to the population inversion of Floquet states by introducing a Schwinger representation of the driven two-level systems in the cavity. This inversion is depleted near Floquet energies that are resonant with the cavity frequency to sustain a coherent light-field. In particular, our model applies to solids within a two-band approximation, in which the electrons act as Schwinger fermions. We propose to use this Floquet-assisted superradiant phase to obtain controllable optical gain for a laser-like operation.

Check for updates

## Contents

# 1   Introduction

Driven dissipative quantum systems display a plethora of intriguing phenomena, including unconventional coherent light sources and amplification mechanisms. Phenomena such as lasing without inversion [1–4], lasing with driven quantum dots [5,6] and population inversion in strongly driven two-level systems [7,8], have been proposed or implemented to extend the conventional lasing mechanism. These examples are based on the non-equilibrium dynamics of the dissipative Rabi model, which presents a minimal example of driven quantum systems. Similarly, driven Dicke models [9] exhibit rich non-equilibrium dynamics of superradiant phase transitions and unconventional lasing states [10–19]. Driving the coupling in cavity-BEC setups, which can be mapped onto the dissipative Dicke model, hosts several non-equilibrium phases [20–25]. Incoherently pumped Strontium transitions have been used to explore the crossover regime of superradiant lasing [26,27]. Nitrogen vacancy (NV) center spins in diamond present a similar platform that has been used to create superradiant lasers [28–30]. In many-body systems, Floquet engineering aims to tune collective properties, such as band topology [31–35], with coherent driving [36–38]. It has been shown that population inversion of Floquet states can occur in driven systems [39–41]. Floquet theory itself presents a method to describe the effective dressed states in driven systems and their population, and is applicable to driven dissipative cavity systems [42,43], in particular.

We present the emergence of a Floquet-assisted superradiant phase (FSP) in the dissipative Dicke model under the influence of circularly polarized driving of the two-level systems, reminiscent of the Rabi model. This superradiant phase is distinct from other recently explored dynamical phases and lasing mechanisms in the Dicke model such as the dynamical phases that emerge under parametric driving of the coupling [20–25], NV room temperature superradiant lasers [28–30] and the Floquet maser realized using magnetic feedback circuits [44]. The FSP presents a mechanism for light-amplification and coherent light sources in two-level systems that is induced by the driven coherences between effective dressed states and is thus not captured by semi-classical rate equations in which population inversion is impossible. We find that this mechanism originates from the effective population inversion of Floquet states that is depleted and transferred into the cavity if the cavity frequency is close to resonance with the Floquet energy difference. This photonic coherent state saturates quickly, leading to a steady state of constant magnitude with respect to the coupling strength. We analytically determine the regime of driving field strengths in which the system displays Floquet state population inversion and is therefore susceptible to the FSP. We further present an analytical prediction of the parameters at which the FSP first emerges in the limit of small coupling strengths.

This work demonstrates that despite the fact that Floquet states are effective descriptions with energies that are only defined modulo multiples of a given driving frequency, their population inversion can induce and sustain a coherent photonic state in a close-to-resonant cavity. The connection between this light-amplification mechanism in two-level systems and effective populations of Floquet states translates into solid-state systems that can be described with two bands, e.g. monolayer graphene. This suggests the possibility of coherent Floquet engineered light-amplification in solids, where the dispersion relation leads to a modification of our model in which the two-level systems are no longer equal and their collective coupling to the cavity becomes more intricate. Such a system would still be susceptible to the mechanisms that underly the FSP which we describe here.

This work is structured as follows. In section 2, we describe the Rabi-Dicke model and its dissipative mean-field description. In section 3, we present numerical results for the phase diagram of the photonic steady state which shows the FSP. We also show the photonic steady state of the FSP in frequency space as a function of the driving field strength. Further, we present analytical calculations of the Dicke superradiant transition in this model. In section

4, we extend our results to a Schwinger representation which we use to calculate two-point correlation functions and Floquet state populations. In this representation we demonstrate the population inversion of the Floquet states and its depletion in the FSP. We then present an approximation of the Floquet energies of the two-level system in the FSP from an approximate bichromatic Floquet description. In section 5, we present analytical bounds for the driving field strengths at which population inversion occurs. Additionally, we demonstrate an accurate description of the onset at which the FSP first occurs for weak coupling to the cavity. In section 6, we conclude and discuss our findings.

## 2 Dissipative Rabi-Dicke Model

We consider a system of $N$ identical two-level systems with level-spacing $\omega_z$ coupled to a single lossy cavity mode with frequency $\omega_c$, as schematically depicted in Fig. 1. We emphasize that the dynamical superradiant state can be realized on any set of well-defined two-level systems, including solids in a two-band approximation, see e.g. [45]. The individual two-level systems experience Rabi-like driving with frequency $\omega_d$ and effective field strength $E_d$. The Hamiltonian of this Rabi-Dicke model is

$$\frac{1}{\hbar}H = \sum_{j=1}^{N}\Big[\frac{\omega_z}{2}\sigma_z^j + \frac{E_d}{\omega_d}(e^{-i\omega_d t}\sigma_+^j + e^{i\omega_d t}\sigma_-^j)\Big] + \omega_c a^\dagger a + \frac{\lambda}{\sqrt{N}}\sum_{j=1}^{N}(a+a^\dagger)\sigma_x^j, \qquad (1)$$

where $\lambda$ is the coupling strength and $\sigma_{x,y,z}^j$ are the Pauli-matrices of the $j$th two-level system. It is $\sigma_\pm = (\sigma_x \pm i\sigma_y)/2$. $a^{(\dagger)}$ is the photon annihilation (creation) operator. This Hamiltonian, that we use as the basis for our analysis, derives from an underlying model such as

$$\frac{1}{\hbar}H_0 = \frac{\omega_z}{2}\sigma_z + \frac{\omega_z}{2\hbar\omega_d}\vec{E}\vec{d}(e^{-i\omega_d t}\sigma_+ + e^{i\omega_d t}\sigma_-). \qquad (2)$$

Here $\vec{E}$ is the driving field and $\vec{d}$ is the dipole moment of the transition. Our effective driving field strength relates to this case as $E_d = \frac{1}{2}\omega_z\vec{E}\vec{d}\hbar^{-1}$, where $2E_d\omega_d^{-1}$ is the Rabi frequency. As a second model that motivates the Hamiltonian $H$, we present the model

$$\frac{1}{\hbar}H_g = v_F(k_x + \frac{eE}{\hbar\omega_d}\cos(\omega_d t))\sigma_x + v_F(k_y + \frac{eE}{\hbar\omega_d}\sin(\omega_d t))\sigma_y \qquad (3)$$

that we used in the context of light-driven graphene [41, 45]. Here $v_F = c/300$ is the Fermi velocity with the speed of light $c$. $e$ is the elementary charge, $E$ is the driving field strength and $k_{x,y}$ are the momentum components. Our effective driving field strength relates to this case as $E_d = ev_F E\hbar^{-1}$. In the following we take $\hbar = 1$.

We use a mean-field approximation of the photon dynamics via the coherent state ansatz $\alpha = \alpha_r + i\alpha_i = \langle a\rangle$, with the system separating into the two-level subsystem A and the cavity subsystem C resulting in the approximate Hamiltonian $H = \sum_j H_A^j + H_C$, with

$$H_A^j = \frac{\omega_z}{2}\sigma_z^j + \frac{E_d}{\omega_d}(e^{-i\omega_d t}\sigma_+^j + e^{i\omega_d t}\sigma_-^j) + \frac{\lambda\langle a+a^\dagger\rangle}{\sqrt{N}}\sigma_x^j, \qquad (4)$$

$$H_C = \omega_c a^\dagger a + \lambda\sqrt{N}\langle\sigma_x\rangle(a+a^\dagger), \qquad (5)$$

We include a cavity loss rate $\kappa$, such that the equation of motion of the photon mode is

$$\dot{\alpha} = -(i\omega_c + \kappa)\alpha - i\lambda\sqrt{N}\langle\sigma_x\rangle. \qquad (6)$$

The Lindblad-von Neumann master equation of the two-level system is

$$\dot{\rho} = i[\rho, \frac{\omega_z}{2}\sigma_z + \frac{E_d}{\omega_d}(e^{-i\omega_d t}\sigma_+ + e^{i\omega_d t}\sigma_-) + \frac{2\lambda\alpha_r}{\sqrt{N}}\sigma_x] + \sum_{l\in\{+,-,z\}}\gamma_l[L_l\rho L_l^\dagger - \frac{1}{2}\{L_l^\dagger L_l,\rho\}], \quad (7)$$

where we omit the superscript $j$, since the two-level systems are all identical, in this approximation. We describe the dissipation of the two-level system in its instantaneous eigenbasis, which has been shown to accurately describe two-band solids [45]. In particular, the Lindblad operators are $L_+ = V\sigma_+ V^\dagger$, $L_- = V\sigma_- V^\dagger$ and $L_z = V\sigma_z V^\dagger$, where $V$ is the unitary transformation into the instantaneous eigenbasis of $H_A(t) = \epsilon_A(t)V\sigma_z V^\dagger$. $\epsilon_A(t)$ is the instantaneous eigenenergy of the Hamiltonian $H_A(t)$. $\gamma_\pm$ and $\gamma_z$ are the coefficients of spontaneous decay and dephasing, respectively. The equation of motion of the two-level system then takes the form (see App. A)

$$\dot{\rho} = i[\rho, H_A(t)] - \gamma_1(\rho - \frac{\mathbb{1}}{2}) - \frac{\gamma_2}{2}H_A(t)\epsilon_A^{-1}(t) - \frac{\gamma_3}{2}\text{Tr}(\rho H_A(t))H_A(t)\epsilon_A^{-2}(t), \quad (8)$$

with

$$\gamma_1 = (\gamma_- + \gamma_+)/2 + 2\gamma_z, \qquad \gamma_2 = \gamma_- - \gamma_+, \qquad \gamma_3 = (\gamma_- + \gamma_+)/2 - 2\gamma_z. \quad (9)$$

Throughout this work we use $\gamma_- + \gamma_+ = \frac{\omega_d}{100\pi}$, $\gamma_+ = \gamma_- e^{-\frac{2\epsilon_A}{k_B T}} \approx 0$, $\gamma_z = \frac{\omega_d}{50\pi}$ and $\kappa = \frac{\omega_c}{100}$. Due to these small values of the decay and dephasing coefficients, the Floquet states are well-resolved in frequency space. The cavity loss rate $\kappa$ is very small compared to $\omega_c$ which constitutes the 'good cavity' regime. We find that the FSP depends on dissipation and is in particular sensitive to the cavity loss rate. However, the scaling behavior with respect to dissipation is not the focus of this work. Rather, we point out the existence of a novel superradiant phase, that emerges in the presence of optical driving. For this purpose we choose a dissipative model. We note that the Lindblad master equation applied to strongly driven two-level systems with weak dissipation has been found to show some deviations from more accurate methods [46]. We understand these deviations to be small enough to not affect the central results of this paper. The specific choice of the dissipative model in the instantaneous eigenbasis is motivated by the natural dissipative environment of electrons in solids [45]. The two-level systems that we consider here can be realized as two electron states, with one electron occupying one or the other. As we describe below, these two states can be embedded in a four-level system that includes both states to be occupied or empty, within a Schwinger construction. While this is the natural Hilbert space for an electronic realization, we emphasize that the results we obtain here can be generated from the Rabi-Dicke model, i.e. Eq. 1.

## 3 Floquet-Assisted Superradiant Phase

We determine the steady state regimes of the system. For that purpose, we solve the equations of motion Eqs. 6 and 7 and find the photonic state $\alpha(t)$, which serves as the order parameter of superradiant phases. In Fig. 2 (a), we show the magnitude of $\alpha$ as a function of the driving field strength $E_d$ and the coupling strength $\lambda$, for $\omega_z = \omega_d/2$ and $\omega_c = \omega_d/4$, as an example. We note that no specific ratio between these frequencies is required. We find two phases of non-zero $|\alpha|$. The phase for small driving field strengths $E_d$ is related to the Dicke superradiant phase and approaches it for $E_d \to 0$, which is an equilibrium phenomenon. In this limit, Eq. 1 recovers the dissipative Dicke-model. To capture this state, we write the equilibrium state of the static two-level system as

$$\rho = \frac{1}{2}(\mathbb{1} - \frac{\gamma_- - \gamma_+}{\gamma_- + \gamma_+}\frac{H_A}{\epsilon_A}), \quad (10)$$
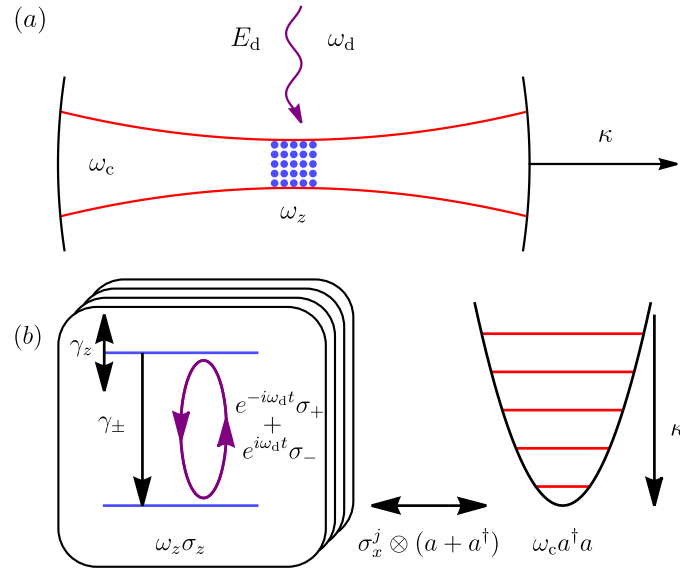
Figure 1: An illustration of the dissipative Rabi-Dicke model (a) and a depiction of its Hamiltonian as in Eq. 1 (b). A cavity (red) contains a set of identical two-level systems (blue) which experience circularly polarized Rabi-like driving (purple). $\gamma_\pm$ and $\gamma_z$ denote the coefficients of dissipative processes in the two-level systems, i.e. spontaneous decay and dephasing. $\kappa$ is the loss rate of the cavity, which determines the coherent output of the cavity.

which solves Eq. 8. We find the corresponding photonic steady state from Eq. 6 by inserting $\dot{\alpha} = 0$ and $\langle \sigma_x \rangle = \rho_x$. It is

$$0 = -(i\omega_c + \kappa)(\alpha_r + i\alpha_i) - i\lambda\sqrt{N}\rho_x \,, \tag{11}$$

with

$$\rho_x = -\frac{\gamma_- - \gamma_+}{\gamma_- + \gamma_+} \frac{4\lambda\alpha_r N^{-\frac{1}{2}}}{\sqrt{\omega_z^2 + 16\lambda^2\alpha_r^2 N^{-1}}} \,, \tag{12}$$

which we solve to find

$$\frac{\alpha}{\sqrt{N}} = (1 + i\frac{\kappa}{\omega_c})\sqrt{\left(\frac{\gamma_- - \gamma_+}{\gamma_- + \gamma_+}\frac{\lambda\omega_c}{\omega_c^2 + \kappa^2}\right)^2 - \left(\frac{\omega_z}{4\lambda}\right)^2} \,. \tag{13}$$

If $\alpha$ is purely imaginary, then $\rho_x$ is zero, because of Eq. 12. This implies that the $\alpha = 0$ solution is the state of the system, based on Eq. 11. If $\alpha$ has a non-vanishing real part, i.e. $\alpha_r \neq 0$, the system is in the Dicke superradiant state. We determine the critical coupling strength $\lambda_c$ of this transition by setting the expression under the root in Eq. 13 equal to zero. It is

$$\lambda_c = \frac{1}{2}\sqrt{\frac{\gamma_- + \gamma_+}{\gamma_- - \gamma_+}\frac{\omega_z}{\omega_c}\left(\kappa^2 + \omega_c^2\right)} \,. \tag{14}$$

In the case of $\kappa = 0$ and $\gamma_+ = \gamma_- e^{-\frac{\omega_z}{k_B T}}$ this reproduces the well-known result for the critical coupling

$$\lambda_c = \frac{1}{2}\sqrt{\omega_z\omega_c \coth(\frac{\omega_z}{2k_B T})} \overset{T \to 0}{\to} \frac{1}{2}\sqrt{\omega_z\omega_c} \,. \tag{15}$$

We show this transition in Fig. 2 (b) compared to the numerical solution, which show excellent agreement. Increasing $E_d$ initially maintains this transition, but increases the critical coupling

strength $\lambda_c|_{E_d>0} - \lambda_c \propto E_d^2$. For the parameters in our example it is $\lambda_c = \frac{\omega_d}{4\sqrt{2}}$ for $E_d = 0$. Further, the phase is separated into two regimes by a boundary $E_d^b \approx 0.02\omega_d^2$ for $\lambda > \sqrt{2}\lambda_c$. For $E_d < E_d^b$ the phase shows similar scaling to the Dicke superradiant phase, i.e. the value of $\alpha$ matches the case of $E_d = 0$. For $E_d > E_d^b$ the system experiences heating in this part of the phase, due to the weak dissipation in the two-level systems.
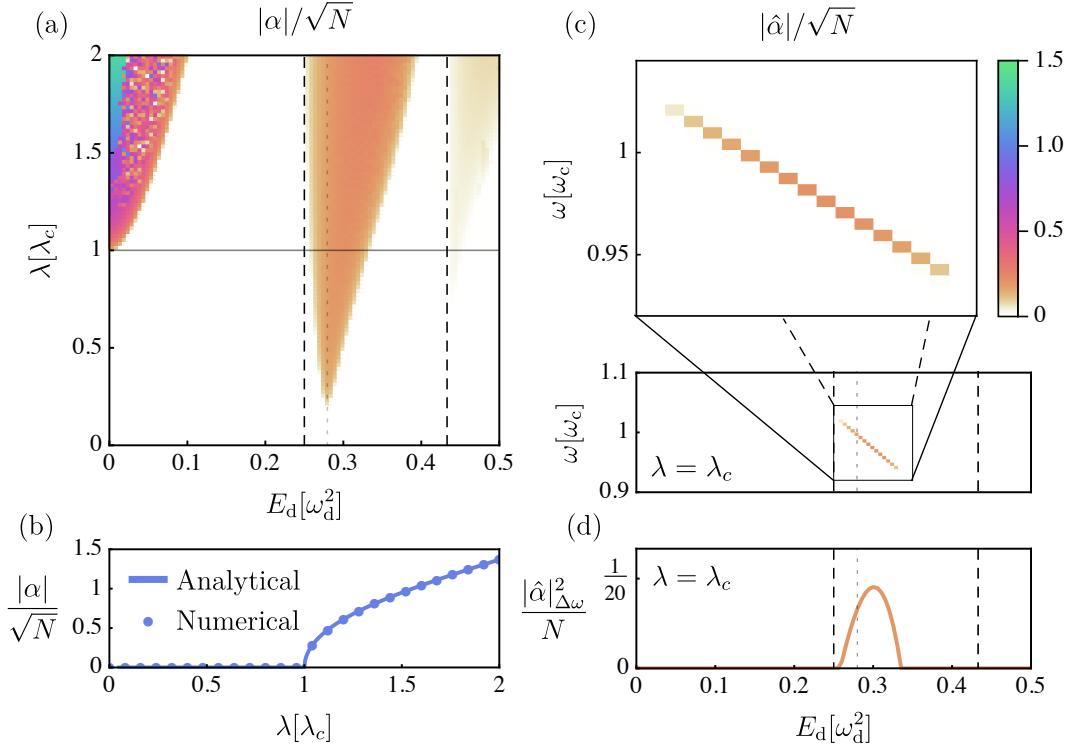


Figure 2: In panel (a) we show the magnitude of the photonic field $\alpha$ as a function of the driving field strength $E_d$ and the coupling strength $\lambda$. For large $E_d$, the Floquet-assisted superradiant phase (FSP) emerges and exhibits an oscillating photonic steady state. In panel (b) we show the $E_d \to 0$ limit, i.e. the Dicke superradiant transition, which is predicted very well analytically. In panel (c) we show the magnitude of the Fourier transform $|\hat{\alpha}|/\sqrt{N}$ as a function of the driving field strength $E_d$ for the coupling strength $\lambda = \lambda_c$. In the FSP, the steady state frequency of the cavity is close to the cavity frequency. We also show a zoomed-in version of the regime in which the FSP occurs. In panel (d) we show the power spectrum $|\hat{\alpha}|^2_{\Delta\omega}N^{-1}$ of the FSP integrated over the frequencies shown in (c) in order to compensate for the frequency shift of the FSP as a function of $E_d$. The dashed lines in (a), (c) and (d) indicate the analytically determined lower bound for the FSP, see Eqs. 25 and 26. The dotted lines in (a), (c) and (d) indicate the driving field strength at which the Floquet energy spacing is equal to the cavity frequency.

For larger field strengths $E_d$, there is a second superradiant phase, the FSP, with a non-zero photon amplitude $|\alpha|$. The existence and properties of this non-equilibrium state is the central point of this paper. For weak coupling, i.e. $\lambda \ll \lambda_c$, this phase emerges at the driving field strength at which the difference of Floquet quasi-energies is resonant with the cavity mode, as we discuss later. For increasing $\lambda$, this domain broadens and gives the tongue structure in Fig. 2 (a). Within this phase, $|\alpha|$ quickly approaches a constant value for increasing coupling strength $\lambda$. The dashed line in Fig. 2 (a) indicates the asymptotic lower bound of the FSP

for increasing $\lambda$. We calculate and present the driving field strengths that bound the FSP in section 5. A natural regime of realizing the FSP is given by two requirements. On the one hand, the instantaneous eigenenergy $\epsilon_A$, which is of the order of the driving frequency $\omega_d$, needs to exceed the temperature. This derives from the ratio $\gamma_2/(\gamma_1 + \gamma_3) = \tanh(\frac{\epsilon_A}{k_B T})$. On the other hand the driving field strengths $E_d$ has to be sufficiently high to drive the system into the FSP, specifically $E_d/\omega_d^2 \approx 0.3$. For the case of graphene, see Eq. 3, for electric fields of the order of $18\mathrm{MV\,m}^{-1}$, and for temperatures of the order of 100K, this results in driving frequencies around $\omega_d \approx 2\pi \times 48\mathrm{THz}$. Note that for very large $E_d$ beyond the point at which the Floquet bands cross, there is a further very faint phase, to be discussed elsewhere.

In Fig. 2 (c) we show the magnitude of the Fourier transform $\hat{\alpha}(\omega)$ of the photonic steady state as a function of the driving field strength $E_d$ at $\lambda = \lambda_c$, indicated by the solid line in Fig. 2 (a). We see that the steady state of the cavity in the FSP oscillates with a frequency close to the cavity frequency $\omega_c$. This differs from the Dicke superradiant phase in which the steady state is not oscillatory. The frequency in the FSP is the effective Floquet energy difference of the two-level system, which is interacting non-linearly with the cavity mode, as we elaborate in the following section. This energy is equal to the cavity frequency $\omega_c$ at the driving field strength indicated by the vertical dotted lines, which is the same as the onset driving field strength at which the FSP emerges for small $\lambda$ in Fig. 2 (a). In Fig. 2 (d) we show the power spectrum of the photon mode $|\hat{\alpha}|^2_{\Delta\omega} = \int |\hat{\alpha}(\omega)|^2 d\omega$, integrated over the range of frequencies shown in Fig. 2 (c) in order to compensate for the shifting frequency of the FSP as a function of the driving field strength $E_d$. In the following section, we show that this profile of the magnitude of the order parameter is related to the depleted population inversion of the Floquet states of the two-level system.

## 4 Floquet State Population Inversion

To understand the underlying mechanism from which the FSP originates, we calculate the Floquet state population of the driven two-level system. We introduce a Schwinger representation of the two-level Hamiltonian in Eq. 4, and calculate the population in frequency space. In this representation the system is embedded into a larger system consisting of two modes $b_1$ and $b_2$. The resulting Hilbert-space is spanned by the creation operators $b_1^\dagger$ and $b_2^\dagger$ of these two modes. Note that these modes can be understood as hard-core bosons in the atomic case of the Dicke model, i.e. $b_1^2 = b_2^2 = 0$, but also as fermions in two-band models of solid-state systems, where these are the electrons, cp. [41, 45]. Our mean-field results are not affected by the specific exchange relations, bosonic or fermionic. The Pauli-matrices are written as

$$\sigma_x = b_1^\dagger b_2 + b_2^\dagger b_1, \qquad \sigma_y = i(b_1^\dagger b_2 - b_2^\dagger b_1), \qquad \sigma_z = b_1^\dagger b_1 - b_2^\dagger b_2. \qquad (16)$$

We calculate the two-point correlation functions $\langle b_j^\dagger(t_2) b_j(t_1) \rangle$ and determine the frequency resolved population of the two-level steady state as

$$n(\omega) = \frac{1}{(\tau_2 - \tau_1)^2} \int_{\tau_1}^{\tau_2} \int_{\tau_1}^{\tau_2} \sum_{j=1}^{2} \langle b_j^\dagger(t_2) b_j(t_1) \rangle \, e^{-i\omega(t_2 - t_1)} dt_2 dt_1, \qquad (17)$$

where the time $\tau_1$ is large enough for the system to have reached a steady state and $(\tau_2 - \tau_1)$ is large enough to contain hundreds of driving periods. Note that in this calculation the operators $b_j(t_1)$ and $b_j^\dagger(t_2)$ act only on one of the $N$ atoms. For large $N$, we assume that the remaining $N-1$ atoms maintain their steady state unaltered, such that the steady state $\alpha(t)$ is also not affected by either action of $b_j(t_1)$ or $b_j^\dagger(t_2)$.
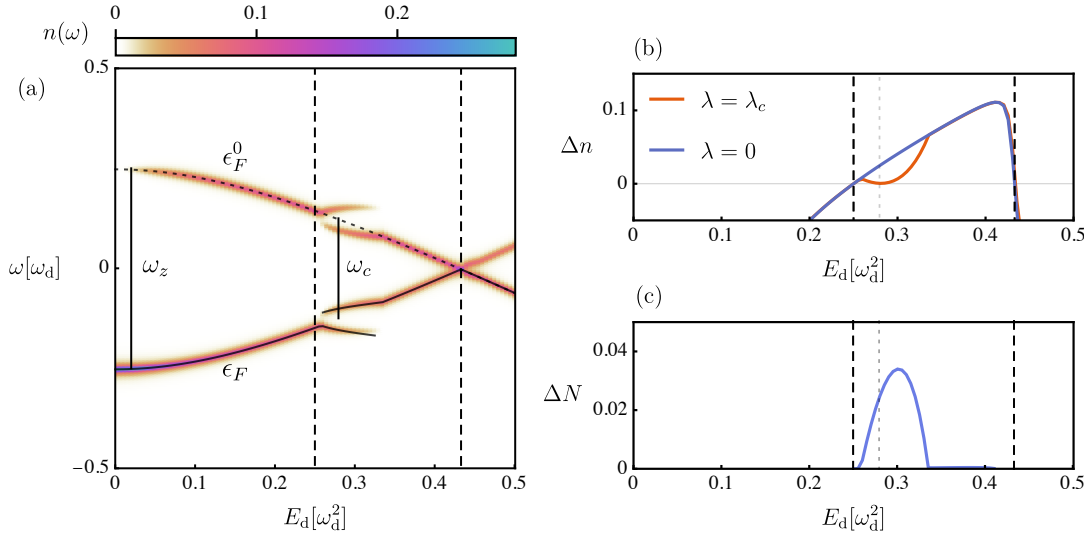
Figure 3: In panel (a) we show the Floquet state population $n(\omega)$ as a function of the driving field strength $E_d$ calculated in the Schwinger formalism. The dotted line indicates the Floquet energies $\epsilon_F^0$ for $\lambda = 0$, the solid lines indicate the approximate Floquet energies $\epsilon_F$ for $\lambda = \lambda_c$ which we obtain from Eq. 21. In panel (b) we show the effective population difference $\Delta n$ between Floquet states for $\lambda = 0$ (blue) and $\lambda = \lambda_c$ (red). The regime in which population inversion occurs also contains the FSP, which depletes the inversion. In panel (c) we show the difference $\Delta N$ between the two populations in panel (b). The dashed lines in all panels indicate the values of $E_d$ that bound the regime in which population inversion occurs, see Eqs. 25 and 26. The dotted gray lines in (b) and (c) indicate the driving field strength at which the Floquet energy difference $\Delta\epsilon_F^0$ is resonant with the cavity frequency $\omega_c$.

We show $n(\omega)$ as a function of the driving field strength $E_d$ in Fig. 3 (a) for $\lambda = \lambda_c$. We use the same values of $\omega_z = \omega_d/2$ and $\omega_c = \omega_d/4$ as for the example in Fig. 2. We see that the state of the probed two-level system is distributed across frequencies that are resonant with the Floquet energies of the system and its replicas $\pm\epsilon_F^0 + m\omega_d$, $m \in \mathbb{Z}$. For $\lambda = 0$, and $\alpha = 0$, these Floquet energies are

$$\epsilon_F^0 = \frac{\omega_d}{2} \pm \sqrt{\frac{E_d^2}{\omega_d^2} + \frac{(\omega_d - \omega_z)^2}{4}} \, . \tag{18}$$

In the regime of the FSP, the Floquet spectrum is modified due to the additional driving that the two-level system experiences from the interaction with the oscillating photonic steady state. We approximate that the FSP oscillates at $\omega_c = \omega_d/4$. The integer ratio of $\omega_d$ and $\omega_c$ is not required, it merely enables a two-frequency Floquet analysis. For this choice of frequencies the two-level Hamiltonian in Eq. 4 is

$$H(t) = e^{-i4\omega_c t} H_{-4} + e^{-i\omega_c t} H_{-1} + H_0 + e^{i\omega_c t} H_1 + e^{i4\omega_c t} H_4 \, , \tag{19}$$

with

$$H_0 = \frac{\omega_z}{2}\sigma_z \, , \qquad\qquad H_{\pm 1} = \frac{\lambda|\alpha|}{\sqrt{N}}\sigma_x \, , \qquad\qquad H_{\pm 4} = \frac{E_d}{\omega_d}\sigma_{\mp} \, . \tag{20}$$

The corresponding Floquet Hamiltonian is

$$
H_F = \begin{pmatrix}
\ldots & H_1 & & & H_4 & & \\
H_{-1} & H_0 + 2\omega_c & H_1 & & & H_4 & \\
& H_{-1} & H_0 + \omega_c & H_1 & & & H_4 \\
& & H_{-1} & H_0 & H_1 & & \\
H_{-4} & & & H_{-1} & H_0 - \omega_c & H_1 & \\
& H_{-4} & & & H_{-1} & H_0 - 2\omega_c & H_1 \\
& & H_{-4} & & & H_{-1} & \ldots
\end{pmatrix} .
\tag{21}
$$

It operates on the Floquet representation of the state

$$
|\psi\rangle\rangle = (\ldots, \psi_{\uparrow,(n-1)\omega_c}, \psi_{\downarrow,(n-1)\omega_c}, \psi_{\uparrow,n\omega_c}, \psi_{\downarrow,n\omega_c}, \ldots)^{\mathrm{T}} .
\tag{22}
$$

Inserting the numerical steady state solutions of $\alpha$ that we find using Eq. 6, and show in Fig. 2 (a), allows us to calculate the Floquet energies $\epsilon_{\mathrm{F}}$ in the FSP using the Floquet Hamiltonian $H_F$. We show these Floquet energies as a function of the driving field strength $E_{\mathrm{d}}$ in Fig. 3 (a) as gray solid lines. We see that these energies match the dominantly populated frequencies in $n(\omega)$ of the two-level system very well. Note that slight mismatches are a consequence of the approximation that the photonic steady state oscillates with the frequency $\omega_c$, which we made to justify the expression of $H_F$.

We sum up the population of all Floquet replicas to calculate the effective relative population of the two-level system as

$$
\Delta n = \sum_{m=-\infty}^{\infty} \left[ \int_{m\omega_{\mathrm{d}}}^{(m+\frac{1}{2})\omega_{\mathrm{d}}} n(\omega)\mathrm{d}\omega - \int_{(m+\frac{1}{2})\omega_{\mathrm{d}}}^{(m+1)\omega_{\mathrm{d}}} n(\omega)\mathrm{d}\omega \right] .
\tag{23}
$$

In Fig. 3 (b), we show this effective relative population $\Delta n$ of the two-level system as a function of the driving field strength $E_{\mathrm{d}}$ for the cases of $\lambda = 0$ and $\lambda = \lambda_c$. We see that there is a regime in which the system experiences an effective population inversion, bracketed by the vertical dashed lines. In the case of non-zero coupling, i.e. $\lambda = \lambda_c$, part of the population inversion is partially depleted to maintain the FSP, i.e. the non-zero steady state of the photon mode. In Fig. 2 (a), we see that the range of the FSP increases for increasing values of $\lambda$, to approach the entire regime in which population inversion occurs. In general, the FSP regime is smaller than the inversion regime, because of the detuning of the cavity frequency $\omega_c$ and the Floquet quasi-energy difference $\Delta\epsilon_F^0$.

In Fig. 3 (c), we show the depletion of the effective population inversion of the two-level system

$$
\Delta N = \Delta n|_{\lambda=0} - \Delta n|_{\lambda=\lambda_c} .
\tag{24}
$$

The behavior of $\Delta N$ agrees very well with that of the photonic steady state that we show in Fig. 2 (d) up to an overall factor. We conclude that the photonic steady state of the FSP originates from the effective population inversion of the Floquet states which is depleted to obtain a non-zero $\alpha$. This explains the constant scaling of the FSP with respect to $\lambda$. In the limit of $\lambda \to \infty$, the intensity of the photonic steady state is limited by the population inversion of the Floquet states.

## 5  Cavity-Resonant Floquet Energies

While the magnitude of the photon amplitude $\alpha$ saturates quickly to a constant value with increasing $\lambda$, here we determine the onset of the FSP for small $\lambda$. For small $\lambda$, the FSP emerges
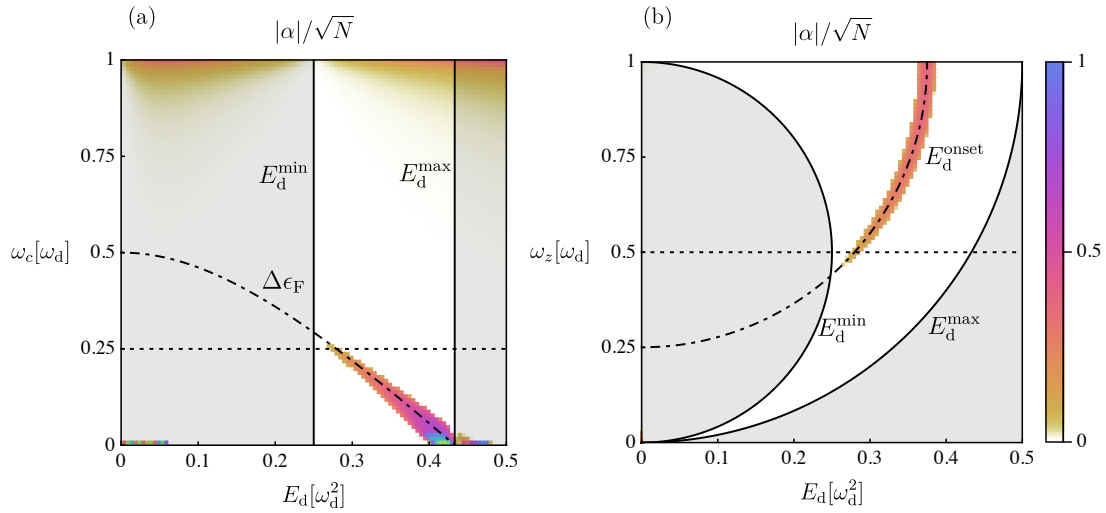
Figure 4: The magnitude of the photonic steady state $\alpha$ as a function of the driving field strength $E_d$, the cavity frequency $\omega_c$ (a) and the two-level energy spacing $\omega_z$ (b). The coupling is small with $\lambda = \omega_d/24$, such that the Floquet-assisted superradiant phase (FSP) appears only close to resonance between the cavity frequency $\omega_c$ and the Floquet energy difference $\Delta\epsilon_F^0$, indicated by dot-dashed lines at $E_d^{onset}$. The gray shaded areas are regimes in which no population inversion of Floquet states occurs. They are bounded by $E_d^{min}$ and $E_d^{max}$. The dotted lines indicate the values of $\omega_c$ and $\omega_z$ of the other subfigure, respectively.

near resonance of the Floquet energy difference $\Delta\epsilon_F^0$ and the cavity frequency $\omega_c$. We therefore present the dependence of the magnitude of $\alpha$ on the cavity frequency $\omega_c$, as well as the two-level energy spacing $\omega_z$. In Fig. 4 (a) we show the magnitude of $\alpha$ as a function of the driving field strength $E_d$ and the cavity frequency $\omega_c$ at $\omega_z = \omega_d/2$ and $\lambda = \omega_d/24$. We see that the FSP emerges near resonance of $\Delta\epsilon_F^0$ and $\omega_c$ with the lower bound of $E_d$ given by the regime of the population inversion of Floquet states. For $\omega_c \to 0$, the critical coupling $\lambda_c$ decreases to values smaller than that of $\lambda$ used here, such that we see the Dicke superradiant phase for small $E_d$. For $\omega_c \to \omega_d$ we see an expected finite population in the cavity as it becomes resonant with the driving field.

We find the analytical solutions of the driven dissipative steady state for $\lambda = 0$ (See App. A) and use them to calculate the driving field strength at which population inversion occurs ($E_d^{min}$). We also calculate the driving field strengths at which the Floquet state energies cross ($E_d^{max}$) and at which the Floquet energy difference is resonant with the cavity frequency ($E_d^{onset}$). They are

$$E_d^{min} = \frac{\omega_d^2}{2}\sqrt{\frac{1}{4} - \left(\frac{1}{2} - \frac{\omega_z}{\omega_d}\right)^2}, \tag{25}$$

$$E_d^{max} = \frac{\omega_d^2}{2}\sqrt{1 - \left(1 - \frac{\omega_z}{\omega_d}\right)^2}, \tag{26}$$

$$E_d^{onset} = \frac{\omega_d^2}{2}\sqrt{\left(1 - \frac{\omega_c}{\omega_d}\right)^2 - \left(1 - \frac{\omega_z}{\omega_d}\right)^2}. \tag{27}$$

We use the regime bound by $E_d^{min}$ and $E_d^{max}$ to estimate where Floquet state population inversion occurs and therefore the system is susceptible to the FSP. $E_d^{onset}$ indicates where the FSP

first emerges for small $\lambda$, i.e. the driving field strength at which the Floquet energy difference is resonant with the cavity frequency. In Fig. 4 (b) we show these regimes and the magnitude of $\alpha$ as a function of the driving field strength $E_d$ and the two-level spacing $\omega_z$ at $\omega_c = \omega_d/4$ and $\lambda = \omega_d/24$. We see that $E_d^{\mathrm{onset}}$ correctly predicts the initial onset of the FSP for small $\lambda$ inside the region of Floquet state population inversion.

# 6  Conclusion

We have demonstrated the emergence of a Floquet-assisted superradiant phase (FSP) in the dissipative Rabi-Dicke model that is directly related to the effective Floquet state population inversion of the two-level system. We propose to tune the Floquet energy difference close to resonance with the cavity, which results in the emergence of the FSP. In the FSP, the population inversion is depleted to populate a coherent photonic steady state that oscillates with a frequency that is close to the cavity frequency. This frequency is the Floquet energy difference of the effectively bichromatically driven two-level systems.

We have presented the frequency resolved state population of the two-level system, calculated in a Schwinger representation, and found that the depletion of the population inversion qualitatively agrees with the magnitude of the photon state. We have characterized the onset of the FSP with respect to the cavity frequency and the two-level energy spacing in the limit of small coupling strengths analytically. This analytical result for the regime that experiences population inversion agrees with the emergence of the FSP with an initial onset for resonant cavity frequency and Floquet energy difference.

We emphasize that the FSP is conceptually distinct from other recently discussed dynamical phases in comparable systems. For instance, the dynamical normal phase [21] emerges in dissipative Dicke models with parametrically driven coupling strength and is characterized by the periodic emission of pulses with opposite phase. The Floquet maser [44] presents continuous superradiance by periodically inducing spin polarization inversion in a noble gas inside a magnetic feedback circuit. This system can be expressed using an undriven Dicke-adjacent model, albeit with different coupling terms. In NV center spins in room temperature diamonds [28–30] and in cold Strontium setups [26, 27], incoherent effective driving can lead to superradiant steady states for cavities that are resonant with the atomic or vacancy center spin transitions. While all of these non-equilibrium phases are captured by models related to the Dicke model, they are all substantially different from the FSP and its underlying mechanism.

The FSP presents a laser-like mechanism using population inverted Floquet states of two-level systems that are brought into resonance with a cavity mode. The model we have proposed is in particular applicable to solid-state systems coupled to a cavity, where the identical two-level systems are replaced by a momentum-dependent two-band model. The master equation approach that we utilized is well-suited for describing such materials dissipatively. In such materials, Floquet state population inversion has been observed which provides motivation to implement this mechanism, with the prospect of creating Floquet-assisted laser systems.

# Acknowledgements

## A Analytical Steady State Solutions

We take a two-level Hamiltonian $H = \vec{H}\vec{\sigma}$, such that $\mathrm{Tr}(H) = 0$. Let $V$ be the transformation into the instantaneous eigenbasis of $H$, such that $VHV^{\dagger} = \epsilon\sigma_z$, where $\epsilon$ sets the energy scale of the Hamiltonian. In general such a Hamiltonian can be written as

$$H = \epsilon \begin{pmatrix} \cos(\theta) & e^{-i\phi}\sin(\theta) \\ e^{i\phi}\sin(\theta) & -\cos(\theta) \end{pmatrix}, \tag{A.1}$$

such that

$$V = e^{i\sigma_y \frac{\theta}{2}} e^{i\sigma_z \frac{\phi}{2}}. \tag{A.2}$$

We write the Lindblad-von Neumann master equation in the original basis of $H$, but include dissipation in the instantaneous eigenbasis, such that $L_z = V^{\dagger}\sigma_z V = H\epsilon^{-1} = h$ and $L_{\pm} = V^{\dagger}\sigma_{\pm}V$. It is

$$\dot{\rho} = i[\rho, H] + \sum_{i \in \{+,-,z\}} \gamma_i (L_i \rho L_i^{\dagger} - \frac{1}{2}\{L_i^{\dagger}L_i, \rho\}) \tag{A.3}$$

$$= i\epsilon[\rho, h] + \gamma_z(\mathrm{Tr}(h\rho)h - 2(\rho - \frac{\mathbb{1}}{2})) \tag{A.4}$$

$$+ \gamma_-(-\frac{1}{2}h - \frac{1}{2}(\rho - \frac{\mathbb{1}}{2}) - \frac{1}{4}\mathrm{Tr}(\vec{h}\vec{\rho})h) + \gamma_+(+\frac{1}{2}h - \frac{1}{2}(\rho - \frac{\mathbb{1}}{2}) - \frac{1}{4}\mathrm{Tr}(\vec{h}\vec{\rho})h), \tag{A.5}$$

with $\rho = \frac{1}{2}(\mathbb{1} + \vec{\rho}\vec{\sigma})$. We simplify this to

$$\partial_t(\vec{\rho}\vec{\sigma}) = i\epsilon[\vec{\rho}\vec{\sigma}, \vec{h}\vec{\sigma}] - \gamma_1\vec{\rho}\vec{\sigma} - \gamma_2\vec{h}\vec{\sigma} - \gamma_3(\vec{h}\vec{\rho})\vec{h}\vec{\sigma}, \tag{A.6}$$

with

$$\gamma_1 = (\gamma_- + \gamma_+)/2 + 2\gamma_z, \qquad \gamma_2 = \gamma_- - \gamma_+, \qquad \gamma_3 = (\gamma_- + \gamma_+)/2 - 2\gamma_z \tag{A.7}$$

and further

$$\dot{\vec{\rho}} = (2\epsilon(h \times \cdot) - \gamma_1 - \gamma_3\vec{h}\langle \vec{h}, \cdot\rangle)\vec{\rho} - \gamma_2\vec{h}. \tag{A.8}$$

We find the steady state solution of the dissipative Rabi model by rewriting $\vec{\rho}(t)$ with respect to the basis $\{\vec{h}, \dot{\vec{h}}, \vec{h} \times \dot{\vec{h}}\}$, such that

$$\vec{\rho}(t) = \rho_1(t)\vec{h} + \rho_2(t)\dot{\vec{h}} + \rho_3(t)(\vec{h} \times \dot{\vec{h}}), \tag{A.9}$$

$$\rho_1(t) = \vec{\rho}(t)\vec{h}, \tag{A.10}$$

$$\rho_2(t) = |\dot{\vec{h}}|^{-2}\vec{\rho}(t)\dot{\vec{h}}, \tag{A.11}$$

$$\rho_3(t) = |\dot{\vec{h}}|^{-2}\vec{\rho}(t)(\vec{h} \times \dot{\vec{h}}). \tag{A.12}$$

Assuming that $|\dot{\vec{h}}|^2$ does not depend on time, the equations of motion become

$$\dot{\rho}_1(t) = \partial_t(\vec{h}\vec{\rho}) = \dot{\vec{h}}\vec{\rho} + \vec{h}\dot{\vec{\rho}} = |\dot{\vec{h}}|^2\rho_2 - (\gamma_1 + \gamma_3)\rho_1 - \gamma_2, \tag{A.13}$$

$$\dot{\rho}_2(t) = |\dot{\vec{h}}|^{-2}\partial_t(\dot{\vec{h}}\vec{\rho}) = |\dot{\vec{h}}|^{-2}(\ddot{\vec{h}}\vec{\rho} + \dot{\vec{h}}\dot{\vec{\rho}}) = -2\epsilon(t)\rho_3 - \gamma_1\rho_2 + |\dot{\vec{h}}|^{-2}\ddot{\vec{h}}\vec{\rho}, \tag{A.14}$$

$$\dot{\rho}_3(t) = |\dot{\vec{h}}|^{-2}\partial_t((\vec{h} \times \dot{\vec{h}})\vec{\rho}) = 2\epsilon(t)\rho_2 - \gamma_1\rho_3 + |\dot{\vec{h}}|^{-2}(\vec{h} \times \ddot{\vec{h}})\vec{\rho}. \tag{A.15}$$

We expand the second derivative of the Hamiltonian vector $\vec{h}$ in this basis as well and find

$$\ddot{\vec{h}}(t) = (\ddot{\vec{h}}\vec{h})\vec{h} + (\ddot{\vec{h}}\dot{\vec{h}})\dot{\vec{h}} + (\ddot{\vec{h}}(\vec{h}\times\dot{\vec{h}}))(\vec{h}\times\dot{\vec{h}}), \tag{A.16}$$

$$\ddot{\vec{h}}(t)\vec{\rho}(t) = \rho_1(\ddot{\vec{h}}\vec{h}) + \rho_2(\ddot{\vec{h}}\dot{\vec{h}})|\dot{\vec{h}}|^2 + \rho_3(\ddot{\vec{h}}(\vec{h}\times\dot{\vec{h}}))|\dot{\vec{h}}|^2 = -\rho_1|\dot{\vec{h}}|^2 + \rho_3(\vec{h}(\dot{\vec{h}}\times\ddot{\vec{h}})), \tag{A.17}$$

$$(\vec{h}\times\ddot{\vec{h}}(t))\vec{\rho}(t) = \rho_2((\vec{h}\times\ddot{\vec{h}}(t))\dot{\vec{h}})|\dot{\vec{h}}|^2 + \rho_3((\vec{h}\times\ddot{\vec{h}}(t))(\vec{h}\times\dot{\vec{h}}))|\dot{\vec{h}}|^2 = -\rho_2(\vec{h}(\dot{\vec{h}}\times\ddot{\vec{h}})). \tag{A.18}$$

We then arrive at the equations of motion

$$\dot{\rho}_1(t) = |\dot{\vec{h}}|^2\rho_2 - (\gamma_1+\gamma_3)\rho_1 - \gamma_2, \tag{A.19}$$

$$\dot{\rho}_2(t) = -2\epsilon(t)\rho_3 - \gamma_1\rho_2 - \rho_1 + \rho_3|\dot{\vec{h}}|^{-2}\vec{h}(\dot{\vec{h}}\times\ddot{\vec{h}}), \tag{A.20}$$

$$\dot{\rho}_3(t) = 2\epsilon(t)\rho_2 - \gamma_1\rho_3 - \rho_2|\dot{\vec{h}}|^{-2}\vec{h}(\dot{\vec{h}}\times\ddot{\vec{h}}). \tag{A.21}$$

In the Rabi-problem in particular it is $\vec{H} = (\frac{E_{\rm d}}{\omega_{\rm d}}\cos(\omega_{\rm d}t), \frac{E_{\rm d}}{\omega_{\rm d}}\sin(\omega_{\rm d}t), \frac{\omega_z}{2})^{\rm T}$ and therefore

$$|\dot{\vec{h}}|^{-2}\vec{h}(\dot{\vec{h}}\times\ddot{\vec{h}}) = \frac{\omega_{\rm d}\omega_z}{2\sqrt{\frac{E_{\rm d}^2}{\omega_{\rm d}^2}+\frac{\omega_z^2}{4}}}, \qquad |\dot{\vec{h}}|^2 = \frac{E_{\rm d}^2}{\frac{E_{\rm d}^2}{\omega_{\rm d}^2}+\frac{\omega_z^2}{4}}, \qquad \epsilon(t) = \sqrt{\frac{E_{\rm d}^2}{\omega_{\rm d}^2}+\frac{\omega_z^2}{4}}, \tag{A.22}$$

which are all constant in time. We assume a periodic steady state $\rho(t) = \rho(t+\frac{2\pi}{\omega_{\rm d}})$ and express the equations of motion in terms of Fourier coefficients

$$im\omega\rho_1^m = |\dot{\vec{h}}|^2\rho_2^m - (\gamma_1+\gamma_3)\rho_1^m - \gamma_2\delta_{m,0}, \tag{A.23}$$

$$im\omega\rho_2^m = -2\epsilon\rho_3^m - \gamma_1\rho_2^m - \rho_1^m + \rho_3^m|\dot{\vec{h}}|^{-2}\vec{h}\vec{f}, \tag{A.24}$$

$$im\omega\rho_3^m = 2\epsilon\rho_2^m - \gamma_1\rho_3^m - \rho_2^m|\dot{\vec{h}}|^{-2}\vec{h}\vec{f}. \tag{A.25}$$

We find that the Fourier modes do not couple in this representation. We solve the system of equations for arbitrary $m$ and find the complete expressions for $\rho_1^m$, $\rho_2^m$ and $\rho_3^m$, fully determining the dissipative steady state

$$\rho_1 = C\gamma_1^2\omega_{\rm d}^4(4E_{\rm d}^2\omega_{\rm d}^{-2}+\omega_z^2) + C\omega_{\rm d}^4\left((4E_{\rm d}^2\omega_{\rm d}^{-2}+\omega_z^2)-\omega_{\rm d}\omega_z\right)^2, \tag{A.26}$$

$$\rho_2 = -C\gamma_1\omega_{\rm d}^4(4E_{\rm d}^2\omega_{\rm d}^{-2}+\omega_z^2), \tag{A.27}$$

$$\rho_3 = -C\omega_{\rm d}^4\left((4E_{\rm d}^2\omega_{\rm d}^{-2}+\omega_z^2)-\omega_{\rm d}\omega_z\right)\sqrt{4E_{\rm d}^2\omega_{\rm d}^{-2}+\omega_z^2}, \tag{A.28}$$

with the prefactor

$$C = \frac{-\gamma_2}{16E_{\rm d}^4\Gamma + \Gamma\omega_{\rm d}^4(\gamma_1^2+(\omega_{\rm d}-\omega_z)^2)\omega_z^2 + 4E_{\rm d}^2\omega_{\rm d}^2(\gamma_1^2\Gamma+\gamma_1\omega_{\rm d}^2+2\Gamma\omega_z(-\omega_{\rm d}+\omega_z))} \tag{A.29}$$

and $\Gamma = \gamma_1 + \gamma_3$. Expressed in the original basis, it is

$$\rho_x(t) = C_2 2E_{\rm d}\omega_{\rm d}^{-1}\left((\gamma_1^2+\omega_z^2-\omega_{\rm d}\omega_z+4E_{\rm d}^2\omega_{\rm d}^{-2})\cos(\omega_{\rm d}t) + \gamma_1E_{\rm d}\sin(\omega_{\rm d}t)\right), \tag{A.30}$$

$$\rho_y(t) = C_2 2E_{\rm d}\omega_{\rm d}^{-1}\left((\gamma_1^2+\omega_z^2-\omega_{\rm d}\omega_z+4E_{\rm d}^2\omega_{\rm d}^{-2})\sin(\omega_{\rm d}t) - \gamma_1E_{\rm d}\cos(\omega_{\rm d}t)\right), \tag{A.31}$$

$$\rho_z(t) = C_2\left((\gamma_1^2+(\omega_{\rm d}-\omega_z)^2)\omega_z - 2E_{\rm d}^2\omega_{\rm d}^{-2}(\omega_{\rm d}-\omega_z)\right), \tag{A.32}$$

with the prefactor

$$C_2 = C\sqrt{4E_{\rm d}^2+\omega_{\rm d}^2\omega_z^2}. \tag{A.33}$$

In Fig. 5, we show the comparison between numerical results and the analytical solutions, which match exactly.
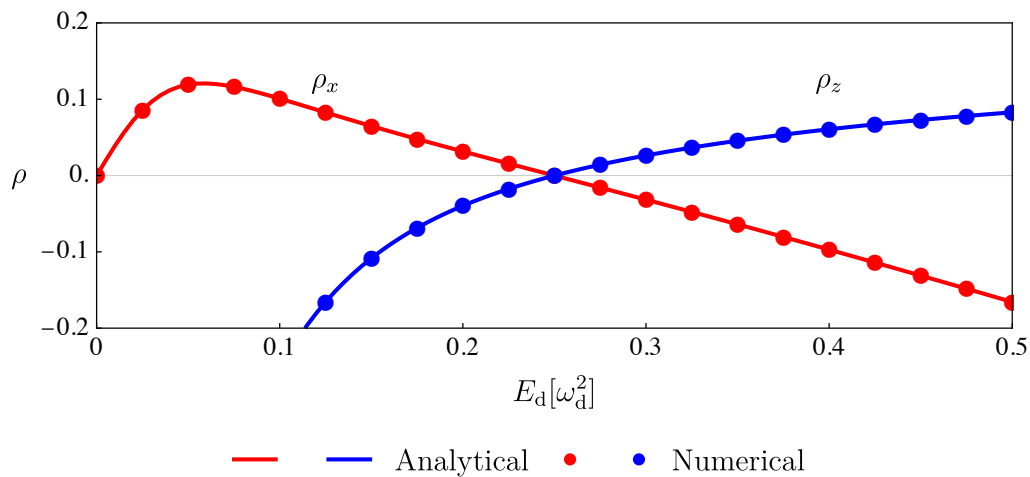
Figure 5: A comparison between the analytical (solid lines) and numerical (dots) results of the dissipative two-level steady state components $\rho_x$ and $\rho_z$ at $t = 2\pi\omega_{\mathrm{d}}^{-1}$ for $\lambda = 0$. It is $\omega_z = \omega_{\mathrm{d}}/2$. The zero-crossing of $\rho_z$ matches the onset of Floquet state population inversion in Fig. 3 (b).

# References

[1] M. O. Scully, S.-Y. Zhu and A. Gavrielides, *Degenerate quantum-beat laser: Lasing without inversion and inversion without lasing*, Phys. Rev. Lett. **62**, 2813 (1989), doi:10.1103/PhysRevLett.62.2813.

[2] J. Mompart and R. Corbalán, *Lasing without inversion*, J. Opt. B: Quantum Semiclassical Opt. **2**, R7 (2000), doi:10.1088/1464-4266/2/3/201.

[3] B. R. Mollow, *Stimulated emission and absorption near resonance for driven systems*, Phys. Rev. A **5**, 2217 (1972), doi:10.1103/PhysRevA.5.2217.

[4] J. Hauss, A. Fedorov, C. Hutter, A. Shnirman and G. Schön, *Single-qubit lasing and cooling at the Rabi frequency*, Phys. Rev. Lett. **100**, 037003 (2008), doi:10.1103/PhysRevLett.100.037003.

[5] I. Yu. Chestnov, V. A. Shahnazaryan, A. P. Alodjants and I. A. Shelykh, *Terahertz lasing in ensemble of asymmetric quantum dots*, ACS Photonics **4**, 2726 (2017), doi:10.1021/acsphotonics.7b00575.

[6] J. V. Koski et al., *Floquet spectroscopy of a strongly driven quantum dot charge qubit with a microwave resonator*, Phys. Rev. Lett. **121**, 043603 (2018), doi:10.1103/PhysRevLett.121.043603.

[7] Y. Zhang, E. Lötstedt and K. Yamanouchi, *Population inversion in a strongly driven two-level system at far-off resonance*, J. Phys. B: At. Mol. Opt. Phys. **50**, 185603 (2017), doi:10.1088/1361-6455/aa8550.

[8] T. M. Stace, A. C. Doherty and S. D. Barrett, *Population inversion of a driven two-level system in a structureless bath*, Phys. Rev. Lett. **95**, 106801 (2005), doi:10.1103/PhysRevLett.95.106801.

[9] R. H. Dicke, *Coherence in spontaneous radiation processes*, Phys. Rev. **93**, 99 (1954), doi:10.1103/PhysRev.93.99.

[10] P. Kirton, M. M. Roses, J. Keeling and E. G. Dalla Torre, *Introduction to the Dicke model: From equilibrium to nonequilibrium, and vice versa*, Adv. Quantum Technol. **2**, 1800043 (2018), doi:10.1002/qute.201800043.

[11] D. Meiser, J. Ye, D. R. Carlson and M. J. Holland, *Prospects for a Millihertz-Linewidth laser*, Phys. Rev. Lett. **102**, 163601 (2009), doi:10.1103/PhysRevLett.102.163601.

[12] J. G. Bohnet, Z. Chen, J. M. Weiner, D. Meiser, M. J. Holland and J. K. Thompson, *A steady-state superradiant laser with less than one intracavity photon*, Nature **484**, 78 (2012), doi:10.1038/nature10920.

[13] M. J. Bhaseen, J. Mayoh, B. D. Simons and J. Keeling, *Dynamics of nonequilibrium Dicke models*, Phys. Rev. A **85**, 013817 (2012), doi:10.1103/PhysRevA.85.013817.

[14] J. Klinder, H. Keßler, M. Wolke, L. Mathey and A. Hemmerich, *Dynamical phase transition in the open Dicke model*, Proc. Natl. Acad. Sci. U.S.A. **112**, 3290 (2015), doi:10.1073/pnas.1417132112.

[15] M. A. Norcia, M. N. Winchester, J. R. K. Cline and J. K. Thompson, *Superradiance on the millihertz linewidth strontium clock transition*, Sci. Adv. **2**, e1601231 (2016), doi:10.1126/sciadv.1601231.

[16] P. Kirton and J. Keeling, *Superradiant and lasing states in driven-dissipative Dicke models*, New J. Phys. **20**, 015009 (2018), doi:10.1088/1367-2630/aaa11d.

[17] T. Laske, H. Winter and A. Hemmerich, *Pulse delay time statistics in a superradiant laser with calcium atoms*, Phys. Rev. Lett. **123**, 103601 (2019), doi:10.1103/PhysRevLett.123.103601.

[18] S. B. Jäger, J. Cooper, M. J. Holland and G. Morigi, *Dynamical phase transitions to optomechanical superradiance*, Phys. Rev. Lett. **123**, 053601 (2019), doi:10.1103/PhysRevLett.123.053601.

[19] F. Damanet, A. J. Daley and J. Keeling, *Atom-only descriptions of the driven-dissipative Dicke model*, Phys. Rev. A **99**, 033845 (2019), doi:10.1103/PhysRevA.99.033845.

[20] V. M. Bastidas, C. Emary, B. Regler and T. Brandes, *Nonequilibrium quantum phase transitions in the Dicke model*, Phys. Rev. Lett. **108**, 043003 (2012), doi:10.1103/PhysRevLett.108.043003.

[21] R. Chitra and O. Zilberberg, *Dynamical many-body phases of the parametrically driven, dissipative Dicke model*, Phys. Rev. A **92**, 023815 (2015), doi:10.1103/PhysRevA.92.023815.

[22] J. G. Cosme, C. Georges, A. Hemmerich and L. Mathey, *Dynamical control of order in a cavity-BEC system*, Phys. Rev. Lett. **121**, 153001 (2018), doi:10.1103/PhysRevLett.121.153001.

[23] H. Keßler, P. Kongkhambut, C. Georges, L. Mathey, J. G. Cosme and A. Hemmerich, *Observation of a dissipative time crystal*, Phys. Rev. Lett. **127**, 043602 (2021), doi:10.1103/PhysRevLett.127.043602.

[24] J. Skulte, P. Kongkhambut, H. Keßler, A. Hemmerich, L. Mathey and J. G. Cosme, *Parametrically driven dissipative three-level Dicke model*, Phys. Rev. A **104**, 063705 (2021), doi:10.1103/PhysRevA.104.063705.

[25] P. Kongkhambut, H. Keßler, J. Skulte, L. Mathey, J. G. Cosme and A. Hemmerich, *Realization of a periodically driven open three-level Dicke model*, Phys. Rev. Lett. **127**, 253601 (2021), doi:10.1103/PhysRevLett.127.253601.

[26] M. A. Norcia and J. K. Thompson, *Cold-strontium laser in the superradiant crossover regime*, Phys. Rev. X **6**, 011025 (2016), doi:10.1103/PhysRevX.6.011025.

[27] K. Debnath, Y. Zhang and K. Mølmer, *Lasing in the superradiant crossover regime*, Phys. Rev. A **98**, 063837 (2018), doi:10.1103/PhysRevA.98.063837.

[28] C. Bradac, M. T. Johnsson, M. van Breugel, B. Q. Baragiola, R. Martin, M. L. Juan, G. K. Brennen and T. Volz, *Room-temperature spontaneous superradiance from single diamond nanocrystals*, Nat. Commun. **8**, 1205 (2017), doi:10.1038/s41467-017-01397-4.

[29] J. D. Breeze, E. Salvadori, J. Sathian, N. McN. Alford and C. W. M. Kay, *Continuous-wave room-temperature diamond maser*, Nature **555**, 493 (2018), doi:10.1038/nature25970.

[30] Q. Wu, Y. Zhang, X. Yang, S.-L. Su, C. Shan and K. Mølmer, *A superradiant maser with nitrogen-vacancy center spins*, Sci. China Phys. Mech. Astron. **65**, 217311 (2021), doi:10.1007/s11433-021-1780-6.

[31] T. Oka and H. Aoki, *Photovoltaic Hall effect in graphene*, Phys. Rev. B **79**, 081406 (2009), doi:10.1103/PhysRevB.79.081406.

[32] J. W. McIver, B. Schulte, F.-U. Stein, T. Matsuyama, G. Jotzu, G. Meier and A. Cavalleri, *Light-induced anomalous Hall effect in graphene*, Nat. Phys. **16**, 38 (2019), doi:10.1038/s41567-019-0698-y.

[33] N. Fläschner, B. S. Rem, M. Tarnowski, D. Vogel, D.-S. Lühmann, K. Sengstock and C. Weitenberg, *Experimental reconstruction of the Berry curvature in a Floquet Bloch band*, Science **352**, 1091 (2016), doi:10.1126/science.aad4568.

[34] M. Aidelsburger, M. Atala, M. Lohse, J. T. Barreiro, B. Paredes and I. Bloch, *Realization of the Hofstadter Hamiltonian with ultracold atoms in optical lattices*, Phys. Rev. Lett. **111**, 185301 (2013), doi:10.1103/PhysRevLett.111.185301.

[35] L. Lu, J. D. Joannopoulos and M. Soljačić, *Topological photonics*, Nat. Photonics **8**, 821 (2014), doi:10.1038/nphoton.2014.248.

[36] T. Oka and S. Kitamura, *Floquet engineering of quantum materials*, Annu. Rev. Condens. Matter Phys. **10**, 387 (2019), doi:10.1146/annurev-conmatphys-031218-013423.

[37] M. Bukov, L. D'Alessio and A. Polkovnikov, *Universal high-frequency behavior of periodically driven systems: From dynamical stabilization to Floquet engineering*, Adv. Phys. **64**, 139 (2015), doi:10.1080/00018732.2015.1055918.

[38] C. Weitenberg and J. Simonet, *Tailoring quantum gases by Floquet engineering*, Nat. Phys. **17**, 1342 (2021), doi:10.1038/s41567-021-01316-x.

[39] J. Stehlik, Y.-Y. Liu, C. Eichler, T. R. Hartke, X. Mi, M. J. Gullans, J. M. Taylor and J. R. Petta, *Double quantum dot Floquet gain medium*, Phys. Rev. X **6**, 041027 (2016), doi:10.1103/PhysRevX.6.041027.

[40] T. M. Stace, A. C. Doherty and D. J. Reilly, *Dynamical steady states in driven quantum systems*, Phys. Rev. Lett. **111**, 180602 (2013), doi:10.1103/PhysRevLett.111.180602.

[41] L. Broers and L. Mathey, *Observing light-induced Floquet band gaps in the longitudinal conductivity of graphene*, Commun. Phys. **4**, 248 (2021), doi:10.1038/s42005-021-00746-6.

[42] C. H. Johansen, J. Lang, A. Morales, A. Baumgärtner, T. Donner and F. Piazza, *Multimode-polariton superradiance via Floquet engineering*, SciPost Phys. **12**, 094 (2022), doi:10.21468/SciPostPhys.12.3.094.

[43] X.-W. Luo and C. Zhang, *Self-adapted Floquet dynamics of ultracold bosons in a cavity*, Phys. Rev. Lett. **120**, 263202 (2018), doi:10.1103/PhysRevLett.120.263202.

[44] M. Jiang, H. Su, Z. Wu, X. Peng and D. Budker, *Floquet maser*, Sci. Adv. **7**, eabe0719 (2021), doi:10.1126/sciadv.abe0719.

[45] M. Nuske, L. Broers, B. Schulte, G. Jotzu, S. A. Sato, A. Cavalleri, A. Rubio, J. W. McIver and L. Mathey, *Floquet dynamics in light-driven solids*, Phys. Rev. Res. **2**, 043408 (2020), doi:10.1103/PhysRevResearch.2.043408.

[46] W. S. Teixeira, F. L. Semião, J. Tuorila and M. Möttönen, *Assessment of weak-coupling approximations on a driven two-level system under dissipation*, New J. Phys. **24**, 013005 (2021), doi:10.1088/1367-2630/ac43ee.

## 3.5 Publication VI: Robustness of the Floquet-assisted superradiant phase and possible laser operation

L. Broers and L. Mathey — **arXiv:2211.01320 (Under review at Phys. Rev. A)**

This work was motivated by the results on the Floquet-assisted superradiant phase (FSP) in Publication V. The emergence of the FSP suggests the possibility of constructing a terahertz laser-source utilizing the FSP of driven graphene inside a cavity. A realistic setup, however, relies on a certain degree of robustness against realistic environmental factors that might affect the underlying mechanism. This work is a preprint, and potentially subject to changes.

I have analyzed the robustness of the FSP with respect to three different types of environmental factors. First, I have considered phase diffusion of the coherent driving field. Introducing a random walk to the phase of the driving field leads to a finite linewidth that in general broadens the responses of the driven system. I have found that across the FSP transition, the linewidth of the photon field in the cavity drastically narrows and overcomes the linewidth of the driving field, as well as the intrinsic linewidth of the cavity. Such line-narrowing is directly connected to a large temporal coherence, which is characteristic of lasing mechanisms. Second, I have considered inhomogeneous broadening in which the two-level systems are randomly detuned around a central frequency. My simulations show that the FSP is robust against this, while experiencing a reduction in efficiency. Since far-detuned systems no longer participate in the collective process of the FSP, the magnitude of the photon field is reduced while stronger coupling is necessary to compensate for this. Third, I have analyzed the effects of increasing both the coefficients of the dissipative processes of the two-level systems, and the cavity loss rate. The results suggest that the FSP is robust up to dissipation scales that are comparable to the values that we used to describe graphene in Publication I. Finally, I have found that weaker dissipation, in particular a higher finesse cavity, leads to a reduction of the critical coupling strength, meaning that the FSP appears for very weak coupling in sufficiently clean setups. I have concluded that the FSP is robust and attainable under experimentally feasible conditions. It qualifies for interpretation as a lasing mechanism, which motivates future work on driven graphene coupled to a single-mode cavity.

My contribution to this work consisted of conceiving the project, creating the numerical code, performing the numerical studies, performing the analytical calculations, analyzing and presenting the results, and writing the manuscript. All of this was done under the supervision and with the guidance of LM.

# Robustness of the Floquet-assisted superradiant phase and possible laser operation

Lukas Broers[1, 2] and Ludwig Mathey[1, 2, 3]

[1]*Center for Optical Quantum Technologies, University of Hamburg, Hamburg, Germany*
[2]*Institute for Quantum Physics, University of Hamburg, Hamburg, Germany*
[3]*The Hamburg Center for Ultrafast Imaging, Hamburg, Germany*

We demonstrate the robustness of the recently established Floquet-assisted superradiant phase of the parametrically driven dissipative Dicke model, inspired by light-induced dynamics in graphene. In particular, we show the robustness of this state against key imperfections and argue for the feasibility of utilizing it for laser operation. We consider the effect of a finite linewidth of the driving field, modelled via phase diffusion. We find that the linewidth of the light field in the cavity narrows drastically across the FSP transition, reminiscent of a line narrowing at the laser transition. We then demonstrate that the FSP is robust against inhomogeneous broadening, while displaying a reduction of light intensity. We show that the depleted population inversion of near-resonant Floquet states leads to hole burning in the inhomogeneously broadened Floquet spectra. Finally, we show that the FSP is robust against dissipation processes, with coefficients up to values that are experimentally available. We conclude that the FSP presents a robust mechanism that is capable of realistic laser operation.

## I. INTRODUCTION

In the superradiant phase transition of the Dicke model [1, 2] the ground state of a set of identical two-level systems (TLS) that are coupled to a cavity is accompanied by symmetry breaking and the emergence of a coherent photon state. Realizations of the Dicke model, and consequently the superradiant phase transition, have been proposed [3–5] and demonstrated experimentally [6–9]. The realization of the Dicke model in cavity-BEC setups leads to intricate non-equilibrium superradiant phases, which can appear in the presence of parametric driving of the coupling parameter [10–20]. Meanwhile, generalizations of the Dicke model have been studied to find rich phase diagrams that display superradiant phases, regular lasing and the unconventional counter-lasing [21–29]. These types of Dicke models are also referred to as driven, due to the tunability of the atom-photon processes [30–32].

The first studies on the superradiant phase were preceeded by studies on the closely related phenomenon of superradiance, introduced in the seminal work by Dicke [33]. Unlike the superradiant phase, superradiance is a transient process of collective coherent spontaneous emission that can be engineered into continuous operation which results in superradiant lasing with ultranarrow linewidths [34–49]. The mechanisms behind regular lasing as well as superradiant lasing rely on incoherent driving which is realized via pumping into higher levels in order to create population inversion. Superradiance has also been studied in the presence of coherent driving of the two-level systems [50–54]. This lead to studies on two-photon dressed-state lasers [55–63] in particular in quantum dot system [64–67], as a type of lasing without inversion [68–71]. Superradiance has also been studied in solid-state systems [72–75]. This relates to Floquet-engineering, which explores the possibilities of dynamically controlling properties such as band populations and topology [76–87].
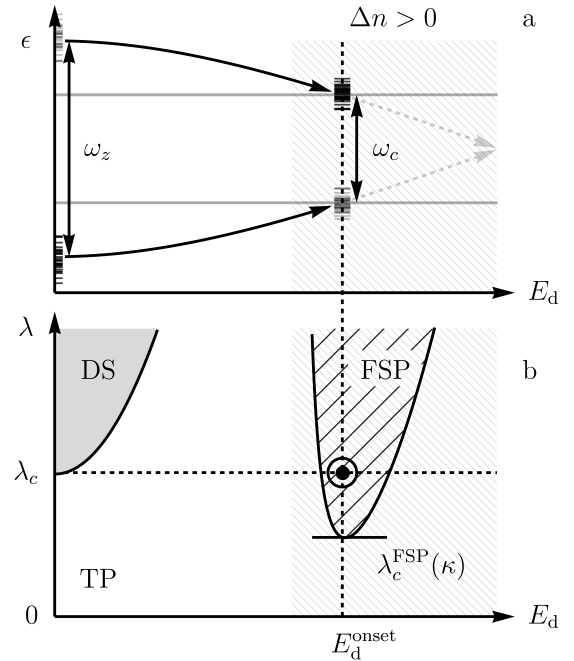


FIG. 1. **Mechanism of the Floquet-assisted superradiant phase.** (a) The bare energy levels $\omega_z$ of a collection of two-level systems are dressed via strong driving field strengths $E_d$ and deformed into Floquet states. Depending on the details of driving and dissipation, this process leads to population inversion in the Floquet states as indicated by the gray hatched areas. At Floquet energies that are resonant with the cavity frequency $\omega_c$, this population inversion is depleted and transferred into a coherent state in the cavity. (b) The phase diagram of the light field in the cavity shows the trivial phase (TP), the Dicke superradiant phase (DS) for small driving field strengths and the Floquet-assisted superradiant phase (FSP) for large driving field strengths around $E_d^{\text{onset}}$. The coupling strength $\lambda_c^{\text{FSP}}$ at which the FSP emerges depends on the cavity loss rate $\kappa$ that increases with $\kappa$.

Generally speaking, one crucial feature of both regular and unconventional lasing is the generation of monochromatic scalable coherent emission that displays line narrowing below the intrinsic linewidth. Further, practical laser operation is expected to be stable in the presence of environmental factors. Such factors include inhomogeneous broadening which in solid-state systems occurs due to material defects, while in gaseous setups it occurs due to the velocity distribution of the atoms. This leads to spectral linewidths that exceed intrinsic linewidths due to shifted energy levels that would be degenerate in the absence of inhomogeneous broadening.

In recent work we have presented the Floquet-assisted superradiant phase (FSP) [88] in a parametrically driven Dicke model in the presence of solid-like dissipation. The underlying mechanism of the FSP consists of strong coherent driving of the TLSs which leads to Floquet states with energies that deviate from the bare transitions. These Floquet states can be tuned into resonance with a cavity while they simulatenously experience effective population inversion due to the interplay of coherent driving and dissipation. This model is motivated by the demonstration of negative optical conductivities as a consequence of population inverted Floquet states in coherently driven graphene [89]. Coupling the TLSs to the cavity results in the population inversion being depleted in order to sustain the oscillating coherent state in the cavity. The mechanism of the FSP is illustrated in Fig. 1. The regime in which inversion occurs as calculated in previous work [88] is indicated with grey hatched lines.

In this paper, we demonstrate the robustness of the FSP. We introduce a phase diffusion process and hence a finite linewidth in the driving field. We show that the transition into the FSP is accompanied by significant narrowing of the linewidth of the cavity light field such that the emergence of the FSP is stable in the presence of finite phase coherence of the driving field. Further, we demonstrate that the FSP is stable in the presence of inhomogeneous broadening. Finally, we show that the FSP is robust with respect to the dissipation of the TLSs up to decay rates of the order of those in recent light-driven graphene experiments. We then identify the cavity loss rate as the most sensitive parameter, as the FSP vanishes comparatively rapidly as a function of cavity losses. Overall, our results suggest the possibility of laser operation based on the FSP in a solid-state system, such as a two-band material, due to the form of the dissipative processes, the magnitude of the dissipation that we consider, the robustness against inhomogeneous broadening, and the strong line narrowing across the transition. This type of laser operation is distinct from regular lasing and superradiant lasing, but comparable to a modified type of dressed-state lasing in solids.

This work is structured as follows. In section II we describe the master equation of the parametrically driven dissipative Dicke model. In section III we introduce phase diffusion into the driving term of the TLS which leads to a broadened linewidth, that is overcome by the drastic line narrowing of the light field in the cavity. In section IV we introduce inhomogeneous broadening into the TLSs which modifies the transition, as not all TLSs participate in the FSP. In section V we show the FSP transition as a function of the cavity loss rate as well as the TLS dissipation rates to show the robustness of the FSP. In section VI we conclude our results and present an outlook for possible implementations of the FSP.

## II. PARAMETRICALLY DRIVEN DICKE MODEL

We consider a dissipative Dicke model that is parametrically driven with circularly polarized light. The Hamiltonian of this system is

$$\frac{1}{\hbar}H = \sum_{j=1}^{N} \frac{\omega_z^j}{2}\sigma_z^j + \sigma_+^j A_-(t) + \sigma_-^j A_+(t)$$
$$+ \omega_c a^\dagger a + \frac{\lambda}{\sqrt{N}}\sum_{j=1}^{N}\sigma_x^j(a + a^\dagger) \qquad (1)$$

with the driving field

$$A_\pm(t) = \frac{E_d}{\omega_d}\exp\{\pm i\omega_d t\}. \qquad (2)$$

$\omega_d$ is the driving frequency and $E_d$ is the effective driving strength that takes the dimension of frequency squared. $E_d$ can be related to electric field strengths of driving terms in other systems that motivate the general form of this Hamiltonian. $\omega_c$ is the cavity frequency. The frequencies $\omega_z^j$ are frequencies of the TLSs. We first choose these to be equal, i.e. $\omega_z^j = \omega_z$, and later consider a distribution of frequencies $\omega_z^j$, to model inhomogeneous broadening. $\sigma_k^j$ is the $k$th Pauli-matrix acting on the $j$th TLS, where $\sigma_\pm^j = (\sigma_x^j \pm i\sigma_y^j)/2$. $a^{(\dagger)}$ is the annihilation (creation) operator of the photon mode in the cavity. $\lambda$ is the coupling strength between the TLSs and the cavity. We consider a mean-field ansatz which separates the model into the two sub-Hamiltonians

$$\frac{1}{\hbar}H^j = \frac{\omega_z^j}{2}\sigma_z^j + \sigma_+^j A_-(t) + \sigma_-^j A_+(t) + \frac{\lambda}{\sqrt{N}}\langle a + a^\dagger\rangle\sigma_x^j$$
$$(3)$$

$$\frac{1}{\hbar}H_c = \omega_c a^\dagger a + \frac{\lambda}{\sqrt{N}}\sum_{j=1}^{N}\langle\sigma_x^j\rangle(a + a^\dagger). \qquad (4)$$

Here $\langle\sigma_x^j\rangle$ and $\langle a + a^\dagger\rangle$ are the expectation values of the respective operators. The dynamics generated by Eq. 4 are solved by a coherent state characterised by $\alpha = \langle a\rangle$ which acts as the order-paramater of superradiant phases. The dynamics of $\alpha$ are governed by the equation of motion

$$\dot{\alpha} = -(i\omega_c + \kappa)\alpha - i\frac{\lambda}{\sqrt{N}}\sum_{j=1}^{N}\langle\sigma_x^j\rangle, \qquad (5)$$

where $\kappa$ is the cavity loss rate. Additionally, we express the dynamics of the $j$th TLS via the Lindblad master equation which we write as

$$\dot{\rho}^j = i[\rho^j, H^j] + \sum_l \gamma_l^j (L_l^j \rho^j L_l^{j,\dagger} - \frac{1}{2}\{L_l^{j,\dagger} L_l^j, \rho^j\}). \quad (6)$$

The Lindblad operators $L_l^j = \sigma_+^j, \sigma_-^j, \sigma_z^j$ are weighted by the dissipation coefficients $\gamma_l^j$ with $l \in \{+, -, z\}$ and act in the instantaneous eigenbasis of the $j$th TLS analogously to the method applied in previous works [88–91]. The coefficients $\gamma_-^j$ and $\gamma_+^j$ describe spontaneous decay and excitation, respectively. The coefficients $\gamma_z^j = \gamma_z$ describe dephasing. This choice of dissipation has been shown to describe the dynamics in light-driven two-band solids [90]. Note that the temperature $T$ is encoded in the ratio of

$$\frac{\gamma_-^j - \gamma_+^j}{\gamma_-^j + \gamma_+^j} = \tanh\left(\frac{\epsilon^j}{k_B T}\right), \quad (7)$$

where the instantaneous eigenenergy scale $\epsilon^j$ of $H^j$ is roughly of the order of the $j$th TLS level spacing $\omega_z^j$. Note that this suggests an ideal range of operation for the FSP. In terms of experimental feasibility it is desirable to keep $E_d$ small but $\frac{\epsilon^j}{k_B T}$ large. This compromise is met up to room temperature for characteristic frequencies of the order of tens to hundreds of terahertz, which is in agreement with the motivational work on light-driven graphene [92]. As an example throughout this work, we use $\omega_d = 2\pi \times 48\text{THz}$ and $\omega_z = 2\pi \times 24\text{THz}$ such that at room temperature $\tanh(\frac{\epsilon^j}{k_B T}) \approx 1$. Therefore, we take $\gamma_+^j \approx 0$.

We further use $\omega_c = 2\pi \times 12\text{THz}$, $\gamma_-^j + \gamma_+^j = \gamma_- + \gamma_+ = 2\text{THz}$, $\gamma_z = 4\text{THz}$, $\kappa = 2\pi \times 120\text{MHz}$ and $\lambda_c = \sqrt{\omega_c \omega_z}/2 \approx 2\pi \times 8.5\text{THz}$, where $\lambda_c$ is the critical coupling strength of the standard Dicke model. The critical coupling $\lambda_c$ does not directly relate to the FSP, but it gives a readily comparable scale of the system parameters. Unless stated otherwise, we take the driving field strength to be adjusted to the onset value of the FSP. This means that the Floquet energies of the driven TLSs are resonant with the cavity frequency $\omega_c$, such that

$$E_d = \frac{\omega_d^2}{2}\sqrt{\left(1 - \frac{\omega_c}{\omega_d}\right)^2 - \left(1 - \frac{\omega_z}{\omega_d}\right)^2}, \quad (8)$$

as we have discussed in previous work [88]. In our example, with $\omega_c/\omega_d = 1/4$ and $\omega_z/\omega_d = 1/2$, this amounts to

$$E_d^{\text{onset}} = \frac{\sqrt{5}}{8}\omega_d^2. \quad (9)$$

The vertical line in Fig. 1 indicates the onset driving field strength.
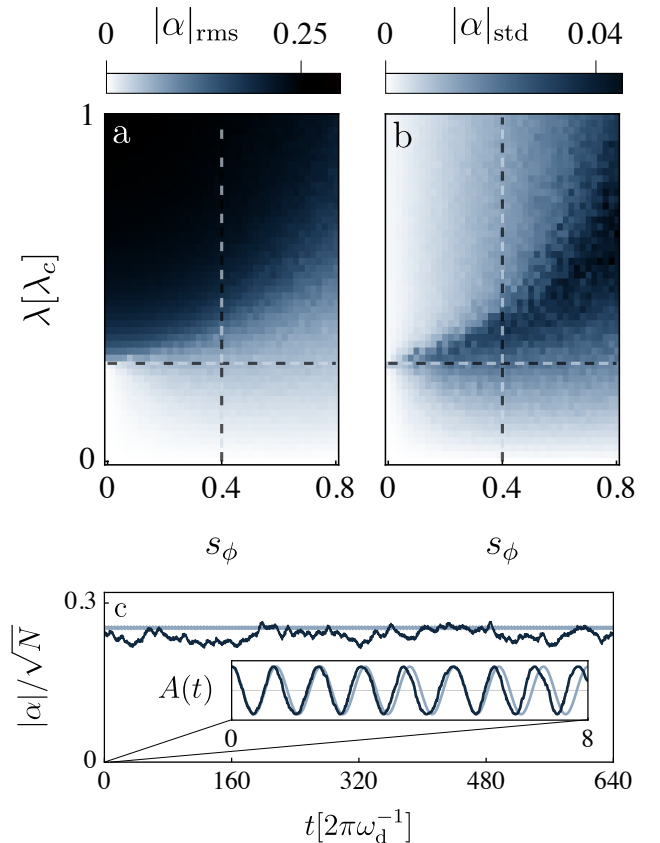


FIG. 2. **Light field fluctuations across the FSP transition.** Panels (a) and (b) show the root-mean-square and the standard deviation of the light field amplitude across the FSP transition as a function of the phase diffusion standard deviation $s_\phi$. The horizontal line indicates the coupling strength at which the FSP transition occurs in the absence of phase diffusion, i.e. $s_\phi = 0$. Panel (c) shows the amplitude of a single-trajectory of the light field for $s_\phi = 0$ (blue) and $s_\phi = 0.4$ (black), as well as an inset of the driving field for the same values of $s_\phi$.

## III. PHASE DIFFUSION

As a first metric for robustness, we consider the influence of a finite linewidth of the driving field on the linewidth of the cavity light field in the FSP. For this purpose we introduce a Gaussian random walk $\phi(t)$ that models phase diffusion in the driving field [93], rather than the monochromatic driving field described in Eq. 2. The standard deviation of $\phi(t)$ after one driving period $2\pi\omega_d^{-1}$ is given by $s_\phi$. This corresponds to a linewidth of $\Delta\omega = \omega_d \frac{s_\phi}{2\pi}$ in the driving field which we now write as

$$A_\pm(t) = \frac{E_d}{\omega_d} \exp\{\pm i(\omega_d t + \phi(t))\}. \quad (10)$$

In Fig. 2 (a), we show the root-mean-square of the light field amplitude $|\alpha|_{\text{rms}}$ across the FSP transition at the onset value of $E_d = E_d^{\text{onset}}$, see Eq. 9, as a function of $\lambda$ and
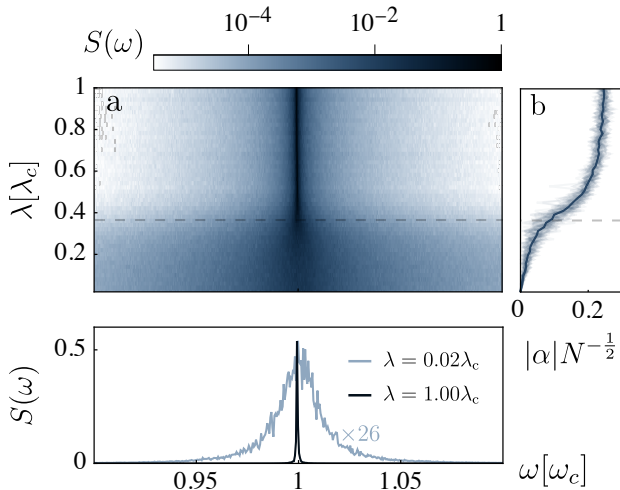
FIG. 3. **Linewidth narrowing in the FSP.** Panel (a) shows the power spectrum averaged over 50 phase diffusion trajectories as a function of the coupling strength $\lambda$ for $s_\phi = 0.4$ on a logarithmic scale. Across the FSP transition indicated by the dashed line, the linewidth of the light field in the cavity narrows drastically. Panel (b) shows the light field amplitude across the FSP transition for the individual trajectories in light colors and their mean in solid dark blue. Panel (c) shows the power spectra for $\lambda = 0.02\lambda_c$, rescaled by a factor of 26 for comparison, and $\lambda = \lambda_c$.

$s_\phi$. We see that the FSP transition is stable against the fluctuations of the driving field, i.e. as a function of $s_\phi$, however the FSP regime is shifted towards larger values of $\lambda$, and the transition regime displays stronger fluctuations. Since the phase diffusion broadens the linewidth of the driving field, the TLSs develop amplitude at many frequencies including the cavity frequency $\omega_c$ which leads to residual occupations in the cavity that contribute to the broadened FSP transition.

In Fig. 2 (b), we show the standard deviation $|\alpha|_{\text{std}}$ of the light field amplitude as a function of $\lambda$ and $s_\phi$. Close to the FSP transition, the amplitude that we show in Fig. 2 (a) displays large fluctuations, that are suppressed both in the FSP and the trivial phase. With increasing phase diffusion, the steady state in the FSP shows an increasing standard deviation and the sharp feature in $|\alpha|_{\text{std}}$ across the transition broadens. For intermediate values of $s_\phi$, the increased standard deviation indicates the shifted location of the FSP transition.

In Fig. 2 (c), we show the amplitude of the light field in the FSP at $\lambda = \lambda_c$ for $s_\phi = 0$ and $s_\phi = 0.4$ on long time scales. The case of $s_\phi = 0.4$ corresponds to a significantly broadened driving field and hence the amplitude of the light field in the FSP jitters considerably. This case corresponds to the vertical dashed lines in Figs. 2 (a) and (b). The inset shows the effect of the phase diffusion on the driving field.

Next we present the line narrowing of the light field across the FSP transition in the presence of phase diffu-

sion. For this purpose we consider the power spectrum

$$S(\omega) = \frac{|\hat{\alpha}(\omega)|^2}{\int_{\mathbb{R}} |\hat{\alpha}(\omega)|^2 d\omega}, \tag{11}$$

where $\hat{\alpha}(\omega)$ is the Fourier transform of $\alpha(t)$.

In Fig. 3 (a) we show $S(\omega)$ at the onset driving field strength with $s_\phi = 0.4$ and averaged over 50 phase diffusion trajectories. Prior to the FSP transition that occurs at approximately $\lambda = 0.37\lambda_c$, there is a broadened signal at the cavity frequency with a linewidth that is given by the cavity loss rate $\kappa$. Across the transition, the linewidth narrows drastically as the occupation of the cavity mode increases. We show the corresponding light field amplitude $|\alpha|$ in Fig. 3 (b) as a transposed plot for the same set of sampled phase diffusion trajectories in light colors, and their mean as a dark solid line.

In Fig. 3 (c) we show the power spectrum $S(\omega)$ prior to ($\lambda = 0.02\lambda_c$) and past ($\lambda = \lambda_c$) the FSP transition, rescaled for comparison. The line narrowing is clearly visible as the full-width half-maximum reduces drastically. The narrowing of the linewidth past the transition corresponds to the coherence times increasing beyond those of the driving field and those given intrinsically by the cavity. This is a hallmark of lasing states.

## IV. INHOMOGENEOUS BROADENING

As a second metric for robustness we consider the consequences of inhomogeneous broadening on the FSP transition. In order to include inhomogeneous broadening, we consider a distribution of detuned two-level spacings $\omega_z^j$ that have the average frequency $\omega_z$. In this model the index of the TLSs is arbitrary, so we label them by their energy for convenience. The relevant quantity for broadening effects is the mode density of the TLSs. We consider $N = 100$ TLSs with normal distributed energy detuning around $\omega_z$ with a relative standard deviation of $s_\omega$. For this purpose, we set the $j$th energy level to

$$\omega_z^j = \omega_z \left( 1 + s_\omega \text{erf}^{-1} \left[ \frac{2j}{N+1} - 1 \right] \right), \tag{12}$$

where $\text{erf}^{-1}$ is the inverse error function, such that the energy levels are evenly distributed as desired without random sampling.

In Fig. 4, we show the amplitude of the light field across the FSP transition as a function of the inhomogeneous broadening standard deviation $s_\omega$. We find that the transition remains sharp for increasing $s_\omega$. However, the value of $\lambda$ at which the FSP transition occurs increases with $s_\omega$ while the amplitude $|\alpha|$ of the light field decreases. This is a consequence of a subset of TLSs not contributing to the FSP due to being far detuned from the cavity frequency. To compensate for this lack of contributing TLSs, the coupling strength needs to increase in order to enter the FSP. If the detuning due to inhomogeneous broadening is larger than the intrinsic linewidth
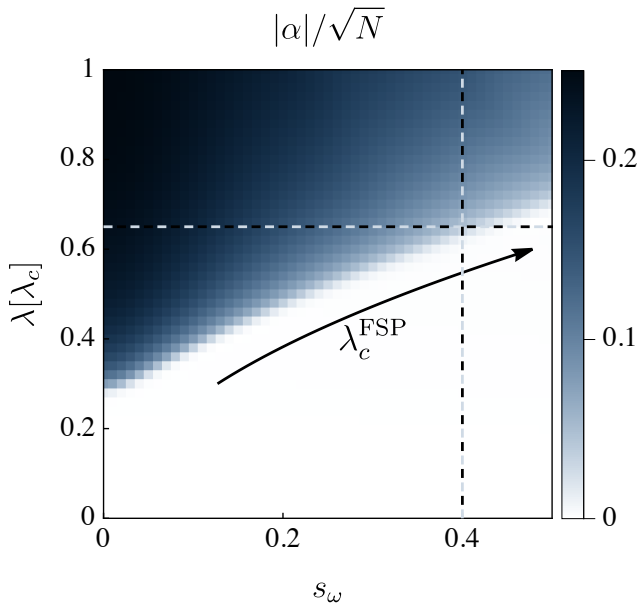
FIG. 4. **Effect of inhomogeneous broadening on the FSP transition.** The FSP transition at the onset driving field strength as a function of the coupling strength $\lambda$ and the inhomogeneous broadening parameter $s_\omega$. The vertical dashed line corresponds to the case that we show in Fig. 5.

of a given TLS, it is not affected by the effective driving that is present due to the interaction with the cavity which contains a non-zero light field.

In order to gain insight into the Floquet states of the system as well as their occupation, we consider the TLSs embedded in a larger space spanned by the creation (annihilation) operators $b_{1,2}^{j,(\dagger)}$. They are connected to the Pauli matrices via

$$\sigma_x^j = b_2^{j,\dagger} b_1^j + b_1^{j,\dagger} b_2^j \tag{13}$$

$$\sigma_y^j = i(b_2^{j,\dagger} b_1^j - b_1^{j,\dagger} b_2^j) \tag{14}$$

$$\sigma_z^j = b_2^{j,\dagger} b_2^j - b_1^{j,\dagger} b_1^j. \tag{15}$$

We note that the operators $b_{1,2}$ can be either fermionic operators or hardcore bosons. While we introduce them as auxiliary operators in this work, a natural platform to implement the dynamical state that we put forth here, is in a two-band material. In that implementation, the electron operators of the two bands coincide with the Schwinger operators that we use here. In this Schwinger representation, individual two-time correlation functions $\langle b_n^{j,\dagger}(t_2) b_n^j(t_1) \rangle$ are accessible, rather than propagators of particle conserving operators Eq. 14–16. We can calculate the steady state distribution [94]

$$n_j(\omega) = \frac{1}{(t_b - t_a)^2} \int_{t_a}^{t_b} \int_{t_a}^{t_b} \mathcal{G}^j(t_2, t_1) e^{i\omega(t_2 - t_1)} dt_2 dt_1 \tag{16}$$

for each of the $N$ TLSs with the correlation function

$$\mathcal{G}^j(t_2, t_1) = \sum_{n=1}^{2} \langle b_n^{j,\dagger}(t_2) b_n^j(t_1) \rangle . \tag{17}$$

Here $t_a$ is a time that is large enough for the system to have formed a steady state and $t_b - t_a$ is an interval that is large enough to ensure sufficient frequency resolution. The distribution $n_j(\omega)$ reveals the energies and occupation of the Floquet states of the $j$th TLS. Collecting the steady state distributions of all $N$ TLSs gives the collective distribution of the entirety of TLSs

$$n(\omega) = N^{-1} \sum_{j=1}^{N} n_j(\omega), \tag{18}$$

which displays the frequency resolved distribution of the ensemble of TLSs, rather than that of individual TLSs. Taking the difference of the collective distribution across opposite frequencies gives the relative collective distribution

$$\Delta n(\omega) = n(\omega) - n(-\omega). \tag{19}$$

$\Delta n(\omega)$ displays the frequency resolved imbalance of the ensemble and reveals the effective population inversion of the entire system and how it is depleted in the FSP.

In Figs. 5 (a) through (c), we show the steady state distributions $n_j(\omega)$ for $s_\omega = 0.4$ and different combinations of $E_d$ and $\lambda$. The horizontal lines indicate the centered two-level spacing $\omega_z$ and the cavity frequency $\omega_c$. The solid line indicates the centered spacing of the Floquet levels that for the $j$th TLS have the energy

$$\epsilon_F^j = \pm \left( \frac{\omega_d}{2} - \sqrt{\frac{E_d^2}{\omega_d^2} + \frac{(\omega_d - \omega_z^j)^2}{4}} \right). \tag{20}$$

In Fig. 5 (a), we show the case of $E_d = 0$ and $\lambda = 0$. In this equilibrium state the lower levels are all fully populated with energies given by Eq. 12. In Fig. 5 (b), we show the case of $E_d = E_d^{\text{onset}}$ and $\lambda = 0$. As expected, the states are dominantly distributed around the Floquet energies given by Eq. 20. At this driving field strength the Floquet states are population inverted. In Fig. 5 (c), we show the case $E_d = E_d^{\text{onset}}$ and $\lambda = \lambda_c$. This case is inside the FSP and the Floquet states that are close to resonant with the cavity frequency are modified due to the presence of the finite photon field in the cavity. Hence, a gap opens and the populations of the Floquet states are modified.

In Fig. 5 (d), we show the relative collective distribution $\Delta n(\omega)$ for $s_\omega = 0.4$, $E_d = E_d^{\text{onset}}$ and for both $\lambda = 0$ (dark blue filling) and $\lambda = \lambda_c$ (black line, white filling), which correspond to Figs. 5 (b) and (c), respectively. We see that inside the FSP and close to the cavity resonance, the Floquet states are not only modified by a gap opening, but the effective population inversion is
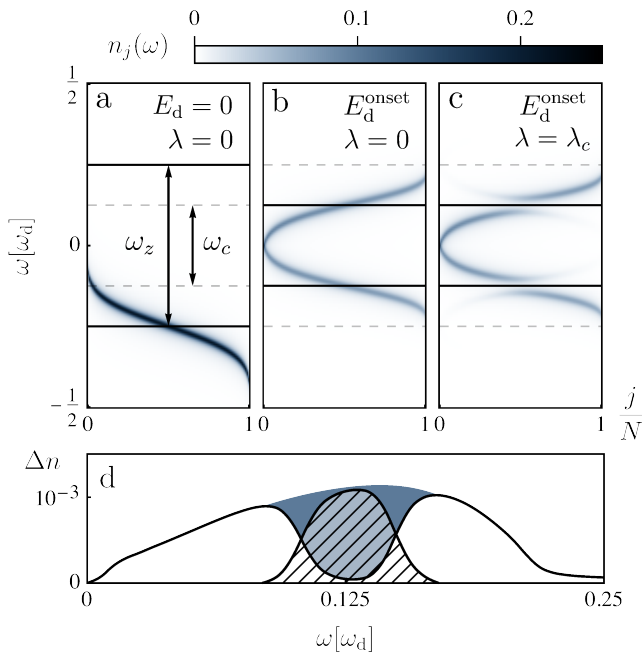
FIG. 5. **Two-level steady state distributions in the presence of inhomogeneous broadening.** Panels (a) through (c) show the steady state distributions $n_j(\omega)$ for $N = 100$ TLSs at $E_d = 0$ (a) and $E_d = E_d^{\mathrm{onset}}$ (b, c) as well as $\lambda = 0$ (a, b) and $\lambda = \lambda_c$ (c). The distributions are concentrated at the Floquet energies of the broadened energy levels. The horizontal lines show the average level spacing $\omega_z$ and the cavity frequency $\omega_c$. Panel (d) shows the relative collective distribution $\Delta n(\omega)$ for $\lambda = \lambda_c$ (black line, white filling) and $\lambda = 0$ (dark blue filling) the difference between the two (hatched filling) is the effective population inversion of Floquet states that is depleted to sustain the FSP.

largely depleted. The inhomogeneous broadening leads to off-resonant TLSs that are unaffected and do not contribute to the FSP mechanism. This type of hole-burning is responsible for the reduced light field amplitude as a function of $s_\omega$ in Fig. 4.

## V. TWO-LEVEL AND CAVITY LOSSES

As a third metric for robustness, we show the effect of the TLS dissipation rates and the cavity loss rate on the FSP. In Fig. 6 we show the magnitude of the light field in the cavity as a function of the effective driving field strength $E_d$ and the coupling strength $\lambda$, as well as the dissipation coefficients. The quantity we show is the intensity per TLS of the light field $|\alpha|^2 N^{-1}$ multiplied with the cavity loss rate $\kappa$. This serves the purpose of quantifying the coherent output of the system rather than the photon count inside the cavity.

In Fig. 6 (a) and (b) we show the effect of the TLS dissipation coefficients. We choose the example $\gamma = \gamma_z = 2(\gamma_- + \gamma_+)$, i.e. we keep the ratio of $\gamma_- + \gamma_+$ and $\gamma_z$
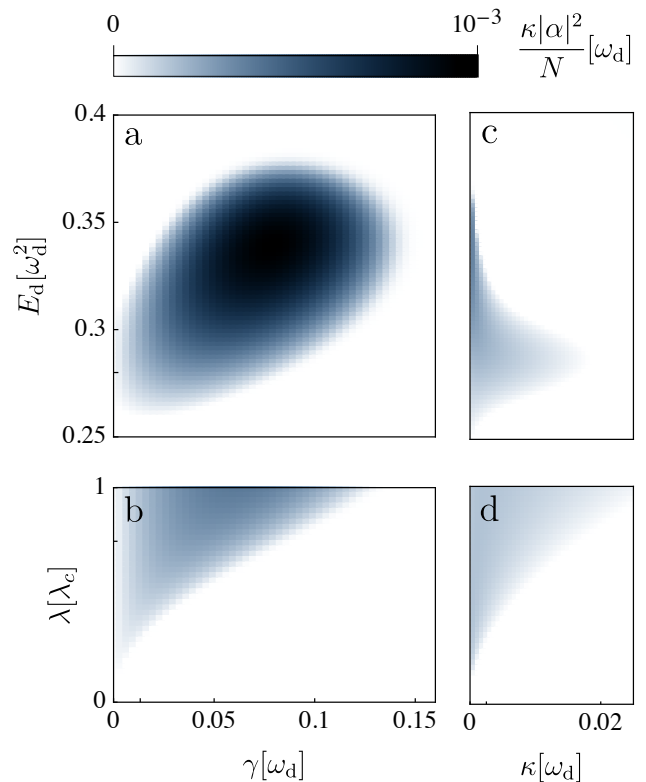


FIG. 6. **Effects of strong dissipation on the FSP.** The output intensity of the light field per TLS $\kappa|\alpha|^2/N$ as functions of combinations of $E_d$, $\lambda$, $\kappa$ and $\gamma$. In panel (a), we show the output intensity per TLS as a function of $\gamma$ and $E_d$ for $\lambda = 0.75\lambda_c$ and $\kappa = \omega_d/400$. In panel (b), we show the output intensity per TLS as a function of $\gamma$ and $\lambda$ for $E_d = E_d^{\mathrm{onset}}$ and $\kappa = \omega_d/400$. In panel (c), we show the output intensity per TLS as a function of $\kappa$ and $E_d$ for $\lambda = 0.75\lambda_c$ and $\gamma = \omega_d/24\pi$. In panel (d), we show the output intensity per TLS as a function of $\kappa$ and $\lambda$ for $E_d = E_d^{\mathrm{onset}}$ and $\gamma = \omega_d/24\pi$.

constant for convenience. We see that the FSP transition is robust for increasing values up to $\gamma \lesssim 0.15\omega_d$ for $\lambda = 0.75\lambda_c$. In our example, that is inspired by light-driven graphene, this corresponds to $\gamma \approx 45\text{THz}$ compared to the characteristic energies of the Hamiltonian of the order of $\omega_d = 2\pi \times 48\text{THz}$. This demonstrates a robustness to dissipation up to rates which are comparable to the coefficients used to describe experimental setups of driven graphene [92, 95–99]. This further supports the viability of graphene as a potential platform for hosting the FSP.

In Fig. 6 (c) and (d) we show the effect of the cavity loss rate $\kappa$ on the FSP. We find a small range of available values for $\kappa$ at which the FSP emerges and further the threshold at which the FSP becomes unsustainable is comparatively small at values of $\kappa \lesssim 0.02\omega_d$ for $\lambda = 0.75\lambda_c$. In our example this corresponds to $\kappa \approx 5\text{THz}$. This demonstrates the sensitivity of the FSP with respect to cavity losses, which we identify as the most sensitive parameter.

For the purpose of realizing the FSP, for driving field strengths close to $E_{\mathrm{d}}^{\mathrm{onset}}$ the FSP will occur for large values of $\kappa$, if $\lambda$ is sufficiently large. Similarly, the given magnitude of $\lambda$ provides an upper limit on $\kappa$ to achieve the realization of the FSP. We note that the FSP can be realized for arbitrarily small values of $\lambda$, given sufficiently small $\kappa$. Therefore, for a given platform, a high-finesse cavity might enable the realization. We note, however, that the optimal output intensity is achieved for intermediate magnitudes of both $\kappa$ and $\lambda$. Stronger dissipation results in a larger inversion of the TLSs, and therefore in a higher output intensity. So for the optimal operation of FSP, intermediate values of the dissipation rates are desirable.

## VI. CONCLUSION

We have demonstrated the robustness of the Floquet-assisted superradiant phase (FSP) in the parametrically driven Dicke model with a dissipative model, that is designed for the electron dynamics in a solid. The photonic steady state in the FSP is robust against inhomogeneous broadening, reasonably strong dissipative processes of the two-level systems and phase diffusion in the driving field. Across the FSP transition, the linewidth of the light field narrows drastically and overcomes the linewidth of the driving field as well as the intrinsic linewidth of the cavity that is given by its loss rate, which is a hallmark of laser mechanisms.

In our model the dissipation is performed in the instantaneous eigenbasis. This choice is motivated by the capabilities of capturing dynamics of two-band solids, as has been demonstrated in previous work [90]. The dependence of the FSP on the ratio of characteristic frequencies and temperature, as well as the driving field strength in units of the driving frequency squared suggests the most promising range of driving frequencies to be of the order of tens to hundreds of terahertz. This energy scale also coincides with the situation in two-band solids such as light-driven graphene [89, 90, 92]. The values of the dissipation coefficients up to which we find the FSP to be stable also agrees with realistic estimates of coherence times in available graphene samples [92, 95–99].

We conclude from the robustness and the small values of the critical coupling of the FSP that it can be utilized for laser operation. The FSP is in principle accessible in two-band solids such as light-driven graphene under realistic conditions. The details of the collective effect of solid-state dispersion relations on the emergence of the FSP will be the subject of future research. Such a demonstration would then constitute a Floquet-assisted solid-state laser system in the terahertz frequency domain. As such, we propose to expand the range of dressed-state laser mechanisms into the domain of Floquet-engineered electron bands in solids, that is accessible with current pump-probe technology.

### ACKNOWLEDGEMENTS

[1] K. Hepp and E. H. Lieb, Phys. Rev. A **8**, 2517 (1973).

[2] Y. K. Wang and F. T. Hioe, Phys. Rev. A **7**, 831 (1973).

[3] P. Domokos and H. Ritsch, Phys. Rev. Lett. **89**, 253003 (2002).

[4] F. Dimer, B. Estienne, A. S. Parkins, and H. J. Carmichael, Phys. Rev. A **75**, 013804 (2007).

[5] D. Nagy, G. Kónya, G. Szirmai, and P. Domokos, Phys. Rev. Lett. **104**, 130401 (2010).

[6] A. T. Black, H. W. Chan, and V. Vuletić, Phys. Rev. Lett. **91**, 203001 (2003).

[7] Z. Zhiqiang, C. H. Lee, R. Kumar, K. J. Arnold, S. J. Masson, A. S. Parkins, and M. D. Barrett, Optica **4**, 424 (2017).

[8] K. Baumann, C. Guerlin, F. Brennecke, and T. Esslinger, Nature **464**, 1301 (2010).

[9] J. Klinder, H. Keßler, M. Wolke, L. Mathey, and A. Hemmerich, Proceedings of the National Academy of Sciences **112**, 3290 (2015), https://www.pnas.org/content/112/11/3290.full.pdf.

[10] V. M. Bastidas, C. Emary, B. Regler, and T. Brandes, Phys. Rev. Lett. **108**, 043003 (2012).

[11] R. Chitra and O. Zilberberg, Phys. Rev. A **92**, 023815 (2015).

[12] Z. Gong, R. Hamazaki, and M. Ueda, Phys. Rev. Lett. **120**, 040404 (2018).

[13] J. G. Cosme, C. Georges, A. Hemmerich, and L. Mathey, Phys. Rev. Lett. **121**, 153001 (2018).

[14] B. Zhu, J. Marino, N. Y. Yao, M. D. Lukin, and E. A. Demler, New Journal of Physics **21**, 073028 (2019).

[15] H. Keßler, P. Kongkhambut, C. Georges, L. Mathey, J. G. Cosme, and A. Hemmerich, Phys. Rev. Lett. **127**, 043602 (2021).

[16] R. J. L. Tuquero, J. Skulte, L. Mathey, and J. G. Cosme, Phys. Rev. A **105**, 043311 (2022).

[17] J. G. Cosme, J. Skulte, and L. Mathey, Phys. Rev. A **100**, 053615 (2019).

[18] J. Skulte, P. Kongkhambut, H. Keßler, A. Hemmerich, L. Mathey, and J. G. Cosme, Phys. Rev. A **104**, 063705 (2021).

[19] P. Kongkhambut, H. Keßler, J. Skulte, L. Mathey, J. G. Cosme, and A. Hemmerich, Phys. Rev. Lett. **127**, 253601 (2021).

[20] J. Skulte, P. Kongkhambut, S. Rao, L. Mathey, H. Keßler, A. Hemmerich, and J. G. Cosme, "Condensate formation in a dark state of a driven atom-cavity system," (2022).

[21] F. T. Hioe, Phys. Rev. A **8**, 1440 (1973).

[22] J. Keeling, M. J. Bhaseen, and B. D. Simons, Phys. Rev. Lett. **105**, 043001 (2010).

[23] M. J. Bhaseen, J. Mayoh, B. D. Simons, and J. Keeling, Phys. Rev. A **85**, 013817 (2012).

[24] A. Baksic and C. Ciuti, Phys. Rev. Lett. **112**, 173601 (2014).

[25] S. Genway, W. Li, C. Ates, B. P. Lanyon, and I. Lesanovsky, Phys. Rev. Lett. **112**, 023603 (2014).

[26] M. Soriente, T. Donner, R. Chitra, and O. Zilberberg, Phys. Rev. Lett. **120**, 183603 (2018).

[27] R. Gutiérrez-Jáuregui and H. J. Carmichael, Phys. Rev. A **98**, 023804 (2018).

[28] O. Chelpanova, A. Lerose, S. Zhang, I. Carusotto, Y. Tserkovnyak, and J. Marino, "Intertwining of lasing and superradiance under spintronic pumping," (2021).

[29] K. C. Stitely, A. Giraldo, B. Krauskopf, and S. Parkins, Phys. Rev. Research **4**, 023101 (2022).

[30] P. Kirton, M. M. Roses, J. Keeling, and E. G. Dalla Torre, Advanced Quantum Technologies **2**, 1800043 (2019).

[31] F. m. c. Damanet, A. J. Daley, and J. Keeling, Phys. Rev. A **99**, 033845 (2019).

[32] P. Kirton and J. Keeling, **20**, 015009 (2018).

[33] R. H. Dicke, Phys. Rev. **93**, 99 (1954).

[34] F. Haake, M. I. Kolobov, C. Fabre, E. Giacobino, and S. Reynaud, Phys. Rev. Lett. **71**, 995 (1993).

[35] S. J. M. Kuppens, M. P. van Exter, and J. P. Woerdman, Phys. Rev. Lett. **72**, 3815 (1994).

[36] D. Meiser, J. Ye, D. R. Carlson, and M. J. Holland, Phys. Rev. Lett. **102**, 163601 (2009).

[37] J. G. Bohnet, Z. Chen, J. M. Weiner, D. Meiser, M. J. Holland, and J. K. Thompson, Nature **484**, 78 (2012).

[38] T. Shi, D. Pan, and J. Chen, Opt. Express **27**, 22040 (2019).

[39] T. Laske, H. Winter, and A. Hemmerich, Phys. Rev. Lett. **123**, 103601 (2019).

[40] M. Tang, S. A. Schäffer, A. A. Jørgensen, M. R. Henriksen, B. T. R. Christensen, J. H. Müller, and J. W. Thomsen, Phys. Rev. Research **3**, 033258 (2021).

[41] D. Meiser and M. J. Holland, Phys. Rev. A **81**, 033847 (2010).

[42] M. A. Norcia and J. K. Thompson, Phys. Rev. X **6**, 011025 (2016).

[43] M. A. Norcia, M. N. Winchester, J. R. K. Cline, and J. K. Thompson, Science Advances **2**, e1601231 (2016).

[44] J. M. Weiner, K. C. Cox, J. G. Bohnet, and J. K. Thompson, Phys. Rev. A **95**, 033808 (2017).

[45] K. Debnath, Y. Zhang, and K. Mølmer, Phys. Rev. A **98**, 063837 (2018).

[46] S. B. Jäger, J. Cooper, M. J. Holland, and G. Morigi, Phys. Rev. Lett. **123**, 053601 (2019).

[47] H. Liu, S. B. Jäger, X. Yu, S. Touzard, A. Shankar, M. J. Holland, and T. L. Nicholson, Phys. Rev. Lett. **125**, 253602 (2020).

[48] Y. Zhang, C. Shan, and K. Mølmer, Phys. Rev. Lett. **126**, 123602 (2021).

[49] Q. Wu, Y. Zhang, X. Yang, S.-L. Su, C. Shan, and K. Mølmer, Science China Physics, Mechanics & Astronomy **65**, 217311 (2021).

[50] B. R. Mollow, Phys. Rev. A **5**, 2217 (1972).

[51] F. Y. Wu, S. Ezekiel, M. Ducloy, and B. R. Mollow, Phys. Rev. Lett. **38**, 1077 (1977).

[52] L. M. Narducci, D. H. Feng, R. Gilmore, and G. S. Agarwal, Phys. Rev. A **18**, 1571 (1978).

[53] D. F. Walls, P. D. Drummond, S. S. Hassan, and H. J. Carmichael, Progress of Theoretical Physics Supplement **64**, 307 (1978), https://academic.oup.com/ptps/article-pdf/doi/10.1143/PTPS.64.307/5292058/64-307.pdf.

[54] D. F. Walls, Journal of Physics B: Atomic and Molecular Physics **13**, 2001 (1980).

[55] A. Lezama, Y. Zhu, M. Kanskar, and T. W. Mossberg, Phys. Rev. A **41**, 1576 (1990).

[56] M. Lewenstein, Y. Zhu, and T. W. Mossberg, Phys. Rev. Lett. **64**, 3131 (1990).

[57] N. Lu and P. R. Berman, Phys. Rev. A **44**, 5965 (1991).

[58] D. J. Gauthier, Q. Wu, S. E. Morin, and T. W. Mossberg, Phys. Rev. Lett. **68**, 464 (1992).

[59] J. Zakrzewski, M. Lewenstein, and T. W. Mossberg, Phys. Rev. A **44**, 7717 (1991).

[60] J. Zakrzewski, M. Lewenstein, and T. W. Mossberg, Phys. Rev. A **44**, 7732 (1991).

[61] J. Zakrzewski, M. Lewenstein, and T. W. Mossberg, Phys. Rev. A **44**, 7746 (1991).

[62] P. Horak, K. M. Gheri, and H. Ritsch, Phys. Rev. A **52**, 554 (1995).

[63] K. M. Gheri, H. Ritsch, D. F. Walls, and V. I. Balykin, Phys. Rev. Lett. **74**, 678 (1995).

[64] A. Muller, E. B. Flagg, P. Bianucci, X. Y. Wang, D. G. Deppe, W. Ma, J. Zhang, G. J. Salamo, M. Xiao, and C. K. Shih, Phys. Rev. Lett. **99**, 187402 (2007).

[65] J. Hauss, A. Fedorov, C. Hutter, A. Shnirman, and G. Schön, Phys. Rev. Lett. **100**, 037003 (2008).

[66] P. Neilinger, M. Rehák, M. Grajcar, G. Oelsner, U. Hübner, and E. Il'ichev, Phys. Rev. B **91**, 104516 (2015).

[67] I. Y. Chestnov, V. A. Shahnazaryan, A. P. Alodjants, and I. A. Shelykh, ACS Photonics **4**, 2726 (2017), https://doi.org/10.1021/acsphotonics.7b00575.

[68] M. O. Scully, S.-Y. Zhu, and A. Gavrielides, Phys. Rev. Lett. **62**, 2813 (1989).

[69] M. Fleischhauer, C. Keitel, M. Scully, and C. Su, Optics Communications **87**, 109 (1992).

[70] Y. Zhu, Phys. Rev. A **45**, R6149 (1992).

[71] J. Mompart and R. Corbalán, **2**, R7 (2000).

[72] K. Cong, Q. Zhang, Y. Wang, G. T. Noe, A. Belyanin, and J. Kono, J. Opt. Soc. Am. B **33**, C80 (2016).

[73] C. Bradac, M. T. Johnsson, M. v. Breugel, B. Q. Baragiola, R. Martin, M. L. Juan, G. K. Brennen, and T. Volz, Nature Communications **8**, 1205 (2017).

[74] J. D. Breeze, E. Salvadori, J. Sathian, N. M. Alford, and C. W. M. Kay, Nature **555**, 493 (2018).

[75] A. Angerer, K. Streltsov, T. Astner, S. Putz, H. Sumiya, S. Onoda, J. Isoya, W. J. Munro, K. Nemoto, J. Schmiedmayer, and J. Majer, Nature Physics **14**, 1168 (2018).

[76] T. Oka and H. Aoki, Phys. Rev. B **79**, 081406 (2009).

[77] K. I. Seetharam, C.-E. Bardyn, N. H. Lindner, M. S. Rudner, and G. Refael, Phys. Rev. X **5**, 041050 (2015).

[78] R. Desbuquois, M. Messer, F. Görg, K. Sandholzer, G. Jotzu, and T. Esslinger, Phys. Rev. A **96**, 053602 (2017).

[79] D. N. Basov, R. D. Averitt, and D. Hsieh, Nature Materials **16**, 1077 (2017).

[80] M. Jiang, H. Su, Z. Wu, X. Peng, and D. Budker, Science Advances **7**, eabe0719 (2021).

[81] V. Peano and M. Thorwart, Phys. Rev. B **82**, 155129 (2010).

[82] V. Peano and M. Thorwart, Europhysics Letters **89**, 17008 (2010).

[83] J. Stehlik, Y.-Y. Liu, C. Eichler, T. R. Hartke, X. Mi, M. J. Gullans, J. M. Taylor, and J. R. Petta, Phys. Rev. X **6**, 041027 (2016).

[84] T. Oka and S. Kitamura, Annual Review of Condensed Matter Physics **10**, 387 (2019).

[85] Y. Zhang, E. Lötstedt, and K. Yamanouchi, **50**, 185603 (2017).

[86] C. H. Johansen, J. Lang, A. Morales, A. Baumgärtner, T. Donner, and F. Piazza, SciPost Phys. **12**, 094 (2022).

[87] M. S. Rudner and N. H. Lindner, Nature Reviews Physics **2**, 229 (2020).

[88] L. Broers and L. Mathey, SciPost Phys. **14**, 018 (2023).

[89] L. Broers and L. Mathey, Communications Physics **4**, 248 (2021).

[90] M. Nuske, L. Broers, B. Schulte, G. Jotzu, S. A. Sato, A. Cavalleri, A. Rubio, J. W. McIver, and L. Mathey, Phys. Rev. Research **2**, 043408 (2020).

[91] L. Broers and L. Mathey, Phys. Rev. Research **4**, 013057 (2022).

[92] J. W. McIver, B. Schulte, F. U. Stein, T. Matsuyama, G. Jotzu, G. Meier, and A. Cavalleri, Nature Physics **16**, 38 (2020).

[93] We write the discretized random walk as

$$\phi_n = \sum_{i=0}^{n} \mathcal{N}\left(0, \frac{s_\phi^2}{n_T}\right), \qquad (21)$$

where $\mathcal{N}(\mu, \nu)$ indicates a randomly sampled value from the normal distribution with mean $\mu$ and variance $\nu$. $n_T$ is the amount of time-steps per driving period, such that $\phi(t)$ is determined by interpolation of $\phi_n$.

[94] Eq. 17 can be transformed such that it is always $t_2 > t_1$. Then the correlation function in Eq. 18 can be calculated by strict forward propagation using the master equation and applying the operators $b_n^j$ and $b_n^{j,\dagger}$ at $t_1$ and $t_2$, respectively.

[95] M. Breusing, S. Kuehn, T. Winzer, E. Malić, F. Milde, N. Severin, J. P. Rabe, C. Ropers, A. Knorr, and T. Elsaesser, Phys. Rev. B **83**, 153410 (2011).

[96] I. Gierz, J. C. Petersen, M. Mitrano, C. Cacho, I. C. E. Turcu, E. Springate, A. Stöhr, A. Köhler, U. Starke, and A. Cavalleri, Nature Materials **12**, 1119 (2013).

[97] D. Brida, A. Tomadin, C. Manzoni, Y. J. Kim, A. Lombardo, S. Milana, R. R. Nair, K. S. Novoselov, A. C. Ferrari, G. Cerullo, and M. Polini, Nature Communications **4**, 1987 (2013).

[98] T. Plötzing, T. Winzer, E. Malic, D. Neumaier, A. Knorr, and H. Kurz, Nano Letters **14**, 5371 (2014).

[99] C. Heide, T. Eckstein, T. Boolakee, C. Gerner, H. B. Weber, I. Franco, and P. Hommelhoff, Nano Letters **21**, 9403 (2021).

# 4 Native and Non-Local Quantum Algorithm Optimization

The early stages of research on quantum computing focused on two central aspects. First, the formulation and development of quantum algorithms that could leverage this new paradigm to efficiently solve classically intractable problems, or gain advantage over classical counterparts. And second, the design and realization of physical platforms, also called architectures, that are used to implement such quantum algorithms. Popular platforms of quantum computing are trapped ions [258–263], superconducting qubits [264–269], photonics [270, 271], quantum dots [25, 272], nuclear spins [273, 274], and neutral atoms [11, 12, 275–278]. The DiVincenzo criteria [279] of proper and scalable quantum computers have been identified fairly early, but each realization faces its own obstacles, such that the identification of a clear ideal candidate is a point of contention. The first major algorithms to demonstrate the prowess of quantum computing were the Deutsch-Jozsa algorithm [280], Grover's algorithm [281], and Shor's algorithm [282]. Later, the field of quantum cryptography [283–286] gained traction with promises of providing fundamentally secure communication channels across large distances in proposed quantum networks [287, 288]. Other intricate approaches have also been proposed, such as quantum error correction [289], topological quantum computing [290], and measurement-based quantum computing [291, 292].

The past decade has also shown tremendous growth in the computer science field of machine learning, which has affected research in physics and in particular quantum computational science. Quantum machine learning (QML) has grown into a sizable branch of quantum computing research [293–296]. As the joint field of quantum computing and machine learning, it promises to utilize noisy intermediate-scale quantum (NISQ) devices effectively. It formalizes neural networks and optimization methods in a manner that synergizes well with the intricacies of quantum information theory and provides a new perspective on the potential utilization of quantum computers.

Throughout this chapter, I provide a brief introduction into quantum information theory with a focus on the native Hamiltonian domain as a contrast to the quantum circuit paradigm. I emphasize the universality condition of gate libraries from the perspective of dynamical Lie algebras. I introduce the concept of variational quantum algorithms (VQAs), the resulting barren plateau phenomenon, and how this necessitates new ansätze to quantum algorithm optimization. I highlight how these topics connect to quantum optimal control methods and use this to provide motivation and context for Publication VII and Publication VIII, in which I studied non-local quantum optimization approaches on the native Hamiltonian level. Literature such as the book by Nielsen and Chuang [297] and review articles [298–300] have inspired this chapter.

## 4.1 Quantum Information Processing

The field of quantum computing addresses the problem of the exponentially increasing complexity of quantum systems as a function of the number of constituents, i.e. the system size. It addresses this by proposing dedicated quantum systems as controllable processing platforms. At the core of this paradigm lies the idea of encoding information into the states of quantum systems, which are manipulated and measured in order to directly perform operations on the information a given state represents. Consequently, the fundamental quantum physical principles of superposition, entanglement, and measurement play a fundamental role in the manner information is manipulated and extracted, and hence how quantum algorithms are constructed. This paradigmatic difference promises a potentially exponential speed-up over classical computers, which are restricted to classical and discrete operations on their information space. The canonical construction of quantum computing takes the concept of the classical bit, which can be in one of the two possible classical logical states 0 and 1, and promotes it to a quantum two-level system with the basis states fittingly denoted as $|0\rangle$ and $|1\rangle$. Such a quantum bit, or *qubit*, can occupy any quantum superposition of these computational states, and further an array of $n$ qubits can occupy any entangled superposition of computational $n$-bit-string states

$$|\psi\rangle = \sum_{q=0}^{2^n-1} c_q [\otimes_{j=1}^n |q_j\rangle_j], \tag{4.1}$$

where $q_j \in \{0, 1\}$ is the $j$th digit of the binary-representation of the index $q$, such that $|q_j\rangle_j$ denotes the $j$th local qubit state and $\otimes$ denotes the generalized tensor product that produces the $n$-qubit computational basis states. $c_q$ is the complex-valued amplitude corresponding to such a computational basis state. By construction, quantum computing tackles dynamical problems that in general explore the entire Hilbert space of a given $n$-qubit system. In accordance with quantum mechanics, information is extracted by measuring the qubit states, where the probability of finding the qubits in the bit-string configuration $q$ is $|c_q|^2$. Similarly, any changes to the quantum state of an array of qubits are governed through the principles of quantum mechanics, e.g. the time-evolution generated through the Schrödinger equation. The time-evolution explicitly determines the transformation that acts on the qubits, the details of which depend on the particular physical realization of the system. In close analogy to classical computing on the binary level, quantum algorithms are conventionally expressed in the language of quantum gates that are arranged in quantum circuits that represent sequences of logical operations.

Mathematically, a quantum circuit is a concatenation of unitary transformations represented by such quantum gates. In the early development of quantum algorithms, this construction of using logical operations on quantum states was studied, due to its intuitive and sequential arrangements of operations of information processing. The Deutsch-Jozsa algorithm [280] is capable of efficiently determining the parity of a given binary function, Shor's algorithm [282] can be utilized to factor large primes efficiently, and Grover's algorithm [281] provides efficient search in a quantum space. The hypothetical consequences of quantum computers utilizing Shor's algorithm to efficiently break RSA

encryption, which relies on large prime factorization, led to widespread interest into the field of quantum computing outside of academia.

In classical computer science, the only single-bit operation is the NOT, which inverts the logical value of a bit. This is contrasted by single-qubit transformations, which are given by the Lie group SU(2), i.e. a continuum of operations that are represented as rotations on the Bloch sphere by arbitrary angles $\theta$ around any axis $\hat{n}$

$$U = \exp\{-i\frac{\theta}{2}\hat{n}\vec{\sigma}\}. \tag{4.2}$$

$\vec{\sigma} = (\sigma_x, \sigma_y, \sigma_z)$ is the vector containing the Pauli matrices. Further, two-qubit gates provide entanglement and are necessary (as well as sufficient) to access the entire Hilbert space of any array of qubits. One such two-qubit gate that is commonly considered is the controlled NOT (CNOT) operation, which is a quantum analog to classical conditional operations. The CNOT performs a $\sigma_x$ transformation on the target qubit only for the component of the control qubit that is in the $|1\rangle$ state. This transformation may be written as

$$\text{CNOT} = P_0 \otimes \mathbb{1} + P_1 \otimes \sigma_x, \tag{4.3}$$

where $P_j = |j\rangle \langle j|$ are projectors onto the logical states. The quantum nature of this construction becomes apparent as soon as the control qubit is in a superposition such as $|\psi\rangle = (|0\rangle + |1\rangle)/\sqrt{2}$. A target qubit that is in the state $|0\rangle$ will after the CNOT has acted on this pair of qubits be in a composite Bell state $|\psi\rangle = (|0\rangle |0\rangle + |1\rangle |1\rangle)/\sqrt{2}$ with the control qubit. This construction is unattainable in classical computers and exemplifies one of the crucial advantages that the quantum computational paradigm provides. Other commonly considered two-qubit gates are the controlled Z (CZ) and the square-root swap ($\sqrt{\text{SWAP}}$).

The specific set of quantum gates L $\subset$ SU($2^n$) that a given physical $n$-qubit system is capable of implementing is called its gate library. A gate library is said to be universal if and only if any unitary transformation $U \in$ SU($2^n$) acting on the corresponding Hilbert space can be implemented to arbitrary precision with an arbitrarily large quantum circuit that contains only quantum gates from that gate library L. It has been proven that universality is guaranteed when arbitrary single-qubit transformations and CNOT gates between all pairs of qubits are possible [297]. Note that the CNOT is not unique here and almost any two-qubit gate fulfills this condition [301]. Specific gate libraries are provided by the details of a given physical implementation, also referred to as the quantum computing architecture, and are formally the result of the generators that make up the underlying Hamiltonian structure. Over time there have been many quantum computing architectures that have been proposed and realized for a steadily increasing amount of qubits. These include trapped ions [258–263], superconducting qubits [264–269], quantum dots [25, 272], photonics [270, 271], nuclear spins [273, 274], and neutral atoms [11, 12, 275–278].

It is instructive to write a general Hamiltonian as

$$H(t) = \sum_j \vartheta_j(t) H_j, \tag{4.4}$$

where $H_j$ are hermitian operators that generate the corresponding gate library. In the context of quantum computing, the $H_j$ most commonly take the form of single-body or two-body Pauli-matrix tensor-products, or sums of such objects. $\vartheta_j(t)$ are the corresponding time-dependent parameters that are manipulated externally in order to implement the quantum gates. If across a time-window $[0, \tau]$, all $\vartheta_{j \neq k}(t \in [0, \tau]) = 0$, except for one $\vartheta_k(t) \neq 0$ which integrates to some value $\frac{1}{\hbar} \int_0^\tau \vartheta_k(t) dt = \theta_k$, then the time-evolution operator over this time-window reads

$$U = e^{-i\theta_k H_k}. \tag{4.5}$$

This implements the gate $U$ corresponding to the generator $H_k$, e.g. as in Eq. 4.2. In this manner a gate library is constructed from a Hamiltonian. Note that by construction, this paradigm omits the implementation of non-commuting generators acting simultaneously on an overlapping subset of qubits, e.g. two simultaneous CNOT operations with different control qubits but the same target qubit. This restriction is a direct consequence of the deliberate choice to represent quantum information processing utilizing discrete quantum gates, and I address the consequences of this in a later section.

The condition of computational universality can alternatively be expressed using the concept of the dynamical Lie algebra of a Hamiltonian such as in Eq. 4.4. The dynamical Lie algebra can be understood as the set of all possible nested commutators of any combination of the generators $H_j$ of a given Hamiltonian [302, 303]. If and only if the dynamical Lie algebra is complete, i.e. it spans the Lie algebra $\mathfrak{su}(2^n)$ of generators of all transformations on the Hilbert space of $n$ qubits, then the gate library, or rather the Hamiltonian, is universal. A minimal example is the single-qubit case, where any two linearly independent generators can be used to construct arbitrary single-qubit gates, such as in Eq. 4.2. This is a consequence of the structure of the $\mathfrak{su}(2)$ algebra that is commonly represented through Pauli matrices that obey the commutation relation $[\sigma_j, \sigma_k] = 2i\epsilon^{jkl}\sigma_l$, where $\epsilon$ is the Levi-Cevita symbol and a sum over $l$ is implied. In a two-qubit example, an arbitrary generator $\sigma_a \otimes \sigma_b$, with $a, b \neq 0$, in addition to full single-qubit control provides the commutators

$$[\sigma_j \otimes \mathbb{1}, \sigma_a \otimes \sigma_b] = 2i\epsilon^{jac}\sigma_c \otimes \sigma_b \tag{4.6}$$

$$[\mathbb{1} \otimes \sigma_k, \sigma_a \otimes \sigma_b] = 2i\epsilon^{kbd}\sigma_a \otimes \sigma_d \tag{4.7}$$

$$[\mathbb{1} \otimes \sigma_k, [\sigma_j \otimes \mathbb{1}, \sigma_a \otimes \sigma_b]] = -4\epsilon^{jac}\epsilon^{kbd}\sigma_c \otimes \sigma_d. \tag{4.8}$$

These provide the generators $\sigma_c \otimes \sigma_b$, $\sigma_a \otimes \sigma_d$, and $\sigma_c \otimes \sigma_d$ with $c \neq a$ and $d \neq b$. Together with the initial generators, this spans $\mathfrak{su}(4)$, i.e. the setup is universal on two qubits.

## 4.2 Variational Quantum Algorithms

The field of quantum machine learning has been increasingly gaining traction [293–296, 298]. Combining classical machine learning with quantum computing promises to be mutually beneficial, and it has brought forth a plethora of methodologies [304–311] such

as quantum neural networks [312–318] and quantum approximate optimization algorithms [319–322], which present new perspectives on the near-term utilization of quantum computers. In particular VQAs present a large class of hybrid quantum-classical algorithms that are widely regarded to be one of the most immediately relevant QML methods for NISQ devices [299, 300, 323–328]. In the conventional setup of VQAs, a quantum circuit with a predetermined arrangement of gates is considered. The gates (usually single-qubit) perform actions that depend on external parameters, denoted as $\theta_j$. In such a quantum circuit, the overall transformation is the product of the individual gate actions determined by the parameters $\theta_j$. The full unitary transformation of such a circuit is then

$$U_\theta = \prod_j e^{-i\theta_j H_j} V_j, \tag{4.9}$$

where the $V_j$ are non-parameterized intermediate gates that commonly provide entanglement such as the CNOT. I show an example of such a quantum circuit in Fig. 4.1 (a). This unitary transformation $U_\theta$, that such a circuit implements is a function of the vector of parameters[1]

$$\theta = \sum_j \theta_j \hat{e}_j, \tag{4.10}$$

where $\hat{e}_j$ denotes the basis vectors of this construction. The construction in Eq. 4.9 is called a parameterized quantum circuit and the initial choice of the arrangement of gates is a direct ingredient of any VQA ansatz of this type. The next ingredient of VQAs is the target transformation that the circuit ideally implements for some *a priori* unknown choice of $\theta$. By constructing an objective function from observable that encodes the desired transformation, the task of finding the ideal $\theta$ becomes an optimization problem, since minimizing the difference between the measured value and the desired value of this objective function is equivalent to having the circuit implement the desired transformation. The objective function is constructed freely and is generalized as some linear combination of simultaneous observables $O_i$ weighted by real numbers $w_i$ such that

$$\mathcal{L}_\theta = \sum_i w_i \langle O_i \rangle. \tag{4.11}$$

As this is inherently measurement-based, the efficient evaluation of objective functions and the tomography of states becomes an important aspect of the construction of efficient optimization algorithms [329–333].

The process of optimization consists of iteratively changing the values of $\theta$ in order to improve the objective $\mathcal{L}_\theta$. It is very common to utilize gradient-based methods for this. In that case, it is necessary to calculate the gradient of the objective function with respect to the parameters $\theta$. The derivative of the transformation $U_\theta$ in Eq. 4.9 with respect to a given parameter $\theta_k$ is [334]

$$\partial_{\theta_k} U_\theta = -i U_{+,k} H_k U_{-,k} \tag{4.12}$$

---

[1]Note that I deliberately write the vector $\theta$ without the arrow-notation, because it is primarily a construction for collecting parameters, and occasionally it is more instructive to represent this as a two-dimensional collection of parameters such as $\theta_{j,k}$ in Eq. 4.19 and Eq. 4.20.

with

$$U_{-,k} = \prod_{j \leq k} e^{-i\theta_j H_j} V_j \qquad U_{+,k} = \prod_{j > k} e^{-i\theta_j H_j} V_j \qquad U_{+,k} U_{-,k} = U_\theta. \qquad (4.13)$$

The derivative of the objective function is then

$$\partial_{\theta_k} \mathcal{L}_\theta = \sum_j w_j \partial_{\theta_k} \langle \psi_0 | U_\theta^\dagger O_j U_\theta | \psi_0 \rangle \qquad (4.14)$$

$$= i \sum_j w_j \langle \psi_0 | U_{-,k}^\dagger [H_k, U_{+,k}^\dagger O_j U_{+,k}] U_{-,k} | \psi_0 \rangle . \qquad (4.15)$$

From this expression it is possible to evaluate the gradient of the objective function analytically, or devise methods of measuring it. Alternatively, it is also possible to evaluate the objective function for the parameters $\theta$ as well as for a slightly altered value $\theta + \delta \hat{e}_k$, for some small $\delta$, and estimate the gradient from finite differences such that

$$\partial_{\theta_k} \mathcal{L}_\theta \approx \frac{\mathcal{L}_{\theta + \delta \hat{e}_k} - \mathcal{L}_\theta}{\delta}. \qquad (4.16)$$

Optimization is then achieved iteratively through processes such as basic gradient descent steps where the parameters are updated as

$$\theta \to \theta - \eta \nabla \mathcal{L}_\theta. \qquad (4.17)$$

Here $\eta$ is a small number called the learning rate, that determines how much the parameters changes per iteration. This update step rule can be made more intricate through methods such as ADAM [335] or the quantum natural gradient [316]. This entire construction and the update rule in Eq. 4.17 in particular, are originally motivated by, and closely related to, neural networks in classical machine learning.

Note that while this methodology is very promising, it has been shown that this class of methods for optimizing parameterized quantum circuits scales unfavorably with the size of the system, which leads to the phenomenon of barren plateaus [334, 336–343]. Barren plateaus are regimes in the parameter space of $\theta$ that grow at an exponential rate as a function of the number of qubits, and across which the gradient $\nabla \mathcal{L}_\theta$ of the objective function decreases in magnitude at an exponential rate as a function of the number of qubits and the circuit depth. Consequently, large systems become exponentially more difficult to optimize, as the gradient becomes practically inaccessible, in particular in the presence of measurement noise, and provides unreliable means of approaching any local minimum in the objective function. This has motivated the search for modified approaches to VQAs that mitigate the barren plateau phenomenon [344–346]. It has been shown that a problem-inspired reduction of the controllability of an ansatz improves learning behavior [347]. In the case of local objective functions, barren plateaus have been demonstrated to occur only in deep circuits [348, 349]. Barren plateaus are explicitly a phenomenon that is determined by the parameterization and the resulting landscape of the objective across the parameter space. This circumstance has motivated
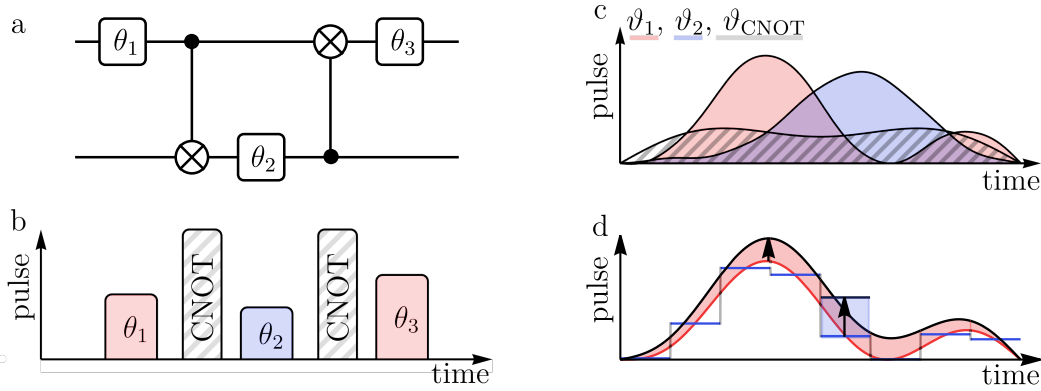
Figure 4.1: The generalization of the underlying native Hamiltonian structure of quantum circuits. Panel (a) shows an example of a parameterized quantum circuit with variational parameters $\theta_1$, $\theta_2$, and $\theta_3$, and two CNOT gates. Panel (b) illustrates the pulses corresponding to the individual quantum gates, as they are implemented on the underlying Hamiltonian level. Panel (c) depicts an example of how pulses are generalized to take non-zero values simultaneously unlike in Panel (b), such that $\theta_1$ and $\theta_3$ are the local pulse-areas of the $\vartheta_1$ pulse. Panel (d) displays the two parameterizations in Eqs. 4.19 (blue) and 4.20 (red) that approximate the pulse $\vartheta_1(t)$. The shaded areas show the change in the pulse induced by varying one of the parameters.

the efforts for devising VQA approaches that differ in their parameterization, controllability, and general construction. This has motivated my work in Publication VII, where I have studied a non-local parameterization at the native Hamiltonian domain, instead of within the quantum circuit paradigm, as I explain in the following section.

## 4.3 Non-local Optimization on the Native Hamiltonian Domain

A crucial advantage is gained by devising a VQA approach beyond the quantum circuit paradigm. As mentioned above, quantum circuits are restrictive by construction. In conventional circuit-based VQAs, the choice of the circuit architecture is a discrete problem that precedes the optimization and is usually tackled with heuristics itself. At the same time, any sequence of gates as expressed in Eq. 4.5 is natively the result of an underlying protocol of time-dependent functions $\vartheta_j(t)$ as in Eq. 4.4. I illustrate this correspondence in Fig. 4.1 (b). In principle, these functions can take arbitrary shape independently of each other, which provides a space of solutions that is not contained in the quantum circuit construction. In this native domain, the unrestricted simultaneous action of the generators is formally recovered from the circuit representations by writing

$\theta_{j,k} = \vartheta_{j,k}\tau/N$ and

$$U = \prod_{k=1}^{N} e^{-\frac{i}{\hbar}\sum_j \vartheta_{j,k} H_j \frac{\tau}{N}} \xrightarrow[N\to\infty]{} \hat{T}[e^{-\frac{i}{\hbar}\int_0^\tau \sum_j \vartheta_j(t) H_j dt}] = \hat{T}[e^{-\frac{i}{\hbar}\int_0^\tau H(t)dt}], \qquad (4.18)$$

where $\tau$ denotes the time during which the transformation $U$ is implemented. In the continuous limit of $N \to \infty$, this reproduces the general time-evolution operator for a Hamiltonian as written in Eq. 4.4. While this in itself may be unsurprising, the shift of perspective on quantum algorithm optimization is very valuable. Applying this generalization to VQAs constitutes the transition to quantum optimal control (QOC) methods [350, 351]. In particular, this makes it possible to devise new classes of parameterizations which do not map onto the circuit paradigm of conventional VQAs. I depict this generalization in Fig. 4.1 (c).

QOC describes a class of methods that aim to provide ideal protocols or pulses for the external manipulation of dynamical quantum systems with respect to a given task [352–356]. Such tasks span a variety of objectives for pulse engineering in quantum systems [357–363]. The parallels between VQAs and QOC are prominent, as they both consider a desired outcome of the dynamics of a quantum system, and transform it into an optimization problem that is solved iteratively. From the construction in Eq. 4.18, a straight-forward parameterization of the $\vartheta_j(t)$ emerges in terms of piece-wise constant functions [352]

$$\vartheta_j(t) = \theta_{j,k}, \qquad\qquad \frac{k-1}{N} < \frac{t}{\tau} < \frac{k}{N}, \qquad (4.19)$$

which is reminiscent of the quantum circuit paradigm in the Trotterized limit. In particular, this generalizes the parameterized quantum circuit approach in Eq. 4.9 and its worth noting that from this perspective, conventional VQAs present a sparsely controlled subset of QOC methods.

An immediate advantage of this generalization is that on the native Hamiltonian level, there is no longer any need for preconceived circuit architectures such as in randomly parameterized quantum circuit approaches. One advantage of the quantum circuit paradigm is the sequential and intuitive construction of discrete logical operations, which provided a framework to devise new quantum algorithms. A central part of optimization methods however, especially machine learning approaches, is that the solutions they provide are found in a manner that is indifferent to intuition, i.e. solutions are often not easily identified as solutions from their structure alone. In addition, the paradigm shift from parameterized quantum circuits to optimization on the native Hamiltonian domain provides a solution space in which all possible gate arrangements are covered by construction. This generalizes the problem in a manner that avoids the task of preconceiving circuits in its entirety. For these reasons, the case can be made that optimization on the native Hamiltonian domain is a natural choice for quantum algorithm optimization.

As studies on barren plateaus have shown, VQAs can benefit from non-locality [344, 347–349]. Similarly, the CRAB [357, 358] algorithm of optimal control theory demonstrates that a shift in the optimization basis is an effective method for improving an

136

algorithm. This motivates a natural choice for an alternative parameterization of $\vartheta_j(t)$ that I have studied in Publication VII. This parameterization optimizes the Fourier coefficients of $\vartheta_j(t)$ and is therefore non-local in time. It is

$$\vartheta_j(t) = \sum_{k=1}^{n_f} \theta_{j,k} \sin(\pi k \frac{t}{\tau}), \tag{4.20}$$

where $n_f$ is the number of Fourier modes and constitutes a hyperparameter that determines the resulting expressibility of $\vartheta_j(t)$. As mentioned earlier, $\tau$ is the time during which this control pulse is applied. This ansatz provides smooth and slowly varying protocols which start and end at zero by construction. I visualize the parameterizations of Eq. 4.19 and Eq. 4.20 in Fig. 4.1 (d). Related types of parameterizations have been considered in optimization methods in different settings [364, 365]. It is worth noting, that the proof of the emergence of barren plateaus [334] relies on the parameterized quantum circuit structure that leads to the expression in Eq. 4.15. In contrast, I have calculated the analogous expression for the Fourier parameterization in Eq. 4.20

$$\partial_{\theta_{j,k}} \mathcal{L}_\theta = i \sum_l w_l \int_0^\tau \sin(k\pi \frac{t}{\tau}) \langle \psi_0 | U_t^0 [U_\tau^t O_l U_t^\tau, H_j] U_0^t | \psi_0 \rangle \, dt, \tag{4.21}$$

which eludes the premises of the aforementioned proof. Hence, it can not be directly inferred that the Fourier parameterization has to display barren plateaus. Here $U_{t_a}^{t_b}$ is the time-evolution operator from time $t_a$ to time $t_b$, for $t_b > t_a$. If $t_a > t_b$, it is $U_{t_a}^{t_b} = (U_{t_b}^{t_a})^\dagger$. In Publication VII, I have analyzed the performance of this Fourier parameterization and compared it to the piece-wise constant parameterization, which acts as a benchmark due to its similarity to circuit-based VQAs. The results showed an improved performance and convergence behavior for the Fourier parameterization across several objectives, such as the energy minimization of randomized problem Hamiltonians and the implementation of the quantum Fourier transform. Additionally, the Fourier parameterization displays a mitigation of the barren plateau phenomenon in a direct comparison to the piece-wise constant parameterization. I showed this by analyzing the uniformly sampled variances of the gradient of the objective function for both parameterizations with respect to the number of qubits.

In Publication VIII, we have considered quantum algorithm optimization in the quantum computing platform of neutral atoms in optical tweezers [12, 276]. We have considered the particular setup in which the logical qubit states $|0\rangle$ and $|1\rangle$ are encoded in metastable hyperfine states of ytterbium atoms [366]. The atoms are individually trapped, which gives high fidelity control over the atomic positions. Entanglement between qubits is achieved via additional highly excited Rydberg states $|R\rangle$. These states display a large polarizability that leads to Van-der-Waals interactions that scale with $r^{-6}$, where $r$ is the distance between two interacting atoms. By introducing Rabi pulses $\Omega_j(t)$ that drive the transition from the logical $|1\rangle$ state of an atom into the Rydberg state $|R\rangle$, it is possible to control the interaction between atoms. Single-qubit operations on the hyperfine states are performed via Raman transition pulses $A_j(t)$. The

corresponding Hamiltonian is

$$\frac{1}{\hbar}H = \sum_{j=1}^{n} A_j(t)\sigma_x^{(j)} + \Omega_{x,j}(t)\tau_x^{(j)} + \Omega_{y,j}(t)\tau_y^{(j)} + \sum_{i\neq j}^{n} |R\rangle_i |R\rangle_j \langle R|_i \langle R|_j \frac{C_6}{|r_i - r_j|^6}, \quad (4.22)$$

where $\tau_x^{(j)} = |R\rangle_j \langle 1|_j + |1\rangle_j \langle R|_j$ and $\tau_y^{(j)} = -i |R\rangle_j \langle 1|_j + i |1\rangle_j \langle R|_j$. $C_6$ is the strength of the Van-der-Waals interaction. We have performed variational optimization on the Rabi and Raman pulses to implement the CNOT gate at various fixed distances. For atoms that are in proximity, the excitation of more than one Rydberg state is highly suppressed, which results in the Rydberg blockade regime [11, 367]. We have analyzed the opposite limit of weak coupling at large distances, and demonstrated its viability under utilization of quantum algorithm optimization. We have then considered the presence of fluctuations in the interatomic distance and how this affects the fidelity of CNOT-implementations at various distances.

We have further considered a class of non-local restrictions in which all the parameters of one subset of transformations are equal, i.e. reduced to one parameter that controls the corresponding processes simultaneously and identically. In particular, we have demonstrated the universality of the Rydberg architecture under such restrictions for many qubits. This means computational universality is maintained even if the Raman pulses that act on the single-qubit subspaces, or the Rabi pulses that control excitation into the Rydberg states, are controlled globally, i.e. $A_j(t) = A(t)$ or $\Omega_j(t) = \Omega(t)$, respectively. Note that this includes acting on qubits which are not involved in the target transformation by cancelling out the overall transformation locally to produce the identity.

This type of restrictions implies that the accessible generators are not the individual $\sigma_x^{(j)}$ or $\tau_x^{(j)}$, but rather $S_x = \sum_{j=1}^{n} \sigma_x^{(j)}$ or $T_x = \sum_{j=1}^{n} \tau_x^{(j)}$, respectively. In general this implies a change in the dynamical Lie algebra. To prove that this restriction preserves universality, it is necessary to demonstrate that the dynamical Lie algebra is unaffected. Therefore, it is sufficient to recover the unrestricted generators from the restricted set of generators. For instance, if the restriction demands that $S_x$ is a generator, but the individual $\sigma_x^{(j)}$ are not, i.e. globally identical Raman pulses, then it is sufficient to show that $\sigma_x^{(j)}$ is accessible through nested commutators of generators. This is the case, since it is

$$[[S_x, \tau_x^{(j)}], \tau_x^{(j)}] \propto \sigma_x^{(j)}. \quad (4.23)$$

Analogously, in the case of the restriction where $T_x$ are generators, but the individual $\tau_x^{(j)}$ are not, i.e. globally identical Rabi pulses, it is

$$[[T_x, \sigma_x^{(j)}], \sigma_x^{(j)}] \propto \tau_x^{(j)}. \quad (4.24)$$

The full proof is detailed in the appendix of Publication VIII, however Eqs. 4.23 and 4.24 already display the central argument of the dynamical Lie algebra being unaltered. We have also presented concrete examples of sequences of transformations that produce the individual local gates under these restrictions. This restriction is interesting, because it is counter-intuitive from a quantum circuit perspective. In principle, the reduced

controllability affects the training behavior in such a setup, but to what degree is yet unclear. The reduced dimensionality of the parameter space is however beneficial to optimization methods. This construction also synergizes well with the optimization of quantum algorithms which we have studied in both Publication VII and Publication VIII, as it constitutes further non-locality. This result implies that it is possible to design a universal quantum computer with this restriction in mind which would result in less intricate machinery and a potentially more robust and less costly architecture.

## 4.4 Publication VII: Mitigated barren plateaus in the time-nonlocal optimization of analog quantum-algorithm protocols

This work was motivated by recent discussions in the literature on variational quantum algorithms (VQAs) and the barren plateau phenomenon that has been shown to occur in VQAs. Barren plateaus are characterized as exponentially growing regimes in parameter space in which the gradients of a given objective function decrease at an exponential rate. Barren plateaus therefore act as a type of *de facto* no-go theorem in a large class of quantum algorithm optimization methods. One particular signature of barren plateaus is given by exponentially decaying variances in the gradient of the objective function with respect to the number of qubits. This motivates modifications of VQA ansätze to circumvent this roadblock.

In this work, I have proposed and analyzed an extended ansatz of VQAs. This extension includes going from the parametrized quantum circuit paradigm to analog quantum information processing on the native Hamiltonian domain. This is related to quantum optimal control in the sense that arbitrary control protocols of the Hamiltonian parameters can be utilized in gradient based optimization of quantum algorithms, e.g. quantum gate compilation. Further, I have proposed a parametrization of these native control protocols in terms of real-valued Fourier coefficients, which provides protocols that are by construction slowly varying, smooth, and are optimized non-locally in time. I have compared this ansatz with the more conventional parametrization of piece-wise constant step-functions, which in the Trotterized limit connects back to discrete quantum circuit constructions. The piece-wise constant parameterization therefore acts as a proper benchmark in a direct comparison.

I have compared the two ansätze in terms of training behavior, fidelity of solutions, and time-efficiency for the tasks of compiling the quantum Fourier transform, as well as minimizing the energy of randomized problem Hamiltonians. I have found that the Fourier based ansatz outperforms the step-wise ansatz in particular in convergence speed and consistency without a loss of time-efficiency of the solutions. Further, I have analyzed and compared the variances of the gradients of an example objective. The piece-wise constant benchmark ansatz shows variances that decay exponentially with the number of qubits, which indicates a clear onset of barren plateaus. This is expected in this ansatz as it is reminiscent of parametrized quantum circuits. In the Fourier based ansatz, the variances decay at a non-exponential rate with the number of qubits, which indicates a mitigation of barren plateaus.

My contribution to this work consisted of conceiving the project, creating the numerical code, performing the numerical studies, performing the analytical calculations, analyzing and presenting the results, and writing the manuscript. All of this was done under the supervision and with the guidance of LM.

# Mitigated barren plateaus in the time-nonlocal optimization of analog quantum-algorithm protocols

Lukas Broers[1,2] and Ludwig Mathey[1,2,3]

[1]*Center for Optical Quantum Technologies, University of Hamburg, 22761 Hamburg, Germany*
[2]*Institute for Quantum Physics, University of Hamburg, 22761 Hamburg, Germany*
[3]*The Hamburg Center for Ultrafast Imaging, 22761 Hamburg, Germany*

Quantum machine learning has emerged as a promising utilization of near-term quantum computation devices. However, algorithmic classes such as variational quantum algorithms have been shown to suffer from barren plateaus due to vanishing gradients in their parameters spaces. We present an approach to quantum algorithm optimization that is based on trainable Fourier coefficients of Hamiltonian system parameters. Our ansatz is exclusive to the extension of discrete quantum variational algorithms to analog quantum optimal control schemes and is non-local in time. We demonstrate the viability of our ansatz on the objectives of compiling the quantum Fourier transform and preparing ground states of random problem Hamiltonians. In comparison to the temporally local discretization ansätze in quantum optimal control and parameterized circuits, our ansatz exhibits faster and more consistent convergence. We uniformly sample objective gradients across the parameter space and find that in our ansatz the variance decays at a non-exponential rate with the number of qubits, while it decays at an exponential rate in the temporally local benchmark ansatz. This indicates the mitigation of barren plateaus in our ansatz. We propose our ansatz as a viable candidate for near-term quantum machine learning.

## I. INTRODUCTION

Quantum machine learning (QML) connects classical machine learning and quantum information processing. This emergent field promises new methods that advance quantum computation [1, 2] and has brought forth a class of approaches referred to as variational quantum algorithms (VQA) [3–6]. In particular, noisy intermediate-scale quantum (NISQ) devices [7–9] are predicted to benefit from the synergies with machine learning found in VQA. These approaches optimize parameters in a sequence of unitary operations, the product of which describes the time-evolution of the system. The optimization is performed with respect to a chosen observable. Examples include quantum approximate optimization algorithms (QAOA) [10, 11], quantum neural networks [12–18], quantum circuit learning [19] and quantum assisted quantum-compiling [20–22].

Similarly, quantum optimal control (QOC) aims to optimize the time-dependent system parameters of a quantum system to attain a given objective [23–29]. QOC has been connected to VQA approaches, and advantages of moving from the discrete circuit picture to the underlying physical system parameters have been demonstrated [30, 31]. Such analog VQA approaches commonly utilize piecewise constant, or step-wise, parameterization ansätze [32–36], which behave like the Trotterized limit of very deep parameterized quantum circuits with very small actions per gate.

A major obstacle of VQA is the existence of barren plateaus in the loss landscapes, i.e. increasingly large regimes in the parameter space with exponentially vanishing gradients, which hinder training [37–44]. The general scaling behavior and emergence of barren plateaus is largely not understood and the dependence of barren plateaus on the details of VQA has been an active

field of research in recent years. The comparison of local to global objective functions, the dependence on circuit depth, and the effects of spatial and temporal locality of parameterizations have been studied in connection to barren plateaus [40–42, 45–47]. In particular, the emergence of barren plateaus has been proven in time-locally parameterized quantum circuits for global objective functions and for local objective functions in the case of non-shallow circuits [40, 42, 45]. Limiting the controllability of such ansätze can reduce the onset of barren plateaus [47–50], which constitutes a trade-off in expressibility [51, 52] in favor of trainability. This includes ansätze that are tailored to a given problem, such as the variational Hamiltonian ansatz [4, 53], the unitary coupled cluster ansatz [54], and QAOA [11]. These results suggest that non-local ansätze that depart from the parameterized circuit paradigm may mitigate barren plateaus without the loss of generality. Overcoming the obstacle of barren plateaus is crucial for the success of near-term QML technologies.

In this paper, we propose a parameterization ansatz for quantum algorithm optimization using generalized analog protocols. In this ansatz we directly control the Fourier coefficients of the system parameters of a Hamiltonian. This constitutes a method that is non-local in time and is exclusive to analog quantum protocols as it does not translate into discrete circuit parameterizations which are conventionally found in VQA. We compare our ansatz to the common optimal control ansatz of step-wise parameterizations for the example objectives of compiling the quantum Fourier transform as well as minimizing the energy of random problem Hamiltonians. This comparison shows that this Fourier based ansatz results in solutions with higher fidelity and in particular superior convergence behavior. Note that the optimization of Fourier coefficients has been proposed for the control
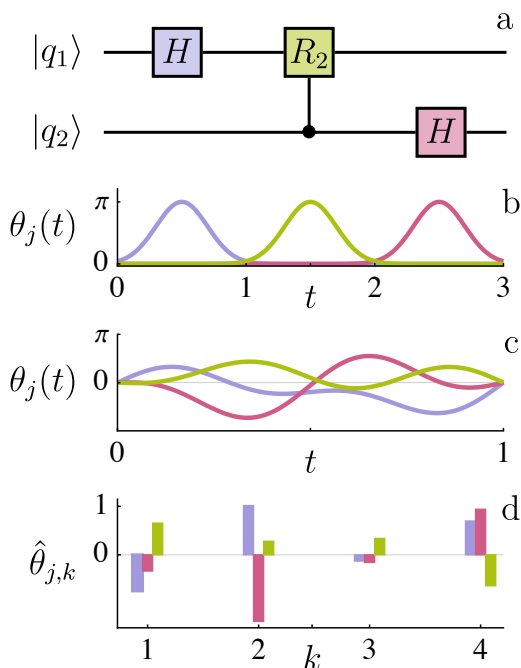
FIG. 1. **Levels of abstraction of quantum algorithms**. A common formulation of quantum circuits consists of a set of discrete gates, see panel (a). The physical realization of these gates consists of temporally isolated control protocols of the system parameters. These are denoted as $\theta_j(t)$ for the different parameters, see panel (b). A more efficient realization utilizes the full space of temporal evolutions of the parameters $\theta_j(t)$. This includes fully parallel protocols which take less time to complete the task, see panel (c). Any such protocol can be expressed via its Fourier coefficients $\hat{\theta}_{j,k}$, which we specifically treat as trainable parameters in our ansatz, see panel (d).

of molecular dynamics [55]. It has also been used in a mixed approach that optimizes in the basis of piecewise constant functions [56], as well as in phase-modulated gradient-free optimization [57]. The Fourier basis has also been used with tuned frequencies in the CRAB algorithm [23, 58]. However, studies on this particular ansatz in the context of analog quantum computing as a natural extension of VQA appear to be lacking. We demonstrate that our ansatz exhibits non-exponential scaling behavior with respect to the number of qubits in the objective gradient variance, which suggests the absence of barren plateaus. We conclude that our ansatz is a promising candidate for efficient training and avoiding barren plateaus in VQA.

## II.  METHODS

In quantum circuits, the time-dependent Hamiltonian parameters that implement the gates are sequential, rather than parallel, and therefore contain long idling

times. This is a consequence of deconstructing unitary transformations into algorithmic sequences of logical gates. Fig. 1 illustrates different levels of abstraction of quantum algorithms. The departure from the conventional quantum circuit paradigm towards a larger and more intricate space of solutions of quantum protocols enables a computational speed-up due to parallelized Hamiltonian operations.

We write a general time-dependent Hamiltonian as

$$H(t) = \sum_j \theta_j(t) H_j, \tag{1}$$

where $H_j$ are Hermitian matrices that define the system. $\theta_j(t)$ are the parameters that determine the time-dependence of the system. The resulting time-evolution operator is formally written as

$$U_{\boldsymbol{\theta}} = \hat{T}[\exp\{-i \int_0^1 \sum_j \theta_j(t) H_j dt\}], \tag{2}$$

where $\hat{T}$ indicates time-ordering. We restrict the time-evolution to $t \in [0, 1]$ and use units in which $\hbar = 1$, for simplicity. The unitary transformation $U_{\boldsymbol{\theta}}$ is explicitly a function of the protocols $\theta_j(t)$. In order to perform numerical optimization, it is necessary to choose a particular parameterization for the $\theta_j(t)$.

In the ansatz which we highlight in this work, we parameterize the $\theta_j(t)$ in terms of the first $n_{\mathrm{f}}$ real-valued Fourier coefficients $\theta_{j,k}$ such that

$$\theta_j(t) = \sum_{k=1}^{n_{\mathrm{f}}} \theta_{j,k} \sin(\pi k t). \tag{3}$$

This ansatz is motivated by its inherent temporal non-locality, as varying a single parameter $\theta_{j,k}$ changes the protocol $\theta_j(t)$ at all points in time. It presents a natural choice for a time-non-local parameterization that results in protocols that are smooth and slowly varying by construction, which is advantageous experimentally. We initialize the parameters $\theta_{j,k}$ randomly between $\pm\pi/k$, such that slow modes are emphasized.

In addition to our ansatz, we consider the step-wise ansatz that uses the common discretization in terms of piecewise constant system parameters.

$$\theta_j(t) = \theta_{j,k}, \quad \frac{k}{n_{\mathrm{f}}} \leq t < \frac{k+1}{n_{\mathrm{f}}}, \tag{4}$$

with $k = 0, \ldots, n_{\mathrm{f}} - 1$. We initialize the $\theta_{j,k}$ randomly between $\pm\pi$. This ansatz is time-local and generates discontinuous step-functions with $n_f$ steps with values $\theta_{j,k}$. These steps are reminiscent of the sequences of parameterized gates in quantum circuits as they are conventionally found in VQA. Due to its connection to conventional parameterized variational circuits, this ansatz serves as a benchmark to which we compare our ansatz of Eq. 3.

In either ansatz, we optimize the parameters

$$\boldsymbol{\theta} = \sum_{j,k} \theta_{j,k} \hat{e}_{j,k}, \tag{5}$$

with respect to a given objective function $\mathcal{L}_{\boldsymbol{\theta}}$, which encodes a target transformation. The exact expression of any objective $\mathcal{L}_{\boldsymbol{\theta}}$ depends on the details of the problem it describes. The $\hat{e}_{j,k}$ are formally constructed unit-vectors that collect the trainable parameters $\theta_{j,k}$ in the vector $\boldsymbol{\theta}$. Successful optimization corresponds to a time-evolution operator $U_{\boldsymbol{\theta}}$ which implements the target transformation. For a single optimization iteration, we vary the individual parameters $\theta_{j,k}$ by a small $\delta$ and evaluate the objective function to estimate the respective derivatives

$$\frac{\partial \mathcal{L}_{\boldsymbol{\theta}}}{\partial \theta_{j,k}} \approx \frac{\mathcal{L}_{\boldsymbol{\theta}+\delta\hat{e}_{j,k}} - \mathcal{L}_{\boldsymbol{\theta}}}{\delta} \qquad (6)$$

such that we obtain the gradient

$$\nabla \mathcal{L}_{\boldsymbol{\theta}} = \sum_{j,k} \frac{\partial \mathcal{L}_{\boldsymbol{\theta}}}{\partial \theta_{j,k}}. \qquad (7)$$

We then update the parameters as

$$\boldsymbol{\theta}_{\text{old}} \to \boldsymbol{\theta}_{\text{new}} = \boldsymbol{\theta}_{\text{old}} - \eta g^{\dagger} \nabla \mathcal{L}_{\boldsymbol{\theta}}, \qquad (8)$$

where $\eta$ is the learning rate, which we update dynamically using the ADAM [59] algorithm. $g$ is the Fubini-Study metric, which contains information on the quantum geometry of the system in order to improve training behavior and makes this approach a quantum natural gradient descent method [60]. For more details see App. A.

Note that in a physical realization, the parameters $\theta_j(t)$ cannot become arbitrarily large, and are limited by physical constraints or features of the realization. In our numerical approach, these parameters are unbounded. However, we find that these parameters remain reasonably small throughout learning, as we show below.

## III. RESULTS

We compare our Fourier ansatz to the step-wise ansatz for the objectives of quantum compiling and energy minimization. Further, we evaluate the scaling behavior of the variances of objective gradients with respect the number of qubits. Throughout this work we use the Ising Hamiltonian [61] with a two-component transverse field for $n_{\text{q}}$ qubits as the controllable system that generates the variational unitary $U_{\boldsymbol{\theta}}$. It is

$$H(t) = \sum_{j=1}^{n_{\text{q}}} \left( B_x^j(t)\sigma_x^j + B_y^j(t)\sigma_y^j \right) + \sum_{j=1}^{n_{\text{q}}-1} J_j(t)\sigma_z^j\sigma_z^{j+1}, \qquad (9)$$

with controllable parameters $B_x^j(t)$, $B_y^j(t)$ and $J_j(t)$. We consider open boundary conditions, such that the index of $J_j(t)$ goes up to $j = n_{\text{q}} - 1$. In total this gives $(3n_{\text{q}}-1)n_{\text{f}}$ trainable parameters in $\boldsymbol{\theta}$, as the $B_x^j(t)$, $B_y^j(t)$ and $J_j(t)$ take the role of the $\theta_j(t)$ in Eq. 1. Our ansatz In
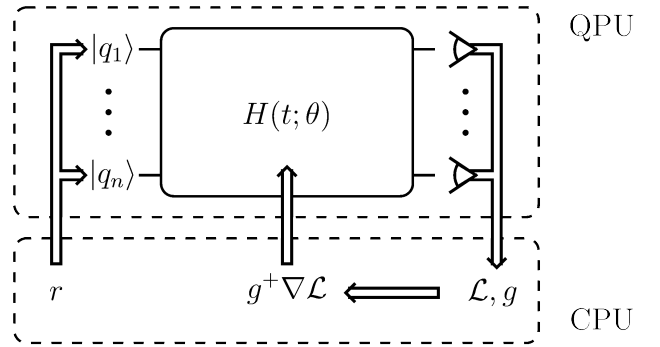


FIG. 2. **Illustration of hybrid quantum optimization**. A quantum processing unit (QPU) is assumed to have controllable parameters $\theta$. Problem-specific input $r$ is mapped onto the initial state of the qubits which the QPU evolves in time according to the parameters $\theta$ and its underlying Hamiltonian $H$. The final qubit state is measured to determine the value of an objective function $\mathcal{L}_{\boldsymbol{\theta}}$ and the Fubini-Study metric $g$. These quantities are used on a classical machine to approximate the quantum natural gradient step to update the parameters $\theta$ and improve $\mathcal{L}_{\boldsymbol{\theta}}$.

Eq. 3 presents a general parameterization of system parameters and therefore the particular choice of the Hamiltonian is not essential. In particular, neither the Fourier ansatz nor the choice of the Hamiltonian are informed *a priori* by any objective at hand. They are agnostic to the optimizational tasks we utilize them for.

### A. Quantum Compiling

We first demonstrate the performance of our ansatz for the example of learning implementations of the QFT represented by the unitary operation $V$, operating on $n_{\text{q}}$ qubits. The matrix elements of $V$ are

$$V_{k,l} = 2^{-\frac{n_{\text{q}}}{2}} \exp\{i2\pi kl2^{-n_{\text{q}}}\}, \qquad (10)$$

where $k, l = 1, \ldots, 2^{n_{\text{q}}}$. For compiling unitary transformations, we utilize the objective function

$$\mathcal{L}_{\boldsymbol{\theta}}^{U} = 1 - \frac{1}{|\{r\}|} \sum_{r} |\langle r|U_{\boldsymbol{\theta}}^{\dagger}V|r\rangle|^2, \qquad (11)$$

where $\{r\}$ is a set of randomized unentangled input states

$$|r\rangle = \otimes_{i=1}^{n_{\text{q}}} [\cos(\frac{\phi_i}{2})|0\rangle + e^{i\psi_i}\sin(\frac{\phi_i}{2})|1\rangle], \qquad (12)$$

which is similar to recent methods [62]. This objective function estimates the implementation error $\epsilon = 1 - |\text{Tr}(U_{\boldsymbol{\theta}}^{\dagger}V)2^{-n_{\text{q}}}|^2$ between the unitaries $U_{\boldsymbol{\theta}}$ and $V$. Note that there exist state estimation and tomography methods [63–67] that are experimentally favorable over the overlap in Eq. 11. Here we use this overlap due to its straightforward numerical accessibility.
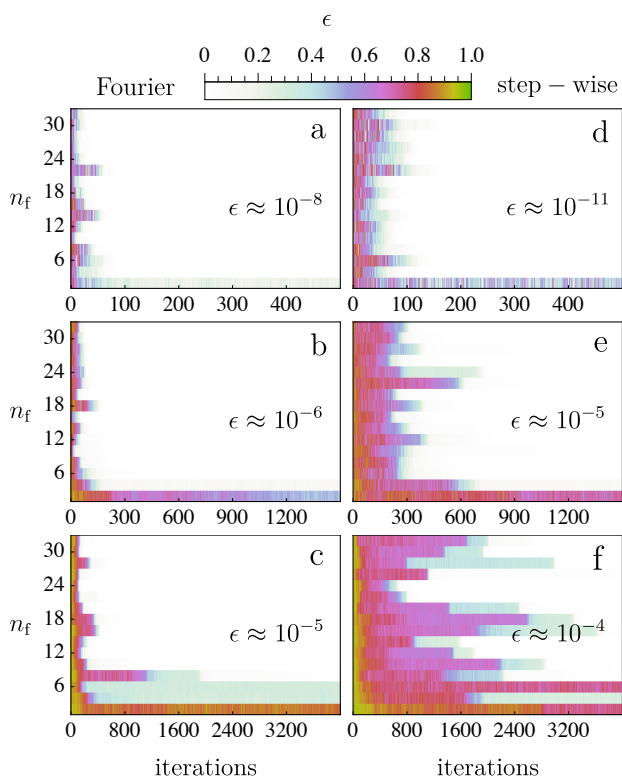
FIG. 3. **Implementation errors during training of the quantum Fourier transform**. The errors $\epsilon$ during training as a function of the hyperparameter $n_{\mathrm{f}}$ for the QFT for $n_{\mathrm{q}} = 2$ (a,d), 3 (b,e) and 4 (c,f) for our Fourier based ansatz (a,b,c) and the step-wise protocol ansatz (d,e,f). For sufficiently large $n_{\mathrm{f}} \geq n_{\mathrm{f,min}}$ both ansätze converge to very small errors. Our Fourier based ansatz outperforms the step-wise ansatz in terms of convergence speed and consistency.

In Fig. 3, we show the estimated implementation error $\epsilon$ during training, as a function of $n_{\mathrm{f}}$ for $n_{\mathrm{q}} \leq 4$. We observe that both implementations converge to the target transformation for sufficiently large $n_{\mathrm{f}}$. For smaller $n_{\mathrm{f}}$ the accessible unitary transformations generated from the ansätze Eqs. 3 and 4 are insufficient and presumably do not contain the QFT on $n_{\mathrm{q}}$ qubits.

We emphasize that our Fourier based ansatz is consistently outperforming the step-wise ansatz in terms of convergence speed. We show in Figs. 3 (a,b,c) that our ansatz tends to converge after roughly 50, 100 and 200 training iterations for $n_{\mathrm{q}} = 2$, 3 and 4, respectively. Figs. 3 (d,e,f) show that the step-wise protocol ansatz tends to converge after roughly 100, 300 and 1800 iterations for $n_{\mathrm{q}} = 2, 3, 4$, respectively. For $n_{\mathrm{q}} = 4$ in Fig. 3 (f), the convergence behavior of the step-wise ansatz is increasingly inconsistent. The step-wise ansatz has the tendency to linger at suboptimal fidelities from which it only moves away very slowly. This behavior becomes more prominent with increasing $n_{\mathrm{q}}$ and is a consequence of the loss landscape that follows from the pa-

rameterization in Eq. 4. Our ansatz does not show this behavior, but rather exhibits faster and more direct convergence. This is an indication for the absence of vanishing gradients, as is apparent when comparing Figs. 3 (c) and (f).

In order to further evaluate the quality of the converged solutions, we show the minimal errors after training $\epsilon_{\mathrm{opt}}$ with respect to the hyperparameter $n_{\mathrm{f}}$ for both ansätze in Figs. 4 (a) and (b). We find the minimal $n_{\mathrm{f}}$ that is necessary for convergence during training to be approximately $n_{\mathrm{f,min}} \approx 4$, 6 and 8 for $n_{\mathrm{q}} = 2$, 3 and 4, respectively. The minimal $n_{\mathrm{f}}$ necessary for convergence appears to be the same for both ansätze in this example. For larger $n_{\mathrm{f}}$, the minimal error converges to very small values that show no strong dependence on $n_{\mathrm{f}}$. For the cases of $n_{\mathrm{q}} = 3$ and $n_{\mathrm{q}} = 4$, the resulting minimal error tends to approach $\epsilon_{\mathrm{opt}} \approx 10^{-5}$. We note that for a concrete experimental realization, additional considerations, e.g. what dissipative processes are present and how well a specific parameter can be tuned dynamically, determine the overall success of these approaches, which will be explored elsewhere.

As a second figure of merit we consider the effective implementation action, which we quantify with the integrated magnitude of the vector of system parameters $\boldsymbol{\theta}(t)$, such that

$$\Phi = \int_0^1 |\boldsymbol{\theta}(t)|\mathrm{d}t. \tag{13}$$

Given that the parameters $\theta_j(t)$ have the units of energy, this quantity is an overall measure of the phase or action that is accumulated during the time-evolution. It therefore quantifies an estimate of both the energy that is required to implement a protocol in a given time, as well as the time that is required given a bound to the magnitude of the parameters $\theta_j(t)$. This figure of merit allows us to determine whether a solution with improved fidelity in our Fourier ansatz merely emerges due to decreased time-efficiency. In Figs. 4 (c) and (d) we show the effective actions $\Phi_{\mathrm{opt}}$ of the same optimal solutions of Figs. 4 (a) and (b), with respect to the hyperparameter $n_{\mathrm{f}}$. We find the two ansätze to be very similar in terms of necessary action and therefore time-efficiency. In both ansätze, there is no strong dependence on the hyperparameter $n_{\mathrm{f}}$ past $n_{\mathrm{f,min}}$. While the implementation actions consistently remain reasonably small, there is a clear and expected tendency of implementations to require larger effective actions with increasing amounts of qubits.

### B. Energy Minimization

As a second optimization task, we consider the energy expectation value of a problem Hamiltonian $H_{\mathrm{p}}$ and its minimization. Specifically, we consider the objective function

$$\mathcal{L}_{\boldsymbol{\theta}}^E = \langle E \rangle_{\boldsymbol{\theta}} = \langle 0|U_{\boldsymbol{\theta}}^\dagger H_{\mathrm{p}} U_{\boldsymbol{\theta}}|0\rangle, \tag{14}$$
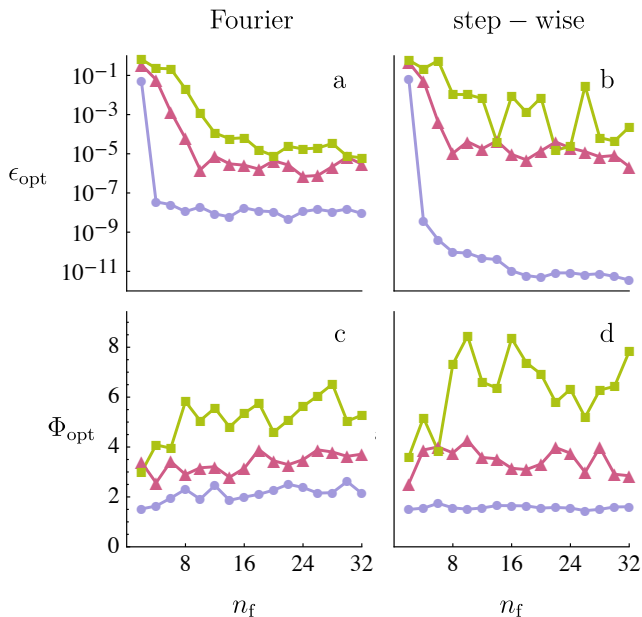
FIG. 4. **Minimal errors and effective actions for training the quantum Fourier transform**. The minimal errors $\epsilon_{\mathrm{opt}}$ (a,b) found during training and the corresponding effective protocol actions $\Phi_{\mathrm{opt}}$ (c,d) of both ansätze. The training results are for the QFT for $n_{\mathrm{q}} = 2$ (blue circles), 3 (red triangles) and 4 (green squares). The inconsistent $\epsilon_{\mathrm{opt}}$ in the step-wise ansatz for $n_{\mathrm{q}} = 4$ (b) is a consequence of the suboptimal convergence behavior, related to the emergence of barren plateaus.

where $U_{\boldsymbol{\theta}}$ is the time-evolution operator of the Hamiltonian given in Eq. 2, which we use to construct the trial state $U_{\boldsymbol{\theta}} |0\rangle$. We use the shortened notation $|0\rangle = |0\rangle^{\otimes n_{\mathrm{q}}}$ of the state where all qubits are in the logical zero state. We perform this ground state search for random problem Hamiltonians for both our ansatz and the step-wise ansatz with $n_{\mathrm{f}} = 16$. In this example we do not apply the QNG, i.e. we set the metric $g = \mathbb{1}$, for simplicity. Fig. 5 shows the energy differences $\Delta E = \langle E \rangle_{\boldsymbol{\theta}} - E_0$ for the training trajectories of three randomized problem Hamiltonians for up to six qubits. We again see that our ansatz outperforms the step-wise ansatz in terms of convergence speed. There is an increasing tendency of gradients to flatten out in the step-wise ansatz. This behavior is not present in our ansatz and indicates the onset of barren plateaus in the optimization of ground state preparation for step-wise protocols.

## C. Objective Gradient Variances

In order to quantify the presence of barren plateaus, we consider the variance of the gradients of the objective function for both our ansatz and the step-wise ansatz. In random parameterized quantum circuits this amounts to
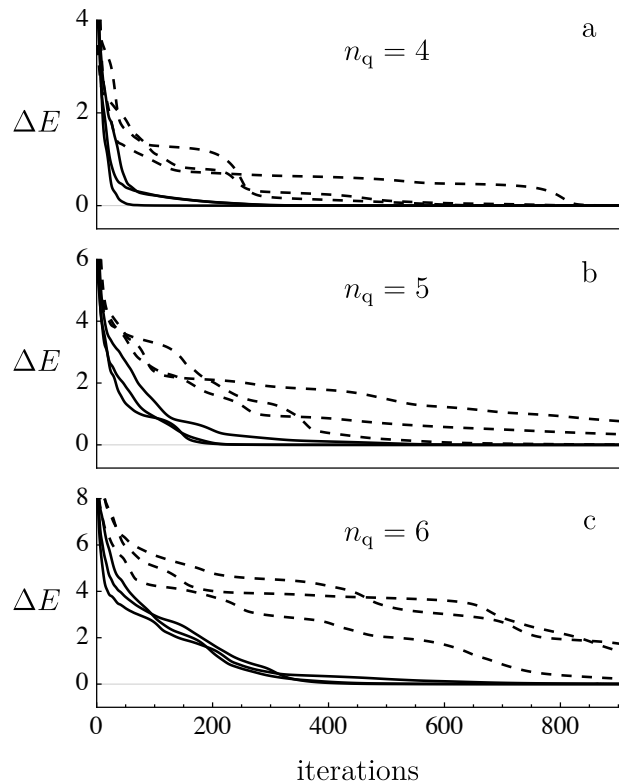


FIG. 5. **Training trajectories for energy minimization**. Learning trajectories for the ground state preparation of three randomly generated problem Hamiltonians for $n_{\mathrm{q}} = 4, 5, 6$ qubits for our ansatz (solid lines) and the step-wise ansatz (dashed lines). $\Delta E = \langle E \rangle_{\boldsymbol{\theta}} - E_0$ is the expected energy of the prepared states relative to the ground state energy. In all cases $n_{\mathrm{f}} = 16$.

uniformly sampling possible initializations in the parameter space of $\boldsymbol{\theta}$ [40]. In analog parameterizations of quantum algorithms, the parameter space is aperiodic and non-compact such that sampling is more intricate. We consider uniformly sampled vectors $\boldsymbol{\theta}$ inside a $(3n_{\mathrm{q}} - 1)$-dimensional ball with radius $|\boldsymbol{\theta}|_{\max}$ for each time-step in the step-wise ansatz, and $|\boldsymbol{\theta}|_{\max}/k$ for each $k$th Fourier mode in our ansatz. The value of $|\boldsymbol{\theta}|_{\max}$ determines the set of reachable states of a given ansatz. We consider the variance of the gradient with respect to the first parameter

$$\mathrm{Var}[\partial_{\theta_{1,1}} \mathcal{L}_{\boldsymbol{\theta}}^E] = \langle (\partial_{\theta_{1,1}} \mathcal{L}_{\boldsymbol{\theta}}^E)^2 \rangle - \langle \partial_{\theta_{1,1}} \mathcal{L}_{\boldsymbol{\theta}}^E \rangle^2 \qquad (15)$$

for the specific problem Hamiltonian

$$H_{\mathrm{p}} = \sigma_z^1 \sigma_z^2 \prod_{j=3}^{n_{\mathrm{q}}} \mathbb{1}^j. \qquad (16)$$

We calculate the variance as a function of $|\boldsymbol{\theta}|_{\max}$ for up to 8 qubits for $n_{\mathrm{f}} = 128$. Analytical arguments on the existence of barren plateaus in RPQCs [40] rely on time-local expressions of the gradient of a loss function

such as Eq. 14. This also applies to the step-wise ansatz. However, in our ansatz given by Eq. 3, the expression is

$$\partial_{\boldsymbol{\theta}_{1,1}}\mathcal{L}_{\boldsymbol{\theta}}^{E} = i \int_0^1 \sin(\pi t') \langle 0|U_{t'}^0 [U_1^{t'} H_{\mathrm{p}} U_{t'}^1, H_1] U_0^{t'}|0\rangle \, dt',$$

$$(17)$$

where $U_a^b$ is the time-evolution operator from the time $a$ to the time $b \geq a$. For $a \geq b$ it is $U_a^b = (U_b^a)^\dagger$. The variance of this expression includes all possible covariances of time-local changes to the protocols $\boldsymbol{\theta}(t)$, which differs substantially from the variances in RPQCs. Further, in the parameter space of $\boldsymbol{\theta}(t)$, the unitaries $U_0^{t'}$ and $U_{t'}^1$ are neither necessarily independent in the sense of the Haar measure nor guaranteed to be 2-designs. Therefore, the analytical argument for RPQCs [40] does not apply to our ansatz. In particular, the argument generates no statement about the scaling behavior.

In Fig. 6 (a), we show the results of the step-wise ansatz. We find that the variance is independent of the amount of qubits $n_{\mathrm{q}}$ for small $|\boldsymbol{\theta}|_{\mathrm{max}}$. For increasing $|\boldsymbol{\theta}|_{\mathrm{max}}$, the variance decays exponentially with $|\boldsymbol{\theta}|_{\mathrm{max}}$ with slopes that are independent of $n_{\mathrm{q}}$. More importantly, the variance decays exponentially as a function of $n_{\mathrm{q}}$ with a log-scale slope of roughly $\ln(\frac{1}{2})$, as indicated by the equally spaced lines. The step-wise ansatz is reminiscent of a continuous Trotterized limit of parameterized circuits and therefore these results are consistent with barren plateau studies on RPQCs [40].

In Fig. 6 (b), we show the results for our ansatz. The variances show asymptotic behavior as functions of $|\boldsymbol{\theta}|_{\mathrm{max}}$. They converge at increasingly large values of $|\boldsymbol{\theta}|_{\mathrm{max}}$, which vastly exceed implementation actions that are necessary for highly entangling unitaries such as the QFT as we show in Fig. 4 (c). Thus, in our ansatz $|\boldsymbol{\theta}|_{\mathrm{max}}$ provides a useful hyperparameter for initialization that can be tuned to comparatively small values where the scaling with $n_{\mathrm{q}}$ is very favorable. Further, we find that the variance decreases as a function of $n_{\mathrm{q}}$ at a decreasing and non-exponential rate. This non-exponential scaling behavior indicates the reduction of barren plateaus in our ansatz, in particular during initialization.

## IV. CONCLUSION

We have proposed a system-agnostic ansatz of analog variational quantum algorithms rooted in quantum optimal control. The central feature of our ansatz is that it treats the Fourier coefficients of the time-controlled system parameters of a given Hamiltonian as trainable. Therefore, our ansatz is non-local in time and has no direct analog in discretized parameterized quantum circuits. By restricting the modes to low-end frequencies we keep the amount of trainable parameters low, while also ensuring smooth quantum protocols and sufficient controllability by construction. We have applied a measurement based stochastic quantum natural gradient optimization scheme to our ansatz to generate protocols
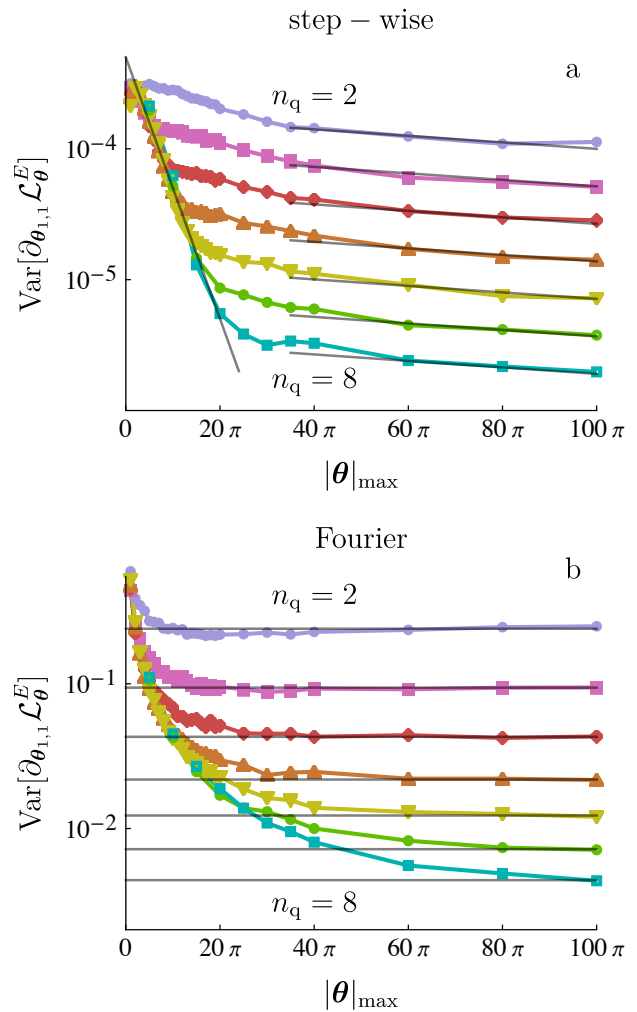


FIG. 6. **Variances of the energy objective gradient.** The variance of the gradient $\partial_{\boldsymbol{\theta}_{1,1}}\mathcal{L}_{\boldsymbol{\theta}}^{E}$ of the loss function $\mathcal{L}_{\boldsymbol{\theta}}^{E} = \langle 0|U_{\boldsymbol{\theta}}^\dagger[\sigma_z^1 \sigma_z^2]U_{\boldsymbol{\theta}}|0\rangle$ for up to 8 qubits for the step-wise ansatz (a) and our Fourier based ansatz (b) on a logarithmic scale. The parameters are sampled uniformly within a radius of $|\boldsymbol{\theta}|_{\mathrm{max}}$ for $n_{\mathrm{f}} = 128$. The lines are visual guides.

for the quantum Fourier transform for up to four qubits. Additionally, we have optimized ground state preparation processes for random problem Hamiltonians for up to six qubits. We compared the results to optimizations of the more commonly utilized step-wise parameterization ansatz. The results we have presented here are limited to few-qubit systems, as the numerical simulations on the native Hamiltonian level are computationally more demanding than the circuit-based counter-parts of conventional VQA. This does not translate into a lack of scalability in a true hybrid realization of the proposed method.

We have demonstrated that the convergence behavior of our ansatz outperforms the step-wise protocols in speed and consistency. We have found the effective im-

plementation action to be comparable and to remain reasonably small in both ansätze. We have analyzed the gradient along the loss landscape for both ansätze, and have shown that our ansatz shows non-exponentially decreasing variances with respect to the amount of qubits, indicating an absence of barren plateaus. The step-wise ansatz shows a characteristic exponential decay with the amount of qubits that is consistent with barren plateau studies on random parameterized quantum circuits. The scaling behavior of objective gradient variances for larger systems, as well as tuning the sampling range for initialization and its relation to expressibility, will be elaborated on elsewhere.

In conclusion, our ansatz is a promising candidate for mitigating barren plateaus in quantum algorithm optimization and presents an alternative to parameterizations that are discrete or local in time. This approach is of direct relevance for current efforts of implementing quantum computing, as it provides realistic and efficient access to optimal quantum algorithm protocols.

## ACKNOWLEDGMENTS

[1] Jacob Biamonte, Peter Wittek, Nicola Pancotti, Patrick Rebentrost, Nathan Wiebe, and Seth Lloyd. Quantum machine learning. *Nature*, 549(7671):195–202, 2017.

[2] M. Cerezo, Guillaume Verdon, Hsin-Yuan Huang, Lukasz Cincio, and Patrick J. Coles. Challenges and opportunities in quantum machine learning. *Nature Computational Science*, 2(9):567–576, 2022.

[3] M. Cerezo, Andrew Arrasmith, Ryan Babbush, Simon C. Benjamin, Suguru Endo, Keisuke Fujii, Jarrod R. McClean, Kosuke Mitarai, Xiao Yuan, Lukasz Cincio, and Patrick J. Coles. Variational quantum algorithms. *Nature Reviews Physics*, 3(9):625–644, 2021.

[4] Dave Wecker, Matthew B. Hastings, and Matthias Troyer. Progress towards practical quantum variational algorithms. *Phys. Rev. A*, 92:042303, Oct 2015.

[5] Alberto Peruzzo, Jarrod McClean, Peter Shadbolt, Man-Hong Yung, Xiao-Qi Zhou, Peter J. Love, Alán Aspuru-Guzik, and Jeremy L. O'Brien. A variational eigenvalue solver on a photonic quantum processor. *Nature Communications*, 5(1):4213, 2014.

[6] Xavier Bonet-Monroig, Hao Wang, Diederick Vermetten, Bruno Senjean, Charles Moussa, Thomas Bäck, Vedran Dunjko, and Thomas E. O'Brien. Performance comparison of optimization methods on variational quantum algorithms. *Phys. Rev. A*, 107:032407, Mar 2023.

[7] Kishor Bharti, Alba Cervera-Lierta, Thi Ha Kyaw, Tobias Haug, Sumner Alperin-Lea, Abhinav Anand, Matthias Degroote, Hermanni Heimonen, Jakob S. Kottmann, Tim Menke, Wai-Keong Mok, Sukin Sim, Leong-Chuan Kwek, and Alán Aspuru-Guzik. Noisy intermediate-scale quantum algorithms. *Rev. Mod. Phys.*, 94:015004, Feb 2022.

[8] John Preskill. Quantum Computing in the NISQ era and beyond. *Quantum*, 2:79, August 2018.

[9] Jarrod R McClean, Jonathan Romero, Ryan Babbush, and Alán Aspuru-Guzik. The theory of variational hybrid quantum-classical algorithms. *New Journal of Physics*, 18(2):023023, feb 2016.

[10] Leo Zhou, Sheng-Tao Wang, Soonwon Choi, Hannes Pichler, and Mikhail D. Lukin. Quantum approximate optimization algorithm: Performance, mechanism, and implementation on near-term devices. *Phys. Rev. X*, 10:021067, Jun 2020.

[11] Stuart Hadfield, Zhihui Wang, Bryan O'Gorman, Eleanor G. Rieffel, Davide Venturelli, and Rupak Biswas. From the quantum approximate optimization algorithm to a quantum alternating operator ansatz. *Algorithms*, 12(2), 2019.

[12] Maria Schuld, Ilya Sinayskiy, and Francesco Petruccione. The quest for a quantum neural network. *Quantum Information Processing*, 13(11):2567–2586, 2014.

[13] Amira Abbas, David Sutter, Christa Zoufal, Aurelien Lucchi, Alessio Figalli, and Stefan Woerner. The power of quantum neural networks. *Nature Computational Science*, 1(6):403–409, 2021.

[14] Kerstin Beer, Dmytro Bondarenko, Terry Farrelly, Tobias J. Osborne, Robert Salzmann, Daniel Scheiermann, and Ramona Wolf. Training deep quantum neural networks. *Nature Communications*, 11(1):808, 2020.

[15] Kunal Sharma, M. Cerezo, Lukasz Cincio, and Patrick J. Coles. Trainability of dissipative perceptron-based quantum neural networks. *Phys. Rev. Lett.*, 128:180505, May 2022.

[16] Iris Cong, Soonwon Choi, and Mikhail D. Lukin. Quantum convolutional neural networks. *Nature Physics*, 15(12):1273–1278, 2019.

[17] Arthur Pesah, M. Cerezo, Samson Wang, Tyler Volkoff, Andrew T. Sornborger, and Patrick J. Coles. Absence of barren plateaus in quantum convolutional neural networks. *Phys. Rev. X*, 11:041011, Oct 2021.

[18] M Cerezo and Patrick J Coles. Higher order derivatives of quantum neural networks with barren plateaus. *Quantum Science and Technology*, 6(3):035006, jun 2021.

[19] K. Mitarai, M. Negoro, M. Kitagawa, and K. Fujii. Quantum circuit learning. *Phys. Rev. A*, 98:032309, Sep 2018.

[20] Sumeet Khatri, Ryan LaRose, Alexander Poremba, Lukasz Cincio, Andrew T. Sornborger, and Patrick J. Coles. Quantum-assisted quantum compiling. *Quantum*, 3:140, May 2019.

[21] M. E. S. Morales, J. D. Biamonte, and Z. Zimborás. On the universality of the quantum approximate optimization algorithm. *Quantum Information Processing*, 19(9):291, 2020.

[22] Jacob Biamonte. Universal variational quantum computation. *Phys. Rev. A*, 103:L030401, Mar 2021.

[23] Patrick Doria, Tommaso Calarco, and Simone Mon-

tangero. Optimal control technique for many-body quantum dynamics. *Phys. Rev. Lett.*, 106:190501, May 2011.

[24] Tommaso Caneva, Tommaso Calarco, and Simone Montangero. Chopped random-basis quantum optimization. *Phys. Rev. A*, 84:022326, Aug 2011.

[25] S. Lloyd and S. Montangero. Information theoretical analysis of quantum optimal control. *Phys. Rev. Lett.*, 113:010502, Jul 2014.

[26] Steffen J. Glaser, Ugo Boscain, Tommaso Calarco, Christiane P. Koch, Walter Köckenberger, Ronnie Kosloff, Ilya Kuprov, Burkhard Luy, Sophie Schirmer, Thomas Schulte-Herbrüggen, Dominique Sugny, and Frank K. Wilhelm. Training schrödinger's cat: quantum optimal control. *The European Physical Journal D*, 69(12):279, 2015.

[27] Jun Li, Xiaodong Yang, Xinhua Peng, and Chang-Pu Sun. Hybrid quantum-classical approach to quantum optimal control. *Phys. Rev. Lett.*, 118:150503, Apr 2017.

[28] Shai Machnes, Elie Assémat, David Tannor, and Frank K. Wilhelm. Tunable, flexible, and efficient optimization of control pulses for practical qubits. *Phys. Rev. Lett.*, 120:150401, Apr 2018.

[29] Christiane P. Koch, Ugo Boscain, Tommaso Calarco, Gunther Dirr, Stefan Filipp, Steffen J. Glaser, Ronnie Kosloff, Simone Montangero, Thomas Schulte-Herbrüggen, Dominique Sugny, and Frank K. Wilhelm. Quantum optimal control in quantum technologies. strategic report on current status, visions and goals for research in europe. *EPJ Quantum Technology*, 9(1):19, 2022.

[30] Alicia B. Magann, Christian Arenz, Matthew D. Grace, Tak-San Ho, Robert L. Kosut, Jarrod R. McClean, Herschel A. Rabitz, and Mohan Sarovar. From pulses to circuits and back again: A quantum optimal control perspective on variational quantum algorithms. *PRX Quantum*, 2:010101, Jan 2021.

[31] Alexandre Choquette, Agustin Di Paolo, Panagiotis Kl. Barkoutsos, David Sénéchal, Ivano Tavernelli, and Alexandre Blais. Quantum-optimal-control-inspired ansatz for variational quantum algorithms. *Phys. Rev. Research*, 3:023092, May 2021.

[32] Navin Khaneja, Timo Reiss, Cindie Kehlet, Thomas Schulte-Herbrüggen, and Steffen J. Glaser. Optimal control of coupled spin dynamics: design of nmr pulse sequences by gradient ascent algorithms. *Journal of Magnetic Resonance*, 172(2):296–305, 2005.

[33] Marin Bukov, Alexandre G. R. Day, Dries Sels, Phillip Weinberg, Anatoli Polkovnikov, and Pankaj Mehta. Reinforcement learning in different phases of quantum control. *Phys. Rev. X*, 8:031086, Sep 2018.

[34] Murphy Yuezhen Niu, Sergio Boixo, Vadim N. Smelyanskiy, and Hartmut Neven. Universal quantum control through deep reinforcement learning. *npj Quantum Information*, 5(1):33, 2019.

[35] Zhi-Cheng Yang, Armin Rahmani, Alireza Shabani, Hartmut Neven, and Claudio Chamon. Optimizing variational quantum algorithms using pontryagin's minimum principle. *Phys. Rev. X*, 7:021027, May 2017.

[36] V.G. Boltyanski, R.V. Gamkrelidze, E.F. Mishchenko, and L.S. Pontryagin. The maximum principle in the theory of optimal processes of control. *IFAC Proceedings Volumes*, 1(1):464–469, 1960. 1st International IFAC Congress on Automatic and Remote Control, Moscow, USSR, 1960.

[37] Samson Wang, Enrico Fontana, M. Cerezo, Kunal Sharma, Akira Sone, Lukasz Cincio, and Patrick J. Coles. Noise-induced barren plateaus in variational quantum algorithms. *Nature Communications*, 12(1):6961, 2021.

[38] Carlos Ortiz Marrero, Mária Kieferová, and Nathan Wiebe. Entanglement-induced barren plateaus. *PRX Quantum*, 2:040316, Oct 2021.

[39] Taylor L. Patti, Khadijeh Najafi, Xun Gao, and Susanne F. Yelin. Entanglement devised barren plateau mitigation. *Phys. Rev. Research*, 3:033090, Jul 2021.

[40] Jarrod R. McClean, Sergio Boixo, Vadim N. Smelyanskiy, Ryan Babbush, and Hartmut Neven. Barren plateaus in quantum neural network training landscapes. *Nature Communications*, 9(1):4812, 2018.

[41] Martin Larocca, Piotr Czarnik, Kunal Sharma, Gopikrishnan Muraleedharan, Patrick J. Coles, and M. Cerezo. Diagnosing Barren Plateaus with Tools from Quantum Optimal Control. *Quantum*, 6:824, September 2022.

[42] Andrew Arrasmith, Zoë Holmes, M Cerezo, and Patrick J Coles. Equivalence of quantum barren plateaus to cost concentration and narrow gorges. *Quantum Science and Technology*, 7(4):045015, aug 2022.

[43] Tyler Volkoff and Patrick J Coles. Large gradients via correlation in random parameterized quantum circuits. *Quantum Science and Technology*, 6(2):025008, jan 2021.

[44] Eric R. Anschuetz and Bobak T. Kiani. Quantum variational algorithms are swamped with traps. *Nature Communications*, 13(1):7760, 2022.

[45] M. Cerezo, Akira Sone, Tyler Volkoff, Lukasz Cincio, and Patrick J. Coles. Cost function dependent barren plateaus in shallow parametrized quantum circuits. *Nature Communications*, 12(1):1791, 2021.

[46] A V Uvarov and J D Biamonte. On barren plateaus and cost function locality in variational quantum algorithms. *Journal of Physics A: Mathematical and Theoretical*, 54(24):245301, May 2021.

[47] Fernando G. S. L. Brandão, Aram W. Harrow, and Michał Horodecki. Local random quantum circuits are approximate polynomial-designs. *Communications in Mathematical Physics*, 346(2):397–434, 2016.

[48] Zoë Holmes, Kunal Sharma, M. Cerezo, and Patrick J. Coles. Connecting ansatz expressibility to gradient magnitudes and barren plateaus. *PRX Quantum*, 3:010313, Jan 2022.

[49] Eric R. Anschuetz. Critical points in quantum generative models, 2023.

[50] Adrián Pérez-Salinas, Radoica Draškić, Jordi Tura, and Vedran Dunjko. Reduce&chop: Shallow circuits for deeper problems, 2023.

[51] Viswanath Ramakrishna and Herschel Rabitz. Relation between quantum computing and quantum controllability. *Phys. Rev. A*, 54:1715–1716, Aug 1996.

[52] S. G. Schirmer, H. Fu, and A. I. Solomon. Complete controllability of quantum systems. *Phys. Rev. A*, 63:063410, May 2001.

[53] Chae-Yeun Park and Nathan Killoran. Hamiltonian variational ansatz without barren plateaus, 2023.

[54] Joonho Lee, William J. Huggins, Martin Head-Gordon, and K. Birgitta Whaley. Generalized unitary coupled cluster wave functions for quantum computation. *Journal of Chemical Theory and Computation*, 15(1):311–324, 01 2019.

[55] Katharina Kormann, Sverker Holmgren, and Hans O. Karlsson. A fourier-coefficient based solution of an opti-

mal control problem in quantum chemistry. *Journal of Optimization Theory and Applications*, 147(3):491–506, 2010.

[56] Yao Song, Junning Li, Yong-Ju Hai, Qihao Guo, and Xiu-Hao Deng. Optimizing quantum control pulses with complex constraints and few variables through autodifferentiation. *Phys. Rev. A*, 105:012616, Jan 2022.

[57] Jiazhao Tian, Haibin Liu, Yu Liu, Pengcheng Yang, Ralf Betzholz, Ressa S. Said, Fedor Jelezko, and Jianming Cai. Quantum optimal control using phase-modulated driving fields. *Phys. Rev. A*, 102:043707, Oct 2020.

[58] Jochen Scheuer, Xi Kong, Ressa S Said, Jeson Chen, Andrea Kurz, Luca Marseglia, Jiangfeng Du, Philip R Hemmer, Simone Montangero, Tommaso Calarco, Boris Naydenov, and Fedor Jelezko. Precise qubit control beyond the rotating wave approximation. *New Journal of Physics*, 16(9):093022, sep 2014.

[59] Diederik P. Kingma and Jimmy Ba. Adam: A method for stochastic optimization. *CoRR*, abs/1412.6980, 2015.

[60] James Stokes, Josh Izaac, Nathan Killoran, and Giuseppe Carleo. Quantum Natural Gradient. *Quantum*, 4:269, May 2020.

[61] R B Stinchcombe. Ising model in a transverse field. i. basic theory. *Journal of Physics C: Solid State Physics*, 6(15):2459, aug 1973.

[62] Matthias C. Caro, Hsin-Yuan Huang, Nicholas Ezzell, Joe Gibbs, Andrew T. Sornborger, Lukasz Cincio, Patrick J. Coles, and Zoë Holmes. Out-of-distribution generalization for learning quantum dynamics. *Nature Communications*, 14(1):3751, 2023.

[63] Ryan Levy, Di Luo, and Bryan K. Clark. Classical shadows for quantum process tomography on near-term quantum computers, 2021.

[64] Marcel Neugebauer, Laurin Fischer, Alexander Jäger, Stefanie Czischek, Selim Jochim, Matthias Weidemüller, and Martin Gärttner. Neural-network quantum state tomography in a two-qubit experiment. *Phys. Rev. A*, 102:042604, Oct 2020.

[65] G. Tóth, W. Wieczorek, D. Gross, R. Krischek, C. Schwemmer, and H. Weinfurter. Permutationally invariant quantum tomography. *Phys. Rev. Lett.*, 105:250403, Dec 2010.

[66] Marcus Cramer, Martin B. Plenio, Steven T. Flammia, Rolando Somma, David Gross, Stephen D. Bartlett, Olivier Landon-Cardinal, David Poulin, and Yi-Kai Liu. Efficient quantum state tomography. *Nature Communications*, 1(1):149, 2010.

[67] Ryan LaRose, Arkin Tikku, Étude O'Neel-Judy, Lukasz Cincio, and Patrick J. Coles. Variational quantum state diagonalization. *npj Quantum Information*, 5(1):57, 2019.

## Appendix A: Quantum Natural Gradient

In order to estimate the gradient of $\mathcal{L}_{\boldsymbol{\theta}}$, we modify a single component $\theta_{j,k}$ by a small amount $\delta = 10^{-7}$. This results in slightly altered time-evolution operators $U_{\boldsymbol{\theta}}^{j,k} = U_{\boldsymbol{\theta}+\delta\hat{e}_{j,k}}$ and values for the objective $\mathcal{L}_{\boldsymbol{\theta}+\delta\hat{e}_{j,k}}$. This gives access to the finite difference estimate

$$\frac{\partial \mathcal{L}_{\boldsymbol{\theta}}}{\partial \theta_{j,k}} \approx \frac{\mathcal{L}_{\boldsymbol{\theta}+\delta\hat{e}_{j,k}} - \mathcal{L}_{\boldsymbol{\theta}}}{\delta}. \tag{A1}$$

We do this for all possible $j$ and $k$ and write

$$\vec{\nabla}\mathcal{L}_{\boldsymbol{\theta}} = \sum_{j,k} \frac{\partial \mathcal{L}_{\boldsymbol{\theta}}}{\partial \theta_{j,k}} \hat{e}_{j,k}. \tag{A2}$$

The quantum natural gradient update $\Delta\boldsymbol{\theta}$ is then given by [60]

$$g(\Delta\boldsymbol{\theta}) = -\eta \vec{\nabla}\mathcal{L}_{\boldsymbol{\theta}} \tag{A3}$$

where $\eta$ is a dynamical learning rate following the ADAM algorithm with standard parameters and a step-size of 0.01 [59]. The quantum natural gradient considers the underlying geometry of the parameterized states using the Fubini-Study metric $g$ which has the components

$$g_{(i,k)}^{(j,l)} = \text{Re}[\langle\partial_{\boldsymbol{\theta}_{i,q}}\psi|\partial_{\boldsymbol{\theta}_{j,l}}\rangle - \langle\partial_{\boldsymbol{\theta}_{i,q}}\psi|\psi\rangle\langle\psi|\partial_{\boldsymbol{\theta}_{j,l}}\psi\rangle]$$
$$\approx \text{Re}[\langle r|U_{\boldsymbol{\theta}}^{\dagger,i,q}U_{\boldsymbol{\theta}}^{j,l}|r\rangle - \langle r|U_{\boldsymbol{\theta}}^{\dagger,i,q}U_{\boldsymbol{\theta}}|r\rangle\langle r|U_{\boldsymbol{\theta}}^{\dagger}U_{\boldsymbol{\theta}}^{j,l}|r\rangle]. \tag{A4}$$

The corresponding operator products are naturally expressed as longer time-evolution operators of the same form as Eq. 2 with the given parameters $\boldsymbol{\theta}$ as

$$U_{\boldsymbol{\theta}}^{\dagger,i,q}U_{\boldsymbol{\theta}} = \hat{T}[e^{-i\int_0^2 \sum_{j,k}(\boldsymbol{\theta}_{j,k}+\delta\hat{e}_{j,k}\hat{e}_{i,q}\Theta(t-1))\sin(\pi kt)H_j dt}], \tag{A5}$$

and analogously $U_{\boldsymbol{\theta}}^{\dagger,i,q}U_{\boldsymbol{\theta}}^{j,l}$ and $U_{\boldsymbol{\theta}}^{\dagger}U_{\boldsymbol{\theta}}^{j,l}$. $\Theta$ is the Heaviside-function such that the parameter $\theta_{i,q}$ is slightly altered by $\delta$ at $t = 1$. The Fubini-Study metric $g$ with respect to $|r\rangle = U_r |0\rangle^{\otimes n}$ can be measured by evaluating $\langle 0|^{\otimes n_q} U_r^{\dagger}U_{\boldsymbol{\theta}}^{\dagger,i,q}U_{\boldsymbol{\theta}}U_r |0\rangle^{\otimes n_q}$. Solving the linear system of Eq. A3 yields the quantum natural gradient descent step. For very large experimental setups, determining the curvature with respect to only a select subset of $\boldsymbol{\theta}$ can be a beneficial compromise in terms of time-efficiency.

## 4.5 Publication VIII: Quantum Gate Optimization for Rydberg Architectures in the Weak-Coupling Limit

N. Heimann, <u>L. Broers</u>, N. Pintul, T. Petersen, K. Sponselee, A. Ilin, C. Becker, and L. Mathey — **arXiv:2306.08691 (Under review at Phys. Rev. Research)**

This collaboration was motivated by the recent advancements of both neutral atom quantum computing architectures, and quantum machine learning methods. The variational optimization of quantum algorithms promises resourceful utilization of noisy intermediate-scale quantum (NISQ) devices. The Rydberg architecture of neutral atoms displays a promising candidate for utilizing such algorithms. This work is a preprint, and potentially subject to changes.

In this work, first-authored by Nicolas Heimann, we have considered the optimization of implementations of the controlled NOT gate on the native Hamiltonian level of neutral atoms in tweezer arrays. In this setup, Raman pulses control the single-qubit actions on a hyperfine sub-space, while a global Rabi pulse controls the transition from this logical sector into highly excited Rydberg states. These Rydberg states have a large polarizability and interact via Van-der-Waals terms. We have optimized the Raman and Rabi pulses under realistic constraints in order to implement a CNOT gate. During this optimization, we have fixed the interatomic distances and considered a global Rabi pulse that acts on both atoms identically. We have found that within these restrictions the optimization works very reliably. In particular, we have highlighted the weak-coupling limit in which the algorithm converges to high-fidelity solutions consistently, provided that the interaction does not go below a critical threshold. Further, introducing fluctuations into the interatomic distances in a high-fidelity solution leads to a transformation error that strongly depends on the mean interatomic distance. For small distances, i.e. in the Rydberg blockade regime, these transformation errors are small. Our results show that they are also small in the weak-coupling limit of large distances. However, the transformation error increases drastically for intermediate distances. Further, we have considered the general restriction of controlling one class of transformations globally, i.e. identically for all qubits, and showed that it maintains the computational universality of the Hamiltonian independent of system size. This result suggests the possibility of NISQ architectures that work on a restricted set of parameters by design while maintaining universality.

My contribution to this work included conceptualizing and implementing the numerics of the quantum simulation and the optimization algorithm together with NH. NH performed and evaluated the numerical studies. I have performed the analytical calculations on the dynamical Lie algebra under the restriction to either global Rabi or global Raman pulses and showed the resulting computational universality. NP, TP, KS, AI provided insight into experimental details that informed the restrictions and energy scales of the parameterization, and have also contributed to the conception of the project and the writing of the manuscript. This collaboration was performed under the joint supervision of CB and LM.

# Quantum Gate Optimization for Rydberg Architectures in the Weak-Coupling Limit

Nicolas Heimann,[1, 2, 3, *] Lukas Broers,[1, 2] Nejira Pintul,[1, 2] Tobias Petersen,[1, 2] Koen Sponselee,[1, 2] Alexander Ilin,[1, 2, 3] Christoph Becker,[1, 2] and Ludwig Mathey[1, 2, 3]

[1] *Zentrum für Optische Quantentechnologien, Universität Hamburg, 22761 Hamburg, Germany*
[2] *Institut für Quantenphysik, Universität Hamburg, 22761 Hamburg, Germany*
[3] *The Hamburg Centre for Ultrafast Imaging, 22761 Hamburg, Germany*

We demonstrate machine learning assisted design of a two-qubit gate in a Rydberg tweezer system. Two low-energy hyperfine states in each of the atoms represent the logical qubit and a Rydberg state acts as an auxiliary state to induce qubit interaction. Utilizing a hybrid quantum-classical optimizer, we generate optimal pulse sequences that implement a CNOT gate with high fidelity, for experimentally realistic parameters and protocols, as well as realistic limitations. We show that local control of single qubit operations is sufficient for performing quantum computation on a large array of atoms. We generate optimized strategies that are robust for both the strong-coupling, blockade regime of the Rydberg states, but also for the weak-coupling limit. Thus, we show that Rydberg-based quantum information processing in the weak-coupling limit is a desirable approach, being robust and optimal, with current technology.

## I. INTRODUCTION

Rydberg tweezer arrays have evolved into an intriguing and promising platform for quantum computing [1–3] and quantum simulation [4, 5]. These devices support the preparation of scalable, nearly defect-free systems [6–8], high fidelity single-qubit operations [9] and the implementation of two-qubit gates via Rydberg states [10–14]. This includes the quantum gate design based on Rydberg blockade, that corresponds to the widely explored regime of strong van-der-Waals interaction strength and small interatomic distances. Furthermore, qubit architectures based on alkaline-earth and alkaline-earth-like atoms [15], such as strontium [16, 17] and ytterbium atoms [18–20], have desirable features such as long-lived decoupled nuclear spin states that are suitable to be used as qubit states, as well as single-photon Rydberg transitions for implementing fast two-qubit gates. The existence of a meta-stable clock state further allows for elaborate qubit schemes allowing novel error correction strategies and shelving operations for non-destructive mid-circuit readout [21]. Further design options include triple magic trapping of qubit and Rydberg states [22], and local Rydberg control via manipulation of inner shell electrons [23].

Optimization methods, such as quantum machine learning and quantum optimal control are a powerful and versatile approach of operating and controlling quantum dynamics in a way that is optimal or near-optimal according to a desired metric. In particular, variational quantum algorithms [24–26] are a class of algorithms which utilize a generalized quantum circuit with parameterized gates to transform the synthesis of quantum algorithm solutions into an optimization problem. This approach can be extended towards quantum optimal control [27–31] and has been utilized in different noisy intermediate-scale quantum devices [32], such as trapped ions [33–36],

superconducting qubits [37–40] and neutral atoms [41–45]. Recently, time-optimal gates have been constructed using quantum optimal control [41] and realized experimentally [46].

In this paper, we demonstrate machine learning assisted design of a controlled-not (CNOT) gate in Rydberg tweezer systems. The logical qubit states are implemented in two hyperfine states of the atoms, which are controlled via Raman pulses. Additionally we consider a Rydberg state in each atom, which can be Rabi-driven from one of the hyperfine states. We demonstrate that using either a global Rabi protocol, driving the Rydberg transition of all atoms, and individual Raman protocols, driving the hyperfine transition of individual atoms, or a global Raman protocol and individual Rabi protocols, are sufficient to support universal quantum computing. We focus on the case of a global Rabi protocol and individual Raman protocols. The parameters of the atomic states and the magnitudes of the Rabi and Raman protocols, as well as an applied magnetic field, are modeled after $^{171}$Yb atom tweezers. However, we emphasize that our analysis and results are directly applicable to all Rydberg tweezer systems, as they include realistic conditions of operation of current devices. We consider a fixed total operation time, and determine fidelity-optimal implementations based on a hybrid quantum-classical optimizer algorithm. We use the van-der-Waals interaction strength as a variable parameter. We identify the minimal van-der-Waals interaction that supports an implementation of a CNOT gate with high fidelity, and find that the fidelity saturates beyond that magnitude. We determine the robustness of our optimal implementations with respect to fluctuations of the distance between the atoms. We find that the implementations are not only robust in the blockade but also in the weak-coupling limit. We propose this regime to be utilized for robust optimal quantum computing under realistic conditions with current technology.

This paper is organized as follows. In Sect. II, we introduce the model and method used throughout the
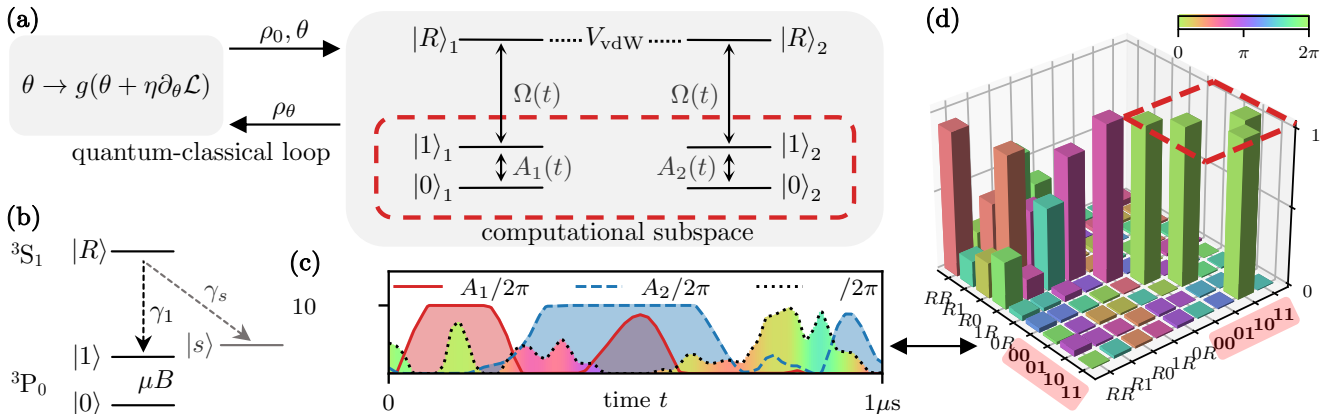
Figure 1. **Optimization platform.** **(a)** Hybrid quantum-classical optimization scheme. The hyperfine states $|0\rangle$ and $|1\rangle$ act as logical states, forming the computational subspace depicted as red-dashed lines, and can be manipulated individually by the control Raman protocol $A_1(t)$ and the target Raman protocol $A_2(t)$, in which qubit 1 is the control qubit and qubit 2 is the target qubit. The Rabi protocol $\Omega(t)$ controls transfer between the state $|1\rangle$ and a highly excited Rydberg state $|R\rangle$. The protocols $\Omega(t)$, $A_j(t)$ and $B$ are parameterized by the transformation parameters $\theta = \{\theta_i\}$. The atoms are coupled via the van-der-Waals interaction $V_{\mathrm{vdW}}$ of the Rydberg states. For a transformation parameter set $\theta$, an initial state $\rho_0$ is propagated yielding the final state $\rho_\theta$. This time propagation in the quantum unit is controlled by a classical unit synthesising the loss function $\mathcal{L}$ from $\rho_\theta$, allowing to optimize the transformation parameters $\theta$. **(b)** Level diagram and dissipation channels, for our main example of $^{171}$Yb. We consider decay from $|R\rangle$ into $|1\rangle$, as well as into $|s\rangle$ which is otherwise decoupled dynamically, and is introduced to model population loss. The magnetic field $B$ defines the Zeeman splitting of the two hyperfine states. **(c)** A high fidelity protocol implementing the CNOT transformation. The Rabi protocol $\Omega(t)$ and the Raman protocols $A_j(t)$ are constrained by a maximal frequency of $\Omega_{\max} = A_{\max} = 2\pi \times 10\mathrm{MHz}$. The phase $\phi(t)$ of the Rabi protocol $\Omega(t)$ is depicted by the filling color. **(d)** The transformation $U$ corresponding to the pulse sequence shown in (c), depicted at the time $\tau = 1\mu\mathrm{s}$. The CNOT operation is clearly visible in the computational subspace, enclosed by the red-dashed square.

manuscript. In Sect. III, we present the performance and the protocols of the hybrid quantum-classical optimizer within the weak-coupling limit. In Sect. IV, we show how spatial fluctuations affect the gate fidelity for a realistic range of interatomic distances. In Sect. V, we conclude.

## II. MODEL

We consider neutral atoms trapped individually in optical tweezers. For each of the atoms we consider two long-lived, low-energy states that constitute a qubit, written as $|0\rangle$ and $|1\rangle$. Additionally we consider a highly excited Rydberg state $|R\rangle$, and a generic state $|s\rangle$ that we use to model the decay of the Rydberg state. The Rydberg state $|R\rangle$ is utilized for its strong van-der-Waals interaction between two atoms in this state, providing a non-linearity to design two-qubit gates. We consider the Hamiltonian

$$H = \sum_j H_j + \sum_{i,j} V_{\mathrm{vdW}}^{i,j} |R\rangle_i |R\rangle_j \langle R|_i \langle R|_j, \quad (1)$$

where

$$V_{\mathrm{vdW}}^{i,j} = \frac{\hbar C_6}{|r_i - r_j|^6} \quad (2)$$

is the van-der-Waals interaction between the $i$th and $j$th atom at the respective positions $r_i$ and $r_j$. $C_6$ is the co-efficient of the van-der-Waals interaction and depends on

the specific atom species and Rydberg state. We choose $C_6 = 1\mathrm{THz} \cdot \mu\mathrm{m}^6$, as inspired by [15, 20], as a typical magnitude for Rydberg atoms of two-electron atoms. $H_j$ is the local Hamiltonian of the $j$th atom. It is

$$H_j = \frac{\hbar}{2} \begin{pmatrix} 0 & \Omega(t) & 0 \\ \Omega^*(t) & 0 & A_j(t) \\ 0 & A_j(t) & 0 \end{pmatrix} + \frac{1}{2} \begin{pmatrix} 0 & 0 & 0 \\ 0 & \mu B & 0 \\ 0 & 0 & -\mu B \end{pmatrix}, \quad (3)$$

and operates on the states $\{|R\rangle, |1\rangle, |0\rangle\}$. The two logical qubit states $|0\rangle$ and $|1\rangle$ are realized as hyperfine states of the atom, and $\mu B$ is the Zeeman splitting between them induced by an external magnetic field $B$, where $2\mu$ is the difference of the magnetic moments. The corresponding Zeeman shift of the Rydberg state is normalized to zero in the rotating frame. $A_j(t)$ is the Raman coupling between the logical qubit states $|0\rangle_j$ and $|1\rangle_j$ of atom $j$, which derives from a two-photon transition, and which we consider to be real-valued. This assumption is realized by optimizing the excitation light homogeneity to select the phases of each coupling $A_j(t)$ [8] to zero. $\Omega(t) = |\Omega(t)|e^{-i\phi(t)}$ is the complex-valued Rabi coupling between the levels $|1\rangle_j$ and $|R\rangle_j$ for all $j$, i.e. in a global fashion. As discussed in App. D, we show that using either a global Rabi coupling and individual Raman couplings, or indvidual Rabi couplings and a global Raman coupling, is sufficient for universal quantum computing. We illustrate the hybrid quantum-classical optimizer in Fig. 1. For a given optimization task, we

limit the Rabi and Raman coupling by maximal values of $\Omega_{\max}$ and $A_{\max}$. Here, we focus on the case of $\Omega_{\max} = A_{\max} = 2\pi \times 10$MHz, but note that our approach equally applies to the general case, i.e. $\Omega_{\max} \neq A_{\max}$. In App. C, we show that a value of $\Omega_{\max} = 2\pi \times 10$MHz is sufficient for our analysis. The maximum gradient of the Rabi phase $\phi(t)$ is $\partial_t \phi_{\max} = \pm\pi/100$ns, motivated by typical acousto-optic modulator bandwidths. The magnetic field $B$ is assumed to be stationary, but can be chosen arbitrarily within the range $B_{\min} \leq B \leq B_{\max}$, where $B_{\min} = 100$G and $B_{\max} = 200$G which corresponds to $0.1$MHz $\leq \mu B/h \leq 0.2$MHz.

The finite lifetime $1/\gamma$ of the Rydberg state leads to decoherence. We consider two contributions to the decay, black body radiation and spontaneous decay [47]. Both black body radiation and spontaneous decay induce transitions out of the Rydberg state $|R\rangle$ to states other than $|0\rangle$, $|1\rangle$, and $|R\rangle$. We model these states with an auxiliary state $|s\rangle$. Spontaneous decay also induces transitions from the Rydberg state $|R\rangle$ to the state $|1\rangle$, i.e. the computational subspace. In Fig. 1 (b) we illustrate this effective dissipation model. The dynamics of the system are governed by the Lindblad master equation

$$\dot{\rho} = -\frac{i}{\hbar}[H, \rho] + \sum_{ij} \mathcal{D}[L_i^j]\rho, \qquad (4)$$

where $\mathcal{D}[L]\rho = L\rho L^\dagger - \frac{1}{2}\{L^\dagger L, \rho\}$, with the Lindblad operators $L_j^s = \sqrt{\gamma_s}|s\rangle_j \langle R|_j$ and $L_j^1 = \sqrt{\gamma_1}|1\rangle_j \langle R|_j$ of the $j$th atom. The total decay rate of the Rydberg state obeys $\gamma = \gamma_s + \gamma_1$ where $\gamma_s = 20\gamma_1$ [21]. Here we choose typical values of the lifetime of the Rydberg state of $1/\gamma = 10\mu$s, $100\mu$s and $500\mu$s [15]. We assume magic-trapping between $|1\rangle$ and $|R\rangle$ and neglect losses arising from turning off the trap during gate operations as well as dephasing contributions [18, 48].

Gradient Ascent Pulse Engineering (GRAPE) [49] is a quantum optimal control technique to construct pulse sequences, which determine the dynamical evolution of the system, such that a desired target transformation $U$ is realized. Note that we employ this method for non-unitary dynamics, given in Eq. 4. We consider a general Hamiltonian $H_\theta(t) = H_0 + \sum_k f_k(t;\theta)h_k + \text{h.c.}$, where $f_k(t;\theta)$ are complex-valued functions, $\theta = \{\theta_i\}$ are parameters, which are to be optimized, and the $h_k$ are hermitian operators. The transformation parameters $\theta$ correspond to a transformation which we evaluate for a given state $\rho_0$ by integrating Eq. (4) over the algorithm time $\tau$. We denote the final state a particular parameter set $\theta$ as $\rho_\theta$. Throughout this work, we fix the algorithm time to $\tau = 1$µs. The optimization is performed with respect to the objective, i.e. the loss function, which in our case we define as

$$\mathcal{L} = 1 - F_\theta = 1 - \frac{1}{4}\langle|\text{Tr}(\rho_\theta^\dagger P U \rho_0 U^\dagger P)|\rangle_{\rho_0}, \qquad (5)$$

where $F_\theta$ is the fidelity and $P = \sum_q |q\rangle\langle q|$ is the projector onto the computational subspace, which is $P =$

$|00\rangle\langle00| + |01\rangle\langle01| + |10\rangle\langle10| + |11\rangle\langle11|$. $\langle\cdot\rangle_{\rho_0}$ is the average over 32 initial random product states $\rho_0 = \bigotimes_i \rho_i$ sampled from the Bloch spheres of the computational subspaces. The batch size of 32 is an empirical value that provides efficient optimization. The optimal transformation parameters $\theta_{\text{opt}} = \text{argmin}_\theta \mathcal{L}$ are inferred via stochastic gradient descent [50]. First, the loss $\mathcal{L}$ is evaluated given the transformation parameters $\theta$. Next, the parameters are varied as $\theta_i \rightarrow \theta_i + \epsilon$ by a small amount $\epsilon = 10^{-8}$, and subsequently the modified loss $\mathcal{L}_i$ is evaluated. The first order gradient is approximated by the finite difference $\partial\mathcal{L}/\partial\theta_i = (\mathcal{L}_i - \mathcal{L})/\epsilon$ and the parameters are then updated as

$$\theta_i \rightarrow g_i\left(\theta_i + \eta_i \frac{\partial\mathcal{L}}{\partial\theta_i}\right), \qquad (6)$$

where $\eta_i$ are dynamically adapted learning rates according to the ADAM method [51]. The functions $g_i$ impose constraints on the protocols. Note that these constraints do not affect the gradient. We refer to this step in the algorithm as a training epoch and illustrate this in Fig. 1 (a). Optimization occurs by iterating over the training epochs until convergence.

The central example that we apply this optimization method to, is the optimal implementation of the CNOT gate. So the number of atoms $N_a = 2$. However, we emphasize that the methodology presented here naturally applies to atom systems with larger numbers. The notion of a global Rabi coupling implies that for $N_a > 2$, any additional atom besides the two involved in the CNOT operation will also experience the global coupling $\Omega(t)$. This results in a transformation on these other qubits, which may be undesired. Our optimization method can also be utilized to learn a coupling $A_{j>2}(t)$ that implements the identity operation, in the presence of the fixed global coupling $\Omega(t)$. We emphasize that this is possible, because even in the case of arbitrarily many neutral atoms, a single global Rabi coupling is sufficient for universal quantum computing. For example, the resulting transformation on the other qubits can be mitigated efficiently by moving the other atoms sufficiently far apart such that the van-der-Waals interaction becomes negligible while additionally applying the control coupling $A_1(t)$. By construction of the CNOT gate, the control coupling $A_1(t)$ will transform the qubit states $|0\rangle$ and $|1\rangle$ into themselves, respectively. This will in general only result in a relative phase between these states which can be corrected. Alternatively, for alkaline-earth-like atoms like $^{171}$Yb, the omg qubit architecture [15] can be employed to realize local two-qubit gates despite the global coupling $\Omega(t)$. Since the Rydberg excitation originates from the meta-stable $^3P_0$ state it is straight forward to site-selectively shelve atoms in the ground state qubit $^1S_0$ if the CNOT gate is not desired. We note that universal quantum computing is equally possible in the case in which there is a global Raman coupling that is equal for all atoms, and the Rabi couplings are applied to the atoms individually. This result is both conceptually in-

teresting, as well as of experimental relevance, because it suggests an alternative, minimal set of experimental control parameters. We expand on this implementation approach elsewhere. In this work, we focus on the case of a global Rabi pulse. For details on the computational universality under these constraints, see App. D.

We optimize the transformation parameters $\theta$, which parameterize $\Omega(t)$ and $A_j(t)$ as stepwise functions which we linearly interpolate in the dynamics, as well as $B$ which we consider to be constant during the time evolution such that it is represented by a single parameter. We refer to these parameterizations as the Rabi protocol $\Omega(t)$, the control Raman protocol $A_1(t)$ and the target Raman protocol $A_2(t)$. We give a detailed account of the parameterization in App. A. We construct the initial protocols $|\Omega^0(t)|$ and $A_j^0(t)$ to be positive and slowly varying. The initial phase of the Rabi protocol $\phi^0(t)$ is generated via a random walk starting at $\phi^0(0) = 0$, see App. B.

In Fig. 1 (c) we illustrate the Rabi protocol $\Omega(t)$ and the Raman protocols $A_j(t)$ of a high fidelity CNOT realization. In Fig. 1 (d) we show the transformation corresponding to this high fidelity realization. The CNOT transformation is visible in the computational subspace, while the transformation on the remaining subspace is arbitrary.

## III.   WEAK-COUPLING SOLUTIONS

In this section, we identify optimal implementations of the CNOT gate in the weak-coupling limit, i.e. based on dynamical phase accumulation. We consider a large interatomic distance $r \approx 10\mu m$, of the two atoms. For this distance, the van-der-Waals interaction is small compared to the maximal Rabi frequency $V_{vdW} \ll \hbar\Omega_{max}$ allowing for occupation of the Rydberg-Rydberg state $|R\rangle \otimes |R\rangle$, where $V_{vdW} = V_{vdW}^{1,2}(r)$, based on the van-der-Waals interaction in Eq. 2, with $r = |r_1 - r_2|$. Hence, the magnitude of the nonlinearity is limited by the algorithm time $\tau$ and the interaction strength $V_{vdW}$. We introduce the dimensionless gate action

$$\Phi = \tau V_{vdW}/\hbar, \qquad (7)$$

as the maximally achievable non-linear phase accumulation. Note that as the algorithm time $\tau = 1\mu s$ is fixed, the gate action $\Phi$ is equivalently a measure of the interaction strength. In this section we treat the interaction strength $V_{vdW}$ as an external parameter rather than a trainable parameter.

In Fig. 2 (a) we show the average of the infidelity $1 - \langle F \rangle_\theta$ over 15 optimized protocols [52] for the target transformation of the CNOT gate. We show this as a function of the gate action $\Phi$ and the number of training epochs in the absence of dissipation, i.e. for $\gamma = 0$. We find that for small gate actions $\Phi \lesssim 2\pi$ the optimization algorithm does not generate a high-fidelity protocol. The fidelity steadily increases with increasing gate action $\Phi$.

We fit the expression $1 - \langle F \rangle_\theta = A(\Phi - \Phi_c)^2$ in the vicinity of the critical gate action $\Phi_c$ and find that $A = 0.37$ and $\Phi_c = 2.018\pi$. For values of $2\pi < \Phi < 3\pi$, the infidelity converges to approximately $1 - \langle F \rangle_\theta \approx 7 \times 10^{-3}$, which indicates sufficient gate action $\Phi$, i.e. it indicates that sufficient time and interaction is provided to generate a two-qubit operation. For gate actions of values $\Phi > 3\pi$ the infidelity decreases further as it converges to approximately $1 - \langle F \rangle_\theta \approx 3 \times 10^{-3}$. In this regime, we observe more efficient optimization behavior that reaches values of $1 - \langle F \rangle_\theta < 10^{-2}$ after roughly 200 training epochs. In the case of no interaction, the transformation consists of single-qubit transformations that cannot implement the CNOT operation.

In Fig. 2 (b) we show representations of transformations in the computational subspace for $\Phi = \pi/2$ and $\Phi = 4\pi$. In the case of insufficient interaction strength, for $\Phi = \pi/2$, the implemented transformation is visibly distinct from a CNOT gate. In the case of sufficiently large interaction strength, for $\Phi = 4\pi$, a high fidelity implementation of the CNOT gate is visible. In Fig. 2 (c) we show the infidelity of optimized protocols as a function of the gate action $\Phi$, with and without dissipation. We use the dissipative parameters discussed in Sect. II. For small values of $\Phi$, the gate fidelity is independent of dissipation, as the Rydberg state is weakly occupied during the protocol. For increasing values of $\Phi$, the protocols approach high fidelities with dissipation, but with an increased infidelity. This increase of the infidelity is also visible along the learning trajectory for $\Phi = 4\pi$ as we show in Fig. 2 (d). Here we see that dissipation results in a lower bound of the infidelity of the optimized protocol. This lower bound is reduced by minimizing the occupation time of the Rydberg states $|R\rangle_j$. The maximal Rabi frequency $\Omega_{max}$ provides a limitation of this optimization in the case of a fixed algorithm time $\tau$.

We find that the optimization method provides high fidelity protocols in the presence of experimentally motivated dissipation. Generally, higher fidelities than what we present can be achieved by increasing the number of training epochs. In a realistic setup, measurement noise, laser phase- and intensity noise, and spatial fluctuations are additional challenges, that can be included in our optimization approach.

## IV.   SPATIAL FLUCTUATIONS

To demonstrate the robustness properties of the optimal implementations that we have obtained, we include fluctuations of the distance between the two Rydberg atoms. In an experimental realization, these fluctuations might derive from thermal motion of each of the atoms in the tweezer potentials, or fluctuations of the tweezer potential itself. We consider spatial distances between the two atoms of $4\mu m$ to $11\mu m$, which interpolates between the blockade regime and the weak-coupling limit.

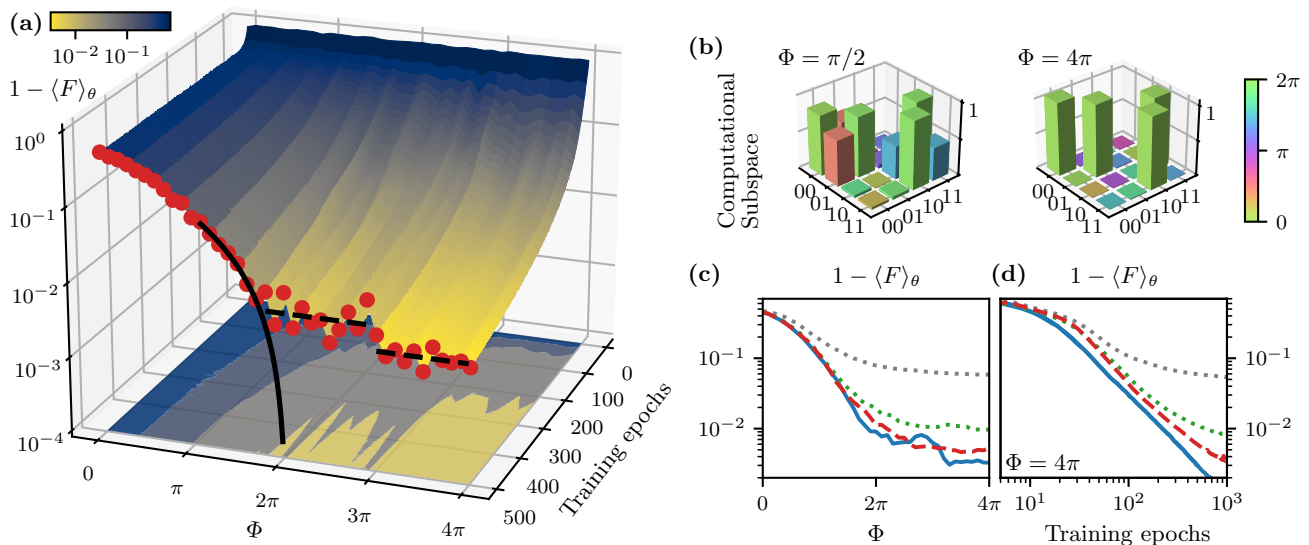We consider a high-fidelity implementation $U$ of the

Figure 2. **Gate optimization in the weak-coupling limit.** **(a)** We display the infidelity $1 - \langle F \rangle_\theta$ as a function of the gate action $\Phi$ and the number of training epochs. The infidelity after 500 training epochs is depicted as red dots. Near $\Phi_c \approx 2\pi$, we fit the infidelity $1 - \langle F \rangle_\theta$ with the fitting function $\Phi = \sqrt{(1 - \langle F \rangle_\theta)/A} + \Phi_c$, which we depict as a black solid line, while the black-dashed lines depict the converged infidelities of $7 \times 10^{-3}$ for $2\pi < \Phi < 3\pi$ and $3 \times 10^{-3}$ for $\Phi > 3\pi$. **(b)** Optimized gate transformations in the computational subspace. For a gate action of $\Phi = \pi/2$ the infidelity is $1 - \langle F \rangle_\theta = 0.25$, indicating that the gate action is insufficient to create a high fidelity protocol. For $\Phi = 4\pi$ we show a transformation having an infidelity of $1 - \langle F \rangle_\theta = 3 \times 10^{-4}$, indicating sufficient gate action. The phases of the matrix elements are encoded on a cyclic color map. **(c-d)** Infidelity without dissipation (blue) and with dissipation of values $1/\gamma = 500\mu s$ (red-dashed), $1/\gamma = 100\mu s$ (green-dotted) and $1/\gamma = 10\mu s$ (grey-dotted). **(c)** Infidelity after 500 training epochs as a function of the gate action $\Phi$. **(d)** The infidelity during training for a fixed gate action $\Phi = 4\pi$ as a function of the number of training epochs. Dissipation results in slower reduction of the infidelity with the number of training epochs and determines the lower bound of the infidelity that is visible for large dissipation, i.e. for large $\gamma$.

CNOT gate, which has been optimized for a specific interaction strength $V_{\mathrm{vdW}}$ and zero dissipation $\gamma = 0$. We now introduce fluctuations of the atom distance, i.e. $r \to r + \delta r(t)$, in which the spatial fluctuations $\delta r(t)$ are sampled from a normal distribution $N(0, \sigma_r)$ at a frequency of 512MHz. Based on a single, stochastic time series $r + \delta r(t)$, we now determine the modified, time-dependent interaction strength

$$V_{\mathrm{vdW}}(t) = \frac{\hbar C_6}{|r + \delta r(t)|^6}. \tag{8}$$

We use this interaction strength to generate the time-evolution $\tilde{U}(\sigma_r)$, while keeping all other features of the protocol unchanged, i.e. we use the same $\Omega(t)$, $A_j(t)$ and $B$ protocol. To quantify to what degree the fidelity is reduced due to the spatial fluctuations, we define the average transformation error as

$$\epsilon(\sigma_r) = 1 - \frac{1}{4} \langle |\mathrm{Tr}(\tilde{U}(\sigma_r)^\dagger \mathrm{CNOT})| \rangle_{\delta r(t), \theta}. \tag{9}$$

Here we take the statistical average of the implementation error over 50 sampled trajectories of $\delta r(t)$ and 10 high fidelity protocols provided by transformation parameters $\theta$ optimized from different initial values.

In Fig. 3 we show the transformation error $\epsilon(\sigma_r)$ as a function of the interatomic distance $r$ for various val-

ues of the standard deviation $\sigma_r$. At large distances of about $r > 9\mu m$, the protocols are only weakly susceptible to spatial fluctuations. Since the van-der-Waals interaction in Eq. 2 scales with $r^{-6}$, the gradient falls off rapidly as the mean distance $r$ increases. Because of this rapid fall-off, fluctuations of $r$ result in a smaller and smaller increase of the error $\epsilon(\sigma_r)$ with increasing $r$. On the other hand, in the blockade regime at distances of $r < 5\mu m$, the interaction strength $V_{\mathrm{vdW}}$ dominates the maximal Rabi frequency $\Omega_{\max}$. In this limit, transitions into the Rydberg-Rydberg state $|R\rangle_1 |R\rangle_2$ are highly suppressed. Therefore, the spatial fluctuations do not induce large errors in this limit either but are more noticeable than in the weak-coupling limit, in this example. However, in the intermediate regime of $5\mu m < r < 8\mu m$, the transformation error $\epsilon(\sigma_r)$ is highly susceptible to spatial fluctuations. At these interatomic distances, the van-der-Waals interaction and the the maximal Rabi frequency are of the same order, i.e. $V_{\mathrm{vdW}} \sim \hbar \Omega_{\max}$. Hence, the optimized protocols are highly susceptible to spatial fluctuations, making these intermediate interatomic distances undesirable in any realization. The robustness with respect to spatial fluctuations is one of the key features that makes the Rydberg blockade regime attractive for quantum computing purposes [10]. However, we emphasize that in the weak-coupling limit, the system is equally
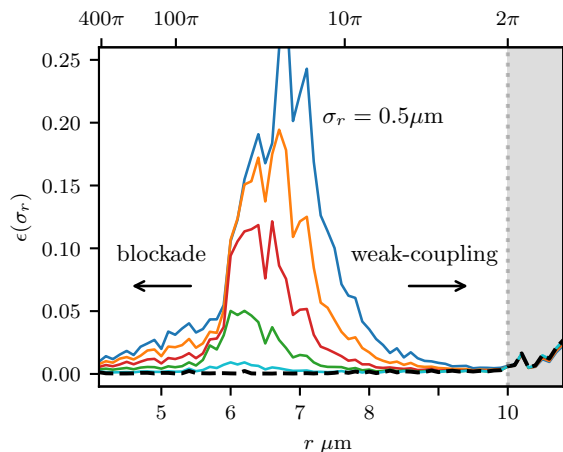
Figure 3. **Robustness against spatial fluctuations.** The transformation error $\epsilon(\sigma_r)$ in the presence of spatial fluctuations, for the noise parameter $\sigma_r = 0.5, 0.4, 0.3, 0.2, 0.1, 0\mu m$ (blue, orange, red, green, cyan, black dashed), and as a function of the interatomic distance $r$. For small ($< 6\mu m$) and large ($> 8\mu m$) distances the optimal implementations are robust against spatial fluctuations. For intermediate distances of $r = 6 - 8\mu m$, the system is strongly susceptible to spatial fluctuations and the relative error grows quickly as a function of $\sigma_r$. The vertical dashed line depicts the minimum distance required to implement the CNOT gate, see Fig. 2 for reference.

robust against spatial fluctuations [53].

## V. CONCLUSION

In conclusion, we have demonstrated quantum gate optimization of a CNOT gate in a Rydberg architecture under experimentally motivated constraints, via machine learning. The two qubit states are two long-lived hyperfine states of each of the two atoms. Additionally, we include a Rydberg state in each atom in our model, as an auxilliary state to provide a van-der-Waals interaction to create a two-qubit gate. These atoms are held in optical tweezers, at fixed distance. The model and parameter choices are based on 171-Yb, such as the dissipative prop-

erties of the Rydberg state. However, we emphasize that our approach is universally applicable to Rydberg architectures. We assume that the long-lived hyperfine states can be driven by Raman protocols, and the transition from one of the hyperfine states to the Rydberg state by a single global Rabi protocol. We show that utilizing either individual Raman protocols for each atom and a global Rabi protocol for both atoms, or individual Rabi protocols for each atom and a global Raman protocol for both atoms, is sufficient for universal quantum computing. Focusing on the case of individual Raman protocols for each atom and a global Rabi protocol, we utilize a hybrid quantum-classical optimization approach, based on gradient ascent pulse engineering (GRAPE), to determine protocols that implement a high fidelity CNOT gate. Keeping the total algorithm time of the protocols fixed at 1µs, we scan the optimal implementations as a function of the interaction strength. Finally, we map out the robustness of the optimal protocols against spatial fluctuations of the interatomic distance. We find that both for the weak-coupling limit and for the blockade regime, the implementations are robust. However, the intermediate regime, at which the maximal Rabi frequency is comparable to the van-der-Waals interaction, is not robust and thus undesirable. Additional imperfections, such as doppler shifts or imperfections in the laser intensities, will be explored elsewhere. We also note that the weak-coupling regime enables gate implementations in tweezer arrays with strongly suppressed next-nearest interactions, resulting in more straight-forward implementations. With these results, we have demonstrated the immediate and significant impact that hybrid quantum-classical optimization, or machine learning inspired methods in general, have on quantum gate design. Going forward, this suggests systematic, large-scale, and in-depth utilization of quantum machine learning methods.

[1] M. Saffman, Quantum computing with atomic qubits and Rydberg interactions: progress and challenges, Journal of Physics B: Atomic, Molecular and Optical Physics **49**, 202001 (2016).

[2] S. R. Cohen and J. D. Thompson, Quantum computing with circular rydberg atoms, PRX Quantum **2**, 030322 (2021).

[3] T. M. Graham, Y. Song, J. Scott, C. Poole, L. Phuttitarn, K. Jooya, P. Eichler, X. Jiang, A. Marra, B. Grinke-meyer, M. Kwon, M. Ebert, J. Cherek, M. T. Lichtman, M. Gillette, J. Gilbert, D. Bowman, T. Ballance, C. Campbell, E. D. Dahl, O. Crawford, N. S. Blunt, B. Rogers, T. Noel, and M. Saffman, Multi-qubit entanglement and algorithms on a neutral-atom quantum computer, Nature **604**, 457 (2022).

[4] M. Morgado and S. Whitlock, Quantum simulation and computing with rydberg-interacting qubits, AVS Quantum Science **3**, 023501 (2021).

[5] A. Browaeys and T. Lahaye, Many-body physics with individually controlled Rydberg atoms, Nature Physics **16**, 132 (2020).

[6] K. Schymik, B. Ximenez, E. Bloch, D. Dreon, A. Signoles, F. Nogrette, D. Barredo, A. Browaeys, and T. Lahaye, In situ equalization of single-atom loading in large-scale optical tweezer arrays, Phys. Rev. A **106**, 022611 (2022).

[7] D. Barredo, S. d. Léséleuc, V. Lienhard, T. Lahaye, and A. Browaeys, An atom-by-atom assembler of defect-free arbitrary two-dimensional atomic arrays, Science **354**, 1021 (2016).

[8] M. Endres, H. Bernien, A. Keesling, H. Levine, E. R. Anschuetz, A. Krajenbrink, C. Senko, V. Vuletic, M. Greiner, and M. D. Lukin, Atom-by-atom assembly of defect-free one-dimensional cold atom arrays, Science **354**, 1024 (2016).

[9] I. S. Madjarov, J. P. Covey, A. L. Shaw, J. Choi, A. Kale, A. Cooper, H. Pichler, V. Schkolnik, J. R. Williams, and M. Endres, High-fidelity entanglement and detection of alkaline-earth rydberg atoms, Nature Physics **16**, 857 (2020).

[10] D. Jaksch, J. I. Cirac, P. Zoller, S. L. Rolston, R. Côté, and M. D. Lukin, Fast Quantum Gates for Neutral Atoms, Physical Review Letters **85**, 2208 (2000).

[11] M. D. Lukin, M. Fleischhauer, R. Cote, L. M. Duan, D. Jaksch, J. I. Cirac, and P. Zoller, Dipole Blockade and Quantum Information Processing in Mesoscopic Atomic Ensembles, Physical Review Letters **87**, 037901 (2001).

[12] M. Saffman and T. G. Walker, Analysis of a quantum logic device based on dipole-dipole interactions of optically trapped Rydberg atoms, Physical Review A **72**, 022347 (2005).

[13] E. Urban, T. A. Johnson, T. Henage, L. Isenhower, D. D. Yavuz, T. G. Walker, and M. Saffman, Observation of Rydberg blockade between two atoms, Nature Physics **5**, 110 (2009).

[14] T. Wilk, A. Gaëtan, C. Evellin, J. Wolters, Y. Miroshnychenko, P. Grangier, and A. Browaeys, Entanglement of Two Individual Neutral Atoms Using Rydberg Blockade, Physical Review Letters **104**, 010502 (2010).

[15] N. Chen, L. Li, W. Huie, M. Zhao, I. Vetter, C. H. Greene, and J. P. Covey, Analyzing the rydberg-based optical-metastable-ground architecture for $^{171}$Yb nuclear spins, Phys. Rev. A **105**, 052438 (2022).

[16] A. Cooper, J. P. Covey, I. S. Madjarov, S. G. Porsev, M. S. Safronova, and M. Endres, Alkaline-Earth Atoms in Optical Tweezers, Physical Review X **8**, 041055 (2018).

[17] M. A. Norcia, A. W. Young, and A. M. Kaufman, Microscopic Control and Detection of Ultracold Strontium in Optical-Tweezer Arrays, Physical Review X **8**, 041054 (2018).

[18] J. T. Wilson, S. Saskin, Y. Meng, S. Ma, R. Dilip, A. P. Burgers, and J. D. Thompson, Trapping alkaline earth rydberg atoms optical tweezer arrays, Phys. Rev. Lett. **128**, 033201 (2022).

[19] A. Jenkins, J. W. Lis, A. Senoo, W. F. McGrew, and A. M. Kaufman, Ytterbium nuclear-spin qubits in an optical tweezer array, Phys. Rev. X **12**, 021027 (2022).

[20] S. Ma, A. P. Burgers, G. Liu, J. Wilson, B. Zhang, and J. D. Thompson, Universal Gate Operations on Nuclear Spin Qubits in an Optical Tweezer Array of Yb 171 Atoms, Physical Review X **12**, 021028 (2022).

[21] Y. Wu, S. Kolkowitz, S. Puri, and J. Thompson, Erasure conversion for fault-tolerant quantum computing in alkaline earth rydberg atom arrays, Nature Communications **13**, 4657 (2022).

[22] T. Topcu and A. Derevianko, Possibility of triple magic trapping of clock and rydberg states of divalent atoms in optical lattices, Journal of Physics B: Atomic, Molecular and Optical Physics **49**, 144004 (2016).

[23] A. P. Burgers, S. Ma, S. Saskin, J. Wilson, M. A. Alarcón, C. H. Greene, and J. D. Thompson, Controlling rydberg excitations using ion-core transitions in alkaline-earth atom-tweezer arrays, PRX Quantum **3**, 020326 (2022).

[24] M. Cerezo, A. Arrasmith, R. Babbush, S. Benjamin, S. Endo, K. Fujii, J. R. McClean, K. Mitarai, X. Yuan, L. Cincio, and P. Coles, Variational quantum algorithms, Nature Reviews Physics (2021).

[25] A. Choquette, A. Di Paolo, P. K. Barkoutsos, D. Sénéchal, I. Tavernelli, and A. Blais, Quantum-optimal-control-inspired ansatz for variational quantum algorithms, Phys. Rev. Res. **3**, 023092 (2021).

[26] Z. Yang, A. Rahmani, A. Shabani, H. Neven, and C. Chamon, Optimizing variational quantum algorithms using pontryagin's minimum principle, Phys. Rev. X **7**, 021027 (2017).

[27] C. Brif, R. Chakrabarti, and H. Rabitz, Control of quantum phenomena: past, present and future, New Journal of Physics **12**, 075008 (2010).

[28] T. Caneva, T. Calarco, and S. Montangero, Chopped random-basis quantum optimization, Physical Review A **84**, 022326 (2011).

[29] A. B. Magann, C. Arenz, M. D. Grace, T. Ho, R. L. Kosut, J. R. McClean, H. A. Rabitz, and M. Sarovar, From pulses to circuits and back again: A quantum optimal control perspective on variational quantum algorithms, PRX Quantum **2**, 010101 (2021).

[30] C. P. Koch, U. Boscain, T. Calarco, G. Dirr, S. Filipp, S. Glaser, R. Kosloff, S. Montangero, T. Schulte-Herbrueggen, D. Sugny, and F. Wilhelm, Quantum optimal control in quantum technologies. strategic report on current status, visions and goals for research in europe, EPJ Quantum Technology **9** (2022).

[31] L. Broers and L. Mathey, Reducing barren plateaus in quantum algorithm protocols (2021), arXiv:2111.08085.

[32] J. Preskill, Quantum Computing in the NISQ era and beyond, Quantum **2**, 79 (2018).

[33] M. Kang, Q. Liang, B. Zhang, S. Huang, Y. Wang, C. Fang, J. Kim, and K. R. Brown, Batch optimization of frequency-modulated pulses for robust two-qubit gates in ion chains, Phys. Rev. Appl. **16**, 024039 (2021).

[34] C. Figgatt, A. Ostrander, N. M. Linke, K. A. Landsman, D. Zhu, D. Maslov, and C. Monroe, Parallel entangling operations on a universal ion-trap quantum computer, Nature **572**, 368 (2019).

[35] T. Choi, S. Debnath, T. A. Manning, C. Figgatt, Z.-X. Gong, L.-M. Duan, and C. Monroe, Optimal quantum control of multimode couplings between trapped ion qubits for scalable entanglement, Phys. Rev. Lett. **112**, 190502 (2014).

[36] V. Nebendahl, H. Häffner, and C. F. Roos, Optimal control of entangling operations for trapped-ion quantum computing, Phys. Rev. A **79**, 012312 (2009).

[37] M. Werninghaus, D. J. Egger, F. Roy, S. Machnes, F. K. Wilhelm, and S. Filipp, Leakage reduction in fast superconducting qubit gates via optimal control, npj Quantum

Information **7**, 14 (2021).

[38] S. Huang and H. Goan, Optimal control for fast and high-fidelity quantum gates in coupled superconducting flux qubits, Phys. Rev. A **90**, 012318 (2014).

[39] D. J. Egger and F. K. Wilhelm, Optimized controlled-z gates for two superconducting qubits coupled through a resonator, Superconductor Science and Technology **27**, 014001 (2013).

[40] P. Rebentrost and F. K. Wilhelm, Optimal control of a leaking qubit, Phys. Rev. B **79**, 060507 (2009).

[41] S. Jandura and G. Pupillo, Time-Optimal Two- and Three-Qubit Gates for Rydberg Atoms, Quantum **6**, 712 (2022).

[42] M. Mohan, R. de Keijzer, and S. Kokkelmans, Robust control and optimal rydberg states for neutral atom two-qubit gates (2022), arXiv:2212.10159.

[43] S. Jandura, J. D. Thompson, and G. Pupillo, Optimizing rydberg gates for logical-qubit performance, PRX Quantum **4** (2023).

[44] M. H. Goerz, E. J. Halperin, J. M. Aytac, C. P. Koch, and K. B. Whaley, Robustness of high-fidelity rydberg gates with single-site addressability, Phys. Rev. A **90**, 032329 (2014).

[45] M. M. Müller, D. M. Reich, M. Murphy, H. Yuan, J. Vala, K. B. Whaley, T. Calarco, and C. P. Koch, Optimizing entangling quantum gates for physical systems, Phys. Rev. A **84**, 042315 (2011).

[46] S. J. Evered, D. Bluvstein, M. Kalinowski, S. Ebadi, T. Manovitz, H. Zhou, S. H. Li, A. A. Geim, T. T. Wang, N. Maskara, H. Levine, G. Semeghini, M. Greiner, V. Vuletic, and M. D. Lukin, High-fidelity parallel entangling gates on a neutral atom quantum computer (2023), arXiv:2304.05420.

[47] I. Cong, H. Levine, A. Keesling, D. Bluvstein, S. Wang, and M. D. Lukin, Hardware-efficient, fault-tolerant quantum computation with rydberg atoms, Phys. Rev. X **12**, 021049 (2022).

[48] S. Zhang, F. Robicheaux, and M. Saffman, Magic-wavelength optical traps for rydberg atoms, Phys. Rev. A **84**, 043408 (2011).

[49] N. Khaneja, T. Reiss, C. Kehlet, T. Schulte-Herbrüggen, and S. J. Glaser, Optimal control of coupled spin dynamics: design of NMR pulse sequences by gradient ascent algorithms, Journal of Magnetic Resonance **172**, 296 (2005).

[50] I. Goodfellow, Y. Bengio, and A. Courville, *Deep Learning* (MIT Press, 2016).

[51] D. Kingma and J. Ba, Adam: A method for stochastic optimization, International Conference on Learning Representations (2014).

[52] We choose the number of optimized protocols, with randomly sampled initial protocols, empirically.

[53] We note that if we expand this optimization to include the optimization of interatomic distances or spatial trajectories of the tweezer locations, this effect may be important to consider. The susceptibility to errors at intermediate distances will create learning pressure away from protocols that cross from the weak-coupling limit at large distances to the Rydberg blockade regime at small distances potentially inhibiting the convergence of the optimization.

## Appendix A: Protocols and parameterization

In the following we detail the parameterization of the protocols in our optimization method. We denote the concatenated parameters of the protocol as $\theta = \{\theta_\Omega, \theta_{\partial\phi}, \theta_{A_1}, \theta_{A_2}, \theta_B\}$. We represent the protocols $|\Omega(t)|$ and $A_j(t)$ in a step-wise discretized manner such that the elements of $\vartheta \in \theta_\Omega, \theta_{A_j}$ represent the amplitudes of respective protocols at $m$ discrete points in time. We linearly interpolate these step-wise representations $\vartheta \in \mathbb{R}^m$ on the temporal lattice with the step-size $\Delta t = \tau/(m-1)$. The interpolation is

$$s(\vartheta, t) = (1 - p_i)\vartheta_i + p_i \vartheta_{i+1}, \tag{A1}$$

where $i = \lfloor t/\Delta t \rfloor$ is the latest index corresponding to the time $t$ and $p_i = t/\Delta t - i$ is an interpolation weight. The amplitudes of the Rabi protocol $|\Omega(t)|$, the control Raman protocol $A_1(t)$ and the target Raman protocol $A_2(t)$ are then given by

$$|\Omega(t)| = s(\theta_\Omega, t) \tag{A2}$$
$$A_1(t) = s(\theta_{A_1}, t) \tag{A3}$$
$$A_2(t) = s(\theta_{A_2}, t). \tag{A4}$$

The phase $\phi(t)$ of the Rabi protocol $\Omega(t)$ is given by the stepwise differential parameterization

$$\phi(t) = s(\theta_\phi, t), \tag{A5}$$

where $\theta_{\phi,i} = \theta_{\phi,i-1} + \theta_{\partial\phi,i}$ and $\theta_{\phi,0} = \theta_{\partial\phi,0}$. This construction creates slowly varying phase protocols and avoids sudden phase-jumps. The magnetic field is given by the constant parameterization

$$B = \theta_B. \tag{A6}$$

In the presented analysis we consider a total number of $4 \times 64 + 1$ parameters, that is $\theta \in \mathbb{R}^{257}$. Further, as mentioned in the main text, we constrain the parameters in between minimal and maximal values. The constraints $g_i(\theta_i)$ in Eq. 6 are defined as follows

$$g_\Omega(\theta_{\Omega,i}) = \max(0, \min(\Omega_{\max}, \theta_{\Omega,i})) \tag{A7}$$
$$g_{A_1}(\theta_{A_1,i}) = \max(0, \min(A_{\max}, \theta_{A_1,i})) \tag{A8}$$
$$g_{A_2}(\theta_{A_2,i}) = \max(0, \min(A_{\max}, \theta_{A_2,i})) \tag{A9}$$
$$g_{\partial\phi}(\theta_{\partial_t\phi,i}) = \max(\partial_t\phi_{\min}, \min(\partial_t\phi_{\max}, \theta_{\partial\phi,i})) \tag{A10}$$
$$g_B(\theta_B) = \max(B_{\min}, \min(B_{\max}, \theta_B)), \tag{A11}$$

with $\Omega_{\max} = 2\pi \times 10\text{MHz}$, $A_{\max} = 2\pi \times 10\text{MHz}$, $\partial_t\phi_{\min} = -\pi/100\text{ns}$, $\partial\phi_{\min} = +\pi/100\text{ns}$, $B_{\min} = 100\text{G}$ and $B_{\max} = 200\text{G}$.

## Appendix B: Protocol initialization

We construct the initial parameters such that the resulting protocols vary slowly, start and end at zero, and
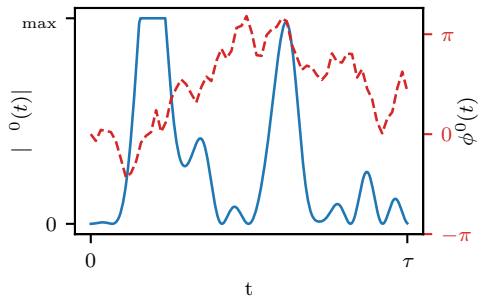
Figure 4. **Protocol initialization.** The initial Rabi protocol $\Omega(t)$ of algorithm time $\tau = 1\mu s$. The amplitude of a sample initial Rabi protocol $|\Omega^0(t)|$ (blue) contains 16 sinosiodal modes and has a maximal Rabi frequency of $\Omega_{max}$. The initial Raman protocols $A_1^0(t)$ and $A_2^0(t)$ are initialized by the same strategy. The phase of the initial Rabi protocol $\phi^0(t)$ (red-dashed) is given by a random walk starting at $\phi^0(0) = 0$.



Figure 5. **Maximal Rabi frequency.** High fidelity protocols are realized for $\Omega_{max} = 2\pi \times 10$MHz, with a gate action of $\Phi = 4\pi$ after 400 training epochs. Lower infidelities can be achieved with more training epochs.

are fairly well-behaved. We first consider a distribution of initial parameterizations

$$S = \left\{ \sum_k \phi_k \sin(k\pi t/\tau) \right\}, \qquad (B1)$$

where $\phi_k$ are random numbers from the uniform distributions $[-1/\sqrt{k}, +1/\sqrt{k}]$. We introduce this dependence on $k$ to emphasize slow modes. We initialize the transformation parameters $\theta_\Omega$, $\theta_{A_1}$ and $\theta_{A_2}$ such that the following initial protocols are realized

$$|\Omega^0(t)| = \Omega_{init} \min(1, s_\Omega^2(t)) \qquad (B2)$$
$$A_1^0(t) = A_{init} \min(1, s_{A_1}^2(t)) \qquad (B3)$$
$$A_2^0(t) = A_{init} \min(1, s_{A_2}^2(t)), \qquad (B4)$$

where we sample $s_\Omega$, $s_{A_1}$ and $s_{A_2}$ from the distribution $S$, $\Omega_{init}$ is the maximal frequency of the initial Rabi protocol and $A_{init}$ is the maximal frequency of the initial Raman protocols. Through out this work we scale the initial protocols by the corresponding maximal frequencies, i.e. $\Omega_{init} = \Omega_{max}$ and $A_{init} = A_{max}$. The parameters of the phase are initialized as $\theta_{\partial_\phi,0}^0 = 0$ and $\theta_{\partial_\phi,i}^0$ is uniformly sampled from $[-\delta, \delta]$. where $\delta \in \mathbb{R}^+$. Here we choose $\delta = 1.5$. Fig. 4 shows an example of a random initial Rabi protocol $\Omega^0(t)$. The initial magnetic field $B^0$ is sampled from the distribution $[B_{min}, B_{max}]$.

### Appendix C: Maximal Rabi frequency

The maximal Rabi frequency $\Omega_{max}$ provides a limitation on the minimally achievable infidelity $1 - F$ of the gate protocol. If $\Omega_{max}$ is not sufficiently large to complete a Rabi oscillation of one of the states $|1\rangle_1$ or $|1\rangle_2$ to one of the Rydberg states $|R\rangle_1$ or $|R\rangle_2$ during the protocol of algorithm time $\tau$, then no protocols with satisfactory fidelity can be constructed. In Fig. 5 we show the average
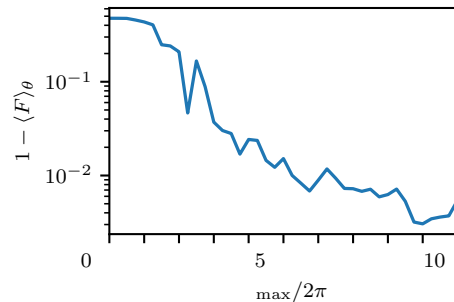
infidelity $1 - \langle F \rangle_\theta$ over several optimized protocols as a function of the Rabi frequency $\Omega_{max}$ for a fixed maximal Raman frequency of $A_{max} = 2\pi \times 10$MHz and a gate action of $\Phi = 4\pi$. For small values of the maximal Rabi frequency $\Omega_{max} < 2\pi \times 2$MHz, the infidelity displays a plateau of large values of roughly $1 - \langle F \rangle_\theta \approx 0.5$. With increasing $\Omega_{max} > 2\pi \times 2$MHz, the infidelity decreases. For $\Omega_{max} > 2\pi \times 8$MHz, the infidelity begins to saturate at values $1 - \langle F \rangle_\theta < 10^{-2}$. Note that the protocols are not necessarily fully converged and lower infidelities can be achieved with more training epochs. Therefore, a maximal Rabi frequency $\Omega_{max} = 2\pi \times 10$MHz is sufficient for our analysis.

### Appendix D: Universal Quantum Computing with Global Pulses

In the following we demonstrate that a single global Rabi coupling for $N_a$ neutral atoms is capable of universal quantum computing. We also show this for the case of a single global Raman coupling and invidiual Rabi couplings. We consider $N_a$ three-level systems consisting of the states $\{|R\rangle, |1\rangle, |0\rangle\}$, and the Hamiltonian

$$H = \mu B \sum_{j=1}^n \sigma_z^j + \sum_{j=1}^n A_j(t)\sigma_x^j + \sum_{j=1}^n (\Omega_x^j(t)\tau_x^j + \Omega_y^j(t)\tau_y^j) + H_I, \qquad (D1)$$

where

$$\sigma_x^j = \begin{pmatrix} 0 & 0 & 0 \\ 0 & 0 & 1 \\ 0 & 1 & 0 \end{pmatrix} \quad \sigma_y^j = \begin{pmatrix} 0 & 0 & 0 \\ 0 & 0 & -i \\ 0 & i & 0 \end{pmatrix} \quad \sigma_z^j = \begin{pmatrix} 0 & 0 & 0 \\ 0 & 1 & 0 \\ 0 & 0 & -1 \end{pmatrix}, \qquad (D2)$$

act on the subspace $\{|1\rangle, |0\rangle\}$ of the $j$th system.

$$\tau_x^j = \begin{pmatrix} 0 & 1 & 0 \\ 1 & 0 & 0 \\ 0 & 0 & 0 \end{pmatrix} \quad \tau_y^j = \begin{pmatrix} 0 & -i & 0 \\ i & 0 & 0 \\ 0 & 0 & 0 \end{pmatrix} \quad \tau_z^j = \begin{pmatrix} 1 & 0 & 0 \\ 0 & -1 & 0 \\ 0 & 0 & 0 \end{pmatrix}, \qquad (D3)$$

act on the subspace $\{|R\rangle, |1\rangle\}$ of the $j$th atom. Analogously, we also define the matrices on the subspace $\{|R\rangle, |0\rangle\}$ of the $j$th atom as

$$\nu_x^j = \begin{pmatrix} 0 & 0 & 1 \\ 0 & 0 & 0 \\ 1 & 0 & 0 \end{pmatrix} \qquad \nu_y^j = \begin{pmatrix} 0 & 0 & -i \\ 0 & 0 & 0 \\ i & 0 & 0 \end{pmatrix}. \qquad \text{(D4)}$$

The interaction term is

$$H_I = \sum_{\langle i,j \rangle} \frac{C_6}{(r_i(t) - r_j(t))^6} |R\rangle_i \otimes |R\rangle_j \langle R|_i \otimes \langle R|_j, \quad \text{(D5)}$$

where $r_j(t)$ is the real-space position of the $j$th atom. $\mu B$ is the Zeeman splitting due to a constant and global magnetic field $B$. $A_j(t)$ is the amplitude of the $j$th Raman coupling of the $j$th atom that control the transition between $|1\rangle_j$ and $|0\rangle_j$. $\Omega_{x,y}^j(t)$ are the Rabi coupling components of the $j$th atom that control the transition between $|1\rangle_j$ and $|R\rangle_j$. For convenience we denote the global sums of local operators as $S_z = \sum_{j=1}^n \sigma_z^j$, $T_x = \sum_{j=1}^n \tau_x^j$, $T_y = \sum_{j=1}^n \tau_y^j$ and $V = \sum_{i,j} V_{i,j}$. We consider the base set of generators contained in Eq. D1,

$$\mathcal{H}_0' = \{\sigma_x^1, \ldots, \sigma_x^n, S_z, \tau_x^1, \ldots, \tau_x^n, \tau_y^1, \ldots, \tau_y^n, V\}. \quad \text{(D6)}$$

We consider that $B > 0$ is always on, which makes controlling individual local rotations more difficult. We consider the rotating frame given by $U = \exp\{i\frac{1}{2}\mu B t S_z\}$, such that we reduce the base set of generators to

$$\mathcal{H}_0'' = \{\sigma_x^1, \ldots, \sigma_x^n, \tau_x^1, \ldots, \tau_x^n, \tau_y^1, \ldots, \tau_y^n, V\}, \quad \text{(D7)}$$

with all generators now being controllable individually from each other.

First, we consider the case in which $\Omega_{x,y}^j = \Omega_{x,y}$, such that the local operators $\tau_{x,y}^i$ are no longer individually controllable. The base set of generators becomes

$$\mathcal{H}_0 = \{\sigma_x^1, \ldots, \sigma_x^n, T_x, T_y, V\}. \quad \text{(D8)}$$

From these base generators we find the commutators

$$[\sigma_x^i, T_x] = \sum_{j=1}^n [\sigma_x^i, \tau_x^j] = -i\nu_y^i \quad \text{(D9)}$$

$$[\nu_y^i, \sigma_x^i] = -i\tau_x^i \quad \text{(D10)}$$

$$[\nu_y^i, T_y] = \sum_{j=1}^n [\nu_y^i, \tau_y^j] = -i\sigma_y^i. \quad \text{(D11)}$$

Eqs. D9 and D10 can be repeated analogously to obtain $\nu_x^i$ and $\tau_y^i$. This means that despite the global Rabi term that determines the transition between $|1\rangle_j$ and $|R\rangle_j$ for all $1 \le j \le N_a$, the local generators $\tau_{x,y}^i$ are part of the dynamical Lie algebra and therefore controllable individually. From Eq. D11 we see that that $\sigma_y^i$ is accessible, and therefore $\sigma_z^i$ is accessible as well. This allows full access to local single-qubit operations. Note that this means

the magnetic field $B$ was not necessary for computational purposes to begin with. However, in experimental setups it serves the purpose of providing non-degenerate levels $|0\rangle$ and $|1\rangle$ at all times. Since the transformation $U$ into the comoving frame does not affect the interaction term, i.e. $UVU^\dagger = V$, we find that the base set of generators in Eq. D8 is computationally universal on the logical space $\otimes_{j=1}^n \{|0\rangle^j, |1\rangle^j\}$. We demonstrate this by constructing specific examples of rotations around $\tau_x^i$, $\tau_y$, $\sigma_y^i$ and $\sigma_z^i$ by an arbitrary angle $\alpha$ as

$$e^{i\alpha\tau_x^i} = e^{i\frac{3\pi}{2}\sigma_x^i} e^{i\frac{3\pi}{2}T_x} e^{i\alpha\sigma_x^i} e^{i\frac{\pi}{2}T_x} e^{i\frac{\pi}{2}\sigma_x^i} \quad \text{(D12)}$$

$$e^{i\alpha\tau_y^i} = e^{i\frac{3\pi}{2}\sigma_x^i} e^{i\frac{3\pi}{2}T_y} e^{i\alpha\sigma_x^i} e^{i\frac{\pi}{2}T_y} e^{i\frac{\pi}{2}\sigma_x^i} \quad \text{(D13)}$$

$$e^{i\alpha\sigma_y^i} = e^{i\frac{3\pi}{2}\sigma_x^i} e^{i\frac{3\pi}{2}T_y} e^{i\frac{3\pi}{2}T_x} e^{i\alpha\sigma_x^i} e^{i\frac{\pi}{2}T_x} e^{i\frac{\pi}{2}T_y} e^{i\frac{\pi}{2}\sigma_x^i} \quad \text{(D14)}$$

$$e^{i\alpha\sigma_z^i} = e^{i\frac{7\pi}{4}\sigma_x^i} e^{i\frac{3\pi}{2}T_y} e^{i\frac{3\pi}{2}T_x} e^{i\alpha\sigma_x^i} e^{i\frac{\pi}{2}T_x} e^{i\frac{\pi}{2}T_y} e^{i\frac{\pi}{4}\sigma_x^i}. \quad \text{(D15)}$$

From these rotations, entanglement between qubits can be achieved utilizing $V$ in the canonical manner of Rydberg architectures.

Second, we consider the case of individual Rabi couplings $\Omega_{x,y}^j(t)$, but a single global Raman coupling $A_j(t) = A(t)$. Analogously to the previous case, the base set of generators then becomes

$$\mathcal{H}_0 = \{S_x, \tau_x^1, \ldots, \tau_x^n, \tau_y^1, \ldots, \tau_y^n, V\}. \quad \text{(D16)}$$

The argument follows analogously and we find that

$$[S_x, \tau_x^j] = \sum_{i=1}^n [\sigma_x^i, \tau_x^j] = -i\nu_y^j \quad \text{(D17)}$$

$$[\nu_y^i, \tau_x^i] = i\sigma_x^i \quad \text{(D18)}$$

$$[\nu_y^i, \tau_y^i] = -i\sigma_y^i, \quad \text{(D19)}$$

and therefore arbitrary single-qubit rotations can be constructed as

$$e^{i\alpha\sigma_x^i} = e^{i\frac{3\pi}{2}\tau_x^i} e^{i\frac{3\pi}{2}S_x} e^{i\alpha\tau_x^i} e^{i\frac{\pi}{2}S_x} e^{i\frac{\pi}{2}\tau_x^i} \quad \text{(D20)}$$

$$e^{i\alpha\sigma_y^i} = e^{i\frac{3\pi}{2}\tau_x^i} e^{i\frac{3\pi}{2}S_x} e^{i\alpha\tau_y^i} e^{i\frac{\pi}{2}S_x} e^{i\frac{\pi}{2}\tau_x^i} \quad \text{(D21)}$$

$$e^{i\alpha\sigma_z^i} = e^{i\frac{3\pi}{2}\tau_x^i} e^{i\frac{3\pi}{2}S_x} e^{i\frac{\pi}{4}\tau_x^i} e^{i\alpha\tau_x^i} e^{i\frac{7\pi}{4}\tau_y^i} e^{i\frac{\pi}{2}S_x} e^{i\frac{\pi}{2}\tau_x^i}, \quad \text{(D22)}$$

despite only global control over $S_x$. It again follows that the dynamical Lie algebra is capable of all necessary operations for universal quantum computing. Note in particular that the generator $S_z$ associated with the magnetic field was again not necessary for constructing arbitrary single-qubit rotations.

In this case of global Raman coupling, the Rabi couplings can be performed individually which means that there is no undesirable population in Rydberg states as overhead of unrelated transformations. The overhead transformation occurs only on the local $\sigma_x$ which is easily circumvented. We can perform a CNOT gate on the 1st

and 2nd qubit while in the Rydberg blockade radius as

$$\text{CNOT} = e^{i\frac{\pi}{2}\tau_x^2} R e^{i\pi\tau_x^1} R e^{i\frac{\pi}{2}\tau_x^2} \tag{D23}$$

$$R = e^{i\frac{\pi}{2}S_x} e^{i\frac{\pi}{4}\tau_x^2} e^{i\frac{\pi}{\sqrt{8}}(\tau_x^2+\tau_y^2)} e^{i\frac{\pi}{4}\tau_x^2} e^{i\frac{3\pi}{2}S_x}, \tag{D24}$$

in the presence of any amount of other qubits which by construction also experience the rotations generated by $S_x$. This transformation will in particular act on all these additional qubits as the identity, as desired. Finally, we note that the controlled-$Y$ gate is implemented more nat-

urally in this case as

$$\text{C(Y)} = e^{-i\frac{\pi}{2}\tau_x^2} e^{-i\frac{\pi}{4}S_x} e^{i\pi\tau_x^1} e^{i\frac{\pi}{4}S_x} e^{i\frac{\pi}{2}\tau_x^2}. \tag{D25}$$

Here it is implied that every transformation also contains the presence of the interaction term $V$ which is large enough to consider the system to be in the Rydberg blockade regime. We emphasize that the Rydberg blockade is not necessary for the arguments we make about universal quantum computing. We only consider the Rydberg blockade for the analytically constructed examples in Eqs. D23, D24 and D25.

# 5 Particle-Hole Symmetry in Superfluids

Superfluidity is the property of frictionless flow, found in ordered phases of ultracold and weakly interacting quantum systems. It is present in Bose-Einstein condensates (BECs) and also Bardeen-Cooper-Schrieffer (BCS) systems of weakly interacting neutral fermions. In the Ginzburg-Landau [368] theory of phase transitions, the order parameter of superfluids at low temperatures is described with a complex-valued scalar field. This order parameter characterizes the second-order phase transition of the particle density of BECs or the pairing-density in BCS theory. The low-energy physics of the order parameter that are captured within such mean-field theories are of immediate relevance for quantum simulators, and atomtronics.

Throughout this chapter, I provide an outline of the effective mean field theory that describes the dynamics of the order parameter of such systems. A defining feature of this theory is that it interpolates between the presence and absence of particle-hole symmetry, which recovers the BEC and BCS limits, respectively. I present the Lagrange density from which I recover the derivation of the equations of motion, the Noether charge, the linearized excitations around the equilibrium state, and the spectra in the presence of a confining potential. This acts as brief introductory material for Publication IX, where we have used this approach to study the dynamics of defects in two-dimensional superfluids, and how these are affected by the presence or absence of particle-hole symmetry. We have used this theory to capture dynamics of the BEC-BCS crossover in two-dimensional fermionic fluids in a yet unpublished collaboration. More in-depth literature is available elsewhere [369, 370]. This chapter goes along the lines of the review article by Pekker and Varma [369]. Further derivations within this chapter were a collaborative effort with my colleague Jim Skulte.

## 5.1 Mixed-Symmetry Superfluid Lagrange Density

We start from the Lagrange density[1] of a complex scalar field $\Psi(\vec{r}, t)$.

$$\mathcal{L} = -i\frac{K_1}{2}(\Psi^*(\vec{r},t)\partial_t\Psi(\vec{r},t) - \Psi(\vec{r},t)\partial_t\Psi^*(\vec{r},t)) - K_2|\partial_t\Psi(\vec{r},t)|^2$$
$$- r|\Psi(\vec{r},t)|^2 + \frac{U}{2}|\Psi(\vec{r},t)|^4 + \xi^2|\nabla\Psi(\vec{r},r)|^2, \tag{5.1}$$

where $r$ is a bias that is reminiscent of a chemical potential and $U$ is the density-density coupling strength that introduces non-linearity. $\xi$ is the characteristic length

---

[1]This theory could be extended to a charged superfluid, i.e. a superconductor, by introducing coupling to the electromagnetic vector potential, which introduces additional local gauge freedom.

scale of the kinetic term. The three corresponding terms are provided by the Ginzburg-Landau theory of phase transitions. The remaining terms contain $K_1$ and $K_2$, which are coefficients that directly determine the character of the emergent dynamics. In particular, they determine whether the action is particle-hole symmetric and whether the equation of motion is Lorentz-invariant, i.e. relativistic. The operation of exchanging the field $\Psi(\vec{r},t)$ with its complex conjugate reflects the transformation of particles and holes into each other in the fermionic BCS Hamiltonian. Imposing the corresponding symmetry requires a Lagrange density that is invariant under this transformation which is reflected in the construction of the dynamical term proportional to $K_2$. The $K_1$-term is the only part of Eq. 5.1 that is not symmetric under this transformation. Invoking the Euler-Lagrange equation yields the equation of motion[2]

$$-K_2\partial_t^2\Psi(\vec{r},t) + iK_1\partial_t\Psi(\vec{r},t) = -\xi^2\nabla^2\Psi(\vec{r},t) - r\Psi(\vec{r},t) + U|\Psi(\vec{r},t)|^2\Psi(\vec{r},t). \quad (5.2)$$

Setting either $K_1 = 0$ or $K_2 = 0$ recovers the non-linear Klein-Gordon equation or the time-dependent Gross-Pitaevskii equation, respectively.

Meanwhile, the canonical conjugate $\Pi(\vec{r},t)$ of the field $\Psi(\vec{r},t)$ is

$$\Pi(\vec{r},t) = \frac{\partial\mathcal{L}}{\partial\dot{\Psi}} = -i\frac{K_1}{2}\Psi^*(\vec{r},t) - K_2\partial_t\Psi^*(\vec{r},t). \quad (5.3)$$

In the Gross-Pitaevskii limit, i.e. $K_2 = 0$, this relation identifies the field $\Psi(\vec{r},t)$ and its complex conjugate $\Psi^*(\vec{r},t)$ as canonical conjugates. In that case, the dynamics are fully captured with $\Psi(\vec{r},t)$ alone which is a manifestation of the first-order time-derivative in the equation of motion and the absence of particle-hole symmetry. In the Klein-Gordon limit, i.e. $K_1 = 0$, the canonical conjugate is identified with the time-derivative $\partial_t\Psi^*(\vec{r},t)$ and the dynamics are fully captured by $\Psi$ and $\dot{\Psi}$, as a consequence of the second-order time-derivative in the equation of motion.

The Lagrange density in Eq. 5.1 displays a U(1)-symmetry that is characterized by the infinitesimal transformation

$$\Psi \to \Psi' = \Psi e^{i\epsilon} = \Psi + i\epsilon\Psi + \mathcal{O}(\epsilon^2) \quad (5.4)$$

$$\Psi^* \to \Psi'^* = \Psi^* e^{-i\epsilon} = \Psi^* - i\epsilon\Psi^* + \mathcal{O}(\epsilon^2). \quad (5.5)$$

By Noether's theorem, this continuous symmetry leads to the conserved current

$$j^\mu = i\frac{\partial\mathcal{L}}{\partial(\partial_\mu\Psi)}\Psi - i\frac{\partial\mathcal{L}}{\partial(\partial_\mu\Psi^*)}\Psi^*, \quad (5.6)$$

which obeys the continuity equation

$$\partial_\mu j^\mu = 0. \quad (5.7)$$

From this follows the corresponding conserved Noether charge

$$J = i\int_{\mathbb{R}^n}(\Pi\Psi - \Pi^*\Psi^*)dr \quad (5.8)$$

$$= \int_{\mathbb{R}^n}K_1|\Psi|^2 + iK_2(\Psi^*\partial_t\Psi - \Psi\partial_t\Psi^*)dr, \quad (5.9)$$

---

[2]There is also an analogous equation of motion for $\Psi^*(\vec{r},t)$.

which in the case of $K_2 = 0$ describes the conservation of the integrated density, i.e. the total number of particles. In the case of $K_1 = 0$, this quantity describes the difference between the total number of particles and holes. In general, the weighted sum of the number of particles and the difference of particles and holes is conserved, such that $K_1$ and $K_2$ determine how many particles may be lifted from the system by creating a hole. This circumstance has profound consequences on the available excitations in the system. In the case of $K_2 > 0$, in which the total number of particles is not conserved, the order parameter hosts global amplitude oscillations. This type of amplitude mode is sometimes identified with the Higgs boson in particle physics, which emerges analogously as excitations in the displacement from a non-zero ground state in the same spontaneously broken continuous symmetry.[3] With decreasing $K_2$, this degree of freedom is continuously lifted as the constraint on the number of particles is imposed to an increasing degree, effectively making the system more stiff with respect to amplitude modes. Calculating the low-energy excitations around the equilibrium quantifies this phenomenon.

## 5.2 Low-Energy Excitations

The equilibrium solution of this theory is obtained by setting the time-derivatives to zero, as well as assuming homogeneity, i.e. a spatially constant $\Psi(\vec{r}, t)$. Independent of $K_1$ and $K_2$, this gives

$$0 = -r\Psi(\vec{r}, t) + U|\Psi(\vec{r}, t)|^2 \Psi(\vec{r}, t) \tag{5.10}$$

which is solved by[4]

$$|\Psi(\vec{r}, t)| = \Psi_0 = \sqrt{\frac{r}{U}}, \tag{5.11}$$

for $r/U > 0$. The competing terms lead to an energy landscape commonly referred to as the *sombrero*-potential, due to its visual similarity to the popular hat, concerning the rim in particular. The ground state manifold $\Phi_0 = \{\Psi_0 e^{i\phi_0} : \phi_0 \in [0, 2\pi)\}$ is then located precisely within the circular minimum of the potential. The linear dynamics around one such equilibrium position are found by introducing a small displacement $\delta\Psi(\vec{r}, t)$ in the amplitude and a small displacement $\delta\phi(\vec{r}, t)$ in the complex phase such that

$$\Psi(\vec{r}, t) = (\Psi_0 + \delta\Psi(\vec{r}, t))e^{i\delta\phi(\vec{r}, t)} \tag{5.12}$$

$$= \Psi_0 + i\delta\phi(\vec{r}, t)\Psi_0 + \delta\Psi(\vec{r}, t) + \mathcal{O}(\delta^2). \tag{5.13}$$

Reinserting this into Eq. 5.2 and separating the real and imaginary parts provides the linearized equations of motion

$$-K_2\partial_t^2\delta\Psi(\vec{r}, t) + K_1\partial_t\Psi_0\delta\phi(\vec{r}, t) = -\xi^2\nabla^2\delta\Psi(\vec{r}, t) + 2r\delta\Psi(\vec{r}, t) \tag{5.14}$$

$$-K_2\partial_t^2\Psi_0\delta\phi(\vec{r}, t) - K_1\partial_t\delta\Psi(\vec{r}, t) = -\xi^2\Psi_0\nabla^2\delta\phi(\vec{r}, t). \tag{5.15}$$

---

[3]The Anderson-Higgs mechanism that emerges as a consequence of local gauge-freedom in particle physics, also emerges in superconductors, but is absent in neutral particle-hole symmetric superfluids.

[4]Due to the U(1)-symmetry, the choice of the global phase of $\Psi_0 e^{i\phi_0}$ is arbitrary, so I set it to $\phi_0 = 0$.
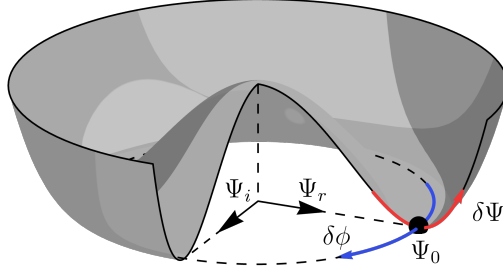
Figure 5.1: The low-energy excitations in the sombrero-potential of the effective field $\Psi = \Psi_r + i\Psi_i$. $\Psi_0$ denotes a symmetry-broken ground state. The amplitude mode is depicted in red and displays a low energy excitation in the radial displacement. The Goldstone mode is depicted in blue and consists of displacement along the manifold of ground states.

Fourier transforming these equations gives the momentum- and frequency-representation

$$(\xi^2 k^2 + 2r - K_2\omega^2)\delta\Psi(\vec{k},\omega) + iK_1\omega\Psi_0\delta\phi(\vec{k},\omega) = 0 \tag{5.16}$$

$$(\xi^2 k^2 - K_2\omega^2)\Psi_0\delta\phi(\vec{k},\omega) - iK_1\omega\delta\Psi(\vec{k},\omega) = 0, \tag{5.17}$$

which couples the modes such that

$$\begin{pmatrix} \xi^2 k^2 + 2r - K_2\omega^2 & iK_1\omega \\ -iK_1\omega & \xi^2 k^2 - K_2\omega^2 \end{pmatrix} \begin{pmatrix} \delta\Psi(\vec{k},\omega) \\ \Psi_0\delta\phi(\vec{k},\omega) \end{pmatrix} = 0. \tag{5.18}$$

The determinant of the matrix in this expression vanishes for

$$\omega_{a,\phi} = \frac{1}{\sqrt{2K_2^2}}\sqrt{K_1^2 + 2K_2\left(\xi^2 k^2 + r\right) \pm \sqrt{K_1^4 + 4K_1^2 K_2\left(\xi^2 k^2 + r\right) + 4K_2^2 r^2}}, \tag{5.19}$$

where $\omega_a$ denotes the amplitude mode that we associate with the positive sign, and $\omega_\phi$ is the phase mode that we associate with the negative sign. Within the sombrero-potential, the phase mode, or Goldstone mode, $\omega_\phi$ describes the angular motion along the equipotential rim, while the amplitude mode $\omega_a$ describes orthogonal radial displacement. As previously remarked, a global excitation along this radial direction, i.e. the amplitude mode, does not conserve the total number of particles and is therefore lifted from the system by divergence in the limit of $K_2 \to 0$. I show the radial and phase displacements within the sombrero-potential in Fig. 5.1

In the limit of $K_1 \to 0$, the expressions for the modes in Eq. 5.19 reduce to

$$\omega_a = \sqrt{\frac{\xi^2 k^2 + 2r}{K_2}} \qquad\qquad \omega_\phi = \frac{\xi|k|}{\sqrt{K_2}}. \tag{5.20}$$

The Goldstone mode is linear and gapless, while the amplitude mode displays a gap of size $\sqrt{2r/K_2}$. The emergence of the gapless linear mode is a consequence of breaking the global continuous U(1) symmetry, as covered by the Goldstone theorem.

For the limit of $K_2 \to 0$, this calculation requires considering the squares $\omega_{a,\phi}^2$. $\omega_a^2$ diverges for $K_2 \to 0$, such that the amplitude mode is effectively lifted from the system, as previously mentioned.[5] This is a manifestation of the increasing density stiffness with a loss of particle-hole symmetry. The limit of $\omega_\phi^2$ is inconclusive as the denominator and the enumerator both approach zero. Invoking L'Hospitâl's rule twice yields

$$\lim_{K_2 \to 0} \omega_\phi^2 = \lim_{K_2 \to 0} \frac{K_1^4 q^2 \left(\xi^2 k^2 + 2r\right)}{\left(K_1^4 + 4K_1^2 K_2 \left(\xi^2 k^2 + r\right) + 4K_2^2 r^2\right)^{3/2}} = \frac{\xi^4 k^4 + 2r\xi^2 k^2}{K_1^2}, \qquad (5.21)$$

which gives the solution to the Goldstone mode

$$\omega_\phi = \frac{\sqrt{\xi^4 k^4 + 2r\xi^2 k^2}}{K_1}. \qquad (5.22)$$

This mode is still gapless and linear for small momenta. By inserting the physical parameters that produce the physics of a BEC, i.e. $\xi = \frac{\hbar}{\sqrt{2m}}$, $r = \mu$ and $K_1 = \hbar$, Eq. 5.22 correctly recovers the well-known Bogoliubov quasi-particle dispersion relation of BECs.

The expression for the amplitude mode $\omega_a$ in the limit of vanishing momenta $k$ describes the onset of the amplitude mode excitation spectrum under consideration of mixed values of $K_1$ and $K_2$. It is[6]

$$\omega_a|_{k \to 0} = \frac{\sqrt{K_1^2 + 2K_2 r}}{K_2}. \qquad (5.23)$$

## 5.3 Spectra in Confining Potentials

It is also possible to introduce an additional external potential into the theory. Revisiting Eq. 5.2 in the absence of the density-density interaction, while including an external potential $V(\vec{r})$ gives

$$-K_2 \partial_t^2 \Psi(\vec{r}, t) + iK_1 \partial_t \Psi(\vec{r}, t) = -\frac{\hbar^2}{2m} \nabla^2 \Psi(\vec{r}, t) + (V(\vec{r}) - r)\Psi(\vec{r}, t) \qquad (5.24)$$

We assume this potential leads to a set of bound eigenstates $\Psi(\vec{r}, t) = \Psi_n e^{-i\omega_n t}$ with eigenenergies $E_n$. We do not assume any relation between frequency and energy in this model and insert such an eigenstate in order to write the Fourier representation

$$K_2 \omega_n^2 \Psi_n + K_1 \omega_n \Psi_n = E_n \Psi_n, \qquad (5.25)$$

---

[5] Alternatively, one could set $K_2 = 0$ in Eq. 5.18 and find that the solution corresponding to $\omega_a$ does not exist in the first place.

[6] The most observant readers might notice the discrepancy between Eq. 5.23 and the corresponding expression in the cited review article by Pekker and Varma. Jim Skulte noticed this discrepancy before I did.

which gives the positive frequency solution

$$\omega_n = \frac{\sqrt{K_1^2 + 4E_n K_2} - K_1}{2K_2} \tag{5.26}$$

such that the difference of frequencies of arbitrary eigenstates is

$$\omega_n - \omega_m = \frac{\sqrt{K_1^2 + 4E_n K_2} - \sqrt{K_1^2 + 4E_m K_2}}{2K_2}. \tag{5.27}$$

In the limit of $K_2 \to 0$, Eq. 5.24 is just the Schrödinger equation, and it is

$$\omega_n - \omega_m = \frac{E_n - E_m}{K_1}, \tag{5.28}$$

which is the well-known energy-frequency relation when $K_1 = \hbar$. In the limit of $K_1 \to 0$ it is

$$\omega_n - \omega_m = \sqrt{\frac{E_n}{K_2}} - \sqrt{\frac{E_m}{K_2}}. \tag{5.29}$$

As a consequence, the spectrum of this system changes as a function of $K_1$ and $K_2$. In a yet unpublished collaboration we have used this model as a starting point for an effective field theory describing an experimental realization of two-dimensional BEC-BCS crossover physics.

## 5.4 Publication IX: Vortex and soliton dynamics in particle-hole symmetric superfluids

J. Skulte, <u>L. Broers</u>, J. G. Cosme and L. Mathey — **Phys. Rev. Research 3, 043109 (2021)**

This work was motivated by the prospect of investigating non-linear dynamics, turbulence, and chaotic behavior in superfluids. These phenomena are rooted in the formation of the dynamics of defects such as vortices and solitons. The differences in the dynamical behavior of such defects in particle-hole (PH) symmetric superfluids to those without such a symmetry are crucial for understanding the formation and characteristics of turbulences in different types of superfluids.

In this work, first-authored by Jim Skulte, we have analyzed the mean-field dynamics of both PH symmetric and asymmetric superfluids in two dimensions inside a radial box potential. We have developed a numerical simulation of an effective field theory that is capable of capturing the dynamics of defects. We have found that vortex-anti-vortex pairs behave very differently in PH symmetric superfluids compared to PH asymmetric ones. In PH asymmetric superfluids, the vortex-anti-vortex pairs move in parallel as they accelerate each other due to the Magnus forces that they impart on each other in the presence of their respective phase-windings. In PH symmetric superfluids, these pairs accelerate directly towards each other and annihilate. We have attributed this to the lack of a Magnus force in balanced PH symmetric superfluids. We have also demonstrated this lack of a Magnus force analytically. These vortex dynamics play an important role for the decay of solitons. In PH asymmetric superfluids, solitons will in the presence of noise start to seed vortex-anti-vortex pairs along their axis. These pairs start to move in different directions, depending on the exact location of their emergence. Consequently, the soliton breaks apart in a process that is referred to as snaking, due to the writhing motion of the vortex-anti-vortex pairs along the soliton. In PH symmetric superfluids, there is also a formation of vortex-anti-vortex pairs along the soliton. However, due to the lack of a Magnus force there is no snaking, but rather the vortices and anti-vortices annihilate as they attract each other along the soliton axis. We have shown that the PH symmetry plays a crucial role in the dynamics of defects which are the principal building blocks of turbulent dynamics in superfluids.

My contribution to this work consisted of conceptualizing and creating large portions of the numerical method, together with JS. JS performed the analytical calculations, as well as the numerical studies, and wrote most of the manuscript. JC and I assisted JS in analyzing the numerical results and in writing the manuscript. This work was done under the supervision of LM.

# Vortex and soliton dynamics in particle-hole-symmetric superfluids

Jim Skulte [1,2] Lukas Broers [1] Jayson G. Cosme [3] and Ludwig Mathey[1,2]

[1]*Zentrum für Optische Quantentechnologien and Institut für Laserphysik, Universität Hamburg, 22761 Hamburg, Germany*
[2]*The Hamburg Centre for Ultrafast Imaging, Luruper Chaussee 149, 22761 Hamburg, Germany*
[3]*National Institute of Physics, University of the Philippines, Diliman, Quezon City 1101, Philippines*

We propose to induce topological defects in particle-hole-symmetric superfluids, with the prime example of the Bardeen-Cooper-Schrieffer state of ultracold atoms, and detect their time evolution and decay. We demonstrate that the time evolution is qualitatively distinct for particle-hole-symmetric superfluids and point out that the dynamics of topological defects is strongly modified in particle-hole-symmetric fluids. We obtain results for different charges and compare them with the standard Gross-Pitaevskii prediction for Bose-Einstein condensates. We highlight the observable signatures of the particle-hole symmetry in the dynamics of decaying solitons and subsequent vortices.

## I. INTRODUCTION

The presence or absence of particle-hole symmetry in a physical system is a fundamental property pervading its dynamical properties. Particle-hole symmetry is realized in Lorentz invariant theories such as the standard model of elementary physics [1], low-energy effective models close to quantum criticality [2], and the famous Bardeen-Cooper-Schrieffer (BCS) theory of superconductivity [3,4].[1] We note that the order parameter dynamics of high-$T_c$ superconductors can be described by an effective particle-hole-symmetric theory, which allows for exploring the dynamics of the Higgs/amplitude mode [5–8]. Similarly, in ultracold neutral atoms the emergence of an effective particle-hole symmetry has been predicted theoretically [9,10] and confirmed experimentally [11,12]. Recently, amplitude oscillations of the order parameter in the Bose-Einstein condensate (BEC) to BCS crossover have been reported [13], suggesting the presence of approximate particle-hole symmetry.

The dynamics of topological defects, such as solitons and quantized vortices, derives from and exemplifies the properties of the underlying quantum fluid. The stability of solitons has been discussed extensively for the nonlinear Schrödinger equation or Gross-Pitaevskii (GP) equation [14–18]. Zakharov and Rubenchik coined the term snaking to refer to the characteristic bending of solitons prior to their decay.

---

[1]Due to the close connection between relativistic Lorentz invariance and particle-hole symmetry, models that are particle-hole symmetric are also sometimes referred to as relativistic models.

Snaking is a manifestation of the Magnus force. This has been discussed for neutral bosonic systems within the GP equation [19–25], in the BEC-BCS crossover [26–28], and in superconductors [29,30].

We propose to determine the influence of particle-hole symmetry on the dynamics of topological defects in two-dimensional neutral superfluids. We focus on the BCS state as our primary example, but our results hold for any approximately particle-hole-symmetric system, e.g., bosons in an optical lattice near unit filling [12]. For this purpose we present the similarities and differences in the dynamics of topological defects in the absence and presence of particle-hole symmetry. We also compare the dynamics of the particle-hole-symmetric theory for zero and nonzero Noether charge, corresponding to a balanced mixture of particles and holes and an imbalanced mixture of particles and holes, respectively. We find that the case with nonzero charge is reminiscent of the dynamics of the GP equation. On the other hand, for vanishing charge, in which the number of particles and holes is balanced, we show that vortices do not experience any Magnus force. This leads to a soliton decay without snaking, setting it apart from soliton dynamics in non-particle-hole-symmetric fluids, such as BECs. To induce soliton dynamics of the quantum fluid in the BCS limit, we propose to imprint a soliton on the BEC side of the crossover in the presence of a potential barrier. As the next step, we propose to ramp the fluid adiabatically across the crossover into the BCS limit while keeping the barrier potential up. Finally, the barrier potential is ramped to zero, to induce the soliton dynamics. This protocol of initializing the dynamics enables imprinting of the phase pattern with an off-resonant optical pulse, whereas direct phase imprinting in the particle-hole-symmetric limit is prohibited. We note that this statement holds only for an exact particle-hole-symmetric case. In experiments such as those in Ref. [27], particle-hole symmetry is only approximately realized. That is, the appropriate effective
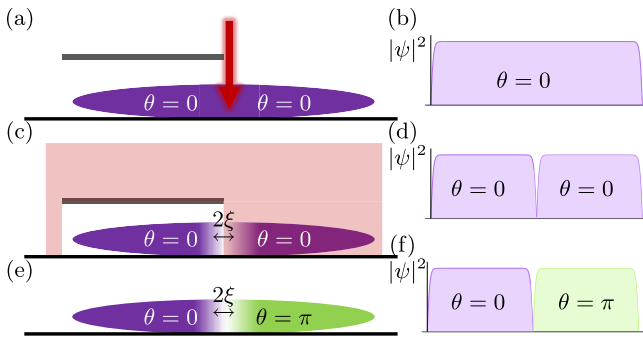
FIG. 1. Schematic representation of (a), (c), and (e) the proposed protocol to imprint a soliton and (b), (d), and (f) the corresponding density profiles $|\psi|^2$ and phase distributions $\theta$. (a) A narrow laser sheet is applied to a quantum fluid on the BEC side of the crossover to create a density depletion in the condensate. (b) and (d) The quantum fluid is split into two subsystems with a relative phase of zero. (c) Next a $\pi$ pulse is applied to half of the condensate to create (e) and (f) the phase pattern of a dark soliton. Next the interaction is adiabatically changed across the crossover deep into the BCS side. The narrow laser sheet separating the two subsystems is removed, which triggers the soliton dynamics. Here $\xi$ is the healing length of the condensate.

action is expected to have both $K_1\partial_t$ and $K_2\partial_t^2$ contributions, as we discuss below. The $K_1\partial_t$ term allows the phase imprinting as it is the dominant term in the BEC regime. The proposed protocol is displayed in Fig. 1.

## II. SYSTEM

We consider a low-energy effective models of the form [3]

$$
\begin{aligned}
\mathcal{S} = \int d^2x\, dt \bigg( & K_2(\partial_t\psi)(\partial_t\bar{\psi}) - iK_1(\partial_t\psi)\bar{\psi} \\
& - \frac{1}{m}\nabla\bar{\psi}\nabla\psi - \mu|\psi|^2 + \frac{g}{2}|\psi|^4 + V_{\text{ext}}|\psi|^2 \\
& - i\mu_Q[(\partial_t\bar{\psi})\psi - \bar{\psi}\partial_t\psi]\bigg),
\end{aligned} \tag{1}
$$

where $K_{1,2}$ are the above-mentioned parameters that determine the time dependence, $\mu$ is the square root of the gap energy, which has the dimensions of a mass term, $g$ is the contact interaction strength, and $V_{\text{ext}}$ is the externally applied potential. A similar effective field theory has been proposed and discussed to model the BEC-BCS crossover in [31–34]. We include a Lagrange multiplier $\mu_Q$ to fix the Klein-Gordon charge (7) (discussed below). By setting $K_2 = 0$, $K_1 = 1$, and $\mu_Q = 0$, we recover the GP equation

$$
i\partial_t\psi(\mathbf{x},t) = \frac{\nabla^2}{2m}\psi(\mathbf{x},t) + V(|\psi|^2)\psi(\mathbf{x},t), \tag{2}
$$

where $V[|\psi(\mathbf{x},t)|^2] = \mu - g|\psi(\mathbf{x},t)|^2 + V_{\text{ext}}(\mathbf{x})$. We refer to a condensate described by the GP equation as a GP fluid. This equation is manifestly not particle-hole symmetric under the exchange $\psi \leftrightarrow \bar{\psi}$. On the other hand, particle-hole symmetry is fulfilled in the action (1) by setting $K_1 = 0$ and $K_2 \neq 0$.

We introduce a dimensionless representation via $\psi = \tilde{\psi}/\xi$, $\nabla = \tilde{\nabla}/\xi$, $\partial_t = c_s/\xi\,\tilde{\partial}_t$, and $V = \mu\tilde{V}$, where $\xi$ is the healing length of the fluid and $c_s$ the speed of sound. This leads to the modified nonlinear Klein-Gordon (NLKG) equation

$$
\partial_{\tilde{t}}^2\tilde{\psi}(\mathbf{x},t) = \tilde{\nabla}^2\tilde{\psi}(\mathbf{x},t) + \tilde{V}(|\tilde{\psi}|^2)\tilde{\psi}(\mathbf{x},t) + i\mu_Q\partial_{\tilde{t}}\tilde{\psi}(\mathbf{x},t). \tag{3}
$$

We refer to condensates evolving according to the NLKG equation as Klein-Gordon (KG) fluids. In the following we drop the tilde. We trap the fluid using a box potential of the form

$$
V_{\text{ext}}(\mathbf{x}) = V_0\{1 + \tanh[(|\mathbf{x}| - r_0)/\xi]\}. \tag{4}
$$

We note that this model is a relativistic BEC [35–37] and a similar equation has been proposed to model cold dark matter [38–40] and relativistic boson stars [41–43].

In the following we show the influence of particle-hole symmetry on the dynamics of topological defects. For the KG fluid, we introduce the canonical momentum $\Pi(x,t) = \partial_t\bar{\psi}(x,t) + i\mu_Q\bar{\psi}(x,t)$ to obtain two coupled first-order partial differential equations

$$
\partial_t\psi(\mathbf{x},t) = \bar{\Pi}(\mathbf{x},t) + i\mu_Q\psi(\mathbf{x},t), \tag{5}
$$

$$
\partial_t\Pi(\mathbf{x},t) = \nabla^2\bar{\psi}(\mathbf{x},t) + V(|\psi|^2)\bar{\psi}(\mathbf{x},t) - i\mu_Q\Pi(\mathbf{x},t). \tag{6}
$$

A crucial feature of a KG fluid is that the particle number $N = \int |\psi(\mathbf{x},t)|^2 dx$ is not conserved, in contrast to a GP fluid. Instead, in the KG fluid, the Noether charge

$$
Q = -i\int[\bar{\Pi}(\mathbf{x},t)\bar{\psi}(\mathbf{x},t) - \Pi(\mathbf{x},t)\psi(\mathbf{x},t)]d^2x \tag{7}
$$

is conserved. The Noether charge $Q$ can be thought of as the difference of particles and holes in the system. That is, a zero Noether charge describes the situation with an equal number of particles and holes. An intuitive example for illustrating the Noether charge is a system of interacting bosons in an optical lattice with unit filling. An excitation corresponds to exciting one atom out of the lattice side and leaving behind a hole. Thus, the Noether charge stays unchanged as the same number of particles and hole were created. Another possible excitation is to excite the atom out of the lattice and further removing it from the system, which leaves a hole behind. The system then slightly goes away from unit filling as there is now an imbalance between the number of holes and particles and this corresponds to an effective nonzero Noether charge. Another example can be envisioned in the BCS regime for nonzero temperature. Here a rf knife can be used to remove some of the atoms occupying the Bogoliubov modes, leading to an imbalance between particle and hole excitations.

We apply the Madelung transformation to the field and the canonical momentum, in which the field $\psi$ is written in an amplitude-phase representation

$$
\psi(\mathbf{x},t) = A(\mathbf{x},t)\exp[i\theta(\mathbf{x},t)], \tag{8}
$$

$$
\Pi(\mathbf{x},t) = \left(\frac{\dot{A}(\mathbf{x},t)}{A(\mathbf{x},t)} + i[\mu_Q - \dot{\theta}(\mathbf{x},t)]\right)\psi(\mathbf{x},t), \tag{9}
$$

and obtain the continuity equation and particle-hole-symmetric Euler equation

$$\partial_t \rho_{\mathrm{KG}} + \frac{\mu_Q}{2}\partial_t \rho_S = -\nabla(\rho_S \mathbf{u}), \tag{10}$$

$$\left(\frac{\rho_{\mathrm{KG}}}{\rho_S} + \frac{\mu_Q}{2}\right)\partial_t \mathbf{u} = \mathbf{u}\nabla\mathbf{u} + \frac{\nabla\rho_S}{2\rho_0} - \frac{\nabla}{2}\left(\frac{\Box\sqrt{\rho_S}}{\sqrt{\rho_S}}\right), \tag{11}$$

where we introduce the GP density $\rho_S = A^2$, the KG density $\rho_{\mathrm{KG}} = A^2 \partial_t \theta$, the velocity $\mathbf{u} = \nabla\theta$, and the box operator $\Box = \partial_t^2 - \nabla^2$. In this representation, the charge simplifies to $Q = \int \rho_{\mathrm{KG}} dx$. In the particle-hole-symmetric Euler equations there is a prefactor $\rho_{\mathrm{KG}}/\rho_S$ in front of the time derivative of the velocity field $\partial_t \mathbf{u}$. This prefactor depends on the charge $Q$. This is a crucial difference to the GP Euler equation where this prefactor is always 1.

The particle-hole-symmetric Euler equation (11) has two quantum pressure terms. One term is due to the kinetic energy of the condensate and is proportional to $\frac{\nabla^2\sqrt{\rho_S}}{\sqrt{\rho_S}}$. It is the zero-point motion of the condensate and becomes dominant if the condensate has spatial variations on short length scales [44]. The second is proportional to $\frac{\partial_t^2\sqrt{\rho_S}}{\sqrt{\rho_S}}$ and originates from the second-order time derivative. It only exists for particle-hole-symmetric condensates.

We present the local velocity field around a single vortex. Therefore, we transform into the Feshbach-Villars basis, which translates the NLKG to coupled GP equations for the particles and antiparticles, respectively [45]

$$\psi = \frac{1}{\sqrt{2}}(\psi^{\mathrm{p}} + \psi^{\mathrm{a}}), \tag{12}$$

$$\Pi = \frac{i}{\sqrt{2}}(\psi^{\mathrm{a}} - \psi^{\mathrm{p}}). \tag{13}$$

Next we expand the field around the vortex core position $r_0$ with the amplitude $A^{\mathrm{i}}$ and phase $\theta^{\mathrm{i}}$ [see Eqs. (8) and (9)] and propagate the location of the vortex core using the equations of motion and compare the new location with the previous location to obtain the local velocity field (for a detailed discussion and derivation see [46–48]). For the two velocity fields we obtain

$$v^{\mathrm{a}} = -\frac{(-i, 1)^{\mathrm{T}} \cdot \nabla(A^{\mathrm{p}} + A^{\mathrm{a}}) + (A^{\mathrm{p}} + A^{\mathrm{a}})(1, i)^{\mathrm{T}} \cdot \nabla\theta}{A^{\mathrm{a}}}, \tag{14}$$

$$v^{\mathrm{p}} = \frac{(-i, 1)^{\mathrm{T}} \cdot \nabla(A^{\mathrm{p}} + A^{\mathrm{a}}) + (A^{\mathrm{p}} + A^{\mathrm{a}})(1, i)^{\mathrm{T}} \cdot \nabla\theta}{A^{\mathrm{p}}}, \tag{15}$$

where the spatial plane $(x, y)$ is represented as the complex plane $z = x + iy$. Translating this back into the $(\psi, \Pi)$ basis, we obtain

$$v^{\psi} = \frac{1}{\sqrt{2}}(v^{\mathrm{p}} + v^{\mathrm{a}}) = \sqrt{2}\left(1 - \frac{A^{\mathrm{a}}}{A^{\mathrm{p}}}\right)v^{\mathrm{p}}. \tag{16}$$

For $Q \neq 0$ we have $A^{\mathrm{a}} \neq A^{\mathrm{p}}$, which means that we obtain a nonzero velocity field. In this case the velocity is proportional to the velocity obtained for GP fluids [47]. For $Q = 0$, we have $A^{\mathrm{p}} = A^{\mathrm{a}}$ and $N^{\mathrm{p}} = N^{\mathrm{a}}$, with $N^i$ the total number of particles/antiparticles. For this balanced scenario the local velocity field vanishes precisely as shown in Fig. 2. As pointed out before and as can be seen from Eq. (16), for a finite charge
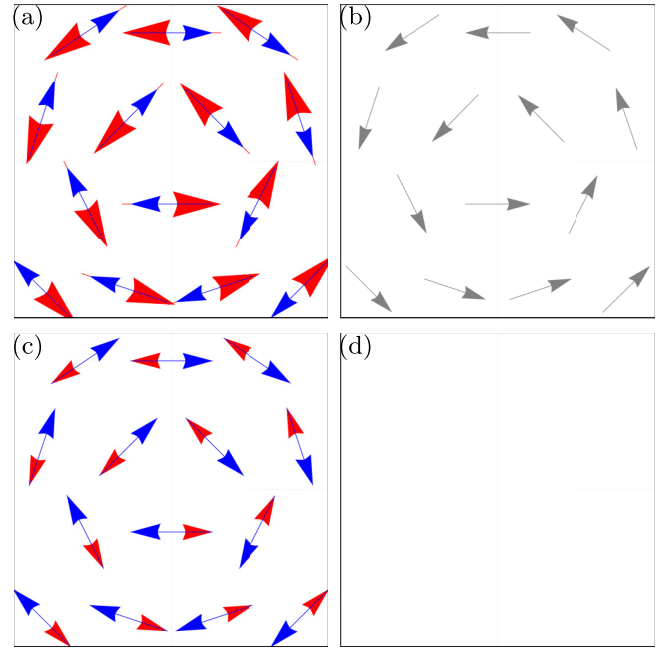


FIG. 2. Schematic sketch of (a) and (c) the local velocity fields of the particles (blue) and antiparticles (red) and (b) and (d) the resulting total local velocity field for the $\psi$ field (gray). (a) An unbalanced mixture of particles and antiparticles with a finite charge $Q$ leads to (b) a nonzero effective velocity field for the $\psi$ field. (c) A balanced mixture of particles and antiparticles with a vanishing charge $Q$ leads to (d) a vanishing effective velocity field for the $\psi$ field.

$Q$ corresponding to an imbalance between particles and antiparticles, the magnitudes of the velocity fields are different [see Fig. 2(a)], which results in a nonzero velocity field for the KG fluid $\psi$ [see Fig. 2(b)]. In contrast, for a balanced mixture the local velocity field magnitudes are the same [see Fig. 2(c)] and due to the opposite direction of the velocity fields the velocity field of the KG fluid vanishes [see Fig. 2(d)].

## III. NUMERICAL RESULTS

To expand on our analytical predictions and to propose an experimental setup to detect vortex dynamics of KG fluids, we simulate the equations using the pseudospectral method [49] for both the GP and KG fluids. We set the ratio between the chemical potential $\mu$ and the contact interaction $g$ to $\mu/g = 10/\xi^2$. In the following we express all length scales in units of $\xi$. Our simulations are discretized in a $256 \times 256$ grid. We choose $r_0/\xi = 25$, where $r_0$ is half of the box size, as defined in Eq. (4), and resolve $\xi$ with three grid points. The phase and density distribution for snapshots in real time are shown for a GP fluid [see Fig. 3(a)] and for a KG fluid with vanishing charge [see Fig. 3(c)]. Circles (KG fluid with $Q = 0$) and diamonds (GP fluid) in red correspond to a phase winding of $+1$, while blue corresponds to $-1$ [see Fig. 3(b)]. The gray arrows show the flow of time in the figure. It can be seen that for a dipole distance $d_{12} > 2\xi$ in the GP fluid the dipole will start to propel forward perpendicular to the dipole axis and will not annihilate. In contrast, the KG vortex dipoles will move along the dipole axis and annihilate each other, due to the absence
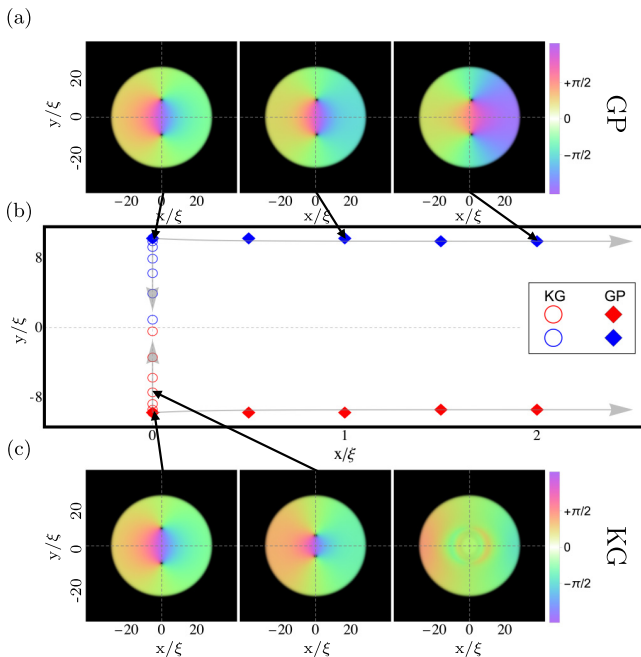
(a)



(b)

(c)

FIG. 3. Dynamics of vortex dipole pairs in a GP and a KG fluid. The phase and the density of (a) the GP fluid and (c) the KG fluid are shown. (b) The symbols display the locations of the vortices and antivortices in red and blue, respectively, of the GP fluid (diamonds) and the KG fluid (circles), and difference times. The snapshots of (a) and (c) are indicated via black arrows. The gray arrows indicate the movement of the vortices in time.

of a velocity field. Related observations of vortex dynamics were reported in Ref. [50]. We note that the particle-hole symmetry is the origin of this qualitatively distinct behavior from GP fluid dynamics. We propose that the data from a future experimental realization of our proposal could be used to numerically fit the ratio of $K_1$ and $K_2$ for different interaction strengths. This links our proposal to the parameters used in the universal effective action of such systems.

To investigate the influence of the particle-hole symmetry on the soliton dynamics, we initialize the condensate with a modified Thomas-Fermi profile [44], as described in the Supplemental Material [48], for a box potential in Eq. (4) with $V_0 = 10$ and $r_0 = 30$ for the GP (KG) fluid and start with a soliton imprinted in the fluid. We let the condensate relax using the imaginary-time propagation [51] extended to particle-hole-symmetric fluids [48]. For the KG fluids, we set the initial canonical momentum as $\Pi = i\frac{\mu_Q}{2}\psi$ with $\mu_Q \in \mathbb{R}$, resulting in a charge of $Q = \mu_Q N$. Furthermore, we add 1% white noise on the initial condensate density to study the stability of solitons.

The system is propagated in time according to Eqs. (2), (5), and (6). At lowest order, the Higgs mode and the Goldstone mode decouple in a particle-hole-symmetric theory [3]. Within this approximation, this initial state only induces the dynamics of the Goldstone mode. However, this approximation fails in soliton and vortex solutions. For the same parameters $\mu$ and $g$, the healing length is twice as large in the KG case compared to GP equation due to the difference in the prefactor of the kinetic energy.

In Fig. 4 we present the real-time dynamics of the complex field $\psi$ shaded from white to black corresponding to decreasing amplitude, i.e., black regions denote areas with vanishing $|\psi|$. The phase of the wave function is represented as color. The wave function is normalized for each snapshot such that the maximum value is set to unity to make it easier to compare GP and KG results.

In the GP fluid, we observe the established soliton instability in Figs. 4(a)–4(c) [16] and the motion of trapped vortices in Figs. 4(c)–4(e) [23,47]. The vortices move towards the edge of the condensate. As they approach the edge, they experience a net force and move along the trap boundary as depicted in Figs. 4(d) and 4(e) [23]. The behavior of the KG fluid with $Q \neq 0$ is similar. As displayed in Figs. 4(f)–4(j), the soliton decays into vortices, which then move around the condensate. Similar to the GP fluid, as the phase rotates in Figs. 4(f)–4(j), the vortices experience a net force leading to their motion along the trap boundary as seen in Figs. 4(i)–4(j).

In contrast, for the KG fluid with $Q = 0$, the soliton decays into vortices that are located along the soliton axis, as shown in Figs. 4(k)–4(m). Similar results have been found in [28]. Moreover, we find that the vortices are not rotating as displayed in Figs. 4(m)–4(o), which is consistent with Eqs. (14) and (16) and Fig. 3. When the vortices reach the trap boundary, they evaporate into the thermal cloud as shown in Figs. 4(n) and 4(o).

## IV. CONCLUSION

In conclusion, we have shown that by measuring the density profile of a two-dimensional condensate after imprinting a soliton in a particle-hole-symmetric superfluid, such as a BCS state of neutral particles, it is possible to test the effective low-energy theoretical description of the system. We have shown analytically and numerically that for particle-hole-symmetric superfluids with vanishing Noether charge, the Magnus force is absent. This allows for a dipole pair of vortices to approach each other without transverse motion and to annihilate, reminiscent of a recent observation in Ref. [50]. Another consequence of the vanishing Magnus force is that a soliton does not bend as it decays into vortices. Probing these effects experimentally will reveal how well particle-hole symmetry is realized in the dynamics of superfluids or whether the non-particle-hole-symmetric term, the first-order derivative in time, is the dominant contribution in the effective theory. This is crucial in understanding the notion of turbulence in particle-hole-symmetric fluids such as superconductors. Our work reveals that turbulence in a BCS superconductor and its scaling laws might deviate from Kolmogorov scaling laws [52], which apply to classical systems as well to GP fluids. We note that our predictions could be experimentally confirmed using refined experimental technique, such as *in situ* observations of two-dimensional Fermi liquids when probing the BEC-BCS crossover in neutral atoms [53,54] or the well-controlled imprinting of vortex dipole pairs [50].
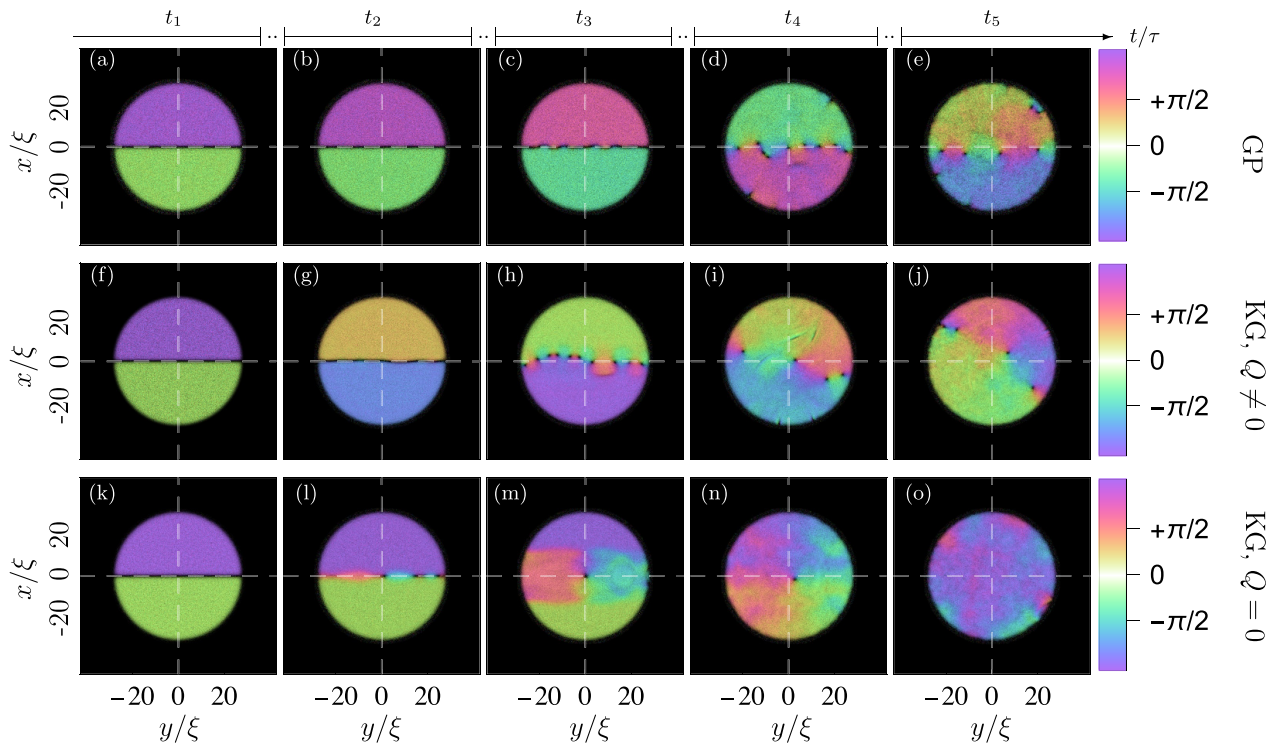
FIG. 4. Overview of the soliton instability for the three distinct cases corresponding to (a)–(e) the GP results, (f)–(j) the KG results with $Q \neq 0$, and (k)–(o) the KG results with $Q = 0$. For a better comparison between the GP and KG results the $\psi$ field density is normalized such that the maximum value is set to unity in each snapshot. The shading of the plots ranging from black to white visualizes the magnitude of the field $|\psi|$, while the colormap indicates the phase. (a), (f), and (k) Initial soliton seeded with white noise. (b), (g), and (l) Soliton bending. (c), (h), and (m) Vortices appearing after the soliton decay. The long-time dynamics of the vortices inside the trap are presented in (d), (i), and (n) and in (e), (j), and (o). White dashed lines indicate the soliton axis and the perpendicular axis. The spatial length is expressed in terms of the healing length $\xi$. A movie showing the dynamics is presented in the Supplemental Material [48].

[1] S. Weinberg, *The Quantum Theory of Fields* (Cambridge University Press, Cambridge, 2013), Vol. 2.

[2] S. Sachdev, *Quantum Phase Transitions*, 2nd ed. (Cambridge University Press, Cambridge, 2011).

[3] D. Pekker and C. Varma, Amplitude/Higgs modes in condensed matter physics, Annu. Rev. Condens. Matter Phys. **6**, 269 (2015).

[4] C. M. Varma, Higgs boson in superconductors, J. Low Temp. Phys. **126**, 901 (2002).

[5] G. Homann, J. G. Cosme, and L. Mathey, Higgs time crystal in a high-$T_c$ superconductor, Phys. Rev. Res. **2**, 043214 (2020).

[6] G. Homann, J. G. Cosme, J. Okamoto, and L. Mathey, Higgs mode mediated enhancement of interlayer transport in high-$T_c$ cuprate superconductors, Phys. Rev. B **103**, 224503 (2021).

[7] Z. Dai and P. A. Lee, Photo-induced superconducting-like response in strongly correlated systems, Phys. Rev. B **104**, 054512 (2021).

[8] Z. Dai and P. A. Lee, Superconducting-like response in driven systems near the Mott transition, arXiv:2106.08354.

[9] E. Altman and A. Auerbach, Oscillating Superfluidity of Bosons in Optical Lattices, Phys. Rev. Lett. **89**, 250404 (2002).

[10] L. Pollet and N. Prokof'ev, Higgs Mode in a Two-Dimensional Superfluid, Phys. Rev. Lett. **109**, 010401 (2012).

[11] J. Léonard, A. Morales, P. Zupancic, T. Donner, and T. Esslinger, Monitoring and manipulating Higgs and Goldstone modes in a supersolid quantum gas, Science **358**, 1415 (2017).

[12] M. Endres, T. Fukuhara, D. Pekker, M. Cheneau, P. Schauss, C. Gross, E. Demler, S. Kuhr, and I. Bloch, The 'Higgs' amplitude mode at the two-dimensional superfluid/Mott insulator transition, Nature (London) **487**, 454 (2012).

[13] A. Behrle, T. Harrison, J. Kombe, K. Gao, M. Link, J. S. Bernier, C. Kollath, and M. Köhl, Higgs mode in a strongly interacting fermionic superfluid, Nat. Phys. **14**, 781 (2018).

[14] V. E. Zakharov and A. M. Rubenchik, Instability of waveguides and solitons in nonlinear media, Sov. Phys.—JETP **38**, 494 (1974).

[15] C. A. Jones, S. J. Putterman, and P. H. Roberts, Motions in a Bose condensate. V. Stability of solitary wave solutions of non-linear Schrodinger equations in two and three dimensions, J. Phys. A: Math. Gen. **19**, 2991 (1986).

[16] J. Brand and W. P. Reinhardt, Solitonic vortices and the fundamental modes of the "snake instability": Possibility of

observation in the gaseous Bose-Einstein condensate, Phys. Rev. A **65**, 043612 (2002).

[17] A. Muñoz Mateo and J. Brand, Chladni Solitons and the Onset of the Snaking Instability for Dark Solitons in Confined Superfluids, Phys. Rev. Lett. **113**, 255302 (2014).

[18] P. G. Kevrekidis, I. Danaila, J.-G. Caputo, and R. Carretero-González, Planar and radial kinks in nonlinear Klein-Gordon models: Existence, stability, and dynamics, Phys. Rev. E **98**, 052217 (2018).

[19] N.-E. Guenther, P. Massignan, and A. L. Fetter, Quantized superfluid vortex dynamics on cylindrical surfaces and planar annuli, Phys. Rev. A **96**, 063608 (2017).

[20] L. A. Toikka and J. Brand, Asymptotically solvable model for a solitonic vortex in a compressible superfluid, New J. Phys. **19**, 023029 (2017).

[21] B. Jackson, J. F. McCann, and C. S. Adams, Vortex line and ring dynamics in trapped Bose-Einstein condensates, Phys. Rev. A **61**, 013604 (1999).

[22] S. A. McGee and M. J. Holland, Rotational dynamics of vortices in confined Bose-Einstein condensates, Phys. Rev. A **63**, 043608 (2001).

[23] D. E. Sheehy and L. Radzihovsky, Vortices in spatially inhomogeneous superfluids, Phys. Rev. A **70**, 063620 (2004).

[24] J. Denschlag, J. E. Simsarian, D. L. Feder, C. W. Clark, L. A. Collins, J. Cubizolles, L. Deng, E. W. Hagley, K. Helmerson, W. P. Reinhardt, S. L. Rolston, B. I. Schneider, and W. D. Phillips, Generating solitons by phase engineering of a Bose-Einstein condensate, Science **287**, 97 (2000).

[25] S. Burger, K. Bongs, S. Dettmer, W. Ertmer, K. Sengstock, A. Sanpera, G. V. Shlyapnikov, and M. Lewenstein, Dark Solitons in Bose-Einstein Condensates, Phys. Rev. Lett. **83**, 5198 (1999).

[26] M. W. Zwierlein, J. R. Abo-Shaeer, A. Schirotzek, C. H. Schunck, and W. Ketterle, Vortices and superfluidity in a strongly interacting Fermi gas, Nature (London) **435**, 1047 (2005).

[27] M. J. H. Ku, W. Ji, B. Mukherjee, E. Guardado-Sanchez, L. W. Cheuk, T. Yefsah, and M. W. Zwierlein, Motion of a Solitonic Vortex in the BEC-BCS Crossover, Phys. Rev. Lett. **113**, 065301 (2014).

[28] W. Van Alphen, H. Takeuchi, and J. Tempere, Crossover between snake instability and Josephson instability of dark solitons in superfluid fermi gases, Phys. Rev. A **100**, 023628 (2019).

[29] J. Bardeen and M. J. Stephen, Theory of the motion of vortices in superconductors, Phys. Rev. **140**, A1197 (1965).

[30] P. Ao and D. J. Thouless, Berry's Phase and the Magnus Force for a Vortex Line in a Superconductor, Phys. Rev. Lett. **70**, 2158 (1993).

[31] S. N. Klimin, J. Tempere, and J. T. Devreese, Finite-temperature effective field theory for dark solitons in superfluid Fermi gases, Phys. Rev. A **90**, 053613 (2014).

[32] S. N. Klimin, J. Tempere, G. Lombardi, and J. T. Devreese, Finite temperature effective field theory and two-band superfluidity in Fermi gases, Eur. Phys. J. B **88**, 122 (2015).

[33] G. Lombardi, W. Van Alphen, S. N. Klimin, and J. Tempere, Soliton-core filling in superfluid Fermi gases with spin imbalance, Phys. Rev. A **93**, 013614 (2016).

[34] W. Van Alphen, G. Lombardi, S. N. Klimin, and J. Tempere, Dark soliton collisions in superfluid Fermi gases, New J. Phys. **20**, 053052 (2018).

[35] S. Fagnocchi, S. Finazzi, S. Liberati, M. Kormos, and A. Trombettoni, Relativistic Bose-Einstein condensates: A new system for analogue models of gravity, New J. Phys. **12**, 095012 (2010).

[36] H. E. Haber and H. A. Weldon, Thermodynamics of an Ultrarelativistic Ideal Bose Gas, Phys. Rev. Lett. **46**, 1497 (1981).

[37] M. Grether, M. de Llano, and G. A. Baker, Bose-Einstein Condensation in the Relativistic Ideal Bose Gas, Phys. Rev. Lett. **99**, 200406 (2007).

[38] K. Huang, H.-B. Low, and R.-S. Tung, Scalar field cosmology II: Superfluidity, quantum turbulence, and inflation, Int. J. Mod. Phys. A **27**, 1250154 (2012).

[39] J. Magaña, T. Matos, A. Suárez, and F. J. Sánchez-Salcedo, Structure formation with scalar field dark matter: The field approach, J. Cosmol. Astropart. Phys. **2012**, 003 (2012).

[40] C. Xiong, M. R. Good, Y. Guo, X. Liu, and K. Huang, Relativistic superfluidity and vorticity from the nonlinear Klein-Gordon equation, Phys. Rev. D **90**, 125019 (2014).

[41] M. Colpi, S. L. Shapiro, and I. Wasserman, Boson Stars: Gravitational Equilibria of Self-Interacting Scalar Fields, Phys. Rev. Lett. **57**, 2485 (1986).

[42] P.-H. Chavanis and T. Harko, Bose-Einstein condensate general relativistic stars, Phys. Rev. D **86**, 064011 (2012).

[43] A. Suárez and P.-H. Chavanis, Hydrodynamic representation of the Klein-Gordon-Einstein equations in the weak field limit: General formalism and perturbations analysis, Phys. Rev. D **92**, 023510 (2015).

[44] C. J. Pethick and H. Smith, *Bose-Einstein Condensation in Dilute Gases*, 2nd ed. (Cambridge University Press, Cambridge, 2008).

[45] H. Feshbach and F. Villars, Elementary relativistic wave mechanics of spin 0 and spin 1/2 particles, Rev. Mod. Phys. **30**, 24 (1958).

[46] O. Törnkvist and E. Schröder, Vortex Dynamics in Dissipative Systems, Phys. Rev. Lett. **78**, 1908 (1997).

[47] A. J. Groszek, D. M. Paganin, K. Helmerson, and T. P. Simula, Motion of vortices in inhomogeneous Bose-Einstein condensates, Phys. Rev. A **97**, 023617 (2018).

[48] See Supplemental Material at http://link.aps.org/supplemental/10.1103/PhysRevResearch.3.043109 for a movie.

[49] W. Bao, D. Jaksch, and P. A. Markowich, Numerical solution of the Gross-Pitaevskii equation for Bose-Einstein condensation, J. Comput. Phys. **187**, 318 (2003).

[50] W. J. Kwon, G. D. Pace, K. Xhani, L. Galantucci, A. M. Falconi, M. Inguscio, F. Scazza, and G. Roati, Sound emission and annihilations in a programmable quantum vortex collider, arXiv:2105.15180.

[51] C. Barenghi and N. G. Parker, *A Primer on Quantum Fluids* (Springer, Cham, 2016).

[52] A. Kolmogorov, The local structure of turbulence in incompressible viscous fluid for very large Reynolds numbers, Dokl. Akad. Nauk SSSR **30**, 301 (1941).

[53] K. Hueck, N. Luick, L. Sobirey, J. Siegl, T. Lompe, and H. Moritz, Two-Dimensional Homogeneous Fermi Gases, Phys. Rev. Lett. **120**, 060402 (2018).

[54] L. Sobirey, N. Luick, M. Bohlen, H. Biss, H. Moritz, and T. Lompe, Observation of superfluidity in a strongly correlated two-dimensional Fermi gas, Science **372**, 844 (2021).

# 6 Conclusion

In this cumulative dissertation, I have presented my work on driven dissipative electron dynamics in graphene, the emergence of a non-equilibrium superradiant phase in a graphene-inspired Dicke model, the benefits of non-local parameterizations in quantum algorithm optimization on the native Hamiltonian domain, and the role of particle-hole symmetry in the dynamics of superfluids. Throughout my work, I have developed and utilized different numerical methods that capture these physics, and that are viable for further use in future research. Controlling the properties of quantum systems through coherent external processes is at the heart of many quantum technologies, and the results of my work contribute to this by providing insight into the dynamical control of non-equilibrium dynamics.

In Publication I, we have introduced a model of driven dissipative two-band solids which utilizes a four-level description. This description includes doubly and unoccupied momentum modes, as well as dissipative processes that act in the instantaneous eigenbasis in a gauge-invariant way, and phenomenologically capture electron exchange with the environment. We have used this to reproduce the anomalous Hall transport in graphene as measured in the experiment by McIver *et al.* [44]. Our model further captures the electron distribution of the non-equilibrium steady state, which reveals the Floquet-Bloch bands and their populations. We have found that the non-equilibrium Floquet-Bloch band populations lead to two primary contributions to the transversal current in the presence of circularly polarized driving. The first contribution emerges directly from the charge carrier imbalance across the momentum space of the driven system. The second contribution is of geometric origin and emerges due to the Berry curvature of the topological Floquet-Bloch bands, which is associated with the anomalous Hall effect. In Publication II, I have studied the longitudinal optical conductivity of graphene driven with circularly polarized terahertz radiation. The optical conductivity provides means of observing light-induced Floquet gaps under realistic conditions through inter-band transitions of Floquet-Bloch bands. The contributions to the current of these inter-band transitions are proportional to the Floquet-Bloch band populations. The driving field leads to gaps in the Floquet-Bloch bands, which increase in size with the field strength up to a certain driving intensity. For very strong driving this behavior changes and the Floquet-Bloch band gaps decrease in size while their location in momentum space changes. It is during this regime of decreasing Floquet band gap size, where I have consistently found population inversion in the Floquet-Bloch bands located at the gaps. This population inversion leads to negative contributions to the optical conductivity, which I have shown to result in a net negative optical conductivity when competing contributions are small. This net negative optical conductivity implies optical gain at terahertz frequencies and suggests the possibility of utilizing this mechanism in a co-

herent light-source. These results have motivated the work in Publications V and VI. In Publication III, I have further used this model to study predictions of time-resolved angle-resolved photoelectron spectroscopy (trARPES) measurements of graphene driven with circularly polarized light under realistic conditions. The experimental observation of the light-induced band gap at the Dirac point in graphene had been obscured through limitations in resolution, Fourier broadening, and undesired signals due to space charge effects and laser-assisted photoelectron replicas. Resolving the gap necessitates an unfavorable compromise between ideally large driving frequencies in the presence of sufficiently large driving intensity. I have proposed that for strong driving, the population at the Dirac point remains largely contained within the Floquet bands that are continuously connected to the undriven bands as a function of the driving field strength. This leads to an energy difference between occupied bands that exceeds the size of the Floquet zone and suggests that it may be possible to overcome these limitations and potentially observe this large light-induced gap at the Dirac point under realistic conditions. In Publication IV, I have studied the non-linear transport in strongly driven graphene in the simultaneous presence of a large DC field. I have studied the resulting non-linear differential photoconductivity which displays a rich structure as a function of the DC field strength and the AC driving field strength with two distinct limits. In one limit, the DC field strength outweighs the AC field strength and the dynamics are captured within a modified Landau-Zener description in momentum space. In this case, the electron distribution in momentum space becomes strongly anisotropic, as the dissipative Landau-Zener transitions lead to wake-field-like features that are modulated by the periodic AC field. I have used this representation in a comoving frame to analytically capture characteristic features of the differential photoconductivity, as well as the temperature dependent and non-linear conductivity in the undriven limit, which agrees well with the numerical results. In the opposite limit, the AC field strength outweighs the DC field strength and the Floquet-Bloch band structure determines the structure of the differential photoconductivity in a type of photon-assisted tunneling.

In Publication V, I have studied a graphene-inspired driven dissipative Dicke model under consideration of solid-like dissipation. For this work, I have implemented and utilized an extended version of the numerical methods developed throughout Publications I — IV, which includes coupling to a single-mode cavity. I have found that this model displays a non-equilibrium superradiant phase in the case of strong driving. Analogous to the results in Publication II, the Floquet states display population inversion in a regime of strong driving. By tuning the cavity to be resonant with these population-inverted Floquet states, a coherent state in the cavity is sustained by depleting this effective population inversion. I refer to this as the Floquet-assisted superradiant phase (FSP), which I have characterized throughout this publication. I have calculated the onset of the FSP for weak-coupling as a function of the cavity frequency and the transition frequency of the two-level systems. The results suggest that the FSP can be utilized in a type of coherent light-source at terahertz frequencies, and that potentially the same mechanism appears in driven material-cavity setups. In Publication VI, I have tested the FSP against environmental factors such as noisy driving, inhomogeneous broadening, and strong dissipation, in order to evaluate whether the FSP qualifies as a type of

laser-like mechanism. I have found that the FSP is robust against all of these factors, and in particular displays sharp line-narrowing across the FSP transition, which overcomes the linewidth of the driving field as well as the inherent linewidth of the cavity. The inhomogeneous broadening affects the critical coupling of the FSP, but the mechanism remains accessible. This suggests that non-trivial band-structures in similar setups change the details of the phase, but do not obscure the FSP mechanism on a qualitative level. On one hand the FSP is viable in the presence of dissipation coefficients that are comparable to the parameters we have used to describe graphene in Publication I. On the other hand, decreasing the dissipation coefficients and the cavity loss rate reduces the critical coupling, which makes the FSP accessible in the case of very weak coupling, in sufficiently pristine setups. These results motivate utilizing the FSP in a setup of driven graphene coupled to an optical cavity to construct a laser-like mechanism.

In Publication VII, I have studied the performance of a time-nonlocal parameterization for quantum algorithm optimization on the native Hamiltonian level. Instead of optimizing the parameterized gates of a preconceived quantum circuit structure as is the case in conventional variational quantum algorithms (VQAs), native optimization acts directly on the control parameters of the underlying Hamiltonian. This generalizes the variational approach to pulses and is reminiscent of quantum optimal control methods. In particular, I have studied a parameterization that optimizes the Fourier coefficients of the Hamiltonian control parameters in order to perform quantum computational tasks. In a direct comparison with the more common piece-wise constant parameterization, the Fourier ansatz displays superior convergence behavior and overall fidelity, without a loss of efficiency of the implementations. Further, I have found that uniformly sampling the variance of the gradient of an example objective displays exponential decay as a function of the number of qubits in the case of the piece-wise constant parameterization. This behavior is characteristic of the barren plateau phenomenon. In the time-nonlocal Fourier ansatz however, these variances decay at a reduced, non-exponential, pace. This suggests a mitigation of the barren plateau phenomenon in the Fourier parameterization and motivates further research on non-local approaches beyond the quantum circuit paradigm, for the purpose of optimization on near-term quantum computers. In Publication VIII, we have studied the performance of native Hamiltonian optimization in the quantum computing architecture of neutral atoms in optical tweezer arrays. We have optimized implementations of the controlled NOT operation under realistic conditions which leads to high fidelity solutions in particular in the canonically unfavorable limit of large distances, i.e. weak coupling. We have tested these solutions against fluctuations of the interatomic distance and found both the small distance limit, and the large distance limit, to be robust against these fluctuations, whereas the regime of intermediate interatomic distances displayed a large susceptibility to fluctuations. Further, we have shown that the computational universality of this system is maintained under restrictions of the controllability in which a single parameter is used to control single-site actions globally, even if this extends to qubits that are not affected under the desired transformation. We have shown this by demonstrating that the dynamical Lie algebra of the Hamiltonian remains unaffected by this class of restrictions. Reducing the controllability of a setup through such restrictions, allows for optimization-inspired architectures that maintain

computational universality, while requiring less intricate machinery. This motivates future research in identifying architectures that benefit from these types of restrictions in particular.

In Publication IX, we have studied the dynamics of vortices and solitons in superfluids in the presence and absence of particle-hole (PH) symmetry. Superfluidity is found in Bose-Einstein condensates (BECs) as well as in BCS-like states of neutral fermions. These systems, however, display distinct physics and host different low-energy excitations. In particular BCS-like superfluids display an amplitude mode, which is absent in BECs due to the conservation of particles. We have developed a two-dimensional simulation of an effective field theory [369] that interpolates between the presence and absence of PH symmetry, i.e. between BEC-like and BCS-like superfluids. The resulting equations of motion continuously connect the limits of the Gross-Pitaevskii equation and the non-linear Klein-Gordon equation, across which the conserved quantities of the theory and the dynamics of excitations change. We have shown how the dynamics of defects such as vortices and solitons differ in these two limits. In particular, in balanced PH symmetric superfluids there is no Magnus force, in contrast to PH asymmetric superfluids. This determines the dynamics of vortex-anti-vortex pairs, which in the PH asymmetric case, propel each other forward through the Magnus forces they exert onto each other. In balanced PH symmetric superfluids, vortex-anti-vortex pairs attract and annihilate each other. These distinct dynamics also affect the dynamics of solitons, which in the presence of the Magnus force decay through a process of vortex-anti-vortex pair formation and a resulting snaking behavior, which breaks the soliton. In the absence of the Magnus force snaking does not occur. These results demonstrate the consequences PH symmetry has on the dynamics of superfluids. This extends to more involved physics in superfluids such as the emergence of turbulences and the intricacies of atomtronic setups. This methodology further presents an intriguing framework to describe the dynamics in the BEC-BCS crossover of neutral fermionic systems.

Non-equilibrium transport phenomena, the Floquet engineering of material properties and superradiance, optimizing the processing of quantum information, and engineering superfluid dynamics through symmetries are all different types of coherent dynamical control of transport and information in quantum systems. The dynamics of quantum systems in the presence of pulses and protocols as means to tailor a desired behavior is at the heart of many quantum technological proposals and future research directions alike. Building on the results of my work in these fields, several future directions of research present themselves. The numerical simulations I have adopted and developed throughout my work capture the dissipative electron dynamics of graphene under various conditions and driving setups. The method extends to different two-band materials, as well as graphene nanoribbon setups. The inclusion of a cavity mode makes it possible to study coherently driven graphene-cavity setups, which as my results suggest, host a robust Floquet-assisted superradiant phase under realistic conditions. My results on quantum algorithm optimization motivate the utilization of non-local parameterizations on the native Hamiltonian level. The generalization of control pulses outside the domain of quantum circuits presents a natural choice for near-term optimization endeavors. The prospect of designing universal quantum computation platforms under restrictions that

leave the dynamical Lie algebra in-tact, while circumventing technological challenges associated with local addressability, presents a promising and underdeveloped line of research.

# Acknowledgements

# Bibliography

[1] K. B. Davis, M. O. Mewes, M. R. Andrews, N. J. van Druten, D. S. Durfee, D. M. Kurn, and W. Ketterle, "Bose-einstein condensation in a gas of sodium atoms," *Phys. Rev. Lett.*, vol. 75, pp. 3969–3973, 22 1995.

[2] M. H. Anderson, J. R. Ensher, M. R. Matthews, C. E. Wieman, and E. A. Cornell, "Observation of bose-einstein condensation in a dilute atomic vapor," *Science*, vol. 269, no. 5221, pp. 198–201, 1995. eprint: `https://www.science.org/doi/pdf/10.1126/science.269.5221.198`.

[3] K. S. Novoselov, A. K. Geim, S. V. Morozov, D. Jiang, Y. Zhang, S. V. Dubonos, I. V. Grigorieva, and A. A. Firsov, "Electric field effect in atomically thin carbon films," *Science*, vol. 306, no. 5696, pp. 666–669, 2004. eprint: `https://www.science.org/doi/pdf/10.1126/science.1102896`.

[4] N. M. R. Peres, F. Guinea, and A. H. Castro Neto, "Electronic properties of disordered two-dimensional carbon," *Phys. Rev. B*, vol. 73, p. 125 411, 12 2006.

[5] A. K. Geim and K. S. Novoselov, "The rise of graphene," *Nature Materials*, vol. 6, no. 3, pp. 183–191, 2007.

[6] R. J. Thompson, G. Rempe, and H. J. Kimble, "Observation of normal-mode splitting for an atom in an optical cavity," *Phys. Rev. Lett.*, vol. 68, pp. 1132–1135, 8 1992.

[7] M. Brune, F. Schmidt-Kaler, A. Maali, J. Dreyer, E. Hagley, J. M. Raimond, and S. Haroche, "Quantum rabi oscillation: A direct test of field quantization in a cavity," *Phys. Rev. Lett.*, vol. 76, pp. 1800–1803, 11 1996.

[8] F. Brennecke, T. Donner, S. Ritter, T. Bourdel, M. Köhl, and T. Esslinger, "Cavity qed with a bose–einstein condensate," *Nature*, vol. 450, no. 7167, pp. 268–271, 2007.

[9] D. N. Basov, R. D. Averitt, and D. Hsieh, "Towards properties on demand in quantum materials," *Nature Materials*, vol. 16, no. 11, pp. 1077–1088, 2017.

[10] T. Oka and S. Kitamura, "Floquet engineering of quantum materials," Tech. Rep. 1, 2019, pp. 387–408. eprint: `https://doi.org/10.1146/annurev-conmatphys-031218-013423`.

[11] D. Jaksch, J. I. Cirac, P. Zoller, S. L. Rolston, R. Côté, and M. D. Lukin, "Fast quantum gates for neutral atoms," *Phys. Rev. Lett.*, vol. 85, pp. 2208–2211, 10 2000.

[12] M. Saffman, T. G. Walker, and K. Mølmer, "Quantum information with rydberg atoms," *Rev. Mod. Phys.*, vol. 82, pp. 2313–2363, 3 2010.

[13] K. S. Novoselov, A. K. Geim, S. V. Morozov, D. Jiang, M. I. Katsnelson, I. V. Grigorieva, S. V. Dubonos, and A. A. Firsov, "Two-dimensional gas of massless dirac fermions in graphene," *Nature*, vol. 438, no. 7065, pp. 197–200, 2005.

[14] P. M. Ostrovsky, I. V. Gornyi, and A. D. Mirlin, "Electron transport in disordered graphene," *Phys. Rev. B*, vol. 74, p. 235 443, 23 2006.

[15] K. I. Bolotin, K. J. Sikes, J. Hone, H. L. Stormer, and P. Kim, "Temperature-dependent transport in suspended graphene," *Phys. Rev. Lett.*, vol. 101, p. 096 802, 9 2008.

[16] M. Müller, M. Bräuninger, and B. Trauzettel, "Temperature dependence of the conductivity of ballistic graphene," *Phys. Rev. Lett.*, vol. 103, p. 196 801, 19 2009.

[17] E. G. Mishchenko, "Dynamic conductivity in graphene beyond linear response," *Phys. Rev. Lett.*, vol. 103, p. 246 802, 24 2009.

[18] J. Schiefele, F. Sols, and F. Guinea, "Temperature dependence of the conductivity of graphene on boron nitride," *Phys. Rev. B*, vol. 85, p. 195 420, 19 2012.

[19] M. Lemme, T. Echtermeyer, M. Baus, and H. Kurz, "A graphene field-effect device," English, *IEEE Electron Device Letters*, vol. 28, no. 4, pp. 282–284, 2007.

[20] F. Schwierz, "Graphene transistors," *Nature Nanotechnology*, vol. 5, no. 7, pp. 487–496, 2010.

[21] Y. Zhang, Y.-W. Tan, H. L. Stormer, and P. Kim, "Experimental observation of the quantum hall effect and berry's phase in graphene," *Nature*, vol. 438, no. 7065, pp. 201–204, 2005.

[22] K. S. Novoselov, Z. Jiang, Y. Zhang, S. V. Morozov, H. L. Stormer, U. Zeitler, J. C. Maan, G. S. Boebinger, P. Kim, and A. K. Geim, "Room-temperature quantum hall effect in graphene," *Science*, vol. 315, no. 5817, pp. 1379–1379, 2007. eprint: https://www.science.org/doi/pdf/10.1126/science.1137201.

[23] Z. Jiang, Y. Zhang, Y.-W. Tan, H. Stormer, and P. Kim, "Quantum hall effect in graphene," *Solid State Communications*, vol. 143, no. 1, pp. 14–19, 2007, Exploring graphene.

[24] C. L. Kane and E. J. Mele, "Quantum spin hall effect in graphene," *Phys. Rev. Lett.*, vol. 95, p. 226 801, 22 2005.

[25] B. Trauzettel, D. V. Bulaev, D. Loss, and G. Burkard, "Spin qubits in graphene quantum dots," *Nature Physics*, vol. 3, no. 3, pp. 192–196, 2007.

[26] N. Tombros, C. Jozsa, M. Popinciuc, H. T. Jonkman, and B. J. van Wees, "Electronic spin transport and spin precession in single graphene layers at room temperature," *Nature*, vol. 448, no. 7153, pp. 571–574, 2007.

[27] W. Han, K. Pi, K. M. McCreary, Y. Li, J. J. I. Wong, A. G. Swartz, and R. K. Kawakami, "Tunneling spin injection into single layer graphene," *Phys. Rev. Lett.*, vol. 105, p. 167 202, 16 2010.

186

[28] W. Han, R. K. Kawakami, M. Gmitra, and J. Fabian, "Graphene spintronics," *Nature Nanotechnology*, vol. 9, no. 10, pp. 794–807, 2014.

[29] J. R. Schaibley, H. Yu, G. Clark, P. Rivera, J. S. Ross, K. L. Seyler, W. Yao, and X. Xu, "Valleytronics in 2d materials," *Nature Reviews Materials*, vol. 1, no. 11, p. 16 055, 2016.

[30] S. A. Vitale, D. Nezich, J. O. Varghese, P. Kim, N. Gedik, P. Jarillo-Herrero, D. Xiao, and M. Rothschild, "Valleytronics: Opportunities, challenges, and paths forward," *Small*, vol. 14, no. 38, p. 1 801 483, 2018. eprint: `https://onlinelibrary.wiley.com/doi/pdf/10.1002/smll.201801483`.

[31] M. S. Mrudul, Álvaro Jiménez-Galán, M. Ivanov, and G. Dixit, "Light-induced valleytronics in pristine graphene," *Optica*, vol. 8, no. 3, pp. 422–427, 2021.

[32] T. Stauber, N. M. R. Peres, and A. K. Geim, "Optical conductivity of graphene in the visible region of the spectrum," *Phys. Rev. B*, vol. 78, p. 085 432, 8 2008.

[33] S. A. Mikhailov and K Ziegler, "Nonlinear electromagnetic response of graphene: Frequency multiplication and the self-consistent-field effects," *Journal of Physics: Condensed Matter*, vol. 20, no. 38, p. 384 204, 2008.

[34] E. Hendry, P. J. Hale, J. Moger, A. K. Savchenko, and S. A. Mikhailov, "Coherent nonlinear optical response of graphene," *Phys. Rev. Lett.*, vol. 105, p. 097 401, 9 2010.

[35] Y. Zhou and M. W. Wu, "Optical response of graphene under intense terahertz fields," *Phys. Rev. B*, vol. 83, p. 245 436, 24 2011.

[36] H. K. Avetissian, A. K. Avetissian, G. F. Mkrtchian, and K. V. Sedrakian, "Creation of particle-hole superposition states in graphene at multiphoton resonant excitation by laser radiation," *Phys. Rev. B*, vol. 85, p. 115 443, 11 2012.

[37] M. Freitag, T. Low, F. Xia, and P. Avouris, "Photoconductivity of biased graphene," *Nature Photonics*, vol. 7, no. 1, pp. 53–59, 2013.

[38] K. Kristinsson, O. V. Kibis, S. Morina, and I. A. Shelykh, "Control of electronic transport in graphene by electromagnetic dressing," *Scientific Reports*, vol. 6, no. 1, p. 20 082, 2016.

[39] T. Oka and H. Aoki, "Photovoltaic hall effect in graphene," *Phys. Rev. B*, vol. 79, p. 081 406, 8 2009.

[40] H. L. Calvo, H. M. Pastawski, S. Roche, and L. E. F. F. Torres, "Tuning laser-induced band gaps in graphene," *Applied Physics Letters*, vol. 98, no. 23, p. 232 103, 2011. eprint: `https://pubs.aip.org/aip/apl/article-pdf/doi/10.1063/1.3597412/14451667/232103\_1\_online.pdf`.

[41] P. M. Perez-Piskunow, G. Usaj, C. A. Balseiro, and L. E. F. F. Torres, "Floquet chiral edge states in graphene," *Phys. Rev. B*, vol. 89, p. 121 401, 12 2014.

[42] G. Usaj, P. M. Perez-Piskunow, L. E. F. Foa Torres, and C. A. Balseiro, "Irradiated graphene as a tunable floquet topological insulator," *Phys. Rev. B*, vol. 90, p. 115 423, 11 2014.

[43] Q. Chen, L. Du, and G. A. Fiete, "Floquet band structure of a semi-dirac system," *Phys. Rev. B*, vol. 97, p. 035 422, 3 2018.

[44] J. W. McIver, B. Schulte, F. U. Stein, T. Matsuyama, G. Jotzu, G. Meier, and A. Cavalleri, "Light-induced anomalous hall effect in graphene," *Nature Physics*, vol. 16, no. 1, pp. 38–41, 2020.

[45] A. C. Neto, F. Guinea, and N. M. Peres, "Drawing conclusions from graphene," *Physics World*, vol. 19, no. 11, p. 33, 2006.

[46] M. Katsnelson and K. Novoselov, "Graphene: New bridge between condensed matter physics and quantum electrodynamics," *Solid State Communications*, vol. 143, no. 1, pp. 3–13, 2007, Exploring graphene.

[47] M. I. Katsnelson, K. S. Novoselov, and A. K. Geim, "Chiral tunnelling and the klein paradox in graphene," *Nature Physics*, vol. 2, no. 9, pp. 620–625, 2006.

[48] T. Wehling, A. Black-Schaffer, and A. Balatsky, "Dirac materials," *Advances in Physics*, vol. 63, no. 1, pp. 1–76, 2014. eprint: `https://doi.org/10.1080/00018732.2014.927109`.

[49] O. Vafek and A. Vishwanath, "Dirac fermions in solids: From high-tc cuprates and graphene to topological insulators and weyl semimetals," *Annual Review of Condensed Matter Physics*, vol. 5, no. 1, pp. 83–112, 2014. eprint: `https://doi.org/10.1146/annurev-conmatphys-031113-133841`.

[50] K. Nakada, M. Fujita, G. Dresselhaus, and M. S. Dresselhaus, "Edge state in graphene ribbons: Nanometer size effect and edge shape dependence," *Phys. Rev. B*, vol. 54, pp. 17 954–17 961, 24 1996.

[51] Y.-W. Son, M. L. Cohen, and S. G. Louie, "Energy gaps in graphene nanoribbons," *Phys. Rev. Lett.*, vol. 97, p. 216 803, 21 2006.

[52] L. Brey and H. A. Fertig, "Electronic states of graphene nanoribbons studied with the dirac equation," *Phys. Rev. B*, vol. 73, p. 235 411, 23 2006.

[53] M. Y. Han, B. Özyilmaz, Y. Zhang, and P. Kim, "Energy band-gap engineering of graphene nanoribbons," *Phys. Rev. Lett.*, vol. 98, p. 206 805, 20 2007.

[54] S. Iijima, "Helical microtubules of graphitic carbon," *Nature*, vol. 354, no. 6348, pp. 56–58, 1991.

[55] G. Mittal, V. Dhand, K. Y. Rhee, S.-J. Park, and W. R. Lee, "A review on carbon nanotubes and graphene as fillers in reinforced polymer nanocomposites," *Journal of Industrial and Engineering Chemistry*, vol. 21, pp. 11–25, 2015.

[56] Y. Cao, V. Fatemi, S. Fang, K. Watanabe, T. Taniguchi, E. Kaxiras, and P. Jarillo-Herrero, "Unconventional superconductivity in magic-angle graphene superlattices," *Nature*, vol. 556, no. 7699, pp. 43–50, 2018.

[57] M. I. Katsnelson, *Graphene: Carbon in Two Dimensions*. Cambridge University Press, 2012.

[58] A. H. Castro Neto, F. Guinea, N. M. R. Peres, K. S. Novoselov, and A. K. Geim, "The electronic properties of graphene," *Rev. Mod. Phys.*, vol. 81, pp. 109–162, 1 2009.

[59] M. J. Allen, V. C. Tung, and R. B. Kaner, "Honeycomb carbon: A review of graphene," *Chemical Reviews*, vol. 110, no. 1, pp. 132–145, 2010.

[60] D. Abergel, V. Apalkov, J. Berashevich, K. Ziegler, and T. Chakraborty, "Properties of graphene: A theoretical perspective," *Advances in Physics*, vol. 59, no. 4, pp. 261–482, 2010. eprint: https://doi.org/10.1080/00018732.2010.487978.

[61] T. Stauber, N. M. R. Peres, and F. Guinea, "Electronic transport in graphene: A semiclassical approach including midgap states," *Phys. Rev. B*, vol. 76, p. 205 423, 20 2007.

[62] K. Nomura and A. H. MacDonald, "Quantum transport of massless dirac fermions," *Phys. Rev. Lett.*, vol. 98, p. 076 602, 7 2007.

[63] S. V. Morozov, K. S. Novoselov, M. I. Katsnelson, F. Schedin, D. C. Elias, J. A. Jaszczak, and A. K. Geim, "Giant intrinsic carrier mobilities in graphene and its bilayer," *Phys. Rev. Lett.*, vol. 100, p. 016 602, 1 2008.

[64] R. Danneau, F. Wu, M. F. Craciun, S. Russo, M. Y. Tomi, J. Salmilehto, A. F. Morpurgo, and P. J. Hakonen, "Evanescent wave transport and shot noise in graphene: Ballistic regime and effect of disorder," *Journal of Low Temperature Physics*, vol. 153, no. 5, pp. 374–392, 2008.

[65] I. Jung, D. A. Dikin, R. D. Piner, and R. S. Ruoff, "Tunable electrical conductivity of individual graphene oxide sheets reduced at "low"temperatures," *Nano Letters*, vol. 8, no. 12, pp. 4283–4287, 2008.

[66] J. Horng *et al.*, "Drude conductivity of dirac fermions in graphene," *Phys. Rev. B*, vol. 83, p. 165 113, 16 2011.

[67] F. T. Vasko and V. Ryzhii, "Voltage and temperature dependencies of conductivity in gated graphene," *Phys. Rev. B*, vol. 76, p. 233 404, 23 2007.

[68] X. Du, I. Skachko, A. Barker, and E. Y. Andrei, "Approaching ballistic transport in suspended graphene," *Nature Nanotechnology*, vol. 3, no. 8, pp. 491–495, 2008.

[69] K. Ziegler, "Minimal conductivity of graphene: Nonuniversal values from the kubo formula," *Phys. Rev. B*, vol. 75, p. 233 407, 23 2007.

[70] G. L. Klimchitskaya and V. M. Mostepanenko, "Conductivity of pure graphene: Theoretical approach using the polarization tensor," *Phys. Rev. B*, vol. 93, p. 245 419, 24 2016.

[71] J. Cserti, "Minimal longitudinal dc conductivity of perfect bilayer graphene," *Phys. Rev. B*, vol. 75, p. 033 405, 3 2007.

[72] M. I. Katsnelson, "Zitterbewegung, chirality, and minimal conductivity in graphene," *The European Physical Journal B - Condensed Matter and Complex Systems*, vol. 51, no. 2, pp. 157–160, 2006.

[73] B. Trauzettel, Y. M. Blanter, and A. F. Morpurgo, "Photon-assisted electron transport in graphene: Scattering theory analysis," *Phys. Rev. B*, vol. 75, p. 035 305, 3 2007.

[74] L. E. F. Foa Torres and G. Cuniberti, "Controlling the conductance and noise of driven carbon-based fabry–pérot devices," *Applied Physics Letters*, vol. 94, no. 22, p. 222 103, 2009. eprint: `https://doi.org/10.1063/1.3147865`.

[75] M. Breusing, C. Ropers, and T. Elsaesser, "Ultrafast carrier dynamics in graphite," *Phys. Rev. Lett.*, vol. 102, p. 086 809, 8 2009.

[76] M. Breusing, S. Kuehn, T. Winzer, E. Malić, F. Milde, N. Severin, J. P. Rabe, C. Ropers, A. Knorr, and T. Elsaesser, "Ultrafast nonequilibrium carrier dynamics in a single graphene layer," *Phys. Rev. B*, vol. 83, p. 153 410, 15 2011.

[77] C. G. Rocha, L. E. F. F. Torres, and G. Cuniberti, "Ac transport in graphene-based fabry-pérot devices," *Phys. Rev. B*, vol. 81, p. 115 435, 11 2010.

[78] A. Iurov, G. Gumbs, O. Roslyak, and D. Huang, "Anomalous photon-assisted tunneling in graphene," *Journal of Physics: Condensed Matter*, vol. 24, no. 1, p. 015 303, 2011.

[79] I. Gierz, J. C. Petersen, M. Mitrano, C. Cacho, I. C. E. Turcu, E. Springate, A. Stöhr, A. Köhler, U. Starke, and A. Cavalleri, "Snapshots of non-equilibrium dirac carrier distributions in graphene," *Nature Materials*, vol. 12, no. 12, pp. 1119–1124, 2013.

[80] G. Jnawali, Y. Rao, H. Yan, and T. F. Heinz, "Observation of a transient decrease in terahertz conductivity of single-layer graphene induced by ultrafast optical excitation," *Nano Letters*, vol. 13, no. 2, pp. 524–530, 2013.

[81] J. N. Heyman, J. D. Stein, Z. S. Kaminski, A. R. Banman, A. M. Massari, and J. T. Robinson, "Carrier heating and negative photoconductivity in graphene," *Journal of Applied Physics*, vol. 117, no. 1, p. 015 101, 2015. eprint: `https://pubs.aip.org/aip/jap/article-pdf/doi/10.1063/1.4905192/13706672/015101\_1\_online.pdf`.

[82] I. Gierz *et al.*, "Tracking primary thermalization events in graphene with photoemission at extreme time scales," *Phys. Rev. Lett.*, vol. 115, p. 086 803, 8 2015.

[83] E. E. Vdovin *et al.*, "Phonon-assisted resonant tunneling of electrons in graphene–boron nitride transistors," *Phys. Rev. Lett.*, vol. 116, p. 186 603, 18 2016.

[84] D. Gagnon, F. Fillion-Gourdeau, J. Dumont, C. Lefebvre, and S. MacLean, "Coherent destruction of tunneling in graphene irradiated by elliptically polarized lasers," *Journal of Physics: Condensed Matter*, vol. 29, no. 3, p. 035 501, 2016.

[85] S. F. Islam and A. Saha, "Driven conductance of an irradiated semi-dirac material," *Phys. Rev. B*, vol. 98, p. 235 424, 23 2018.

[86] V. Kumar, "Linear and nonlinear optical properties of graphene: A review," *Journal of Electronic Materials*, vol. 50, no. 7, pp. 3773–3799, 2021.

[87] H. Tang, S. G. Menabde, T. Anwar, J. Kim, M. S. Jang, and G. Tagliabue, "Photo-modulated optical and electrical properties of graphene," *Nanophotonics*, vol. 11, no. 5, pp. 917–940, 2022.

[88] T. Higuchi, C. Heide, K. Ullmann, H. B. Weber, and P. Hommelhoff, "Light-field-driven currents in graphene," *Nature*, vol. 550, no. 7675, pp. 224–228, 2017.

[89] C. Heide, T. Eckstein, T. Boolakee, C. Gerner, H. B. Weber, I. Franco, and P. Hommelhoff, "Electronic coherence and coherent dephasing in the optical control of electrons in graphene," *Nano Letters*, vol. 21, no. 22, pp. 9403–9409, 2021.

[90] C. Heide, T. Boolakee, T. Higuchi, H. B. Weber, and P. Hommelhoff, "Interaction of carrier envelope phase-stable laser pulses with graphene: The transition from the weak-field to the strong-field regime," *New Journal of Physics*, vol. 21, no. 4, p. 045 003, 2019.

[91] C. Heide, T. Boolakee, T. Eckstein, and P. Hommelhoff, "Optical current generation in graphene: Cep control vs. w + 2w control," *Nanophotonics*, vol. 10, no. 14, pp. 3701–3707, 2021.

[92] S. A. Sato and A. Rubio, "Nonlinear electric conductivity and thz-induced charge transport in graphene," *New Journal of Physics*, vol. 23, no. 6, p. 063 047, 2021.

[93] T. N. Ikeda, S. Tanaka, and Y. Kayanuma, "Floquet-landau-zener interferometry: Usefulness of the floquet theory in pulse-laser-driven systems," *Phys. Rev. Res.*, vol. 4, p. 033 075, 3 2022.

[94] M. Bukov, L. D'Alessio, and A. Polkovnikov, "Universal high-frequency behavior of periodically driven systems: From dynamical stabilization to floquet engineering," *Advances in Physics*, vol. 64, no. 2, pp. 139–226, 2015. eprint: `https://doi.org/10.1080/00018732.2015.1055918`.

[95] U. D. Giovannini and H. Hübener, "Floquet analysis of excitations in materials," *Journal of Physics: Materials*, vol. 3, no. 1, p. 012 001, 2019.

[96] H. Dehghani, T. Oka, and A. Mitra, "Dissipative floquet topological systems," *Phys. Rev. B*, vol. 90, p. 195 429, 19 2014.

[97] H. Dehghani, T. Oka, and A. Mitra, "Out-of-equilibrium electrons and the hall conductance of a floquet topological insulator," *Phys. Rev. B*, vol. 91, p. 155 422, 15 2015.

[98] A. Kumar, M. Rodriguez-Vega, T. Pereg-Barnea, and B. Seradjeh, "Linear response theory and optical conductivity of floquet topological insulators," *Phys. Rev. B*, vol. 101, p. 174 314, 17 2020.

[99] M. Wackerl, P. Wenk, and J. Schliemann, "Floquet-drude conductivity," *Phys. Rev. B*, vol. 101, p. 184 204, 18 2020.

[100] T. Kitagawa, E. Berg, M. Rudner, and E. Demler, "Topological characterization of periodically driven quantum systems," *Phys. Rev. B*, vol. 82, p. 235 114, 23 2010.

[101] N. H. Lindner, G. Refael, and V. Galitski, "Floquet topological insulator in semiconductor quantum wells," *Nature Physics*, vol. 7, no. 6, pp. 490–495, 2011.

[102] T. Kitagawa, T. Oka, A. Brataas, L. Fu, and E. Demler, "Transport properties of nonequilibrium systems under the application of light: Photoinduced quantum hall insulators without landau levels," *Phys. Rev. B*, vol. 84, p. 235 108, 23 2011.

[103] M. Aidelsburger, M. Atala, M. Lohse, J. T. Barreiro, B. Paredes, and I. Bloch, "Realization of the hofstadter hamiltonian with ultracold atoms in optical lattices," *Phys. Rev. Lett.*, vol. 111, p. 185 301, 18 2013.

[104] M. C. Rechtsman, J. M. Zeuner, Y. Plotnik, Y. Lumer, D. Podolsky, F. Dreisow, S. Nolte, M. Segev, and A. Szameit, "Photonic floquet topological insulators," *Nature*, vol. 496, no. 7444, pp. 196–200, 2013.

[105] N. Fläschner, B. S. Rem, M. Tarnowski, D. Vogel, D.-S. Lühmann, K. Sengstock, and C. Weitenberg, "Experimental reconstruction of the berry curvature in a floquet bloch band," *Science*, vol. 352, no. 6289, pp. 1091–1094, 2016. eprint: https://science.sciencemag.org/content/352/6289/1091.

[106] G. Jotzu, M. Messer, R. Desbuquois, M. Lebrat, T. Uehlinger, D. Greif, and T. Esslinger, "Experimental realization of the topological haldane model with ultracold fermions," *Nature*, vol. 515, no. 7526, pp. 237–240, 2014.

[107] S. Mukherjee, A. Spracklen, M. Valiente, E. Andersson, P. Öhberg, N. Goldman, and R. R. Thomson, "Experimental observation of anomalous topological edge modes in a slowly driven photonic lattice," *Nature Communications*, vol. 8, no. 1, p. 13 918, 2017.

[108] G. Ma, M. Xiao, and C. T. Chan, "Topological phases in acoustic and mechanical systems," *Nature Reviews Physics*, vol. 1, no. 4, pp. 281–294, 2019.

[109] M. Sameti and M. J. Hartmann, "Floquet engineering in superconducting circuits: From arbitrary spin-spin interactions to the kitaev honeycomb model," *Phys. Rev. A*, vol. 99, p. 012 333, 1 2019.

[110] M. Rudner and N. Lindner, "Band structure engineering and non-equilibrium dynamics in floquet topological insulators," English, *Nature Reviews Physics*, vol. 2, no. 5, pp. 229–244, 2020.

[111] F. D. M. Haldane, "Model for a quantum hall effect without landau levels: Condensed-matter realization of the "parity anomaly"," *Phys. Rev. Lett.*, vol. 61, pp. 2015–2018, 18 1988.

[112] D. Manzano, "A short introduction to the Lindblad master equation," *AIP Advances*, vol. 10, no. 2, p. 025 106, 2020. eprint: https://pubs.aip.org/aip/adv/article-pdf/doi/10.1063/1.5115323/12881278/025106\_1\_online.pdf.

[113] J. K. Freericks, H. R. Krishnamurthy, and T. Pruschke, "Theoretical description of time-resolved photoemission spectroscopy: Application to pump-probe experiments," *Phys. Rev. Lett.*, vol. 102, p. 136 401, 13 2009.

[114]    B. Lv, T. Qian, and H. Ding, "Angle-resolved photoemission spectroscopy and its application to topological materials," *Nature Reviews Physics*, vol. 1, no. 10, pp. 609–626, 2019.

[115]    G. Saathoff, L. Miaja-Avila, M. Aeschlimann, M. M. Murnane, and H. C. Kapteyn, "Laser-assisted photoemission from surfaces," *Phys. Rev. A*, vol. 77, p. 022 903, 2 2008.

[116]    Y. H. Wang, D. Hsieh, D. Pilon, L. Fu, D. R. Gardner, Y. S. Lee, and N. Gedik, "Observation of a warped helical spin texture in $Bi_2Se_3$ from circular dichroism angle-resolved photoemission spectroscopy," *Phys. Rev. Lett.*, vol. 107, p. 207 602, 20 2011.

[117]    C. M. Cacho *et al.*, "Ultrafast tr-arpes with artemis xuv beamline," in *Research in Optical Sciences*, Optical Society of America, 2012, JT2A.43.

[118]    S. Eich *et al.*, "Time- and angle-resolved photoemission spectroscopy with optimized high-harmonic pulses using frequency-doubled ti:sapphire lasers," *Journal of Electron Spectroscopy and Related Phenomena*, vol. 195, pp. 231–236, 2014.

[119]    G. Rohde, A. Hendel, A. Stange, K. Hanff, L.-P. Oloff, L. X. Yang, K. Rossnagel, and M. Bauer, "Time-resolved arpes with sub-15 fs temporal and near fourier-limited spectral resolution," *Review of Scientific Instruments*, vol. 87, no. 10, p. 103 102, 2016. eprint: `https://doi.org/10.1063/1.4963668`.

[120]    R. Liu *et al.*, "Femtosecond to picosecond transient effects in wse2 observed by pump-probe angle-resolved photoemission spectroscopy," *Scientific Reports*, vol. 7, no. 1, p. 15 981, 2017.

[121]    M. Puppin *et al.*, "Time- and angle-resolved photoemission spectroscopy of solids in the extreme ultraviolet at 500 khz repetition rate," *Review of Scientific Instruments*, vol. 90, no. 2, p. 023 104, 2019. eprint: `https://doi.org/10.1063/1.5081938`.

[122]    S. Peli, D. Puntel, D. Kopic, B. Sockol, F. Parmigiani, and F. Cilento, "Time-resolved vuv arpes at 10.8 ev photon energy and mhz repetition rate," *Journal of Electron Spectroscopy and Related Phenomena*, vol. 243, p. 146 978, 2020.

[123]    D. Kutnyakhov *et al.*, "Time- and momentum-resolved photoemission studies using time-of-flight momentum microscopy at a free-electron laser," *Review of Scientific Instruments*, vol. 91, no. 1, p. 013 109, 2020. eprint: `https://doi.org/10.1063/1.5118777`.

[124]    J. Maklar, S. Dong, S. Beaulieu, T. Pincelli, M. Dendzik, Y. W. Windsor, R. P. Xian, M. Wolf, R. Ernstorfer, and L. Rettig, "A quantitative comparison of time-of-flight momentum microscopes and hemispherical analyzers for time- and angle-resolved photoemission spectroscopy experiments," *Review of Scientific Instruments*, vol. 91, no. 12, p. 123 112, 2020. eprint: `https://doi.org/10.1063/5.0024493`.

[125] S. Dong *et al.*, "Direct measurement of key exciton properties: Energy, dynamics, and spatial distribution of the wave function," *Natural Sciences*, vol. 1, no. 1, e10010, 2021. eprint: `https://onlinelibrary.wiley.com/doi/pdf/10.1002/ntls.10010`.

[126] Y. H. Wang, H. Steinberg, P. Jarillo-Herrero, and N. Gedik, "Observation of floquet-bloch states on the surface of a topological insulator," *Science*, vol. 342, no. 6157, pp. 453–457, 2013. eprint: `https://science.sciencemag.org/content/342/6157/453`.

[127] I. Gierz, S. Link, U. Starke, and A. Cavalleri, "Non-equilibrium dirac carrier dynamics in graphene investigated with time- and angle-resolved photoemission spectroscopy," *Faraday Discuss.*, vol. 171, pp. 311–321, 0 2014.

[128] S. Ulstrup *et al.*, "Ultrafast electron dynamics in epitaxial graphene investigated with time- and angle-resolved photoemission spectroscopy," *Journal of Physics: Condensed Matter*, vol. 27, no. 16, p. 164 206, 2015.

[129] L. Peralta Gavensky, G. Usaj, and C. A. Balseiro, "Photo-electrons unveil topological transitions in graphene-like systems," *Scientific Reports*, vol. 6, no. 1, p. 36 577, 2016.

[130] I. Gierz, "Probing carrier dynamics in photo-excited graphene with time-resolved arpes," *Journal of Electron Spectroscopy and Related Phenomena*, vol. 219, pp. 53–56, 2017, SI: The electronic structure of 2D and layered materials.

[131] H. Soifer *et al.*, "Band-resolved imaging of photocurrent in a topological insulator," *Phys. Rev. Lett.*, vol. 122, p. 167 401, 16 2019.

[132] S. Beaulieu *et al.*, "Revealing hidden orbital pseudospin texture with time-reversal dichroism in photoelectron angular distributions," *Phys. Rev. Lett.*, vol. 125, p. 216 404, 21 2020.

[133] S. Aeschlimann *et al.*, "Survival of floquet–bloch states in the presence of scattering," *Nano Letters*, vol. 21, no. 12, pp. 5028–5035, 2021, PMID: 34082532. eprint: `https://doi.org/10.1021/acs.nanolett.1c00801`.

[134] M. Schüler, U. De Giovannini, H. Hübener, A. Rubio, M. A. Sentef, T. P. Devereaux, and P. Werner, "How circular dichroism in time- and angle-resolved photoemission can be used to spectroscopically detect transient topological states in graphene," *Phys. Rev. X*, vol. 10, p. 041 013, 4 2020.

[135] I. Gierz, M. Mitrano, J. C. Petersen, C. Cacho, I. C. E. Turcu, E. Springate, A. Stöhr, A. Köhler, U. Starke, and A. Cavalleri, "Population inversion in monolayer and bilayer graphene," *Journal of Physics: Condensed Matter*, vol. 27, no. 16, p. 164 204, 2015.

[136] F. Mahmood, C. Chan, Z. Alpichshev, D. Gardner, Y. Lee, P. A. Lee, and N. Gedik, "Selective scattering between floquet–bloch and volkov states in a topological insulator," *Nature Physics*, vol. 12, no. 4, pp. 306–310, 2016.

194

[137]  S. Aeschlimann *et al.*, "Direct evidence for efficient ultrafast charge separation in epitaxial ws2/graphene heterostructures," *Science Advances*, vol. 6, no. 20, 2020. eprint: `https://advances.sciencemag.org/content/6/20/eaay0761.full.pdf`.

[138]  R. Krause *et al.*, "Ultrafast charge separation in bilayer ws2/graphene heterostructure revealed by time- and angle-resolved photoemission spectroscopy," *Frontiers in Physics*, vol. 9, p. 184, 2021.

[139]  T. O. Wehling, A. V. Balatsky, M. I. Katsnelson, A. I. Lichtenstein, K. Scharnberg, and R. Wiesendanger, "Local electronic signatures of impurity states in graphene," *Phys. Rev. B*, vol. 75, p. 125 425, 12 2007.

[140]  S. Ihnatsenka and G. Kirczenow, "Dirac point resonances due to atoms and molecules adsorbed on graphene and transport gaps and conductance quantization in graphene nanoribbons with covalently bonded adsorbates," *Phys. Rev. B*, vol. 83, p. 245 442, 24 2011.

[141]  M. Inglot and V. K. Dugaev, "Impurity states in graphene with intrinsic spin-orbit interaction," *Journal of Applied Physics*, vol. 109, no. 12, p. 123 709, 2011. eprint: `https://doi.org/10.1063/1.3598130`.

[142]  Y. G. Pogorelov, V. M. Loktev, and D. Kochan, "Impurity resonance effects in graphene versus impurity location, concentration, and sublattice occupation," *Phys. Rev. B*, vol. 102, p. 155 414, 15 2020.

[143]  S. Hellmann, K. Rossnagel, M. Marczynski-Bühlow, and L. Kipp, "Vacuum space-charge effects in solid-state photoemission," *Phys. Rev. B*, vol. 79, p. 035 402, 3 2009.

[144]  J. Graf, S. Hellmann, C. Jozwiak, C. L. Smallwood, Z. Hussain, R. A. Kaindl, L. Kipp, K. Rossnagel, and A. Lanzara, "Vacuum space charge effect in laser-based solid-state photoemission spectroscopy," *Journal of Applied Physics*, vol. 107, no. 1, p. 014 912, 2010. eprint: `https://doi.org/10.1063/1.3273487`.

[145]  S. Hellmann, T. Ott, L. Kipp, and K. Rossnagel, "Vacuum space-charge effects in nano-arpes," *Phys. Rev. B*, vol. 85, p. 075 109, 7 2012.

[146]  L.-P. Oloff, K. Hanff, A. Stange, G. Rohde, F. Diekmann, M. Bauer, and K. Rossnagel, "Pump laser-induced space-charge effects in hhg-driven time- and angle-resolved photoelectron spectroscopy," *Journal of Applied Physics*, vol. 119, no. 22, p. 225 106, 2016. eprint: `https://doi.org/10.1063/1.4953643`.

[147]  M. Gross and S. Haroche, "Superradiance: An essay on the theory of collective spontaneous emission," *Physics Reports*, vol. 93, no. 5, pp. 301–396, 1982.

[148]  H. Haken, *Laser Theory*. Springer Berlin Heidelberg, 1984.

[149]  M. O. Scully and M. S. Zubairy, *Quantum Optics*. Cambridge University Press, 1997.

[150]  D. Walls and G. J. Milburn, Eds., *Quantum Optics*. Springer Berlin Heidelberg, 2008.

[151] P. Kirton, M. M. Roses, J. Keeling, and E. G. Dalla Torre, "Introduction to the dicke model: From equilibrium to nonequilibrium, and vice versa," *Advanced Quantum Technologies*, vol. 2, no. 1-2, p. 1 800 043, 2019. eprint: `https://onlinelibrary.wiley.com/doi/pdf/10.1002/qute.201800043`.

[152] R. H. Dicke, "Coherence in spontaneous radiation processes," *Phys. Rev.*, vol. 93, pp. 99–110, 1 1954.

[153] K. Hepp and E. H. Lieb, "On the superradiant phase transition for molecules in a quantized radiation field: The dicke maser model," *Annals of Physics*, vol. 76, no. 2, pp. 360–404, 1973.

[154] M. Tavis and F. W. Cummings, "Exact solution for an $N$-molecule—radiation-field hamiltonian," *Phys. Rev.*, vol. 170, pp. 379–384, 2 1968.

[155] E. Jaynes and F. Cummings, "Comparison of quantum and semiclassical radiation theories with application to the beam maser," *Proceedings of the IEEE*, vol. 51, no. 1, pp. 89–109, 1963.

[156] F. T. Hioe, "Phase transitions in some generalized dicke models of superradiance," *Phys. Rev. A*, vol. 8, pp. 1440–1445, 3 1973.

[157] Y. K. Wang and F. T. Hioe, "Phase transition in the dicke model of superradiance," *Phys. Rev. A*, vol. 7, pp. 831–836, 3 1973.

[158] K. Rzażewski, K. Wódkiewicz, and W. Żakowicz, "Phase transitions, two-level atoms, and the $A^2$ term," *Phys. Rev. Lett.*, vol. 35, pp. 432–434, 7 1975.

[159] I. Bialynicki-Birula and K. Rzażewski, "No-go theorem concerning the superradiant phase transition in atomic systems," *Phys. Rev. A*, vol. 19, pp. 301–303, 1 1979.

[160] K. Rzażewski and K. Wódkiewicz, "Stability of matter interacting with photons," *Phys. Rev. A*, vol. 43, pp. 593–594, 1 1991.

[161] J. Keeling, "Coulomb interactions, gauge invariance, and phase transitions of the dicke model," *Journal of Physics: Condensed Matter*, vol. 19, no. 29, p. 295 213, 2007.

[162] L. Garziano, A. Settineri, O. Di Stefano, S. Savasta, and F. Nori, "Gauge invariance of the dicke and hopfield models," *Phys. Rev. A*, vol. 102, p. 023 718, 2 2020.

[163] S. Hughes, C. Gustin, and F. Nori, *Reconciling quantum and classical spectral theories of ultrastrong coupling: Role of cavity bath coupling and gauge corrections*, 2023. arXiv: `2309.15788 [quant-ph]`.

[164] F. Dimer, B. Estienne, A. S. Parkins, and H. J. Carmichael, "Proposed realization of the dicke-model quantum phase transition in an optical cavity qed system," *Phys. Rev. A*, vol. 75, p. 013 804, 1 2007.

[165] M. P. Baden, K. J. Arnold, A. L. Grimsmo, S. Parkins, and M. D. Barrett, "Realization of the dicke model using cavity-assisted raman transitions," *Phys. Rev. Lett.*, vol. 113, p. 020 408, 2 2014.

[166] Z. Zhiqiang, C. H. Lee, R. Kumar, K. J. Arnold, S. J. Masson, A. S. Parkins, and M. D. Barrett, "Nonequilibrium phase transition in a spin-1 dicke model," *Optica*, vol. 4, no. 4, pp. 424–429, 2017.

[167] P. Nataf and C. Ciuti, "No-go theorem for superradiant quantum phase transitions in cavity qed and counter-example in circuit qed," *Nature Communications*, vol. 1, no. 1, p. 72, 2010.

[168] S. Genway, W. Li, C. Ates, B. P. Lanyon, and I. Lesanovsky, "Generalized dicke nonequilibrium dynamics in trapped ions," *Phys. Rev. Lett.*, vol. 112, p. 023 603, 2 2014.

[169] A. Safavi-Naini, R. J. Lewis-Swan, J. G. Bohnet, M. Gärttner, K. A. Gilmore, J. E. Jordan, J. Cohn, J. K. Freericks, A. M. Rey, and J. J. Bollinger, "Verification of a many-ion simulator of the dicke model through slow quenches across a phase transition," *Phys. Rev. Lett.*, vol. 121, p. 040 503, 4 2018.

[170] P. Domokos and H. Ritsch, "Collective cooling and self-organization of atoms in a cavity," *Phys. Rev. Lett.*, vol. 89, p. 253 003, 25 2002.

[171] A. T. Black, H. W. Chan, and V. Vuletić, "Observation of collective friction forces due to spatial self-organization of atoms: From rayleigh to bragg scattering," *Phys. Rev. Lett.*, vol. 91, p. 203 001, 20 2003.

[172] K. Baumann, C. Guerlin, F. Brennecke, and T. Esslinger, "Dicke quantum phase transition with a superfluid gas in an optical cavity," *Nature*, vol. 464, no. 7293, pp. 1301–1306, 2010.

[173] D. Nagy, G. Kónya, G. Szirmai, and P. Domokos, "Dicke-model phase transition in the quantum motion of a bose-einstein condensate in an optical cavity," *Phys. Rev. Lett.*, vol. 104, p. 130 401, 13 2010.

[174] J. Keeling, M. J. Bhaseen, and B. D. Simons, "Collective dynamics of bose-einstein condensates in optical cavities," *Phys. Rev. Lett.*, vol. 105, p. 043 001, 4 2010.

[175] M. J. Bhaseen, J. Mayoh, B. D. Simons, and J. Keeling, "Dynamics of nonequilibrium dicke models," *Phys. Rev. A*, vol. 85, p. 013 817, 1 2012.

[176] V. M. Bastidas, C. Emary, B. Regler, and T. Brandes, "Nonequilibrium quantum phase transitions in the dicke model," *Phys. Rev. Lett.*, vol. 108, p. 043 003, 4 2012.

[177] F. Brennecke, R. Mottl, K. Baumann, R. Landig, T. Donner, and T. Esslinger, "Real-time observation of fluctuations at the driven-dissipative dicke phase transition," *Proceedings of the National Academy of Sciences*, vol. 110, no. 29, pp. 11 763–11 767, 2013. eprint: `https : / / www . pnas . org / doi / pdf / 10 . 1073 / pnas . 1306993110`.

[178] J. Klinder, H. Keßler, M. Wolke, L. Mathey, and A. Hemmerich, "Dynamical phase transition in the open dicke model," *Proceedings of the National Academy of Sciences*, vol. 112, no. 11, pp. 3290–3295, 2015. eprint: `https://www.pnas. org/content/112/11/3290.full.pdf`.

[179] S. Haroche and F. Hartmann, "Theory of saturated-absorption line shapes," *Phys. Rev. A*, vol. 6, pp. 1280–1300, 4 1972.

[180] B. R. Mollow, "Stimulated emission and absorption near resonance for driven systems," *Phys. Rev. A*, vol. 5, pp. 2217–2222, 5 1972.

[181] F. Y. Wu, S. Ezekiel, M. Ducloy, and B. R. Mollow, "Observation of amplification in a strongly driven two-level atomic system at optical frequencies," *Phys. Rev. Lett.*, vol. 38, pp. 1077–1080, 19 1977.

[182] L. M. Narducci, D. H. Feng, R. Gilmore, and G. S. Agarwal, "Transient and steady-state behavior of collective atomic systems driven by a classical field," *Phys. Rev. A*, vol. 18, pp. 1571–1576, 4 1978.

[183] D. F. Walls, P. D. Drummond, S. S. Hassan, and H. J. Carmichael, "Non-Equilibrium Phase Transitions in Cooperative Atomic Systems," *Progress of Theoretical Physics Supplement*, vol. 64, pp. 307–320, 1978. eprint: `https://academic.oup.com/ptps/article-pdf/doi/10.1143/PTPS.64.307/5292058/64-307.pdf`.

[184] D. F. Walls, "Cooperative fluorescence from n coherently driven two-level atoms," *Journal of Physics B: Atomic and Molecular Physics*, vol. 13, no. 10, p. 2001, 1980.

[185] A. Muller, E. B. Flagg, P. Bianucci, X. Y. Wang, D. G. Deppe, W. Ma, J. Zhang, G. J. Salamo, M. Xiao, and C. K. Shih, "Resonance fluorescence from a coherently driven semiconductor quantum dot in a cavity," *Phys. Rev. Lett.*, vol. 99, p. 187 402, 18 2007.

[186] V. Peano and M. Thorwart, "Quasienergy description of the driven jaynes-cummings model," *Phys. Rev. B*, vol. 82, p. 155 129, 15 2010.

[187] V. Peano and M. Thorwart, "Dynamical bistability in the driven circuit qed," *Europhysics Letters*, vol. 89, no. 1, p. 17 008, 2010.

[188] A. Baksic and C. Ciuti, "Controlling discrete and continuous symmetries in "superradiant" phase transitions with circuit qed systems," *Phys. Rev. Lett.*, vol. 112, p. 173 601, 17 2014.

[189] C. Bradac, M. T. Johnsson, M. v. Breugel, B. Q. Baragiola, R. Martin, M. L. Juan, G. K. Brennen, and T. Volz, "Room-temperature spontaneous superradiance from single diamond nanocrystals," *Nature Communications*, vol. 8, no. 1, p. 1205, 2017.

[190] R. Gutiérrez-Jáuregui and H. J. Carmichael, "Dissipative quantum phase transitions of light in a generalized jaynes-cummings-rabi model," *Phys. Rev. A*, vol. 98, p. 023 804, 2 2018.

[191] A. Angerer *et al.*, "Superradiant emission from colour centres in diamond," *Nature Physics*, vol. 14, no. 12, pp. 1168–1172, 2018.

[192] J. Hannukainen and J. Larson, "Dissipation-driven quantum phase transitions and symmetry breaking," *Phys. Rev. A*, vol. 98, p. 042 113, 4 2018.

[193] J. V. Koski, A. J. Landig, A. Pályi, P. Scarlino, C. Reichl, W. Wegscheider, G. Burkard, A. Wallraff, K. Ensslin, and T. Ihn, "Floquet spectroscopy of a strongly driven quantum dot charge qubit with a microwave resonator," *Phys. Rev. Lett.*, vol. 121, p. 043 603, 4 2018.

[194] S. B. Jäger, J. Cooper, M. J. Holland, and G. Morigi, "Dynamical phase transitions to optomechanical superradiance," *Phys. Rev. Lett.*, vol. 123, p. 053 601, 5 2019.

[195] C. H. Johansen, J. Lang, A. Morales, A. Baumgärtner, T. Donner, and F. Piazza, "Multimode-polariton superradiance via Floquet engineering," *SciPost Phys.*, vol. 12, p. 094, 2022.

[196] O. Chelpanova, A. Lerose, S. Zhang, I. Carusotto, Y. Tserkovnyak, and J. Marino, "Intertwining of lasing and superradiance under spintronic pumping," *Phys. Rev. B*, vol. 108, p. 104 302, 10 2023.

[197] R. Chitra and O. Zilberberg, "Dynamical many-body phases of the parametrically driven, dissipative dicke model," *Phys. Rev. A*, vol. 92, p. 023 815, 2 2015.

[198] J. G. Cosme, C. Georges, A. Hemmerich, and L. Mathey, "Dynamical control of order in a cavity-bec system," *Phys. Rev. Lett.*, vol. 121, p. 153 001, 15 2018.

[199] M. Soriente, T. Donner, R. Chitra, and O. Zilberberg, "Dissipation-induced anomalous multicritical phenomena," *Phys. Rev. Lett.*, vol. 120, p. 183 603, 18 2018.

[200] J. A. Muniz, D. Barberena, R. J. Lewis-Swan, D. J. Young, J. R. K. Cline, A. M. Rey, and J. K. Thompson, "Exploring dynamical phase transitions with cold atoms in an optical cavity," *Nature*, vol. 580, no. 7805, pp. 602–607, 2020.

[201] J. Skulte, P. Kongkhambut, H. Keßler, A. Hemmerich, L. Mathey, and J. G. Cosme, "Parametrically driven dissipative three-level dicke model," *Phys. Rev. A*, vol. 104, p. 063 705, 6 2021.

[202] P. Kongkhambut, H. Keßler, J. Skulte, L. Mathey, J. G. Cosme, and A. Hemmerich, "Realization of a periodically driven open three-level dicke model," *Phys. Rev. Lett.*, vol. 127, p. 253 601, 25 2021.

[203] J. Skulte, P. Kongkhambut, S. Rao, L. Mathey, H. Keßler, A. Hemmerich, and J. G. Cosme, "Condensate formation in a dark state of a driven atom-cavity system," *Phys. Rev. Lett.*, vol. 130, p. 163 603, 16 2023.

[204] Z. Gong, R. Hamazaki, and M. Ueda, "Discrete time-crystalline order in cavity and circuit qed systems," *Phys. Rev. Lett.*, vol. 120, p. 040 404, 4 2018.

[205] J. G. Cosme, J. Skulte, and L. Mathey, "Time crystals in a shaken atom-cavity system," *Phys. Rev. A*, vol. 100, p. 053 615, 5 2019.

[206] B. Zhu, J. Marino, N. Y. Yao, M. D. Lukin, and E. A. Demler, "Dicke time crystals in driven-dissipative quantum many-body systems," *New Journal of Physics*, vol. 21, no. 7, p. 073 028, 2019.

[207] H. Keßler, P. Kongkhambut, C. Georges, L. Mathey, J. G. Cosme, and A. Hemmerich, "Observation of a dissipative time crystal," *Phys. Rev. Lett.*, vol. 127, p. 043 602, 4 2021.

[208] R. J. L. Tuquero, J. Skulte, L. Mathey, and J. G. Cosme, "Dissipative time crystal in an atom-cavity system: Influence of trap and competing interactions," *Phys. Rev. A*, vol. 105, p. 043 311, 4 2022.

[209] M. O. Scully and W. E. Lamb, "Quantum theory of an optical maser. i. general theory," *Phys. Rev.*, vol. 159, pp. 208–226, 2 1967.

[210] M. O. Scully, S.-Y. Zhu, and A. Gavrielides, "Degenerate quantum-beat laser: Lasing without inversion and inversion without lasing," *Phys. Rev. Lett.*, vol. 62, pp. 2813–2816, 24 1989.

[211] N. Lu and P. R. Berman, "Lasing without inversion in dressed-state lasers," *Phys. Rev. A*, vol. 44, pp. 5965–5972, 9 1991.

[212] M. Fleischhauer, C. Keitel, M. Scully, and C. Su, "Lasing without inversion and enhancement of the index of refraction via interference of incoherent pump processes," *Optics Communications*, vol. 87, no. 3, pp. 109–114, 1992.

[213] Y. Zhu, "Lasing without inversion in a closed three-level system," *Phys. Rev. A*, vol. 45, R6149–R6152, 9 1992.

[214] J Mompart and R Corbalán, "Lasing without inversion," vol. 2, no. 3, R7–R24, 2000.

[215] Y. Shchadilova, M. M. Roses, E. G. Dalla Torre, M. D. Lukin, and E. Demler, "Fermionic formalism for driven-dissipative multilevel systems," *Phys. Rev. A*, vol. 101, p. 013 817, 1 2020.

[216] K. C. Stitely, A. Giraldo, B. Krauskopf, and S. Parkins, "Lasing and counter-lasing phase transitions in a cavity-qed system," *Phys. Rev. Research*, vol. 4, p. 023 101, 2 2022.

[217] A. Lezama, Y. Zhu, M. Kanskar, and T. W. Mossberg, "Radiative emission of driven two-level atoms into the modes of an enclosing optical cavity: The transition from fluorescence to lasing," *Phys. Rev. A*, vol. 41, pp. 1576–1581, 3 1990.

[218] M. Lewenstein, Y. Zhu, and T. W. Mossberg, "Two-photon gain and lasing in strongly driven two-level atoms," *Phys. Rev. Lett.*, vol. 64, pp. 3131–3134, 26 1990.

[219] J. Zakrzewski, M. Lewenstein, and T. W. Mossberg, "Theory of dressed-state lasers. i. effective hamiltonians and stability properties," *Phys. Rev. A*, vol. 44, pp. 7717–7731, 11 1991.

[220] J. Zakrzewski, M. Lewenstein, and T. W. Mossberg, "Theory of dressed-state lasers. ii. phase diffusion and squeezing," *Phys. Rev. A*, vol. 44, pp. 7732–7745, 11 1991.

[221] J. Zakrzewski, M. Lewenstein, and T. W. Mossberg, "Theory of dressed-state lasers. iii. pump-depletion effects," *Phys. Rev. A*, vol. 44, pp. 7746–7758, 11 1991.

[222] D. J. Gauthier, Q. Wu, S. E. Morin, and T. W. Mossberg, "Realization of a continuous-wave, two-photon optical laser," *Phys. Rev. Lett.*, vol. 68, pp. 464–467, 4 1992.

[223] P. Horak, K. M. Gheri, and H. Ritsch, "Recoil-induced lasing of cold atoms," *Phys. Rev. A*, vol. 52, pp. 554–565, 1 1995.

[224] K. M. Gheri, H. Ritsch, D. F. Walls, and V. I. Balykin, "How large photon recoil can make cold atoms lase," *Phys. Rev. Lett.*, vol. 74, pp. 678–681, 5 1995.

[225] J. Hauss, A. Fedorov, C. Hutter, A. Shnirman, and G. Schön, "Single-qubit lasing and cooling at the rabi frequency," *Phys. Rev. Lett.*, vol. 100, p. 037003, 3 2008.

[226] P. Neilinger, M. Rehák, M. Grajcar, G. Oelsner, U. Hübner, and E. Il'ichev, "Two-photon lasing by a superconducting qubit," *Phys. Rev. B*, vol. 91, p. 104516, 10 2015.

[227] I. Y. Chestnov, V. A. Shahnazaryan, A. P. Alodjants, and I. A. Shelykh, "Terahertz lasing in ensemble of asymmetric quantum dots," *ACS Photonics*, vol. 4, no. 11, pp. 2726–2737, 2017. eprint: `https://doi.org/10.1021/acsphotonics.7b00575`.

[228] R. Sawant and S. A. Rangwala, "Lasing by driven atoms-cavity system in collective strong coupling regime," *Scientific Reports*, vol. 7, no. 1, p. 11432, 2017.

[229] J. D. Breeze, E. Salvadori, J. Sathian, N. M. Alford, and C. W. M. Kay, "Continuous-wave room-temperature diamond maser," *Nature*, vol. 555, no. 7697, pp. 493–496, 2018.

[230] M. Jiang, H. Su, Z. Wu, X. Peng, and D. Budker, "Floquet maser," *Science Advances*, vol. 7, no. 8, eabe0719, 2021. eprint: `https://www.science.org/doi/pdf/10.1126/sciadv.abe0719`.

[231] F. Haake, M. I. Kolobov, C. Fabre, E. Giacobino, and S. Reynaud, "Superradiant laser," *Phys. Rev. Lett.*, vol. 71, pp. 995–998, 7 1993.

[232] S. J. M. Kuppens, M. P. van Exter, and J. P. Woerdman, "Quantum-limited linewidth of a bad-cavity laser," *Phys. Rev. Lett.*, vol. 72, pp. 3815–3818, 24 1994.

[233] D. Meiser, J. Ye, D. R. Carlson, and M. J. Holland, "Prospects for a millihertz-linewidth laser," *Phys. Rev. Lett.*, vol. 102, p. 163601, 16 2009.

[234] D. Meiser and M. J. Holland, "Steady-state superradiance with alkaline-earth-metal atoms," *Phys. Rev. A*, vol. 81, p. 033847, 3 2010.

[235] J. G. Bohnet, Z. Chen, J. M. Weiner, D. Meiser, M. J. Holland, and J. K. Thompson, "A steady-state superradiant laser with less than one intracavity photon," *Nature*, vol. 484, no. 7392, pp. 78–81, 2012.

[236] M. A. Norcia and J. K. Thompson, "Cold-strontium laser in the superradiant crossover regime," *Phys. Rev. X*, vol. 6, p. 011025, 1 2016.

[237] M. A. Norcia, M. N. Winchester, J. R. K. Cline, and J. K. Thompson, "Superradiance on the millihertz linewidth strontium clock transition," *Science Advances*, vol. 2, no. 10, e1601231, 2016. eprint: `https://www.science.org/doi/pdf/10.1126/sciadv.1601231`.

[238] J. M. Weiner, K. C. Cox, J. G. Bohnet, and J. K. Thompson, "Phase synchronization inside a superradiant laser," *Phys. Rev. A*, vol. 95, p. 033 808, 3 2017.

[239] P. Kirton and J. Keeling, "Superradiant and lasing states in driven-dissipative dicke models," vol. 20, no. 1, p. 015 009, 2018.

[240] K. Debnath, Y. Zhang, and K. Mølmer, "Lasing in the superradiant crossover regime," *Phys. Rev. A*, vol. 98, p. 063 837, 6 2018.

[241] T. Laske, H. Winter, and A. Hemmerich, "Pulse delay time statistics in a superradiant laser with calcium atoms," *Phys. Rev. Lett.*, vol. 123, p. 103 601, 10 2019.

[242] K. Debnath, Y. Zhang, and K. Mølmer, "Collective dynamics of inhomogeneously broadened emitters coupled to an optical cavity with narrow linewidth," *Phys. Rev. A*, vol. 100, p. 053 821, 5 2019.

[243] H. Liu, S. B. Jäger, X. Yu, S. Touzard, A. Shankar, M. J. Holland, and T. L. Nicholson, "Rugged mhz-linewidth superradiant laser driven by a hot atomic beam," *Phys. Rev. Lett.*, vol. 125, p. 253 602, 25 2020.

[244] Q. Wu, Y. Zhang, X. Yang, S.-L. Su, C. Shan, and K. Mølmer, "A superradiant maser with nitrogen-vacancy center spins," *Science China Physics, Mechanics & Astronomy*, vol. 65, no. 1, p. 217 311, 2021.

[245] Y. Zhang, C. Shan, and K. Mølmer, "Ultranarrow superradiant lasing by dark atom-photon dressed states," *Phys. Rev. Lett.*, vol. 126, p. 123 602, 12 2021.

[246] I. I. Rabi, "Space quantization in a gyrating magnetic field," *Phys. Rev.*, vol. 51, pp. 652–654, 8 1937.

[247] T. M. Stace, A. C. Doherty, and D. J. Reilly, "Dynamical steady states in driven quantum systems," *Phys. Rev. Lett.*, vol. 111, p. 180 602, 18 2013.

[248] J. Eisert, M. Friesdorf, and C. Gogolin, "Quantum many-body systems out of equilibrium," *Nature Physics*, vol. 11, no. 2, pp. 124–130, 2015.

[249] C. Weitenberg and J. Simonet, "Tailoring quantum gases by floquet engineering," *Nature Physics*, 2021.

[250] T. M. Stace, A. C. Doherty, and S. D. Barrett, "Population inversion of a driven two-level system in a structureless bath," *Phys. Rev. Lett.*, vol. 95, p. 106 801, 10 2005.

[251] K. I. Seetharam, C.-E. Bardyn, N. H. Lindner, M. S. Rudner, and G. Refael, "Controlled population of floquet-bloch states via coupling to bose and fermi baths," *Phys. Rev. X*, vol. 5, p. 041 050, 4 2015.

[252] J. Stehlik, Y.-Y. Liu, C. Eichler, T. R. Hartke, X. Mi, M. J. Gullans, J. M. Taylor, and J. R. Petta, "Double quantum dot floquet gain medium," *Phys. Rev. X*, vol. 6, p. 041 027, 4 2016.

[253] R. Desbuquois, M. Messer, F. Görg, K. Sandholzer, G. Jotzu, and T. Esslinger, "Controlling the floquet state population and observing micromotion in a periodically driven two-body quantum system," *Phys. Rev. A*, vol. 96, p. 053 602, 5 2017.

[254] Y. Zhang, E. Lötstedt, and K. Yamanouchi, "Population inversion in a strongly driven two-level system at far-off resonance," vol. 50, no. 18, p. 185 603, 2017.

[255] D. Hagenmüller and C. Ciuti, "Cavity qed of the graphene cyclotron transition," *Phys. Rev. Lett.*, vol. 109, p. 267 403, 26 2012.

[256] L. Chirolli, M. Polini, V. Giovannetti, and A. H. MacDonald, "Drude weight, cyclotron resonance, and the dicke model of graphene cavity qed," *Phys. Rev. Lett.*, vol. 109, p. 267 404, 26 2012.

[257] Y.-X. Zhang, Y. Zhang, and K. Mølmer, "Dicke phase transition in a disordered emitter–graphene-plasmon system," *Phys. Rev. A*, vol. 98, p. 033 821, 3 2018.

[258] J. I. Cirac and P. Zoller, "Quantum computations with cold trapped ions," *Phys. Rev. Lett.*, vol. 74, pp. 4091–4094, 20 1995.

[259] C. Monroe, D. M. Meekhof, B. E. King, W. M. Itano, and D. J. Wineland, "Demonstration of a fundamental quantum logic gate," *Phys. Rev. Lett.*, vol. 75, pp. 4714–4717, 25 1995.

[260] F. Schmidt-Kaler, H. Häffner, M. Riebe, S. Gulde, G. P. T. Lancaster, T. Deuschle, C. Becher, C. F. Roos, J. Eschner, and R. Blatt, "Realization of the cirac–zoller controlled-not quantum gate," *Nature*, vol. 422, no. 6930, pp. 408–411, 2003.

[261] S. Gulde, M. Riebe, G. P. T. Lancaster, C. Becher, J. Eschner, H. Häffner, F. Schmidt-Kaler, I. L. Chuang, and R. Blatt, "Implementation of the deutsch–jozsa algorithm on an ion-trap quantum computer," *Nature*, vol. 421, no. 6918, pp. 48–50, 2003.

[262] H. Häffner, C. Roos, and R. Blatt, "Quantum computing with trapped ions," *Physics Reports*, vol. 469, no. 4, pp. 155–203, 2008.

[263] C. D. Bruzewicz, J. Chiaverini, R. McConnell, and J. M. Sage, "Trapped-ion quantum computing: Progress and challenges," *Applied Physics Reviews*, vol. 6, no. 2, p. 021 314, 2019.

[264] Y. Nakamura, Y. A. Pashkin, and J. S. Tsai, "Coherent control of macroscopic quantum states in a single-cooper-pair box," *Nature*, vol. 398, no. 6730, pp. 786–788, 1999.

[265] A. Blais, R.-S. Huang, A. Wallraff, S. M. Girvin, and R. J. Schoelkopf, "Cavity quantum electrodynamics for superconducting electrical circuits: An architecture for quantum computation," *Phys. Rev. A*, vol. 69, p. 062 320, 6 2004.

[266] J. Koch, T. M. Yu, J. Gambetta, A. A. Houck, D. I. Schuster, J. Majer, A. Blais, M. H. Devoret, S. M. Girvin, and R. J. Schoelkopf, "Charge-insensitive qubit design derived from the cooper pair box," *Phys. Rev. A*, vol. 76, p. 042 319, 4 2007.

[267] G Wendin, "Quantum information processing with superconducting circuits: A review," *Reports on Progress in Physics*, vol. 80, no. 10, p. 106 001, 2017.

[268] M. Kjaergaard, M. E. Schwartz, J. Braumüller, P. Krantz, J. I.-J. Wang, S. Gustavsson, and W. D. Oliver, "Superconducting qubits: Current state of play," *Annual Review of Condensed Matter Physics*, vol. 11, no. 1, pp. 369–395, 2020.

[269] A. Blais, A. L. Grimsmo, S. M. Girvin, and A. Wallraff, "Circuit quantum electrodynamics," *Rev. Mod. Phys.*, vol. 93, p. 025 005, 2 2021.

[270] E. Knill, R. Laflamme, and G. J. Milburn, "A scheme for efficient quantum computation with linear optics," *Nature*, vol. 409, no. 6816, pp. 46–52, 2001.

[271] P. Kok, W. J. Munro, K. Nemoto, T. C. Ralph, J. P. Dowling, and G. J. Milburn, "Linear optical quantum computing with photonic qubits," *Rev. Mod. Phys.*, vol. 79, pp. 135–174, 1 2007.

[272] D. Loss and D. P. DiVincenzo, "Quantum computation with quantum dots," *Phys. Rev. A*, vol. 57, pp. 120–126, 1 1998.

[273] I. L. Chuang, N. Gershenfeld, and M. Kubinec, "Experimental implementation of fast quantum searching," *Phys. Rev. Lett.*, vol. 80, pp. 3408–3411, 15 1998.

[274] B. E. Kane, "A silicon-based nuclear spin quantum computer," *Nature*, vol. 393, no. 6681, pp. 133–137, 1998.

[275] L. Isenhower, E. Urban, X. L. Zhang, A. T. Gill, T. Henage, T. A. Johnson, T. G. Walker, and M. Saffman, "Demonstration of a neutral atom controlled-not quantum gate," *Phys. Rev. Lett.*, vol. 104, p. 010 503, 1 2010.

[276] M Saffman, "Quantum computing with atomic qubits and rydberg interactions: Progress and challenges," *Journal of Physics B: Atomic, Molecular and Optical Physics*, vol. 49, no. 20, p. 202 001, 2016.

[277] H. Levine *et al.*, "Parallel implementation of high-fidelity multiqubit gates with neutral atoms," *Phys. Rev. Lett.*, vol. 123, p. 170 503, 17 2019.

[278] D. Bluvstein *et al.*, "Logical quantum processor based on reconfigurable atom arrays," *Nature*, 2023.

[279] D. P. DiVincenzo, "The physical implementation of quantum computation," *Fortschritte der Physik*, vol. 48, no. 9-11, pp. 771–783, 2000. eprint: `https://onlinelibrary.wiley.com/doi/pdf/10.1002/1521-3978%28200009%2948%3A9/11%3C771%3A%3AAID-PROP771%3E3.0.CO%3B2-E`.

[280] D. Deutsch and R. Jozsa, "Rapid solution of problems by quantum computation," *Proceedings of the Royal Society of London. Series A: Mathematical and Physical Sciences*, vol. 439, no. 1907, pp. 553–558, 1992. eprint: `https://royalsocietypublishing.org/doi/pdf/10.1098/rspa.1992.0167`.

[281] L. K. Grover, "A fast quantum mechanical algorithm for database search," in *Proceedings of the Twenty-Eighth Annual ACM Symposium on Theory of Computing*, ser. STOC '96, Philadelphia, Pennsylvania, USA: Association for Computing Machinery, 1996, 212–219.

[282] P. W. Shor, "Polynomial-time algorithms for prime factorization and discrete logarithms on a quantum computer," *SIAM Journal on Computing*, vol. 26, no. 5, pp. 1484–1509, 1997. eprint: `https://doi.org/10.1137/S0097539795293172`.

[283] A. K. Ekert, "Quantum cryptography based on bell's theorem," *Phys. Rev. Lett.*, vol. 67, pp. 661–663, 6 1991.

[284] C. H. Bennett, G. Brassard, and N. D. Mermin, "Quantum cryptography without bell's theorem," *Phys. Rev. Lett.*, vol. 68, pp. 557–559, 5 1992.

[285] N. Gisin, G. Ribordy, W. Tittel, and H. Zbinden, "Quantum cryptography," *Rev. Mod. Phys.*, vol. 74, pp. 145–195, 1 2002.

[286] S. Pirandola *et al.*, "Advances in quantum cryptography," *Adv. Opt. Photon.*, vol. 12, no. 4, pp. 1012–1236, 2020.

[287] J. I. Cirac, P. Zoller, H. J. Kimble, and H. Mabuchi, "Quantum state transfer and entanglement distribution among distant nodes in a quantum network," *Phys. Rev. Lett.*, vol. 78, pp. 3221–3224, 16 1997.

[288] H. J. Kimble, "The quantum internet," *Nature*, vol. 453, no. 7198, pp. 1023–1030, 2008.

[289] P. W. Shor, "Scheme for reducing decoherence in quantum computer memory," *Phys. Rev. A*, vol. 52, R2493–R2496, 4 1995.

[290] A. Kitaev, "Fault-tolerant quantum computation by anyons," *Annals of Physics*, vol. 303, no. 1, pp. 2–30, 2003.

[291] R. Raussendorf and H. J. Briegel, "A one-way quantum computer," *Phys. Rev. Lett.*, vol. 86, pp. 5188–5191, 22 2001.

[292] H. J. Briegel, D. E. Browne, W. Dür, R. Raussendorf, and M. Van den Nest, "Measurement-based quantum computation," *Nature Physics*, vol. 5, no. 1, pp. 19–26, 2009.

[293] I. S. Maria Schuld and F. Petruccione, "An introduction to quantum machine learning," *Contemporary Physics*, vol. 56, no. 2, pp. 172–185, 2015. eprint: `https://doi.org/10.1080/00107514.2014.964942`.

[294] C. Ciliberto, M. Herbster, A. D. Ialongo, M. Pontil, A. Rocchetto, S. Severini, and L. Wossnig, "Quantum machine learning: A classical perspective," *Proceedings of the Royal Society A: Mathematical, Physical and Engineering Sciences*, vol. 474, no. 2209, p. 20170551, 2018. eprint: `https://royalsocietypublishing.org/doi/pdf/10.1098/rspa.2017.0551`.

[295] V. Dunjko and H. J. Briegel, "Machine learning & artificial intelligence in the quantum domain: A review of recent progress," *Reports on Progress in Physics*, vol. 81, no. 7, p. 074001, 2018.

[296] M. Cerezo, G. Verdon, H.-Y. Huang, L. Cincio, and P. J. Coles, "Challenges and opportunities in quantum machine learning," *Nature Computational Science*, vol. 2, no. 9, pp. 567–576, 2022.

[297] M. A. Nielsen and I. L. Chuang, *Quantum Computation and Quantum Information: 10th Anniversary Edition*. Cambridge University Press, 2010.

[298] J. Biamonte, P. Wittek, N. Pancotti, P. Rebentrost, N. Wiebe, and S. Lloyd, "Quantum machine learning," *Nature*, vol. 549, no. 7671, pp. 195–202, 2017.

[299] D. Wecker, M. B. Hastings, and M. Troyer, "Progress towards practical quantum variational algorithms," *Phys. Rev. A*, vol. 92, p. 042 303, 4 2015.

[300] M. Cerezo *et al.*, "Variational quantum algorithms," *Nature Reviews Physics*, vol. 3, no. 9, pp. 625–644, 2021.

[301] S. Lloyd, "Almost any quantum logic gate is universal," *Phys. Rev. Lett.*, vol. 75, pp. 346–349, 2 1995.

[302] V. Ramakrishna and H. Rabitz, "Relation between quantum computing and quantum controllability," *Phys. Rev. A*, vol. 54, pp. 1715–1716, 2 1996.

[303] S. G. Schirmer, H. Fu, and A. I. Solomon, "Complete controllability of quantum systems," *Phys. Rev. A*, vol. 63, p. 063 410, 6 2001.

[304] V. Dunjko, J. M. Taylor, and H. J. Briegel, "Quantum-enhanced machine learning," *Phys. Rev. Lett.*, vol. 117, p. 130 501, 13 2016.

[305] Z.-C. Yang, A. Rahmani, A. Shabani, H. Neven, and C. Chamon, "Optimizing variational quantum algorithms using pontryagin's minimum principle," *Phys. Rev. X*, vol. 7, p. 021 027, 2 2017.

[306] M. Y. Niu, S. Boixo, V. N. Smelyanskiy, and H. Neven, "Universal quantum control through deep reinforcement learning," *npj Quantum Information*, vol. 5, no. 1, p. 33, 2019.

[307] S. Khatri, R. LaRose, A. Poremba, L. Cincio, A. T. Sornborger, and P. J. Coles, "Quantum-assisted quantum compiling," *Quantum*, vol. 3, p. 140, 2019.

[308] J. Lee, W. J. Huggins, M. Head-Gordon, and K. B. Whaley, "Generalized unitary coupled cluster wave functions for quantum computation," *Journal of Chemical Theory and Computation*, vol. 15, no. 1, pp. 311–324, 2019.

[309] M. C. Caro, H.-Y. Huang, N. Ezzell, J. Gibbs, A. T. Sornborger, L. Cincio, P. J. Coles, and Z. Holmes, "Out-of-distribution generalization for learning quantum dynamics," *Nature Communications*, vol. 14, no. 1, p. 3751, 2023.

[310] A. Pérez-Salinas, R. Draškić, J. Tura, and V. Dunjko, *Reduce&chop: Shallow circuits for deeper problems*, 2023. arXiv: 2212.11862 [quant-ph].

[311] E. R. Anschuetz, *Critical points in quantum generative models*, 2023. arXiv: 2109.06957 [quant-ph].

[312] M. Schuld, I. Sinayskiy, and F. Petruccione, "The quest for a quantum neural network," *Quantum Information Processing*, vol. 13, no. 11, pp. 2567–2586, 2014.

[313] K. Mitarai, M. Negoro, M. Kitagawa, and K. Fujii, "Quantum circuit learning," *Phys. Rev. A*, vol. 98, p. 032 309, 3 2018.

[314] I. Cong, S. Choi, and M. D. Lukin, "Quantum convolutional neural networks," *Nature Physics*, vol. 15, no. 12, pp. 1273–1278, 2019.

[315] A. Abbas, D. Sutter, C. Zoufal, A. Lucchi, A. Figalli, and S. Woerner, "The power of quantum neural networks," *Nature Computational Science*, vol. 1, no. 6, pp. 403–409, 2021.

[316] J. Stokes, J. Izaac, N. Killoran, and G. Carleo, "Quantum Natural Gradient," *Quantum*, vol. 4, p. 269, 2020.

[317] K. Sharma, M. Cerezo, L. Cincio, and P. J. Coles, "Trainability of dissipative perceptron-based quantum neural networks," *Phys. Rev. Lett.*, vol. 128, p. 180 505, 18 2022.

[318] M Cerezo and P. J. Coles, "Higher order derivatives of quantum neural networks with barren plateaus," *Quantum Science and Technology*, vol. 6, no. 3, p. 035 006, 2021.

[319] E. Farhi, J. Goldstone, and S. Gutmann, "A quantum approximate optimization algorithm," 2014.

[320] L. Zhou, S.-T. Wang, S. Choi, H. Pichler, and M. D. Lukin, "Quantum approximate optimization algorithm: Performance, mechanism, and implementation on near-term devices," *Phys. Rev. X*, vol. 10, p. 021 067, 2 2020.

[321] S. Hadfield, Z. Wang, B. O'Gorman, E. G. Rieffel, D. Venturelli, and R. Biswas, "From the quantum approximate optimization algorithm to a quantum alternating operator ansatz," *Algorithms*, vol. 12, no. 2, 2019.

[322] M. E. S. Morales, J. D. Biamonte, and Z. Zimborás, "On the universality of the quantum approximate optimization algorithm," *Quantum Information Processing*, vol. 19, no. 9, p. 291, 2020.

[323] J. Preskill, "Quantum Computing in the NISQ era and beyond," *Quantum*, vol. 2, p. 79, 2018.

[324] J. R. McClean, J. Romero, R. Babbush, and A. Aspuru-Guzik, "The theory of variational hybrid quantum-classical algorithms," *New Journal of Physics*, vol. 18, no. 2, p. 023 023, 2016.

[325] M. Cerezo, A. Poremba, L. Cincio, and P. J. Coles, "Variational Quantum Fidelity Estimation," *Quantum*, vol. 4, p. 248, 2020.

[326] J. Biamonte, "Universal variational quantum computation," *Phys. Rev. A*, vol. 103, p. L030401, 3 2021.

[327] K. Bharti *et al.*, "Noisy intermediate-scale quantum algorithms," *Rev. Mod. Phys.*, vol. 94, p. 015 004, 1 2022.

[328] X. Bonet-Monroig, H. Wang, D. Vermetten, B. Senjean, C. Moussa, T. Bäck, V. Dunjko, and T. E. O'Brien, "Performance comparison of optimization methods on variational quantum algorithms," *Phys. Rev. A*, vol. 107, p. 032 407, 3 2023.

[329] M. Cramer, M. B. Plenio, S. T. Flammia, R. Somma, D. Gross, S. D. Bartlett, O. Landon-Cardinal, D. Poulin, and Y.-K. Liu, "Efficient quantum state tomography," *Nature Communications*, vol. 1, no. 1, p. 149, 2010.

[330] G. Tóth, W. Wieczorek, D. Gross, R. Krischek, C. Schwemmer, and H. Weinfurter, "Permutationally invariant quantum tomography," *Phys. Rev. Lett.*, vol. 105, p. 250 403, 25 2010.

[331] R. LaRose, A. Tikku, É. O'Neel-Judy, L. Cincio, and P. J. Coles, "Variational quantum state diagonalization," *npj Quantum Information*, vol. 5, no. 1, p. 57, 2019.

[332] M. Neugebauer, L. Fischer, A. Jäger, S. Czischek, S. Jochim, M. Weidemüller, and M. Gärttner, "Neural-network quantum state tomography in a two-qubit experiment," *Phys. Rev. A*, vol. 102, p. 042 604, 4 2020.

[333] R. Levy, D. Luo, and B. K. Clark, "Classical shadows for quantum process tomography on near-term quantum computers," *arXiv:2110.02965*, vol. preprint, 2021. arXiv: 2110.02965 [quant-ph].

[334] J. R. McClean, S. Boixo, V. N. Smelyanskiy, R. Babbush, and H. Neven, "Barren plateaus in quantum neural network training landscapes," *Nature Communications*, vol. 9, no. 1, p. 4812, 2018.

[335] D. P. Kingma and J. Ba, "Adam: A method for stochastic optimization," *CoRR*, vol. abs/1412.6980, 2015.

[336] F. G. S. L. Brandão, A. W. Harrow, and M. Horodecki, "Local random quantum circuits are approximate polynomial-designs," *Communications in Mathematical Physics*, vol. 346, no. 2, pp. 397–434, 2016.

[337] A. Arrasmith, Z. Holmes, M Cerezo, and P. J. Coles, "Equivalence of quantum barren plateaus to cost concentration and narrow gorges," *Quantum Science and Technology*, vol. 7, no. 4, p. 045 015, 2022.

[338] S. Wang, E. Fontana, M. Cerezo, K. Sharma, A. Sone, L. Cincio, and P. J. Coles, "Noise-induced barren plateaus in variational quantum algorithms," *Nature Communications*, vol. 12, no. 1, p. 6961, 2021.

[339] C. Zhao and X.-S. Gao, "Analyzing the barren plateau phenomenon in training quantum neural networks with the ZX-calculus," *Quantum*, vol. 5, p. 466, 2021.

[340] M. Larocca, P. Czarnik, K. Sharma, G. Muraleedharan, P. J. Coles, and M. Cerezo, "Diagnosing Barren Plateaus with Tools from Quantum Optimal Control," *Quantum*, vol. 6, p. 824, 2022.

[341] C. Ortiz Marrero, M. Kieferová, and N. Wiebe, "Entanglement-induced barren plateaus," *PRX Quantum*, vol. 2, p. 040 316, 4 2021.

[342] T. L. Patti, K. Najafi, X. Gao, and S. F. Yelin, "Entanglement devised barren plateau mitigation," *Phys. Rev. Research*, vol. 3, p. 033 090, 3 2021.

[343] E. R. Anschuetz and B. T. Kiani, "Quantum variational algorithms are swamped with traps," *Nature Communications*, vol. 13, no. 1, p. 7760, 2022.

[344] T. Volkoff and P. J. Coles, "Large gradients via correlation in random parameterized quantum circuits," *Quantum Science and Technology*, vol. 6, no. 2, p. 025 008, 2021.

[345] A. Pesah, M. Cerezo, S. Wang, T. Volkoff, A. T. Sornborger, and P. J. Coles, "Absence of barren plateaus in quantum convolutional neural networks," *Phys. Rev. X*, vol. 11, p. 041 011, 4 2021.

[346] C.-Y. Park and N. Killoran, *Hamiltonian variational ansatz without barren plateaus*, 2023. arXiv: 2302.08529 [quant-ph].

[347] Z. Holmes, K. Sharma, M. Cerezo, and P. J. Coles, "Connecting ansatz expressibility to gradient magnitudes and barren plateaus," *PRX Quantum*, vol. 3, p. 010 313, 1 2022.

[348] M. Cerezo, A. Sone, T. Volkoff, L. Cincio, and P. J. Coles, "Cost function dependent barren plateaus in shallow parametrized quantum circuits," *Nature Communications*, vol. 12, no. 1, p. 1791, 2021.

[349] A. V. Uvarov and J. D. Biamonte, "On barren plateaus and cost function locality in variational quantum algorithms," *Journal of Physics A: Mathematical and Theoretical*, vol. 54, no. 24, p. 245 301, 2021.

[350] A. B. Magann, C. Arenz, M. D. Grace, T.-S. Ho, R. L. Kosut, J. R. McClean, H. A. Rabitz, and M. Sarovar, "From pulses to circuits and back again: A quantum optimal control perspective on variational quantum algorithms," *PRX Quantum*, vol. 2, p. 010 101, 1 2021.

[351] A. Choquette, A. Di Paolo, P. K. Barkoutsos, D. Sénéchal, I. Tavernelli, and A. Blais, "Quantum-optimal-control-inspired ansatz for variational quantum algorithms," *Phys. Rev. Research*, vol. 3, p. 023 092, 2 2021.

[352] N. Khaneja, T. Reiss, C. Kehlet, T. Schulte-Herbrüggen, and S. J. Glaser, "Optimal control of coupled spin dynamics: Design of nmr pulse sequences by gradient ascent algorithms," *Journal of Magnetic Resonance*, vol. 172, no. 2, pp. 296–305, 2005.

[353] S. J. Glaser *et al.*, "Training schrödinger's cat: Quantum optimal control," *The European Physical Journal D*, vol. 69, no. 12, p. 279, 2015.

[354] S. Lloyd and S. Montangero, "Information theoretical analysis of quantum optimal control," *Phys. Rev. Lett.*, vol. 113, p. 010 502, 1 2014.

[355] J. Li, X. Yang, X. Peng, and C.-P. Sun, "Hybrid quantum-classical approach to quantum optimal control," *Phys. Rev. Lett.*, vol. 118, p. 150 503, 15 2017.

[356] C. P. Koch *et al.*, "Quantum optimal control in quantum technologies. strategic report on current status, visions and goals for research in europe," *EPJ Quantum Technology*, vol. 9, no. 1, p. 19, 2022.

[357] P. Doria, T. Calarco, and S. Montangero, "Optimal control technique for many-body quantum dynamics," *Phys. Rev. Lett.*, vol. 106, p. 190 501, 19 2011.

[358] T. Caneva, T. Calarco, and S. Montangero, "Chopped random-basis quantum optimization," *Phys. Rev. A*, vol. 84, p. 022 326, 2 2011.

[359] J. Scheuer *et al.*, "Precise qubit control beyond the rotating wave approximation," *New Journal of Physics*, vol. 16, no. 9, p. 093 022, 2014.

[360] S. Machnes, E. Assémat, D. Tannor, and F. K. Wilhelm, "Tunable, flexible, and efficient optimization of control pulses for practical qubits," *Phys. Rev. Lett.*, vol. 120, p. 150 401, 15 2018.

[361] M. Bukov, A. G. R. Day, D. Sels, P. Weinberg, A. Polkovnikov, and P. Mehta, "Reinforcement learning in different phases of quantum control," *Phys. Rev. X*, vol. 8, p. 031 086, 3 2018.

[362] J. Tian, H. Liu, Y. Liu, P. Yang, R. Betzholz, R. S. Said, F. Jelezko, and J. Cai, "Quantum optimal control using phase-modulated driving fields," *Phys. Rev. A*, vol. 102, p. 043 707, 4 2020.

[363] Y. Song, J. Li, Y.-J. Hai, Q. Guo, and X.-H. Deng, "Optimizing quantum control pulses with complex constraints and few variables through autodifferentiation," *Phys. Rev. A*, vol. 105, p. 012 616, 1 2022.

[364] D. Zax, G Goelman, and S Vega, "Amplitude-modulated composite pulses," *Journal of Magnetic Resonance (1969)*, vol. 80, no. 2, pp. 375–382, 1988.

[365] K. Kormann, S. Holmgren, and H. O. Karlsson, "A fourier-coefficient based solution of an optimal control problem in quantum chemistry," *Journal of Optimization Theory and Applications*, vol. 147, no. 3, pp. 491–506, 2010.

[366] N. Chen, L. Li, W. Huie, M. Zhao, I. Vetter, C. H. Greene, and J. P. Covey, "Analyzing the rydberg-based optical-metastable-ground architecture for $^{171}$Yb nuclear spins," *Phys. Rev. A*, vol. 105, p. 052 438, 5 2022.

[367] E. Urban, T. A. Johnson, T. Henage, L. Isenhower, D. D. Yavuz, T. G. Walker, and M. Saffman, "Observation of rydberg blockade between two atoms," *Nature Physics*, vol. 5, no. 2, pp. 110–114, 2009.

[368] V. L. Ginzburg and L. D. Landau, "On the Theory of superconductivity," *Zh. Eksp. Teor. Fiz.*, vol. 20, D. ter Haar, Ed., pp. 1064–1082, 1950.

[369] D. Pekker and C. Varma, "Amplitude/higgs modes in condensed matter physics," *Annual Review of Condensed Matter Physics*, vol. 6, no. 1, pp. 269–297, 2015. eprint: https://doi.org/10.1146/annurev-conmatphys-031214-014350.

[370] M. Faccioli and L. Salasnich, "Spontaneous symmetry breaking and higgs mode: Comparing gross-pitaevskii and nonlinear klein-gordon equations," *Symmetry*, vol. 10, no. 4, 2018.

# Eidesstattliche Versicherung

Hiermit versichere ich an Eides statt, die vorliegende Dissertationsschrift selbst verfasst und keine anderen als die angegebenen Hilfsmittel und Quellen benutzt zu haben.

Hamburg, den _19.12.23_

_____
Unterschrift des Doktoranden